Constraints upon the Cosmological Density Parameter from Tully-Fisher Observations of *IRAS* Galaxies

Thesis by Joshua Roth

In Partial Fulfillment of the Requirements

for the Degree of

Doctor of Philosophy

California Institute of Technology

1994

(defended 16 June 1993)

Acknowledgements

Caltech Professor Jeremy R. Mould served as thesis advisor to J. Roth throughout the years 1989 - 1993 during which the work described herein was performed. Additional scientific guidance was provided by Caltech professor S. Djorgovski and by Drs. Michael Strauss and Jefferey Willick. Ming-Sheng Han provided essential assistance with galaxy photometry and with discussions of Tully-Fisher experiments. Nicholas Weir patiently walked the author through a maze of statistical concepts. Discourse with E. Bertschinger, S. Courteau, M. Davis, A. Dekel, A. Dressler, R. Giovanelli, G. Helou, B. Madore, M. Pierce, R. Schommer and A. Szalay contributed to this thesis.

This project would have been impossible without the continuous assistance of Michael Strauss (the predictions of whose thesis it vainly seeks to test), and by the generous provision (before publication) of the *IRAS* '4KVL' sample and distance predictions for same by the *IRAS* redshift survey team of M. Davis, K. Fisher, J. Huchra, M. Strauss, and A. Yahil. Through them we acknowledge the Infrared Astronomical Satellite developed and operated by the United States National Aeronautics and Space Administration, the Netherlands Agency for Aerospace Programs, and the United Kingdom Science and Engineering Research Council.

We acknowledge the use of the Huchtmeier and Richter (1989) catalog of HI observations of galaxies in the work described below, and the use of the NASA Extragalactic Database provided by the Infrared Processing and Analysis Center. N. Suntzeff and I. Thompson are thanked for providing magnitudes and finding charts for new Landolt (1992) standard stars that played an essential role in calibrating our galaxy photometry. Thanks are due Don Mathewson for providing linewidth data from his Parkes survey on magnetic tape. Robinson Hall librarians Helen Knudsen and Anne Snyder are thanked for expert assistance with astronomical literature.

The Jodrell Bank MkIA, Parkes 64 m and Arecibo 300 m radio telescopes, and the Mount Palomar 60 inch, Cerro Tololo 36 inch and Cerro Tololo Schmidt optical telescopes all provided the author and his collaborators observing time with which to gather most of the data reported herein. The assistance provided by the staff at each observatory is gratefully acknowledged. Thanks are due Professor R. D. Davies for assistance at Jodrell Bank, Dr. L. Staveley-Smith for the same at Parkes, and Dr. R. Schommer for the same at Cerro Tololo.

Heavy use was made of software generously provided by several members of the research community for public use: the 'FIGARO' CCD image processing software of K. Shortridge and the Caltech astronomy department, the 'SFOTO' surface photometry package of Ming-Sheng Han, the 'GASP' program of M. Cawson, the 'IRAF' image processing software of the National Optical Observatories, the 'SLAP' spectral line reduction package of L. Staveley-Smith, the 'Numerical Recipes' of Press *et al.* (1986), the 'MONGO' graphics program of J. Tonry, and the 'PGPLOT' graphics program of T. Pearson. Typesetting made use of D. Knuth's 'TeX'. Computing was performed primarily with the Digital VAX cluster of the Caltech astronomy department and secondarily with Sun workstations at Caltech and at Cerro Tololo.

J. Roth enjoyed the support of a National Science Foundation Graduate Fellowship, of a Lewis A. Kingsley Fellowship, and from NSF grant AST 93-23646 to J. R. Mould. Travel for J. Roth to the Jodrell Bank and Parkes facilities was funded by the NRAO Unique Foreign Telescopes program. It is the author's sincere hope that the results of this work, although modest, may soon be shared with the generous taxpayers of the United States who, despite the turbulent social and economic state of our nation, continue to support basic scientific research.

Thanks are due the candidacy committee members T. de Zeeuw, A. Dressler, J. R. Mould, J. B. Oke, and A. C. Readhead, and the thesis defense committee of S. Djorgovski, P. Goldreich, B. F. Madore, J. R. Mould, and W. L. W. Sargent for their attention and patience.

Study at Caltech has provided a fulfilling diversity of friendship and experience. I particularly wish to thank the Caltech 'Y' for promoting community service, and the Caltech (Shotokan) Karate Club and 'IMPACT' self defense community for the gentle care with which they share their art.

Thanks (and another Friday night talk) are due the members of the Santa Monica Amateur Astronomy Club for rekindling my interest in the stars, and for their unwavering support throughout my research career.

I thank and embrace my friends Joel, Robin and Jeff for their help during the deepest challenges of my adult life.

To my family – Rachel, David, Helen, and Amil – I dedicate this work.

in loving memory

Helen Roth

(born Helen Adler; New York, N.Y.)

1937 - 1992

Abstract

Mapping galaxy peculiar velocities, or departures from the uniform expansion of the universe, on megaparsec scales promises to indicate whether number density fluctuations in galaxy counts trace density fluctuations in the underlying matter (to within some factor b), and, if so, to constrain the cosmological density parameter Ω, which dictates whether space will expand forever or one day collapse. To sample the peculiar velocity field to distances approaching that of the Hydra-Centaurus complex (but in all directions) we have extracted an all sky, quasi volume limited sample to 4000 km sec^{-1} from the 1.9 Jy 60 micron *IRAS* redshift survey of Michael Strauss and collaborators. These objects enjoy distance predictions as functions of $\beta \equiv \Omega^{0.6}/b$ derived from iterative correction of their redshifts for mutual peculiar gravity, which scales with β. Our volume limited sample most efficiently probes the cosmic flowfield and enjoys objective and uniform selection criteria whose effects upon inferred quantities can be probed with simulations.

We have sought to measure relative distances to the 251 objects in this sample judged *a priori* suitable for use in the Tully-Fisher (luminosity - linewidth) relation. The requisite neutral hydrogen radio spectra and near infrared CCD photometry have been obtained for about one half of these objects. Methods of reducing the radio and CCD data are explained in detail. Isophotal I band magnitudes are reproduced by independent observations to ~ 0.05 magnitudes precision. Errors and biases in neutral hydrogen linewidths at low signal to noise ratio are quantified.

The I band magnitude and 21 cm. linewidth data imply a Tully-Fisher (TF) relation at each value of β from 0.05 to 2.00 used by Strauss *et al.* to iterate the *IRAS* redshift catalog. The β value producing minimum apparent TF scatter is investigated as a diagnostic with extensive Monte Carlo simulations. Such simulations suggest that, if the β knob setting producing minimum apparent TF scatter were found to equal unity, ~ 100 galaxy distance moduli to ~ 0.5 magnitudes precision would constrain the actual value of β to lie within the range $0.7 \lesssim \beta \lesssim 1.3$ at a $\sim 95\%$ confidence level.

'β response profiles' (apparent TF scatter versus β) observed in various subsets of our provisional database are presented. Our provisional database yields minimum apparent TF scatter at a β value of ~ 0.9. Excising the apparently problematic Virgo cluster region yields a response profile favoring β values of $\sim 0.6 \pm 0.2$, or $\Omega \sim 0.4 \pm 0.3$. Excising data points disfavored by statistical estimates of leverage upon β likewise favors low values of $\beta \sim 0.5$. Limitations to our current data analysis which preclude our asserting strong constraints upon the density parameter at present are discussed in detail.

Table of Contents

Copyright — ii
Acknowledgements — iii
Abstract — vii
Table of contents — ix

— **Chapter 1** —

The Cosmological Density Parameter and Peculiar Velocities

Section I: Ω and cosmological models — 1-1
Section II: Ω and peculiar velocities — 1-5
Section III: Extant peculiar velocity surveys — 1-9
Section IV: The *IRAS* 60μ 2 Jy redshift survey and the 4KVL sample — 1-13
Section V: Thesis outline — 1-15
Tables — 1-17
Figures — 1-24

— **Chapter 2** —

Photometric Observations and Reductions

Section I: Introduction — 2-1
Section II: Bias and overscan correction — 2-4
Section III: Flatfielding — 2-5
Section IV: Aperture photometry of standard stars — 2-7
Section V: Extinction and photometric transformation coefficient determination — 2-12
Section VI: Galaxy surface photometry — 2-15
Section VII: Repeatability of photometric results — 2-22
Tables — 2-26
Figures — 2-43

— **Chapter 3** —

Corrections to Photometric Quantities

Section I: Introduction — 3-1
Section II: Cosmological corrections — 3-1
Section III: Galactic absorption corrections — 3-3
Section IV: Internal absorption and reddening correction — 3-5
Tables — 3-11
Figures — 3-21

— Chapter 4 —

HI Observations of *IRAS* 4KVL Objects from Jodrell Bank

Section I: Introduction — 4-1
Section II: 21 cm. observations — 4-1
Section III: Flux scale definition and constancy — 4-3
Section IV: Program object reduction — 4-4
Section V: Data presentation — 4-6
Section VI: Monte Carlo perturbation of high S/N spectra with radiometer noise — 4-7
Tables — 4-10
Figures — 4-14

— Chapter 5 —

HI Observations of *IRAS* 4KVL Objects at Parkes

Section I: Observations — 5-1
Section II: Data reduction — 5-2
Section III: Flux scale consistency — 5-4
Section IV: Repeatability of spectral line parameters — 5-5
Tables — 5-7
Figures — 5-10

— Chapter 6 —

Monte Carlo Models of the *IRAS* 4KVL Tully-Fisher Experiment

Section I: Introduction — 6-1
Section II: Properties of *IRAS* Model Predictions — 6-2
Section III: Monte Carlo generation of synthetic datasets — 6-6
Section IV: Distributions of inferred Tully-Fisher relation properties — 6-15
Section V: Bayes' theorem and confidence limits on X_{true} — 6-18
Section VI: Conclusions and caveats — 6-21
Tables — 6-28
Figures — 6-32

— Chapter 7 —

Analysis of Current *IRAS* 4KVL Tully-Fisher Dataset

Section I: Introduction — 7-1
Section II: External HI sources and JAN93 sample definition — 7-1
Section III: *IRAS* model distances and JAN93 Tully-Fisher properties — 7-3
Section IV: Comments - Conclusions - Caveats — 7-18
Tables — 7-25
Figures — 7-37

References — R-1

Let me make one thing clear: this theory that the universe, after having reached an extremity of rarefaction, will be condensed again has never convinced me. And yet many of us are counting on that, continually making plans for the time when we'll all be back there again.

Qwfwq, in

Cosmicomics (Le cosmicomiche) – Italo Calvino – 1965

Chapter 1: The Cosmological Density Parameter and Peculiar Velocities

This thesis attempts to set bounds upon the cosmological density parameter Ω by measuring gravitational distortions upon the uniform expansion of the universe (on $\sim$ 10 Mpc scales) and comparing these to predictions based on the assumption that galaxies reflect the distribution of the matter generating those distortions (as well as providing 'test particles' with which to measure them). In this introductory chapter we briefly review some properties of cosmological models and observational limits on some parameters of those models. We then discuss the specific models motivating this thesis and the method used to select our study sample. We close the chapter with an outline of the main text.

I. Ω and Cosmological Models

We begin by reviewing the conceptual framework in which the density parameter Ω is defined.

Motivated by special relativity, we describe 'spacetime' separation between events by a metric element

$$ds^2 = c^2dt^2 - dl^2 \qquad (1-1)$$

whose 'spacelike' component

$$dl^2 = R^2(t)[dr^2(1-kr^2)^{-1} + r^2d\omega^2], \qquad (1-2)$$

$$d\omega^2 = d\theta^2 + sin^2(\theta)d\psi^2, \qquad (1-3)$$

is the physical (*e.g.*, megaparsecs) separation between two points on a coordinate grid with radial coordinate r and angular coordinates θ, ψ. The time varying scale factor $R(t)$ converts from 'tic marks' on the 'comoving' coordinate grid (r, θ, ψ) to physical units. The curvature term k takes values of +1, -1 or 0; this reflects the 'spherelike', 'saddlelike' or 'flat' nature of space.

If the scale factor $R(t)$ is increasing with time, then an observer at any point on the comoving grid will see other points on that grid receding at a rate proportional to its distance from said observer. Thus the observation that nearly all 'extragalactic nebulae' show shifts of spectral features towards wavelengths redder than laboratory values by amounts implying recession velocities in apparent proportion to galaxy distances (Hubble, 1929) need not invalidate the Copernican prejudice that we do not live at a central point in the universe.

General relativity provides predictions for the dynamical evolution of the scale factor $R(t)$. Their exposition is given by Weinberg (1972) and Lawden (1982), among others. A heuristic 'Newtonian' thought experiment leads to similar results, excellent development of which is given by Harrison (1981). A test particle is placed at the edge of a sphere drawn around some portion of space sufficiently large so that the outside surroundings appear isotropic to some degree. Let the sphere's radius be $l = Rr$ and the interior matter have density $\rho(t)$. The gravitational acceleration upon the test particle by the matter interior to l is given by

$$d^2R(t)/dt^2 = -(4/3)\pi G\rho R \qquad (1-4)$$

where G is Newton's gravitational constant. For 'ordinary matter' the equation of state $\rho(t) = \rho_0 R_0^3 R_0^{-3}(t)$ (where subscript '0' denotes the present epoch) allows the integration of (1-4) to

$$(dR(t)/dt)^2 = (8/3)\pi G\rho R^2(t) - kc^2 \qquad (1-5)$$

where the speed of light c accompanies a dimensionless integration constant k equivalent to that in the metric (1-2) above. The history of Eqns. 1-4, 1-5 and properties of their solutions are thoroughly described by Felten and Isaacman (1986).

If in addition to 'ordinary matter' a mass-energy density associated with 'empty' space or 'vacuum' is posited to exist, Eqn. (1-4) becomes

$$(dR(t)/dt)^2 = 8/3\pi G\rho R^2(t) - kc^2 + (\Lambda/3)R^2(t) \qquad (1-6)$$

where Λ is referred to as the *cosmological constant* describing a 'vacuum energy density' $\rho_{vac} = \Lambda/(4\pi G)$ (Carroll, Press and Turner 1992).

Defining a 'curvature' $K \equiv kR^{-2}$, a 'Hubble parameter' $H \equiv 1/R(t) \times dR(t)/dt$ and a 'deceleration parameter' $q \equiv -\, d^2R(t)/dt^2 \times R(t) \times (dR(t)/dt)^{-2}$ allows equations (1-4) and (1-6) to be recast as

$$c^2K = 4\pi G\rho - H^2(q+1), \tag{1-7}$$

$$\Lambda = 4\pi G\rho - 3H^2q. \tag{1-8}$$

We see from Eqn. 1-8 that when Λ is zero, a proportional relationship between q and density results; when Λ dominates the energy density, on the other hand, Eqn. 1-6 integrates to exponential expansion: $R(t) \propto exp[(\Lambda/3)^{1/2}t]$. Although Λ was introduced to provide stationary (if unstable) solutions to Eqn. 1-3, it most recently has been invoked to describe the 'inflationary' epoch in the early history of the universe (*cf.* Kolb and Turner 1990). Only when $\Lambda = 0$ is the correspondence between density and curvature as simple as asserted in most popular expositions of the subject.

The Hubble parameter is currently believed to lie within the range 50 to 100 km sec^{-1} Mpc^{-1}; individual estimates generally differ by amounts greater than their stated uncertainties. For the simple $q_0 = 0.5$, $\Lambda = 0$ models, such Hubble parameters imply ages for the universe of $\sim$ 7 to 13 billion years. Galaxy count studies do not strongly constrain q but are consistent with $q = 0.5$ (Loh and Spillar 1986). Gravitational lens statistics promise to place strong upper limits upon Λ that might preclude its playing a significant role in the post-inflationary universe (Carroll, Press and Turner 1992). Because nonzero Λ allow flat space to be reconciled with a purely baryonic universe, and because they allow the high H_0 universes apparently favored by recent Tully-Fisher work to accomodate $\gtrsim$ 13 billion year globular star cluster ages, nonzero Λ models still enjoy serious consideration despite the lack of a compelling physical model for a current vacuum energy density of the requisite magnitude.

Models with $\Lambda = 0$ and $q > 0$ correspond to an expanding universe of ordinary matter whose expansion is slowing as the kinetic energy thereof fights against the mutual gravitational attraction of its contents. At a given time t, a critical density

$$\rho_{crit}(t) \equiv 3H^2(t)/(8\pi G) \qquad (1-9)$$

exists such that, should the actual density $\rho(t)$ at time t exceed $\rho_{crit}(t)$, the scale factor $R(t)$ will reach a maximum value at some finite time t, and thereafter contract. If we take the Hubble parameter H_0 to be 50 km sec^{-1} Mpc^{-1}, the present critical value for the cosmic density amounts to $\rho_{crit} \sim 5 \times 10^{-27}$ kg m^{-3}, equivalent to a few hydrogen atoms per cubic meter. If we define

$$\Omega(t) \equiv \rho(t)/\rho_{crit}(t) \qquad (1-10)$$

as the *cosmological density parameter*, we find that $\Omega = 2q$ when $\Lambda = 0$. Ω values of $> 1, 1, < 1$ then correspond to positively curved, flat, and negatively curved comoving coordinate systems, respectively. $\Omega > 1$ universes are those which suffer an eventual contraction. When $\Omega = 1$, the scale factor evolves as $R(t) \propto t^{2/3}$, and the time since the 'Big Bang' is simply given as $2/(3H_0)$.

The correspondence of Ω with qualitatively different futures for our universe provides some incentive for its measurement. Another incentive derives from the 'inflationary' theory, which predicts that space should currently appear flat on scales like that of the lookback time times c. This is equivalent to predicting unit Ω (*if* Λ is zero). Gravitational evolution is expected to relate the (recently quantified) small (angular) scale microwave background radiation (hereafter MBR) anisotropies (Smoot *et al.* 1992) to large-scale features in the current galaxy distribution; the efficiency at which gravity can 'amplify' the initial density variations reflected in the MBR fluctuations depends on Ω (*cf.* Kolb and Turner 1990), with low values believed unable to generate the current galaxy clustering. Finally, nucleosynthesis arguments appear to limit the cosmic density of baryonic matter to $\lesssim 0.2$ of the critical value; thus a dynamical measurement of $\Omega \sim 1$ would strengthen

the case for the nonbaryonic matter whose detection with solid-state detectors is an area of current research.

II. Ω and Peculiar Velocities

We have alluded to a 'dynamical' measurement of Ω; here we follow Gunn (1978) in motivating such a measurement.

We return to our test particle, now placed on the edge of a sphere of radius l drawn around some region of space enjoying higher matter density than the universal mean $\overline{\rho}$. The *net* gravitational acceleration upon the particle induced by the excess mass $\Delta M = (4/3)\pi\Delta\rho l^3$ is given by

$$\Delta g = -(4/3)\pi G\Delta\rho l. \qquad (1-11)$$

Acting for a time Δt, this acceleration changes the particle's velocity by an amount

$$\Delta v = -(4/3)f\pi G\Delta\rho l\Delta t, \qquad (1-12)$$

where f is the inevitable 'fudge factor' of order unity. Substituting the relations between Ω and the mean density $\overline{\rho}$, and that between the critical ρ_{crit} and the Hubble parameter, we find the fractional perturbation upon the Hubble flow at the edge of a sphere enclosing overdensity $\Delta\rho = \rho - \overline{\rho}$ to be

$$(\Delta v/H_0 l) = (f/2)\ \Omega\ (\Delta\rho/\overline{\rho})\ \Delta t\ H_0. \qquad (1-13)$$

As universes with higher Ω_0 (given a fixed Hubble parameter value H_0) are younger, they offer less time for such forces to act and we expect $\Delta v/H_0 l$ to be proportional to some power of Ω less than unity. Furthermore, the overdensity $\Delta\rho/\overline{\rho}$ relative to the mean is enhanced as the universe continues to expand; this suggests an even lower power of Ω will suffice to generate a given $\Delta v/H_0 l$.

The result stemming from perturbation theory that describes the net fractional deceleration as a function of present fractional overdensity is:

$$\Delta v/v_{Hub} \sim (1/3)\ (\Omega^{0.6})\ (\Delta\rho/\overline{\rho}) \qquad (1-14)$$

(*cf.* Kolb and Turner 1990), where $v_{Hub} \equiv H_0 l$ denotes the velocity at which the particle would expand from the center of the sphere if matter between it and that point enjoyed exactly the average cosmic density. The difference between the expected average expansion rate between two points and the actual value is referred to as a *peculiar velocity.*

Thus to constrain the cosmic density parameter we need to measure the fractional deceleration $\Delta v/v_{Hub}$ at the edge of one or more volumes containing overdense regions, and the mass overdensity $\Delta\rho/\overline{\rho}$ contained within them.

We note that elaborations of Eqn 1-14 for nonlinear dynamics have been developed by Villumsen and Davis (1986) and by Gramann (1992), among others. Given the spatial smoothing required for peculiar velocity measurements (which individually suffer from less than unity signal to noise ratio), and the severe biases in effect when 'test particles' sampling the velocity field are strongly clustered), nonlinear extensions of Eqn. 1-14 are unlikely to be profitably exploited with the distance indicators of several tenths of magnitudes' precision upon which the bulk of extant peculiar velocity results is based.

We first discuss $\Delta\rho/\overline{\rho}$. Although for over half a century the relative velocities of galaxies in clusters have been known to exceed what we would expect the galaxies to generate by their own mutual gravity (Zwicky 1933; Smith 1936), we may still posit that regions more populous in galaxies also enjoy higher underlying 'dark' matter density. Thus, if the galaxy number density is n_{gal}, we might expect

$$\Delta\rho/\overline{\rho} = \Delta n_{gal}/\overline{n}_{gal}. \qquad (1-15)$$

If the process that makes galaxies operates with an efficiency that itself varies with mass density, we might generalize Eqn 1-15 to

$$\Delta\rho/\overline{\rho} = b_{gal}\ (\Delta n_{gal}/\overline{n}_{gal}), \qquad (1-16)$$

where the galaxy - mass density contrast ratio b_{gal} (regrettably known in the literature as the 'bias' factor; Kaiser 1984) exceeds unity if galaxies are made more efficiently in denser regions, and vice versa. Eqn. 1-14 can now be rewritten as

$$\Delta v/v_{Hub} \sim (1/3)\ (\Omega^{0.6}/b_{gal})\ (\Delta n_{gal}/\overline{n}_{gal}). \qquad (1-17)$$

A crucial degeneracy is illuminated by this equation: without independent constraint upon b_{gal}, Ω cannot be uniquely determined. Thus in what follows we use the parameter

$$\beta \equiv \Omega^{0.6}/b_{gal}, \qquad (1-18)$$

which scales galaxy number overdensity to fractional deceleration, to distinguish competing models.

Redshift surveys (*e.g.*, Davis *et al.* 1982; Strauss 1989, hereafter ST) exploit the proportionality of recession velocity to distance expected in an expanding frame to map (relative) galaxy distances, and hence to identify regions of high, low and average galaxy number density. Either in their raw state, or after self consistent correction for expected peculiar velocities (*e.g.*, Yahil *et al.* 1991), such surveys may be used to estimate $\Delta n_{gal}/\overline{n}_{gal}$.

Given a catalog of galaxies with redshifts, the net gravity on a test particle at a given point in space may be assessed by equating the density with a delta function at the position of each catalog member, weighting each member for the fraction of the intrinsic population below the catalog inclusion thresholds at the member's distance, and adding terms like 1-17 produced by each member vectorially.

To assess the fractional deceleration $\Delta v/v_{Hub}$ one generally exploits a 'standard candle' or 'standard ruler' property of tracer galaxies to obtain their distances relative to others in a sample, or relative to a reference system such as the Coma cluster. This can yield an estimate of v_{Hub}, the tracer's expected 'uniform density' recession velocity. The peculiar velocity,

$$v_{pec} = cz - v_{Hub} \qquad (1-19)$$

takes a value that depends upon the reference frame from which recession velocity cz (hereafter loosely called 'redshift') is measured. We note that only the component of v_{pec} that lies along our line of sight is reflected in differences 1-19.

Perhaps the most straightforward determinations of v_{Hub} derive from obtaining the distance modulus in magnitude units $\delta M_j^{cal} = m_j - m_{cal}$ of galaxy j from a calibrating system like the Coma cluster whose peculiar velocity is believed to be no more than a small fraction of its redshift cz_{cal}. v_{pec} then follows from:

$$v_{pec_j} = cz_j - cz_{cal} \times 10^{0.2\delta M_j^{cal}}. \qquad (1-20)$$

Such methods are called 'direct peculiar velocity mapping' in the present text, 'Method 1' in several previous studies (*e.g.*, Aaronson *et al.* 1982; Faber and Burstein 1988), and the 'inferred distance' problem by Willick (1992, hereafter WT; 1993).

Less direct methods use some parameterized model for the velocity field predicting the peculiar velocity of objects at given distance d_j, right ascension α_j, and declination δ_j, or inverting such predictions to predict the distance d_j of object j at α_j, δ_j exhibiting redshift cz_j. The models' parameter 'knobs' are then adjusted until some measure of predicted distance ratios d_i/d_j between galaxies in all possible pairs i, j most closely matches that implied by observed relative distance moduli $m_i - m_j$:

$$d_i/d_j = 10^{0.4(m_i - m_j)}. \qquad (1-21)$$

Such methods are referred to here as 'indirect peculiar velocity mapping' or 'flowfield model fitting', as 'Method 2' or 'Schechter's (1980) method' by previous workers, and the 'calibration' problem by Willick (WT; 1993). We will use only this latter approach in the present study, with a single parameter 'knob' for β (equation 1-18) free for 'tuning' to data.

III. Extant Peculiar Velocity Studies

The study of galaxy peculiar velocities has mushroomed since the pioneering work of Rubin *et al.* (1976) to consume a substantial fraction of the time on major optical and radio facilities. Progress reports on most major developments in the field can be found in two conference proceedings volumes: that of the 1986 A.S.P. Conference on Galaxy Distances and Deviations from Uniform Expansion (Madore and Tully 1986) and of the 1988 Vatican Observatory Study Week on Large-Scale Motions in the Universe (Rubin and Coyne 1988). We will provide only the most skeletal notes here, as much of the preliminary developments are likely to be eclipsed by work currently in progress.

Since the discovery of a dipolar asymmetry in the apparent temperature of the cosmic microwave background radiation (MBR), we presume we know the net motion of the solar neighborhood with respect to the comoving frame (an apparently anti-Copernican state of affairs). Some component of this motion we attribute to our neighborhood's rotation about the center of the Milky Way and to motion normal to its plane. Some further originates from our Galaxy's largely binary motion with respect to the mass center of the Local Group. Further components are presumed to result from linear superposition of peculiar gravity arising from local asymmetries in the galaxy distribution and 'infall' into the Virgo cluster and other attracting overdense regions. We note that 'infall', or positive peculiar velocity, towards an overdense region does not imply that a test particle is losing absolute distance from that region; space continues to expand between them, only not as fast as it would if the underlying density were uniform at the cosmic mean value.

Models for the peculiar velocity field fall into two classes: those that ascribe perturbations to the Hubble expansion to one or a few discrete entities (*e.g.*, the Virgo cluster, the 'Great Attractor'), and those that assume some extragalactic objects delineated with uniform selection criteria trace mass density fluctuations $\Delta\rho/\overline{\rho}$ within some range of spatial scales. Early studies belonged principally to the first class; the present study, to the second.

The bulk of distance moduli used in the peculiar velocity literature to date derive from distance indicators that seem to rely on some constancy or simple scaling behavior of galaxy mass to light (M/L) ratios and something like the virial theorem relating the internal motions of galaxies' contents to the galaxy's mass (Djorgovski, de Carvalho and Han 1989). For elliptical galaxies, the 'Faber-Jackson' (Faber and Jackson 1976) and the related $D_n - \sigma$, or diameter - velocity dispersion (Djorgovski and Davis 1987; Dressler *et al.* 1987) relations appear to provide relative distance moduli to $\sim$ 0.4 magnitudes accuracy. For spiral galaxies, the 'Tully-Fisher', or luminosity - linewidth relation (Tully and Fisher 1977), when implimented with high-quality CCD measurements (*e.g.*, Han 1991; hereafter HT; Willick WT; Courteau 1992, hereafter CT), appears to provide relative distance moduli to $\sim$ 0.3 magnitudes accuracy. Both the $D_n - \sigma$ and Tully - Fisher (hereafter, TF) methods require measurement of galaxy apparent magnitude m and some measure of internal velocity amplitude w (whether from coherent rotation of spiral disks or from isotropic stellar velocities within ellipticals). Should the M/L ratios that 'zero' these relations vary systematically with ambient matter or galaxy density, application of Eqn. 1-20 could mimic the dynamical action of large β in a universe without nonbaryonic matter (Silk 1989). Only highly accurate distance indicators based on completely different physics (*e.g.*, supernovae - Branch 1992; surface brightness fluctuations - Tonry and Schneider 1988) offer robust alternatives to this disquieting possibility.

Scatter in relative distance moduli of $\sim$ 0.3 magnitudes results in $\sim$ 15% distance errors; at a redshift of 4000 km sec^{-1} , this translates to 600 km sec^{-1} spurious peculiar velocity. This is comparable to the Local Group's peculiar velocity as inferred from the MBR dipole. Thus peculiar

velocity measurements at distances like those of the Hydra-Centaurus and Perseus-Pisces superclusters typically enjoy a signal to noise ratio less than unity.

Application of the TF and $D_n - \sigma$ relations to field and cluster galaxies have detected the retardation of universal expansion by the Virgo cluster (Schecter 1980; Aaronson *et al.* 1982; Han and Mould 1990), the reflection of the Local Group motion inferred from the microwave background dipole in the peculiar velocities of distant clusters (Aaronson *et al.* 1986), and large ($\sim$ 500 km sec^{-1}) streaming motions on $\sim$ 50 Mpc scales (Lynden-Bell *et al.* 1988; Dressler and Faber 1990; Mould *et al.* 1991; Mathewson, Ford and Buchhorn 1992) that may originate in part from the Hydra-Centaurus / 'Great Attractor' complex in the southern sky and in part from the relatively unpopulated void between us and the Perseus - Pisces system on the other side of the sky.

Biases, or systematic departures of model parameters inferred from observational data from their actual values, have plagued the field since its inception. Worse perhaps than these biases is the confusion surrounding their nomenclature (the name of Malmquist inevitably being invoked, even when effects more nearly parallel those described by Lutz and Kelker 1973), the conditions under which they apply, and the procedures which are claimed to render one immune to their effects. The subject has perhaps been best elucidated by Willick in his Ph. D. thesis and derivative papers (WT; Willick 1993). An orthogonal view of pitfalls that may arise from covariant residuals from distance indicator relations has been offered by Gould (1993). Past 'bias' problems that may have led to substantial misinterpretation of peculiar velocity data include (a) incomplete sky coverage skewing bulk flow direction in the Rubin *et al.* 1976 (James, Joseph and Collins 1991) and Aaronson *et al.* (1986) studies (Willick, pers. comm.), (b) asymmetric scattering of tracers from overdense regions mimicing or enhancing 'infall' towards overdense regions (*e.g.*, Faber and Burstein 1988; WT; Roth 1991; Landy and Szalay 1992), which may be responsible for the 'detection' of 'backside infall' towards the 'Great Attractor', and (c) sample selection limits or detection thresholds applied to quantities correlated with distance indicator residuals (*e.g.*, Mould *et al.* 1991), which can lead to

spurious inferred peculiar velocities. In the present study we perform Monte Carlo simulations to identify which of several 'nuisance parameters' affecting our experiment may systematically skew the β best fitting our data from the true value, and found that one ritual often blindly performed (that of minimizing linewidth residuals) yields biased estimates of β. In performing simulations particular to our sample selection, observations and analysis we follow the lead of Staveley-Smith and Davies (1989), of Han and Mould (1990) and of Han (HT).

The physically most compelling approach to peculiar velocity data in the literature to date (once one accepts the paradigm of universal distance indicators!) is that developed by Bertschinger and Dekel (1989). Known as 'POTENT', their method exploits the curl-free nature of forces derived from potentials to reconstruct the unobservable tangential peculiar velocity components. (The radial components are those provided by traditional 'method 1' analyses of TF and $D_n - \sigma$ data.) The flowfield is then integrated to map the underlying density. Comparison of this density field with that derived from iterative correction of the *IRAS* redshift survey for peculiar gravity then addresses the questions: (a) does mass trace light (more truthfully, do *IRAS* galaxy number density fluctuations reflect those in the underlying mass field)?, and (b) for which value of β do the *IRAS* density maps best match that provided by 'POTENT'? The most recent application of 'POTENT' to extant peculiar velocity data (Dekel *et al.* 1993) provides 95% confidence limits on β of $1.26^{+0.75}_{-0.59}$. Since 'POTENT' uses 'method 1' peculiar velocities as input, β can be augmented by perhaps one or two tenths by the 'enhanced infall' effect (regrettably called 'inhomogeneous Malmquist bias' in most of the literature). Another complication to the 'POTENT' / *IRAS* procedure is the heavy and asymmetric smoothing that must be applied to the peculiar velocity data.

The method used in the present study amounts to a 'method 2' complement to 'POTENT'. We assess no peculiar velocities directly. Rather, we use the distance predictions offered by the *IRAS* mass maps for each of our objects to convert apparent to (inferred) absolute magnitude, and plot the latter versus log linewidth. The value of β that minimizes the scatter of this inferred TF

relation is then taken as the statistic of interest, and the run of TF scatter versus β (hereafter called the 'response profile') provides a diagnostic whose behavior is extensively explored with Monte Carlo simulations.

IV. The *IRAS* 60μ 2 Jy Redshift Survey and the 4KVL Sample

The uniform response of the far infrared detectors aboard the *IRAS* satellite and the nearly complete sky coverage of its observations allowed Michael Strauss and his collaborators (Marc Davis, John Huchra, Amos Yahil and Karl Fisher among others) to extract a flux limited catalog of point sources whose 'colors' (flux ratios in various far infrared bands) matched those expected for galaxies. Redshifts were obtained for these objects to make a uniform map of the local universe. Strauss's thesis sample resulted in over 2500 galaxy redshifts for objects with 60μ fluxes above 1.9 Janskys (Strauss 1989, hereafter ST; Strauss *et al.* 1992). Karl Fisher (1992; hereafter FT) extended the program, obtaining redshifts for galaxies with 60μ fluxes down to 1.2 Janskys.

Iterative calculation of these objects' gravity upon one another, followed by redshifts' correction for peculiar velocities induced thereby, has yielded distance estimates for these objects. The method is outlined and properties of their results briefly discussed in Chapter 6 (section II) below. In 1989 J. R. Mould and I decided to test the predictions for the 1.9 Jy object distances by extracting a subsample for which Tully-Fisher distance moduli might be obtainable. Michael Strauss and his collaborators provided us with a list of 440 objects satisfying the criteria:

$$F_{60_\mu} > 1.9\ Jy\ \times\ (4000/cz_{LG})^2, \qquad (1-22)$$

OR

$$F_{60_\mu} > 1.9\ Jy\ \times\ (4000/cz_{MB})^2, \qquad (1-23)$$

where cz_{LG}, cz_{MB} are object redshifts (in km sec^{-1}) in the Local Group and Microwave Background 'rest frames', respectively. Our goal was to create a nominally volume limited sample, which would sample space in a uniform and efficient manner, using redshift in these two frames as nominal distance indicators encompassing the extreme possibilities that (a) the microwave dipole is generated locally, in which case cz_{MB} is a better distance estimator for galaxies, or that (b) the microwave dipole is generated by mass asymmetries on very large (several hundred Mpc) scales (or is unrelated to galaxy motions!), in which case cz_{LG} serves better. We denote this sample '4KVL' ('4000 km sec^{-1} volume limited') throughout the text.

Of the 440 objects so selected, 251 passed our *a priori* screening for usefulness in the Tully-Fisher relation. (Said subsample is hereafter called 'OKOBJ'.) Objects were rejected if (a) the axial ratio suggested an inclination angle between the disk's normal vector and the line of sight of less than 40 degrees, (b) the object was an interacting, obviously disturbed, peculiar or nonspiral galaxy, (c) crowding with objects of similar redshift made HI profile confusion likely (or if such was evident in already published HI profiles), or (d) the object was too large to encompass within the field of view of any CCD imaging system available to us. These 251 objects are listed in order of increasing right ascension in Table I. The first column gives a master object number used to refer to that object throughout this thesis. The second column reflects under which of the two conditions 1-22 or 1-23 the object was accepted, with (1) denoting 'both conditions satisfied', (2) denoting 'condition 1-22 only satisfied', and condition (3) denoting 'condition 1-23 only satisfied'. Object names in the NGC, UGC or ESO catalogs follow. Right ascension and declination in 1950 epoch from the *IRAS* point source catalog come next, followed by heliocentric redshift in km sec^{-1} . Such redshifts derived from a variety of literature sources and from original observations by Strauss *et al.*

The catalog was provided well in advance of publication, and we thank Michael Strauss and collaborators for their generosity with this data.

Figure 1 shows a sky map of the 251 objects' positions. The *IRAS* survey's ability to very nearly approach the Galactic plane is evident. Figure 2 offers a histogram of Local Group frame redshift cz_{LG}, illustrating the quasi volume limited nature of the sample.

We stress that we are using objects, which were originally selected to trace the matter distribution, as 'test particles' to sample the flow, and there is no guarantee that objects well suited to one purpose are ideal for the other. (In particular, before obtaining the data presented in this thesis, the disquieting possibility existed that infrared luminous objects, being dusty, would exhibit irregular photometric properties prohibiting internal absorption correction. After the fact, we have found that their photometric properties seem rather well behaved; their neutral hydrogen spectra, rather less so.)

V. Thesis Outline

In Chapter 2 we describe the photometric observations and reductions that led to calibrated I band isophotal magnitudes for about 75 percent of the 'OKOBJ' sample.

In Chapter 3 the 'bootstrap' method we use to remove systematic inclination related trends in the photometry is described and applied to our data. Our results suggest that infrared luminous galaxies suffer greater opacity at near infrared wavelengths than do those selected by photographic magnitude or diameter.

Chapters 4 and 5 describe the observations and data reduction carried out at Jodrell Bank and Parkes observatories in order to obtain neutral hydrogen linewidths for (an unfortunately small fraction of) those sample objects lacking them in the literature. Chapter 4 also describes Monte Carlo perturbation of high quality profiles performed to estimate biases suffered by linewidth measurements in the presence of substantial radiometer noise.

Chapter 6 describes a comprehensive Monte Carlo simulation of our actual experiment. Objects for which we currently have magnitude and linewidth data are placed at the distances predicted by Strauss *et al.* for a given value of β. 60 micron luminosities are drawn from the luminosity function calibrated by Yahil *et al.* (1991), assigned neutral hydrogen masses, linewidths and I band luminosities that reflect the correlations between these quantities (including the Tully-Fisher relation), and assigned realistic observational errors and, in the case of linewidths, signal to noise related bias. The resulting synthetic datasets are then analyzed in the method we apply to the actual data in Chapter 7, and the utility of estimating β by minimizing apparent TF scatter is quantified.

Finally, Chapter 7 describes the provisional dataset remaining after culling of disturbed HI profiles and merging of independent photometric observations. The 'response profiles' of this dataset, and geographic subsets thereof, are discussed, and provisional constraints upon the density parameter inferred. We conclude by listing the shortcomings of the present work and suggestions for further research.

Table I - *IRAS* '4KVL' TULLY-FISHER SAMPLE - N=251

obj	set	NGC	UGC	ESO	α_{1950}	δ_{1950}	$cz_{\odot}$
1	2	7817	19		0 01	20 28	2342
2	3		148		0 13	15 48	4156
3	2	134		350 23	0 27	-33 31	1581
5	1			79 3	0 29	-64 31	2704
6	2	157			0 32	- 8 40	1678
7	1	174		411 1	0 34	-29 45	3471
8	3	192	401		0 36	0 35	4210
11	2	253		474 29	0 45	-25 33	245
12	3	259			0 45	- 3 02	4089
15	2			352 24	1 11	-32 54	3564
18	1	491		352 53	1 19	-34 19	3899
19	1		903		1 19	17 19	2320
22	1	613		413 11	1 31	-29 40	1487
25	1	643B		29 53	1 38	-75 15	3966
28	1	697	1317		1 48	22 06	3109
29	1	772	1466		1 56	18 45	2489
30	1				1 58	68 07	3675
33	1	827	1640		2 06	7 44	3438
39	1	871	1759		2 14	14 19	3740
43	1	972	2045		2 31	29 05	1548
44	1	986			2 31	-39 15	1983
45	3	992			2 34	20 53	4121
47	1	1050	2178		2 39	34 33	3844
49	3	1061			2 40	32 15	3993
50	1	1084			2 43	- 7 47	1410
51	1	1097		416 20	2 44	-30 29	1275
52	1				2 49	-16 51	3297
53	1				2 50	66 11	3544
54	1	1134	2365		2 50	12 48	3595
55	1		2368		2 51	12 38	3577
56	3		2409		2 53	50 23	3867
58	1		2456		2 56	36 37	3632
59	2	1186	2521		3 02	42 38	2762
62	1	1266			3 13	- 2 36	2194
64	1		2789		3 31	67 23	3055
65	1	1365		358 17	3 31	-36 18	1652
66	1	1385		482 16	3 35	-24 39	1503
67	1	1421			3 40	-13 38	2099
68	1		2855		3 43	69 58	1152
69	1		2866		3 45	69 56	1232

Table I - *IRAS* '4KVL' TULLY-FISHER SAMPLE - page 2

obj	set	NGC	UGC	ESO	α_{1950}	δ_{1950}	$cz_{\odot}$
70	3				3 50	32 09	4076
71	1	1482		549 33	3 52	-20 38	1655
73	1		2936		4 00	1 49	3823
75	2		2985		4 10	27 24	3912
77	1	1559		84 10	4 17	-62 53	1292
78	1	1530	3013		4 17	75 10	2407
79	1	1566		157 20	4 18	-55 03	1487
80	2	1591		484 25	4 27	-26 49	4127
82	1				4 29	29 23	2047
83	1		3097		4 33	2 09	3580
84	1		3147		4 41	72 46	2948
87	1				4 55	- 7 51	3773
90	1	1792		305 6	5 03	-38 02	1216
91	2	1803		203 18	5 04	-49 38	4145
92	1	1808		305 8	5 05	-37 34	977
93	1			553 20	5 09	-20 29	3997
94	1	1821			5 09	-15 11	3608
96	1				5 30	-13 57	3444
98	2		3354		5 43	56 05	3085
99	1	2076			5 44	-16 48	2422
100	3		3367		5 51	15 09	3931
101	3		3405		6 05	80 27	3839
105	1				6 16	3 11	2769
106	1		3511		6 38	65 15	3567
109	1	2339	3693		7 05	18 51	2252
110	1		3714		7 06	71 49	2889
111	1			491 20	7 07	-27 29	2876
112	1			492 2	7 09	-26 37	2611
114	2		3780		7 14	34 10	3980
115	1	2369		122 18	7 16	-62 15	3237
116	1			428 23	7 20	-29 08	3068
117	1		3828		7 20	58 03	3217
118	3			428 28	7 21	-29 57	2374
125	1		4041		7 46	73 37	3449
126	1	2469	4111		7 54	56 48	3493
129	1	2566		495 3	8 16	-25 20	1649
130	2		4336		8 16	4 48	4073
131	2			60 4	8 22	-69 36	3924
132	3	2601		60 5	8 25	-67 57	3234
133	2				8 36	-14 30	4184

Table I - *IRAS* '4KVL' TULLY-FISHER SAMPLE - page 3

obj	set	NGC	UGC	ESO	α_{1950}	δ_{1950}	$cz_{\odot}$
134	1	2633	4574		8 42	74 16	2156
136	1			563 28	8 48	-21 46	2611
139	3	2738			9 01	22 10	3102
141	3	2764			9 05	21 38	2707
143	1	2785	4876		9 12	41 07	2737
145	1			126 3	9 13	-60 13	2857
150	3	2903			9 29	21 43	539
151	3			91 16	9 36	-63 15	2069
154	1	2990	5229		9 43	5 56	3198
156	3			374 10	9 52	-32 54	2960
157	1	3095		435 26	9 57	-31 18	2849
158	1	3079	5387		9 58	55 55	1114
159	1	3094	5390		9 58	16 00	2477
161	1			127 11	10 10	-62 17	3370
163	3			263 23	10 12	-43 22	3032
164	3			375 4	10 14	-33 18	2893
165	3			213 11	10 14	-48 37	2747
167	1	3183	5582		10 17	74 25	3076
169	1	3223		375 12	10 19	-34 00	2900
170	2	3221	5601		10 19	21 49	4085
171	2			500 34	10 22	-23 17	3670
172	1			317 23	10 22	-39 03	2804
174	2			436 26	10 26	-30 46	4272
175	1	3263		263 I43	10 27	-43 51	2842
176	1	3278		317 43	10 29	-39 41	2961
179	1	3318		317 52	10 35	-41 22	2910
181	2	3333		376 2	10 37	-35 46	4104
182	3			264 29	10 38	-46 50	3310
188	2	3453		569 17	10 51	-21 31	4039
189	1	3471	6064		10 56	61 47	2076
193	3	3521	6150		11 03	0 14	804
195	1	3568		377 20	11 08	-37 10	2476
198	1	3620		38 10	11 14	-75 56	1755
199	3	3621		377 37	11 15	-32 32	734
203	3	3672			11 22	- 9 31	1861
204	1	3683	6458		11 24	57 09	1686
206	3	3717		439 15	11 29	-30 01	1731
207	1	3735	6567		11 33	70 48	2696
208	3	3749		320 8	11 33	-37 43	2720
210	3			266 15	11 38	-44 12	3113

Table I - *IRAS* '4KVL' TULLY-FISHER SAMPLE - page 4

obj	set	NGC	UGC	ESO	α_{1950}	δ_{1950}	$cz_{\odot}$
212	1	3882		170 11	11 43	-56 06	1901
213	1	3885		440 7	11 44	-27 38	1948
216	3			320 26	11 47	-38 30	2703
223	1	4030			11 57	- 0 49	1463
225	1		7017		11 59	30 08	3174
226	3	4045			12 00	2 15	1942
228	1	4102	7096		12 03	52 59	862
229	2			379 30	12 06	-36 25	3915
231	1			380 1	12 12	-35 13	2689
232	1	4219		267 37	12 13	-43 02	1993
233	2	4253			12 15	30 05	3876
239	1	4332	7453		12 20	66 07	2843
240	3	4388	7520		12 23	12 56	2545
241	1	4418			12 24	- 0 36	2045
243	1	4433			12 25	- 8 00	2978
245	1	4500	7667		12 29	58 14	3149
246	3	4501	7675		12 29	14 41	2321
247	1	4527	7721		12 31	2 55	1730
248	1	4536	7732		12 31	2 27	1814
251	3	4602			12 38	- 4 51	2559
254	3	4626			12 39	- 6 41	2874
255	3	4658			12 42	- 9 48	2407
256	1	4666			12 42	- 0 11	1516
257	3			507 13	12 45	-27 18	3184
258	3	4691			12 45	- 3 03	1123
260	2			323 25	12 49	-38 45	4060
262	2			507 37	12 50	-27 11	3694
263	1	4785		219 4	12 50	-48 28	3750
264	1			323 38	12 51	-41 32	3371
265	1	4793	8033		12 52	29 12	2487
267	3	4818			12 54	- 8 15	1155
269	1	4835		269 19	12 55	-45 59	2185
271	3	4939			13 01	-10 04	3117
272	1	4945		219 24	13 02	-49 12	563
274	3	4990			13 06	- 5 00	3181
275	1			323 90	13 07	-41 17	2950
276	3		8248		13 08	18 42	3650
278	1				13 09	-17 16	2748
280	3			219 41	13 10	-49 12	3518
281	1				13 12	-15 41	2231

Table I - *IRAS* '4KVL' TULLY-FISHER SAMPLE - page 5

obj	set	NGC	UGC	ESO	α_{1950}	δ_{1950}	$cz_{\odot}$
282	2				13 12	24 52	3866
284	3	5054			13 14	-16 22	1743
285	3	5064		220 2	13 16	-47 38	2982
286	1	5073			13 16	-14 35	2715
287	1			269 85	13 16	-47 01	2893
288	1	5078		508 48	13 17	-27 08	2148
293	1			173 15	13 24	-57 13	3006
295	1			383 5	13 26	-34 00	3579
298	1	5188		383 9	13 28	-34 32	2326
303	3	5248	8616		13 35	9 08	1156
306	3			221 7	13 47	-52 24	3674
309	2				13 48	-52 40	3973
310	1	5351	8809		13 51	38 09	3631
311	1	5371	8846		13 53	40 42	2561
312	2			174 3	13 54	-52 31	4059
313	3	5383	8875		13 55	42 05	2258
315	1			174 5	13 58	-53 18	3775
316	1	5430	8937		13 59	59 34	2819
320	3	5506			14 10	- 2 58	1753
321	2				14 13	-55 18	3954
323	3			373 5	14 17	-46 04	1719
328	3	5656	9332		14 28	35 32	3192
332	1	5678	9358		14 30	58 08	1929
333	1	5676	9366		14 31	49 40	2104
334	3			272 23	14 36	-44 06	2911
336	2	5716			14 38	-17 15	3970
337	3	5719			14 38	- 0 06	1688
338	1	5728			14 39	-17 02	2834
344	1	5786		327 37	14 55	-41 48	3055
345	3	5792	09631		14 55	- 0 53	1930
347	3		9668		15 00	83 43	3917
348	1	5861			15 06	-11 07	1855
349	1	5833		42 3	15 06	-72 40	3071
350	3			581 25	15 10	-20 29	2277
351	1				15 10	7 24	3528
352	1	5900	9790		15 13	42 23	2551
353	1	5905	9797		15 14	55 41	3391
354	1	5908	9805		15 15	55 35	3309
357	1	5937			15 28	- 2 39	2754
358	1	5938		99 7	15 31	-66 41	3580

Table I - *IRAS* '4KVL' TULLY-FISHER SAMPLE - page 6

obj	set	NGC	UGC	ESO	α_{1950}	δ_{1950}	$cz_{\odot}$
360	1	5962	9926		15 34	16 46	1963
361	1	5990	10024		15 43	2 34	3809
366	1			137 14	16 12	-58 11	2703
367	1			69 2	16 15	-70 01	3452
368	1			100 23	16 22	-63 04	3846
369	1				16 25	-61 25	3332
370	1	6181	10439		16 30	19 55	2372
373	1	6221		138 3	16 48	-59 08	1478
375	3	6361	10815		17 18	60 39	3862
376	1				17 28	-43 13	2548
377	3				17 57	- 4 00	3968
378	1	6574	11144		18 09	14 58	2261
379	1			140 12	18 09	-60 06	3157
380	2	6643	11218		18 21	74 32	1491
382	3	6701	11348		18 42	60 36	3983
384	3				19 05	28 55	3927
385	1	6764	11407		19 07	50 51	2379
387	1	6754		231 25	19 07	-50 43	3325
389	1	6782		142 1	19 19	-60 01	3736
391	1	6808		73 3	19 38	-70 45	3468
392	1	6810		142 35	19 39	-58 46	1975
393	1	6824	11470		19 42	55 59	3386
394	2	6835			19 51	-12 41	1581
395	2				20 16	- 5 28	3400
396	2		11540		20 19	66 34	2490
397	1			285 7	20 20	-44 09	2902
399	1				20 27	-15 23	3494
400	1	6931			20 30	-11 32	3549
401	1	6925		463 4	20 31	-32 09	2799
404	1			107 7	21 05	-63 29	3097
405	2				21 08	65 57	2894
406	3		11703		21 11	1 58	4009
407	1			402 26	21 19	-36 53	2796
408	1	7074			21 27	6 27	3476
409	1			48 2	21 30	-76 34	3901
410	3				21 31	42 30	4075
411	1	7083			21 31	-64 07	3049
412	3			27 1	21 45	-81 45	2500
414	2			404 36	22 07	-36 20	3028
417	1			405 5	22 13	-37 05	3447

Table I - *IRAS* '4KVL' TULLY-FISHER SAMPLE - page 7

obj	set	NGC	UGC	ESO	α_{1950}	δ_{1950}	$cz_{\odot}$
418	3		11973		22 14	41 15	4148
421	2	7331	12113		22 34	34 09	826
422	1			534 9	22 35	-26 06	3395
423	2	7448	12294		22 57	15 42	2192
424	1	7479	12343		23 02	12 03	2399
426	1	7541	12447		23 12	4 15	2607
427	1	7552		291 12	23 13	-42 51	1589
433	1	7677	12610		23 25	23 15	3543
434	1	7678	12614		23 25	22 08	3489
435	3				23 27	15 29	4236
437	3		12773		23 43	11 47	4261

Figure Captions - Chapter 1

Figure 1: Positions in celestial coordinates α, δ (degrees) of the 251 *IRAS* '4KVL' sample objects selected for Tully-Fisher (TF) observations.

Figure 2: Histogram of recession velocities (in the Local Group rest frame) in km sec^{-1} for the 251 *IRAS* '4KVL' objects selected for TF observations.

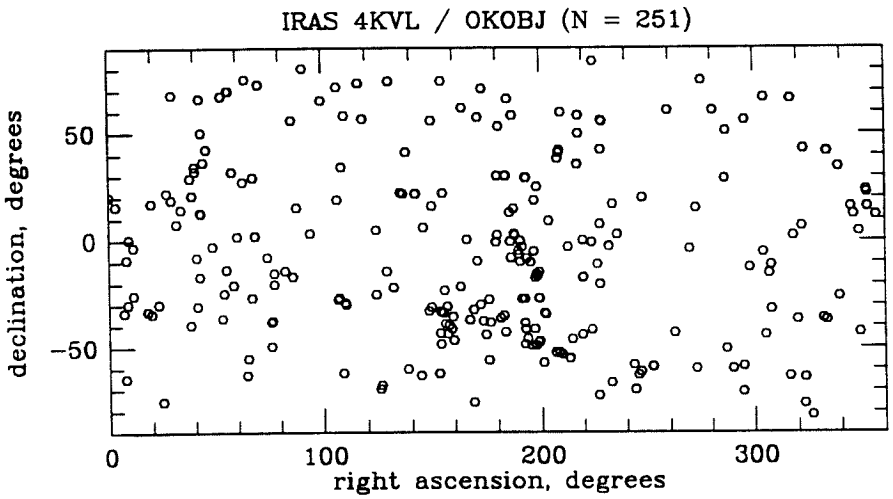

Figure 1

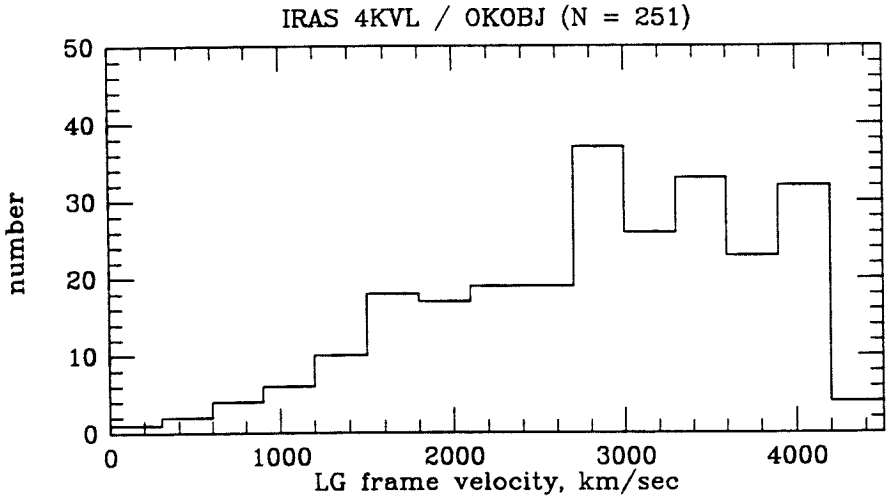

Figure 2

Chapter 2: Photometric observations and reductions

I. Introduction

The ostensible goal of the present study is to estimate distances to the *IRAS* 4KVL galaxies by using Tully-Fisher techniques, that is, by exploiting a 'standard candle' property of spiral galaxies. We predict the absolute magnitude of galaxies with the rotational linewidth of the 21 centimeter neutral hydrogen emission line; the apparent brightnesses of the objects are then needed to estimate (relative) distances. In this chapter we discuss the means by which galaxy brightnesses were measured.

Over a period of two years we (principally J. Roth, but also J. R. Mould, R. Schommer, and others) photometered a large subset of the *IRAS* 4KVL sample at Mount Palomar, Cerro Tololo and Cerro Las Campanas observatories. Runs producing data used in this thesis are listed in Table I along with the collecting aperture, image scale and field of view for each camera. (After learning of a 'bug' in the observing system at Las Campanas which allowed the shutter to remain open by an unknown excess amount during long exposures, we decided to skip reducing data obtained at Las Campanas; most objects observed there were reobserved at Cerro Tololo. Hence Campanas does not appear in Table I.)

Images were taken of program objects and standard stars in the I (near infrared) and V (visual) bandpasses. The I band is least affected by Galactic and internal absorption of any accesible to standard CCDs ($A_I = 0.4A_B$; HT) and gives greater weight to the main sequence and giant star contributions to a galaxy's light and less to the HII regions and young stars whose abundance presumably depends on the strength of density wave or tidal perturbation and structural parameters of the ISM as well as upon a galaxy's mass. The $V - I$ color ($m_V - m_I$) may provide a second parameter to the TF relation in *IRAS* galaxies and, in principle, allows inferred galaxy magnitudes

to be corrected for spectral shape differences across the I bandpass (although, in practice, 'color terms' were found to be negligable in all cameras we used).

All observations used charge coupled devices (CCDs) at the telescope focus to detect incoming photons (Janesick, 1992). CCDs are thin silicon wafers divided into arrays of (generally) square pixels which accumulate mobile electrons in numbers proportional to the numbers of incident photons that photoelectrically liberate them; cycling the electrical barriers maintained between pixels allows a current proportional to the number of mobile electrons to be measured and digitized, one pixel at a time; the result is a two-dimensional array of numbers each proportional to the number of mobile electrons contained in one pixel. (The number of electrons represented by 1 data number, or DN, is called the gain and is generally set so the noise associated with the baseline current from reading an empty chip, known as 'read noise', is just resolved.) CCDs resemble photographic plates in that they soak up light for some time and are then 'developed'; they are unlike photographic plates in that they can be used over and over, and that accidental exposure to bright light generally leaves them unharmed.

CCDs are quite linear devices over a large dynamic range (Janesick 1992). In line with common usage of well-tested CCDs at visible and near infrared wavelengths, we assumed rather than tested this linearity. Repeat exposures of standard stars with different exposure times, when performed, generally supported this assumption to within the error bars, but did not provide a sensitive test. Deferred charge, or nonlinearity at low light levels, is a commonly overlooked error source (Gilliland, 1992) not explicitly addressed by current versions of the 'IRAF' or 'FIGARO' reduction packages used in this work. Because of the large areal extent of our program objects and the generally high sky counts obtained in our broadband images we expect our results have not been compromised by neglecting this correction.

CCD pixels do have a finite capacity for electrons, but this generally exceeds by several times the maximum value the DN is allowed to take given the 16 bits provided by the A/D converters.

Short exposures were generally taken of all program objects to insure that the deeper (generally 10 minute) integrations would not saturate the detector; occasional objects' bright nuclei forced shorter exposures.

The filter, along with the reflectivity curves for the mirrors and the quantum efficiency curve for the CCD, defines the effective bandpass of observation.

Quantum efficiency, the fraction of incident photons that successfully generate a mobile electron (hereafter 'QE') is generally quite high in the red end of the visible spectrum: values of 0.4 to 0.8 were encountered in this project. We note that implicit in our reduction method lies the assumption that CCD QE is stable over the course of a night – an assumption borne out by laboratory experience and supported *a posteriori* by photon counts from standard stars observed many times a night. The assumption was not explicitly tested, however. Gross variations in QE seen in standard star data were generally taken as evidence for nonphotometric weather. One night (N3 of P60/90 = run 3) showed QE variations of around 0.3 magnitude on single CCD frames with multiple exposures of standard stars; data from that night remain uncalibrated. A shutter failure is suspected responsible.

In general terms, photometry of extended objects with CCDs requires the following steps:

(1) - establishing differential sensitivity of different CCD pixels so that correcting all to one mean sensitivity can be performed ('flat fielding');

(2) - establishing the throughput of the entire camera, by observing 'standard' stars whose apparent magnitudes have been carefully calibrated and catalogued;

(3) - establishing atmospheric transmission variation with zenith angle ('extinction coefficients');

(4) - observing extended objects and applying 'flat field' corrections determined in step (1) for differential CCD sensitivity;

(5) - assessing and subtracting the mean sky level from an extended object's image;

(6) - placing appropriate (in this case, elliptical) apertures upon the extended object image and summing all pixel counts contained within them;

(7) - converting this sum to a standard magnitude by using the relation between counts and catalogued magnitudes established in step (2) and correcting for atmospheric transmission using results of step (3);

(8) - plotting the results as a surface brightness profile by using knowledge of the 'plate scale' (angular sky coverage per CCD pixel).

These steps are discussed in greater detail in the following sections.

CCD properties, observing and data reduction techniques are discussed extensively in the proceedings of the 1991 September Tucson School on CCD use put together by Steve Howell (1992); had this meeting taken place two years earlier, notably better data would have been acquired for this thesis.

II. Bias and overscan correction

The underlying constant current level registered by the amplifier(s) when reading out a CCD which has seen no light manifests itself as a roughly constant number of counts per pixel across the CCD. This additive base must be subtracted from all images before further processing. Zero second 'exposures' followed by chip readout provide a two-dimensional map of this 'bias', which is generally featureless; these were taken in large numbers and averaged at Tololo but generally not at Palomar. Unless spatial structure is seen in the bias frames they are not essential (Gilliland, 1992) and their subtraction may even add noise (although in amounts inconsequential to this program).

Amplifier 'zero' level can drift even during one chip readout; thus an 'overscan' region of the image (in the column direction) is produced by continuing to read current off the chip by scrolling the inter-pixel gates even after the pixels have been emptied in a given row (Gilliland, 1992). When

using 'IRAF' we generally fit a polynomial of higher than zero order to the overscan region; the fit is then expanded in the row direction and subtracted from the entire image. When 'FIGARO' was used, each row's overscan level was directly subtracted.

Poisson-like fluctuations in bias counts add noise to the images. (We say 'Poisson-like' because the noise is NOT generally the square root of the absolute bias level, which can be several hundred DN, but typically several times smaller.) A typical noise level might be equivalent to 5 or 10 electrons. Read noise levels for our cameras are listed in Table I.

III. Flatfielding

No CCD detector offers an identical quantum efficiency for each pixel. Pixel to pixel variations in QE must be mapped and corrected for in program data. These variations depend on wavelength and thus the correction array for a given observation becomes effectively a weighted average of monochromatic correction arrays; the weighting by wavelength in this average depends on the camera's total throughput (as function of wavelength) AND upon the spectrum of the source. Three methods commonly used to determine the differential QE, or 'flatfield response' of a CCD camera are:

(1) to observe light produced by a high temperature continuum light source generally reflected off a white spot on the interior of the telescope dome;

(2) to observe twilight skies, wherein the twilight substantially exceeds the cosmic background in brightness;

(3) to average nighttime observations in such a manner that all discrete sources disappear, leaving the overall detector response to uniform illumination. Generally at each pixel, the median of all values for that pixel taken in a given band during the night is used; this generally rejects frames wherein

this pixel beheld a cosmic source (star, galaxy) and provides a measure of the pixel's response to background skyglow.

Subtleties in flatfielding are further discussed in the Tucson school CCD book (Howell 1992).

Method (1) offers the advantages of many repeat exposures, high signal to noise, and stable conditions, but suffers from disadvantages including (a) subtle differences between the white spot reflectivity function and true isotropic illumination, and (b) spectral differences between the interior light source (which generally has an effective spectral temperature below 2000°K) and the objects of study (which, in this case, generally show effective spectral temperatures typical of stars and spiral galaxies; *i.e.*, one to several thousand degrees Kelvin hotter than the lamps we used). 'Color balance' filters were used at Cerro Tololo to give domelamps a hotter apparent spectrum.

Method (2) offers the advantage of truer illumination, but suffers from (a) short working time during which twilight is neither too bright nor too dim, which lets one get only a few good frames each night, (b) generally poorer counting statistics from dimmer twilight frames or noisy median statistics, and (c) bright stars which, if present, must be somehow removed (generally by median averaging several frames). The aforementioned spectral difference problem also plagues method (2), if at a lesser level.

Method (3) in principle offers a calibration of differential QE under conditions exactly like those used to obtain program data (since it simply uses program data as input), but suffers from (a) substantial shot noise in the flatfield determination, since far fewer photons are obtained and the median required to reject cosmic sources is a noisy statistic, and (b) requirement for each pixel to see blank sky more often than not throughout a night. Since our program objects generally occupied a substantial fraction of the available field of view, central pixels were rarely free of object signal and Method (3) could not be used in this project.

Methods (1) and (2) can be combined to exploit the high signal nature of dome/lamp flatfields and the truer illumination of twilight flats, and we generally did so here.

No traditional high temperature domelamp and whitespot were available at the Cerro Tololo Schmidt. The images taken with that Schmidt were best flattened with images of diffuse daylight allowed to enter a barely opened domeslit oriented opposite the Sun's position in late afternoon, with the telescope pointed to a position on the dome opposite the slit in azimuth and at zenith angle of roughly 40 degrees.

The numerous emission lines provided by the ionosphere in the I band night sky spectrum have been known to produce thin film like interference patterns in some CCDs; this 'fringeing' generally must be determined by median averaged sky frames or by deep observations of nearly blank sky fields and subtracted from object frames. Only our unused Campanas data were plagued with visible fringeing; hence we do not describe any recipe for removing the effect. Defringeing techniques are described by Gilliland (1992). Variability in the brightness and relative line strengths in the I band skyglow, plus some very low level fringeing, may be responsible for our failure, and that of many other observers queried by us, to get I band frames flat at the few thousands level reported in the R band (*e.g.*, WT).

IV. Aperture photometry of standard stars

A. Introduction

Once bias and/or overscan corrected, flatfielded images have been produced, we determine the throughput of a given camera+filter+atmosphere combination on a given night. In principle, continuous monitoring of 'standard' stars of 'known' (*i.e.*, previously measured) apparent brightness will permit the throughput to be determined on an hourly basis. In practice, however, we utilize data only from nights appearing clear from start to finish and yielding consistent count rates from standard stars observed at various times of night. In part this was due to practice learned from seniors, in part from the finite readout time of CCDs (one to two minutes) which produces significant telescope

deadtime when numerous short exposures are made. Run P60/11/89 utilized a minimal number of standard stars and is least well calibrated; run P60/8/90 might also be considered undercalibrated.

B. Standard star references

Standard star finding charts and calibrated magnitudes in the Kron-Cousins I and V bandpasses (Cousins 1976) were obtained from several sources and are listed in Table II; those providing the bulk of our photometric calibrations were:

L1: Landolt (1983; charts in Landolt 1973): CCD magnitudes in I and V for stars in equatorially located 'Selected Areas'.

L2: Landolt (1992) new fainter standards with CCD-determined magnitudes. The charts and magnitudes actually used in this project were obtained before publication by I. Thompson (OCIW) and N. Suntzeff (CTIO) and from them in turn by J. Roth. These are denoted **L/T** and **L/S**, respectively, in Table II.

These fainter standards allowed longer exposure times to be taken by cameras (such as ours) whose sensitivity generally required short exposures and defocused images to observe the L1 objects without saturating the detector. We note that magnitudes and names for L2 stars in Table II may differ from those published in Landolt (1992) because we used provisional, prepublished versions of that catalog. Their positions, however, allow cross-identification.

G: Graham (1982) photoelectrically determined magnitudes for stars in wide fields at declinations around $\delta \sim -45$ degrees.

Occasional use was made of stars in the M67 'dipper' asterism calibrated by CCD observation by Schild (1983). Cluster fields in Christian *et al.* (1985) were observed but not used for calibration owing to great crowding of standard stars; they did enter into extinction coefficient assessment on one run.

Standard stars actually used to determine photometric transformations in this project are listed along with their stated I and $V-I$ magnitudes and positions in Table II.

C. Instrumental magnitude determination

Because of the linear response of CCDs to incident light we expect that we can define an instrumental magnitude $m_{instr} = -2.5\ log(N_{photons}/\Delta t_{exp})$ (where log is taken to mean log_{10}) that will be related to the catalogued magnitude m_I by a simple offset reflecting the throughput of the camera. The number $N_{photons}$ of photons obtained from a star during exposure of length t_{exp} seconds can be determined in principle by placing a circle or box around the star's image, adding up all pixel counts therein, and subtracting a sky value $N_{sky} = n_{sky}\ (counts/pixel)\ \times\ area\ (pixels)$. The sky level n_{sky} can be assessed either locally or globally. Local sky assessment is more robust against imperfect flatfielding, while global sky assessment does not run the risk of contamination by very low level wings of the point spread function (PSF), which can vary with atmospheric conditions and ambient temperature.

In this work we have utilized a modified version of 'FIGARO' routine 'FOTO' to assess instrumental magnitudes m_I, m_V. The mechanics of this routine and our use of it very closely follow the discussion of point source photometry in DaCosta (1992). 'FOTO' places concentric circles of increasing radius r centered on star center previously determined by moments of the light distribution. The sky is assessed in an annulus of inner radius r_{sky_1}, outer radius r_{sky_2} with the same center. Sky is assessed by composing a histogram of pixel counts for all pixels within the annulus, determining an average and width for the distribution, rejecting points beyond about 3 times the width from the average, and reassessing the average and width of the counts distribution in an iterative manner. The average may be the mean or median of the pixel values; most commonly the estimated mode

$$mode\ =\ 3\ \times\ median\ -\ 2\ \times\ mean \qquad (2-1)$$

is used to enjoy the mode's robustness to stellar and cosmic ray contamination without requiring the actual intensive calculation of the true mode. On one run (P60/89) we found the photometric solutions improved by using $sky = mean$ and on one run (P60/90) we chose to use global estimates of n_{sky} for each frame.

Once n_{sky} (photons/pixel) has been determined, it is subtracted from each pixel within aperture r and the sum of pixel values (after sky subtraction) $N_{net}(r)$ within aperture r yields an 'aperture magnitude'

$$m(r) = -2.5\ log[N_{net}(r)] + \ offset + \ 2.5log(t_{exp}) \qquad (2-2)$$

given an exposure time in seconds of t_{exp}. Aperture magnitudes $m(r)$ are assessed for a sequence of successively larger radii from r_1 to r_2 with radial step Δr. In what follows we have set the arbitrary offset to 31.

The sequence of magnitude values $m(r)$ is referred to as a *growth curve*. Direct growth curve measurement has the advantage over PSF function fitting of model independence and computational speed but the disadvantage of being dominated by noise and possible systematic effects for fainter point sources. Growth curve shape depends upon the functional form of the PSF but is expected to converge in any case to an asymptotic value for the total magnitude of the point source. We find that the convergence to asymptotic magnitude generally depends on the sky estimation algorithm chosen, with the differences between the curves exceeding by several times the formal (photon counting statistics) errors on the magnitudes $m(r)$. This emphasizes the important possibility of systematic error.

For each run, standards were identified on CCD frames with the help of finding charts and coordinates registered by cursor on the CCD image display. Centroids were then assessed and star positions, sky radii, sky estimator type, aperture radii r and instrumental gain (required to estimate

Poisson noise contribution to magnitude error) specified to 'FOTO'. 'FOTO' parameters used on each run appear on Tables I and III.

Our growth curves were generally found to converge more slowly than do Gaussian PSFs with $\sigma(pixels)$ = actual 'seeing' value, presumably because of diffraction spikes and imperfect telescope focus. Thus in initial reduction of run 1 we took the instrumental magnitude to equal $m(r)$ at the point where the (absolute value of the) slope of the growth curve dropped below

$$|m(r) - m(r - \Delta r)|/\Delta r \; < \; 0.001 \; mag \; arcsec^{-1}. \qquad (2-3)$$

All standard star growth curves deemed acceptable from the 1989 run satisfied this criterion at some r and at that r each instrumental magnitude was assessed. We note that this run alone relied principally upon relatively bright L1 standards that had to be observed badly out of focus to avoid CCD saturation; thereafter, the much fainter L2 and Graham standards became known to us.

For all other runs the method of *aperture corrections* was adopted. (Aperture corrections are well discussed by Da Costa and Howell in the Tucson CCD volume and in references therein.) The topic arises as follows: we wish to place a sufficiently large aperture upon the star image to count most of its light. At low starlight levels and with large aperture areas, however, Poisson noise in the sky counts and readout noise dominate. Furthermore faint stars are more sensitive to error in sky estimation, and sky estimation error can cause growth curves to remain steep (sky underestimated) or to turn over (sky overestimated). In practice we found that bright (but unsaturated!) stars on the same frame as faint standards generally show growth curves with acceptable properties as they are least affected by sky subtraction error or noise.

The difference in aperture magnitudes between radii r_1 and r_2:

$$\Delta m(r_1, r_2) = m_{template}(r_2) - m_{template}(r_1) \qquad (2-4)$$

measured from one or more bright template stars on a given frame can be applied to correct a faint star's magnitude at small radius r_1, which is relatively robust against shot noise and sky error, to the larger radius r_2:

$$m_{star}^{corr}(r_2) = m_{star}(r_1) + \Delta m(r_1, r_2) \qquad (2-5)$$

Template growth curve gradients generally lay below $|\Delta m/\Delta r| < 0.005\ mag\ arcsec^{-1}$ at r_2. The aperture correction for a given frame was generally the average of values from several individual stars. Apertures r_1 and r_2 were set constant for each run and are listed in pixel and arcsecond units in Table III. Aperture choices were influenced by degree of diffraction (extreme in the case of the Tololo Schmidt data) and overall focus quality.

Template growth curves, apertures r_1, r_2 and sky radii r_{sky_1}, r_{sky_2} were admittedly chosen in nonalgorithmic fashion; thus the possibility of further systematic differences between runs could be introduced. In part the many months separating reductions of different runs contributed to inconsistency in procedure. We merely claim that *a posteriori* our procedure seems secure as multiply observed galaxy magnitudes generally matched to within the errors (section VII below).

V. Extinction and photometric transformation coefficient determination

The methods described in the preceding section provided instrumental magnitudes

$$m(j,n) = -2.5\ log[N_{net}(j,n;r_1)] + 2.5log(t_exp) + offset + \Delta m(n;r_1,r_2) \qquad (2-6)$$

for standard star j viewed at airmass (= secant of zenith angle) $secz(j,n)$ on frame n for which an average aperture correction $\Delta m(n;r_1,r_2)$ has been determined for frame n from one or more template point sources. $N_{net}(j,n;r_1)$ is the summed counts within aperture r_1 centered on stardard star after sky subtraction. From these numbers we need to assess the dimming effects of the atmosphere at each band, correct instrumental magnitudes for atmospheric dimming, and determine offsets between

catalogued and instrumental values. We then can relate photon counts from extended sources (*i.e.*, galaxies) to traditional magnitude units.

A. Extinction coefficients

Ideally, extinction coefficients are determined by observing several stars j at two or more airmasses $secz(j,n)$ and, in a given bandpass, assessing:

$$k_{band} = <_j [m(j,n_1) - m(j,n_2)]/[secz(j,n_1) - secz(j,n_2)] > \qquad (2-7)$$

where m are instrumental magnitudes obtained in the specified bandpass in frames n_1, n_2. When this was performed separately for different stars observed at adequate range in airmass the resultant k were averaged as shown above. The actual numbers involved at I and V bands over the airmass range 1.0 - 1.7 are small, however, and not infrequently absurdly large or negative k resulted; these were rejected. On run 1 (P60/89) extinction coefficients for Palomar suggested by J.R.M. were adopted. On run 6 (TSC/91), coefficients measured and averaged over four previous nights at the Tololo 36 inch were used. Table IV lists the extinction coefficients adopted for each independent run or night.

We note that as long as galaxies were observed at airmasses similar to those of the calibrating standard star exposures, error in assessing the extinction coefficient is largely absorbed into the photometry zero point. The only subsample with consistently large (around 1.5) airmass values, the P60/91 overlap objects as observed at the Tololo Schmidt, gave isophotal galaxy magnitudes in agreement with P60/91 to within the errors on average (Table VIII and Section VII B below).

Once extinction coefficients were determined, instrumental magnitudes in the I and V bandpasses were assessed for observation n of star j in each run:

$$m_I^{obs}(j,n) = m_I(j,n) - k_I secz(j,n); \qquad (2-8a)$$

$$m_V^{obs}(j,n) = m_V(j,n) - k_V secz(j,n). \qquad (2-8b)$$

B. Photometric transformation coefficients

With extinction-corrected ('zero air') instrumental magnitudes m_I^{obs}, m_V^{obs} in hand, we solved for coefficients (a,b,c,d) in the (hereafter 'JRM') system:

$$m_I^{obs} - m_I^{cat} = a(m_V^{obs} - m_I^{obs}) + b; \qquad (2-9a)$$

$$m_V^{cat} - m_I^{cat} = c(m_V^{obs} - m_I^{obs}) + d \qquad (2-9b)$$

by fitting linear relations to sets of points :

$$[m_I^{obs}(j,n) - m_I^{cat}(j)) \ , \ (m_V^{obs}(j,n) - m_I^{obs}(j,n)];$$

$$[m_V^{cat}(j) - m_I^{cat}(j)) \ , \ (m_V^{obs}(j,n) - m_I^{obs}(j,n)],$$

respectively. Solutions were performed independently one night at a time. When star s was observed at several $secz$ values, only observations n at lower $secz(j,n)$ were employed. Numerical Recipes' MEDFIT routine (Press *et al.* 1986) was used on random subsamples of the (m_I^{obs}, m_V^{obs}) lists ('bootstrapping') to establish average values and error bars for (a,b,c,d). (MEDFIT fits lines to lists of points (x,y) by minimizing absolute value deviations, rather than squared deviations, from the lines; this decreases sensitivity to outliers.) Lists of residuals were then inspected, gross outliers removed when necessary, and lines refit. We assume that the uncertainties in (a,b,c,d) are dominated by point to point variance induced primarily by instantaneous seeing and transparency variations; thus we do not propogate the individual instrumental magnitude error bars (which principally reflect photon counting statistics) into (a,b,c,d). Occasionally too few points were available for stable MEDFITs to bootstrapped subsamples and error bars were instead based on the scatter of individual points about the fit line. Error bars in (a,b,c,d) are a principal source of uncertainty in isophotal galaxy

magnitudes described below and must be estimated conservatively. The scatter of each point set about its adopted fit to Eqns. (2-9) was typically 0.01 - 0.03 magnitudes.

VI. Galaxy surface photometry

Table VI lists photometric observations of *IRAS* 4KVL galaxies resulting in calibrated surface photometry. Column 1 lists 4KVL database number, column 2, the telescope used (Palomar 60 inch, Tololo 36 inch, Tololo Schmidt), column 3, the year, and column 4, the sky transparency (P = photometric, N = nonphotometric, ? = unsure at time of observation) and moonlight content of sky (D = dark, L = light). As mentioned before, no data from Las Campanas resulted in calibrated surface brightness profiles for this project.

In what follows we describe how isophotal and total magnitudes and surface brightness profiles were obtained from flatfielded I and V band galaxy images taken on nights enjoying photometric calibration obtained with methods described in the previous section. Extensive use was made of program 'SFOTO' written by Ming-Sheng Han (HT). 'SFOTO' allows interactive labeling of star and cosmic ray regions to be ignored by ellipse fitting programs, allows interactive sky level measurements, allows stars, cosmic rays, defective rows and columns and other undesired image components to be replaced with a smooth interpolation of the surrounding brightness field before photon counting, and converts photon count rates to standard magnitudes given photometric transformation coefficients. 'SFOTO' makes use of individual 'FIGARO' and 'PGPLOT' routines. We are indebted to Ming-Sheng Han for continued support to 'SFOTO' users.

A. Aperture determination

We wish to measure the total light output from each spiral galaxy for which we will estimate distance via Tully-Fisher techniques. In principle we might proceed as we do with stars: estimate sky,

subtract sky, place circular aperture large enough to encompass entire galaxy, and count photons. In practice, however, we only directly measure galaxy magnitudes down to some limiting surface brightness (*i.e.*, countrate coming from given angular area of sky; generally expressed in units of magnitudes per square arcsecond) at which sky estimation errors and Poisson statistics dominate. Determining the total galaxy magnitude then depends upon extrapolating the directly measured radial trend in surface brightness (SB); insofar as spiral galaxies obey exponential disk surface brightness laws this extrapolation is straightforward. Radial trends in surface brightness also pertain to studies of galaxy structure. Thus a series of concentric apertures whose shape more closely matches galaxies' is favored.

Elliptical apertures seem adequate to trace the shape of the outer regions of spiral galaxies, which are taken to be circular disks of finite thickness seen at some tilt angle. Contour plots of photon counts from galaxies generally tend towards ellipses at the fainter, outer isophotes. Ellipses fit to the outer portions of spiral galaxies also invite use to estimate the inclination of the disk, a quantity essential to deprojecting observed linewidths to disk rotation velocities. For these reasons concentric elliptical apertures positioned most nearly normal to the gradient in photon countrate have been fit to sky-subtracted I band galaxy images by the 'GASP' program.

'GASP' fits ellipses increasing in major axis by a constant multiplicative factor whose centroids, position angles and eccentricities are allowed to vary (but by no more than set maximum amounts) with each radial step outward. Ellipse major axes grow by a constant multiplicative factor. We adopted Han's (HT) values for most 'GASP' parameters; the threshold value for counts above sky at which to stop integrating ($TRSH$) was frequently modified, however, to prevent fit ellipses from diverging wildly from galaxy appearance or from running beyond the CCD frame. Ellipse centroids rarely wandered by more than a couple of pixels; position angles and ellipticities changed abruptly in the presence of prominent arms and bars. As interior ellipses are strongly skewed by such features when prominent, the inner portions of surface brightness profiles presented below should

not be taken to reflect the azimuthally averaged radial surface brightness profile; nor are our SB profiles generally well suited for bulge – disk decomposition.

Once 'GASP' provided a set of fit ellipses for a given galaxy image frame, these were laid over that frame on a TV display and inspected. When $TRSH$ was set too low, outer ellipses wandered far from the galaxy and went unused in subsequent photometry. When $TRSH$ was set too high, ellipses did not extend far enough to encompass the entire object and the outermost fit ellipse was generally copied outward by hand until encompassing the entire disk visible at levels a few percent above sky. Occasionally ellipse parameters (ellipticity, position angle) were user modified to provide more sensible fit to the underlying disk when perturbed at outer radii by spiral arm or bar structure.

B. Photometric calibration

The use of 'GASP' output and corresponding I and V band CCD frames to obtain galaxy surface photometry was described in Han Ming-Sheng's thesis (HT), which we follow closely as we used his software essentially unmodified.

Given the sequence of elliptical apertures of semimajor axis $r(i)$, eccentricity $\epsilon(i)$, position angle $\psi(i)$ and differential angular area $\delta\Omega(i)$, differential and integral photon counts within the ellipses are obtained in I and V. Reference stars common to I and V frames were marked interactively, centroids assessed and ellipses shifted before overlying upon V frame; this operation assumes no image rotation took place between paired I and V exposures. 'SFOTO' requires as input the I and $V-I$ extinction coefficients k_I, $k_{V-I} = k_V - k_I$ and constants (A,B,C,D) in the equations

$$m_I^{cat} = A + m_I^{obs} - k_I secz + B(m_V^{cat} - m_I^{cat}); \qquad (2-10a)$$

$$m_V^{cat} - m_I^{cat} = C + D(m_V^{obs} - m_i - k_{V-I} secz). \qquad (2-10b)$$

where '*cat*' and '*obs*' refer as before to catalogued and instrumental magnitudes, respectively. Transformation from 'JRM' coeffiecients (a,b,c,d) to 'HMS' coefficients (A,B,C,D) to second order follows:

$$A = ad/c - b - offset, \tag{2-11a}$$

$$B = -a/c, \tag{2-11b}$$

$$C = d, \tag{2-11c}$$

$$D = c, \tag{2-11d}$$

with corresponding approximate error bar transformations:

$$dA = db, \tag{2-12a}$$

$$dB = (da)/c \tag{2-12b}$$

$$dC = d(d) \tag{2-12c}$$

$$dD = dc. \tag{2-12d}$$

'HMS' coefficients for each night of photometry are tabulated in Table V.

In some cases, the color term B in the 'HMS' system was so small that it was defined to be zero. In these cases, its actual value times the assumed average galaxy color $m_V - m_I = 1.5$ was added to the zeropoint A. Zeropoint offsets for nights with color terms set to zero could have been reassessed in light of the measured average galaxy color, but were not. We later found the average integrated galaxy color at last favored isophote to be 1.23 for the observed sample; assuming a typical color term amplitude of 0.02, our initial adoption of 1.5 induces a systematic error in I band magnitudes of $(0.02)(1.5 - 1.23) = .005$ magnitudes. We did not revise the zeropoint offsets in light of this average difference.

Error bars for photometric quantities are derived by 'SFOTO' following the precepts of Han (HT). Included are Poisson noise and sky uncertainty contributions, and the (generally dominant)

error bars in the photometric transformation coefficients. We note that one error source not included by Han nor 'SFOTO' in the error budget for surface brightness is uncertainty in plate scale. Telescope apertures, f/ratios and focal lengths are often only approximately specified to users; plate scales should ideally be directly measured by telescope shifting and multiple exposures, or imaging of astrometrically calibrated fields. We did not do so. In fact, we entered an incorrect plate scale (2.608 in place of 2.635 arcsec per pixel) when reducing the Schmidt (run 6) data. Surface brightnesses were thus overestimated in this case by 2.5 $log(2.635^2/2.608^2) = 0.022$ mag arcsec^{-2} and this error times the slope of the integrated isophotal aperture magnitude m_{I_Σ} versus the local isophotal surface brightness Σ_I relation gives the error in isophotal magnitude. Since that slope is typically ~ 0.1 at $\Sigma_I \sim 24$ mag arcsec^{-2}, isophotal magnitudes for run 6 have been left unchanged.

Radial profiles of I band surface brightness, of integrated I band magnitude, and of integrated $V - I$ color are presented in Figure 1 for objects enjoying calibrated V and I band photometry.

C. Isophotal magnitude extraction

Isophotal magnitudes for 189 calibrated photometric observations of 159 different objects are given in Table VI. I band magnitudes are listed at the $\Sigma_I = 22.5$, 23.0, 23.5 and 24.0 mag arcsec^{-2} level, along with their associated error bars. Letters 'I' and 'E' denote whether isophotal magnitudes were obtained by interpolation between directly determined points on the (m_{I_Σ}, Σ_I) curve or by extrapolation using the exponential disk law fit described below.

Isophotal magnitudes at surface brightness levels bracketed by values in column 2 of an SFB file, that is, bracketed by values determined directly by photon counts, are assessed by fitting a line $m_{I_\Sigma} = a\ \Sigma_I + b$ to the points bracketing the desired isophote.

Extrapolated isophotal and 'total' magnitudes were obtained by user selecting a portion of the radial surface brightness profile $\Sigma_I(r)$ by cursor, a line being fit to the points therein, and by picking a point (not necessarily the last one in the profile) from which extrapolation is to be made. Frequently

the last one or two isophotes contained imperfectly smoothed out starlight and exponential disk law extrapolation was performed from a point further in. (Courteau (CT) automated this procedure to fit the exponential law between radii containing fixed fractions of the detected light.)

The term 'exponential disk law' implies that light intensity falls off exponentially as a function of radial distance from the center of a galaxy. If the count rate per unit solid angle from an isophote at (angular) distance r along the major axis from the galaxy center can be described by

$$dN/dt/d\Omega(r) = K_0 exp(-r/r_0) \qquad (2-13)$$

then the surface brightness profile $\Sigma(r)$ in magnitudes per arcsecond squared will read

$$\Sigma = Ar + B, \qquad (2-14)$$

where

$$r_0 = 1.0857/A \qquad (2-15)$$

is the exponential disk law (EDL) scale length, and

$$B = -2.5\ log(K_0) \qquad (2-16)$$

is the EDL central surface brightness. The magnitude increment $\Delta m(r_1, r_2)$ from radius r_1 to r_2 is given by

$$\Delta m(r_1, r_2) = -2.5\ log[1+ < b/a > (q(x_1) - q(x_2)) \times\ 10^{-0.4I_t+0.4I(r_1)}], \qquad (2-17)$$

where $< b/a >$ is the average axial ratio of the outer galaxy ellipses, which is related to the inclination angle i_{disk} inferred for the galaxy by:

$$r = max[q_0, < b/a >]; \qquad (2-18)$$

$$if\ \ r\ =\ q_0,\ i_{disk}\ =\ 90^\circ \qquad (2-19)$$

$$else \;\; cos(i_{disk}) = \sqrt{(r^2 - q_0^2)/(1 - q_0^2)}; \qquad (2-20)$$

where

$$q_0 = 0.2 \qquad (2-21)$$

is taken to be the intrinsic axial ratio of an edge on spiral galaxy (HT). Further quantities include

$$x = r/r_0, \qquad (2-22)$$

$$q(x) = (1+x)exp(-x), \qquad (2-23)$$

and

$$I_t \;=\; B \;-\; 5\; log(r_0) \;-\; 2.5\; log(2\pi) \qquad (2-24)$$

is the total magnitude for a galaxy wholly described by the EDL. $I(r_1)$ is the actual integrated magnitude at the point r_1 from which the extrapolation is to be applied (HT). As r_2 goes to infinity this yields the estimated total extrapolated magnitude for the galaxy. To assess the isophotal magnitude at some surface brightness level Σ_E beyond those determined directly, the r_2 satisfying

$$\Sigma_E \;=\; A\; r_2 + B \qquad (2-25)$$

is found and Eqn. 2-17 above solved for $\Delta m(r_1, r_2)$. The isophotal magnitude is then

$$m_{I_{\Sigma_E}} = I(r_1) + \Delta m(r_1, r_2). \qquad (2-26)$$

Error bars for Δm were assessed by differentiating the above expression for Δm by all pertinent quantities bearing error bars (r_0, K_0, $< b/a >$, and $I(r_1)$) and adding all contributions $(\partial \Delta m \;/\; \partial_x) \times \Delta_x$ in quadrature. Total galaxy magnitudes were assessed by setting r_2 to infinity in Eqn. 2-17 above; the explicit formulae are given in HT.

In addition to contents already described, Table VI contains the inclination angle i_{disk} assessed from the median axial ratio $< a/b >$ of ellipses selected by user from the radial ellipticity profile, and r_0 and $B = \Sigma_0$ from the line fit to the EDL portion of the SB profile.

'Isophotal' $V - I$ colors for 183 observations of 157 objects are listed in Table VII. Since 'SFOTO' does not extrapolate V band or $V - I$ profiles, $V - I$ are only determined when directly assessed by photon counts within elliptical apertures used for the I band counts. Table VII lists interpolated values of cumulative, or integral, $V - I$ values at Σ_I = 20.0, 20.5, 21.0, 21.5 and 22.0 mag arcsec^{-2} levels.

VII. Repeatability of photometric results

27 objects observed more than once (hence, enjoying two or more entries in Table VI) allow us to estimate the repeatability of the entire observing and data reduction procedure described above. If quantities measured twice on different dates and/or at different sites differed by amounts substantially greater than their error bars we would be forced to conclude that systematic effects limit the confidence we may place on those quantities; fortunately this did not prove to be the case.

A. Repeatability of I band isophotal magnitudes

For each of 27 objects a pair of observations was taken from Table VI. The absolute value of the I band magnitude difference Δm_{I_Σ} between each pair of observations was then assessed, and averages and variances of $|\Delta m_{I_\Sigma}|$ at each isophotal level from 22.5 to 24.0 mag arcsec^{-2} computed. The averages were assessed for the 27 objects. These objects were broken down as well into groups based on how each isophotal magnitude was determined:

i - both magnitudes interpolated from the run of direct counts within the elliptical apertures provided by 'GASP' (INT/INT),

ii - both extrapolated using the exponential disk law fit (EXT/EXT), or

iii - one of each (INT/EXT).

Results are given in Table VIII. Note that overall, $m_{I_{22.5}}$ is repeated to within 0.04 mag on average, while $m_{I_{24.0}}$ is repeated to about $\sim$ 0.06 mag. Table VIII also shows the averages and variances for magnitude differences $|\Delta m_{I_\Sigma}|$ divided by measurement errors in same; should this dimensionless quantity notably exceed unity, systematic errors would be said to dominate. We see that repeated measurements of isophotal magnitudes generally differ by amounts comparable to the measurement errors.

B. Run to run offsets in isophotal I magnitudes

One may also seek systematic differences between runs for the few run pairs enjoying several overlap objects. 8 objects common to T36/3/90 (run 2) and T36/3/91 (run 5) show $m_{I_{24.0}}(1990)$ brighter than $m_{I_{24.0}}(1991)$ by 0.05 $\pm$0.07 magnitudes. 6 objects common to P60/4/91 (run 7) and TSC/3/91 (run 6) give a similar result. All run pairs with at least two overlap objects are listed in Table IX. N_I and N_E list the numbers of magnitudes in each group produced by INTerpolation or EXTrapolation, respectively. Although greater numbers of overlap observations would have been useful, the results suggest that strong systematic differences between runs, which could induce spurious large-scale features into the inferred peculiar velocity field, are not present in our I band photometry.

The matchup between runs 6 and 7 is particularly gratifying since the former data, taken on the Tololo Schmidt, had unique plate scale and diffraction properties, required heavier use of aperture correction techniques on standard star growth curves, and the overlap objects were generally observed through higher than ideal ($\sim$ 1.5) airmasses at Tololo. The Palomar data in that comparison, for their part, had sky assessed only in very small portions of the field of view, since these overlap

objects were generally larger than the P60/CCD 11 field of view (this being the motivation for using the Schmidt in the first place).

We nevertheless underscore the desire for greater numbers of overlap objects for photometric projects spanning several observing seasons and using a mixture of cameras, detectors and observing sites.

C. Repeatability of 'isophotal' V-I magnitudes

Averages and variances for the absolute values of differences in integrated $V-I$ values between paired independent observations of galaxies at isophotal Σ_I levels 20.0 to 22.0 mag arcsec^{-2} are listed in Table X. (Since neither V nor $V-I$ profiles were not extrapolated beyond the last ellipse provided by 'GASP', $V-I$ values were often unavailable at deeper Σ_I levels.) $V-I$ did not reproduce quite as nicely as m_I: on average, independent measurements of 'isophotal' $V-I$ differ by 0.055 magnitude; furthermore, these differences exceed the measurement errors (estimated from photon counting statistics and from stated error bars on photometric transformation coefficients) on $V-I$ typically by $\sim$ 40 percent. Poorer flatfielding, shorter exposures in V, and the reliance on establishing the spatial X-Y translation from the I to the V frame required to prepare the $V-I$ profile with generally few reference stars presumably all contribute to the error budget.

Systematic differences in 'isophotal' $V-I$ values between the two March Tololo runs (1990, 1991) came in at 0.04$\pm$0 .05 mag; in any case a wide range of offsets between galaxies is reflected in the 0.05 - 0.06 mag variances listed in Table XI. Neither run pair listed in Table XI shows a glaring systematic trend in $V-I$ offset, nor a statistically significant one.

D. Repeatability of magnitude extrapolation via exponential disk law fitting

Unlike Courteau (CT), we did not design an algorithm to objectively select the region of the surface brightness profile in which to fit a line to the plot of $\Sigma_I = Ar + B$.

The fit region was selected by eye, and considerable uncertainty derived from the frequently seen steep falloff region followed by a shallower portion at outermost radii: the shallower outermost portion might sensibly be attributed to sky subtraction error or imperfect removal of contaminating starlight, and was usually excluded from the fit. Objective separation of inclined spiral galaxy SB profiles into bulge and disk components is nontrivial and profiles often show little evidence of pure EDL behavior.

Putting aside objections to the EDL fitting procedure, we may ask about its repeatability. 71 profiles enjoyed two independent EDL fits each (by J. Roth), one set performed in December 1991 and the second in April 1992. In each case a total integrated galaxy magnitude I was assessed following the prescription of equation 2-16 in section VI C above, with r_2 set to infinity. The difference between $m_I^{tot}(1991)$ and $m_I^{tot}(1992)$ for each profile, as well as its absolute value, was assessed and Δ_I, $|\Delta_I|$ each averaged within individual nights; the results are in Table XII.

Generally the extrapolation procedure reproduces m_I^{tot} to about 0.025 mag (with appreciable scatter in that value). The column $< m_I^{tot}(2) - m_I^{tot}(1) >$, where assessed, shows that systematic, not random, differences in approach between 1991 and 1992 are responsible for most of $< m_I^{tot}(2) - m_I^{tot}(1) >$; thus a more explicit or objective algorithm for fitting the EDL could notably reduce the additional scatter in m_I^{tot} produced by EDL fitting and extrapolation (Courteau CT). The tabulated $< m_I^{tot}(2) - m_I^{tot}(1) >$ are no greater than the limits to photometric repeatability established in subsections A – B above; in quadrature, EDL fitting and extrapolation does not appear to dominate the error budget.

In practice we restricted ourselves to working with isophotal magnitudes m_{I_Σ} at the $\Sigma_I = 23.5\ mag\ arcsec^{-2}$ level when fitting models predicting galaxy distances to the data.

Table I: Imaging Systems Used in 4KVL Project

RUN:	P60/11/89 (1)	T36/3/90 (2)	P60/8/90 (3)	T36/9/90 (4)	T36/3/91 (5)	TSC/3/91 (6)	P60/4/91 (7)
TEL:	PAL 60	CTIO 36	PAL 60	CTIO 36	CTIO 36	CTIO SCHMT	PAL 60
APERTURE: (inches)	60	36	60	36	36	24	60
f/RATIO:	3.2	13.5	8.75	13.5	13.5	3.5	8.75
CCD:	TI 365 (4)	TEK 4	TEK (11)	TEK 4	THOMPSON 2	TEK (4?)	TEK (11)
N_{PIX}: (side)	800	512	1024	512	512 (binned)	512	1024
S_{PIX}: (microns)	15	27	24	27	38 (binned)	27	24
S_{PIX}: (arcsec)	0.64	0.445	0.376	0.445	0.626 (binned)	2.635	0.376
FOV: (arcmin)	8.5	3.8	6.4	3.8	5.3	22.5	6.4
GAIN: (e-/DN)	2.0	2.6	2.4	3.1	2.7	2.9	2.4
RD NSE: (e-/pix)	8	9	5.5	7	4	7	5.5
Nr CLEAR: NIGHTS	2	4	2	2	4	2	3
NOTES:	w/reducing optics				CCD ghosts if satur. ——— 2x2 binned	Scale mis-speced in SFB files as 2.608	

Table II - standard stars employed in photometric solutions - page 1

name	ref	α			δ				epoch	m_I	$m_V - m_I$	runs
HD 2892	L1	00	31	26	+	01	06	13	(1985)	9.366	+1.319	1
HD 5505	L1	00	56	05	+	01	36	00	(1985)	9.001	+1.056	1, 4
HD 16581	L1	02	38	46	+	01	17	26	(1985)	8.195	-0.063	1
36395	L1	05	30	43	-	03	41	39	(1985)	7.960	+2.076	1
SA 97 346	L1	05	56	41	+	00	13	17	(1985)	9.260	+0.662	1
BD+5 1668	L1	07	26	36	+	05	16	16	(1985)	9.843	+2.714	1
SA 99 6	L1	07	52	48	-	00	47	12	(1985)	11.054	+1.229	2
SA 100 162	L1	08	52	29	-	00	40	03	(1985)	9.148	+1.204	1
SA 101 281	L1	09	56	19	-	00	27	20	(1985)	11.579	+0.866	7, 5, 6
SA 101 282	L1						25	42	(1985)	10.002	+0.520	7, 5, 6
SA 107 970	L1	15	36	40	+	00	21	30	(1985)	10.910	+2.567	2, 7
SA 108 475	L1	16	36	14	-	00	32	53	(1985)	11.308	+1.408	2
SA 109 231	L1	17	44	34	-	00	25	31	(1985)	9.331	+1.492	2
E3 T	G	06	41	50	-	45	08	00	(1980)	8.953	+1.100	6
E3 t	G		42	00	-		02	12	(1980)	14.666	+0.848	6
E3 e	G		42	01	-		07	56	(1980)	12.174	+0.693	6
E3 o	G		42	11	-		09	36	(1980)	14.142	+0.662	6
E3 k	G		42	19	-		07	42	(1980)	13.418	+0.660	6
E3 R	G		42	39	-		13	17	(1980)	10.620	+0.039	2, 4, 5, 6
E3 X	G		42	45	-		11	44	(1980)	10.799	+0.546	2, 4, 5, 6
E4 57-a	G	09	23	07	-	45	17	15	(1980)	9.829	+1.514	2
E5 o	G	12	04	02	-	45	27	03	(1980)	15.718	+0.807	6
E5 m	G		04	02	-		27	30	(1980)	15.016	+0.798	6
E5 k	G		04	09	-		27	07	(1980)	14.747	+0.629	6
E5 h	G		04	20	-		30	00	(1980)	12.920	+1.305	6
E5 Y	G		04	22	-		24	52	(1980)	12.814	+0.055	2, 5, 6
E5 c	G		04	26	-		25	50	(1980)	12.437	+0.962	2, 5, 6
E5 S	G		03	28	-		22	01	(1980)	9.897	+0.689	6
E5 U	G		02	50	-		22	46	(1980)	9.295	+1.224	6
E7 m	G	17	25	54	-	45	00	34	(1980)	11.293	+1.295	3
E7 s	G		25	56	-		01	01	(1980)	13.457	+0.768	3
E549	W	12	05	00	-	45	29	03	(1986.5)	7.391	+1.938	2
E708	W	17	25	16	-		09	48	(1986.5)	10.548	+0.255	2
E756	W		26	08	-		07	14	(1986.5)	0.190	+1.216	2

Table II - standard stars employed in photometric solutions - page 2

name	ref	α	δ	epoch	m_I	$m_V - m_I$	runs
M67 81	S				10.075	-0.068	7
M67 117	S				11.765	+0.912	7
M67 124	S	08 48 37	+ 11 57 33	(1950)	11.582	+0.565	7
M67 127	S				12.144	+0.672	7
M67 135	S				10.396	+1.069	7
SA110A L	L/T				11.29	+2.36	7
SA110A M	L/T	18 40 08	+ 00 01 00	(1987)	13.11	+1.22	7
SA110A N	L/T				11.64	+0.88	7
SA110A O	L/T				11.21	+1.60	7
SA110C D	L/T				11.73	+0.70	7, 3, 4
SA110C E	L/T	18 42 17	+ 00 08 20	(1990.5)	12.34	+1.28	7, 3, 4
SA110C F	L/T				10.84	+2.63	7, 3, 4
SA113D A	L/T	21 40 20	+ 00 24 00	(1987)	11.56	+0.69	3
SA113D B	L/T				9.81	+1.70	3
SA114 750	L/T	22 40 59	+ 01 07 54	(1985)	11.913	+0.013	4
PG1323 *	L/S				13.608	-0.127	7
PG1323 B	L/S	13 23 02	- 08 33 41	(1950)	12.573	+0.833	7
PG1323 C	L/S				13.244	+1.141	7
PG16 A	L/S				16.264	+1.010	6
PG16 B	L/S	16 33 01	+ 09 53 56	(1950)	11.872	+1.094	7, 5, 6
PG16 C	L/S				12.083	+1.141	7, 5, 6
PG16 D	L/S				11.399	+0.681	5, 6

Table III - Aperture Photometry (modified FIGARO/FOTO) parameters

RUN:	P60/11/89	T36/3/90	T36/9/90	P60/8/90	T36/3/91	TSC/3/91	P60/4/91	units
$r_1 - r_2$	N/A	6–30 2.7–15	6-30 2.7–15	6.5–32 2.4–11.8	5–25 3.1–15.6	3–15 7.8–39	6.5–32 2.4–11.8	pixels arcsec
$\Delta m/\Delta r$:	-.001	N/A	N/A	N/A	N/A	N/A	N/A	mag/arcsec
r_{sky_1} – r_{sky_2}:	71–80 45–51	37–47 16–21	37–47 26–21	N/A	31–40 19–25	25–31 65–81	40–52 15–19	pixels arcsec
sky est:	mean	'mode'	'mode'	global	'mode'	'mode'	'mode'	
scale:	0.64	0.44	0.44	0.37	0.63	2.6	0.37	arcsec/pix
notes:	many defoc stds; all grth crvs satisfied gradient	same as T36 9/90	same as T36 3/90	same CCD, ap cor as P60/91		gross difn spikes fm lrg 2ndry mirror; good g.crv templates rare	same CCD, ap cor as P60/90	

Table IV: extinction coefficients

run	night	k_I	k_V	notes
P60/11/89	all	.05	.14	by fiat per JRM
T36/3/90	n19	.07	.13	measured
	n20	.09	.22	measured
	n21	.06	.14	measured
	n22	.05	.13	measured
P60/8/90	n2	.03	.11	measured
T36/9/90	all	.05	.14	measured and averaged over run
T36/3/91	all	.05	.18	measured and averaged over run
TSC/3/91	all	.05	.18	taken from T36/3/91 prev 4 nts
P60/4/91	all	.05	.16	measured and averaged over run

Table V - Photometric transformation coefficients for SFOTO

m_I^{obs}, m_V^{obs} = instrumental magnitudes; m_I^{cat}, m_V^{cat} = catalogued magnitudes

'HMS' system: $m_I^{cat} = A + m_I^{obs} + B(m_V^{cat} - m_I^{cat})$, $m_V^{cat} - m_I^{cat} = C + D(m_V^{obs} - m_I^{obs})$;

A ◁ A + 31 (31 being 'FOTO' magnitude offset)

RUN: (night)	A ΔA	B ΔB	C ΔC	D ΔD	k_I k_V
P60/11/89	21.541	-.030	1.599	1.072	.05
(n5)	(.025)	(.025)	(.10)	(.025)	.14
P60/11/89	21.577	-.046	1.540	0.976	.05
(n7)	(.010)	(.020)	(.020)	(.020)	.14
T36/3/90	21.681	-0.013	0.609	0.988	.070
(n19)	(.007)	(.009)	(.004)	(.009)	.128
T36/3/90	21.663	-0.019	0.698	0.972	.088
(n20)	(.009)	(.012)	(.015)	(.023)	.224
T36/3/90	21.627	0.006	0.642	0.968	.060
(n21)	(.012)	(.010)	(.01)	(.011)	.141
T36/3/90	21.651	-0.0086	0.640	0.981	.053
(n22)	(.014)	(.011)	(.006)	(.009)	.127
P60/8/90	21.761	-0.034	0.600	1.102	.032
(n2)	(.025)	(0.10)	(.025)	(0.10)	.107
P60/8/90	Unexplained QE glitches				
(n3)	prevent calibration				
T36/9/90	21.637	-0.005	0.716	1.053	.048
(n6)	(.009)	(.03)	(.007)	(.02)	.140
T36/9/90	21.647	-0.0043	0.719	0.957	.048
(n7)	(.017)	(.018)	(.006)	(.02)	.140
T36/3/91	20.690	-0.027	0.877	1.012	.053
(n1)	(.015)	(.015)	(.012)	(.021)	.182
T36/3/91	20.660	-0.044	0.966	1.061	.053
(n2)	(.006)	(.025)	(.026)	(.04)	.182
T36/3/91	20.665	-0.0073	0.940	1.048	.053
(n3)	(.006)	(.014)	(.02)	(.05)	.182
T36/3/91	20.648	-0.0066	0.951	1.012	.053
(n4)	(.005)	(.014)	(.014)	(.03)	.182
TSC/3/91	20.168	≡ 0	0.803	≡ 1.0	.053
(n1)	(.02)	(.02)	(.02)	(.02)	.182
TSC/3/91	20.201	≡ 0	0.790	≡ 1.0	.053
(n2)	(.02)	(.02)	(.02)	(.02)	.182
P60/4/91	21.792	≡ 0	0.657	1.082	.054
(n2)	(.009)	(.019)	(.007)	(.016)	.160
P60/4/91	21.748	≡ 0	0.633	1.090	.054
(n4)	(.004)	(.007)	(.006)	(.018)	.160
P60/4/91	21.757	-0.010	0.642	1.089	.054
(n5)	(.004)	(.008)	(.004)	(.013)	.160

Table VI - Observed surface brightness profiles, 4KVL objects – page 1

obj	obs	i	m_I^{tot}	$m_I^{22.5}$	σ		$m_I^{23.0}$	σ		$m_I^{23.5}$	σ		$m_I^{24.0}$	σ		Σ_0	r_0
1	P60 89 PL	79	10.64	10.73	0.04	I	10.70	0.04	I	10.67	0.05	I	10.66	0.05	E	16.73	17.24
2	P60 90 PD	75	12.58	12.73	0.10	I	12.68	0.10	I	12.64	0.10	I	12.61	0.11	E	16.67	7.96
7	T36 90 PD	63	11.94	12.04	0.03	I	12.01	0.03	I	11.98	0.03	I	11.97	0.14	E	16.92	7.71
7	T36 90 PD	63	11.90	12.00	0.02	I	11.96	0.02	I	11.94	0.09	E	11.92	0.09	E	17.60	8.89
8	P60 90 PD	66	11.31	11.49	0.12	I	11.44	0.12	I	11.40	0.12	I	11.38	0.12	I	18.74	15.56
15	T36 90 PD	81	11.58	11.68	0.03	I	11.64	0.03	I	11.62	0.03	I	11.60	0.18	E	16.86	12.06
15	T36 90 PD	82	11.56	11.67	0.01	I	11.64	0.01	I	11.62	0.01	I	11.60	0.01	I	12.34	7.17
18	T36 90 PD	44	11.49	11.55	0.03	I	11.53	0.03	I	11.52	0.04	E	11.51	0.04	E	17.05	6.81
19	P60 90 PD	84	12.23	12.31	0.15	I	12.28	0.15	E	12.26	0.15	E	12.25	0.15	E	17.56	10.50
19	P60 89 PL	77	12.24	12.38	0.03	I	12.34	0.03	I	12.30	0.03	I	12.27	0.03	E	18.67	12.72
25	T36 90 PD	73	12.44	12.59	0.03	I	12.54	0.03	I	12.50	0.03	I	12.47	0.03	I	16.79	7.74
28	P60 89 PL	73	10.65	10.87	0.04	I	10.81	0.04	I	10.75	0.04	I	10.70	0.05	E	19.10	30.76
31	P60 89 PL	77	12.35	12.43	0.03	I	12.40	0.03	I	12.38	0.03	I	12.36	0.45	E	16.08	6.73
33	P60 89 PL	66	11.81	12.15	0.04	I	12.09	0.04	I	12.02	0.04	I	11.94	0.05	I	21.17	28.03
42	P60 89 PL	73	13.06	13.15	0.02	I	13.11	0.02	I	13.08	0.03	I	13.07	0.03	E	16.98	4.72
43	P60 89 PL	65	9.87	10.06	0.04	I	9.99	0.05	E	9.95	0.05	E	9.92	0.05	E	19.65	42.03
44	T36 90 PD	58	9.88	10.04	0.03	I	9.97	0.03	I	9.91	0.04	E	9.90	0.04	E	17.35	20.11
49	P60 90 PD	52	12.68	12.87	0.13	I	12.81	0.13	I	12.78	0.13	I	12.74	0.13	E	19.52	8.96
53	P60 90 ?D	61	12.80	13.04	0.22	I	12.97	0.21	I	12.91	0.20	I	12.87	0.20	E	19.00	10.02
53	P60 89 PL	63	12.73	13.03	0.05	I	12.93	0.06	I	12.85	0.07	E	12.81	0.07	E	19.40	12.66
54	P60 89 PL	72	11.07	11.22	0.03	I	11.18	0.03	I	11.13	0.03	I	11.09	0.29	E	16.32	12.94
55	P60 89 PL	38	12.02	12.16	0.03	I	12.10	0.47	E	12.07	0.46	E	12.04	0.45	E	14.19	6.65
59	P60 89 PL	72	10.63	10.74	0.03	I	10.70	0.04	I	10.67	0.06	E	10.65	0.06	E	16.94	17.24
62	T36 90 PD	39	11.65	11.79	0.01	I	11.74	0.01	I	11.70	0.01	E	11.68	0.01	E	18.00	10.07
64	P60 89 PL	58	11.77	12.06	0.06	I	11.96	0.06	I	11.88	0.15	E	11.84	0.16	E	18.82	16.17
66	P60 89 PL	55	9.94	10.28	0.04	I	10.19	0.04	I	10.10	0.04	I	10.04	0.04	E	20.48	48.56
69	P60 89 PL	50	11.23	11.38	0.06	I	11.31	0.06	I	11.28	0.07	E	11.26	0.07	E	18.67	13.30
71	P60 89 PL	58	10.88	11.01	0.05	I	10.98	0.05	E	10.94	0.06	E	10.92	0.06	E	19.05	20.25
77	T36 91 PD	60	9.76	9.86	0.04	I	9.82	0.04	I	9.80	0.05	E	9.79	0.05	E	18.04	24.51
79	TSC 91 PD	45	8.74	8.90	0.03	E	8.85	0.03	E	8.82	0.03	E	8.79	0.03	E	18.81	47.06
80	T36 90 PD	53	12.13	12.25	0.02	I	12.21	0.02	I	12.19	0.03	I	12.17	0.03	I	15.02	5.31
82	P60 89 PL	56	11.90	12.53	0.05	I	12.39	0.05	I	12.19	0.05	I	12.13	0.06	I	20.90	24.99
83	P60 89 PL	60	13.56	13.72	0.03	I	13.64	0.03	I	13.60	0.03	I	13.59	0.05	E	18.05	4.25
87	T36 90 PD	73	12.23	12.35	0.01	I	12.33	0.01	I	12.30	0.01	I	12.27	0.01	I	16.74	7.22
90	TSC 91 PD	62	9.09	9.18	0.03	I	9.15	0.03	I	9.13	0.03	I	9.12	0.03	I	17.28	29.50
91	T36 90 PD	45	12.02	12.11	0.01	I	12.08	0.01	I	12.06	0.02	E	12.05	0.02	E	18.09	7.13
91	T36 90 ?D	46	12.05	12.12	0.01	I	12.10	0.01	I	12.08	0.08	E	12.07	0.08	E	17.76	6.54
92	TSC 91 PD	45	8.78	9.01	0.03	I	8.93	0.03	I	8.85	0.03	I	8.82	0.03	I	14.28	26.92
93	T36 90 PD	67	11.76	11.96	0.03	I	11.91	0.03	I	11.84	0.03	I	11.81	0.03	I	17.59	10.46
94	T36 91 PD	41	12.40	12.60	0.02	I	12.53	0.02	I	12.48	0.02	I	12.45	0.03	E	19.04	8.71

Table VI - Observed surface brightness profiles, 4KVL objects – page 2

obj	obs	i	m_I^{tot}	$m_I^{22.5}$	σ		$m_I^{23.0}$	σ		$m_I^{23.5}$	σ		$m_I^{24.0}$	σ		Σ_0	r_0
94	T36 90 PD	42	12.32	12.61	0.01	I	12.54	0.01	I	12.47	0.01	I	12.39	0.02	I	18.19	6.03
96	T36 91 PD	73	11.78	11.94	0.03	I	11.91	0.03	I	11.88	0.03	I	11.85	0.03	I	17.99	11.69
98	P60 91 PD	76	12.03	12.27	0.03	I	12.18	0.03	I	12.13	0.03	E	12.10	0.03	E	19.32	19.37
99	T35 91 PD	51	10.70	11.18	0.03	I	11.07	0.03	I	10.95	0.03	I	10.84	0.03	I	20.78	38.15
99	P60 89 PL	75	10.89	11.14	0.05	I	11.02	0.05	I	10.97	0.05	E	10.95	0.05	E	20.29	33.66
101	P60 91 PD	84	12.77	12.91	0.03	I	12.86	0.03	I	12.83	0.03	E	12.81	0.03	E	17.93	10.38
105	P60 89 PL	65	11.23	11.32	0.05	I	11.28	0.16	E	11.26	0.16	E	11.25	0.16	E	16.69	11.41
106	P60 89 PL	43	11.47	11.61	0.04	I	11.58	0.04	I	11.55	0.04	I	11.50	0.04	I	17.33	8.81
109	P60 89 PL	44	10.56	10.72	0.03	I	10.66	0.03	I	10.62	0.05	E	10.60	0.05	E	18.68	19.55
110	P60 91 ND	41	11.26	11.59	0.01	I	11.51	0.01	I	11.43	0.01	I	11.36	0.02	E	20.87	24.94
114	P60 89 PL	86	12.93	13.21	0.03	I	13.12	0.03	I	13.05	0.04	I	13.00	0.04	E	20.08	17.24
115	T36 91 PD	83	10.88	11.01	0.03	I	10.96	0.03	I	10.93	0.03	I	10.91	0.09	E	17.27	21.94
115	TSC 91 PD	80	10.89	11.01	0.03	I	10.97	0.03	I	10.94	0.03	I	10.92	0.59	E	15.74	17.16
117	P60 91 ?D	52	11.21	11.37	0.01	I	11.34	0.01	I	11.31	0.01	I	11.27	0.01	I	18.55	13.64
118	T36 90 ?D	90	11.88	12.03	0.02	I	11.97	0.02	I	11.93	0.26	E	11.91	0.26	E	16.94	15.48
126	P60 89 PL	47	12.38	12.46	0.04	I	12.43	0.04	I	12.41	0.04	I	12.40	0.15	E	15.88	4.60
132	T36 90 PD	47	11.34	11.50	0.02	I	11.44	0.02	I	11.40	0.02	I	11.38	0.03	E	18.50	13.23
134	P60 91 ?D	49	11.07	11.17	0.01	I	11.13	0.22	E	11.11	0.22	E	11.10	0.22	E	16.61	10.41
134	P60 89 PL	50	11.01	11.19	0.04	I	11.15	0.04	I	11.10	0.04	I	11.06	0.04	I	17.60	13.05
136	T36 91 PD	73	11.84	11.93	0.05	I	11.90	0.09	E	11.88	0.09	E	11.87	0.09	E	16.50	9.76
139	P60 91 PD	65	12.23	12.36	0.02	I	12.32	0.02	I	12.29	0.02	I	12.27	0.02	I	16.81	7.32
141	P60 91 ?D	66	11.93	12.04	0.01	I	11.99	0.01	I	11.97	0.02	E	11.96	0.02	E	17.87	9.24
143	P60 91 PD	71	12.00	12.19	0.01	I	12.14	0.01	I	12.10	0.01	I	12.06	0.01	I	17.44	9.78
150	P60 91 ?D	60	7.99	8.05	0.03	E	8.03	0.03	E	8.02	0.03	E	8.01	0.03	E	17.40	45.02
150	TSC 91 PD	65	7.91	8.05	0.03	I	8.02	0.03	I	7.99	0.03	I	7.97	0.03	I	19.28	82.17
151	T36 91 PD	76	12.09	12.17	0.08	E	12.14	0.08	E	12.12	0.08	E	12.11	0.08	E	17.26	9.42
151	T36 90 PD	76	11.99	12.07	0.03	E	12.05	0.03	E	12.03	0.03	E	12.01	0.03	E	17.67	10.73
154	P60 91 ?D	59	11.96	12.02	0.01	I	12.00	0.01	I	11.98	0.01	I	11.97	0.09	E	15.90	5.43
154	T36 91 PD	55	11.94	12.00	0.04	I	11.98	0.04	I	11.96	0.04	I	11.95	0.17	E	14.53	4.42
159	T36 91 PD	42	11.72	11.82	0.02	E	11.79	0.02	E	11.77	0.02	E	11.75	0.02	E	18.51	8.77
163	T36 90 PD	85	12.11	12.32	0.02	I	12.25	0.02	I	12.20	0.02	I	12.16	0.07	E	18.54	17.03
167	P60 89 PL	55	10.93	11.16	0.03	I	11.09	0.04	I	11.03	0.04	I	10.99	0.04	E	18.93	21.02
169	T36 91 PD	49	9.69	9.85	0.07	E	9.80	0.08	E	9.76	0.08	E	9.74	0.09	E	18.77	30.90
170	P60 91 ?D	85	11.36	11.50	0.01	I	11.46	0.01	I	11.43	0.01	I	11.40	0.01	I	11.83	8.54
171	T36 91 PD	57	12.25	12.35	0.04	I	12.32	0.04	I	12.30	0.04	I	12.29	0.04	I	17.14	6.21
172	T36 91 PD	64	11.64	11.77	0.03	I	11.73	0.03	I	11.69	0.10	E	11.67	0.10	E	17.25	10.89
176	T36 90 PD	50	11.39	11.45	0.06	E	11.43	0.07	E	11.42	0.07	E	11.41	0.07	E	17.16	7.95
179	T36 91 PD	58	10.98	11.09	0.04	I	11.05	0.04	I	11.02	0.40	E	11.01	0.40	E	16.44	11.44
181	T36 90 PD	78	11.99	12.12	0.01	I	12.08	0.01	I	12.06	0.01	I	12.02	0.06	E	17.94	12.10
189	P60 90 PL	53	11.56	11.69	0.01	I	11.66	0.01	I	11.63	0.01	I	11.60	0.01	I	16.96	8.42

Table VI - Observed surface brightness profiles, 4KVL objects – page 3

obj	obs	i	m_I^{tot}	$m_I^{22.5}$	σ		$m_I^{23.0}$	σ		$m_I^{23.5}$	σ		$m_I^{24.0}$	σ		Σ_0	r_0
193	P60 91 ?D	62	7.87	7.95	0.02	E	7.92	0.02	E	7.91	0.02	E	7.89	0.02	E	18.46	60.02
193	TSC 91 PD	57	7.68	7.94	0.03	I	7.89	0.03	I	7.84	0.03	I	7.79	0.03	I	20.91	37.75
194	T36 90 PD	57	11.19	11.44	0.02	I	11.37	0.02	I	11.30	0.02	I	11.26	0.10	E	19.19	20.75
198	T36 91 PD	65	10.22	10.37	0.05	I	10.32	0.07	E	10.29	0.07	E	10.27	0.07	E	18.56	27.82
203	T36 91 PD	70	10.24	10.32	0.04	I	10.29	0.21	E	10.27	0.21	E	10.26	0.21	E	16.04	17.20
204	P60 91 ?D	69	11.06	11.18	0.01	I	11.15	0.01	I	11.12	0.01	I	11.10	0.02	E	19.24	17.77
206	TSC 91 PD	83	9.79	10.01	0.03	I	9.95	0.03	I	9.91	0.03	I	9.87	0.03	I	19.53	53.88
207	P60 91 PD	85	10.75	10.85	0.02	I	10.82	0.02	I	10.80	0.02	I	10.78	0.02	I	16.96	19.61
210	T36 91 PD	46	11.70	11.79	0.04	I	11.76	0.04	I	11.74	0.04	I	11.72	0.17	E	16.19	7.11
210	T36 90 ?D	45	11.65	11.75	0.01	I	11.72	0.01	I	11.70	0.02	I	11.68	0.06	E	16.98	8.31
213	T36 91 PD	70	10.53	10.65	0.05	I	10.61	0.05	I	10.59	0.08	E	10.57	0.08	E	18.61	22.61
216	T36 90 PD	72	10.86	11.00	0.02	E	10.95	0.02	E	10.93	0.02	E	10.91	0.03	E	18.57	22.10
223	T36 91 PD	39	9.33	9.44	0.04	I	9.40	0.04	I	9.38	0.04	I	9.36	0.04	I	18.09	23.70
225	P60 91 PD	83	12.65	12.76	0.02	I	12.73	0.02	I	12.70	0.02	I	12.68	0.02	I	17.03	8.38
226	P60 91 PD	54	10.66	10.90	0.01	I	10.83	0.01	I	10.77	0.01	I	10.73	0.01	I	19.24	22.65
228	P60 91 PD	56	9.92	10.00	0.03	I	9.98	0.03	I	9.96	0.03	I	9.94	0.03	I	16.33	13.95
229	T36 91 PD	67	12.94	13.05	0.03	I	13.02	0.03	I	12.99	0.03	I	12.96	0.03	I	17.36	5.54
231	T36 90 PD	59	10.61	10.75	0.02	I	10.70	0.02	I	10.67	0.29	E	10.65	0.29	E	16.69	16.87
232	T36 91 PD	75	10.49	10.59	0.05	I	10.56	0.08	E	10.54	0.08	E	10.52	0.08	E	17.95	23.54
239	P60 91 PD	45	11.22	11.41	0.01	I	11.35	0.01	I	11.30	0.01	I	11.26	0.01	I	17.42	11.16
240	P60 91 ?D	84	10.03	10.16	0.02	E	10.12	0.03	E	10.09	0.03	E	10.07	0.03	E	18.82	41.04
240	TSC 91 PD	77	9.96	10.15	0.03	I	10.09	0.03	I	10.05	0.03	I	10.02	0.03	I	18.20	38.82
246	TSC 91 PD	63	8.33	8.47	0.03	I	8.44	0.03	I	8.42	0.03	I	8.39	0.03	I	20.60	85.19
247	P60 91 ?D	77	9.25	9.33	0.01	I	9.29	0.01	I	9.27	0.11	E	9.26	0.11	E	15.16	24.41
247	TSC 91 PD	76	9.27	9.39	0.03	I	9.35	0.03	I	9.32	0.03	I	9.30	0.03	I	15.45	25.40
248	P60 91 ?D	73	9.62	9.78	0.05	E	9.73	0.05	E	9.69	0.06	E	9.67	0.06	E	18.89	45.83
248	TSC 91 PD	73	9.47	9.69	0.03	I	9.61	0.03	I	9.57	0.03	I	9.55	0.03	I	19.19	54.51
251	T36 91 PD	73	10.64	10.75	0.04	I	10.72	0.04	I	10.69	0.07	E	10.68	0.07	E	17.87	20.28
251	T36 91 PD	73	10.61	10.75	0.04	I	10.71	0.04	I	10.67	0.04	I	10.64	0.04	I	17.44	17.98
254	T36 91 PD	76	11.61	11.78	0.05	I	11.75	0.05	I	11.71	0.05	I	11.68	0.05	I	20.18	20.57
255	T36 91 PD	66	11.47	11.63	0.04	I	11.58	0.04	I	11.54	0.04	I	11.52	0.05	E	18.96	16.87
256	TSC 91 PD	81	9.52	9.59	0.03	I	9.57	0.03	I	9.54	0.03	I	9.54	0.04	E	17.38	29.12
257	T36 90 PD	85	12.33	12.41	0.03	E	12.38	0.03	E	12.36	0.03	E	12.35	0.03	E	17.07	9.86
258	T36 91 PD	35	10.00	10.18	0.03	I	10.12	0.03	I	10.08	0.03	I	10.05	0.13	E	18.56	23.45
260	T36 90 PD	61	11.62	11.84	0.01	I	11.79	0.01	I	11.74	0.01	I	11.69	0.02	I	19.40	16.40
262	T36 90 PD	78	12.74	12.83	0.01	I	12.80	0.04	E	12.78	0.04	E	12.76	0.04	E	17.79	8.03
265	P60 91 PD	56	10.93	11.03	0.02	I	10.98	0.02	I	10.97	0.03	E	10.95	0.03	E	17.65	12.66
267	T36 91 PD	74	10.04	10.16	0.03	I	10.12	0.03	I	10.09	0.03	I	10.07	0.26	E	16.39	21.38
269	TSC 91 PD	81	10.51	10.60	0.03	I	10.57	0.05	E	10.55	0.05	E	10.54	0.05	E	17.41	22.90
271	TSC 91 PD	62	10.17	10.46	0.03	I	10.37	0.03	I	10.31	0.03	I	10.26	0.03	I	18.18	31.42

Table VI - Observed surface brightness profiles, 4KVL objects – page 4

obj	obs	i	m_I^{tot}	$m_I^{22.5}$	σ		$m_I^{23.0}$	σ		$m_I^{23.5}$	σ		$m_I^{24.0}$	σ		Σ_0	r_0
276	T36 91 PD	66	12.73	12.82	0.03	I	12.79	0.03	I	12.77	0.03	I	12.75	0.80	E	15.22	4.38
278	T36 91 PD	75	11.12	11.23	0.04	I	11.19	0.04	I	11.17	0.04	I	11.15	0.04	I	16.54	13.19
278	T36 90 ?D	70	11.03	11.17	0.02	I	11.14	0.02	I	11.11	0.02	I	11.08	0.02	I	17.01	14.76
280	T36 91 PD	80	11.06	11.15	0.05	I	11.14	0.08	E	11.11	0.08	E	11.10	0.09	E	18.68	21.91
281	T36 91 PD	79	11.60	11.68	0.02	I	11.66	0.02	I	11.64	0.02	I	11.63	0.02	I	16.58	8.66
284	TSC 91 PD	54	9.53	9.78	0.03	I	9.71	0.03	I	9.66	0.03	I	9.62	0.03	I	18.91	40.30
284	TSC 91 PD	55	9.52	9.77	0.03	I	9.71	0.03	I	9.65	0.03	I	9.61	0.03	I	19.25	44.26
285	T36 91 PD	61	10.30	10.44	0.05	I	10.36	0.05	I	10.35	0.05	E	10.33	0.05	E	18.52	20.65
285	T36 90 ?D	53	10.26	10.44	0.02	I	10.38	0.02	I	10.33	0.02	I	10.31	0.03	E	19.30	26.54
286	T36 91 PD	90	11.40	11.50	0.05	I	11.47	0.05	I	11.44	0.05	I	11.43	0.17	E	16.62	16.55
287	T36 91 PD	57	10.82	10.99	0.03	I	10.93	0.03	I	10.89	0.05	E	10.87	0.05	E	18.10	18.77
295	T36 90 PD	82	12.07	12.37	0.02	I	12.29	0.02	I	12.23	0.02	I	12.18	0.02	I	19.59	23.33
298	T36 91 PD	65	10.66	10.83	0.03	I	10.79	0.03	I	10.75	0.03	I	10.72	0.03	I	18.84	22.82
298	TSC 91 PD	63	10.71	10.87	0.03	I	10.83	0.03	I	10.79	0.03	I	10.76	0.03	I	18.66	21.85
303	P60 91 ?D	56	9.25	9.36	0.01	I	9.31	0.01	I	9.29	0.10	E	9.28	0.10	E	17.65	29.24
303	TSC 91 PD	46	9.17	9.41	0.03	I	9.36	0.03	I	9.30	0.03	I	9.25	0.03	I	19.19	45.24
306	T36 90 PD	57	11.85	12.04	0.08	E	11.98	0.09	E	11.94	0.09	E	11.91	0.09	E	18.55	13.07
310	P60 91 PD	61	11.12	11.30	0.02	I	11.23	0.02	I	11.20	0.02	I	11.18	0.02	I	15.70	11.48
313	P60 91 PD	39	10.53	10.65	0.01	I	10.61	0.01	I	10.58	0.01	I	10.56	0.16	E	16.59	12.92
315	T36 90 PD	42	12.19	12.63	0.04	E	12.49	0.05	E	12.39	0.05	E	12.32	0.05	E	19.88	16.66
316	P60 91 PD	53	11.00	11.14	0.02	I	11.09	0.02	I	11.06	0.02	I	11.04	0.02	I	16.40	10.45
320	P60 91 PD	83	10.97	11.03	0.08	E	11.01	0.08	E	10.99	0.08	E	10.99	0.08	E	16.64	15.56
320	T36 91 PD	76	10.88	10.99	0.04	I	10.96	0.04	I	10.92	0.04	I	10.90	0.04	I	16.05	13.58
328	P60 91 PD	48	11.36	11.44	0.02	I	11.41	0.03	E	11.39	0.03	E	11.38	0.03	E	17.77	9.11
332	P60 91 PD	59	10.32	10.42	0.03	I	10.39	0.02	I	10.36	0.03	E	10.35	0.03	E	18.18	19.29
333	P60 91 ?D	63	10.06	10.16	0.01	I	10.14	0.01	I	10.12	0.01	I	10.10	0.01	I	15.00	13.93
334	T36 90 PD	90	11.79	11.88	0.09	E	11.85	0.10	E	11.83	0.10	E	11.81	0.10	E	17.16	14.95
336	T36 91 PD	39	11.63	11.90	0.02	I	11.82	0.02	I	11.78	0.02	I	11.74	0.02	I	18.61	12.80
336	T36 90 PD	48	11.61	11.90	0.01	I	11.81	0.01	I	11.75	0.01	I	11.70	0.02	I	19.29	15.55
337	T36 91 PD	71	10.48	10.63	0.05	I	10.57	0.05	I	10.52	0.05	I	10.51	0.05	E	18.69	23.43
338	T36 91 PD	66	10.21	10.43	0.05	I	10.33	0.05	I	10.26	0.09	E	10.24	0.09	E	18.00	22.01
346	T36 90 ?D	73	11.66	11.89	0.02	I	11.83	0.02	I	11.78	0.02	I	11.72	0.02	I	19.42	18.16
348	T36 91 PD	55	10.58	10.70	0.04	I	10.66	0.04	I	10.63	0.04	I	10.61	0.13	E	15.98	13.45
348	T36 90 ?D	58	10.51	10.62	0.02	I	10.58	0.02	I	10.55	0.12	E	10.54	0.12	E	16.46	14.83
349	T36 91 PD	69	10.69	10.78	0.07	E	10.75	0.07	E	10.74	0.07	E	10.72	0.07	E	17.82	17.25
350	T36 91 PD	88	11.50	11.67	0.05	I	11.62	0.05	E	11.58	0.05	E	11.56	0.05	E	18.68	24.50
350	T36 90 PD	81	11.36	11.60	0.02	I	11.54	0.02	I	11.49	0.02	I	11.42	0.03	E	18.94	26.92
352	P60 91 ?D	76	11.87	12.30	0.01	I	12.22	0.01	I	12.14	0.01	I	12.03	0.02	I	21.16	32.56
353	P60 91 PD	50	10.76	11.38	0.02	I	11.19	0.02	I	11.11	0.02	I	11.00	0.03	I	19.43	27.33
353	P60 91 ?D	47	10.61	11.30	0.01	I	11.12	0.01	I	11.03	0.01	I	10.90	0.02	I	20.05	33.41

Table VI - Observed surface brightness profiles, 4KVL objects – page 5

obj	obs	i	m_I^{tot}	$m_I^{22.5}$	σ		$m_I^{23.0}$	σ		$m_I^{23.5}$	σ		$m_I^{24.0}$	σ		Σ_0	r_0
354	P60 91 ?D	90	10.57	10.74	0.01	I	10.69	0.01	I	10.66	0.01	I	10.64	0.01	I	19.03	19.35
357	T36 91 PD	55	11.31	11.41	0.04	I	11.36	0.04	I	11.35	0.07	E	11.34	0.07	E	17.72	10.11
360	P60 91 ?D	48	10.35	10.55	0.01	I	10.48	0.01	I	10.45	0.01	I	10.42	0.01	I	18.73	19.68
361	P60 91 PD	50	11.29	11.42	0.01	I	11.39	0.01	I	11.37	0.01	I	11.35	0.01	I	17.40	8.61
361	T36 91 PD	53	11.33	11.41	0.04	I	11.39	0.04	I	11.37	0.04	I	11.35	0.04	I	17.66	9.25
367	T36 91 PD	90	11.38	11.55	0.03	I	11.49	0.03	I	11.43	0.03	I	11.40	0.13	E	15.61	13.09
367	T36 90 PD	90	11.49	11.57	0.02	I	11.53	0.26	E	11.52	0.25	E	11.51	0.25	E	16.06	13.93
370	P60 90 PD	64	10.69	10.77	0.11	I	10.75	0.11	I	10.73	0.11	I	10.71	0.10	I	16.83	12.54
375	P60 91 PD	81	11.56	11.68	0.01	I	11.64	0.01	I	11.61	0.01	I	11.58	0.01	I	17.58	13.90
378	P60 90 PD	48	10.68	10.73	0.13	I	10.71	0.13	I	10.70	0.13	E	10.69	0.13	E	17.33	9.74
380	P60 91 PD	61	10.09	10.17	0.01	I	10.13	0.01	I	10.12	0.38	E	10.11	0.38	E	15.63	15.08
382	P60 90 PD	26	11.28	11.37	0.12	E	11.34	0.12	E	11.32	0.12	E	11.31	0.12	E	17.44	8.79
385	P60 89 PL	59	11.07	11.21	0.02	I	11.15	0.45	E	11.13	0.45	E	11.12	0.44	E	15.17	10.42
387	T36 90 PD	63	11.12	11.18	0.08	E	11.16	0.07	E	11.15	0.07	E	11.14	0.07	E	15.89	9.53
391	T36 90 PD	53	11.33	11.40	0.20	I	11.37	0.20	I	11.35	0.20	I	11.34	0.23	E	15.90	6.72
392	T36 90 PD	72	10.07	10.14	0.01	I	10.10	0.01	I	10.09	0.02	E	10.08	0.02	E	16.36	15.03
394	T36 90 PD	86	11.29	11.37	0.03	I	11.34	0.03	I	11.31	0.20	E	11.30	0.20	E	16.72	13.71
396	P60 90 PL	61	11.52	11.69	0.05	I	11.64	0.05	I	11.59	0.11	E	11.56	0.11	E	18.22	15.05
399	T36 90 PD	56	12.79	13.04	0.01	I	12.98	0.01	I	12.93	0.01	I	12.89	0.01	I	19.85	9.85
401	T36 91 PD	77	10.18	10.27	0.04	I	10.24	0.04	I	10.21	0.10	E	10.20	0.10	E	17.25	21.56
405	P60 89 PL	55	12.11	12.29	0.05	I	12.22	0.05	I	12.17	0.05	I	12.14	0.05	I	13.28	4.49
406	P60 89 PD	68	12.30	12.40	0.12	I	12.36	0.12	E	12.34	0.12	E	12.33	0.12	E	17.16	7.61
409	T36 90 PD	81	12.42	12.66	0.03	I	12.57	0.03	I	12.51	0.03	I	12.47	0.10	E	17.67	14.09
411	T36 90 PD	59	10.27	10.43	0.03	I	10.37	0.13	E	10.34	0.14	E	10.31	0.14	E	18.74	26.25
414	T36 90 PD	78	11.78	11.95	0.03	I	11.88	0.03	I	11.83	0.03	I	11.80	0.24	E	16.76	10.58
418	P60 90 PD	81	11.18	11.33	0.14	I	11.30	0.14	I	11.27	0.14	I	11.24	0.13	I	18.51	22.18
422	T36 90 PD	77	11.57	11.74	0.01	I	11.67	0.17	E	11.64	0.18	E	11.62	0.18	E	18.49	18.83
426	P60 90 PD	74	10.55	10.64	0.12	I	10.62	0.12	I	10.60	0.12	I	10.58	0.12	I	16.90	16.88
434	P60 89 PL	47	10.28	10.62	0.05	E	10.50	0.06	E	10.42	0.07	E	10.37	0.08	E	19.90	38.96

Table VII - Observed isophotal $V-I$ colors, 4KVL objects – page 1

obj	obs	$V-I$	σ	$V-I$	σ	$V-I$	σ
		$\Sigma_I = 20.0$		$\Sigma_I = 21.0$		$\Sigma_I = 22.0$	
1	P60 89 PL	1.372	0.100	1.342	0.100	1.322	0.100
2	P60 90 PD	1.075	0.057	1.035	0.054	1.020	0.052
7	T36 90 PD	1.353	0.116	1.300	0.115	1.283	0.114
7	T36 90 PD	1.281	0.012	1.245	0.012	1.236	0.012
8	P60 90 PD	1.273	0.073	1.250	0.072	1.227	0.070
15	T36 90 PD	1.297	0.010	1.276	0.010	1.249	0.010
18	T36 90 PD	1.309	0.115	1.278	0.114	1.269	0.114
19	P60 89 PL	1.554	0.011	1.477	0.012	1.437	0.014
19	P60 90 PD	1.622	0.102	1.526	0.094	1.475	0.091
25	T36 90 PD	1.514	0.119	1.462	0.118	1.427	0.117
28	P60 89 PL	1.394	0.100	1.332	0.100	1.277	0.100
31	P60 89 PL	1.212	0.011	1.186	0.012	1.173	0.014
33	P60 89 PL	1.325	0.100	1.275	0.100	1.248	0.100
42	P60 89 PL	1.045	0.022	1.049	0.022	1.040	0.022
43	P60 89 PL	1.323	0.100	1.273	0.100	1.242	0.100
44	T36 90 PD	1.363	0.115	1.317	0.115	1.303	0.115
49	P60 90 PD	1.327	0.077	1.318	0.076	1.304	0.077
53	P60 89 PL	2.424	0.202	2.354	0.197	2.231	0.190
54	P60 89 PL	1.379	0.020	1.311	0.021	1.279	0.023
55	P60 89 PL	1.424	0.020	1.291	0.022	1.245	0.024
59	P60 89 PL	1.322	0.021	1.300	0.021	1.293	0.023
62	T36 90 PL	1.389	0.011	1.370	0.011	1.365	0.012
64	P60 89 PL	2.154	0.101	2.012	0.101	1.923	0.101
66	P60 89 PL	0.855	0.101	0.837	0.101	0.828	0.101
69	P60 89 PL	2.050	0.101	2.007	0.101	1.963	0.101
71	P60 89 PL	1.634	0.100	1.511	0.101	1.424	0.102
77	T36 91 PD	0.857	0.013	0.827	0.013	0.819	0.015
79	TSC 91 PD	1.027	0.022	1.003	0.022	0.989	0.021
80	T36 90 PD	1.155	0.113	1.096	0.112	1.095	0.112
82	P60 89 PD	2.528	0.030	2.459	0.030	2.427	0.031
83	P60 89 PL	1.183	0.021	1.169	0.022	1.168	0.023
87	T36 90 PD	1.469	0.011	1.440	0.011	1.425	0.011
90	TSC 91 PD	1.099	0.022	1.094	0.022	1.087	0.022
91	T36 90 ?D	1.154	0.010	1.117	0.010	1.105	0.010
92	TSC 91 PD	1.181	0.023	1.161	0.023	1.156	0.023
93	T36 90 PD	1.560	0.120	1.440	0.117	1.401	0.116
94	T36 90 PD	1.101	0.010	1.107	0.010	1.098	0.011
94	T36 91 PD	0.960	0.022	0.954	0.022	0.929	0.023
96	T36 91 PD	1.601	0.045	1.558	0.044	1.528	0.043
98	P60 91 PD	1.765	0.021	1.674	0.020	1.577	0.022

Table VII - Observed isophotal $V-I$ colors, 4KVL objects – page 2

obj	obs	$V-I$	σ	$V-I$	σ	$V-I$	σ
		$\Sigma_I = 20.0$		$\Sigma_I = 21.0$		$\Sigma_I = 22.0$	
99	P60 89 PL	1.580	0.100	1.496	0.100	1.394	0.102
99	T36 91 PD	1.668	0.049	1.569	0.045	1.468	0.041
101	P60 91 PD	1.534	0.018	1.441	0.019	1.393	0.020
105	P60 89 PD	2.003	0.024	1.965	0.024	1.930	0.026
106	P60 89 PL	1.220	0.100	1.142	0.100	1.114	0.101
109	P60 89 PL	1.341	0.020	1.239	0.021	1.188	0.023
110	P60 91 ND	1.200	0.013	1.191	0.014	1.180	0.015
114	P60 89 NL	1.294	0.021	1.214	0.023	1.202	0.024
115	T36 91 PD	1.432	0.026	1.392	0.026	1.366	0.025
117	P60 91 ?D	1.141	0.009	1.105	0.009	1.087	0.012
118	T36 90 ?D	1.799	0.018	1.639	0.017	1.571	0.018
126	P60 89 PL	0.887	0.101	0.853	0.102	0.825	0.102
132	T36 90 PD	1.252	0.009	1.230	0.009	1.237	0.010
134	P60 89 PL	1.275	0.011	1.238	0.011	1.173	0.016
134	P60 91 ?D	1.186	0.100	1.150	0.100	1.083	0.101
136	T36 91 PD	1.656	0.023	1.504	0.021	1.469	0.022
139	P60 91 PD	1.131	0.012	1.052	0.011	1.039	0.013
141	P60 91 ?D	1.169	0.009	1.157	0.010	1.143	0.012
143	P60 91 PD	1.692	0.021	1.538	0.019	1.469	0.020
150	TSC 91 PD	1.105	0.023	1.084	0.022	1.081	0.023
150	P60 91 ?D	1.169	0.011	1.139	0.014	—	—
151	T36 90 PD	1.505	0.028	1.451	0.027	1.421	0.027
151	T36 91 PD	1.587	0.045	1.533	0.043	1.503	0.042
154	T36 91 PD	0.914	0.026	0.867	0.026	0.853	0.026
154	P60 91 ?D	0.905	0.007	0.861	0.007	0.849	0.008
159	T36 91 PD	1.202	0.030	1.167	0.029	1.140	0.028
163	T36 90 PD	1.215	0.022	1.174	0.021	1.147	0.022
167	P60 89 PL	1.214	0.012	1.158	0.013	1.121	0.018
169	T36 91 PD	1.372	0.035	1.309	0.033	1.278	0.032
170	P60 91 ?D	1.457	0.017	1.342	0.016	1.256	0.016
171	T36 91 PD	1.379	0.035	1.333	0.034	1.304	0.032
172	T36 91 PD	1.506	0.040	1.440	0.038	1.382	0.035
176	T36 90 PD	1.045	0.006	1.033	0.006	—	—
179	T36 91 PD	1.140	0.015	1.064	0.015	1.029	0.016
181	T36 90 PD	1.336	0.008	1.246	0.008	1.211	0.008
189	P60 91 ?D	1.116	0.009	1.098	0.009	1.088	0.012
193	TSC 91 PD	1.242	0.023	1.218	0.023	1.219	0.024
193	P60 91 ?D	1.237	0.012	1.221	0.015	—	—
194	T36 90 PD	1.257	0.009	1.291	0.009	1.265	0.012
198	T36 91 PD	1.870	0.051	1.798	0.049	1.758	0.049

Table VII - Observed isophotal $V-I$ colors, 4KVL objects – page 3

obj	obs	$V-I$	σ	$V-I$	σ	$V-I$	σ
		$\Sigma_I = 20.0$		$\Sigma_I = 21.0$		$\Sigma_I = 22.0$	
203	T36 91 PD	1.226	0.016	1.153	0.015	1.093	0.016
204	P60 91 ?D	1.368	0.016	1.332	0.015	1.301	0.015
206	TSC 91 PD	1.402	0.026	1.403	0.026	1.365	0.025
207	P60 91 PD	1.316	0.014	1.223	0.013	1.178	0.014
210	T36 90 ?D	1.084	0.012	1.015	0.012	0.997	0.012
210	T36 91 PD	1.107	0.015	1.026	0.014	0.997	0.016
213	T36 91 PD	1.337	0.017	1.316	0.017	1.289	0.017
216	T36 90 PD	1.341	0.009	1.291	0.009	1.276	0.010
223	T36 91 PD	1.217	0.031	1.178	0.030	1.148	0.030
225	P60 91 PD	1.248	0.013	1.196	0.012	1.121	0.012
226	P60 91 PD	1.297	0.015	1.241	0.014	1.202	0.016
228	P60 91 PD	1.344	0.014	1.244	0.013	1.230	0.014
229	T36 91 PD	1.386	0.035	1.352	0.034	1.321	0.033
231	T36 90 PD	1.462	0.026	1.301	0.024	1.259	0.025
232	T36 91 PD	1.405	0.019	1.365	0.019	1.335	0.020
239	P60 91 PD	1.313	0.007	1.271	0.007	1.249	0.009
240	TSC 91 PD	1.137	0.023	1.100	0.022	1.071	0.022
240	P60 91 ?D	1.227	0.010	1.183	0.010	1.146	0.014
246	TSC 91 PD	1.245	0.024	1.209	0.023	1.188	0.023
247	P60 91 PD	1.360	0.025	1.322	0.024	1.278	0.024
247	P60 91 ?D	1.446	0.012	1.380	0.013	1.335	0.015
248	TSC 91 PD	1.254	0.024	1.113	0.023	1.077	0.022
248	P60 91 ?D	1.325	0.011	1.170	0.011	1.101	0.014
251	T36 91 PD	1.300	0.033	1.250	0.032	1.215	0.031
251	T36 91 PD	1.304	0.033	1.255	0.032	1.222	0.031
254	T36 91 PD	1.448	0.036	1.397	0.035	1.370	0.035
255	T36 91 PD	1.034	0.028	0.999	0.027	1.000	0.028
256	TSC 91 PD	1.335	0.024	1.292	0.024	1.267	0.024
257	T36 90 PD	1.445	0.012	1.351	0.014	1.316	0.017
260	T36 90 PD	1.176	0.007	1.110	0.007	1.087	0.007
262	T36 90 PD	1.057	0.006	1.029	0.006	1.020	0.007
265	P60 91 PD	1.072	0.011	1.041	0.011	1.018	0.011
267	T36 91 PD	1.355	0.034	1.289	0.032	1.265	0.031
269	TSC 91 PD	1.230	0.023	1.192	0.023	1.159	0.023
271	TSC 91 PD	1.217	0.023	1.169	0.023	1.108	0.022
276	T36 91 PD	1.308	0.035	1.257	0.033	1.233	0.033
278	T36 91 PD	1.329	0.033	1.257	0.032	1.223	0.031
278	T36 90 ?D	1.243	0.022	1.173	0.021	1.146	0.021
280	T36 91 PD	1.525	0.021	1.493	0.020	1.463	0.022
281	T36 91 PD	1.153	0.027	1.161	0.027	1.162	0.027

Table VII - Observed isophotal $V-I$ colors, 4KVL objects – page 4

obj	obs	$V-I$	σ	$V-I$	σ	$V-I$	σ
		$\Sigma_I = 20.0$		$\Sigma_I = 21.0$		$\Sigma_I = 22.0$	
284	TSC 91 PD	1.310	0.024	1.212	0.023	1.200	0.023
284	TSC 91 PD	1.309	0.024	1.223	0.023	1.192	0.023
285	T36 91 PD	1.451	0.019	1.424	0.019	1.407	0.020
285	T36 90 ?D	1.435	0.014	1.419	0.014	1.411	0.015
286	T36 91 PD	1.342	0.018	1.311	0.018	1.281	0.018
287	T36 90 ?D	1.414	0.038	1.170	0.030	1.116	0.030
295	T36 90 PD	1.625	0.011	1.602	0.012	1.528	0.015
298	T36 91 PD	1.405	0.036	1.337	0.034	1.289	0.032
298	TSC 91 PD	1.352	0.024	1.283	0.024	1.254	0.023
303	TSC 91 PD	1.135	0.023	1.073	0.022	1.067	0.022
303	P60 91 ?D	1.207	0.010	1.109	0.010	1.088	0.012
306	T36 90 PD	1.640	0.030	1.588	0.031	1.543	0.034
310	P60 91 PD	1.222	0.013	1.137	0.012	1.099	0.014
313	P60 91 PD	1.102	0.006	1.097	0.008	1.072	0.013
315	T36 90 PD	1.683	0.031	1.533	0.028	1.450	0.028
316	P60 91 PD	1.197	0.012	1.147	0.012	1.108	0.014
320	T36 91 PD	1.359	0.034	1.343	0.034	1.326	0.034
320	P60 91 PD	1.315	0.015	1.295	0.016	1.279	0.017
328	P60 91 PD	1.142	0.011	1.102	0.012	1.079	0.013
332	P60 91 PD	1.291	0.014	1.247	0.014	1.221	0.015
333	P60 91 ?D	1.213	0.006	1.168	0.007	1.138	0.009
334	T36 90 PD	1.422	0.010	1.374	0.010	1.349	0.012
336	T36 91 PD	1.148	0.007	1.020	0.007	0.989	0.009
336	T36 91 PD	1.186	0.028	1.040	0.024	0.995	0.023
337	T36 91 PD	1.581	0.040	1.543	0.039	1.496	0.038
338	T36 91 PD	1.336	0.017	1.292	0.017	1.267	0.018
346	T35 90 ?D	1.490	0.015	1.454	0.015	1.427	0.015
348	T36 90 ?D	1.286	0.013	1.157	0.013	1.123	0.013
348	T36 91 PD	1.314	0.018	1.138	0.016	1.091	0.018
349	T36 91 PD	1.437	0.037	1.363	0.035	1.323	0.035
350	T36 90 PD	1.436	0.026	1.324	0.024	1.238	0.023
350	T36 91 PD	1.563	0.039	1.444	0.036	1.348	0.035
352	P60 91 ?D	1.563	0.013	1.480	0.013	1.420	0.014
353	P60 90 PL	1.243	0.013	1.155	0.013	1.093	0.015
353	P60 91 PD	1.255	0.010	1.160	0.010	1.103	0.012
354	P60 90 PL	1.454	0.012	1.389	0.012	1.347	0.013
357	T36 91 PD	1.319	0.033	1.275	0.032	1.253	0.032
360	P60 91 PD	1.185	0.006	1.124	0.007	1.086	0.009
361	T36 91 PD	1.294	0.032	1.281	0.032	1.277	0.032
361	P60 91 PD	1.252	0.006	1.238	0.007	1.233	0.009

Table VII - Observed isophotal $V-I$ colors, 4KVL objects – page 5

obj	obs	$V-I$	σ	$V-I$	σ	$V-I$	σ
		$\Sigma_I = 20.0$		$\Sigma_I = 21.0$		$\Sigma_I = 22.0$	
367	T36 90 PD	1.574	0.011	1.453	0.012	1.404	0.014
367	T36 91 PD	1.595	0.030	1.473	0.027	1.419	0.027
370	P60 90 PD	1.102	0.063	1.076	0.060	1.046	0.058
375	P60 91 PD	1.452	0.007	1.401	0.007	1.357	0.009
378	P60 90 PD	1.311	0.076	1.296	0.075	1.284	0.074
380	P60 89 PL	1.148	0.013	1.103	0.013	1.083	0.015
382	P60 90 PD	1.100	0.060	1.074	0.057	1.047	0.056
387	T36 90 PD	1.200	0.022	1.159	0.022	1.143	0.022
391	T36 90 PD	1.387	0.116	1.381	0.116	1.381	0.116
392	T36 90 PD	1.467	0.011	1.454	0.012	1.447	0.012
394	T36 90 PD	1.415	0.116	1.426	0.117	1.430	0.117
396	P60 90 ?D	1.995	0.101	1.860	0.101	1.818	0.102
399	T36 90 PD	1.378	0.011	1.367	0.011	1.364	0.011
401	T36 91 PD	1.254	0.121	1.179	0.107	1.133	0.098
405	P60 89 PL	1.566	0.100	1.471	0.101	1.404	0.101
406	P60 90 PD	1.245	0.071	1.217	0.069	1.199	0.067
409	T36 90 PD	1.968	0.132	1.790	0.126	1.668	0.123
411	T36 90 PD	1.359	0.116	1.297	0.115	1.249	0.114
414	T36 90 PD	1.500	0.118	1.410	0.116	1.396	0.116
418	P60 90 PD	1.507	0.093	1.433	0.086	1.382	0.083
422	T36 90 PD	1.463	0.011	1.441	0.011	1.415	0.012
426	P60 90 PD	1.259	0.072	1.207	0.069	1.172	0.065
434	P60 89 PL	1.173	0.021	1.067	0.022	1.121	0.024

Table VIII - Independent photometry on 4KVL objects: m_I reproduction

A. Average absolute difference, magnitudes

Σ_I	Δm_I	*rms*	N_{pts}	Δm_I	*rms*	N_{pts}	Δm_I	*rms*	N_{pts}	Δm_I	*rms*	N_{pts}
	(INT/INT)			(INT/EXT)			(EXT/EXT)			(all pairs)		
22.5	0.035	0.027	21	0.030	0.033	5	0.100	—	1	0.036	0.030	27
23.0	0.034	0.024	17	0.049	0.032	9	0.090	—	1	0.041	0.029	27
23.5	0.029	0.025	10	0.052	0.032	15	0.055	0.035	2	0.044	0.032	27
24.0	0.050	0.033	5	0.062	0.036	11	0.055	0.042	11	0.057	0.039	27

B. Average absolute difference / mag errors:

Σ_I	Δm_I	σ	N_{pts}	Δm_I	σ	N_{pts}	Δm_I	σ	N_{pts}	Δm_I	σ	N_{pts}
	(INT/INT)			(INT/EXT)			(EXT/EXT)			all pairs)		
22.5	0.90	0.82	21	0.51	0.54	5	1.17	—	1	0.84	0.77	27
23.0	1.00	0.79	17	0.72	0.62	9	1.05	—	1	0.91	0.73	27
23.5	0.93	1.00	10	0.72	0.59	15	0.65	0.40	2	0.79	0.77	27
24.0	1.34	0.90	5	1.10	0.83	11	0.52	0.66	11	0.91	0.85	27

Table IX - Systematic offsets in isophotal magnitudes between pairs of runs

run A run B N_{obj}	$< \|\|\Delta M_I^{22.5}\|\| >$ (*rms*) N_I / N_E	$< \|\|\Delta M_I^{23.0}\|\| >$ (*rms*) N_I / N_E	$< \|\|\Delta M_I^{23.5}\|\| >$ (*rms*) N_I / N_E	$< \|\|\Delta M_I^{24.0}\|\| >$ (*rms*) N_I / N_E
T36/3/90	-.04	-.04	-.04	-.05
T36/3/91	(.04)	(.05)	(.06)	(.07)
8	14 / 2	12 / 4	10 / 6	4 / 12
P60/4/91	-.01	-.02	-.04	-.05
TSC/3/91	(.05)	(.06)	(.06)	(.06)
6	8 / 4	8 / 4	7 / 5	5 / 7
P60/4/91	-.02	-.03	-.05	-.06
T36/3/91	(.02)	(.02)	(.04)	(.06)
3	4 / 2	4 / 2	4 / 2	4 / 2
T36/3/91	+.02	+.02	+.02	+.02
TSC/3/91	(.03)	(.03)	(.03)	(.03)
2	4 / 0	4 / 0	4 / 0	4 / 0

Table X - Independent photometry on 4KVL objects: $m_V - m_I$ reproduction

$||\Delta V - I||$ refers to absolute value of difference between two $m_V - m_I$ measurements for one object
Listed are averages over N_{pts} observations

Σ_I	$< \|\|\Delta V - I\|\| >$	*rms*	$< \|\|\Delta V - I\|\| >$	*rms*	N_{pts}
	($\Delta V - I$, mag)		($\Delta V - I/\sigma_{V_I}$)		
20.0	0.062	0.035	1.66	1.66	5
20.5	0.058	0.038	1.53	1.53	9
21.0	0.053	0.038	1.43	1.43	15
21.5	0.050	0.040	1.34	1.34	11
22.0	0.047	0.041	1.24	1.24	11

Table XI - systematic offsets in $V - I$ colors $m_V - m_I$ between pairs of runs

run 1 run 2	$< \|\|\Delta V - I\|\| >$ (*rms*) $\Sigma_I = 20.0$	$< \|\|\Delta V - I\|\| >$ (*rms*) $\Sigma_I = 20.5$	$< \|\|\Delta V - I\|\| >$ (*rms*) $\Sigma_I = 21.0$	$< \|\|\Delta V - I\|\| >$ (*rms*) $\Sigma_I = 21.5$	$< \|\|\Delta V - I\|\| >$ (*rms*) $\Sigma_I = 22.0$	N_{pts}
T36/3/90	+.053	+.047	+.040	+.037	+.032	8
T36/3/91	(.041)	(.049)	(.048)	(.049)	(.051)	
P60/4/91	+.011	+.003	+.020	+.002	+.001	6
TSC/3/91	(.064)	(.061)	(.054)	(.050)	(.051)	

Table XII - Repeatability of extrapolated magnitudes

I_1 = extrapolated 'total' I band magnitude; exp disk law fit Dec '91
I_2 = extrapolated 'total' I band magnitude; exp disk law fit Apr '92

run	N_{obj}	$< I_2 - I_1 >$	*rms*	$< \|\|I_2 - I_1\|\| >$	*rms*
P60/91/n2	12	—	—	.013	.015
P60/91/n4	13	—	—	.022	.031
T36/91/n1	15	+.027	.036	.027	.036
T36/91/n2	15	+.023	.039	.029	.034
T36/91/n3+4	16	+.033	.058	.035	.056

Figure Captions - Chapter 2

Figure 1 (36 pages): Radial profiles of I band surface brightness $\Sigma_I(r)$ (left column), integrated isophotal I band magnitude $m_{\Sigma_I}(r)$ (center column), and integrated isophotal $V-I$ color $[m_I - m_V]_{\Sigma_I}(r)$ (right column) for 4KVL galaxies enjoying calibrated I and V band CCD surface photometry.

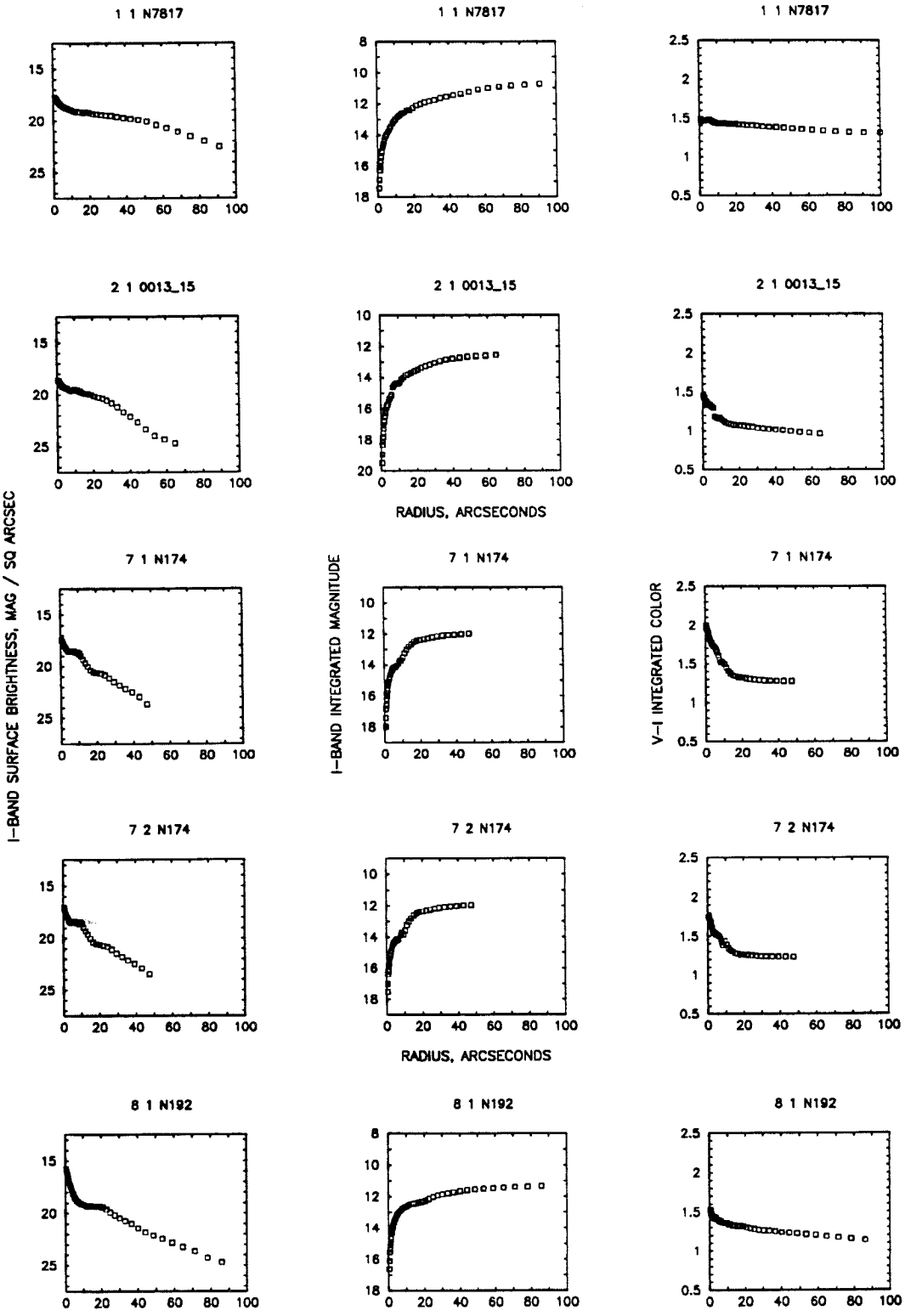
1 1 N7817
1 1 N7817
1 1 N7817
2 1 0013_15
2 1 0013_15
2 1 0013_15
7 1 N174
7 1 N174
7 1 N174
7 2 N174
7 2 N174
7 2 N174
8 1 N192
8 1 N192
8 1 N192
I-BAND SURFACE BRIGHTNESS, MAG / SQ ARCSEC
I-BAND INTEGRATED MAGNITUDE
V-I INTEGRATED COLOR
RADIUS, ARCSECONDS
RADIUS, ARCSECONDS

Figure 1(1)

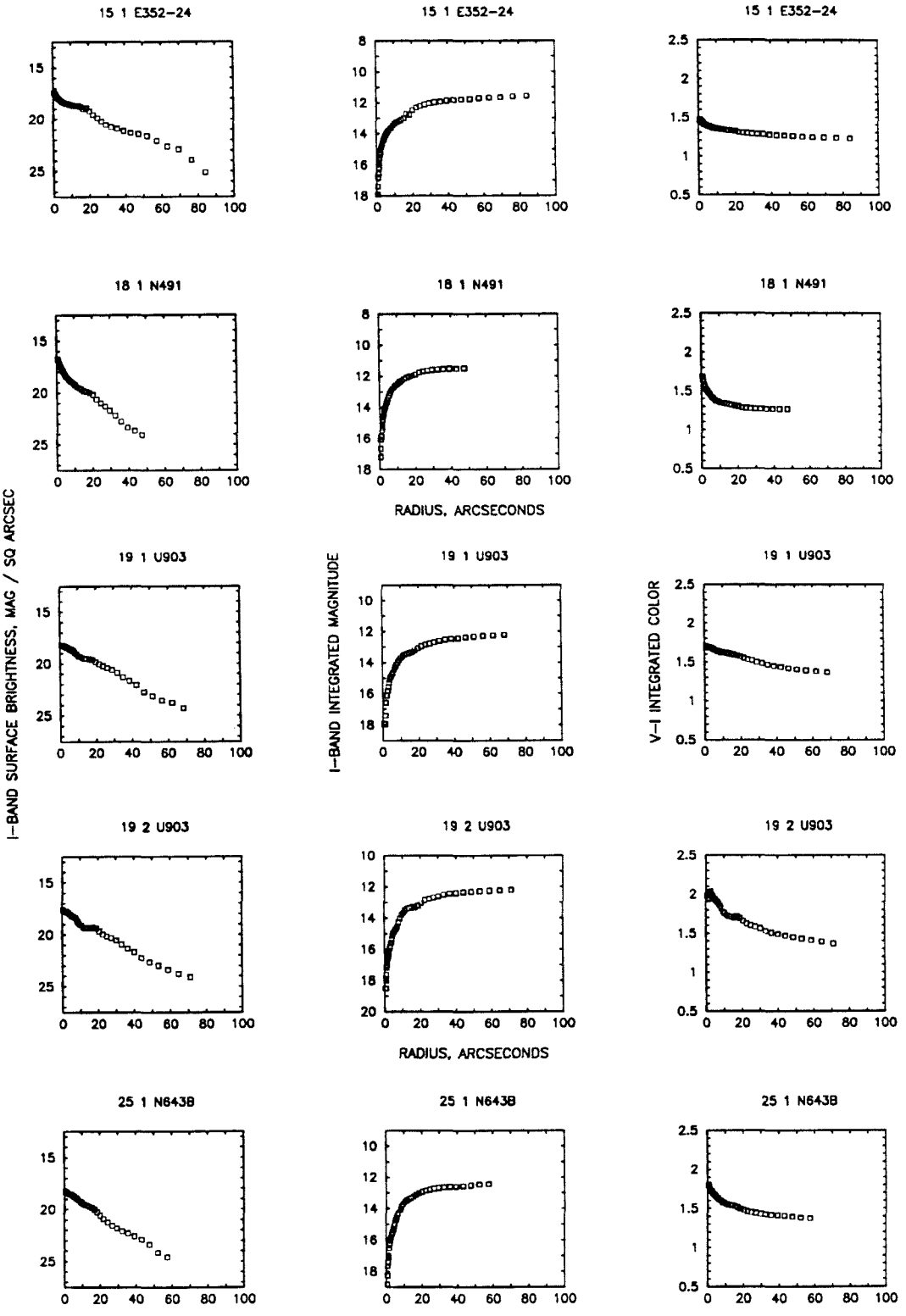
15 1 E352-24
15 1 E352-24
15 1 E352-24
18 1 N491
18 1 N491
18 1 N491
19 1 U903
19 1 U903
19 1 U903
19 2 U903
19 2 U903
19 2 U903
25 1 N643B
25 1 N643B
25 1 N643B
I-BAND SURFACE BRIGHTNESS, MAG / SQ ARCSEC
I-BAND INTEGRATED MAGNITUDE
V-I INTEGRATED COLOR
RADIUS, ARCSECONDS
RADIUS, ARCSECONDS

Figure 1(2)

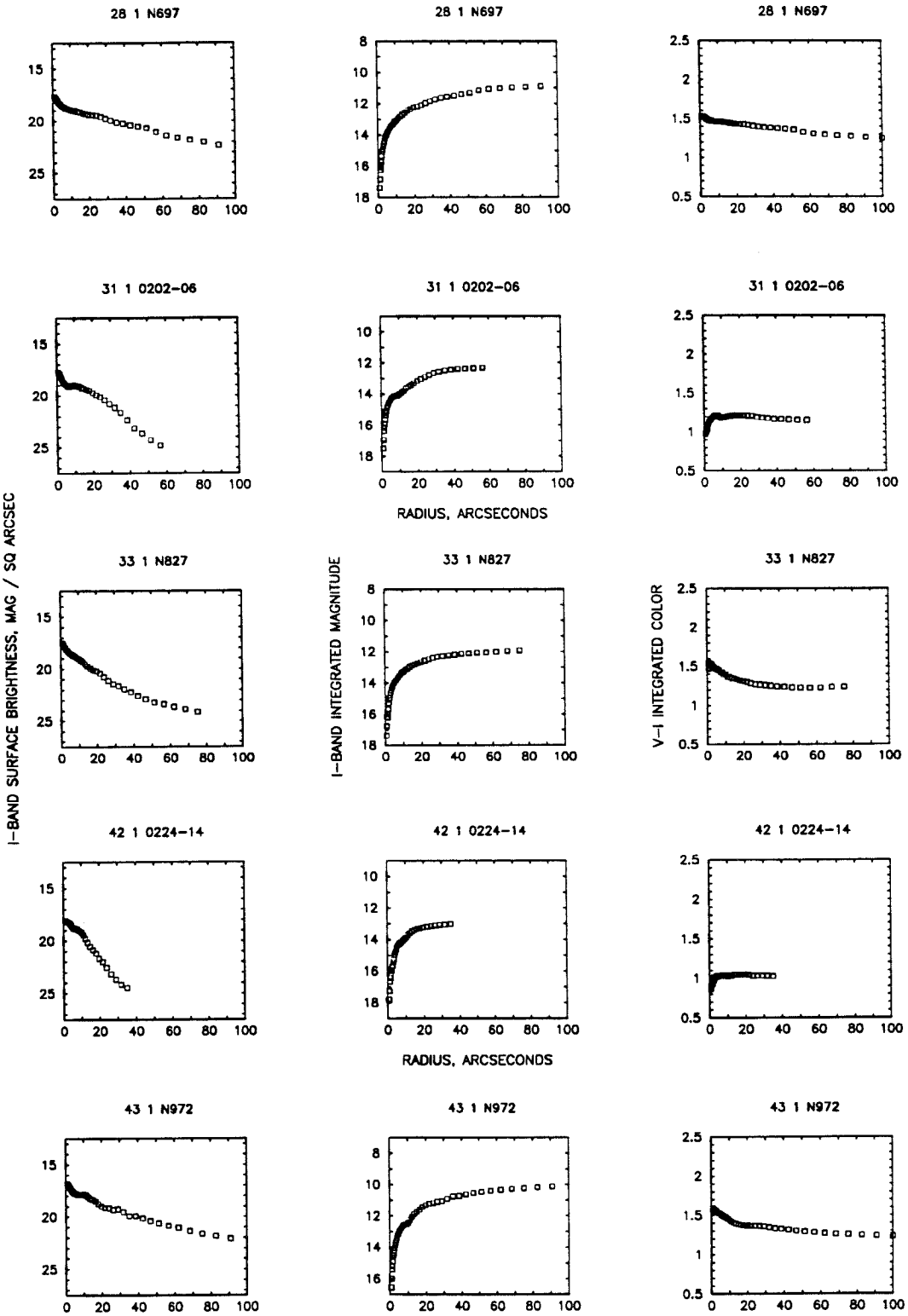
28 1 N697
28 1 N697
28 1 N697
31 1 0202-06
31 1 0202-06
31 1 0202-06
33 1 N827
33 1 N827
33 1 N827
42 1 0224-14
42 1 0224-14
42 1 0224-14
43 1 N972
43 1 N972
43 1 N972
I-BAND SURFACE BRIGHTNESS, MAG / SQ ARCSEC
I-BAND INTEGRATED MAGNITUDE
V-I INTEGRATED COLOR
RADIUS, ARCSECONDS
RADIUS, ARCSECONDS

Figure 1(3)

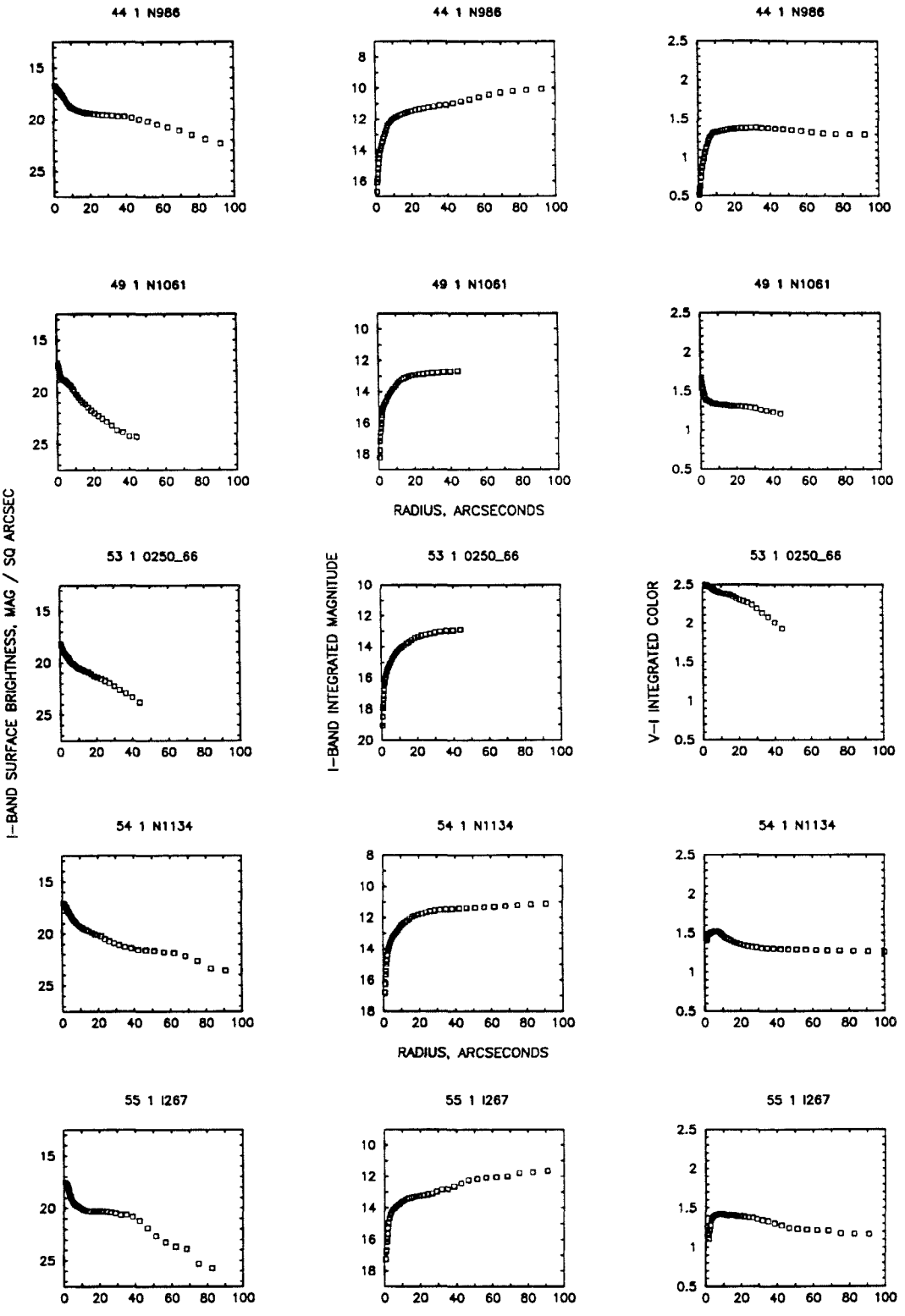
44 1 N986
44 1 N986
44 1 N986
49 1 N1061
49 1 N1061
49 1 N1061
I-BAND SURFACE BRIGHTNESS, MAG / SQ ARCSEC
RADIUS, ARCSECONDS
53 1 0250_66
53 1 0250_66
53 1 0250_66
I-BAND INTEGRATED MAGNITUDE
V-I INTEGRATED COLOR
54 1 N1134
54 1 N1134
54 1 N1134
RADIUS, ARCSECONDS
55 1 I267
55 1 I267
55 1 I267

Figure 1(4)

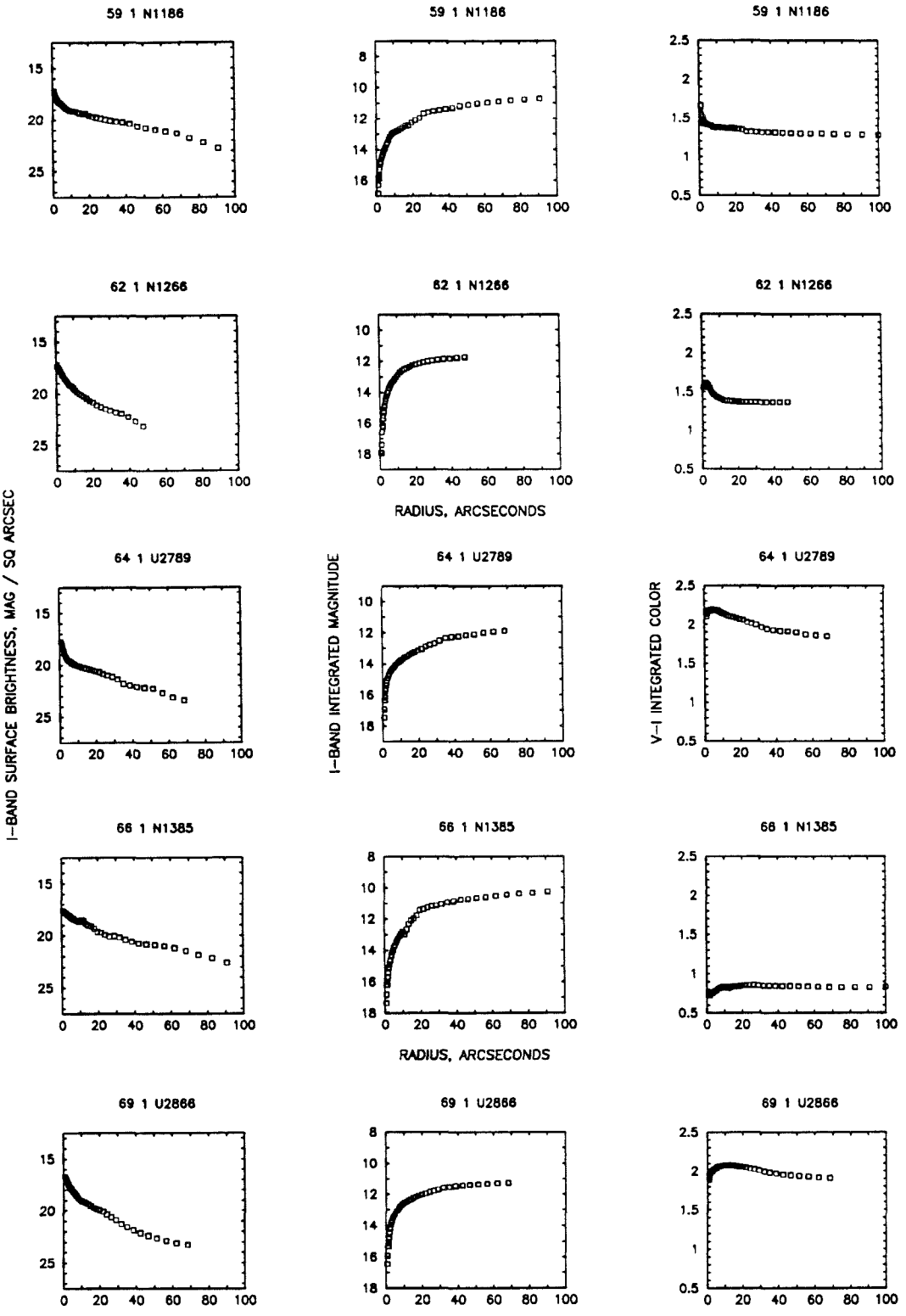
59 1 N1186
59 1 N1186
59 1 N1186
62 1 N1266
62 1 N1266
62 1 N1266
64 1 U2789
64 1 U2789
64 1 U2789
66 1 N1385
66 1 N1385
66 1 N1385
69 1 U2866
69 1 U2866
69 1 U2866
I-BAND SURFACE BRIGHTNESS, MAG / SQ ARCSEC
I-BAND INTEGRATED MAGNITUDE
V-I INTEGRATED COLOR
RADIUS, ARCSECONDS
RADIUS, ARCSECONDS

Figure 1(5)

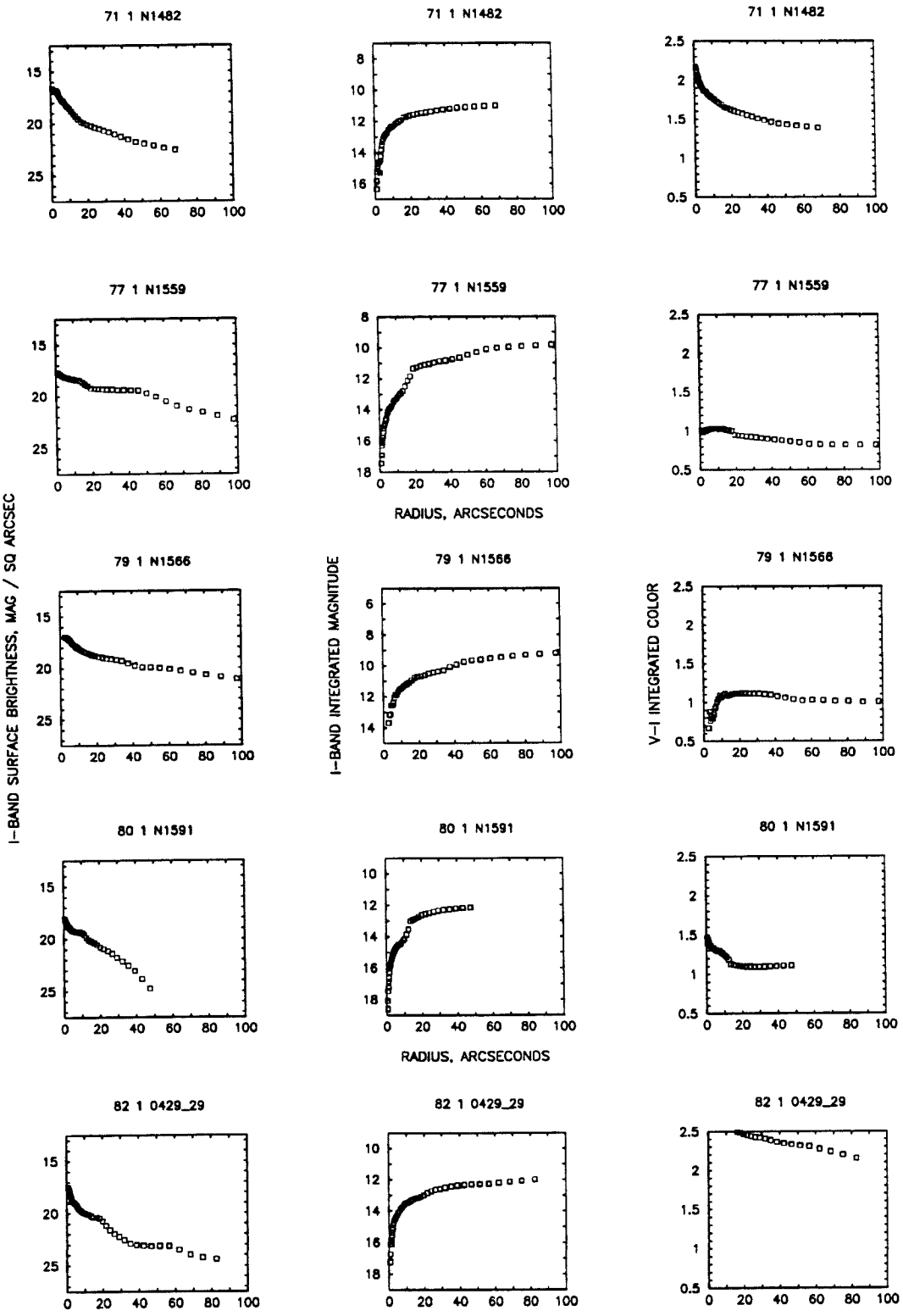
71 1 N1482
71 1 N1482
71 1 N1482
77 1 N1559
77 1 N1559
77 1 N1559
79 1 N1566
79 1 N1566
79 1 N1566
80 1 N1591
80 1 N1591
80 1 N1591
82 1 0429_29
82 1 0429_29
82 1 0429_29
I-BAND SURFACE BRIGHTNESS, MAG / SQ ARCSEC
I-BAND INTEGRATED MAGNITUDE
V-I INTEGRATED COLOR
RADIUS, ARCSECONDS
RADIUS, ARCSECONDS

Figure 1(6)

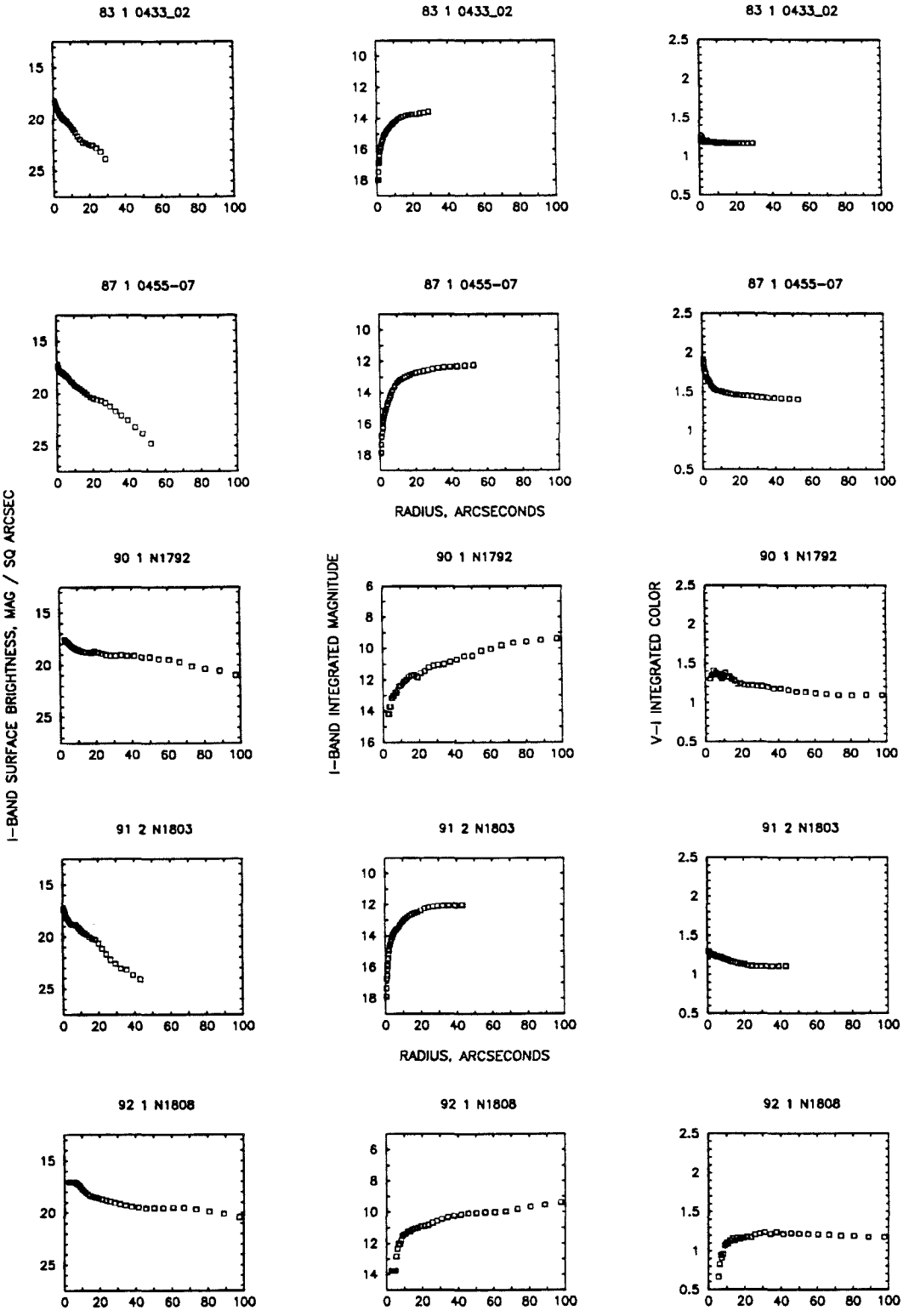
83 1 0433_02
83 1 0433_02
83 1 0433_02
87 1 0455-07
87 1 0455-07
87 1 0455-07
90 1 N1792
90 1 N1792
90 1 N1792
91 2 N1803
91 2 N1803
91 2 N1803
92 1 N1808
92 1 N1808
92 1 N1808
I-BAND SURFACE BRIGHTNESS, MAG / SQ ARCSEC
I-BAND INTEGRATED MAGNITUDE
V-I INTEGRATED COLOR
RADIUS, ARCSECONDS
RADIUS, ARCSECONDS

Figure 1(7)

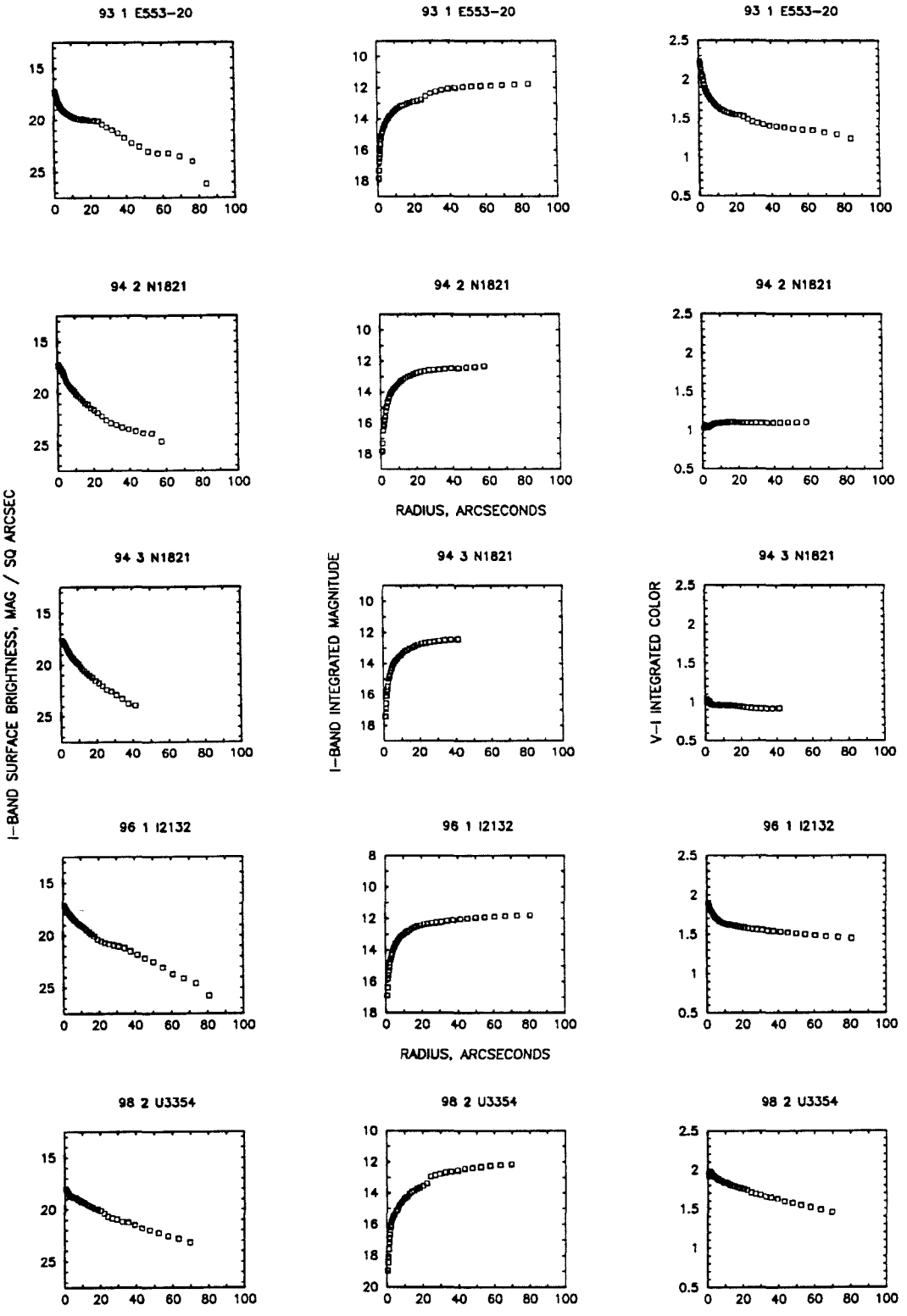
93 1 E553-20
93 1 E553-20
93 1 E553-20
94 2 N1821
94 2 N1821
94 2 N1821
94 3 N1821
94 3 N1821
94 3 N1821
96 1 I2132
96 1 I2132
96 1 I2132
98 2 U3354
98 2 U3354
98 2 U3354
I-BAND SURFACE BRIGHTNESS, MAG / SQ ARCSEC
I-BAND INTEGRATED MAGNITUDE
V-I INTEGRATED COLOR
RADIUS, ARCSECONDS
RADIUS, ARCSECONDS

Figure 1(8)

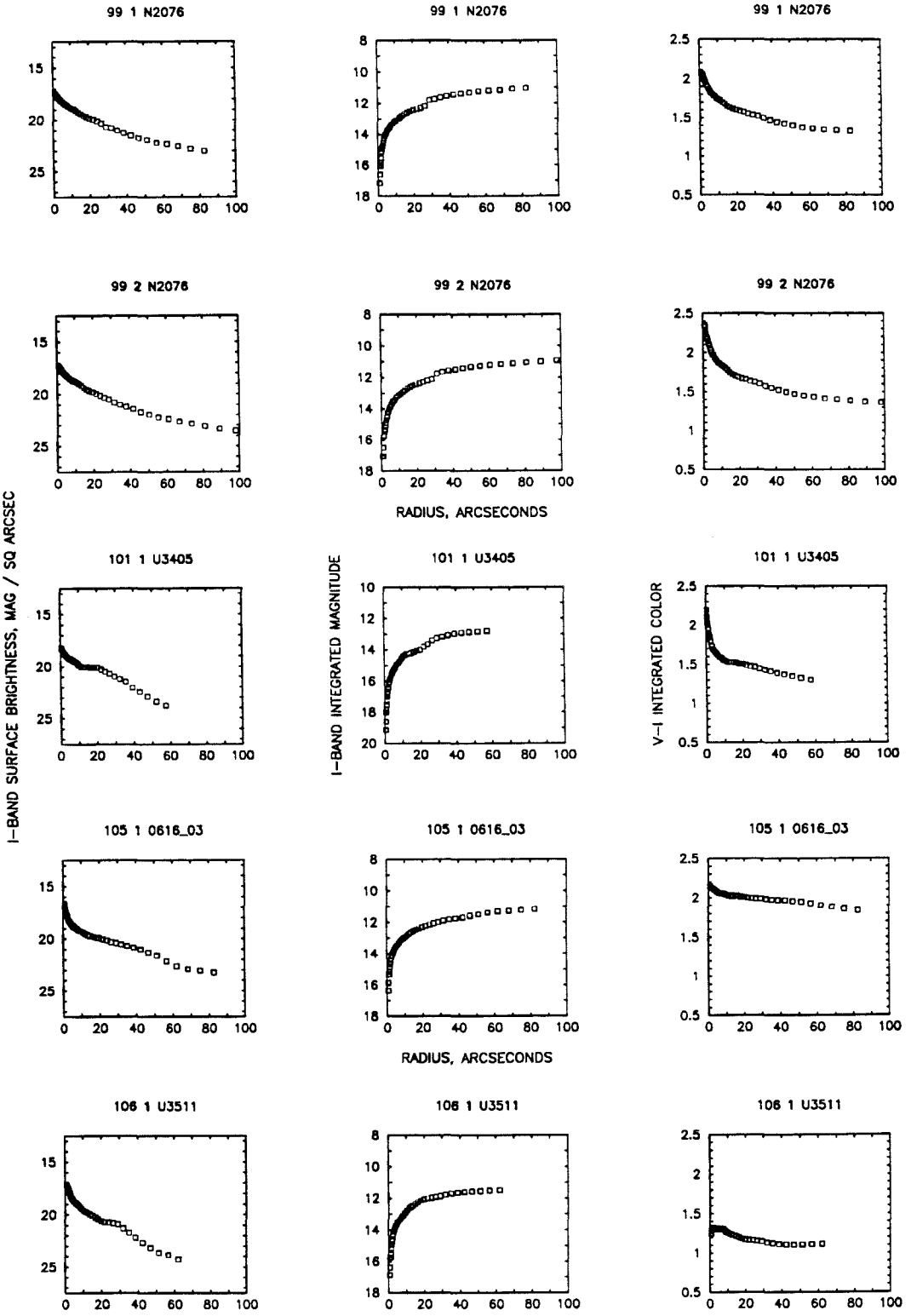
99 1 N2076
99 1 N2076
99 1 N2076
99 2 N2076
99 2 N2076
99 2 N2076
101 1 U3405
101 1 U3405
101 1 U3405
105 1 0616_03
105 1 0616_03
105 1 0616_03
106 1 U3511
106 1 U3511
106 1 U3511
I-BAND SURFACE BRIGHTNESS, MAG / SQ ARCSEC
I-BAND INTEGRATED MAGNITUDE
V-I INTEGRATED COLOR
RADIUS, ARCSECONDS
RADIUS, ARCSECONDS

Figure 1(9)

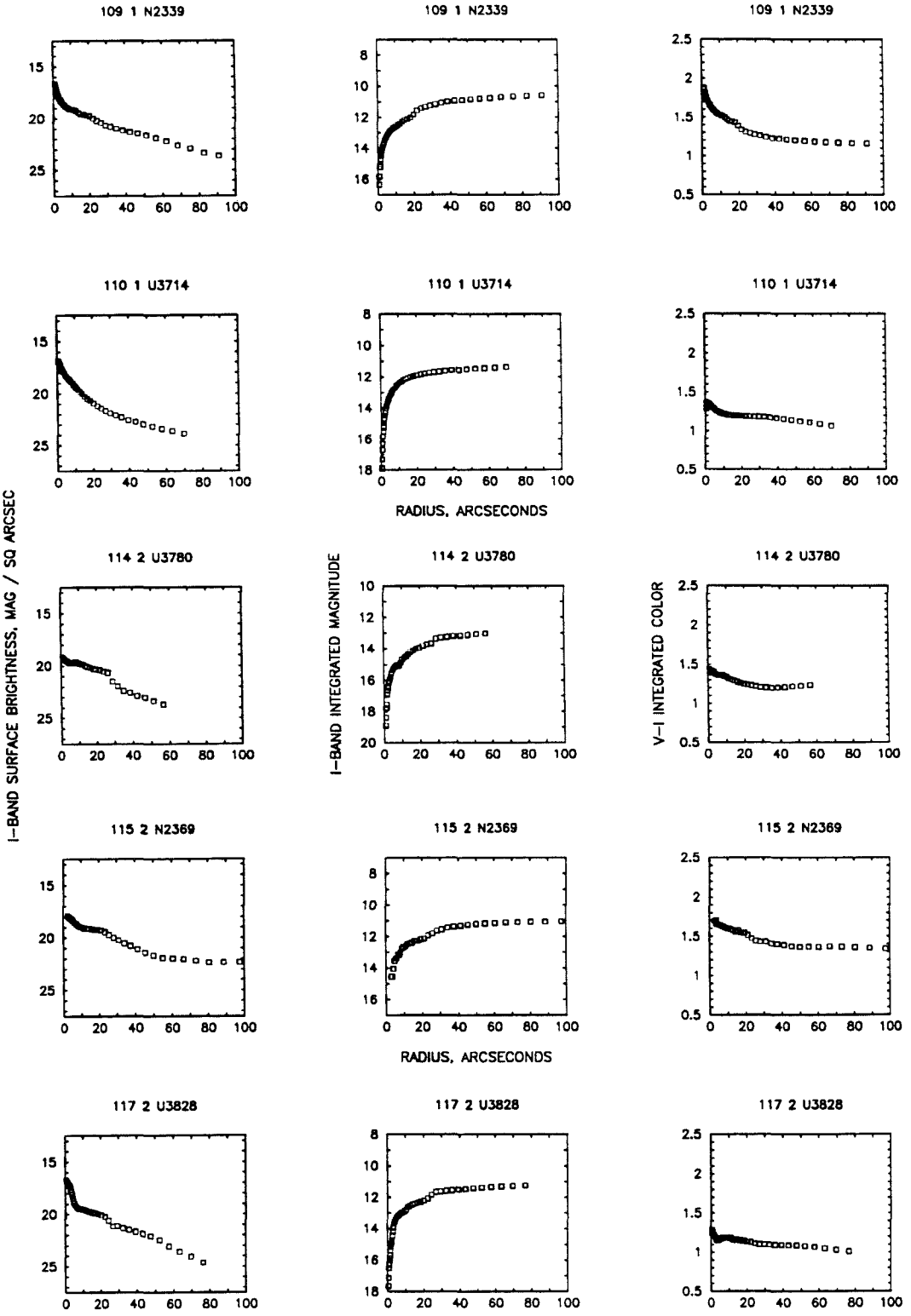
109 1 N2339
109 1 N2339
109 1 N2339
110 1 U3714
110 1 U3714
110 1 U3714
I-BAND SURFACE BRIGHTNESS, MAG / SQ ARCSEC
RADIUS, ARCSECONDS
114 2 U3780
114 2 U3780
114 2 U3780
I-BAND INTEGRATED MAGNITUDE
V-I INTEGRATED COLOR
115 2 N2369
115 2 N2369
115 2 N2369
RADIUS, ARCSECONDS
117 2 U3828
117 2 U3828
117 2 U3828

Figure 1(10)

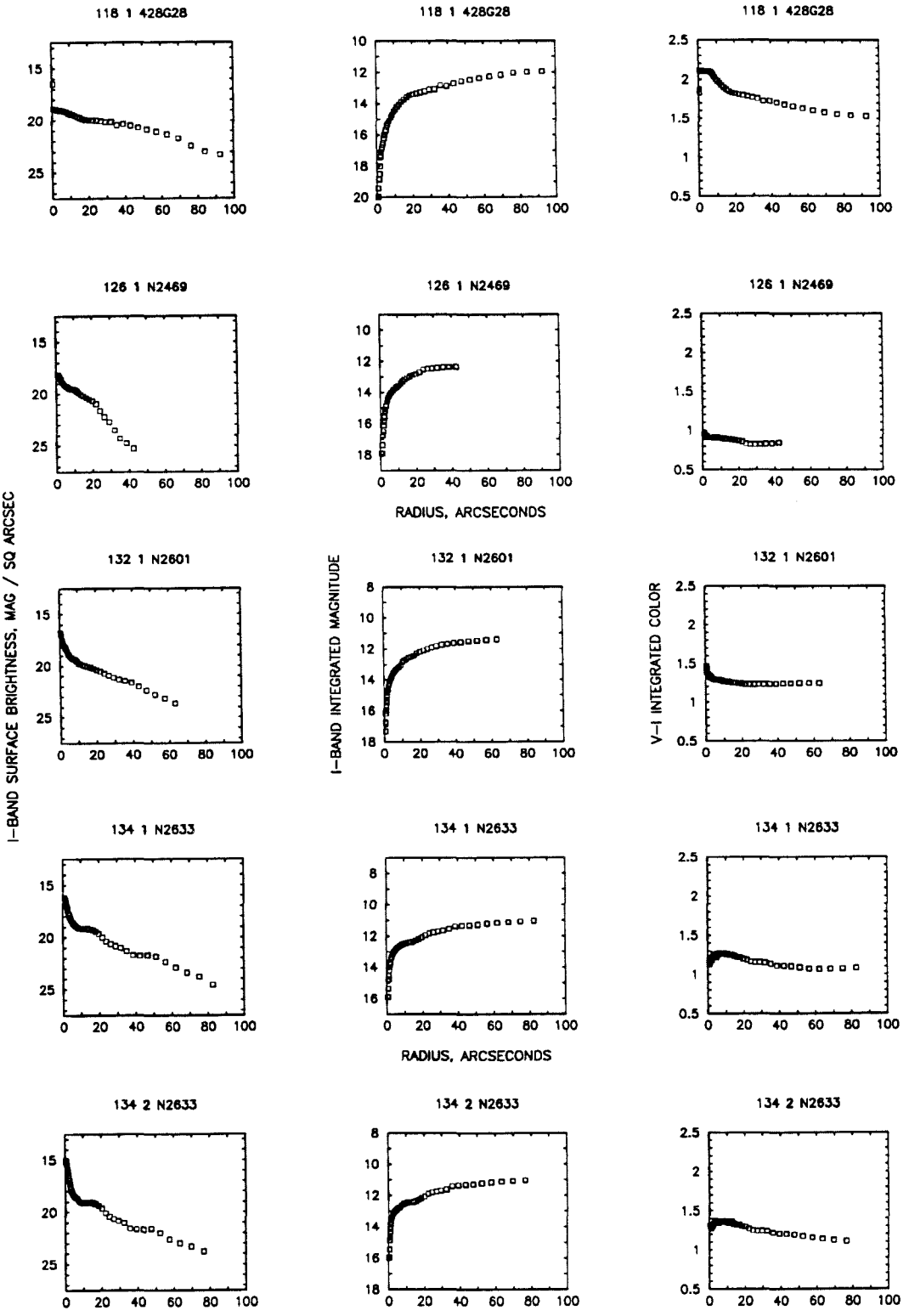
118 1 428G28
118 1 428G28
118 1 428G28
126 1 N2469
126 1 N2469
126 1 N2469
132 1 N2601
132 1 N2601
132 1 N2601
134 1 N2633
134 1 N2633
134 1 N2633
134 2 N2633
134 2 N2633
134 2 N2633
I-BAND SURFACE BRIGHTNESS, MAG / SQ ARCSEC
I-BAND INTEGRATED MAGNITUDE
V-I INTEGRATED COLOR
RADIUS, ARCSECONDS
RADIUS, ARCSECONDS

Figure 1(11)

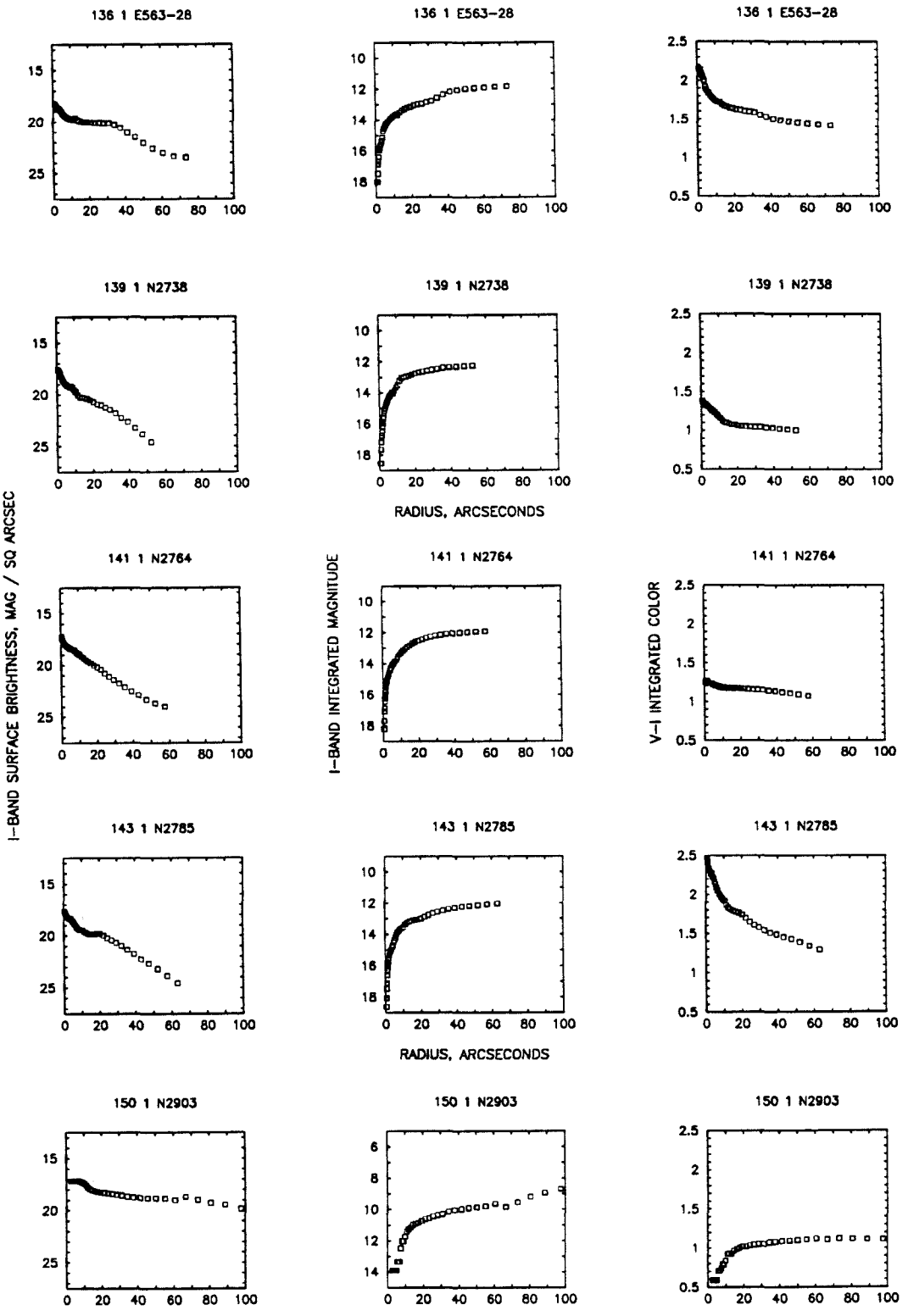
136 1 E563-28
136 1 E563-28
136 1 E563-28
139 1 N2738
139 1 N2738
139 1 N2738
141 1 N2764
141 1 N2764
141 1 N2764
143 1 N2785
143 1 N2785
143 1 N2785
150 1 N2903
150 1 N2903
150 1 N2903
I-BAND SURFACE BRIGHTNESS, MAG / SQ ARCSEC
I-BAND INTEGRATED MAGNITUDE
V-I INTEGRATED COLOR
RADIUS, ARCSECONDS
RADIUS, ARCSECONDS

Figure 1(12)

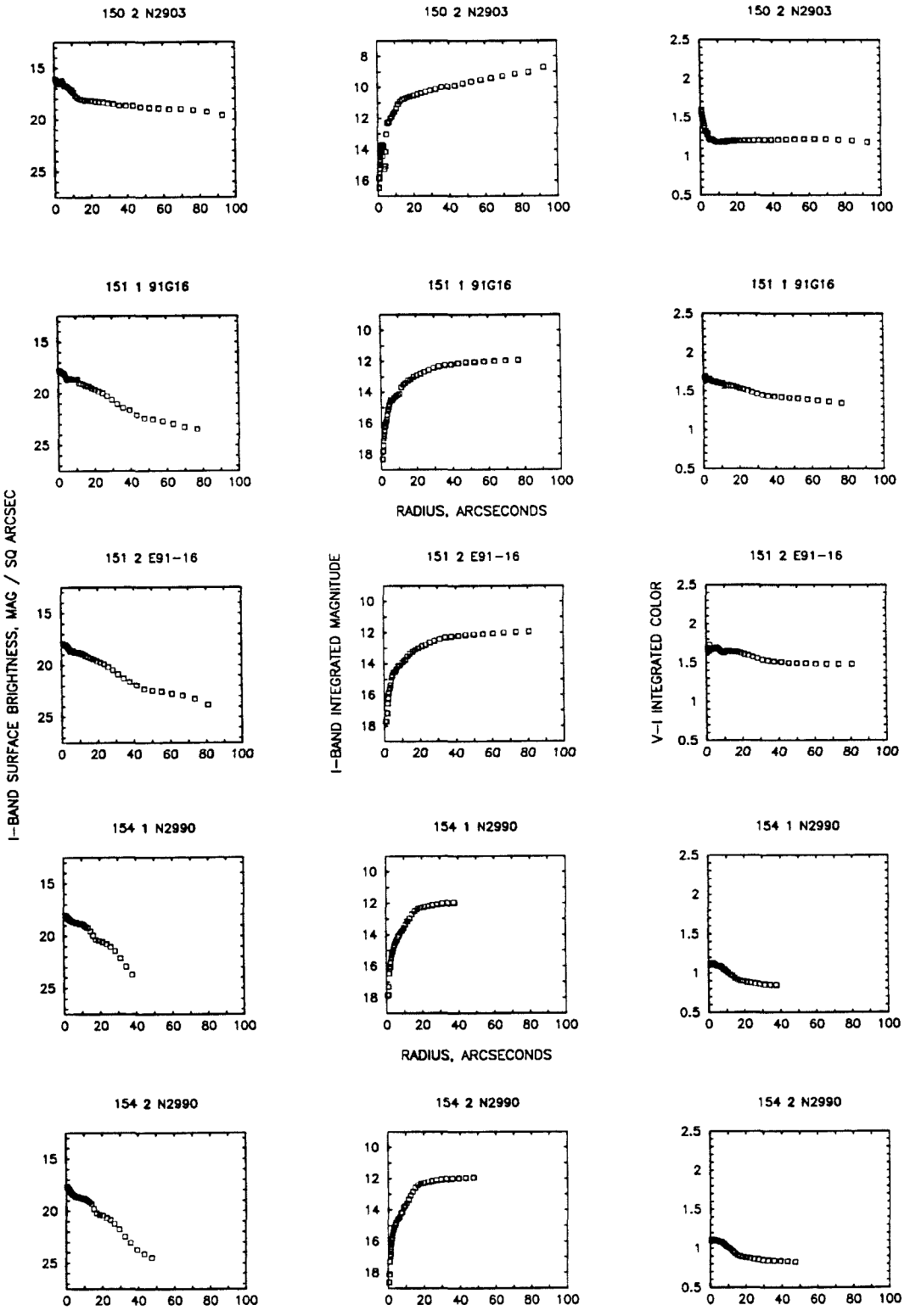
150 2 N2903
150 2 N2903
150 2 N2903
151 1 91G16
151 1 91G16
151 1 91G16
151 2 E91-16
151 2 E91-16
151 2 E91-16
154 1 N2990
154 1 N2990
154 1 N2990
154 2 N2990
154 2 N2990
154 2 N2990
I-BAND SURFACE BRIGHTNESS, MAG / SQ ARCSEC
I-BAND INTEGRATED MAGNITUDE
V-I INTEGRATED COLOR
RADIUS, ARCSECONDS
RADIUS, ARCSECONDS

Figure 1(13)

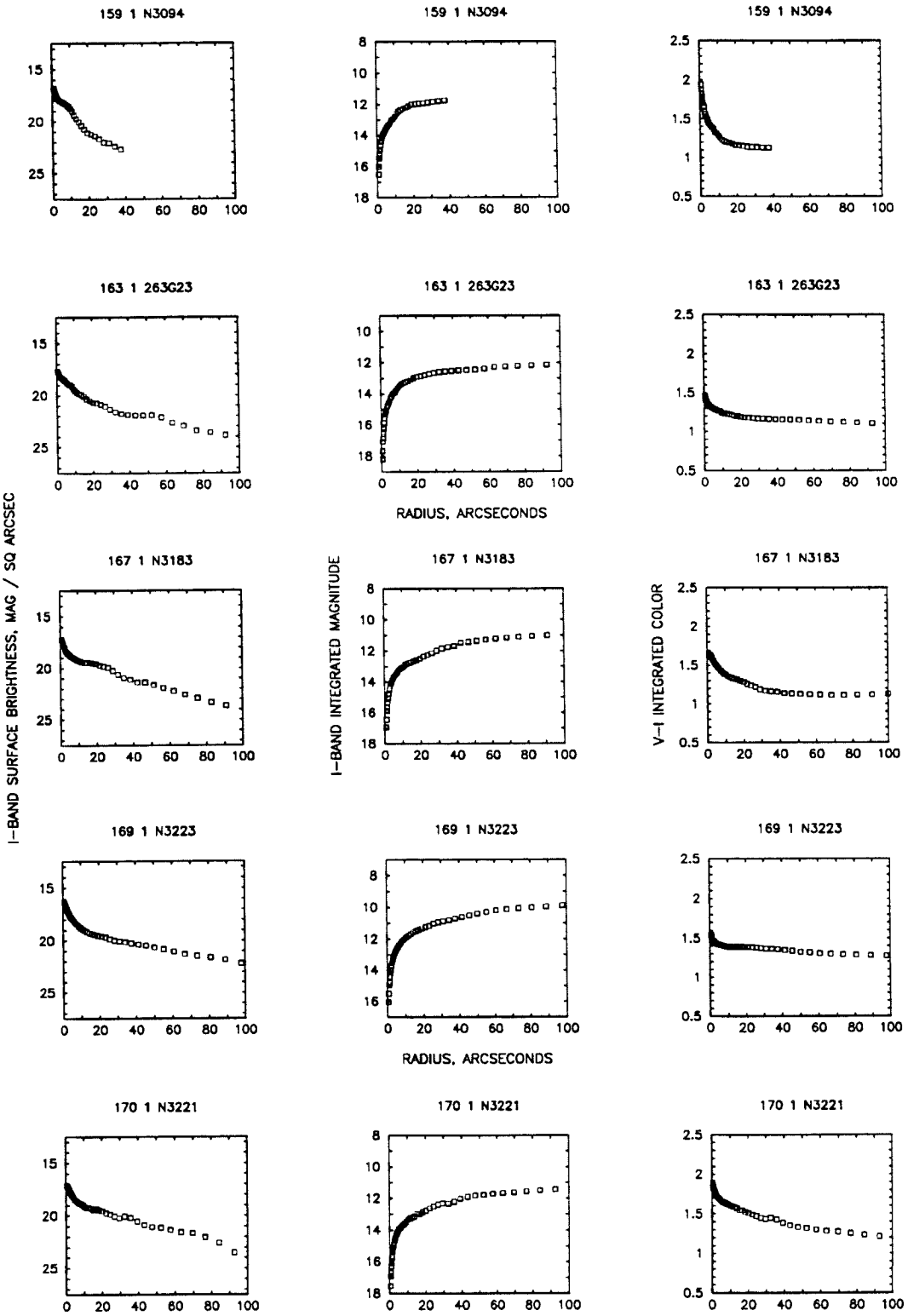
159 1 N3094
159 1 N3094
159 1 N3094
163 1 263G23
163 1 263G23
163 1 263G23
167 1 N3183
167 1 N3183
167 1 N3183
169 1 N3223
169 1 N3223
169 1 N3223
170 1 N3221
170 1 N3221
170 1 N3221
I-BAND SURFACE BRIGHTNESS, MAG / SQ ARCSEC
I-BAND INTEGRATED MAGNITUDE
V-I INTEGRATED COLOR
RADIUS, ARCSECONDS
RADIUS, ARCSECONDS

Figure 1(14)

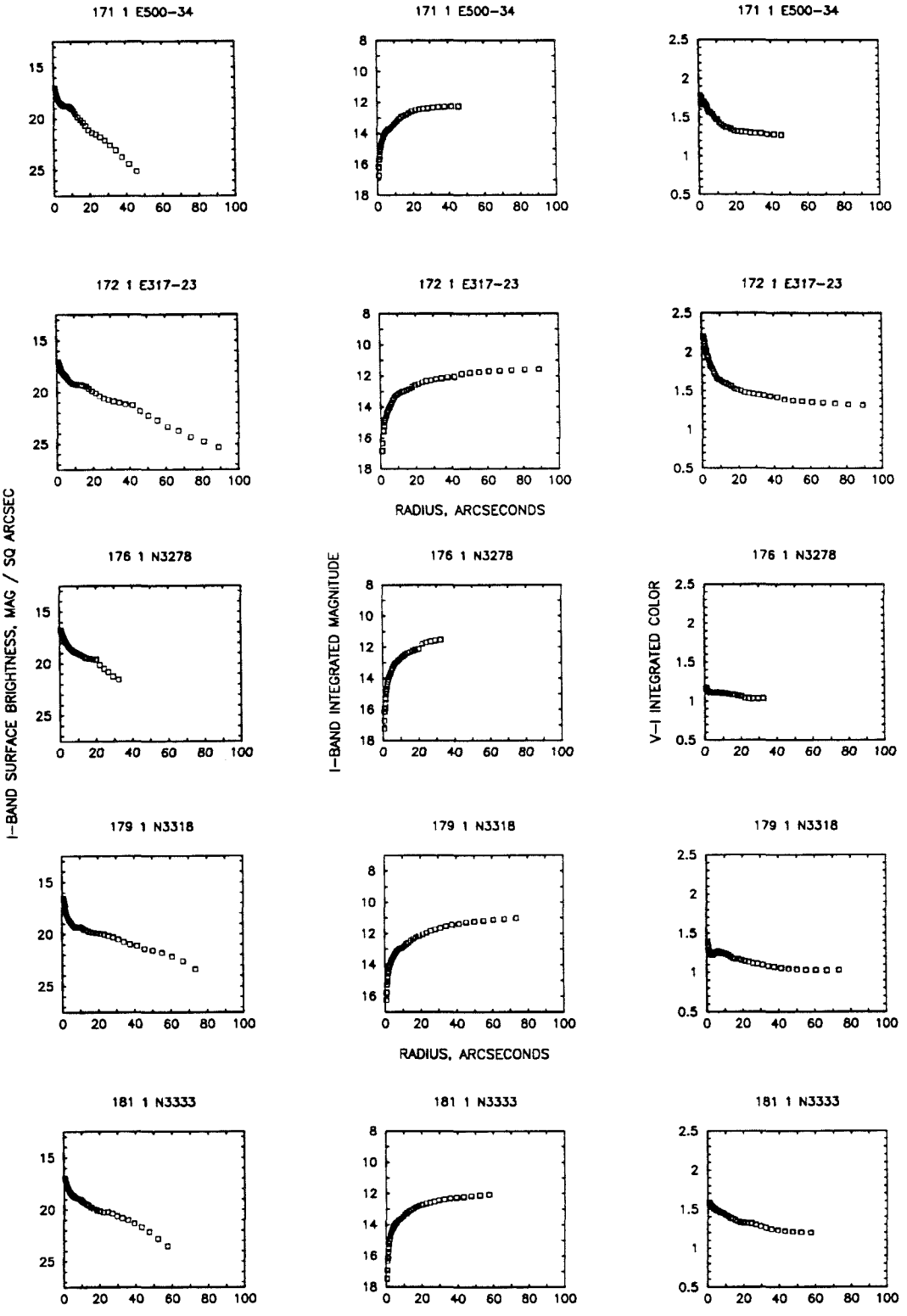
171 1 E500-34
171 1 E500-34
171 1 E500-34
172 1 E317-23
172 1 E317-23
172 1 E317-23
176 1 N3278
176 1 N3278
176 1 N3278
179 1 N3318
179 1 N3318
179 1 N3318
181 1 N3333
181 1 N3333
181 1 N3333
I-BAND SURFACE BRIGHTNESS, MAG / SQ ARCSEC
I-BAND INTEGRATED MAGNITUDE
V-I INTEGRATED COLOR
RADIUS, ARCSECONDS
RADIUS, ARCSECONDS

Figure 1(15)

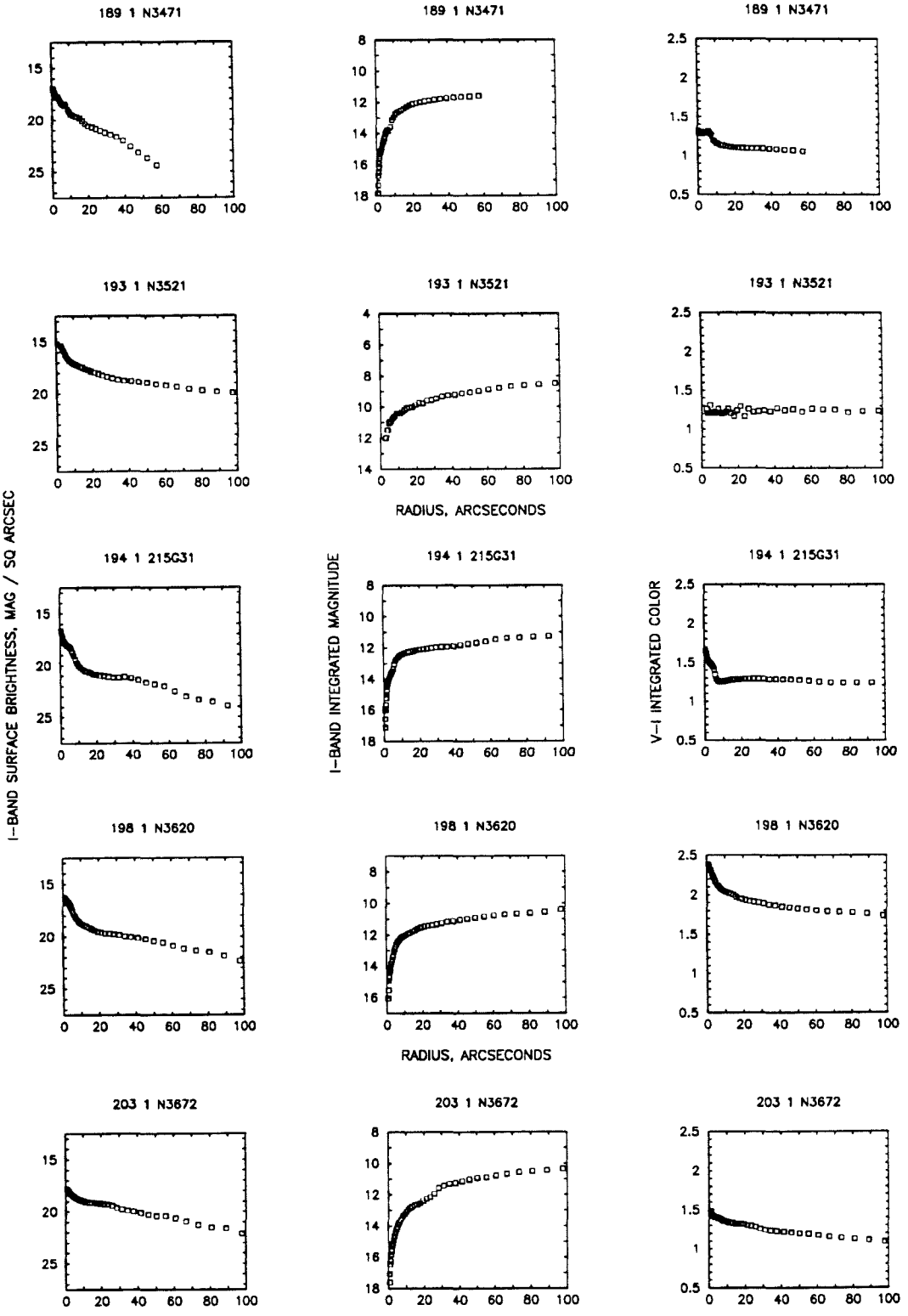
189 1 N3471
189 1 N3471
189 1 N3471
193 1 N3521
193 1 N3521
193 1 N3521
194 1 215G31
194 1 215G31
194 1 215G31
198 1 N3620
198 1 N3620
198 1 N3620
203 1 N3672
203 1 N3672
203 1 N3672
I-BAND SURFACE BRIGHTNESS, MAG / SQ ARCSEC
I-BAND INTEGRATED MAGNITUDE
V-I INTEGRATED COLOR
RADIUS, ARCSECONDS
RADIUS, ARCSECONDS

Figure 1(16)

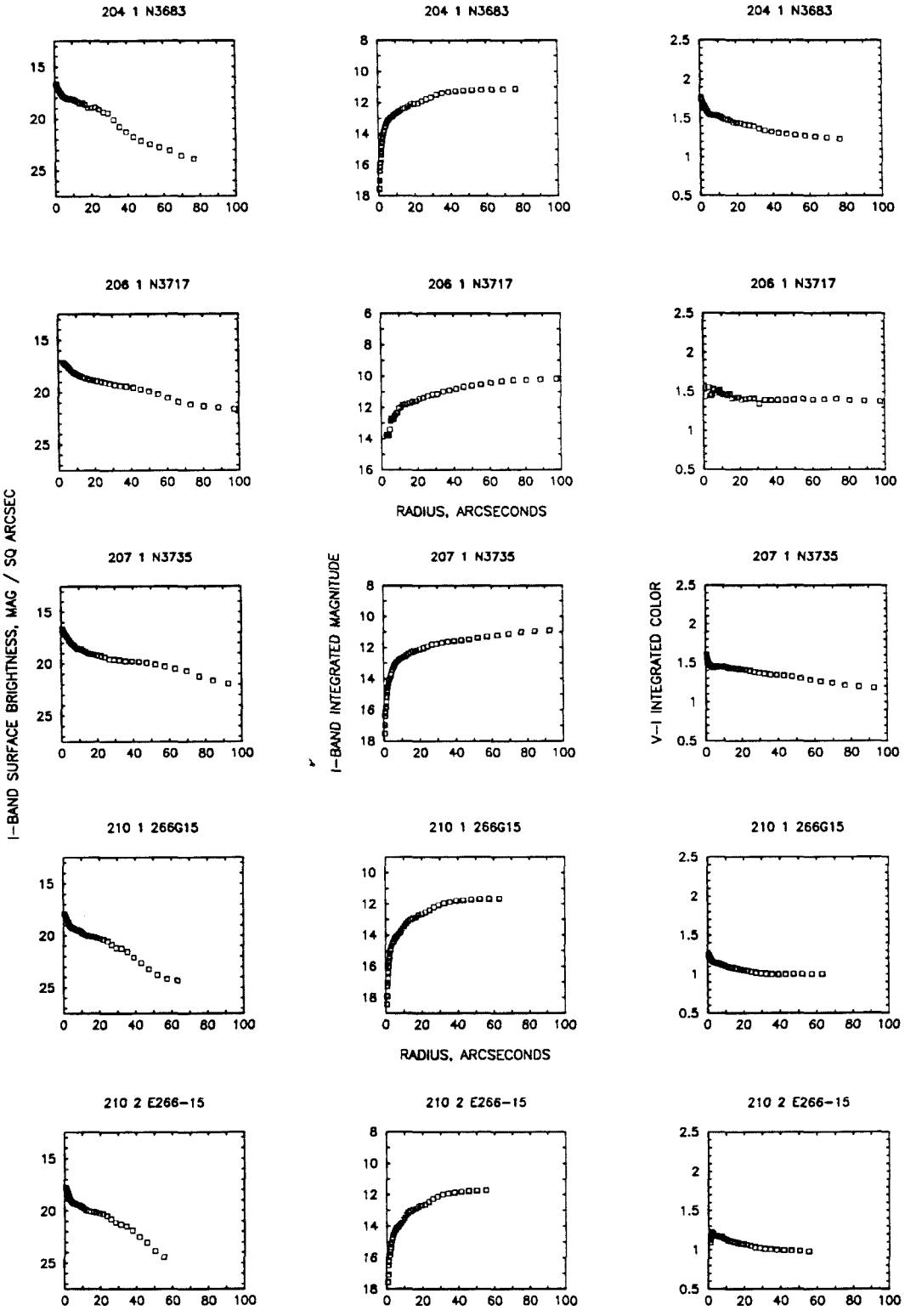
204 1 N3683
204 1 N3683
204 1 N3683
206 1 N3717
206 1 N3717
206 1 N3717
207 1 N3735
207 1 N3735
207 1 N3735
210 1 266G15
210 1 266G15
210 1 266G15
210 2 E266-15
210 2 E266-15
210 2 E266-15
I-BAND SURFACE BRIGHTNESS, MAG / SQ ARCSEC
I-BAND INTEGRATED MAGNITUDE
V-I INTEGRATED COLOR
RADIUS, ARCSECONDS
RADIUS, ARCSECONDS

Figure 1(17)

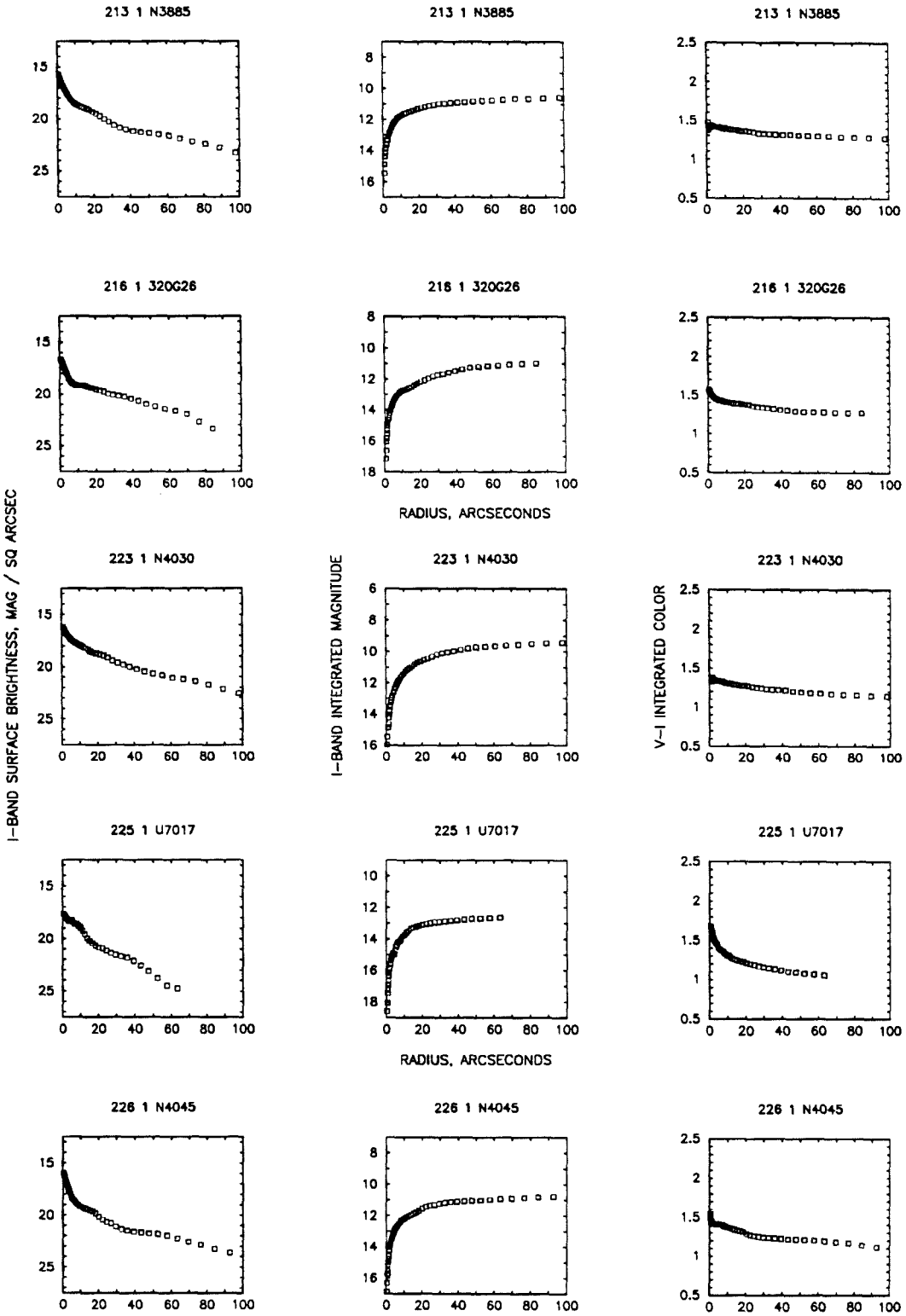
213 1 N3885
213 1 N3885
213 1 N3885
216 1 320G26
216 1 320G26
216 1 320G26
223 1 N4030
223 1 N4030
223 1 N4030
225 1 U7017
225 1 U7017
225 1 U7017
226 1 N4045
226 1 N4045
226 1 N4045
I-BAND SURFACE BRIGHTNESS, MAG / SQ ARCSEC
I-BAND INTEGRATED MAGNITUDE
V-I INTEGRATED COLOR
RADIUS, ARCSECONDS
RADIUS, ARCSECONDS

Figure 1(18)

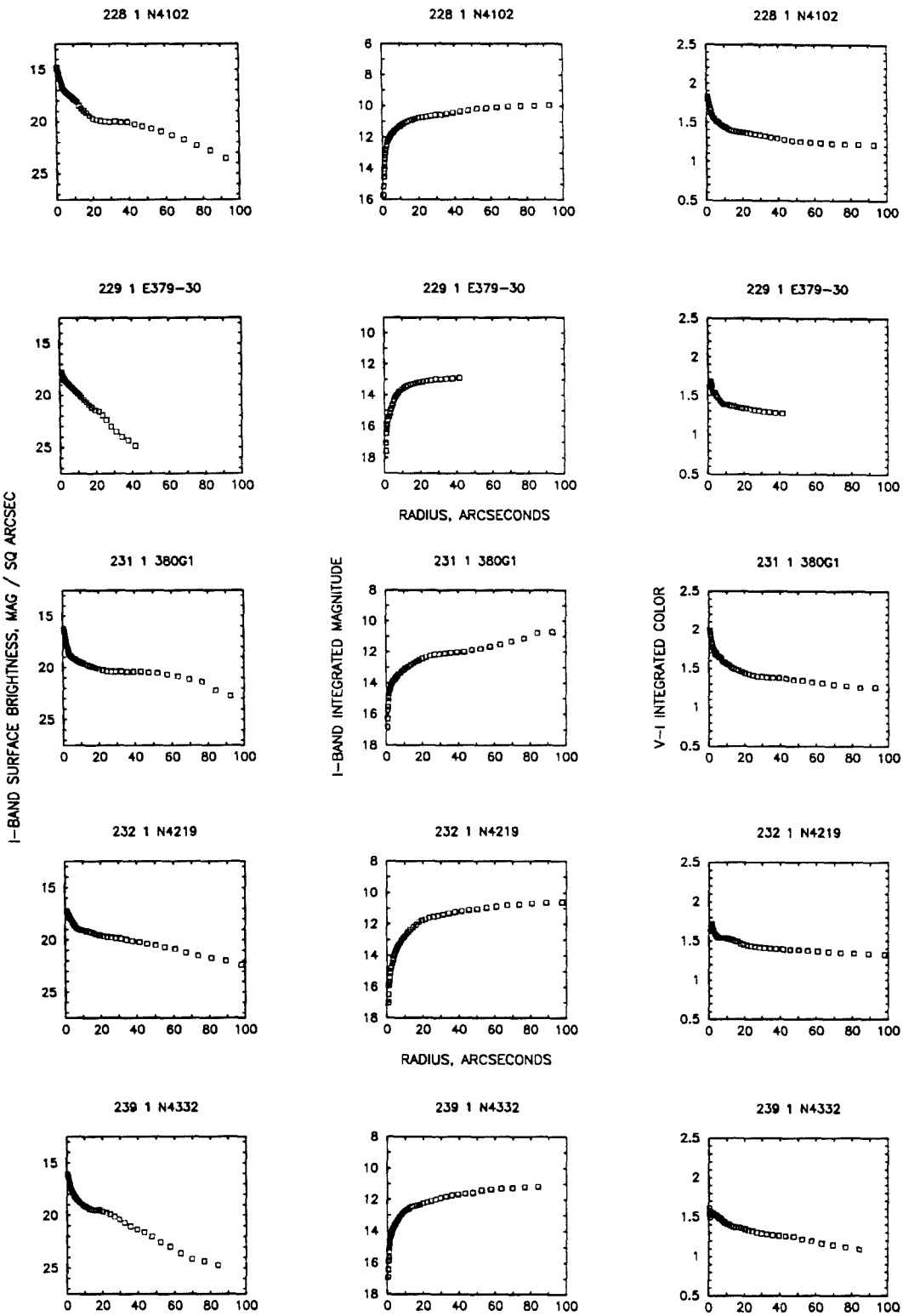
228 1 N4102
228 1 N4102
228 1 N4102
229 1 E379-30
229 1 E379-30
229 1 E379-30
231 1 380G1
231 1 380G1
231 1 380G1
232 1 N4219
232 1 N4219
232 1 N4219
239 1 N4332
239 1 N4332
239 1 N4332
I-BAND SURFACE BRIGHTNESS, MAG / SQ ARCSEC
I-BAND INTEGRATED MAGNITUDE
V-I INTEGRATED COLOR
RADIUS, ARCSECONDS
RADIUS, ARCSECONDS

Figure 1(19)

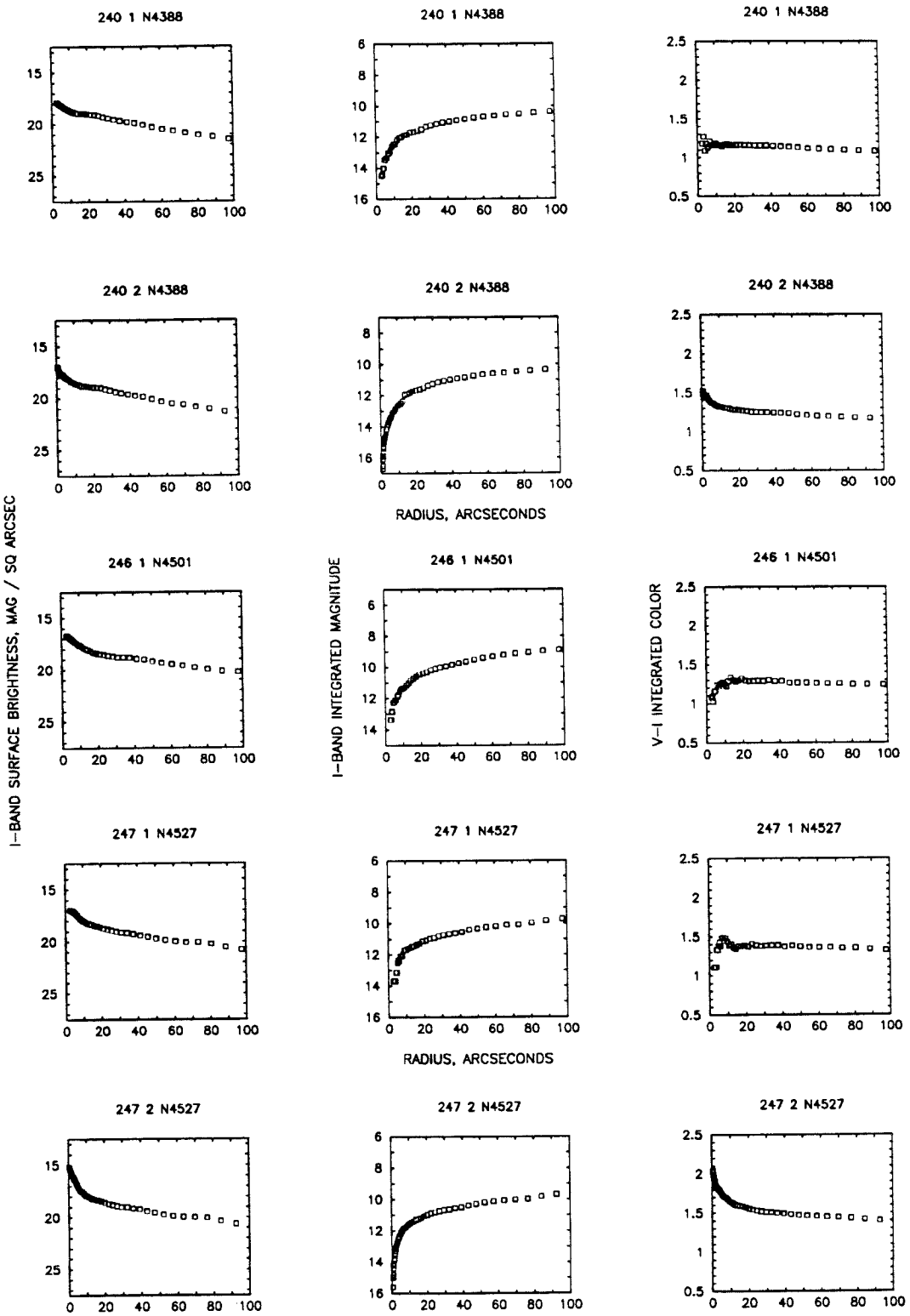
240 1 N4388
240 1 N4388
240 1 N4388
240 2 N4388
240 2 N4388
240 2 N4388
246 1 N4501
246 1 N4501
246 1 N4501
247 1 N4527
247 1 N4527
247 1 N4527
247 2 N4527
247 2 N4527
247 2 N4527
I-BAND SURFACE BRIGHTNESS, MAG / SQ ARCSEC
I-BAND INTEGRATED MAGNITUDE
V-I INTEGRATED COLOR
RADIUS, ARCSECONDS
RADIUS, ARCSECONDS

Figure 1(20)

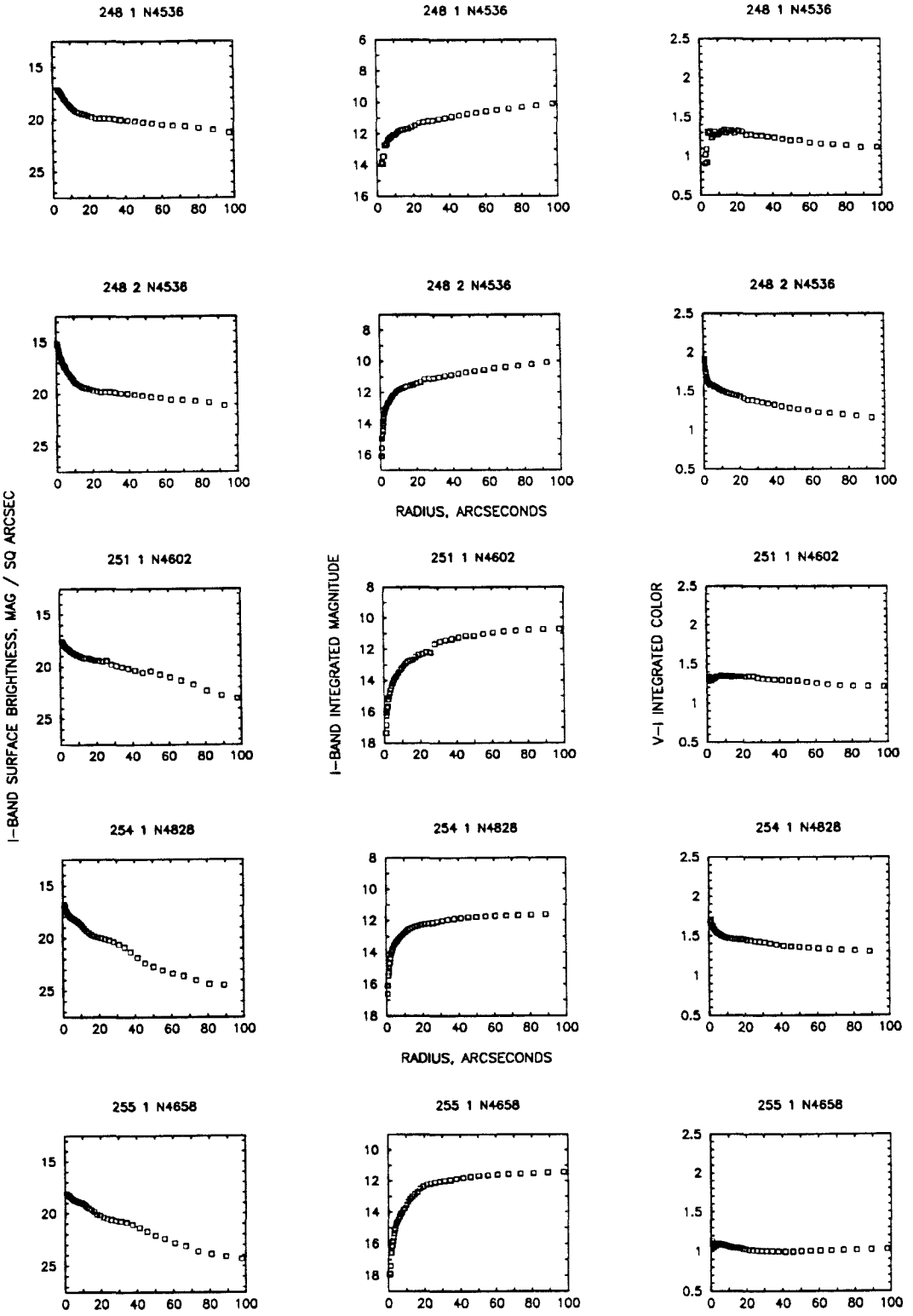
248 1 N4536
248 1 N4536
248 1 N4536
248 2 N4536
248 2 N4536
248 2 N4536
251 1 N4602
251 1 N4602
251 1 N4602
254 1 N4828
254 1 N4828
254 1 N4828
255 1 N4658
255 1 N4658
255 1 N4658
I-BAND SURFACE BRIGHTNESS, MAG / SQ ARCSEC
I-BAND INTEGRATED MAGNITUDE
V-I INTEGRATED COLOR
RADIUS, ARCSECONDS
RADIUS, ARCSECONDS

Figure 1(21)

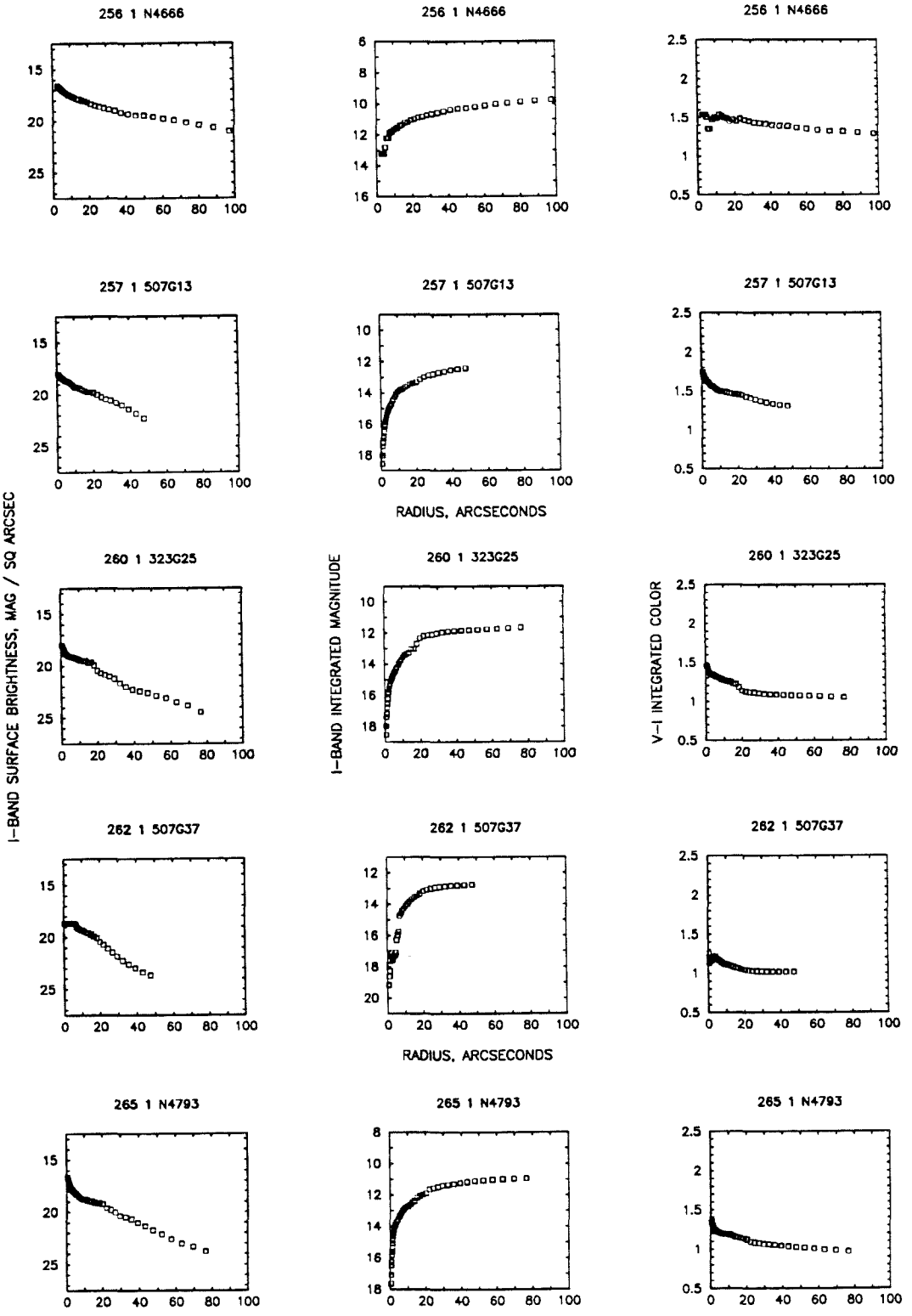
256 1 N4666
256 1 N4666
256 1 N4666
257 1 507G13
257 1 507G13
257 1 507G13
I-BAND SURFACE BRIGHTNESS, MAG / SQ ARCSEC
RADIUS, ARCSECONDS
260 1 323G25
260 1 323G25
260 1 323G25
I-BAND INTEGRATED MAGNITUDE
V-I INTEGRATED COLOR
262 1 507G37
262 1 507G37
262 1 507G37
RADIUS, ARCSECONDS
265 1 N4793
265 1 N4793
265 1 N4793

Figure 1(22)

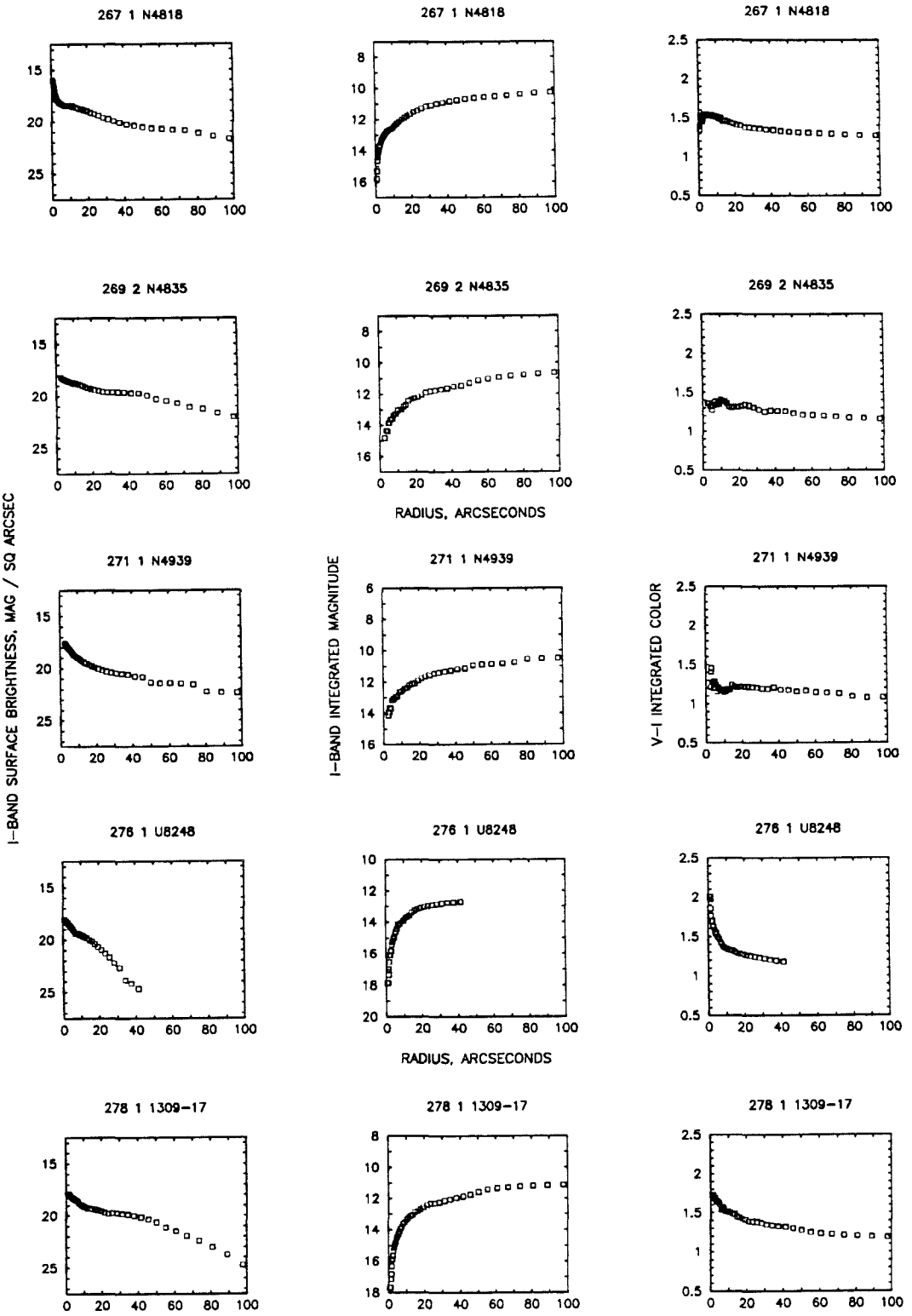
267 1 N4818
269 2 N4835
271 1 N4939
276 1 U8248
278 1 1309-17
I-BAND SURFACE BRIGHTNESS, MAG / SQ ARCSEC
I-BAND INTEGRATED MAGNITUDE
V-I INTEGRATED COLOR
RADIUS, ARCSECONDS

Figure 1(23)

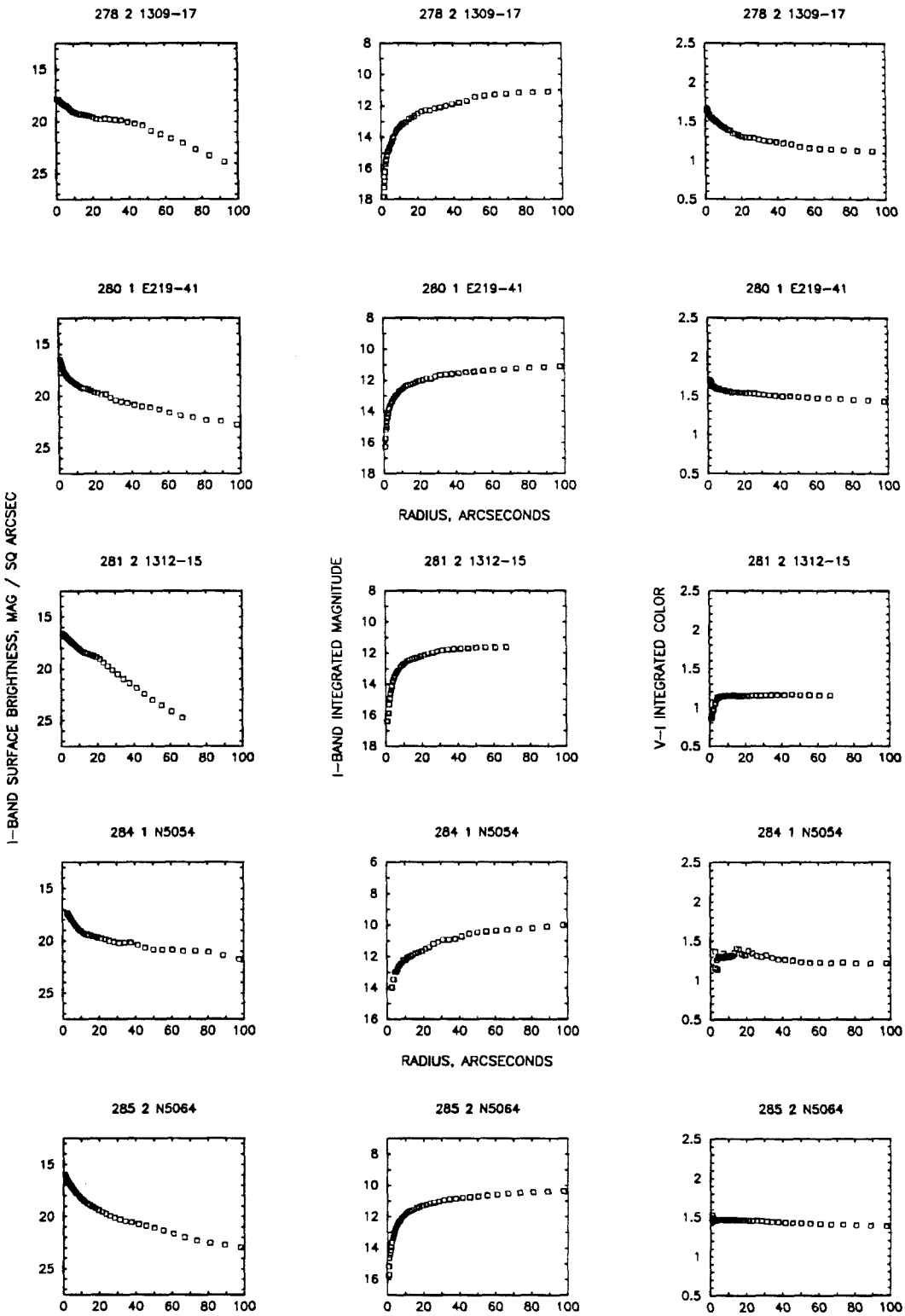
278 2 1309-17
278 2 1309-17
278 2 1309-17
280 1 E219-41
280 1 E219-41
280 1 E219-41
281 2 1312-15
281 2 1312-15
281 2 1312-15
284 1 N5054
284 1 N5054
284 1 N5054
285 2 N5064
285 2 N5064
285 2 N5064
I-BAND SURFACE BRIGHTNESS, MAG / SQ ARCSEC
I-BAND INTEGRATED MAGNITUDE
V-I INTEGRATED COLOR
RADIUS, ARCSECONDS
RADIUS, ARCSECONDS

Figure 1(24)

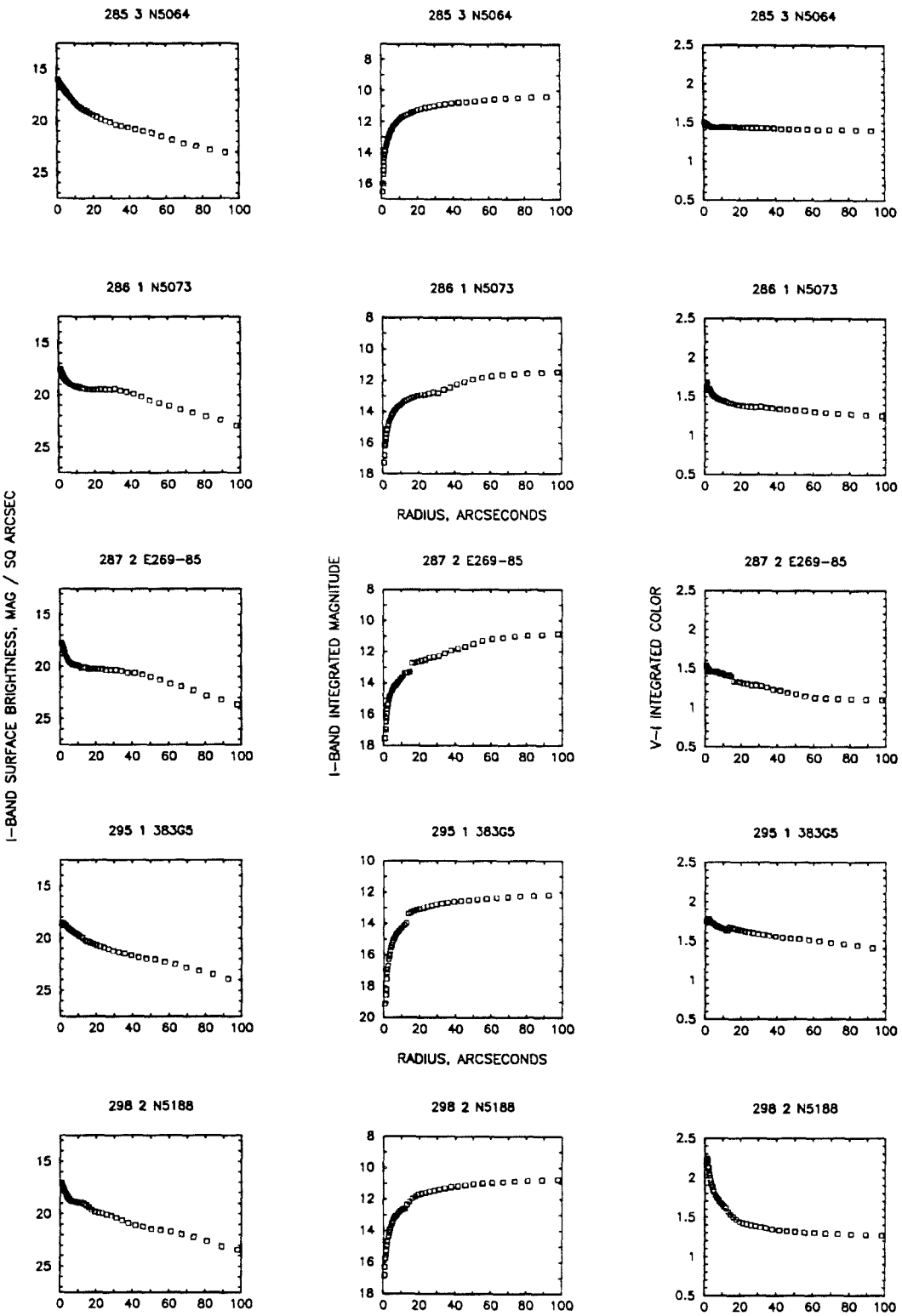
285 3 N5064
285 3 N5064
285 3 N5064
286 1 N5073
286 1 N5073
286 1 N5073
287 2 E269-85
287 2 E269-85
287 2 E269-85
295 1 383G5
295 1 383G5
295 1 383G5
298 2 N5188
298 2 N5188
298 2 N5188
I-BAND SURFACE BRIGHTNESS, MAG / SQ ARCSEC
I-BAND INTEGRATED MAGNITUDE
V-I INTEGRATED COLOR
RADIUS, ARCSECONDS
RADIUS, ARCSECONDS

Figure 1(25)

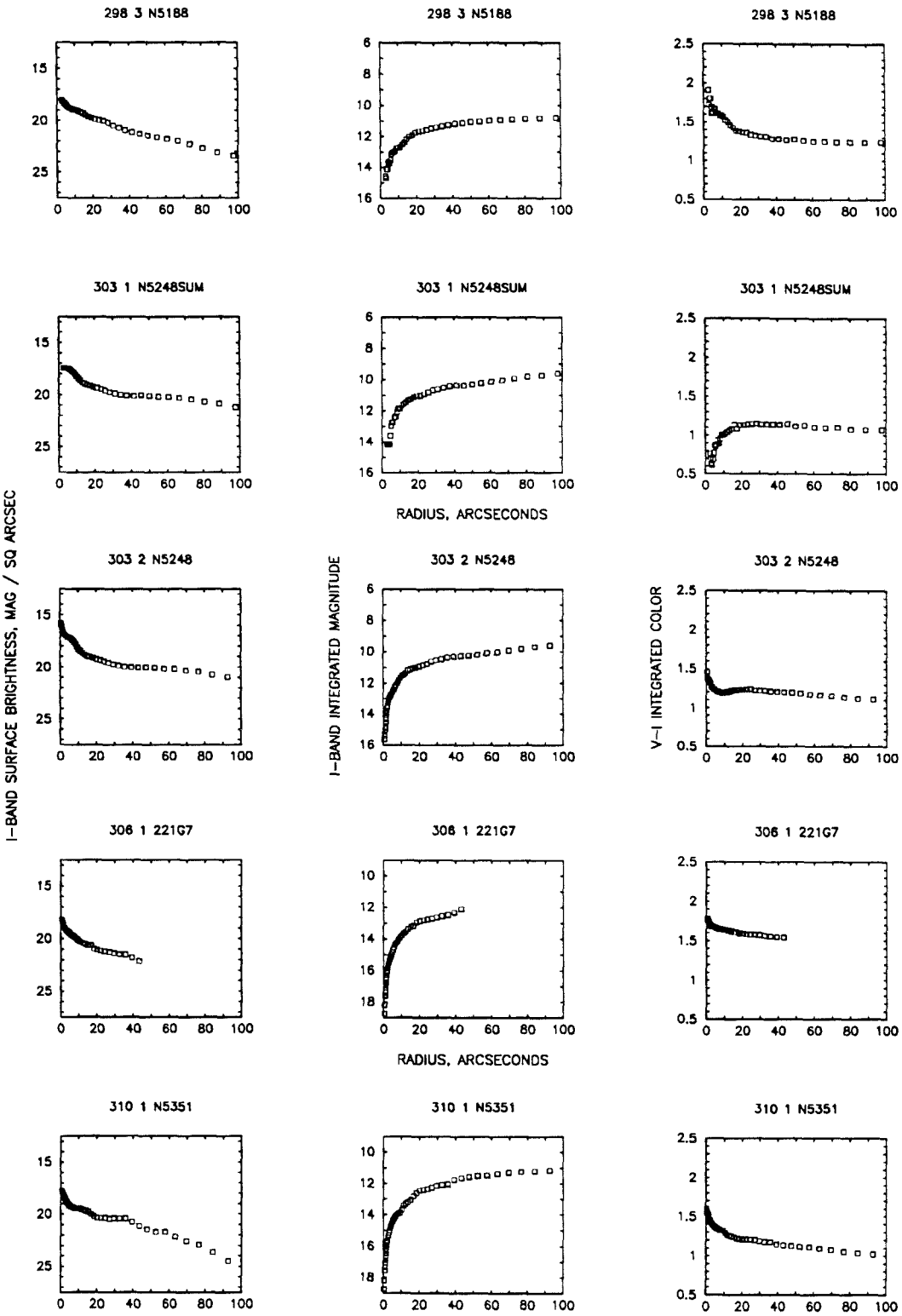
298 3 N5188
298 3 N5188
298 3 N5188
303 1 N5248SUM
303 1 N5248SUM
303 1 N5248SUM
303 2 N5248
303 2 N5248
303 2 N5248
306 1 221G7
306 1 221G7
306 1 221G7
310 1 N5351
310 1 N5351
310 1 N5351
I-BAND SURFACE BRIGHTNESS, MAG / SQ ARCSEC
I-BAND INTEGRATED MAGNITUDE
V-I INTEGRATED COLOR
RADIUS, ARCSECONDS
RADIUS, ARCSECONDS

Figure 1(26)

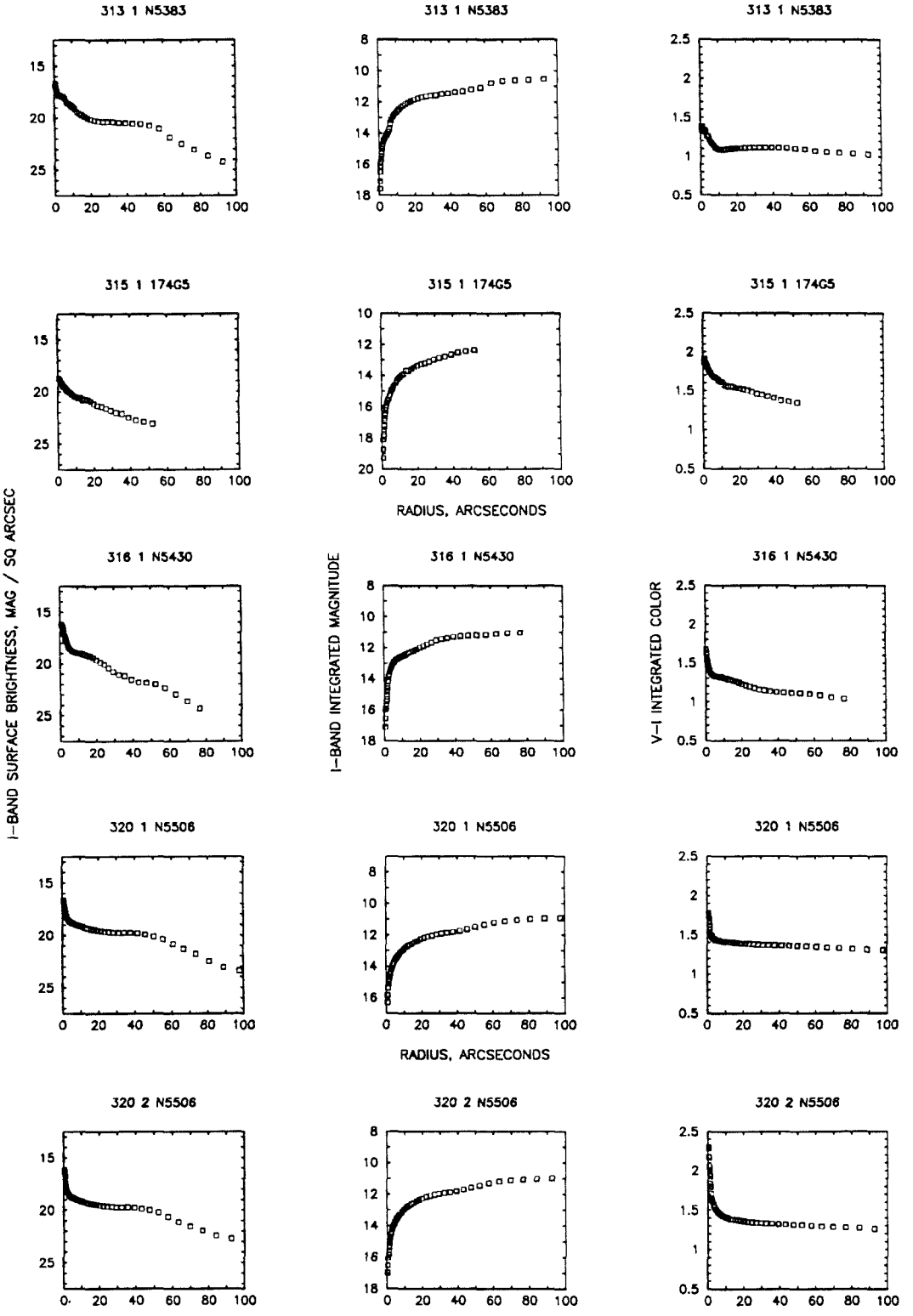
313 1 N5383
313 1 N5383
313 1 N5383
315 1 174G5
315 1 174G5
315 1 174G5
316 1 N5430
316 1 N5430
316 1 N5430
320 1 N5506
320 1 N5506
320 1 N5506
320 2 N5506
320 2 N5506
320 2 N5506
I-BAND SURFACE BRIGHTNESS, MAG / SQ ARCSEC
I-BAND INTEGRATED MAGNITUDE
V-I INTEGRATED COLOR
RADIUS, ARCSECONDS
RADIUS, ARCSECONDS

Figure 1(27)

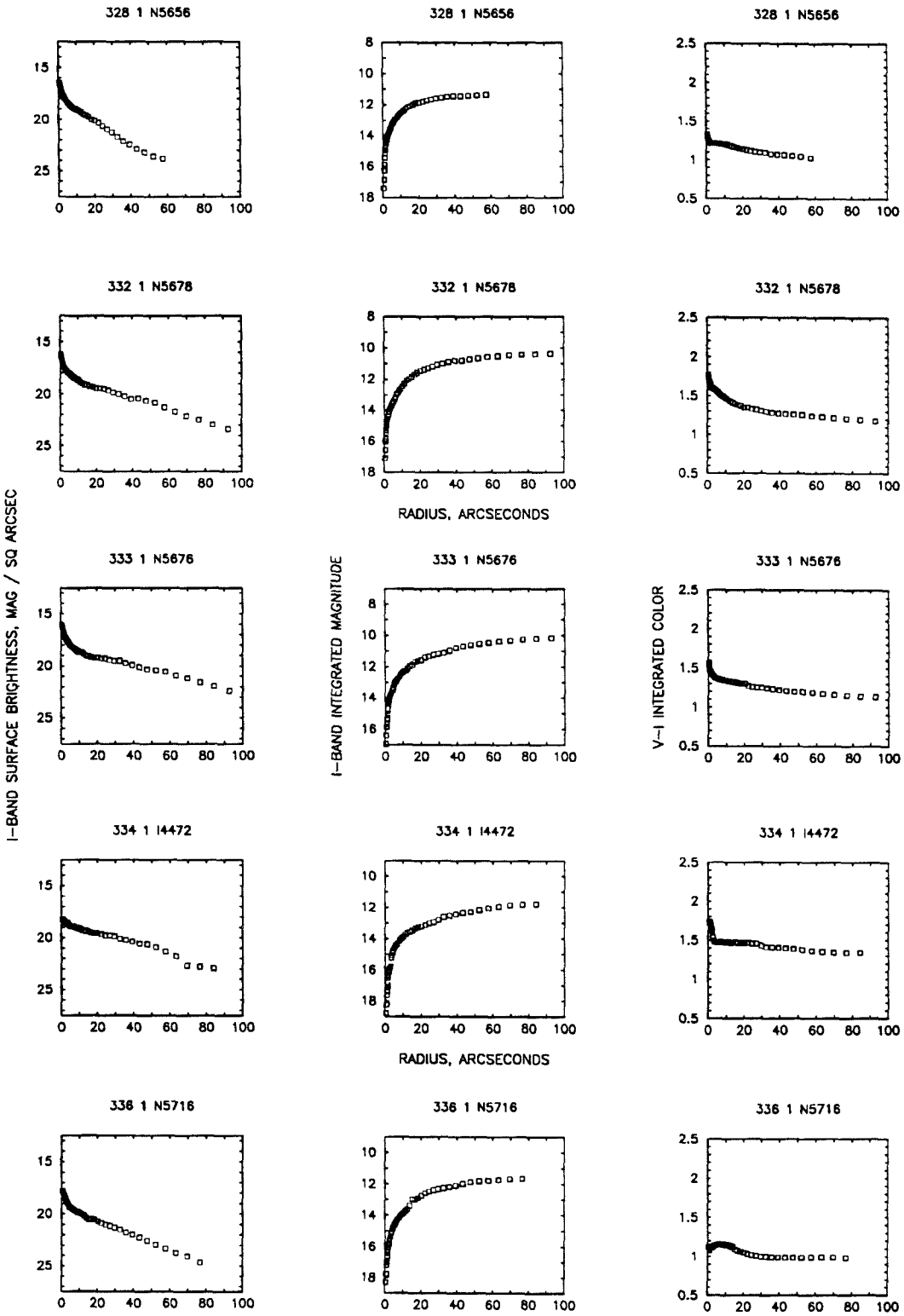
328 1 N5656
328 1 N5656
328 1 N5656
332 1 N5678
332 1 N5678
332 1 N5678
I-BAND SURFACE BRIGHTNESS, MAG / SQ ARCSEC
RADIUS, ARCSECONDS
I-BAND INTEGRATED MAGNITUDE
333 1 N5676
333 1 N5676
333 1 N5676
V-I INTEGRATED COLOR
334 1 I4472
334 1 I4472
334 1 I4472
RADIUS, ARCSECONDS
336 1 N5716
336 1 N5716
336 1 N5716

Figure 1(28)

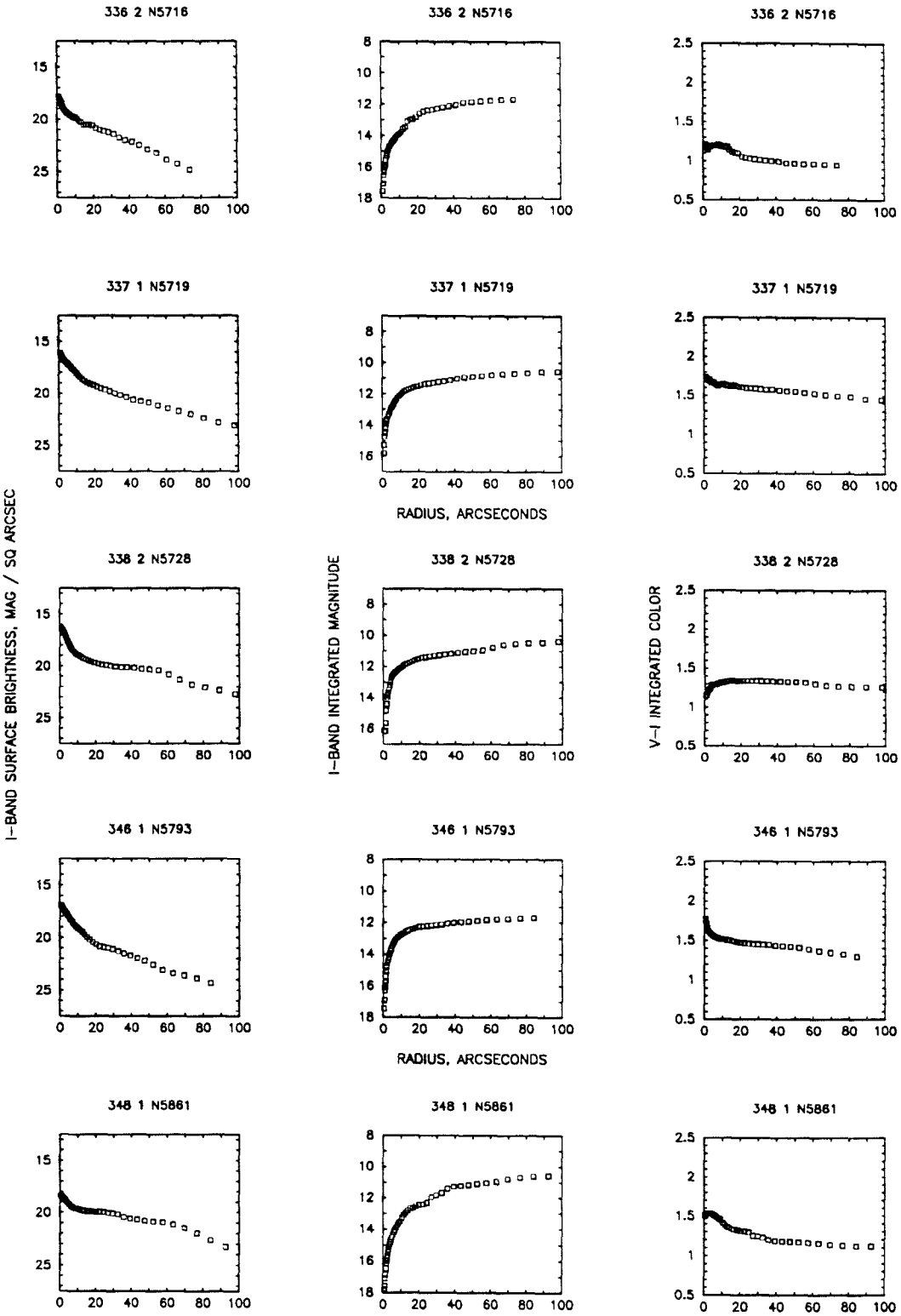
336 2 N5716
336 2 N5716
336 2 N5716
337 1 N5719
337 1 N5719
337 1 N5719
338 2 N5728
338 2 N5728
338 2 N5728
346 1 N5793
346 1 N5793
346 1 N5793
348 1 N5861
348 1 N5861
348 1 N5861
I-BAND SURFACE BRIGHTNESS, MAG / SQ ARCSEC
I-BAND INTEGRATED MAGNITUDE
V-I INTEGRATED COLOR
RADIUS, ARCSECONDS
RADIUS, ARCSECONDS

Figure 1(29)

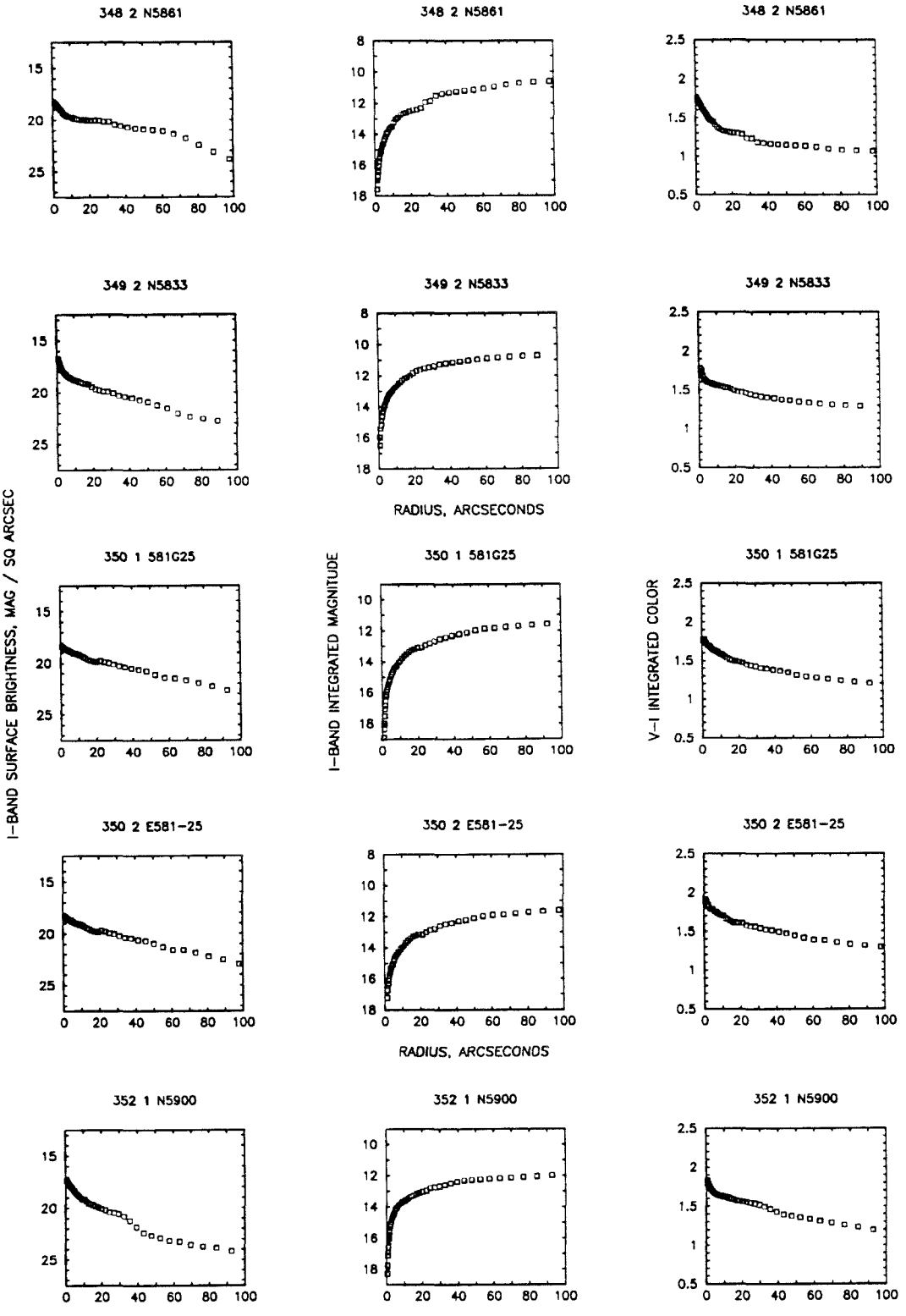
348 2 N5861
348 2 N5861
348 2 N5861
349 2 N5833
349 2 N5833
349 2 N5833
RADIUS, ARCSECONDS
I-BAND SURFACE BRIGHTNESS, MAG / SQ ARCSEC
350 1 581G25
350 1 581G25
350 1 581G25
I-BAND INTEGRATED MAGNITUDE
V-I INTEGRATED COLOR
350 2 E581-25
350 2 E581-25
350 2 E581-25
RADIUS, ARCSECONDS
352 1 N5900
352 1 N5900
352 1 N5900

Figure 1(30)

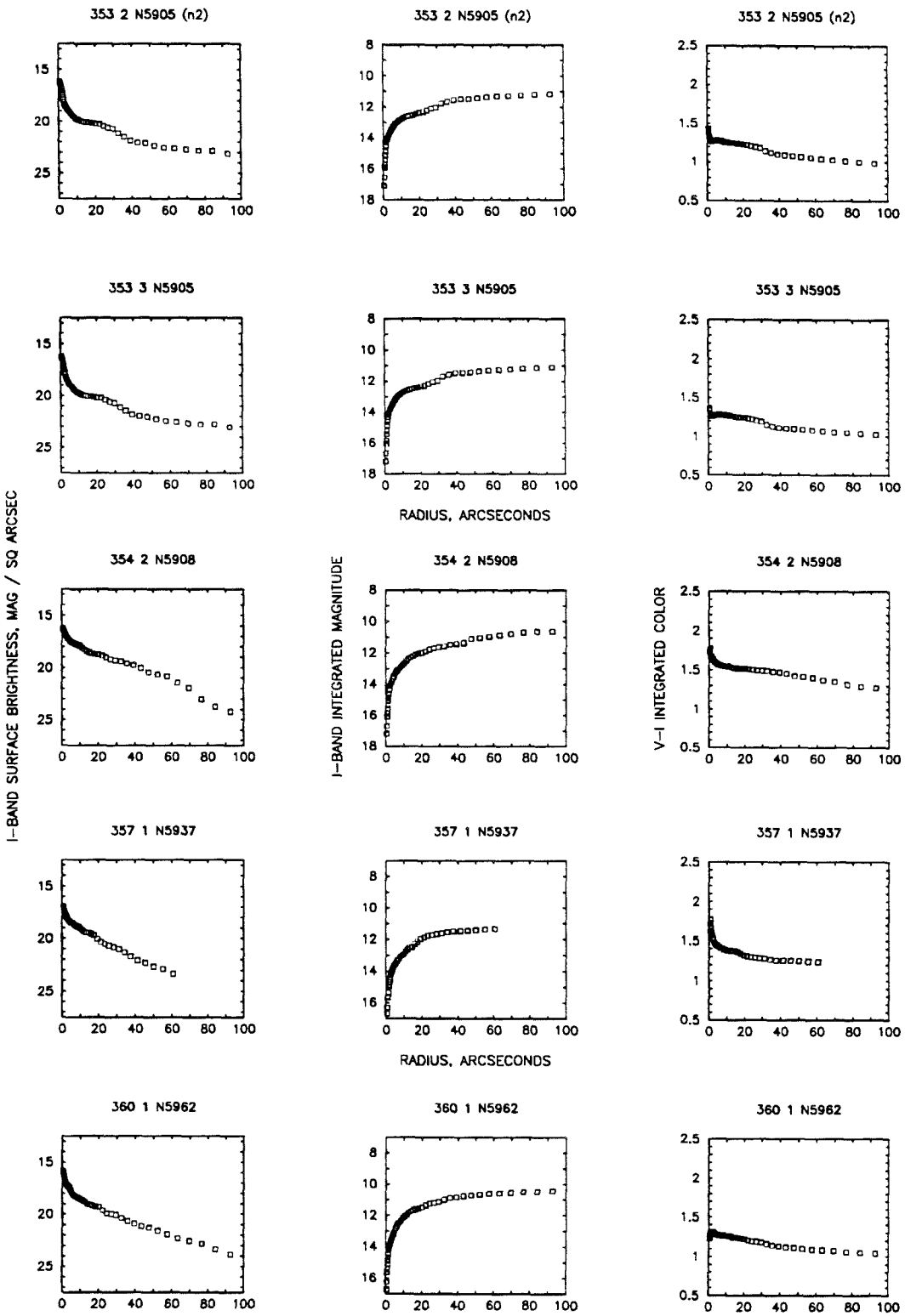
353 2 N5905 (n2)
353 2 N5905 (n2)
353 2 N5905 (n2)
353 3 N5905
353 3 N5905
353 3 N5905
354 2 N5908
354 2 N5908
354 2 N5908
357 1 N5937
357 1 N5937
357 1 N5937
360 1 N5962
360 1 N5962
360 1 N5962
I-BAND SURFACE BRIGHTNESS, MAG / SQ ARCSEC
I-BAND INTEGRATED MAGNITUDE
V-I INTEGRATED COLOR
RADIUS, ARCSECONDS
RADIUS, ARCSECONDS

Figure 1(31)

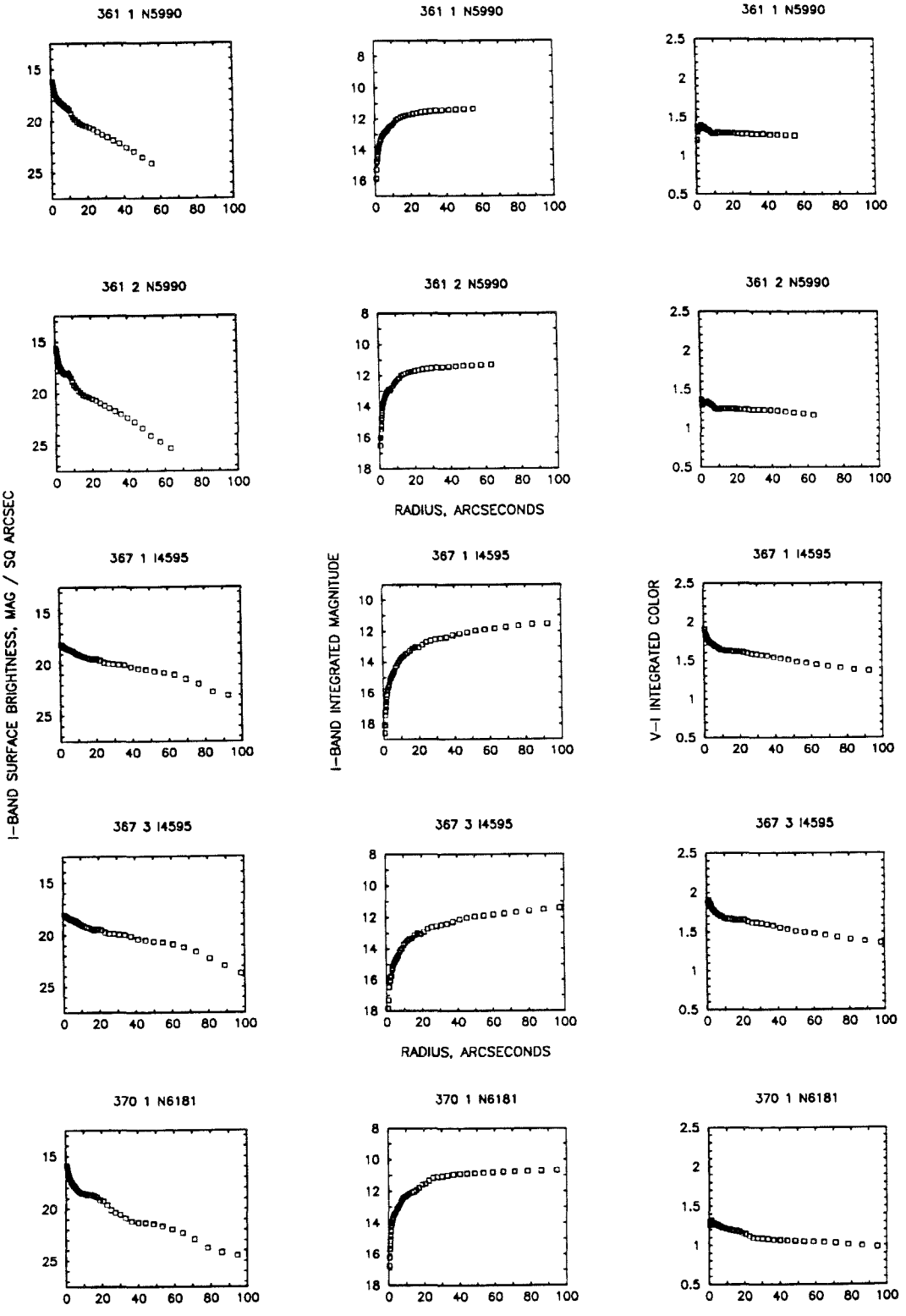
361 1 N5990
361 1 N5990
361 1 N5990
361 2 N5990
361 2 N5990
361 2 N5990
I-BAND SURFACE BRIGHTNESS, MAG / SQ ARCSEC
I-BAND INTEGRATED MAGNITUDE
V-I INTEGRATED COLOR
RADIUS, ARCSECONDS
367 1 I4595
367 1 I4595
367 1 I4595
367 3 I4595
367 3 I4595
367 3 I4595
RADIUS, ARCSECONDS
370 1 N6181
370 1 N6181
370 1 N6181

Figure 1(32)

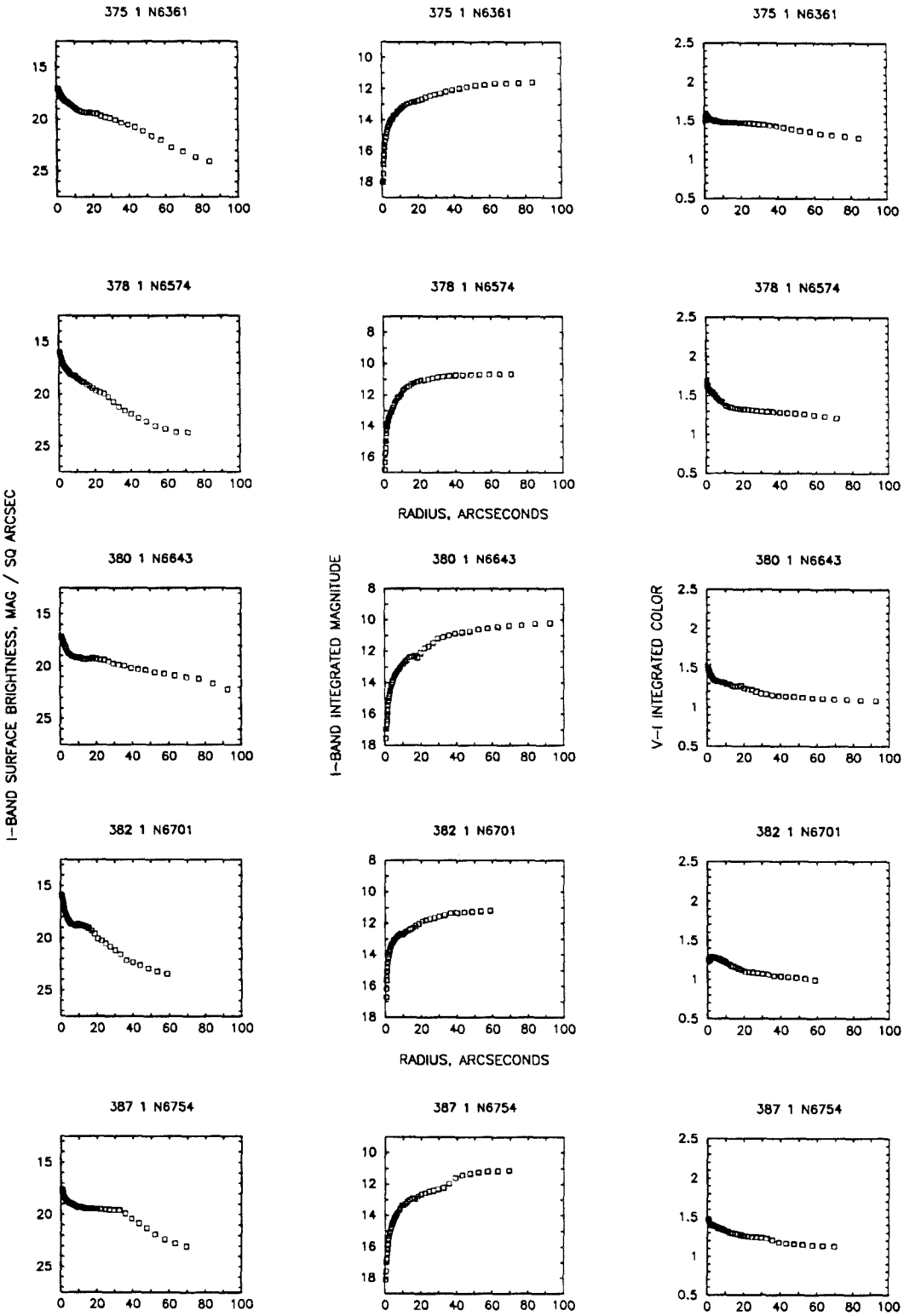
375 1 N6361
375 1 N6361
375 1 N6361
378 1 N6574
378 1 N6574
378 1 N6574
I-BAND SURFACE BRIGHTNESS, MAG / SQ ARCSEC
RADIUS, ARCSECONDS
I-BAND INTEGRATED MAGNITUDE
V-I INTEGRATED COLOR
380 1 N6643
380 1 N6643
380 1 N6643
382 1 N6701
382 1 N6701
382 1 N6701
RADIUS, ARCSECONDS
387 1 N6754
387 1 N6754
387 1 N6754

Figure 1(33)

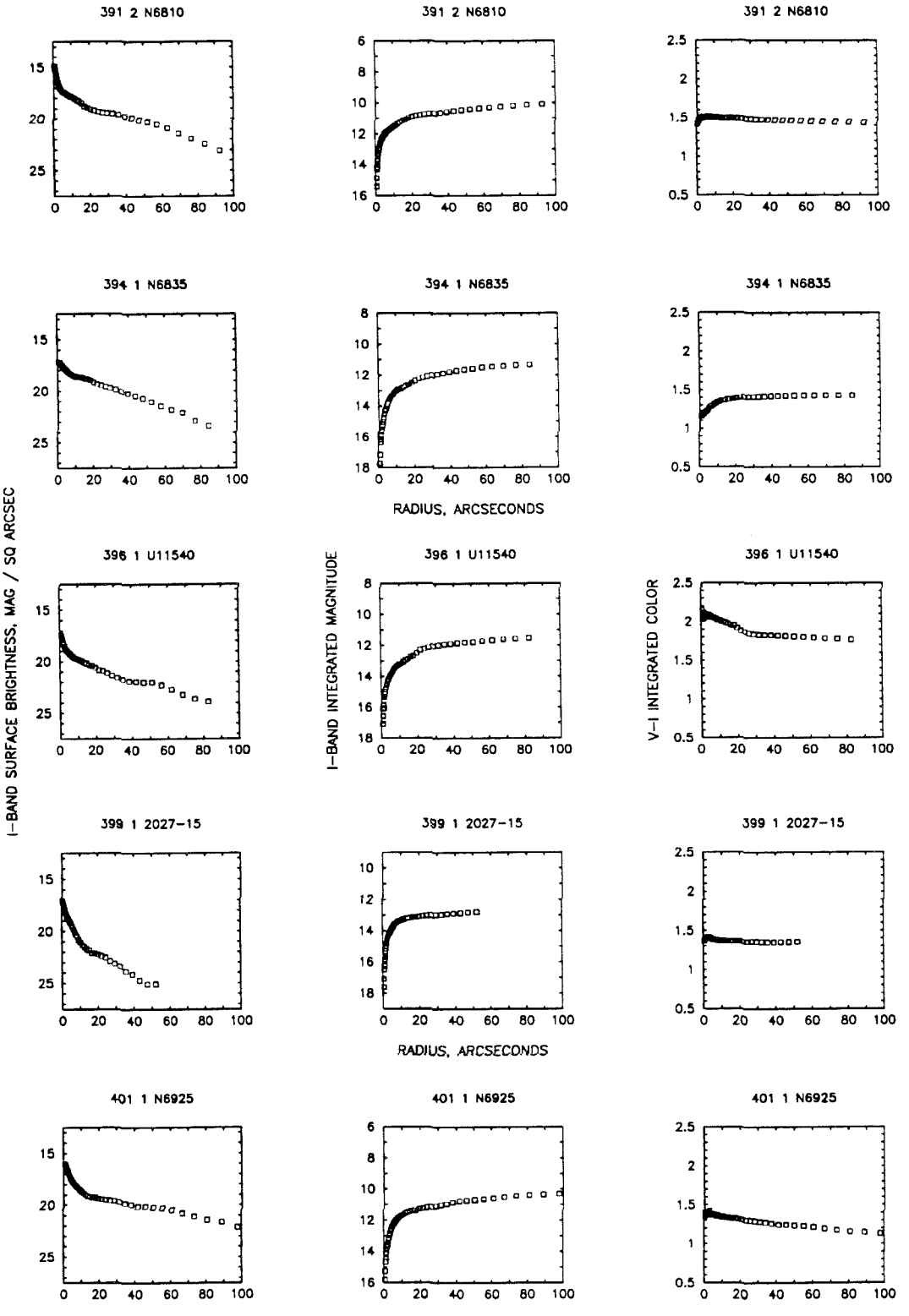
391 2 N6810
391 2 N6810
391 2 N6810
394 1 N6835
394 1 N6835
394 1 N6835
I-BAND SURFACE BRIGHTNESS, MAG / SQ ARCSEC
RADIUS, ARCSECONDS
396 1 U11540
396 1 U11540
396 1 U11540
I-BAND INTEGRATED MAGNITUDE
V-I INTEGRATED COLOR
399 1 2027-15
399 1 2027-15
399 1 2027-15
RADIUS, ARCSECONDS
401 1 N6925
401 1 N6925
401 1 N6925

Figure 1(34)

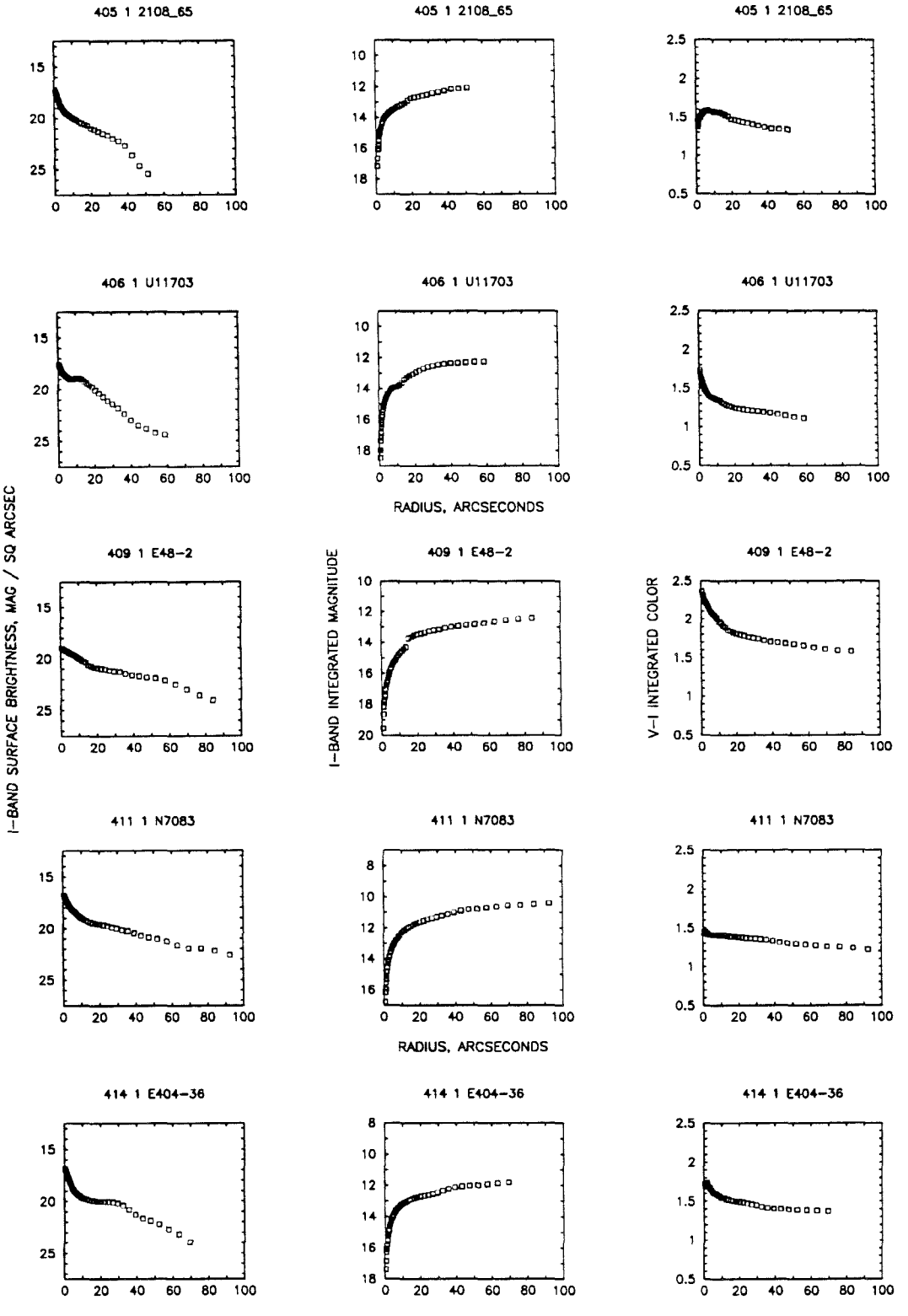
405 1 2108_65
405 1 2108_65
405 1 2108_65
406 1 U11703
406 1 U11703
406 1 U11703
409 1 E48-2
409 1 E48-2
409 1 E48-2
411 1 N7083
411 1 N7083
411 1 N7083
414 1 E404-36
414 1 E404-36
414 1 E404-36
I-BAND SURFACE BRIGHTNESS, MAG / SQ ARCSEC
I-BAND INTEGRATED MAGNITUDE
V-I INTEGRATED COLOR
RADIUS, ARCSECONDS
RADIUS, ARCSECONDS

Figure 1(35)

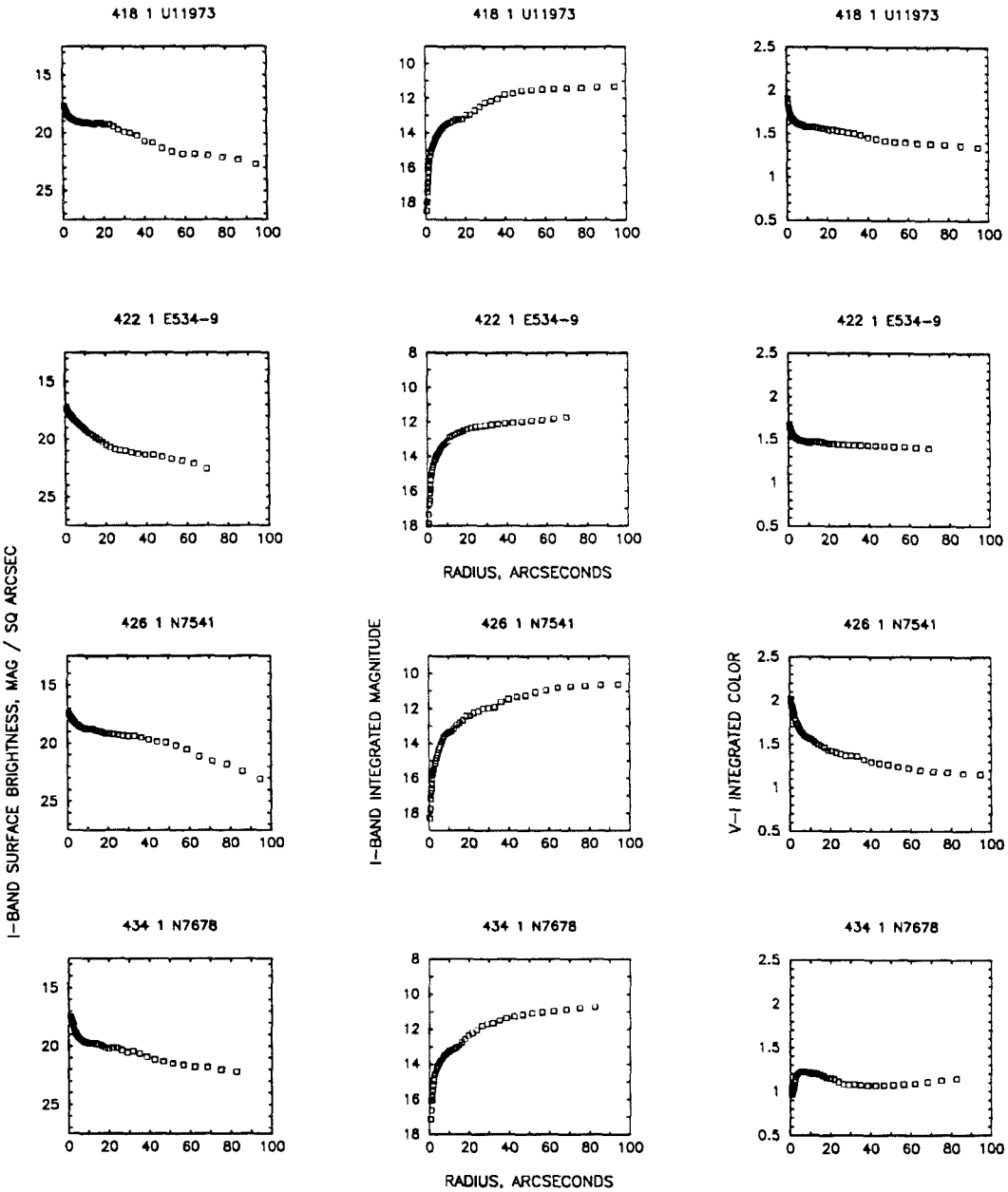
418 1 U11973
418 1 U11973
418 1 U11973
422 1 E534-9
422 1 E534-9
422 1 E534-9
426 1 N7541
426 1 N7541
426 1 N7541
434 1 N7678
434 1 N7678
434 1 N7678
I-BAND SURFACE BRIGHTNESS, MAG / SQ ARCSEC
I-BAND INTEGRATED MAGNITUDE
V-I INTEGRATED COLOR
RADIUS, ARCSECONDS
RADIUS, ARCSECONDS

Figure 1(36)

Chapter 3 - Corrections to Photometric Quantities

I. Introduction

The previous chapter showed how galaxy magnitudes were obtained by counting photons with CCDs, instrument throughputs having been calibrated with standard stars. The resulting observed surface brightness profiles $\Sigma_I(r)$, $[\Sigma_V - \Sigma_I](r)$ require corrections before the isophotal or estimated total magnitudes can be used as 'standard candles' to assess relative distances. The apparent size, brightness and colors of sources are altered by redshift effects (*e.g.*, Weinberg 1972). The apparent brightness of any portion of a given extragalactic object is diminished by the intervening dust and gas in our own Galaxy. Finally, the dust and gas contained in spiral galaxies themselves absorbs and scatters their own stellar light emission by amounts expected to depend upon the galaxy's inclination to our line of sight. Correction to a hypothetical face on standard is necessary to reduce scatter and remove systematic inclination related biases in the estimated distances we will infer for this sample. Because nobody has yet shown how to correct I and V band photometry on far infrared luminous galaxies for internal absorption, we must derive this correction self consistently for our own data. To do so we follow the methods of Han (HT; 1992), who determined inclination corrections to photometric quantities for his sample of optically selected cluster spirals. As expected, inclination effects on galaxy magnitudes and colors are stronger for our (presumably) dustier objects than they are for his samples based on the Palomar Sky Survey plates.

II. Cosmological corrections

The effect of cosmological recession velocity $v_{rec} = cz$, $z \sim \delta\lambda/\lambda_0$ upon the angular size of a standard ruler of angular size D is to increase the apparent angular size by a factor $(1 + z)$; thus

linear dimensions (in arcseconds) in all surface brightness profiles were divided by this factor to yield corrected angular size

$$r_{rest} = r_z \times (1+z)^{-1}. \qquad (3-1)$$

Area and surface brightness are correspondingly affected; thus, for example, the apparent density of luminous energy coming from a given solid angle of source surface must be multiplied by $(1+z)^4$ to correct it to rest frame units and surface brightness, in magnitudes per unit solid angle, becomes:

$$\Sigma_{rest} = \Sigma_z - 10log(1+z). \qquad (3-2)$$

Because the expansion of space through which photons travel between emission and observation increases their wavelength, the portion of an object spectrum falling within the bandpass of an astronomical detector depends upon source z value. Corrections for this effect (known as K correction; Sandage 1963) depend upon the details of the bandpass and of the object spectrum. Han (HT) calculated K corrections for a range of model galaxy spectra and a range of redshifts (z) from 0 to 0.03; he then fit simple functions to describe the corrections to I and V band magnitudes. He found that galaxies of type T and redshift z required the subtraction of terms

$$K_I = (0.5876 - 0.1658\ T)\ z; \qquad (3-3a)$$

$$K_V = (1.9728 - 0.4109\ T)\ z \qquad (3-3b)$$

from their I and V band magnitudes, respectively. Adopting provisional average type $< T >= 2$ for the present sample, we subtracted terms of $K_I = 0.256z$ from our I band surface brightness and integrated magnitude columns, and $K_{(V-I)} = 0.895z$ from our differential and integral color $(V-I)$ columns in each SFB file before extracting isophotal radii, magnitudes and colors. Uncertainty in galaxy type of amplitude $\delta T = 3$ leads to a maximum error (at the sample redshift limit of $cz = 4000$ km sec^{-1}) of $\Delta K_I = 0.006$, $\Delta K_{(V-I)} = 0.010$, which we deem acceptable in light of the ~ 0.05 mag limits to our I and $V-I$ magnitudes inferred from repeat galaxy observations in the previous

chapter. Of course, the correction depends on the details of the galaxy spectral models, but its amplitude at such low redshifts suggests that we may ignore this uncertainty for our purposes.

To sum up, then, the following quantities in each SFB file were corrected in the following manner:

$$m_I \triangleleft m_I - 0.256\ z; \tag{3-4}$$

$$\Sigma_I \triangleleft \Sigma_I - 10log(1+z) - 0.256\ z; \tag{3-5}$$

$$r \triangleleft r \times (1+z)^{-1}. \tag{3-6}$$

$$(m_V - m_I) \triangleleft (m_V - m_I) - 0.895\ z. \tag{3-7}$$

Error bars in photometric quantities (as previously determined from photon counting statistics, sky level precision, and uncertainty in the photometric solutions) were unaltered; that is, uncertainty in the magnitude of K correction was not added to the error budget. We note that, as objects in the present study all lie at $cz_\odot < 5000$ km sec^{-1} , z related corrections to both photometric and spectroscopic observables are in practice dwarfed by random and systematic measurement errors.

III. Galactic absorption correction

The absolute decrement suffered by light at a given wavelength while passing through a given line of sight through our Milky Way is difficult to determine. External galaxies suffer their own internal absorption and reddening effects which are hard to separate from those of the Milky Way.

Most extragalactic astronomers have followed the example of Burstein and Heiles (1982; hereafter BH) in assuming a proportionality between dust column density (which is chiefly responsible for scattering light at visible wavelengths) and neutral hydrogen column density. The former may

be indirectly measureable with the *IRAS* 100 micron intensity maps, although at a fairly coarse angular scale (Boulanger, Helou, pers. comm.).

The Galactic HI column density is easily observable with narrowband radio spectrometers at 1420 MHz using techniques of frequency (rather than spatial) switching to provide the system baseline above which integrated intensity directly reflects HI column density (since the Galaxy is believed to be optically thin in the hyperfine transition at 1420 MHz). BH utilized Galactic HI column density maps and Lick Observatory large-scale galaxy counts by Shane and Wirtanen to prepare a map of inferred extinction coefficients $E(B-V)$. From this quantity absorption coefficients in magnitudes are set by:

$$A_B = 4.3\ E(B-V); \tag{3-8a}$$

$$A_V = 0.74\ A_B; \tag{3-8b}$$

$$A_I = 0.44\ A_B \tag{3-8c}$$

(Whitford 1958). The precise fractional attenuation in a given lightbeam observed with a broadband detector will depend upon the source spectrum, of course, but these values are typically applied to the principally starlike spectra of galaxies. I band surface brightness and integrated magnitude for each galaxy had corrections

$$\Sigma_I \triangleleft \Sigma_I - A_I \tag{3-9a}$$

$$m_I \triangleleft m_I - A_I, \tag{3-9b}$$

and $V-I$ colors,

$$(m_V - m_I) \triangleleft (m_V - m_I) - (A_V - A_I), \tag{3-9c}$$

applied following those of the previous section before isophotal magnitudes and radii were extracted in what follows.

Large-scale gradients now known to exist in the distribution of galaxies, which cannot be attributed solely to the effects of Galactic absorption (Picard 1991), weaken any inference made about small scale Galactic absorption differentials by studying number counts of extragalactic objects. Nevertheless the BH values have become standards for extragalactic distance indicator work.

We obtained BH values for 148 of our 159 photometered objects from the NASA/IPAC Extragalactic Database (hereafter 'NED'). We obtained values for 356 of our 440 *a priori* sample members. The average value and *rms* of the latter are $< A_B^{BH} >= 0.246 \pm .293$. Sampling the RC2 function for $A_B(l,b)$ (de Vaucauleurs, de Vaucauleurs and Corwin 1976; hereafter RC2) at the same points provided $< A_B^{RC2} >= 0.099 \pm .11$, a substantially lower value.

IV. Internal absorption and reddening corrections

We presume that, as galaxies are seen more nearly edge on, their starlight passes through an increasing amount of absorbing and scattering material. At the same time, a greater number of stars populates a column of fixed angular area. Formulae derived empirically from other samples, or theoretically from simple models for galaxies, are available in the literature (*e.g.*, Tully and Fouque 1985). We are not content to use them, however, since (a) the galaxies used in these studies may differ systematically from far infrared luminous ones like ours, and (b) the spatial distribution of stars and gas in the galaxy, which critically affects the inclination corrections, may be very different in our galaxies than in the models. In this section we closely follow the methods of Han (1992), who set out to determine in somewhat 'bootstrap' fashion the corrections to be placed upon isophotal magnitudes and colors for absorption and reddening of visible light by a galaxy's own interstellar media. His sample was composed of cluster spirals selected principally by Zwicky magnitude in the northern hemisphere and by ESO diameter in the south. His approach could be summarized as follows:

(1) Fit an exponential disk law (hereafter EDL)

$$\Sigma_I(r) = \Sigma_0 + A\ r, \qquad (3-10a)$$

$$A = 1.0857/r_0 \qquad (3-10b)$$

to the outer part of surface brightness profile; the scale radius r_0 provides some sort of standard ruler or aperture, and inferred central surface brightness Σ_0 reflects the overall disk brightness density.

(2) Use nominal distances to objects to verify that scale radius (in physical units like kiloparsecs) does not correlate with galaxy inclination angle; if it does, it cannot serve as an unbiased aperture.

(3) Plot EDL central surface brightness Σ_0 versus log galaxy axial ratio $log(R)$ where R = major axis / minor axis; slope is -2.5 if galaxies are optically (and geometrically) thin to starlight because of pure geometrical projection. A lesser slope indicates that galaxies are not 'limb brightening' as much as would be expected and hence, offer some opacity to their own starlight.

(4) Determine average ratio of (uncorrected) isophotal radius r^i_Σ at some observed surface brightness level Σ_I^{corr} (corrected for cosmological and Galactic effects but not otherwise) to scale radius r_0 to provide statistical correction of observed isophotal radii r^i_Σ to face-on values:

$$r_\Sigma^{corr} = r^i_\Sigma \times [1 - 0.92\ s_1\ log(R)/ < r^i_\Sigma/r_0 >], \qquad (3-11)$$

where s_1 equals the slope of $\Sigma_0 - log(R)$ relation, and 'i' denotes a quantity derived before correction for galaxy inclination.

(5) Use r_Σ^{corr} as a standard aperture within which to assess an average interior surface brightness

$$\Sigma^i_r = m^i_{I_\Sigma} + 5\ log(r_\Sigma^{corr}), \qquad (3-12)$$

where $m^i_{I_\Sigma}$ is the observed isophotal magnitude at the specified SB level Σ.

(6) Plot Σ_r^i versus $log(R)$; use the resulting slope s_2 to correct isophotal magnitudes $m_{I_\Sigma}^i$ to face on value:

$$m_{I_\Sigma}^{corr} = m_{I_\Sigma}^i - s_2 log(R). \qquad (3-13)$$

Note that while slope s_1 simply indicates the inclination effects upon the surface brightness of the outer part of galaxy disks, where EDLs have been fitted, s_2 indicates the dimming of all the light interior to the radius at which I band surface brightness equals Σ.

(7) Plot observed isophotal color $(m_V - m_I)_\Sigma^i$ versus $log(R)$ and utilize the slope s_3 to correct isophotal colors to face on values:

$$(m_V - m_I)_\Sigma^{corr} = (m_V - m_I)_\Sigma^i - s_3 log(R). \qquad (3-14)$$

The application of this approach to the photometered *IRAS* 4KVL sample is described here. As might have been expected, inclination effects are generally stronger in this $L_{60\mu}$ restricted sample than in the photographic magnitude and diameter selected sample of Han (HT).

Lines were fit to data by using the 'MEDFIT' routine of Numerical Recipes (Press *et al.* 1986) which minimizes absolute vertical deviation from the line, weakening the skewing effect of outliers. To get a robust estimate of the slope and intercept, 500 samples with half the points of the original were drawn (with replacement) at random from a given point list ('bootstrapping'). Error bars stated for slope and intercept, however, come from the straightforward minimum squared residuals' line fit (Recipes' 'FIT'). Our results can be summarized as follows:

(i) $Log(1.0857/r_0 \times d)$ [$= log(\alpha/d)$] versus $log(R)$, where d is the provisional distance to object (estimated here by applying the 'bi-infall' model (minus 'local anomaly'), of Han and Mould (1990)) is plotted as Figure 1*a*. The fit line is

$$y \;=\; -0.32\ (\pm 0.09)\ x \;-\; 2.64\ (\pm 0.04).$$

On the face of it, this invalidates assumption (2) above, that apparent scale radii of EDL fits do not vary with inclination. However, excluding objects with inclination angles above 75 degrees left no significant slope within this diagram. Since the isophotal radius to scale radius ratios $< r^i_\Sigma/r_0 >$ described shortly below changed by only a few percent between intermediately inclined and edge on galaxies, we retained Han's procedure without modification. An *a posteriori* justification might be the small scatter of highly inclined objects about mean relations derived herein, as well as the noncorrelation of Tully-Fisher residuals with galaxy inclination angle found in Chapter 7.

(ii) Σ_0 versus $log(R)$, plotted in Figure 1*b*, is fit by the line:

$$y = -1.31\ (\pm 0.66)\ x + 18.09\ (\pm 0.27).$$

The slope is -2.5 in the absence of absorption. Han obtained a slope of -1.90 for his sample. Thus the effect of galaxy contents and/or geometry in preventing outer disks from brightening as turned edge on is roughly twice as strong for our IR selected galaxies as it is for Han's photographically selected ones.

(iii) Average values $< r^i_\Sigma/r)0 >$ used for statistical correction of isophotal diameters:

$$< r^i_{22.5}/r_0 >= 4.52 \pm 1.42$$

$$< r^i_{23.0}/r_0 >= 4.99 \pm 1.43$$

$$< r^i_{23.5}/r_0 >= 5.47 \pm 1.45$$

$$< r^i_{24.0}/r_0 >= 5.92 \pm 1.45.$$

Han obtained values in different galaxy type ranges of:

$$< r^i_{23.5}/r_0 >= 4.58, \quad 0 \leq T \leq 3,$$

$$< r^i_{23.5}/r_0 >= 4.45, \quad 4 \leq T \leq 5,$$

$$< r^i_{23.5}/r_0 >= 3.76, \quad 6 \leq T$$

(his values being medians, ours means). The rather subjective nature of choosing the EDL fit region by eye allows for the possibility that a systematic difference would arise between Han's ratios and ours.

(iv) Given slope s_1 = -1.31 and average $< r^i_\Sigma/r)0 >$ values, we could assess average interior surface brightness Σ^i_r and plot versus $log(R)$; at levels 22.5 to 24.0, these were described by

$$y = 1.53(\pm 0.13)x + 19.43(\pm 0.05), \quad \Sigma_I = 22.5 \ mag \ arcsec^{-2},$$

$$y = 1.47(\pm 0.14)x + 19.65(\pm 0.06), \quad \Sigma_I = 23.0 \ mag \ arcsec^{-2},$$

$$y = 1.47(\pm 0.15)x + 19.85(\pm 0.06), \quad \Sigma_I = 23.5 \ mag \ arcsec^{-2},$$

$$y = 1.43(\pm 0.16)x + 20.02(\pm 0.06), \quad \Sigma_I = 24.0 \ mag \ arcsec^{-2},$$

and are plotted at the $\Sigma_I = 23.5$ level in Figure 2*a*. Note the systematic zeropoint shift, as expected, to dimmer average surface brightness within larger (corrected) isophotal apertures, and the slowly weakening dependence on axial ratio with increasing photometric depth. These slopes (s_2) provide the correction of isophotal magnitude with inclination angle. Note that the 23.5 level slope (1.47) exceeds those given by Han (1992):

$$s_2 = 0.73(\pm 0.16), \quad 0 \leq T \leq 3,$$

$$s_2 = 0.90(\pm 0.18), \quad 4 \leq 5,$$

$$s_2 = 0.51(\pm 0.23), \quad 6 \leq T,$$

by average factor ~ 2. Corrected isophotal magnitudes $m^{corr}_{I_\Sigma}$ at levels Σ_I 22.5, 23.0, 23.5 and 24.0 mag arcsec^{-2}, and error bars for same, are given in Table I. The tight appearance of Figure 2*a* suggests that infrared luminous galaxies in fact enjoy a degree of regularity in their structure.

(v) Isophotal $V-I$ colors ($m_V - m_I$) at Σ_I levels 20.0, 21.0 and 22.0 versus $log(R)$ are described by:

$$y = 0.39(\pm 0.08)x + 1.07(\pm 0.03), \Sigma_I = 20.0\ mag\ arcsec^{-2},$$

$$y = 0.36(\pm 0.07)x + 1.03(\pm 0.03), \Sigma_I = 21.0\ mag\ arcsec^{-2},$$

$$y = 0.32(\pm 0.07)x + 1.02(\pm 0.03), \Sigma_I = 22.0\ mag\ arcsec^{-2},$$

and are plotted at the $\Sigma_I = 21.5$ level in Figure 2*b*. We cannot directly compare these slopes (s_3) with Han's value of $0.22(\pm 0.09)$ since his $m_V - m_I$ are assessed at the $\Sigma_I = 23.5$ level. We note the decreasing slope at increasing depth, suggesting that reddening is less severe as one progresses radially outward through the disk. Corrected isophotal $V-I$ colors at the $\Sigma_I = 20.0$, 21.0, and 22.0 mag arcsec^{-2} levels, and errors for same, are listed in Table II.

Residuals from the lines fit to the $log(\alpha/d) - log(R)$ and $\Sigma_r - log(R)$ relations were plotted against 60 micron flux, against object distance d (from the 'bi-infall' model) and against $|b^{II}|$ in Figures $3a-c$ and $4a-c$, respectively. The lack of correlation shown in these diagrams provides some *a posteriori* justification for the procedure followed above. Thus we consider isophotal quantities listed in Tables I and II to be adequately corrected for use in the I band Tully-Fisher relation.

Table I - Corrected isophotal I band magnitudes, 4KVL objects – page 1

obj	obs	$m_I^{22.5}$	σ	$m_I^{23.0}$	σ	$m_I^{23.5}$	σ	$m_I^{24.0}$	σ
1	P60 89 PL	9.801	0.147	9.804	0.150	9.785	0.155	9.794	0.161
2	P60 90 PD	11.910	0.225	11.893	0.224	11.854	0.228	11.847	0.234
8	P60 90 PD	10.932	0.144	10.911	0.144	10.873	0.145	10.863	0.145
19	P60 89 PL	11.494	0.159	11.483	0.161	11.434	0.166	11.438	0.169
19	P60 90 PD	11.228	0.219	11.237	0.221	11.222	0.226	11.238	0.229
25	T36 90 PD	11.794	0.120	11.777	0.122	11.742	0.127	11.728	0.130
28	P60 89 PL	10.008	0.120	9.979	0.123	9.920	0.127	9.902	0.133
31	P60 89 PL	11.610	0.209	11.616	0.209	11.593	0.214	11.604	0.510
33	P60 89 PL	11.509	0.088	11.474	0.090	11.406	0.093	11.337	0.097
42	P60 89 PL	12.434	0.185	12.425	0.185	12.396	0.190	12.401	0.192
43	P60 89 PL	9.363	0.076	9.330	0.079	9.293	0.083	9.280	0.086
49	P60 90 PD	12.326	0.137	12.296	0.135	12.253	0.134	12.236	0.136
54	P60 89 PL	10.359	0.176	10.349	0.176	10.291	0.180	10.296	0.353
55	P60 89 PL	11.803	0.500	11.767	0.482	11.740	0.471	11.727	0.464
59	P60 89 PL	9.762	0.105	9.753	0.108	9.734	0.122	9.742	0.125
62	T36 90 PD	11.518	0.107	11.480	0.105	11.451	0.106	11.437	0.104
66	P60 89 PL	9.921	0.103	9.843	0.103	9.752	0.106	9.706	0.108
69	P60 89 PL	10.238	0.153	10.258	0.156	10.243	0.158	10.240	0.157
71	P60 89 PL	10.608	0.120	10.575	0.120	10.542	0.122	10.529	0.123
77	T36 91 PD	9.373	0.053	9.359	0.055	9.337	0.062	9.335	0.065
79	TSC 91 PD	8.680	0.172	8.637	0.168	8.602	0.170	8.584	0.168
80	T36 90 PD	11.906	0.091	11.882	0.091	11.860	0.093	11.848	0.094
82	P60 89 PL	11.336	0.076	11.201	0.078	11.121	0.080	11.027	0.130
83	P60 89 PL	13.027	0.134	12.986	0.133	12.944	0.136	12.962	0.141
87	T36 90 PD	11.574	0.226	11.573	0.224	11.545	0.229	11.539	0.229
90	TSC 91 PD	8.700	0.150	8.693	0.149	8.672	0.152	8.669	0.152
91	T36 90 ?D	11.888	0.083	11.874	0.082	11.858	0.115	11.852	0.116
91	T36 90 PD	11.885	0.026	11.868	0.028	11.848	0.033	11.841	0.034
92	TSC 91 PD	8.758	0.182	8.686	0.177	8.606	0.179	8.586	0.176
93	T36 90 PD	11.374	0.159	11.347	0.159	11.276	0.163	11.262	0.163
94	T36 90 PD	12.307	0.170	12.247	0.165	12.176	0.167	12.102	0.164
94	T36 91 PD	12.296	0.098	12.247	0.096	12.203	0.097	12.182	0.098
96	T36 91 PD	11.047	0.107	11.044	0.110	11.016	0.114	11.003	0.118
98	P60 91 PD	10.907	0.095	10.889	0.100	10.855	0.104	10.853	0.109
99	P60 89 PL	10.272	0.120	10.195	0.124	10.158	0.129	10.151	0.133
99	T36 91 PD	10.779	0.057	10.676	0.058	10.558	0.060	10.464	0.062
101	P60 91 PD	11.761	0.207	11.757	0.209	11.729	0.215	11.739	0.218
106	P60 89 PL	11.301	0.053	11.277	0.053	11.245	0.054	11.202	0.056
109	P60 89 PL	10.224	0.087	10.185	0.086	10.150	0.094	10.137	0.094
110	P60 91 ND	11.330	0.075	11.261	0.074	11.181	0.076	11.130	0.076

Table I - Corrected isophotal I band magnitudes, 4KVL objects – page 2

obj	obs	$m_I^{22.5}$	σ	$m_I^{23.0}$	σ	$m_I^{23.5}$	σ	$m_I^{24.0}$	σ
114	P60 89 PL	12.060	0.414	12.012	0.408	11.950	0.415	11.937	0.414
115	T36 91 PD	9.819	0.088	9.823	0.094	9.799	0.134	9.811	0.139
115	TSC 91 PD	9.866	0.196	9.866	0.197	9.841	0.203	9.850	0.641
117	P60 91 ?D	10.985	0.068	10.967	0.068	10.934	0.070	10.907	0.071
126	P60 89 PL	12.162	0.212	12.148	0.207	12.126	0.254	12.123	0.251
132	T36 90 PD	11.007	0.040	10.967	0.041	10.936	0.050	10.925	0.051
134	P60 89 PL	10.891	0.142	10.858	0.140	10.812	0.142	10.779	0.141
134	P60 91 ?D	10.871	0.078	10.848	0.242	10.829	0.242	10.823	0.241
136	T36 91 PD	10.944	0.123	10.949	0.126	10.934	0.129	10.942	0.131
139	P60 91 PD	11.808	0.082	11.790	0.084	11.762	0.087	11.754	0.090
141	P60 91 ?D	11.433	0.176	11.414	0.174	11.395	0.178	11.397	0.178
143	P60 91 PD	11.534	0.229	11.513	0.227	11.473	0.231	11.452	0.231
150	TSC 91 PD	7.505	0.074	7.488	0.076	7.460	0.079	7.455	0.082
150	P60 91 ?D	7.598	0.124	7.593	0.124	7.579	0.127	7.580	0.128
154	T36 91 PD	11.626	0.128	11.621	0.126	11.604	0.128	11.605	0.214
154	P60 91 ?D	11.584	0.083	11.582	0.084	11.567	0.086	11.569	0.125
159	T36 91 PD	11.591	0.073	11.569	0.072	11.549	0.074	11.541	0.073
163	T36 90 PD	10.989	0.225	10.981	0.226	10.910	0.233	10.935	0.247
167	P60 89 PL	10.752	0.078	10.697	0.079	10.636	0.082	10.611	0.087
169	T36 91 PD	9.353	0.093	9.321	0.098	9.292	0.103	9.279	0.105
170	P60 91 ?D	10.463	0.290	10.467	0.288	10.432	0.295	10.436	0.296
171	T36 91 PD	11.847	0.074	11.836	0.075	11.820	0.077	11.815	0.078
172	T36 91 PD	11.079	0.075	11.057	0.077	11.032	0.124	11.031	0.125
176	T36 90 PD	10.992	0.084	10.986	0.085	10.974	0.087	10.973	0.088
179	T36 91 PD	10.532	0.072	10.515	0.073	10.493	0.418	10.493	0.417
181	T36 90 PD	11.176	0.288	11.176	0.285	11.132	0.297	11.140	0.296
189	P60 91 ?D	11.373	0.084	11.352	0.083	11.324	0.085	11.307	0.086
193	TSC 91 PD	7.537	0.088	7.503	0.088	7.452	0.091	7.417	0.092
194	T36 90 PD	10.680	0.083	10.629	0.084	10.566	0.086	10.553	0.136
198	T36 91 PD	9.667	0.082	9.647	0.085	9.619	0.088	9.613	0.090
203	T36 91 PD	9.647	0.151	9.644	0.257	9.629	0.259	9.635	0.259
204	P60 91 ?D	10.571	0.224	10.557	0.221	10.535	0.225	10.524	0.225
206	TSC 91 PD	8.928	0.196	8.915	0.198	8.874	0.204	8.863	0.208
207	P60 91 PD	9.831	0.248	9.843	0.248	9.821	0.254	9.826	0.257
210	T36 90 ?D	11.351	0.059	11.331	0.059	11.309	0.060	11.302	0.083
210	T36 91 PD	11.382	0.065	11.364	0.066	11.346	0.067	11.341	0.186
213	T36 91 PD	9.860	0.076	9.852	0.079	9.833	0.103	9.835	0.107
216	T36 90 PD	10.127	0.134	10.117	0.136	10.092	0.140	10.092	0.143
223	T36 91 PD	9.261	0.062	9.232	0.062	9.210	0.063	9.195	0.063
225	P60 91 PD	11.778	0.131	11.785	0.136	11.761	0.142	11.766	0.147

Table I - Corrected isophotal I band magnitudes, 4KVL objects – page 3

obj	obs	$m_I^{22.5}$	σ	$m_I^{23.0}$	σ	$m_I^{23.5}$	σ	$m_I^{24.0}$	σ
226	P60 91 PD	10.551	0.072	10.497	0.073	10.439	0.075	10.404	0.076
228	P60 91 PD	9.637	0.079	9.625	0.080	9.605	0.082	9.598	0.083
229	T36 91 PD	12.365	0.099	12.355	0.101	12.327	0.105	12.318	0.129
231	T36 90 PD	10.197	0.063	10.164	0.065	10.141	0.303	10.135	0.301
232	T36 91 PD	9.562	0.109	9.567	0.129	9.548	0.133	9.556	0.137
239	P60 91 PD	11.184	0.174	11.130	0.169	11.081	0.171	11.048	0.168
240	TSC 91 PD	9.275	0.202	9.250	0.202	9.210	0.207	9.206	0.209
240	P60 91 ?D	9.105	0.181	9.107	0.184	9.081	0.191	9.089	0.195
246	TSC 91 PD	7.948	0.116	7.941	0.117	7.917	0.120	7.903	0.121
247	TSC 91 PD	8.589	0.201	8.581	0.201	8.549	0.206	8.546	0.208
247	P60 91 ?D	8.520	0.166	8.509	0.167	8.489	0.202	8.503	0.204
248	TSC 91 PD	8.979	0.190	8.932	0.190	8.890	0.195	8.885	0.196
248	P60 91 ?D	9.064	0.145	9.041	0.148	9.007	0.153	9.001	0.157
251	T36 91 PD	10.023	0.121	10.012	0.124	9.972	0.128	9.963	0.131
254	T36 91 PD	10.981	0.204	10.976	0.204	10.937	0.209	10.926	0.210
255	T36 91 PD	11.043	0.144	11.013	0.144	10.978	0.147	10.972	0.151
256	TSC 91 PD	8.648	0.154	8.660	0.157	8.640	0.163	8.656	0.170
257	T36 90 PD	11.237	0.178	11.254	0.181	11.239	0.188	11.255	0.192
260	T36 90 PD	11.232	0.160	11.196	0.158	11.149	0.161	11.119	0.161
262	T36 90 PD	11.840	0.163	11.847	0.169	11.830	0.174	11.841	0.177
265	P60 91 PD	10.639	0.037	10.613	0.044	10.595	0.046	10.592	0.048
267	T36 91 PD	9.391	0.106	9.381	0.109	9.349	0.113	9.352	0.284
269	TSC 91 PD	9.473	0.207	9.486	0.208	9.470	0.214	9.483	0.217
271	TSC 91 PD	9.943	0.182	9.880	0.180	9.822	0.183	9.787	0.182
276	T36 91 PD	12.235	0.238	12.229	0.234	12.207	0.237	12.203	0.860
278	T36 91 PD	10.412	0.162	10.410	0.163	10.385	0.168	10.389	0.170
278	T36 90 ?D	10.466	0.268	10.458	0.264	10.430	0.268	10.417	0.267
280	T36 91 PD	9.854	0.147	9.863	0.152	9.846	0.158	9.857	0.162
281	T36 91 PD	10.779	0.119	10.792	0.123	10.778	0.128	10.787	0.132
284	TSC 91 PD	9.364	0.054	9.322	0.055	9.265	0.057	9.241	0.059
285	T36 91 PD	9.639	0.165	9.630	0.165	9.613	0.168	9.614	0.168
285	T36 90 ?D	9.780	0.072	9.739	0.073	9.703	0.075	9.693	0.078
286	T36 91 PD	10.274	0.126	10.289	0.133	10.266	0.140	10.285	0.226
287	T36 91 PD	10.320	0.052	10.286	0.066	10.258	0.068	10.248	0.070
295	T36 90 PD	11.347	0.155	11.309	0.158	11.254	0.164	11.230	0.169
298	T36 91 PD	10.231	0.069	10.211	0.071	10.171	0.075	10.156	0.077
298	TSC 91 PD	10.313	0.108	10.291	0.108	10.255	0.111	10.241	0.113
303	TSC 91 PD	9.179	0.081	9.133	0.081	9.076	0.082	9.032	0.083
303	P60 91 ?D	9.002	0.068	8.970	0.069	8.949	0.120	8.944	0.121
310	P60 91 PD	10.849	0.057	10.803	0.059	10.773	0.062	10.763	0.064

Table I - Corrected isophotal I band magnitudes, 4KVL objects – page 4

obj	obs	$m_I^{22.5}$	σ	$m_I^{23.0}$	σ	$m_I^{23.5}$	σ	$m_I^{24.0}$	σ
313	P60 91 PD	10.489	0.187	10.456	0.181	10.423	0.182	10.411	0.241
316	P60 91 PD	10.806	0.172	10.776	0.168	10.744	0.170	10.730	0.168
320	T36 91 PD	10.144	0.144	10.141	0.146	10.107	0.152	10.108	0.169
320	P60 91 PD	10.011	0.237	10.029	0.238	10.016	0.244	10.032	0.246
328	P60 91 PD	11.185	0.134	11.169	0.132	11.152	0.133	11.148	0.132
332	P60 91 PD	9.996	0.065	9.984	0.066	9.958	0.072	9.955	0.074
333	P60 91 ?D	9.662	0.156	9.655	0.154	9.635	0.158	9.628	0.158
334	T36 90 PD	10.488	0.385	10.510	0.382	10.494	0.390	10.513	0.391
336	T36 90 PD	11.445	0.163	11.384	0.159	11.332	0.160	11.290	0.159
336	T36 91 PD	11.558	0.053	11.493	0.053	11.458	0.054	11.423	0.055
337	T36 91 PD	9.929	0.186	9.898	0.185	9.852	0.189	9.859	0.190
338	T36 91 PD	9.706	0.070	9.610	0.072	9.580	0.111	9.582	0.114
346	T36 90 ?D	10.968	0.234	10.941	0.232	10.882	0.237	10.854	0.237
348	T36 90 ?D	10.036	0.226	10.015	0.221	9.996	0.254	9.994	0.252
348	T36 91 PD	10.157	0.099	10.132	0.099	10.103	0.101	10.098	0.163
349	T36 91 PD	9.980	0.124	9.980	0.126	9.963	0.129	9.968	0.132
350	T36 90 PD	10.437	0.305	10.419	0.302	10.373	0.308	10.337	0.309
350	T36 91 PD	10.370	0.135	10.365	0.143	10.335	0.149	10.343	0.155
352	P60 91 ?D	11.483	0.314	11.442	0.310	11.357	0.315	11.266	0.313
353	P60 91 PD	11.077	0.033	10.907	0.035	10.821	0.037	10.722	0.039
353	P60 91 ?D	11.027	0.023	10.870	0.025	10.781	0.027	10.654	0.029
354	P60 91 ?D	9.641	0.381	9.640	0.377	9.614	0.384	9.616	0.383
357	T36 91 PD	10.874	0.087	10.845	0.087	10.845	0.107	10.844	0.108
360	P60 91 ?D	10.240	0.082	10.189	0.082	10.158	0.083	10.132	0.083
361	T36 91 PD	10.961	0.072	10.950	0.073	10.932	0.075	10.926	0.076
361	P60 91 PD	11.004	0.089	10.992	0.088	10.971	0.090	10.959	0.090
367	T36 90 PD	10.271	0.334	10.292	0.424	10.280	0.430	10.303	0.431
367	T36 91 PD	10.354	0.373	10.337	0.369	10.275	0.376	10.288	0.397
370	P60 90 PD	10.163	0.184	10.161	0.183	10.142	0.185	10.133	0.185
375	P60 91 PD	10.717	0.266	10.714	0.265	10.687	0.271	10.681	0.274
378	P60 90 PD	10.100	0.136	10.099	0.136	10.091	0.137	10.092	0.137
380	P60 91 PD	9.623	0.166	9.605	0.420	9.591	0.419	9.594	0.417
382	P60 90 PD	11.186	0.116	11.161	0.116	11.143	0.117	11.133	0.117
387	T36 90 PD	10.605	0.095	10.604	0.096	10.592	0.098	10.595	0.099
391	T36 90 PD	10.939	0.255	10.926	0.253	10.904	0.254	10.909	0.278
392	T36 90 PD	9.381	0.256	9.374	0.253	9.366	0.257	9.378	0.256
394	T36 90 PD	10.081	0.263	10.091	0.263	10.076	0.336	10.096	0.338
396	P60 89 PL	10.858	0.078	10.824	0.127	10.796	0.129	10.789	0.131
399	T36 90 PD	12.533	0.070	12.495	0.071	12.451	0.074	12.415	0.075
401	T36 91 PD	9.363	0.121	9.362	0.125	9.340	0.160	9.352	0.163

Table I - Corrected isophotal I band magnitudes, 4KVL objects – page 5

obj	obs	$m_I^{22.5}$	σ	$m_I^{23.0}$	σ	$m_I^{23.5}$	σ	$m_I^{24.0}$	σ
405	P60 89 PL	10.757	0.124	10.752	0.123	10.734	0.125	10.738	0.141
406	P60 90 PD	11.679	0.141	11.668	0.145	11.652	0.147	11.656	0.149
409	T36 90 PD	11.513	0.358	11.472	0.353	11.415	0.374	11.416	0.373
411	T36 90 PD	9.981	0.122	9.944	0.180	9.911	0.187	9.899	0.191
414	T36 90 PD	11.109	0.303	11.073	0.299	11.028	0.305	11.020	0.390
418	P60 90 PD	9.973	0.211	9.984	0.213	9.950	0.215	9.937	0.222
422	T36 90 PD	10.917	0.197	10.892	0.265	10.859	0.273	10.858	0.278
426	P60 90 PD	9.811	0.154	9.818	0.156	9.798	0.159	9.798	0.161
434	P60 89 PL	10.294	0.112	10.194	0.116	10.120	0.122	10.076	0.124

Table II - Corrected isophotal $V - I$ colors, 4KVL objects – page 1

obj	obs	$m_V - m_I$	σ	$m_V - m_I$	σ	$m_V - m_I$	σ
		$\Sigma_I = 20.0$		$\Sigma_I = 21.0$		$\Sigma_I = 22.0$	
1	P60 89 PL	1.091	0.118	1.082	0.114	1.091	0.113
2	P60 90 PD	0.829	0.093	0.804	0.085	0.811	0.082
8	P60 90 PD	1.110	0.082	1.095	0.078	1.093	0.076
19	P60 89 PL	1.261	0.065	1.207	0.059	1.189	0.057
19	P60 90 PD	1.278	0.125	1.204	0.113	1.180	0.110
25	T36 90 PD	1.248	0.130	1.219	0.126	1.206	0.125
28	P60 89 PL	1.102	0.112	1.035	0.109	1.012	0.109
31	P60 89 PL	0.987	0.078	0.975	0.070	0.981	0.067
33	P60 89 PL	1.108	0.106	1.065	0.105	1.059	0.105
42	P60 89 PL	0.864	0.072	0.869	0.065	0.869	0.062
43	P60 89 PL	1.060	0.105	1.027	0.104	1.013	0.104
49	P60 90 PD	1.094	0.079	1.084	0.078	1.083	0.079
54	P60 89 PL	1.043	0.068	1.018	0.062	1.009	0.060
55	P60 89 PL	1.245	0.021	1.086	0.024	1.072	0.024
59	P60 89 PL	0.945	0.050	0.939	0.046	0.950	0.046
62	T36 90 PD	1.272	0.034	1.261	0.031	1.264	0.029
66	P60 89 PL	0.761	0.107	0.745	0.106	0.748	0.105
69	P60 89 PL	1.419	0.110	1.383	0.109	1.356	0.109
71	P60 89 PL	1.491	0.107	1.371	0.107	1.305	0.107
77	T36 91 PD	0.730	0.026	0.719	0.024	0.724	0.024
79	TSC 91 PD	0.969	0.055	0.952	0.050	0.935	0.047
80	T36 90 PD	0.974	0.117	0.996	0.116	1.007	0.115
82	P60 89 PL	1.932	0.039	1.910	0.037	1.873	0.039
83	P60 89 PL	0.920	0.051	0.919	0.047	0.922	0.045
87	T36 90 PD	1.224	0.080	1.203	0.072	1.215	0.068
90	TSC 91 PD	0.955	0.056	0.974	0.052	0.985	0.049
91	T36 90 PD	1.075	0.016	1.037	0.015	1.042	0.015
92	TSC 91 PD	1.086	0.057	1.077	0.053	1.088	0.049
93	T36 90 PD	1.348	0.132	1.259	0.128	1.249	0.126
94	T36 90 PD	0.983	0.050	0.986	0.046	0.981	0.042
94	T36 91 PD	0.841	0.037	0.830	0.035	0.808	0.034
96	T36 91 PD	1.276	0.066	1.244	0.060	1.233	0.059
98	P60 91 PD	1.148	0.051	1.062	0.046	0.984	0.046
99	P60 89 PL	1.291	0.112	1.212	0.110	1.131	0.111
99	P60 91 PD	1.508	0.053	1.400	0.048	1.311	0.045
101	P60 91 PD	1.123	0.084	1.076	0.076	1.049	0.074
106	P60 89 PL	1.070	0.101	1.000	0.101	0.980	0.102
109	P60 89 PL	1.057	0.034	0.983	0.032	0.951	0.033
110	P69 91 ND	1.100	0.028	1.096	0.026	1.082	0.026
114	P60 89 PL	0.925	0.138	0.886	0.126	0.913	0.117

Table II - Corrected isophotal $V - I$ colors, 4KVL objects – page 2

obj	obs	$m_V - m_I$	σ	$m_V - m_I$	σ	$m_V - m_I$	σ
		$\Sigma_I = 20.0$		$\Sigma_I = 21.0$		$\Sigma_I = 22.0$	
115	TSC 91 PD	1.015	0.081	0.990	0.073	1.006	0.070
117	P60 91 ?D	0.993	0.028	0.963	0.025	0.958	0.026
126	P60 89 PL	0.780	0.118	0.727	0.116	0.727	0.114
132	T36 90 PD	1.017	0.018	1.019	0.017	1.033	0.018
134	P60 89 PL	1.069	0.109	1.050	0.107	0.987	0.107
134	P60 91 ?D	1.161	0.030	1.132	0.028	1.075	0.029
136	T36 91 PD	1.159	0.048	1.118	0.043	1.113	0.043
139	P60 91 PD	0.939	0.038	0.893	0.034	0.892	0.033
141	P60 91 ?D	0.986	0.062	0.977	0.056	0.974	0.053
143	P60 91 PD	1.464	0.081	1.341	0.073	1.293	0.069
150	TSC 91 PD	0.946	0.040	0.935	0.037	0.951	0.037
150	P60 91 ?D	1.031	0.045	1.013	0.042	-0.089	0.037
154	T36 91 PD	0.786	0.049	0.751	0.046	0.749	0.044
154	P60 91 ?D	0.761	0.034	0.732	0.031	0.735	0.030
159	T36 91 PD	1.115	0.038	1.075	0.036	1.062	0.034
163	T36 90 PD	0.742	0.091	0.734	0.082	0.725	0.078
167	P60 89 PL	1.043	0.031	1.026	0.028	1.002	0.030
169	T36 91 PD	1.136	0.040	1.083	0.037	-0.055	0.018
170	P60 91 ?D	1.153	0.106	1.054	0.096	1.000	0.090
171	T36 91 PD	1.180	0.043	1.140	0.041	1.130	0.040
172	T36 91 PD	1.214	0.051	1.163	0.047	1.133	0.045
176	T36 90 PD	0.840	0.023	0.844	0.020	-0.059	0.019
179	T36 91 PD	0.895	0.031	0.840	0.028	0.840	0.028
181	T36 90 PD	1.029	0.099	0.948	0.089	0.948	0.084
189	P60 91 ?D	1.019	0.032	1.016	0.029	1.011	0.028
193	TSC 91 PD	1.131	0.040	1.128	0.037	1.104	0.036
194	T36 90 PD	0.941	0.033	0.954	0.030	0.925	0.030
198	T36 91 PD	1.586	0.057	1.545	0.054	1.493	0.055
203	T36 91 PD	1.026	0.059	0.958	0.053	0.910	0.051
204	P60 91 ?D	1.175	0.077	1.169	0.070	1.157	0.066
206	TSC 91 PD	1.098	0.083	1.112	0.075	1.083	0.072
207	P60 91 PD	1.016	0.095	0.943	0.085	0.942	0.081
210	T36 90 ?D	0.874	0.024	0.828	0.022	0.831	0.022
210	T36 91 PD	0.893	0.024	0.831	0.023	0.822	0.023
213	T36 91 PD	1.055	0.038	1.052	0.035	1.039	0.034
216	T36 90 PD	1.018	0.055	0.997	0.049	1.002	0.047
223	T36 91 PD	1.154	0.035	1.120	0.034	1.095	0.033
225	P60 91 PD	0.981	0.064	0.938	0.057	0.891	0.056
226	P60 91 PD	1.177	0.032	1.139	0.029	1.110	0.029
228	P60 91 PD	1.233	0.033	1.147	0.030	1.144	0.029

Table II - Corrected isophotal $V - I$ colors, 4KVL objects – page 3

obj	obs	$m_V - m_I$	σ	$m_V - m_I$	σ	$m_V - m_I$	σ
		$\Sigma_I = 20.0$		$\Sigma_I = 21.0$		$\Sigma_I = 22.0$	
229	T36 91 PD	1.137	0.054	1.112	0.050	1.100	0.049
231	T36 90 PD	1.214	0.038	1.081	0.034	1.049	0.034
232	T36 91 PD	1.017	0.052	0.992	0.047	0.984	0.046
239	P60 91 PD	1.231	0.051	1.200	0.047	1.161	0.044
240	TSC 91 PD	0.879	0.079	0.855	0.072	0.855	0.068
240	P60 91 ?D	0.918	0.077	0.898	0.069	0.885	0.067
246	TSC 91 PD	1.089	0.049	1.048	0.045	1.040	0.043
247	TSC 91 PD	1.147	0.079	1.107	0.071	1.091	0.068
247	P60 91 ?D	1.214	0.068	1.168	0.061	1.131	0.059
248	TSC 91 PD	1.050	0.074	0.946	0.066	0.900	0.063
248	P60 91 ?D	1.110	0.057	0.974	0.051	0.935	0.050
251	T36 91 ?D	1.096	0.060	1.055	0.055	1.046	0.053
254	T36 91 PD	1.218	0.083	1.180	0.075	1.178	0.072
255	T36 91 PD	0.851	0.058	0.833	0.054	0.857	0.052
256	TSC 91 PD	1.067	0.071	1.042	0.064	1.049	0.062
257	T36 90 PD	1.039	0.077	0.977	0.069	0.983	0.067
260	T36 90 PD	0.894	0.055	0.881	0.049	0.881	0.046
262	T36 90 PD	0.722	0.067	0.721	0.060	0.739	0.058
265	P60 91 PD	0.949	0.022	0.926	0.020	0.914	0.020
267	T36 91 PD	1.130	0.059	1.079	0.053	1.084	0.052
269	TSC 91 PD	0.824	0.082	0.809	0.074	0.827	0.071
271	TSC 91 PD	1.061	0.064	1.004	0.059	0.932	0.055
276	T36 91 PD	1.104	0.084	1.083	0.077	1.073	0.072
278	T36 91 PD	1.075	0.071	1.000	0.064	1.004	0.062
278	T36 90 ?D	1.011	0.090	0.955	0.082	0.956	0.077
280	T36 91 PD	0.997	0.061	0.978	0.056	0.964	0.055
281	T36 91 PD	0.900	0.062	0.925	0.056	0.950	0.055
284	TSC 91 PD	1.162	0.032	1.083	0.030	1.075	0.030
285	T36 91 PD	1.112	0.057	1.097	0.052	1.092	0.050
285	T36 91 ?D	1.135	0.031	1.124	0.029	1.129	0.028
286	T36 91 PD	0.994	0.068	0.981	0.061	0.984	0.060
287	T36 91 PD	1.001	0.040	0.848	0.035	0.842	0.036
295	T36 90 PD	1.396	0.069	1.306	0.061	1.252	0.060
298	T36 91 PD	1.192	0.048	1.144	0.044	1.119	0.042
298	TSC 91 PD	1.144	0.047	1.118	0.044	1.088	0.042
303	TSC 91 PD	1.080	0.035	1.010	0.032	1.016	0.031
303	P60 91 ?D	1.107	0.030	1.011	0.027	0.996	0.027
310	P60 91 PD	1.088	0.030	1.011	0.027	0.974	0.027
313	P60 91 PD	1.060	0.053	1.031	0.049	1.017	0.045
316	P60 91 PD	1.084	0.054	1.051	0.050	1.020	0.046

Table II - Corrected isophotal $V - I$ colors, 4KVL objects – page 4

obj	obs	$m_V - m_I$	σ	$m_V - m_I$	σ	$m_V - m_I$	σ
		$\Sigma_I = 20.0$		$\Sigma_I = 21.0$		$\Sigma_I = 22.0$	
320	T36 91 PD	1.114	0.068	1.104	0.063	1.110	0.061
320	P60 91 PD	1.027	0.088	1.016	0.079	1.029	0.076
328	P60 91 PD	1.059	0.043	1.025	0.039	1.008	0.037
332	P60 91 PD	1.164	0.031	1.127	0.028	1.110	0.028
333	P60 91 ?D	1.062	0.055	1.028	0.050	1.012	0.047
334	T36 90 PD	0.951	0.130	0.924	0.118	0.938	0.111
336	T36 91 PD	0.942	0.050	0.825	0.045	0.812	0.042
336	T36 91 PD	1.018	0.032	0.865	0.028	0.820	0.028
337	T36 91 PD	1.361	0.077	1.336	0.071	1.306	0.067
338	T36 91 PD	1.074	0.034	1.023	0.031	1.036	0.032
346	T36 90 ?D	1.162	0.083	1.141	0.075	1.127	0.070
348	T36 90 ?D	0.968	0.071	0.914	0.064	0.910	0.059
348	T36 91 PD	0.958	0.037	0.907	0.034	0.871	0.033
349	T36 91 PD	1.113	0.058	1.061	0.053	1.045	0.052
350	T36 90 PD	1.004	0.109	0.914	0.098	0.864	0.092
350	T36 91 PD	1.102	0.076	0.989	0.068	0.942	0.066
352	P60 91 ?D	1.328	0.105	1.240	0.095	1.196	0.089
353	P60 91 PD	1.151	0.019	1.026	0.018	1.007	0.020
353	P60 91 ?D	1.169	0.016	1.040	0.015	1.027	0.016
354	P60 91 ?D	1.130	0.131	1.089	0.118	1.070	0.111
357	T36 91 PD	1.089	0.044	1.056	0.042	1.056	0.041
360	P60 91 ?D	1.070	0.029	1.013	0.027	0.989	0.026
361	T36 91 PD	1.113	0.040	1.110	0.039	1.105	0.038
361	P60 91 PD	1.081	0.031	1.073	0.029	1.073	0.027
367	T36 90 PD	1.159	0.122	1.071	0.110	1.059	0.104
367	T36 91 PD	1.207	0.132	1.118	0.119	1.088	0.112
370	P60 90 PD	0.887	0.082	0.865	0.077	0.858	0.074
375	P60 91 PD	1.163	0.096	1.120	0.086	1.100	0.082
378	P60 90 PD	0.978	0.078	0.973	0.076	0.963	0.075
380	P60 91 PD	0.953	0.057	0.920	0.052	0.912	0.049
382	P60 90 PD	0.990	0.059	0.963	0.057	0.943	0.055
387	T36 90 PD	0.964	0.036	0.962	0.033	0.962	0.033
391	T36 90 PD	1.200	0.126	1.208	0.124	1.218	0.123
392	T36 90 PD	1.236	0.086	1.233	0.078	1.245	0.073
394	T36 90 PD	0.991	0.153	1.019	0.147	1.046	0.144
396	P60 90 PL	1.591	0.105	1.485	0.104	1.459	0.106
399	T36 90 PD	1.189	0.031	1.189	0.028	1.189	0.027
401	T36 91 PD	0.951	0.132	0.887	0.114	0.868	0.108
405	P60 89 PL	0.637	0.108	0.573	0.108	0.543	0.109
406	P60 90 PD	0.990	0.079	0.978	0.075	0.972	0.074

Table II - Corrected isophotal $V - I$ colors, 4KVL objects – page 5

obj	obs	$m_V - m_I$	σ	$m_V - m_I$	σ	$m_V - m_I$	σ
		$\Sigma_I = 20.0$		$\Sigma_I = 21.0$		$\Sigma_I = 22.0$	
409	T36 90 PD	1.516	0.176	1.390	0.165	1.294	0.158
411	T36 90 PD	1.220	0.124	1.161	0.121	1.117	0.120
414	T36 90 PD	1.238	0.156	1.196	0.148	1.208	0.145
418	P60 90 PD	0.906	0.113	0.891	0.105	0.855	0.100
422	T36 90 PD	1.242	0.076	1.236	0.068	1.229	0.065
426	P60 90 PD	0.964	0.086	0.944	0.079	0.931	0.077
434	P60 89 PL	1.037	0.038	0.966	0.036	1.057	0.036

Figure Captions - Chapter 3

Figure 1: (a) $log(\alpha/d)$ versus $log(R)$, where α is the slope of the exponential disk law (EDL) fit to outer portion of surface brightness profile $\alpha = 1.0857/r_0$, and r_0, the EDL scale length. R is the major to minor axis ratio. (b) Σ_0 versus $log(R)$, where Σ_0 is the central surface brightness of the EDL disk law fit to outer portion of surface brightness profile.

Figure 2: (a) Average interior surface brightness (within inclination corrected isophotal radius) Σ_r versus $log(R)$, at isophotal level $\Sigma_I = 23.5$ mag arcsec^{-2}. (b) Isophotal integrated color $(m_V - m_I)$ versus $log(R)$ at level $\Sigma_I = 21.5$ mag arcsec^{-2}.

Figure 3: Residuals from $log(\alpha/d) - log(R)$ relation versus: (a) log 60 micron flux, (b) bi-infall model distance, Mpc, (c) $|b^{II}|$.

Figure 4: Residuals from $\Sigma_0 - log(R)$ relation versus: (a) log 60 micron flux, (b) bi-infall model distance, Mpc, (c) $|b^{II}|$.

IRAS 4KVL CCD SURVEY / bi-infall distances

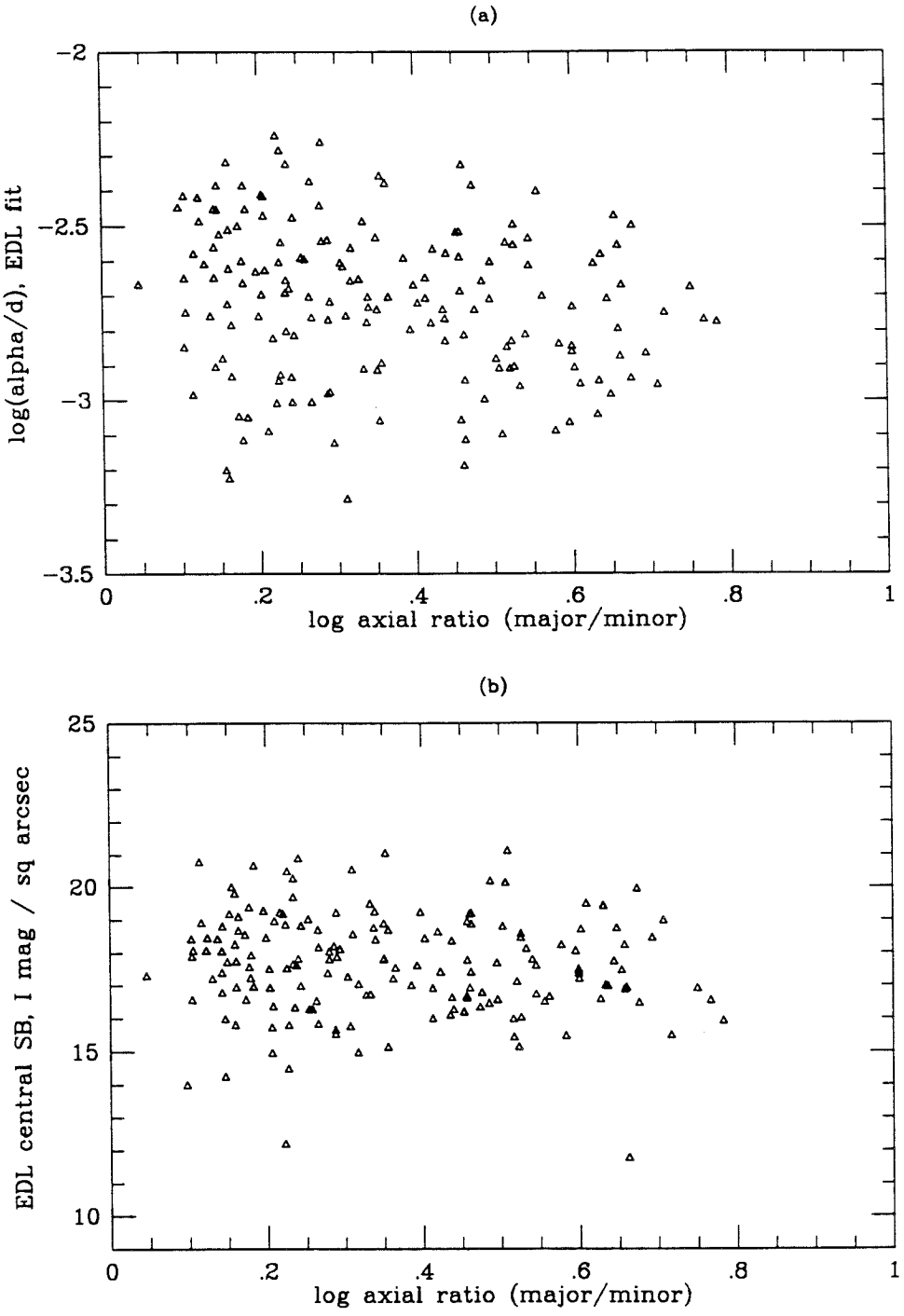

Figure 1

IRAS 4KVL CCD SURVEY

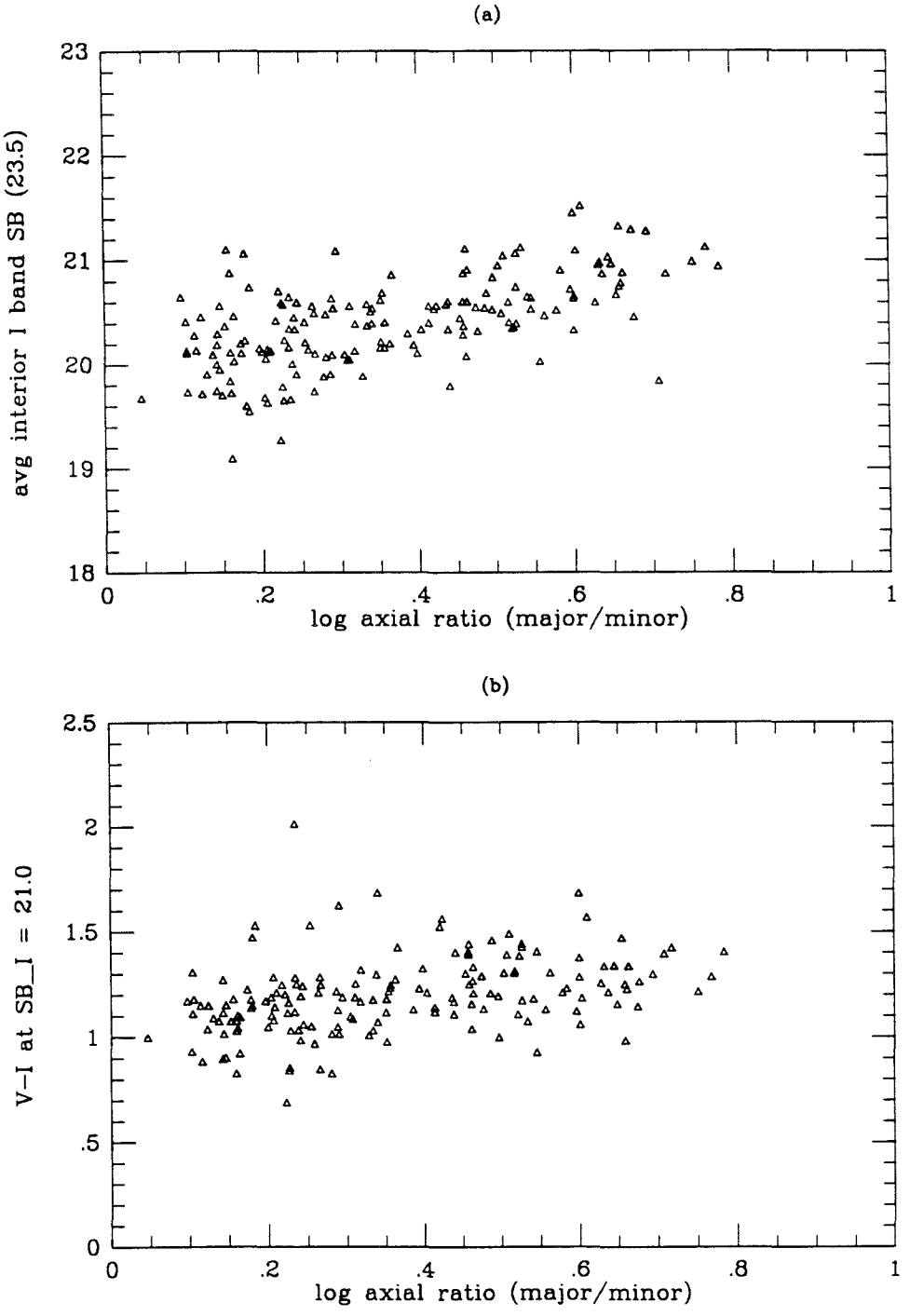

Figure 2

disk scale length | axial ratio residuals

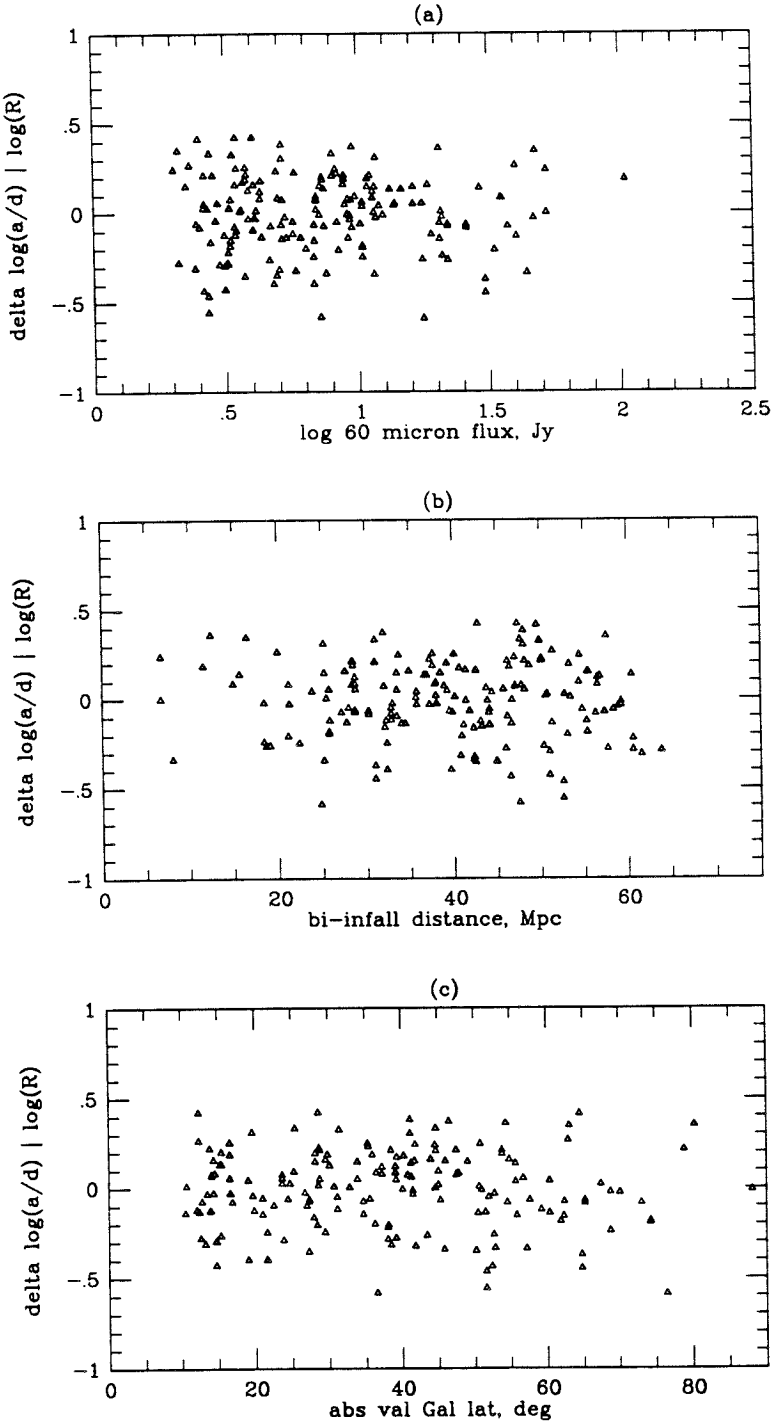

Figure 3

EDL central SB | axial ratio residuals

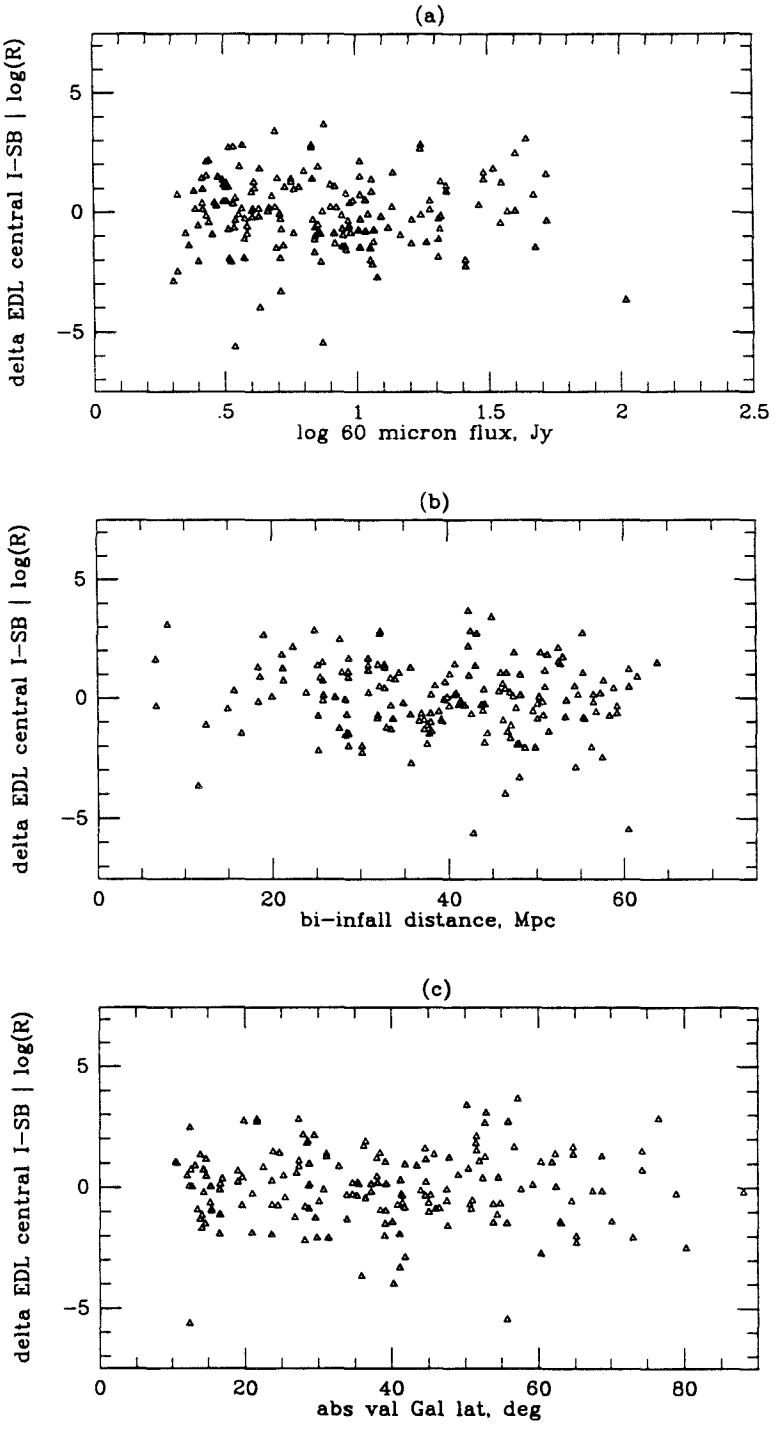

Figure 4

Chapter 4 - HI observations of *IRAS* 4KVL objects from Jodrell Bank

I. Introduction

The Tully-Fisher relation presumably relies on some constancy of spiral galaxy mass to light ratios, and to exploit it to use those objects as 'standard candles' we need some measure of galaxies' mass. The width of the emission line from neutral hydrogen at 21 centimeters indirectly reflects the amplitude of rotational velocities in the galaxy's gravitational potential. The emission line spectra used in this thesis all derive from correlator based spectrometers, which offer much higher frequency resolution than do filter bank systems. Such systems essentially obtain the spectrum within some bandpass as follows:

1 - The signal is mixed down by a frequency signal from the 'local oscillator' (LO) nearly equal to the difference between the mean sky frequency of interest and the bandwidth (BW) of the spectrum desired;

2 - The signal's power level is crudely digitized (with as little as one bit's resolution) and multiplied by delayed copies of itself to generate an autocorrelation function.

3 - The Fourier transform of the autocorrelation function then yields the power spectrum.

The theory behind correlator based radio spectrometers is not lucidly discussed in any reference known to us, although Kraus (1986) provides some informative discussion.

The steepness of the Tully-Fisher relation dictates that the highest spectral (and, hence, velocity) resolution obtainable be used. The resolution in spectrometers such as used at Jodrell Bank and Parkes is limited in part by the correlator hardware, and further by the intrinsic tradeoff between resolution and signal to noise.

II. 21 cm observations

The data reported here were obtained by R. D. Davies, J. R. Mould and J. Roth with the Jodrell Bank Lovell 76 m radiotelescope largely during a two week run in September of 1989. Four objects were observed during other programs in spring of 1990 by J. V. Smoker and R. D. Davies. J. Cohen, K. Hummel and A. Pedlar provided valuable assistance with observing techniques and data management and reduction to visiting astronomers J. R. and J. R. M.

Our instrumental setup, observing, calibration and data reduction largely follow those of Staveley-Smith and Davies (1987, hereafter SSDI, and 1988, hereafter SSDII) and are described in detail in the Ph. D. thesis of Lister Staveley-Smith (1985; hereafter SST). The feeds and amplifiers reside in an assembly held at the prime focus of the 76 m dish by a single pedestal arising from the center of the dish. The telescope is altazimuthally mounted. The dual circular polarization feed system was connected to cryogenically cooled HEMT receivers showing approximate zenith system temperatures of 45 degrees Kelvin. The system illuminated a beam of about 12 arcminutes' diameter on the sky. The Jodrell Bank 1024 channel autocorrelation spectrometer was split into two 512 channel banks for the two orthogonal polarizations; each bank spanned a 10 MHz bandpass, giving a dispersion of 4.13 km sec^{-1} per channel and just over 2100 km sec^{-1} effective velocity coverage at a given local oscillator (LO) setting. Integrations generally ran 10 minutes on source, 10 minutes off, with a calibration diode fired at the end of every 10 minutes' integration.

Individual net (object minus sky) spectra were provided by the observing system in format readable to 'SLAP', the Spectral Line Analysis Package written by Lister Staveley-Smith and used by the present author to reduce all *IRAS* 4KVL data from Jodrell Bank and Parkes. To avoid a faulty region in the Jodrell correlator the frequency corresponding to the heliocentric redshift of the source was placed four tenths of the way from the left (low frequency) end of the bandpass rather than at the center (0.5). This region of the bandpass was, however, occasionally plagued by interference at intermediate (post-LO) frequency (IF) which placed spiky signals in object spectra regardless of their redshift; the staff attributed this to transmissions from the airport nearby the observatory. The

occasional object whose emission features stray from the 0.4 BW position apparently have systemic gas velocities significantly different from the (generally optical) redshift provided by Strauss *et al.*

III. Flux scale definition and constancy

The absolute flux density scale for the 1989 observations was calibrated by pointed observations of 3C286 through the same range of local oscillator settings used during the program observations. The calibration diode was defined *a priori* as 20 Jy in the observing software. Pointed observations of 3C 286 performed by R. D. Davies at three local oscillator settings calibrated the diode in each channel; the calibration coefficients determined by him at the telescope are given in Table I. The values, averaged over the run and divided by 20 Jy, were used as scaling factors for the galaxy flux scale when the spectral line data were reduced.

The nearby, face on galaxies NGC 1058 and NGC 4214 used by SSDI as flux monitor objects were observed by us as well throughout the run; their narrow profiles yield fluxes relatively robust against change in baseline shape. Individual spectra were weighted by inverse system temperature before summation, and sums in each channel were scaled by the appropriate factor from Table I before averaging, baseline subtraction and integral assessment. Corrections for the change of telescope gain with zenith angle determined by Staveley-Smith (SST) were applied to the individual object spectra. Table II*a* gives the run of measured fluxes for NGC 1058 and Table II*b* the same for NGC 4214. No systematic trend with date was seen for either object. Observed fluxes in Jy km sec^{-1} for these objects averaged over the run came out to:

NGC 1058: F_{HI} = 82.3 ± 2.6 (ch. A), 83.7 ± 3.3 (ch. B);

NGC 4214: F_{HI} = 208.0 ± 4.8 (ch. B), 216.4 ± 5.9 (ch. B).

SSDI published fluxes of 74.9 ± 0.4 and 191.0 ± 2.5 Jy km sec^{-1} for these objects; we thus find we measured fluxes in the 1989 IRAS/4KVL campaign that were higher than those of SSDI by factors:

NGC 1058: F_A (Roth) = 1.10 F(SSD); F_B (Roth) = 1.12 F(SSD);

NGC 4214: F_A (Roth) = 1.09 F(SSD); F_B (Roth) = 1.13 F(SSD).

The origin of this discrepancy remains unclear. (A discrepancy of similar sign and magnitude is described in Chapter 3, where our Parkes observations of monitor and calibrator objects are compared to values published by Davies, Staveley-Smith and Murray 1989; hereafter DSSM.) The ratios of raw power received in channel A to that received in B from 3C 286, NGC 1058 and NGC 4214 differ by several percent and apparently depend on object angular size.

The 1990 data provided by J. V. S. and R. D. D. include observations of NGC 1058 and NGC4214 but no absolute flux density calibration. The gain was calibrated by these face-on galaxies alone by equating their fluxes to those measured by us in 1989. This led to raw fluxes in each channel of 1990 data being multiplied by factors $f_A = 1.04$, $f_B = 0.87$, respectively.

Because HI fluxes are not being used by us either as a primary 'standard candle' nor as a second parameter in the TF relation, such few percent irregularities in the flux scale can be neglected. Furthermore, they are dwarfed by the systematic disagreements in flux scale for observations of even bright, nearby objects by different observers with different flux calibration procedures.

IV. Program object reduction

Program objects were reduced using the 'SLAP' (Spectral Line Analysis Package) written and provided by Lister Staveley-Smith.

Individual net (object minus sky) spectra were reviewed and rejected if plagued by unusually disturbed baselines, gross interference, or evidence of correlator malfunction (usually manifesting itself as apparent periodicity in the spectral plot of received power versus heliocentric velocity). During reduction, velocities along the x axis are those derived from reception frequency by 'radio' convention $\delta v/c = \delta\nu/\nu_0$. Spectra were summed separately for each channel. To remove baselines

from the summed spectra, polynomials were fitted to hand picked regions of baseline free from signal or interference and subtracted from the spectra. When detections were strong this procedure was applied separately to each channel sum; elsewhere the two channels were summed before baseline subtraction.

Review of data reduction logs shows that the author added the two channels' spectra without individual flux correction, contrary to ideal procedure, and then multiplied object fluxes by the average correction factor (1.05 ± 0.02). This procedure avoids gross systematic error but does make less than ideal use of the calibration provided by 3C 286.

The reference points on a canonical two horned rectangular profile are those at which the flux reached 20, 25 and 50 percent of the peak value on a given side. Following baseline subtraction, systemic velocity and line width at these reference points were determined using two algorithms. Method 'MAX' comes in from points beyond the profile edges towards the center until it first encounters a velocity at which the power equals fraction f (20, 25 or 50 percent) of peak power on that side of the profile. Method 'MAX' is thus presumably biased towards higher linewidth by greater radiometer noise, since random noise spikes will intercept the incoming f level 'detector'. Method 'GAUS' fits a one-sided Gaussian function to the profile edge, guided initially by the location of the local maximum. Since radiometer noise frequently provides false spectral peaks inward of the actual profile 'horns', 'GAUS' is not infrequently fooled into fitting a skewed Gaussian providing a too narrow 50 percent width and at times too wide, at times too narrow a 20 percent width. Monte Carlo simulations exploring these effects are discussed below in Section V. We note that Chapter 5 on our Parkes observations offers a plot of the difference between widths provided by 'MAX' and 'GAUS' and that the 'MAX' widths generally exceed those provided by 'GAUS'.

Line fluxes were assessed by integrating all flux above the zero line and between the two points marked by the cursor as delineating the edge of the profile. Error bars were not placed on program object fluxes since systematic differences in subjective signal / baseline separation and polynomial

order choice in baseline fitting dominate the uncertainty in fluxes of broad emission line spectra. Two independent reductions of Parkes 4KVL detections discussed in Chapter 5 offer an empirical estimate of the magnitude of flux uncertainty introduced by variation in reduction procedure. In any case we would suggest a minimum fractional error of 10 percent be applied to any program object flux reported here. In cases of $S/N < 5$, we presume fluxes are determined to no better than perhaps 30 percent. The poorest baselines generally resulted when we were forced to observe objects within 30 or 40 degrees of the Sun's position.

Finally, fluxes remained uncorrected for differential gain across the beam (DSSM) or for cosmological effects. Neglecting the correction for differential gain underestimates fluxes by an amount depending on object size but not exceeding 5 percent (SSDI, DSSM).

V. Data presentation

Figures 1 show the spectra of all (41) detected *IRAS* 4KVL objects observed in 1989/90 after summation, flux rescaling, baseline removal and Hanning smoothing. Figures 2 show the spectra of (16) nondetections after summation, flux rescaling and Hanning smoothing. Velocities are determined here by 'optical' convention $\delta v/c = \delta\lambda/\lambda_0$.

Table III lists for each detected object its database number, HI flux in Jy km sec^{-1} , systemic velocity between the 20 percent reference points in km sec^{-1} , signal to noise ratio S/N defined as F_{HI}/W_{20} divided by the per channel *rms* baseline noise in Jy assessed in a signal free portion of the spectrum after Hanning smoothing, and velocity spacing (width) between the two equal level markers at 50, 25 and 20 percent levels, respectively. Widths and velocities are averages of 'MAX' and 'GAUS' output and have been converted to 'optical' convention by

$$v_{opt} = v_{rad}/(1 - v_{rad}/c), \qquad (4-1)$$

$$W_{opt} = W_{rad}\ \delta V_{opt}/\delta V_{rad}, \qquad (4-2a)$$

$$\delta V_{opt}/\delta V_{rad} = W_{rad}[1/(1 - v_{rad}/c) + (v_{rad}/c)/(1 - v_{rad}/c)^2] \qquad (4 - 2b)$$

(SST). Staveley-Smith also shows that 'optical convention' widths equal their rest frame values at nonzero z, while 'radio' widths require division by $1+z$.

Table IV lists, for nondetections, their heliocentric velocity as provided by Strauss *et al.* in the sample definition and the *rms* per channel noise in mJy after Hanning smoothing from a clean portion of the baseline. Detected galaxies showed an average HI flux of 13.7 Jy km sec^{-1} and average signal to noise ratio of 12. Nondetections showed an average baseline noise of 3.8 mJy channel $^{-1}$ after Hanning smoothing.

VI. Monte Carlo perturbation of high S/N spectra with radiometer noise

To quantify the above discussion of bias effects on linewidths produced by 'MAX' and 'GAUS' we perturbed the spectra of three intrinsically high S/N Jodrell Bank 1989/90 spectra (for objects 0250+66, N772 and N2566) with Gaussian random deviates of standard deviation σ_f (mJy) varying independently in each correlator channel, then reassessed linewidths with both methods. This follows the lead of Lewis (1983) and Bicay and Giovanelli (1986), who performed similar Monte Carlo experiments to study biases in measures of HI profile width. Such perturbation was performed 300 times for a given σ_f, velocity widths assessed each time, and the results averaged. The three template spectra run a range in 'steepness', where

$$\text{steepness} = (W_{20}+W_{50})/[2(W_{20}-W_{50})],$$

from 18.8 (0250+66) to 3.9 (N2566). The results are shown in Figures 3 and 4. S/N is defined, as before, as integral HI flux divided by linewidth divided by average radiometer noise per channel.

As expected, 'MAX' is biased towards greater linewidth as noise heats up. Steep profiles are most susceptible at 20 percent but least at 50 percent. Shallow profiles are most susceptible at 50 percent. Generally linewidth bias seems to set in at $S/N \sim 10$ and increases steeply to ~ 10

km sec^{-1} 'extra' linewidth at $S/N \sim 5$. The amount of linewidth bias suffered sensitively depends on profile shape, however.

'GAUS' linewidths generally drop as S/N decreases. In this case we find steep profiles most immune at both 20 and 50 percent levels, while N772's profile (steepness = 7.5) suffers worst (both W_{20} and W_{50} spuriously drop by 10 km sec^{-1} at $S/N = 5$). Again $S/N \sim 5$ appears to be a critical value, an impression supported by comparing repeat reductions of Parkes data presented in Chapter 3.

The bias in inferred galaxy magnitude (from the TF relation) induced by a given linewidth bias depends upon the actual galaxy linewidth and the line of sight inclination angle, but as an example, if we consider an edge on object with apparent width 300 km sec^{-1} and linewidth bias 15 km sec^{-1} , then

$$\delta W/W = 0.05 = \delta ln(W) = 2.3\ \delta log(W)$$

and a corresponding Tully-Fisher magnitude shift of

$$|\delta M| = 8\ \delta log(W) = 0.17\ mag$$

if the TF slope is taken as -8. The resultant distance error is 8 percent, which translates to false peculiar velocity of 320 km sec^{-1} at the 4KVL sample edge of 4000 km sec^{-1} . Since intrinsically narrow profiles suffer greater fractional bias $\delta W/W$ at a given S/N, radiometer noise might be expected to bias the TF relation towards steeper slope at low linewidth if 'MAX'-like algorithms assess velocity width. This could be a possible source of the curvature in the TF relation reported by Aaronson *et al.* (1982).

The above experiment highlights the need to know the detailed algorithm used by a given author, and the S/N inherent in his/her data, before using that author's linewidths in a TF application. As such information is unavailable for the bulk of linewidth data we have drawn from the literature, we can only make statistical allowances for the bias effects described here and do so in Monte Carlo simulations of our experiment in Chapter 6. We implore future authors of HI

papers to provide methodology and S/N information. The creation of an on-line database from which astronomers may pull raw or reduced spectral line data is a currently feasible development, and one that should be actively encouraged.

Table I - Calibration diode measured power

Dates are UT September 1989; Power values are in Jy

Local oscillator frequencies in Mhz correspond to heliocentric

velocities = (4 ν_{LO} - 1420 MHz - 155 MHz)/1420 MHz $\times c$

μ_{LO}	389 MHz		392 MHz		395 MHz	
v	4014 km s^{-1}		1479 km s^{-1}		-1056 km s^{-1}	
date:	ch. A	ch. B	ch. A	ch. B	ch. A	ch. B
11	21.5	19.9	19.1	19.8	18.9	17.4
16	20.5	21.0	19.1	20.4	19.2	19.8
18	21.2	21.2	20.3	21.4	19.5	20.4
22	22.1	21.9	22.6	21.6	20.7	20.6
25	22.3	21.4	21.8	23.4	21.2	21.2
28	21.5	21.1	19.4	21.2	20.0	20.1
avg:	21.5	21.1	20.4	21.2	19.8	19.9
rms:	(0.6)	(0.7)	(1.5)	(1.4)	(1.0)	(1.3)
scale:	1.075	1.055	1.020	1.060	0.990	0.995

Table II*a* - Flux integral measurements for NGC 1058

Date is UT September 1989; Fluxes are in units of Jy km s^{-1}

date:	F_{HI}, ch. A	F_{HI}, ch. B
16	86.3	87.2
17	82.0	83.8
19	82.2	82.6
20	85.5	86.1
21	84.2	85.6
22	82.2	86.1
23	85.9	90.0
24	79.4	81.8
25	80.1	79.0
26	78.6	79.2
27	83.3	83.4
28	81.6	83.4
29	79.1	79.4

Table II*b* - Flux integral measurements for NGC 4214

Date is UT September 1989; Fluxes are in units of Jy km s^{-1}

date:	F_{HI}, ch. A	F_{HI}, ch. B
16	212.6	220.2
17	202.8	208.4
19	214.0	225.8
20	209.8	217.3
21	212.4	225.8
22	204.0	216.1
23	202.7	208.3
24	207.8	212.3
26	203.9	215.7
27	213.4	213.2
28	204.4	217.2

Table III - HI detections of *IRAS* 4KVL objects at Jodrell Bank

obj	name	F_{HI}	V_{HI}^{hel}	S/N	W_{50}	W_{25}	W_{20}
1	N 7817	14.8	2299	10	398	422	431
29	N 772	8.3	2436	16	412	460	471
33	N 827	12.2	3430	9	360	375	378
43	N 972	9.0	1536	13	260	304	315
53	0250+66	9.6	3241	9	373	388	394
56*	U 2409	16.4	3898	7	286	318	324
64	U 2789	11.3	3150	15	358	383	387
66	N 1385	26.2	1495	25	183	213	234
69	U 2866	31.1	1334	33	237	275	285
71	N 1482	5.5	1859	4	243	273	280
83	U 3097	7.4	3351	15	116	172	188
84	U 3147	11.2	2868	10	255	296	303
94	N 1821	10.4	3612	17	145	186	196
98	U 3354	10.6	3109	5	400	417	421
99	N 2076	39.3	2128	13	358	396	410
106	U 3511	10.9	3565	7	315	347	354
117	U 3828	3.5	3276	7	237	264	268
126	N 2469	7.2	3254	7	218	290	303
129	N 2566	17.9	1630	14	168	209	233
134	N 2633	17.3	2164	16	257	288	296
136	E563-28	10.8	2694	13	245	270	275
204	N 3683	20.9	1758	11	274	391	421
228	N 4102	7.5	842	5	306	334	336
245	N 4500	3.8	2911	3	305	319	321
265	N 4793	16.9	2510	18	295	324	336
316*	N 5430	8.8	2965	12	314	344	351
338	N 5728	10.4	2786	4	389	409	414
340	E580-27	7.0	3286	19	136	183	197
348	N 5861	28.6	1842	16	321	351	358
352	N 5900	9.2	2694	5	399	422	424
357	N 5937	9.9	2805	7	355	407	418
361	N 5990	1.6	3889	2	251	269	283
382*	N 6701	7.4	4013	7	274	308	315
385	N 6764	14.8	2415	20	275	296	302
394	N 6835	15.6	1613	20	117	168	190
396	U 11540	7.3	2477	7	345	356	359
400	N 6931	2.5	3343	5	112	140	144
405	2108+65	9.4	2888	17	147	196	205
408	N 7074	2.9	3551	2	265	293	299
423	N 7448	30.4	2180	20	277	305	308
424	N 7479	32.1	2393	30	349	369	374

F_{HI} in Jy km s^{-1}; V_{HI} and W in km s^{-1}.
$S/N = F_{HI}/W_{20}/\sigma_f$, where σ_f is baseline noise per channel
Asterisk (*) denotes objects observed in 1990 by J. V. S. and R. D. D.

Table IV - HI nondetections of *IRAS* 4KVL objects at Jodrell Bank

obj	name	V	σ_{mJy}
31	0202-06	3919	3.7
42	0224-14	3766	5.1
59	N 1186	2762	3.7
62	N 1266	2194	2.6
87	0455-07	3773	3.2
93	E553-20	3997	5.5
125*	U 4041	3449	2.4
133	0836-14	4184	4.5
143	N 2785	2737	3.1
171	E500-34	3670	7.1
188	N 3453	4039	4.4
239	N 4332	2843	1.4
281	1312-15	2231	3.3
393	N 6824	3386	3.4
395	2016-05	3400	3.9
399	2027-15	3494	3.6

σ_{mJy} is average baseline noise in mJy after Hanning-smoothing.

V is heliocentric in km s^{-1} from Strauss *et al.*

UGC 4041 appears to have been detected but uncertainty in baseline subtraction leave its flux and width undetermined; raw spectrum is shown in Figure 2.

Asterisk (*) denotes object observed in 1990 by J.V.S. and R.D.D.

Figure Captions - Chapter 4

Figure 1 (7 pages): 21 cm. line spectra of detected objects, flux corrected, baseline subtracted and Hanning smoothed. Velocities obtain from reception wavelength following 'optical' convention $v/c = \delta\lambda/\lambda_0$.

Figure 2 (3 pages): 21 cm. line spectra of nondetections, flux corrected and Hanning smoothed. Velocities obtain from reception wavelength following 'optical' convention $v/c = \delta\lambda/\lambda_0$.

Figure 3: (a) Bias in 'MAX' algorithm's W_{20} as function of S/N, averaged at each S/N over 300 Monte Carlo perturbations of original high S/N profile by independent Gaussian random deviates in each radiometer channel. Three template spectra originating from Figure 1 are represented by different symbols. (b) Bias in 'MAX' algorithm's W_{50}, from the same experiment.

Figure 4: (a) Bias in 'GAUS' algorithm's W_{20} for the same perturbed profiles described in Figure 3. (b) Bias in 'GAUS' algorithm's W_{50} from the same experiment.

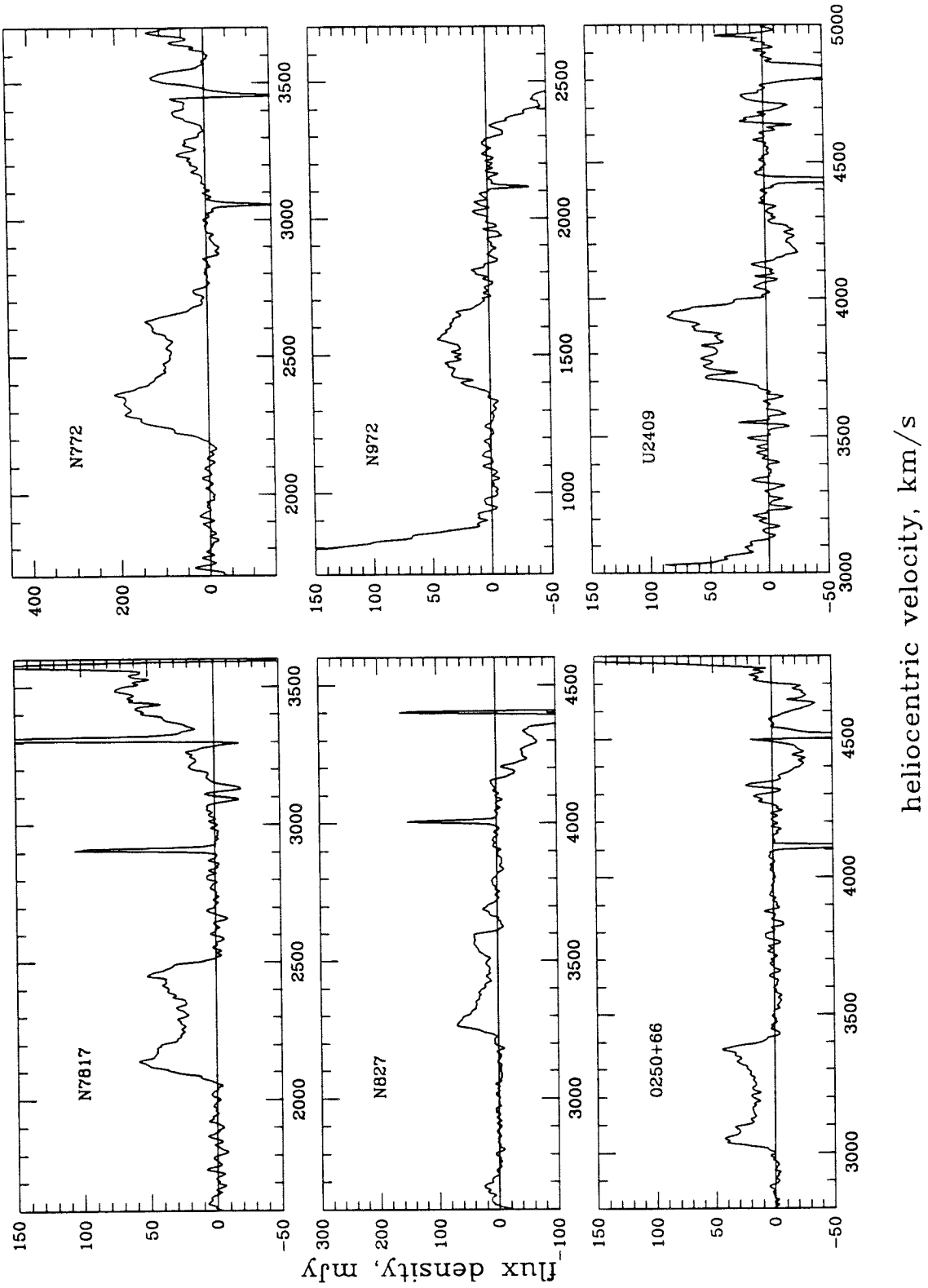
N7817
N772
N827
N972
0250+66
U2409
flux density, mJy
heliocentric velocity, km/s

Figure 1(1)

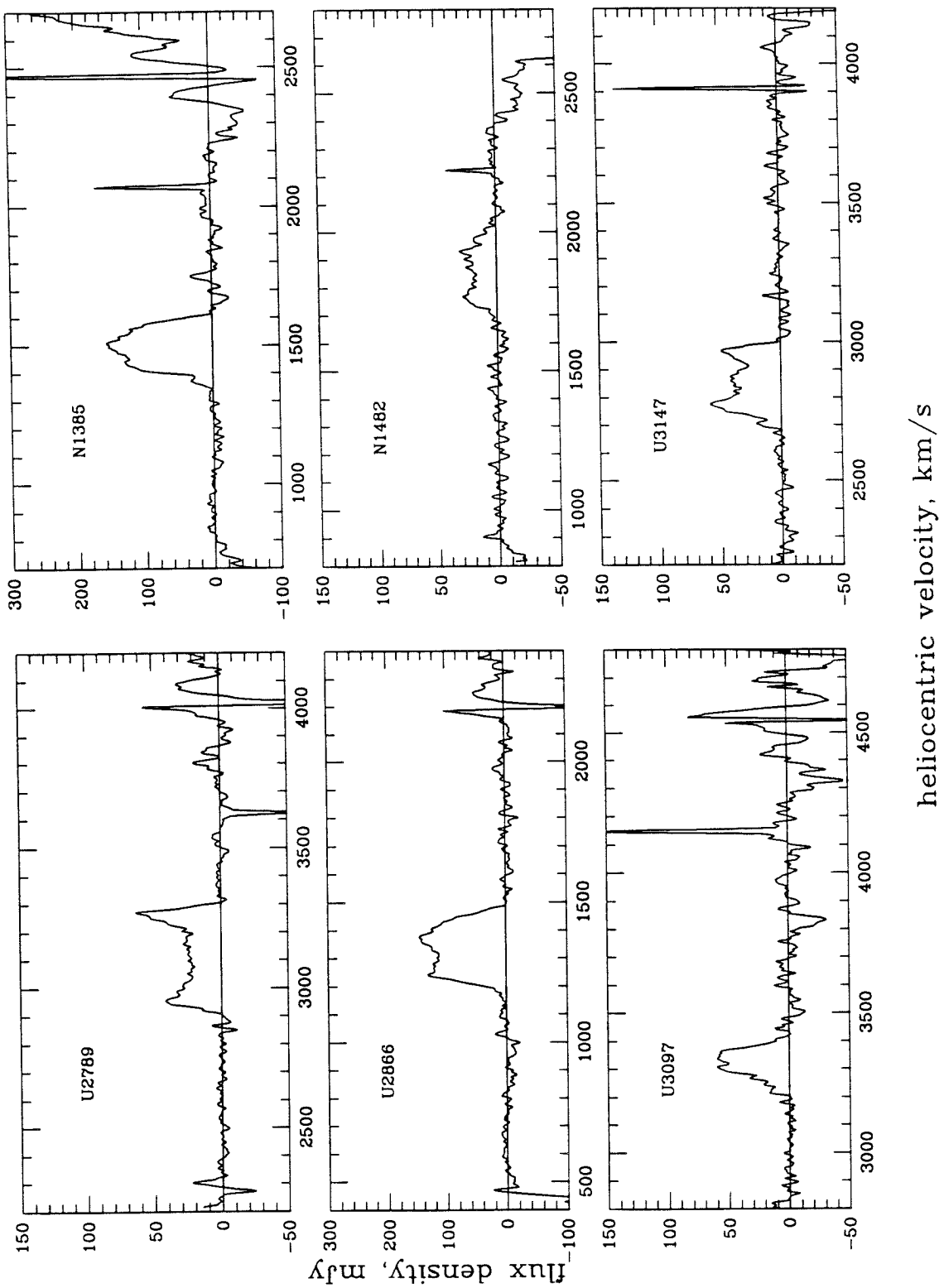
N1385
N1482
U3147
U2789
U2866
U3097
flux density, mJy
heliocentric velocity, km/s

Figure 1(2)

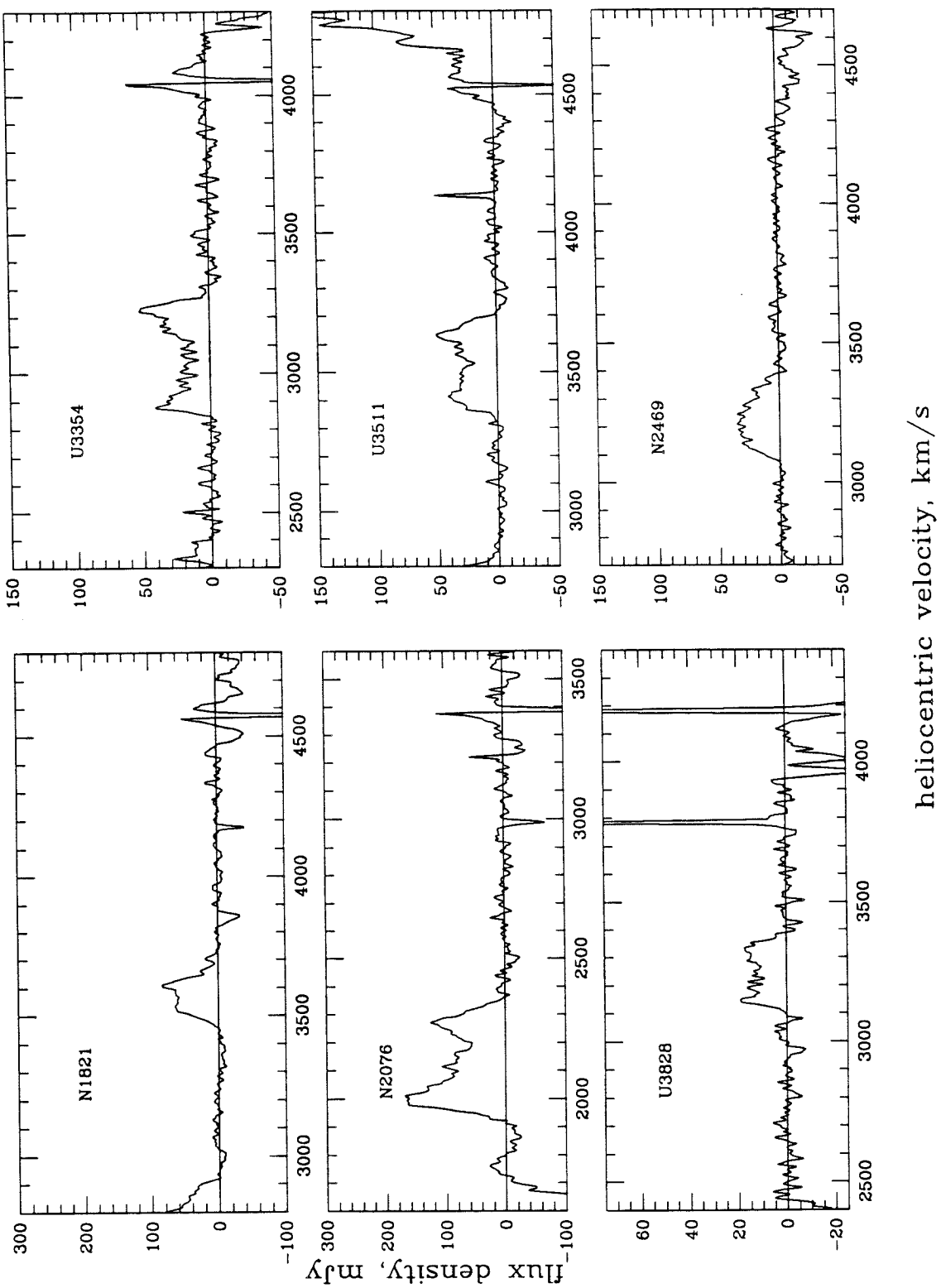
N1821
N2076
U3828
U3354
U3511
N2469
flux density, mJy
heliocentric velocity, km/s

Figure 1(3)

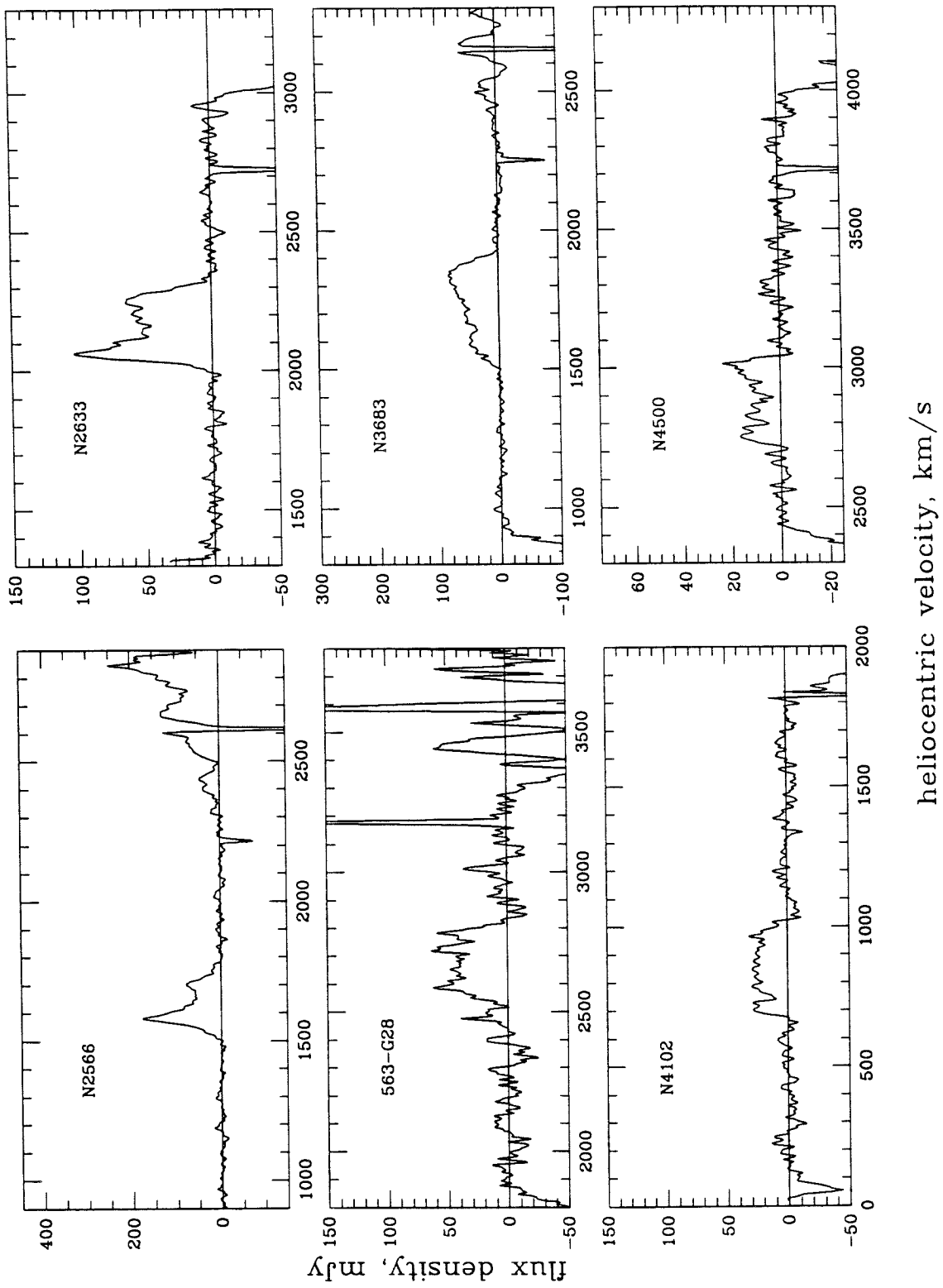
N2566
563-G28
N4102
N2633
N3683
N4500
flux density, mJy
heliocentric velocity, km/s

Figure 1(4)

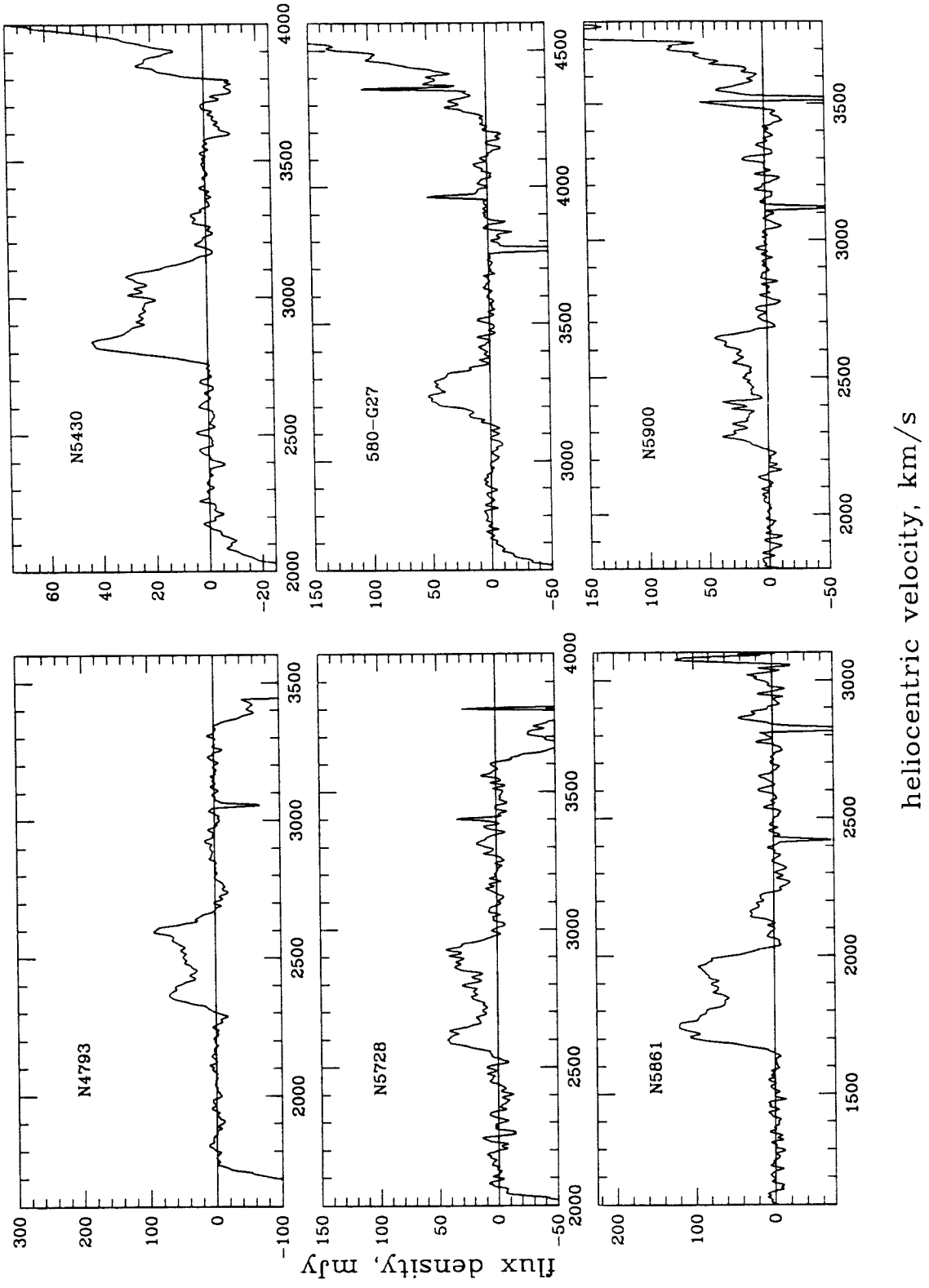
N5430
580-G27
N5900
N4793
N5728
N5861
flux density, mJy
heliocentric velocity, km/s

Figure 1(5)

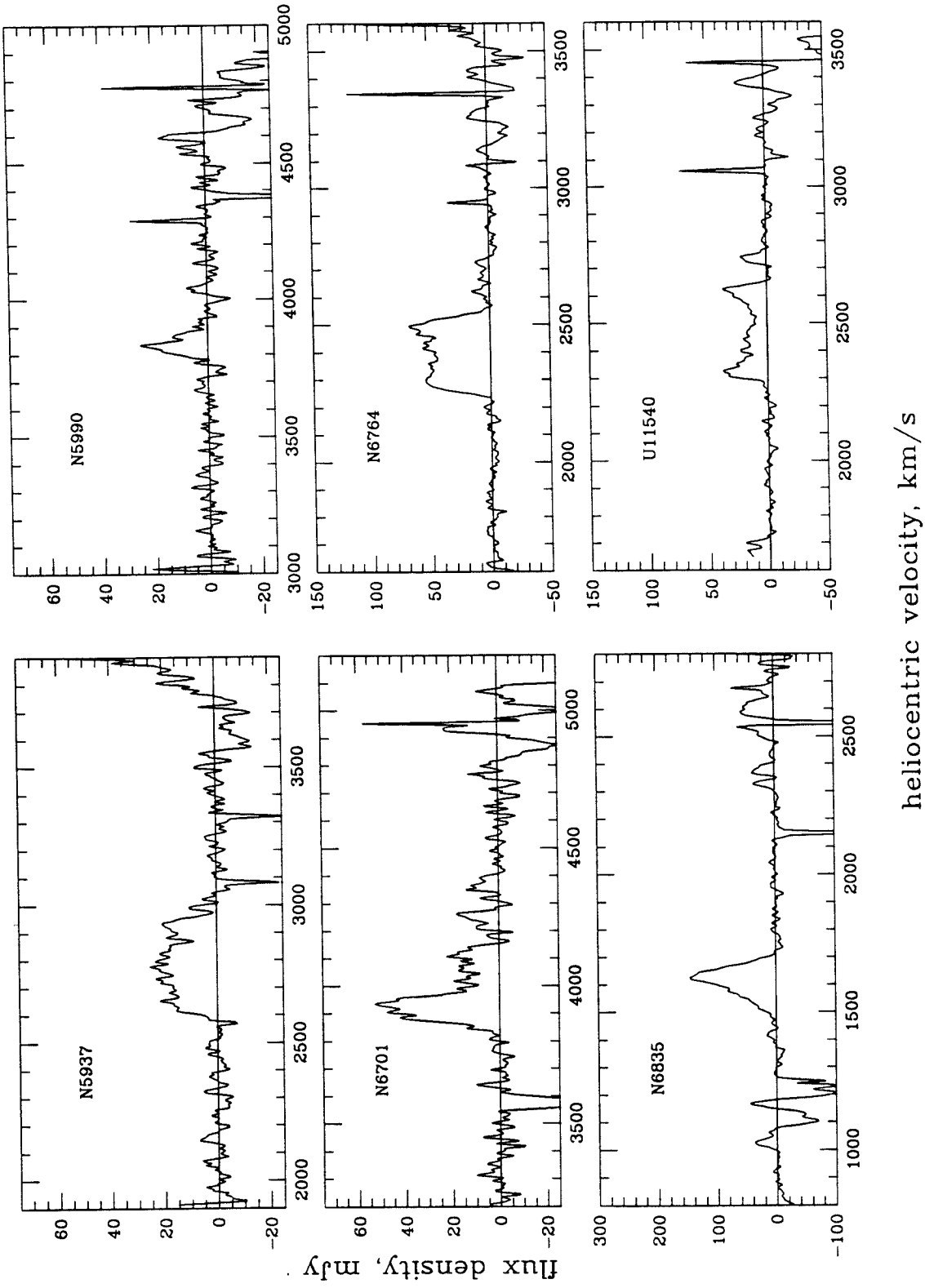
N5990
N6764
U11540
N5937
N6701
N6835
flux density, mJy
heliocentric velocity, km/s

Figure 1(6)

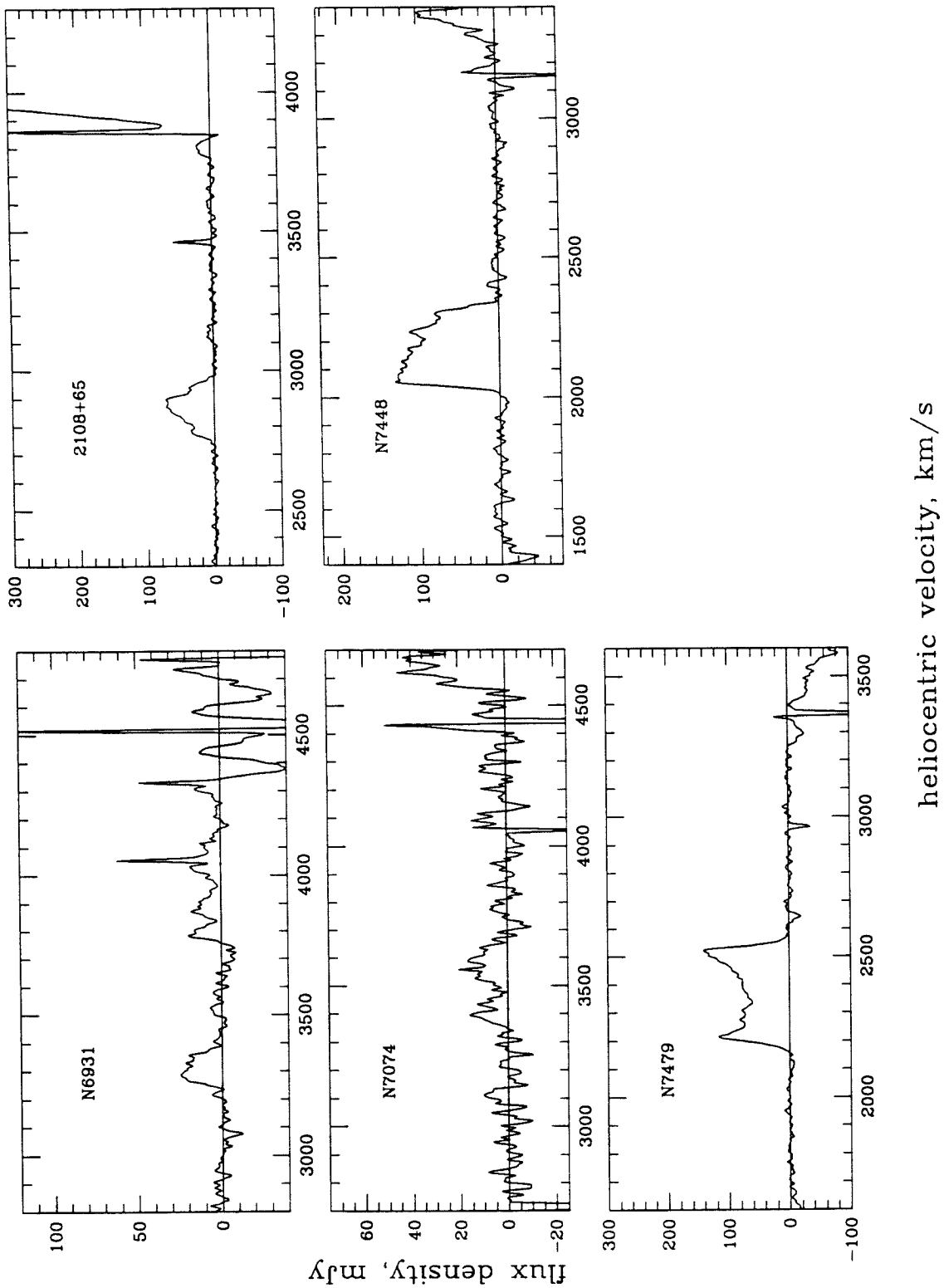
2108+65
N7448
N6931
N7074
N7479
flux density, mJy
heliocentric velocity, km/s

Figure 1(7)

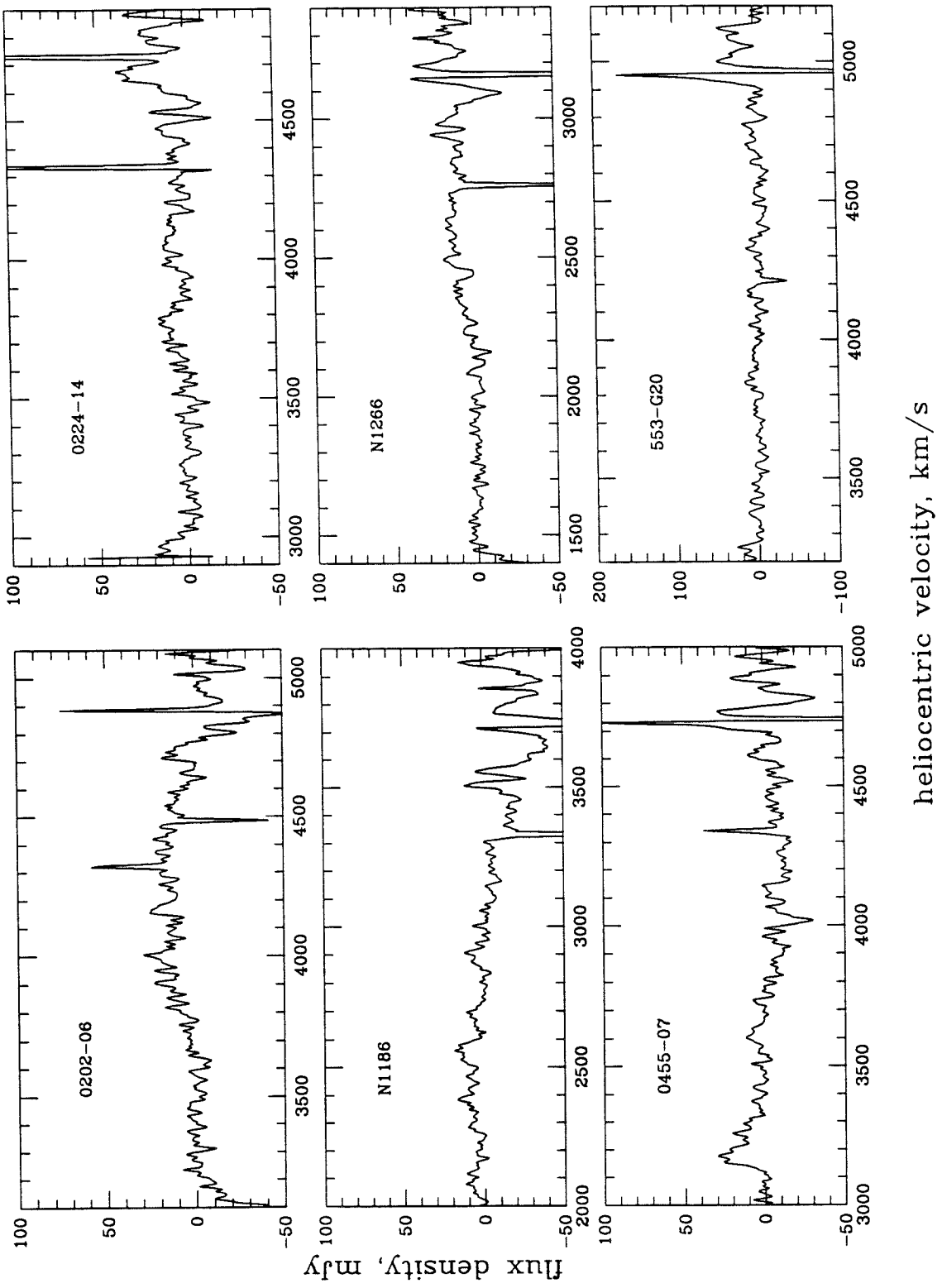
0202-06
N1186
0455-07
0224-14
N1266
553-G20
flux density, mJy
heliocentric velocity, km/s

Figure 2(1)

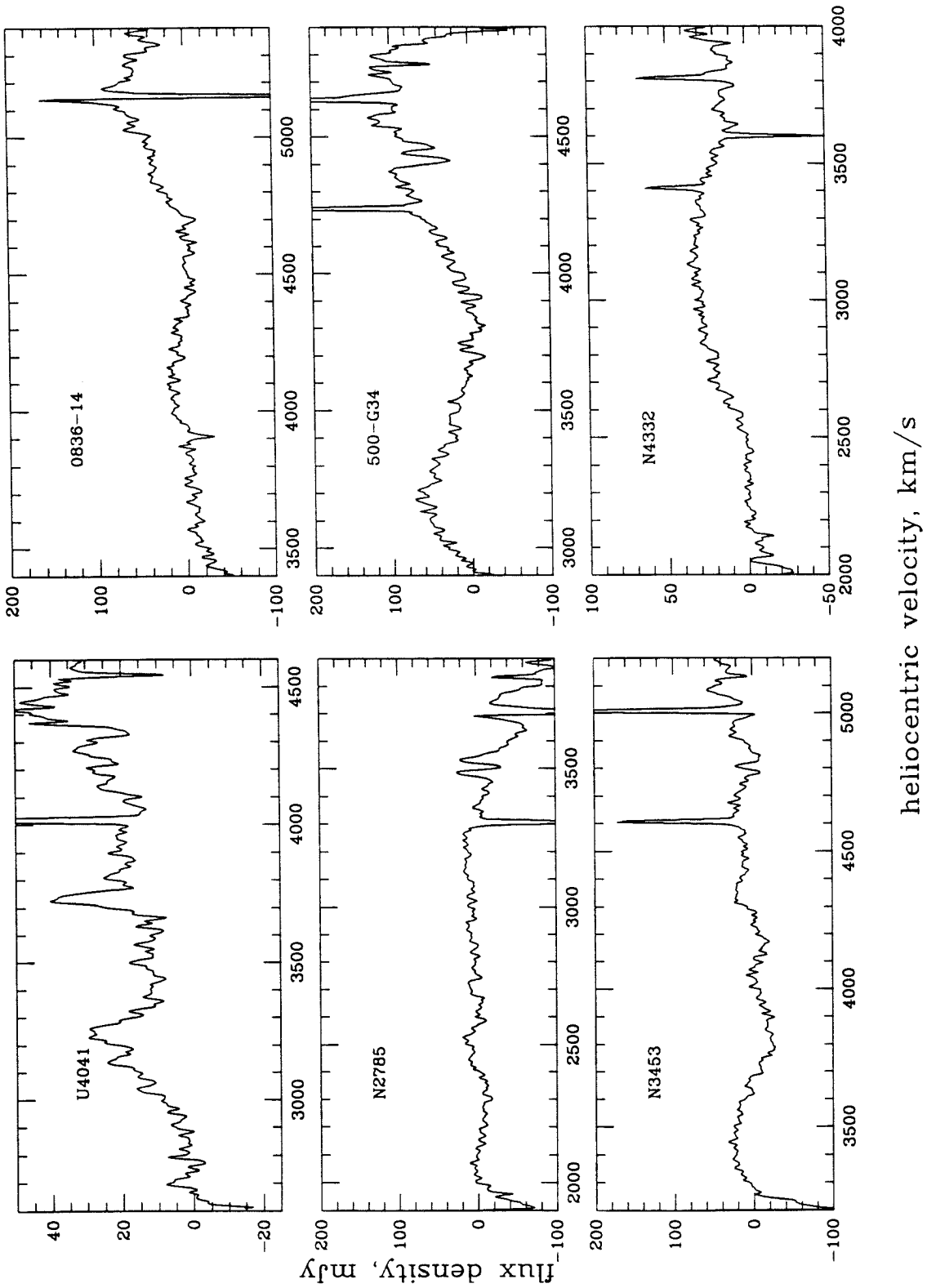
0836-14
500-G34
N4332
U4041
N2785
N3453
flux density, mJy
heliocentric velocity, km/s

Figure 2(2)

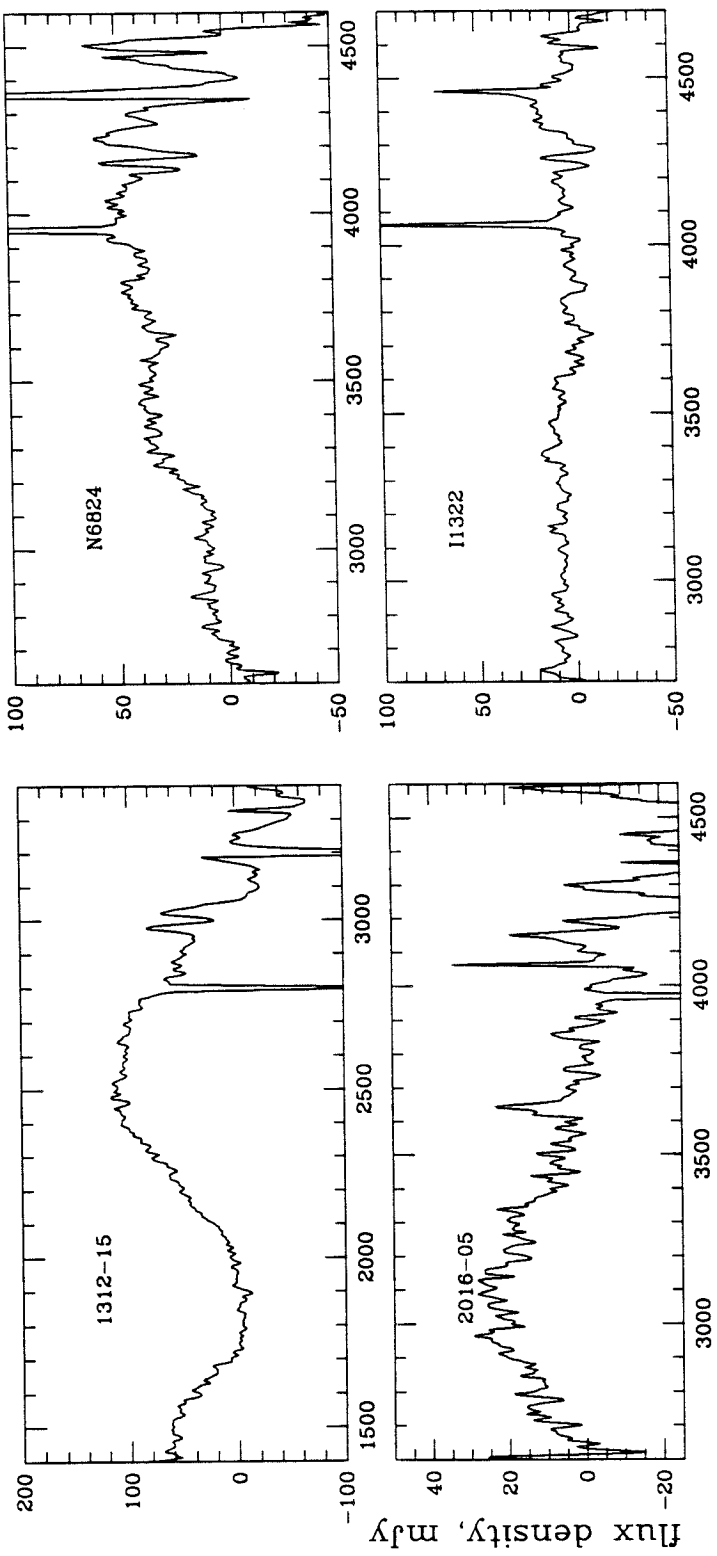
flux density, mJy
heliocentric velocity, km/s
1312-15
2016-05
N6824
I1322

Figure 2(3)

Monte Carlo perturbation of high S/N HI profiles

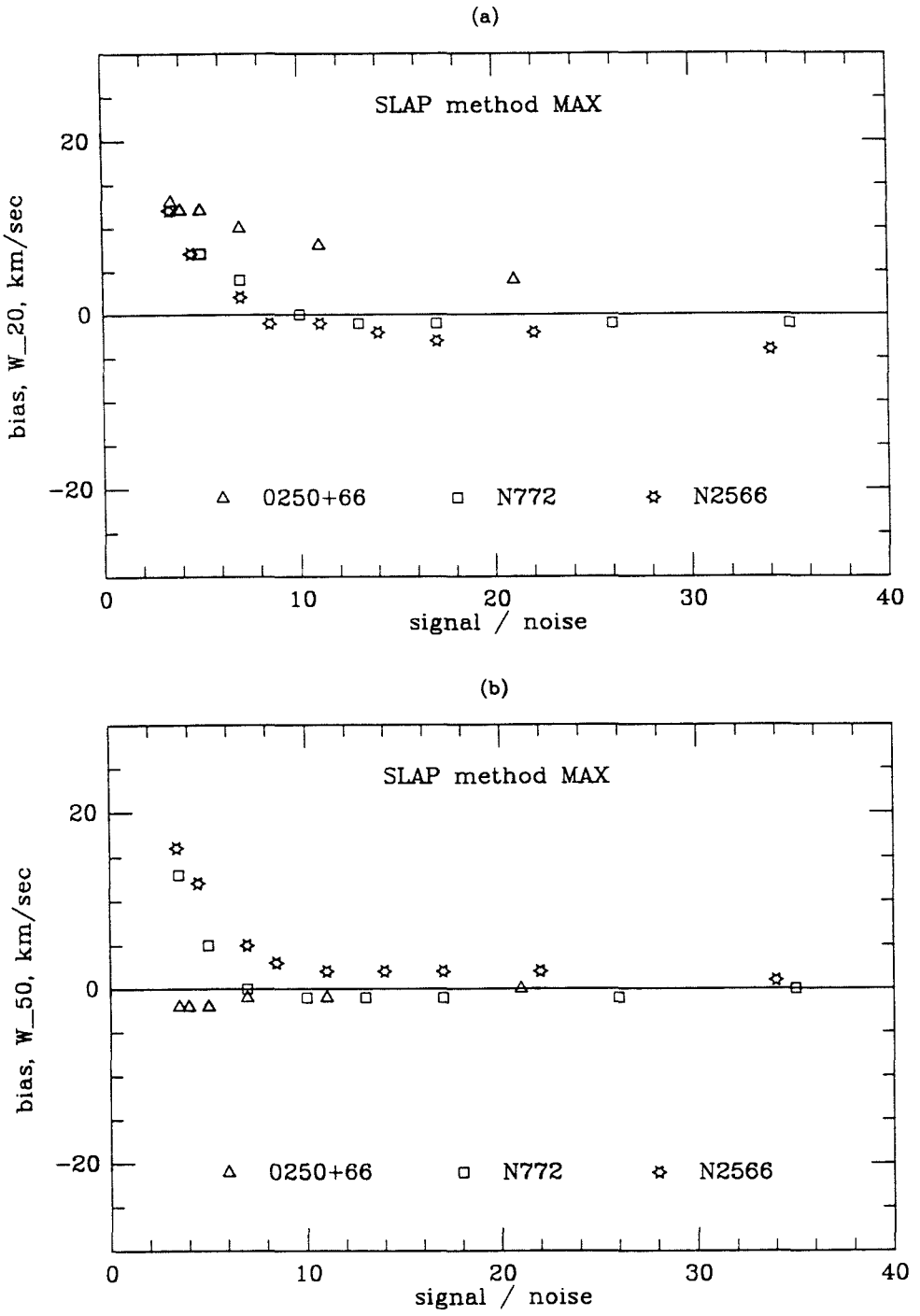

Figure 3

Monte Carlo perturbation of high S/N HI profiles

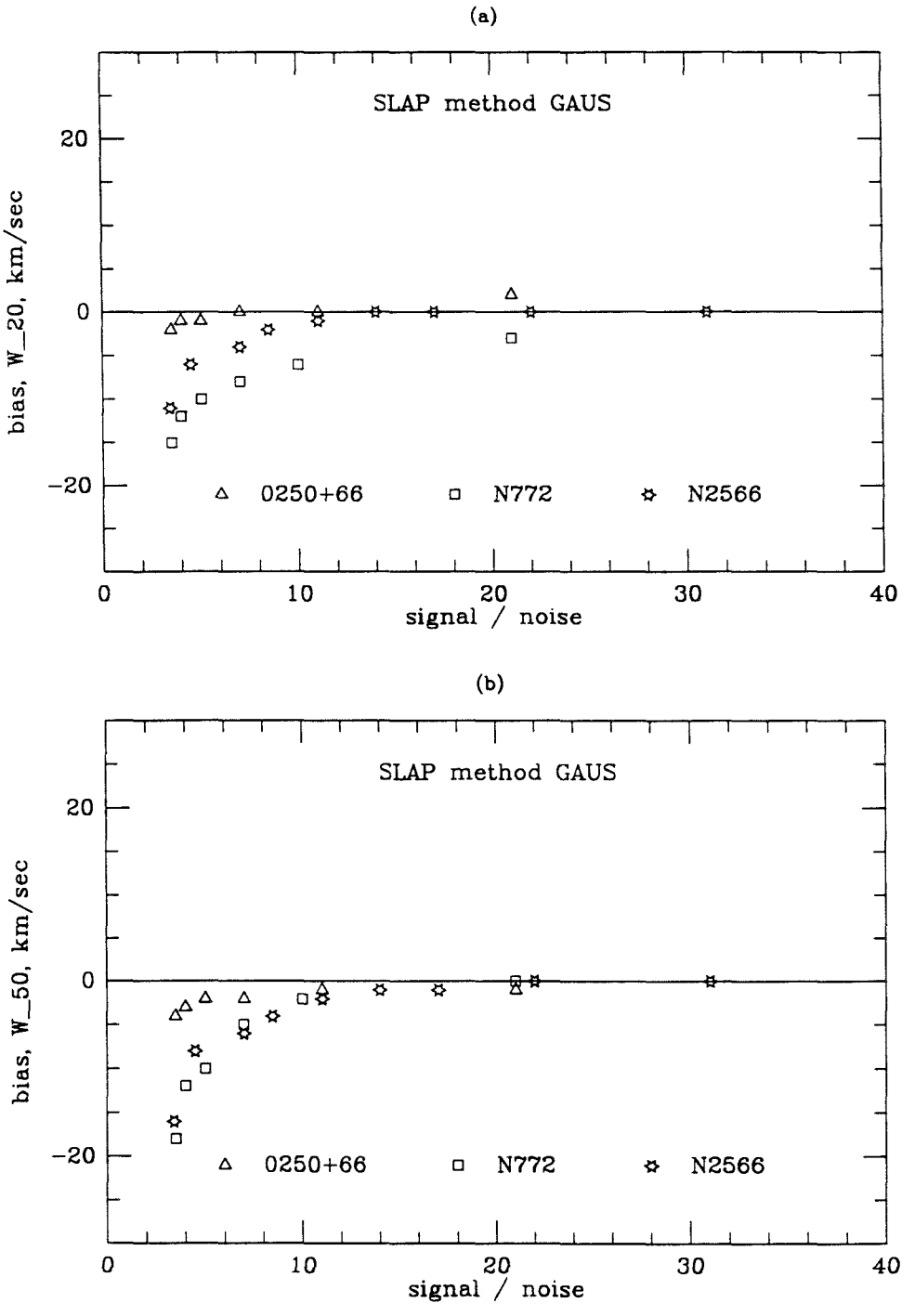

Figure 4

Chapter 5: HI observations of *IRAS* 4KVL objects at Parkes

I. Observations

Eight full days of observing time were made available to the *IRAS* 4KVL project in December 1989 at the 64 meter radio telescope of the Australian CSIRO at Parkes, New South Wales. The Parkes telescope has a beamwidth of 15 arcminutes at 21 cm, a gain of 0.63 °K Jy^{-1}, and was equipped with a cryogenically cooled receiver with a system temperature of about 40°K. The 1024 channel 1 bit autocorrelator was split into two banks of 512 channels for each of two linear polarizations for the 1989 run. As 512 channels spanned the 10 MHz bandwidth, the resulting dispersion was 19.5 kHz (4.1 km sec^{-1}) per channel, as in our Jodrell setup. The primary observers during the 1989 Parkes *IRAS* 4KVL run were Lister Staveley-Smith, Jeremy Mould and Joshua Roth. Davies, Staveley-Smith and Murray (DSSM) further discuss the instrumental configuration as well as the absolute flux calibration (such as we used) tied to Hydra A.

A few 4KVL objects were observed by L. Staveley-Smith and J. R. Mould in 1990 at which time the correlator was divided into four quadrants of 256 channels. Those objects are noted with an asterisk (*) in Tables I and II.

The Parkes telescope features an altazimuth mount. Feeds and cooled FET amplifiers reside in the chamber held at the focus of the 64 meter dish by three support members arising therefrom.

Net galaxy spectra were obtained by integrating on program objects for N minutes (N being set by the observers at 3, 4, or 5 depending on baseline stability) and then upon 'blank' sky, generally at the same altitude-azimuth setting as the program object, for an equal length of time. Sky regions N (time, not arc) minutes E and W of program objects were checked for other galaxies whose HI line emission might overlap a program objects'; on two occasions we failed to note such objects until anomalous apparent absorption features were seen in program object spectra. Individual net

galaxy spectra were generally immediately added to a running sum using the crude data reduction package on the observing system at Parkes until the observers deemed the signal to noise ratio (S/N) adequate (or a nondetection likely). Several objects, although detected, were returned to once or twice later in the run to enhance S/N. An average of about 3 hours' integration time was spent on each of the objects listed in the tables that follow.

The telescope was generally 'tuned' (*i.e.*, the local oscillator set) so that the heliocentric redshift provided by Strauss *et al.* for a given *IRAS* 4KVL object appeared at the center of the band (VC = 0.5 in 'SLAP' lingo). Objects whose emission features appear far from the bandpass center thus have discrepant optical and radio recession velocities.

II. Data reduction

Individual net object spectra provided by the Parkes operating system were converted to 'SLAP' format and processed with that package twice at Caltech in 1990 and 1992 by J. Roth. Individual scans were rejected if horribly curvey, subject to interference near the bandpass center, or if a correlator failure was evident (usually seen as artificial looking periodicity in the spectral plot of power versus recession velocity).

Summed spectra for each channel were multiplied by gain correction factors determined by pointed observations of the continuum flux standard source Hydra A which, when compared to the calibration source in each channel, provided the gain correction factors (DSSM). The calibration diodes were defined to be 5 Jy in the data acquisition system in 1989. Observations of Hydra A showed their equivalent power to be 4.94 Jy in Channel A and 4.77 Jy in Channel B; thus raw spectral data were multiplied by correction factors of 0.99 (A) and 0.95 (B), respectively, before summation. Flux calibration coefficients for the 1990 data, also based on pointed observations of Hydra A, were provided to J.R. by L.S.S. and applied to the 1990 spectra.

Generally the two channels' spectral sums were then added, a polynomial baseline fit to signal-free portions of the spectrum and subtracted, and 'MAX' and 'GAUS' linewidth measuring algorithms applied to assess the linewidths and velocities at the 50, 25 and 20 percent of peak power levels as discussed in the previous Chapter. Hanning smoothing was then applied before plotting in Figure 1 and before assessing per channel noise from signal free portions of the spectrum after baseline subtraction (but generally after assessing linewidths). On a few especially strong detections baselines were subtracted separately from channels A and B, as we more often did with the Jodrell data described in Chapter 4.

Objects observed in 1990 by L.S.S. and J.R.M. had scans added, baselines removed and smoothing applied by those observers at Parkes; J. R. then applied 'MAX' and 'GAUS' to these net spectra to obtain widths. The poorer resolution and consequent greater smoothness of these spectra is apparent in Figure 1.

Table I lists detected objects' fluxes, linewidths and velocity centroids as determined by 'SLAP' methods 'MAX' and 'GAUS'. Figure 1 shows net summed spectra after baseline subtraction and Hanning smoothing. Velocities in Figure 1 are derived from reception frequency by 'optical convention' $v/c = \delta\lambda/\lambda_0$. Velocity centroids and widths were determined in 'SLAP' with velocities in 'radio' convention and then converted (as before) using Equations 4-1, 4-2 before listing in Table I or plotting in Figures 1 and 2. Figure 2 shows net summed spectra for nondetections after Hanning smoothing. Table II lists nondetections' heliocentric velocities and noise in mJy per channel after Hanning smoothing.

Beam dilution factors (DSSM) due to differential gain across the galaxy disk were not applied to the fluxes in Table I as most objects observed by us show an apparent angular diameter much smaller than the beamsize of 15 arcminutes. Cosmological corrections have not been applied to fluxes or velocities and SST shows that 'optical' convention linewidths are z invariant.

The greatest limit to sensitivity to weak sources was arguably the generally curvey and time variable baselines offered by the Parkes system, especially during daylight hours. Baseline curvature is evident in some of the nondetections' spectra shown in Figure 2 even after summing many independent scans. Some baselines were so perverse as to offer a pronounced shear in the center of the bandpass, badly distorting any object signal present. It is difficult to quantify this effect, however, so we define signal to noise for detections (Table I), as:

$$S/N \; = \; F_{HI} \; (Jy \; km/s) \; / \; W_{20} \; (km \; s^{-1}) \; / \; \sigma_f \; (Jy) \qquad (5-1)$$

and tabulate noise per channel σ_f in mJy for nondetections, even though baseline curvature and variability may dominate radiometer noise in preventing detection of weak sources.

We note that Figures 1 and 2 represent 50 and 11 objects, respectively, while Tables I and II list 48 and 13 objects, ditto. N174 (4KVL object 7) and E436-26 (174) were apparently detected but did not yield sufficiently clear signal/baseline separation or S/N in our judgement to warrant linewidth or flux measurement.

III. Flux scale consistency

Calibration galaxies NGC 1073 and DDO 36 used by DSSM to tie their Jodrell and Parkes flux scales together, and flux monitor galaxies UKS 1457-480, NGC 7424 and IC 4824, used by DSSM to monitor flux scale constancy at Parkes, were observed by us in the 1989 run to compare our flux scale to theirs. We observed UGC 1457 five times, IC 4824 three times, NGC 7424 twice and the others once each. The fluxes we obtained, those tabulated for these objects by DSSM, and the ratios of our fluxes to theirs are given in Table III. On average our fluxes exceed theirs by ~ 8 percent. (Recall we had a similar experience at Jodrell Bank, where we consistently measured fluxes for Jodrell monitor objects NGC 1058 and NGC 4214 about 11 percent higher than those published by SSDI.) The five UGC 1457 fluxes averaged 100.01 Jy km sec^{-1} with scatter 3.5 Jy km sec^{-1} ,

or 3.5 percent. The enhanced flux values may come from a change of feeds performed at Parkes between the DSSM and *IRAS* 4KVL runs (Staveley-Smith, pers. comm.).

IV. Repeatability of spectral line parameters

Most of the 1989 run detections enjoyed two independent reductions from raw data on by J.R. in 1990 and 1992 (the latter values are tabulated in Table I). Two independent reductions allow the repeatability of derived parameters (particularly linewidths) to be assessed. Given the steepness of the Tully-Fisher relation, any estimate of linewidth uncertainty that exceeds the formal error bars on linewidth needs to be taken into account when fitting models of the velocity field to TF data.

Absolute value of the difference between 1990 and 1992 values for flux (divided by the average flux value; *i.e.*, fractional variation), velocities and widths provided by 'MAX' are plotted versus S/N ratio in Figure 3 and the analogous plots for 'GAUS' follow in Figure 4. The figures suggest that (a) as expected, fluxes, widths and systemic velocities are all more poorly reproduced as S/N drops, (b) S/N of about 5 is a critical value, as previously suggested (Chapter 4) by our Monte Carlo simulations, and (c) 'GAUS' provides slightly more repeatability than does 'MAX' for widths and systemic velocities. Averaged over all S/N, the sample average and *rms* values for the absolute values of differences between 1992 and 1990 quantities are:

'MAX':

fractional flux $|F_{HI}^{92} - F_{HI}^{90}|/[F_{HI}^{92}+F_{HI}^{90}] = 0.14 \pm 0.12$;

width at 20% level $|W_{20}^{92}$ - $W_{20}^{90}| = 16 \pm 15$ km sec^{-1} ;

width at 50% level $|W_{50}^{92}$ - $W_{50}^{90}| = 21 \pm 27$ km sec^{-1} ;

$V_{\odot}$ at 20% level $|V_{HI}^{92}$ - $V_{HI}^{90}| = 9.9 \pm 12$ km sec^{-1} .

'GAUS':

fractional flux $|F_{HI}^{92} - F_{HI}^{90}|/[F_{HI}^{92}+F_{HI}^{90}] = 0.15 \pm 0.12$;

$$\text{width at 20\% level } |W_{20}^{92} - W_{20}^{90}| = 13 \pm 16 \text{ km sec}^{-1} ;$$

$$\text{width at 50\% level } |W_{50}^{92} - W_{50}^{90}| = 18 \pm 23 \text{ km sec}^{-1} ;$$

$$V_{\odot} \text{ at 20\% level } |V_{HI}^{92} - V_{HI}^{90}| = 4.9 \pm 4.6 \text{ km sec}^{-1} .$$

The S/N ratio for the contributing observations averaged 4.5 $\pm$ 2.0.

Averaging 'MAX' and 'GAUS' results before differencing 1992 and 1990 reductions might have been expected to show a greater stability in linewidth based on the simulations discussed in Chapter 4. Yet we found negligable gain in width reproduceability by averaging 'MAX' and 'GAUS' widths.

Some functional fit to the width differences as functions of S/N described herein can offer a curve providing an empirical estimate of the error bars to be placed upon widths provided by 'SLAP' or comparable routines. We utilize a simple approximation for the uncertainty in W_{20}^{MAX} in our Monte Carlo models for the 4KVL experiment in Chapter 6.

Finally, we plot the difference between 'MAX' and 'GAUS' widths from the latest (1992) reduction in Figure 5. Radiometer noise spikes occasionally arise on the flanks of an HI profile, intercepting a given flux level and biasing 'MAX' towards higher linewidths; noise spikes tend to bias 'GAUS' towards lower linewidths, as noise spikes interior to true local maxima (horns on canonical two horned profiles) are mistaken for same and skew one sided Gaussian fit inwards; this can be seen on the 'SLAP' reduction screen to bias W_{50} notably worse than it does W_{20} and this is reflected in Figure 5.

Table I - HI detections of *IRAS* 4KVL objects at Parkes

obj	name	F_{HI}	W_{50}	W_{25}	W_{20}	V_{20}	S/N
5*	E 79-3	16.0	433	479	486	2621	7.3
25	N 643B	5.0	270	295	296	3893	5.0
44	N 986	15.0	94	178	207	1984	15.7
77	N 1559	50.4	244	277	289	1297	22.7
80	N 1591	6.1	319	345	345	4112	7.1
91	N 1803	7.9	292	322	325	4122	6.5
92	N 1808	70.9	264	346	348	1000	32.0
93	E 553-20	7.9	400	420	421	4045	7.9
112	0709-26	45.0	291	350	362	2594	16.9
115	N 2369	12.4	450	476	477	3268	6.0
116	0720-29	11.3	316	330	333	3026	10.2
118	E 428-28	8.6	407	419	420	2251	8.1
131	E 60-4	5.2	293	298	299	3980	11.9
132	N 2601	3.4	364	407	424	3298	8.0
145	E 126-3	26.2	365	371	372	2925	13.6
151	E 91-6	5.4	208	226	229	1996	5.8
163	E 263-23	35.8	347	448	453	3039	10.4
176	N 3278	6.9	295	330	332	2997	10.0
179*	N 3318	20.2	351	384	389	2782	6.5
181	N 3333	11.5	383	425	471	4132	13.3
182	E 264-29	12.8	352	382	382	3204	8.6
198*	N 3620	8.1	374	407	412	1774	4.4
210	E 266-15	11.5	260	268	269	–	9.2
216	E 320-26	27.7	509	527	528	2835	13.4
262	E 507-37	9.6	193	222	223	3603	9.6
263	E 219-4	16.7	529	572	585	3669	10.9
264	E 323-38	4.2	248	253	254	3339	7.9
280	E 219-41	27.9	447	474	475	3474	17.0
287*	E 269-85	21.0	306	334	339	2865	7.9
293	E 173-15	27.0	296	316	324	2910	16.5
306	E 221-7	24.9	307	315	317	3661	17.2
312	E 174-3	20.9	211	247	255	4018	17.1
315	E 175-5	20.2	207	272	274	3773	9.6
321	1413-55	17.6	388	408	413	3949	15.2
323	I 4402	20.8	335	356	357	1654	17.9
334	I 4472	19.6	370	375	391	2864	10.5
344	N 5786	36.8	298	360	373	2980	13.3
349	N 5833	58.7	409	448	449	3028	33.5
358	N 5938	43.3	342	386	387	3477	21.9
366	E 137-14	12.5	231	250	252	2764	11.1

Table I - HI detections of 4KVL objects at Parkes - cont

obj	name	F_{HI}	W_{50}	W_{25}	W_{20}	V_{20}	S/N
379*	E 140-12	23.7	243	276	297	3160	9.7
387	N 6754	14.0	312	370	371	3246	12.7
397	2020-44	3.7	182	192	194	2916	9.2
404	I 5084	10.5	374	385	389	3135	10.1
407	E 402-6	13.2	182	209	211	2570	16.8
409*	E 48-2	18.2	407	434	438	3929	9.8
414	E 404-36	6.4	359	371	379	3095	5.3
422	E 534-9	10.4	386	414	415	3382	12.4

Fluxes in Jy km s^{-1}; velocities and 'MAX' widths in km s^{-1} via $v/c = \delta\lambda/\lambda_0$
$S/N = F_{HI}/W_{20}/\sigma$, where σ is *rms* baseline noise after Hanning smoothing
Asterisk (*) denotes 1990 L.S.S./J.R.M. observation

Table II - *IRAS* 4KVL HI nondetections at Parkes, 1989/90

obj	name	V	σ
7	N 174	3471	11.0
27	E 353-36	3626	8.2
172	E 317-23	2804	7.1
174*	E 436-26	4272	7.4
177	N 3281	3395	12.6
178	I 2596	3390	19.1
229	E 379-30	3915	8.8
270	E 269-38	3262	8.5
275	E 323-90	2950	18.9
289	E 270-7	3750	13.7
298	E 383-9	2326	17.8
391	N 6808	3468	10.9
392	N 6810	1975	8.3

σ is *rms* baseline noise, mJy, after Hanning smoothing
V is heliocentric recession velocity in km s^{-1} from Strauss *et al.*
Asterisk (*) denotes 1990 L.S.S./J.R.M. observation

Table III - 1989 observations of DSSM calibrator / monitor galaxies

name	obs	our flux Jy km s^{-1}	DSSM flux Jy km s^{-1}	ratio
UKS 1457	1	97.84	91.4	1.07
	2	103.69		1.13
	3	101.35		1.11
	4	101.82		1.11
	5	98.37		1.08
I 4824	1	18.55	19.0	0.98
	2	20.92		1.10
	3	21.3		1.12
N 7424	1	221.24	207.8	1.06
	2	222.4		1.07
DDO 36	1	21.05	18.3	1.15
N 1073	1	65.57	70.5	0.93

Figure Captions - Chapter 5

Figure 1 (9 pages): HI line spectra of objects detected at Parkes, summed, flux corrected, baseline subtracted and Hanning smoothed. Velocities derive from reception wavelength via 'optical convention' $v/c = \delta\lambda/\lambda_0$. NGC 174 and ESO 436-26 were apparently detected but fluxes and linewidths were not assessed. Spectra with smoother or low resolution appearance derive from 1990 L.S.S./J.R.M. run and summation.

Figure 2 (2 pages): Spectra of objects not detected at Parkes, summed, flux corrected and Hanning smoothed. Velocities derive from reception wavelength via 'optical convention' as in Figure 1.

Figure 3: Absolute value of difference between quantity Y assessed in 1992 and quantity Y assessed in 1990 (from same raw data), versus signal to noise ratio: (a) Y = fractional difference in integrated HI line flux; (b) Y = linewidth at 50 percent of peak power level; (c) Y = linewidth at 20 percent of peak power level; (d) Y = systemic velocity at 20 percent of peak power level, where quantities Y were assessed using 'MAX' method of 'SLAP'.

Figure 4: Panels analogous to those in Figure 3, but quantities Y provided by 'GAUS' method of 'SLAP'.

Figure 5: (a) Linewidth at 50 percent level, assessed by 'MAX', minus that assessed by 'GAUS'. (b) Analogue with 20 percent linewidths.

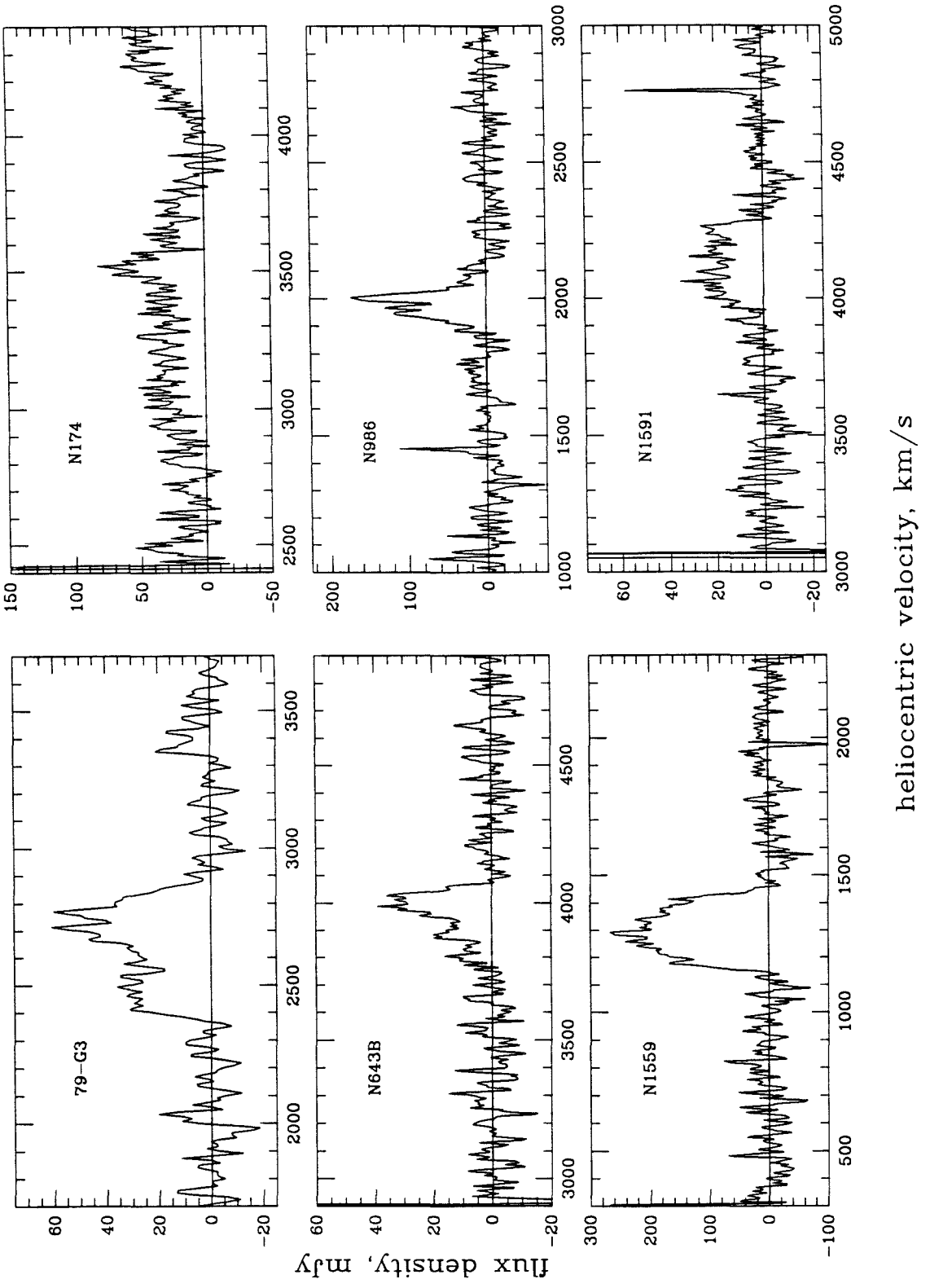
79-G3
N643B
N1559
N174
N986
N1591
flux density, mJy
heliocentric velocity, km/s

Figure 1(1)

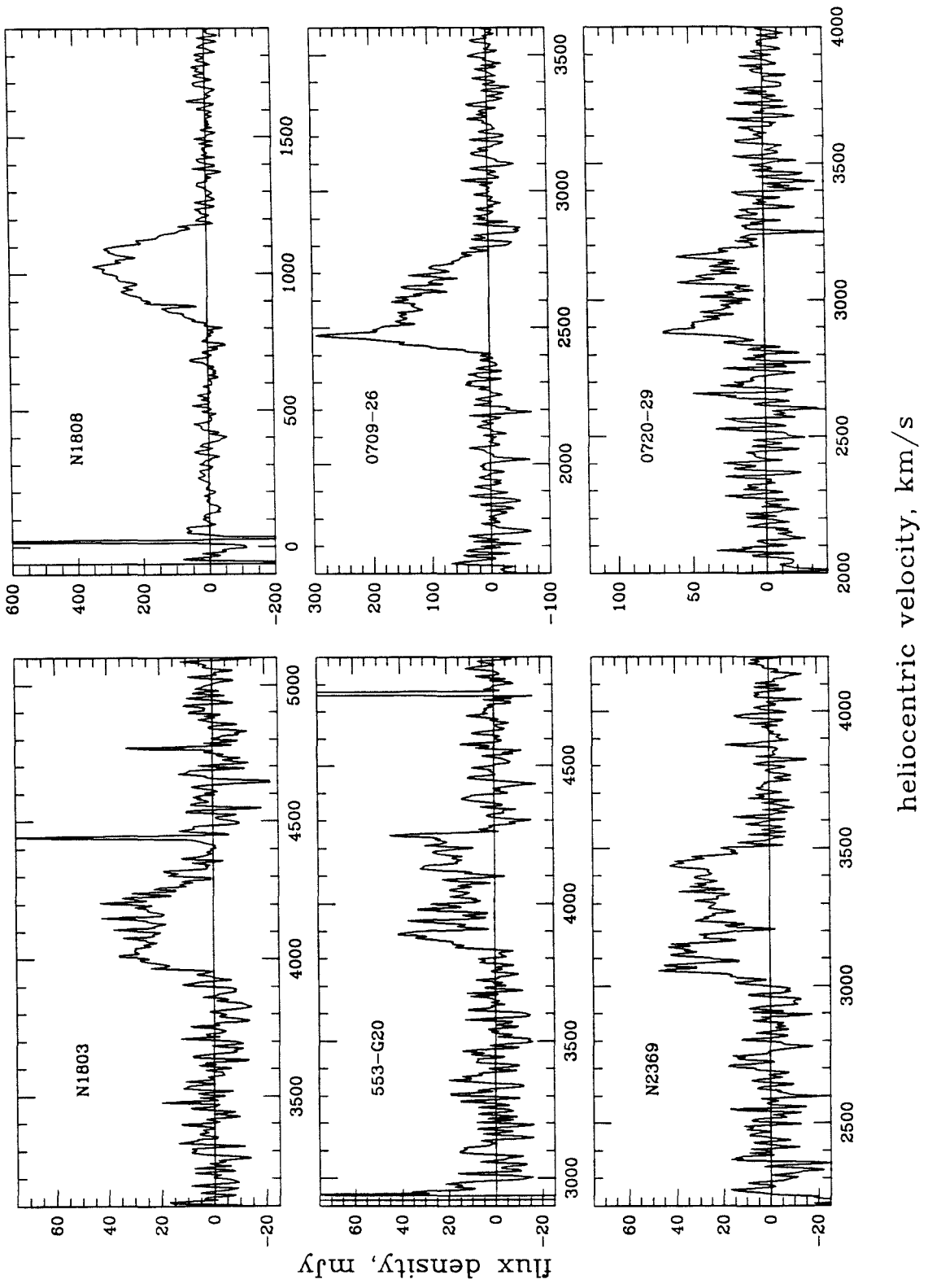
N1808
0709-26
0720-29
N1803
553-G20
N2369
flux density, mJy
heliocentric velocity, km/s

Figure 1(2)

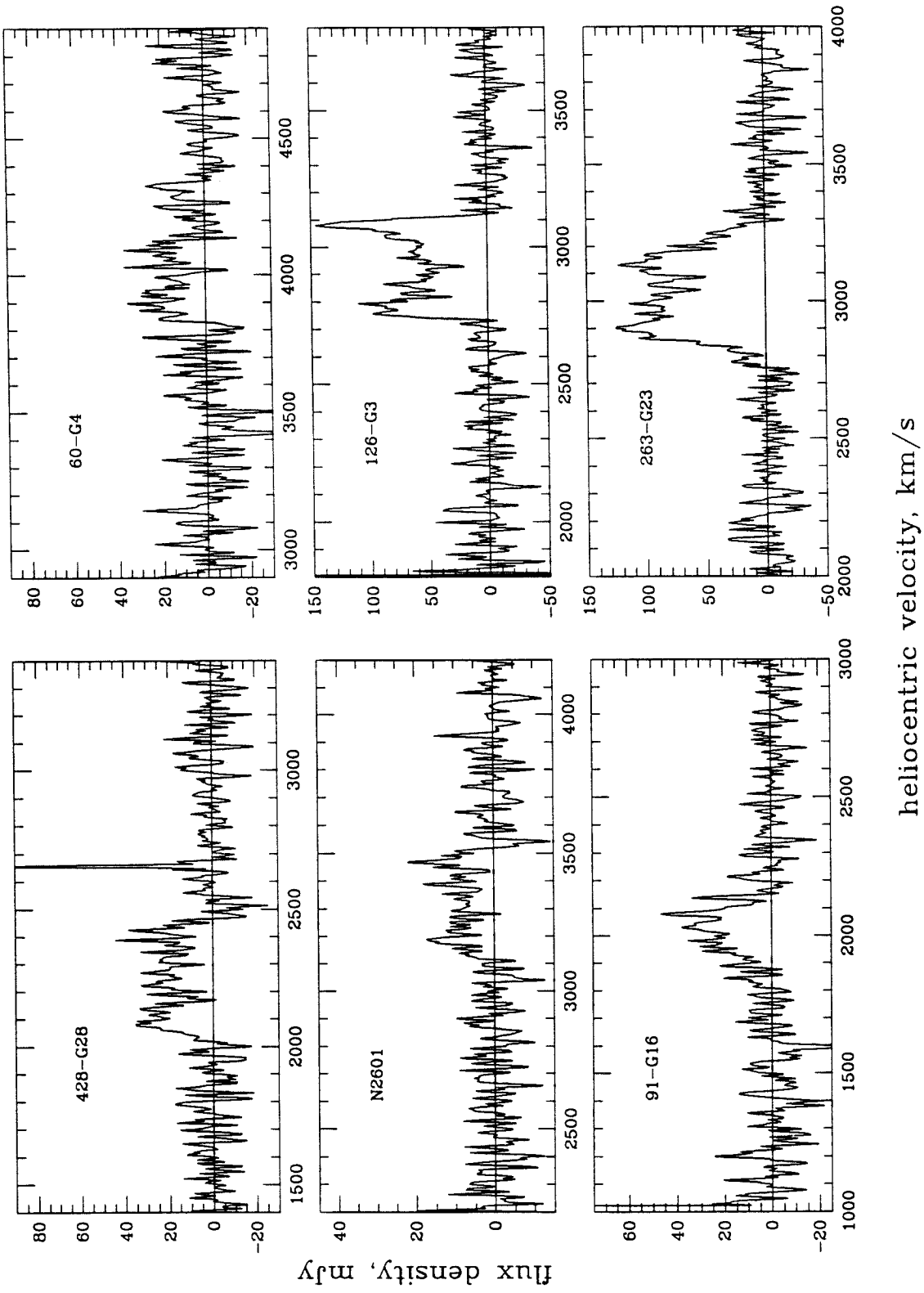
428-G28
N2601
91-G16
60-G4
126-G3
263-G23
flux density, mJy
heliocentric velocity, km/s

Figure 1(3)

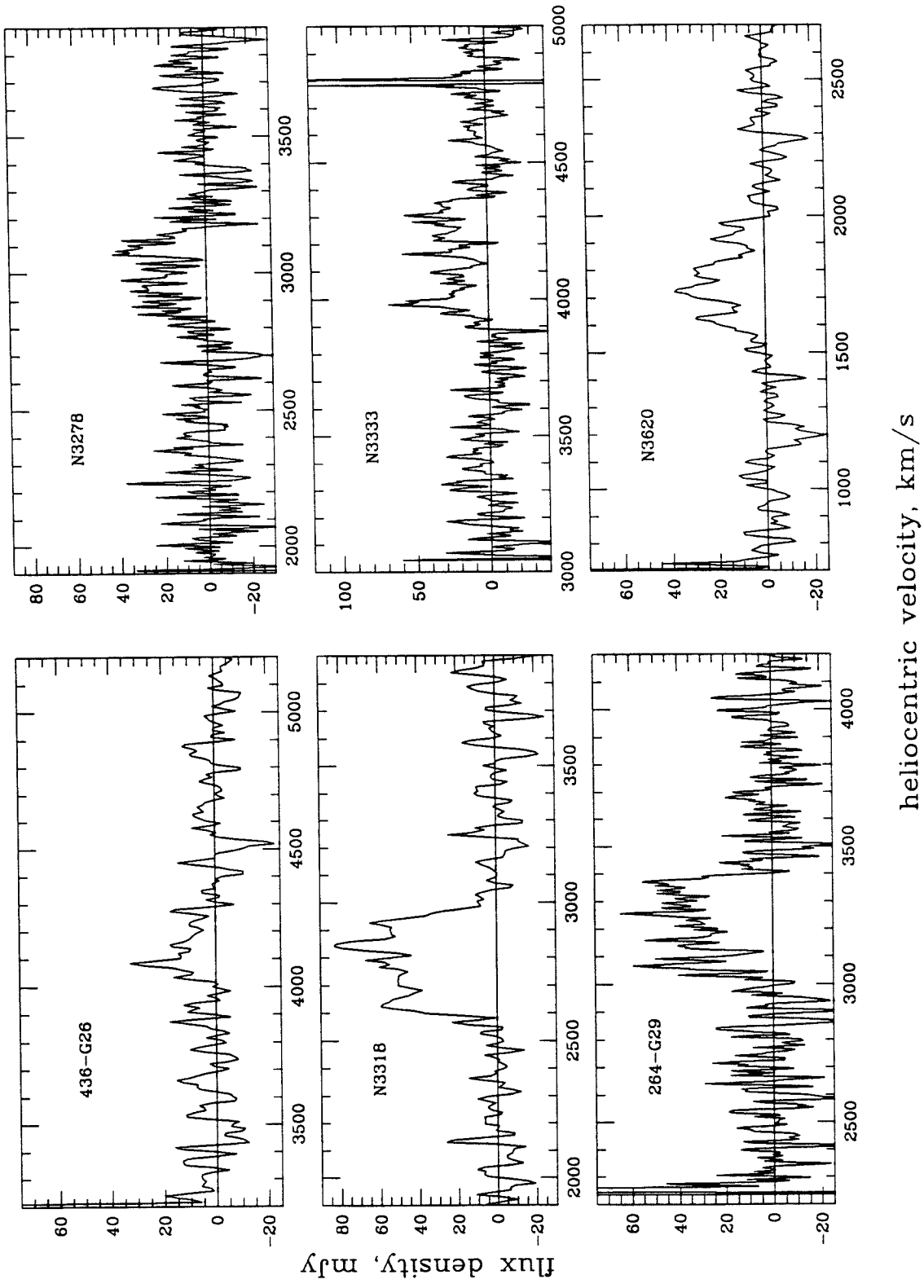
N3278
N3333
N3620
436-G26
N3318
264-G29
flux density, mJy
heliocentric velocity, km/s

Figure 1(4)

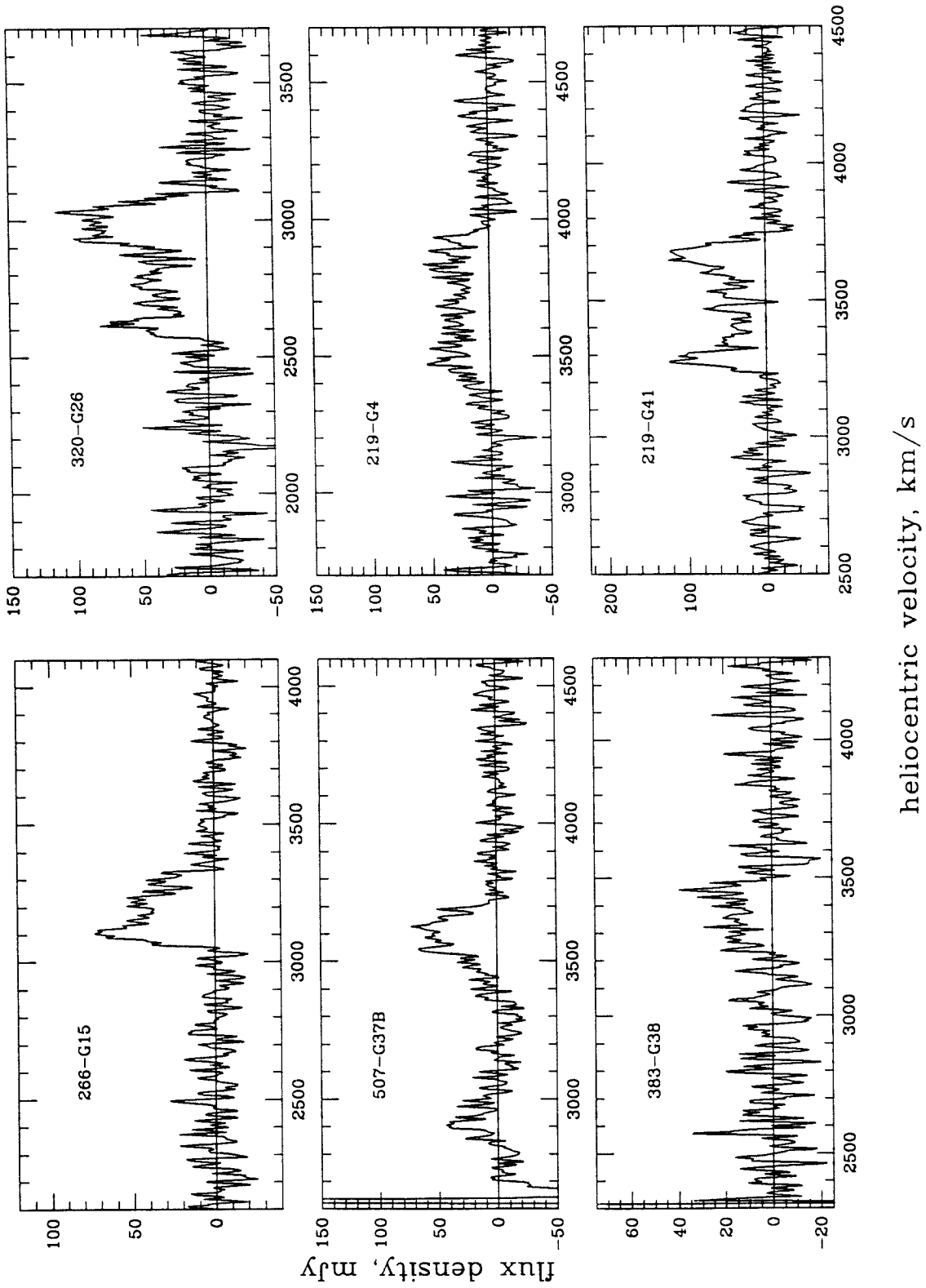
320-G26
219-G4
219-G41
266-G15
507-G37B
383-G38
flux density, mJy
heliocentric velocity, km/s

Figure 1(5)

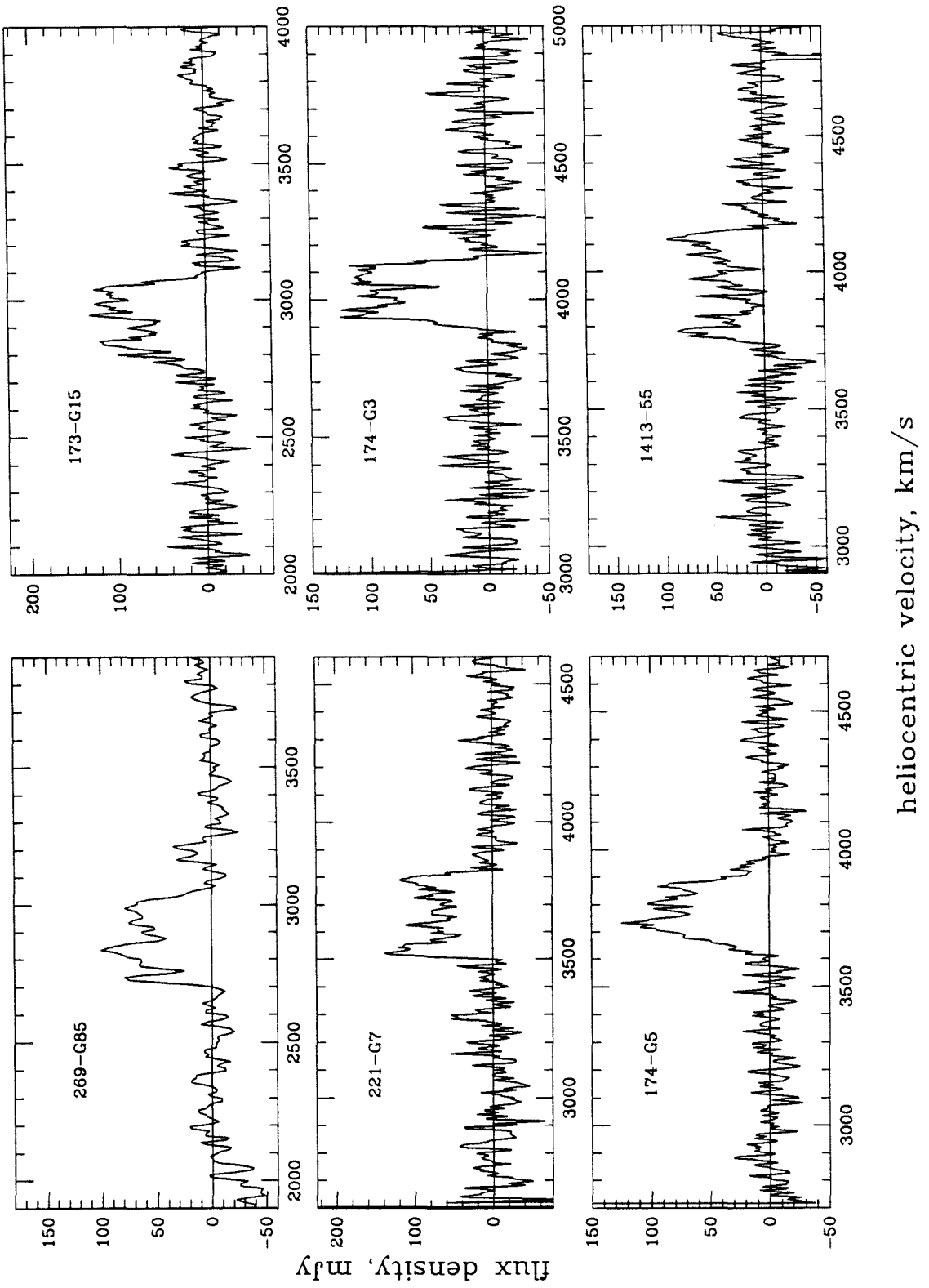
269-G85
221-G7
174-G5
173-G15
174-G3
1413-55
flux density, mJy
heliocentric velocity, km/s

Figure 1(6)

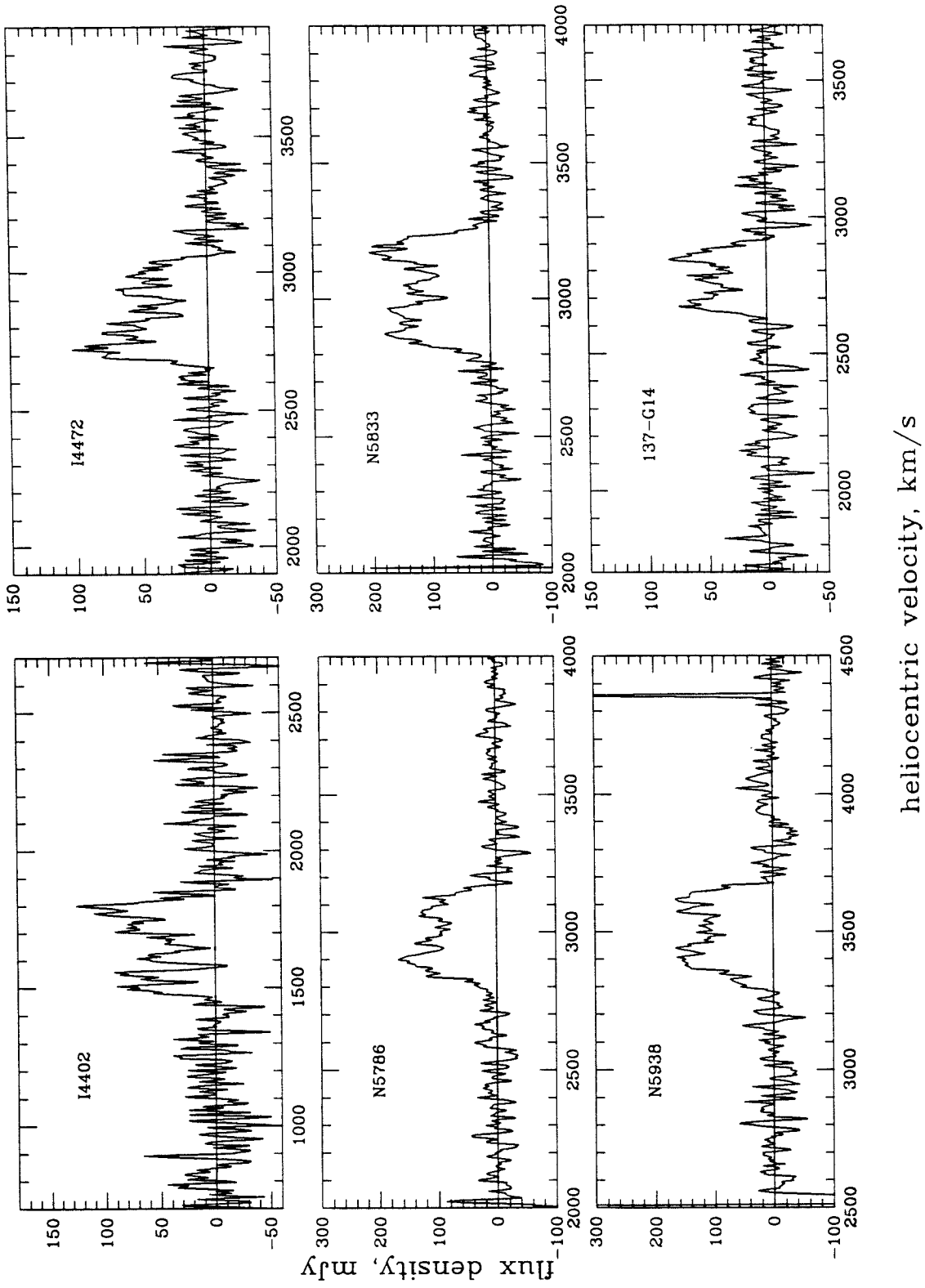
I4402
N5786
N5938
I4472
N5833
137-G14
flux density, mJy
heliocentric velocity, km/s

Figure 1(7)

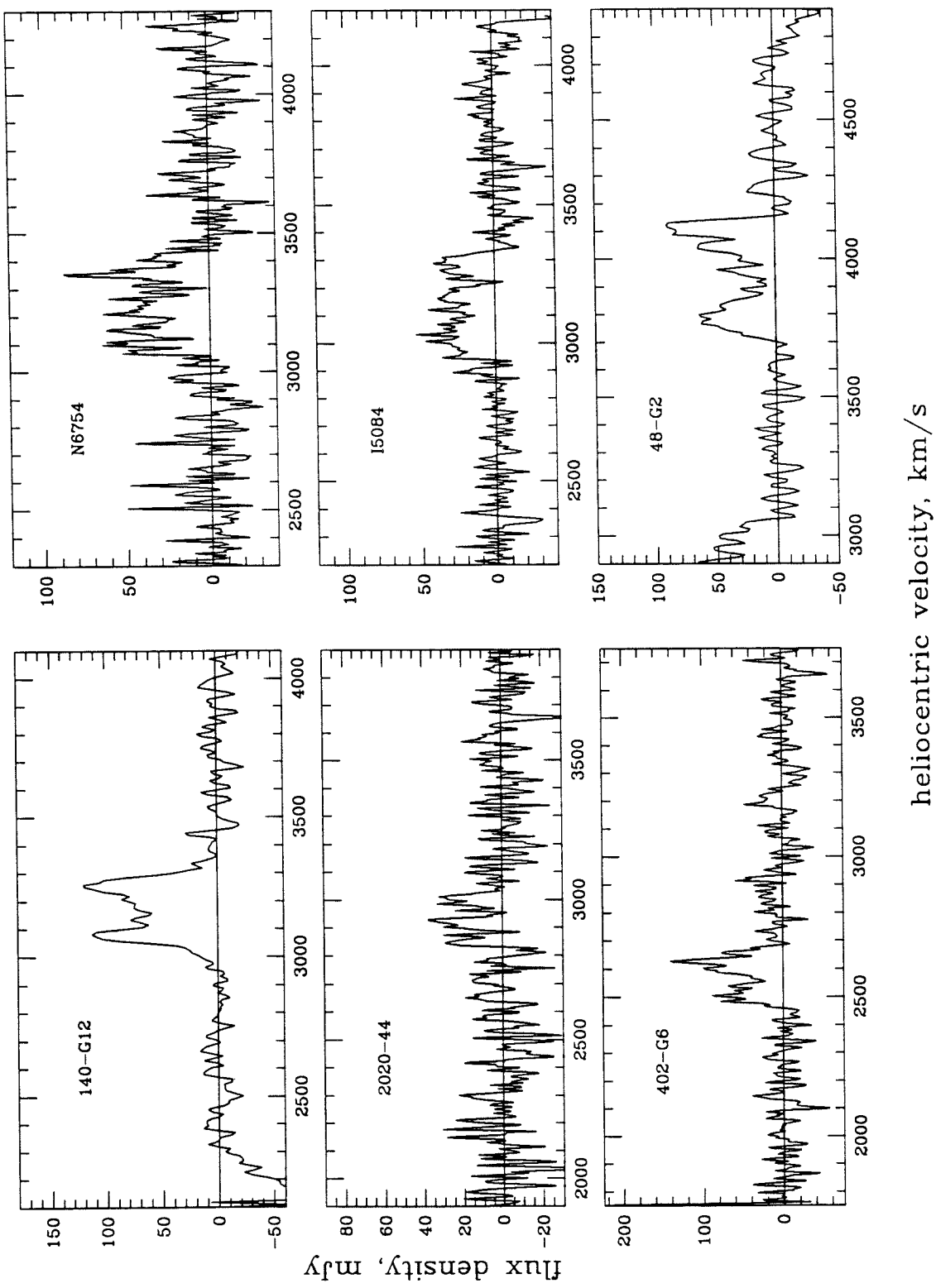
N6754
I5084
48-G2
140-G12
2020-44
402-G6
flux density, mJy
heliocentric velocity, km/s

Figure 1(8)

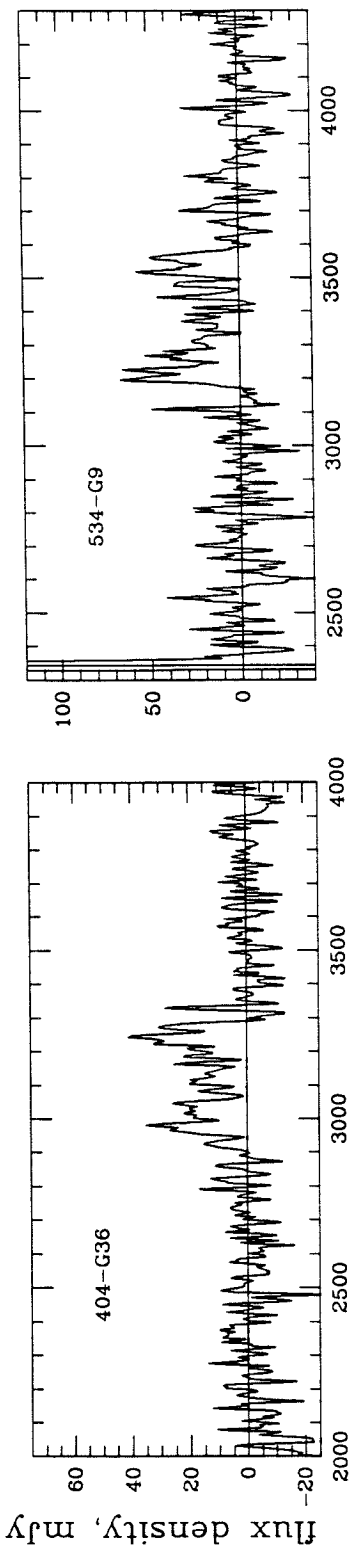

Figure 1(9)

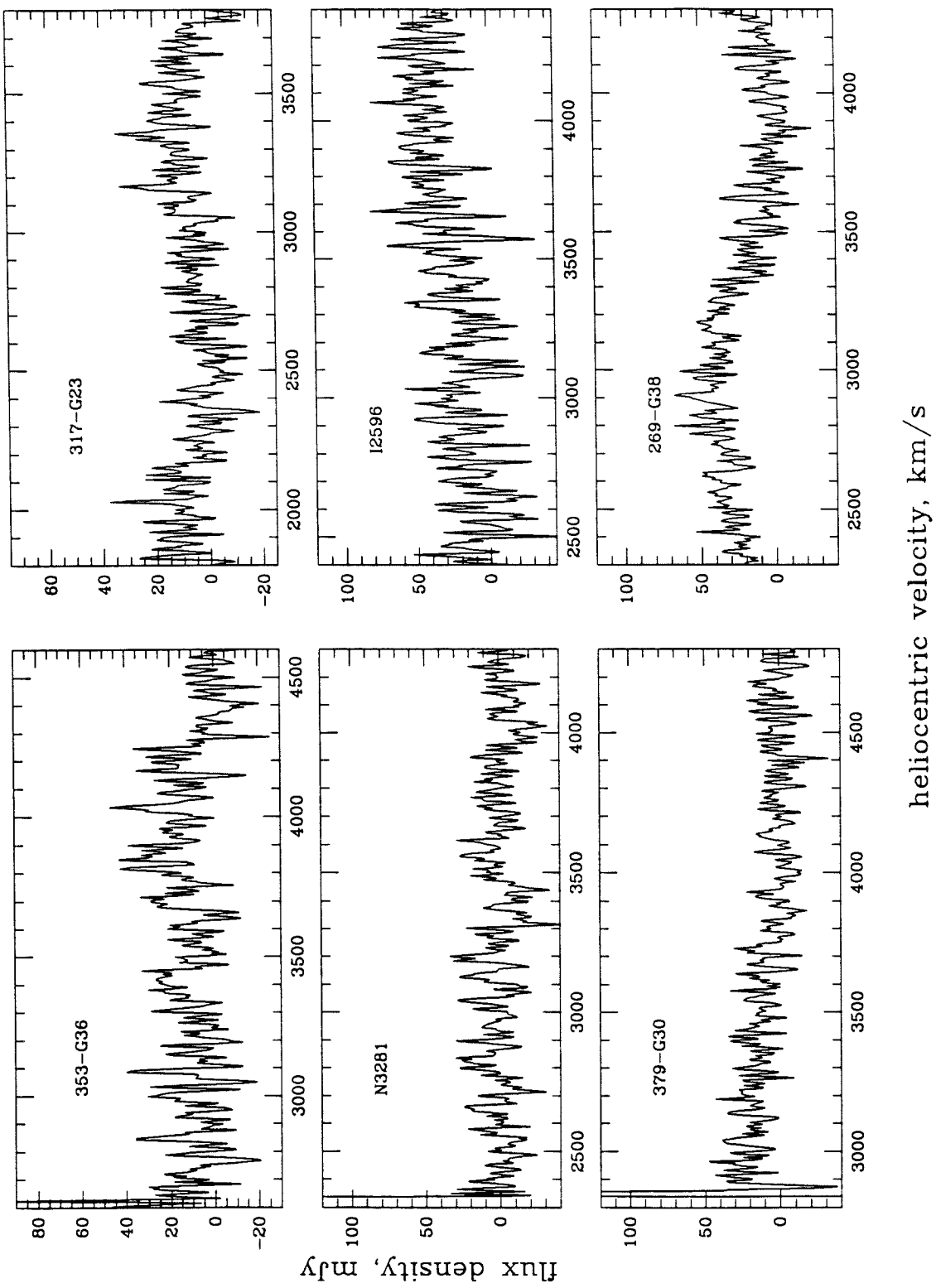
353-G36
N3281
379-G30
317-G23
I2596
269-G38
flux density, mJy
heliocentric velocity, km/s

Figure 2(1)

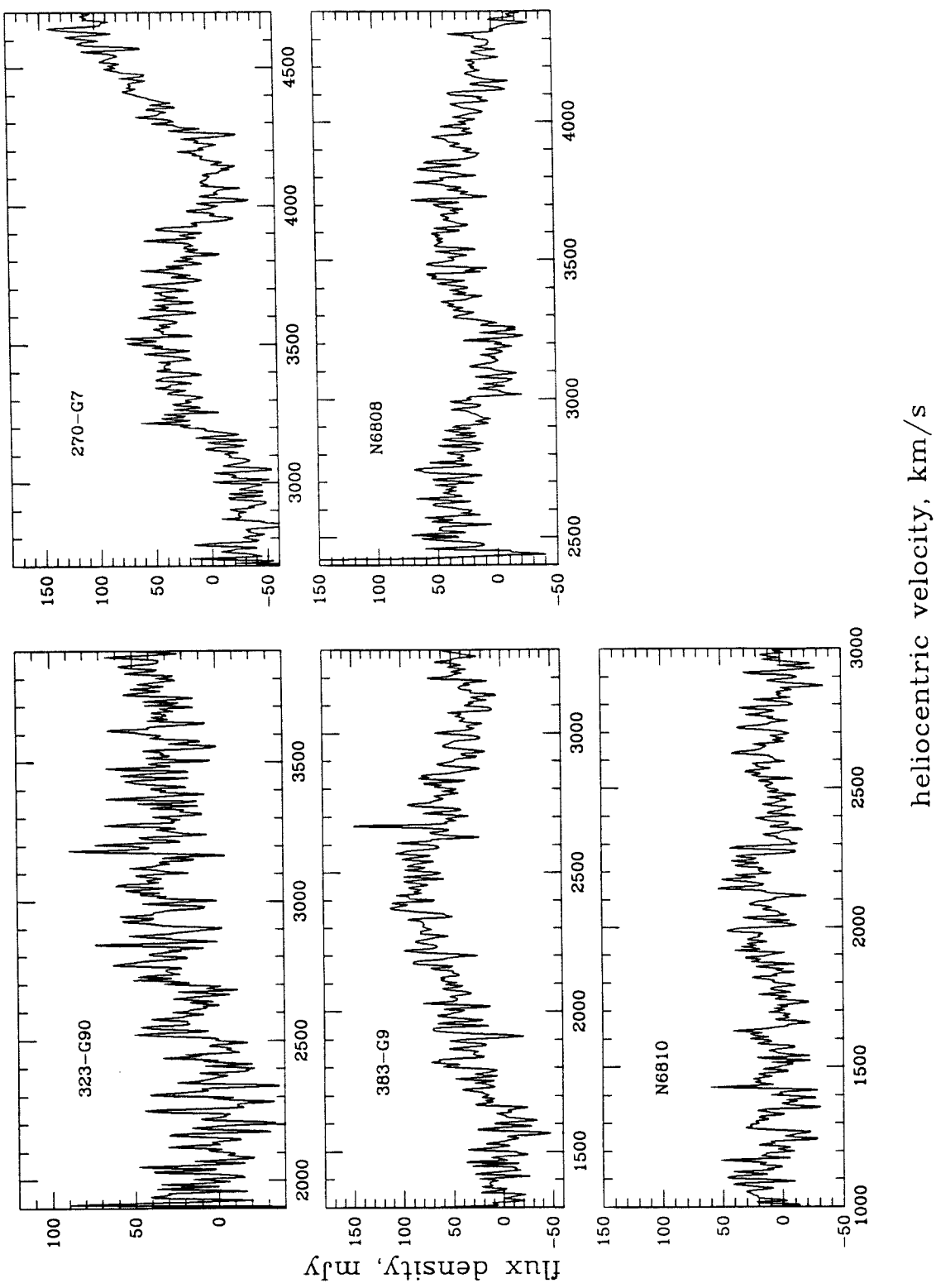
270-G7
N6808
323-G90
383-G9
N6810
flux density, mJy
heliocentric velocity, km/s

Figure 2(2)

MAX, 1992-1990

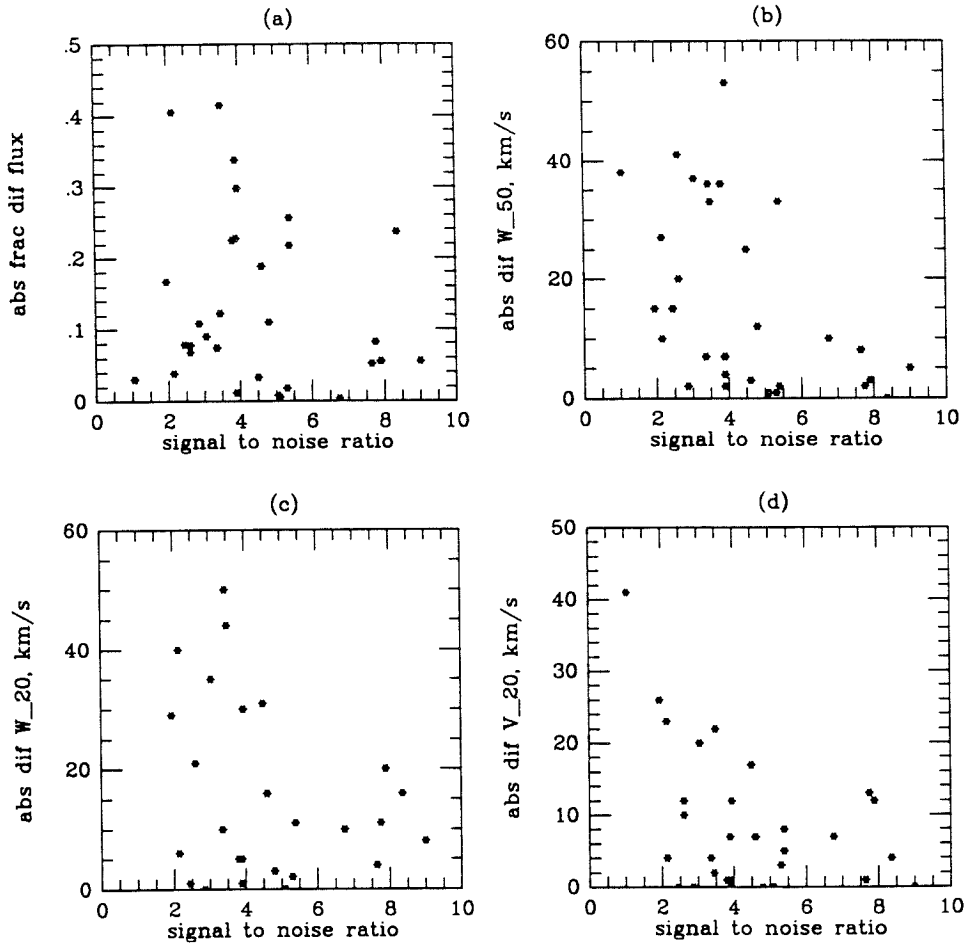

Figure 3

GAUS, 1992–1990

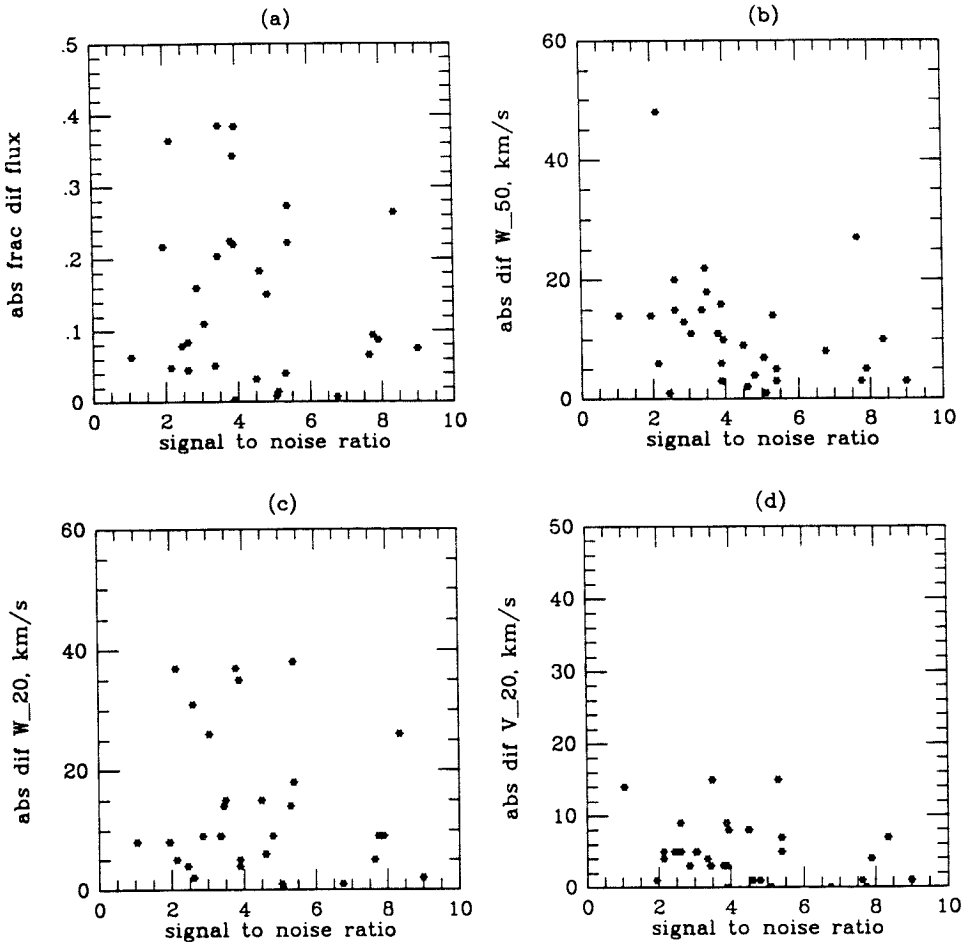

Figure 4

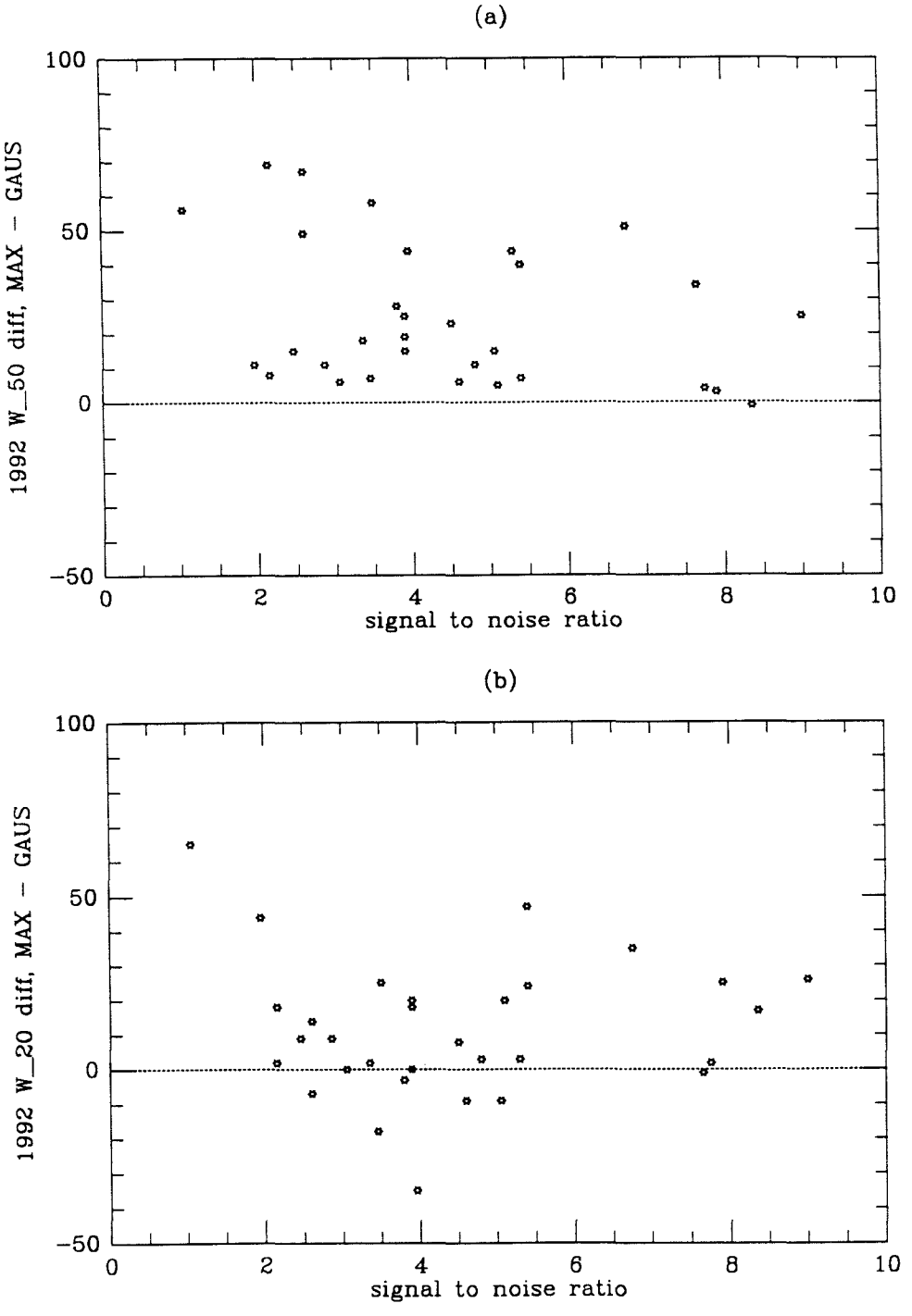
(a)
100
50
0
−50
0
2
4
6
8
10
1992 W_50 diff, MAX − GAUS
signal to noise ratio
(b)
100
50
0
−50
0
2
4
6
8
10
1992 W_20 diff, MAX − GAUS
signal to noise ratio

Figure 5

Chapter 6 - Monte Carlo Models of the *IRAS* 4KVL Tully-Fisher Experiment

Section I: Introduction

As motivated in Chapter 1, we have obtained the photometry and HI spectroscopy described in the preceeding chapters with the hope of constraining the cosmic density parameter Ω. Our experiment is motivated by Strauss *et al.* 's iterative calculations of their 2 Jy galaxy distances, in which one free parameter ($\beta = \Omega^{0.6}/b_{IRAS}$; recall Eqn. 1-18) determines the distance to an object at position (α, δ) and recession velocity (hereafter called 'redshift') cz.

Here we pose the question: once we accept the paradigm that the *IRAS* galaxies' density contrast field reflects that of the underlying matter distribution and assume further that infrared luminous spiral galaxies obey a linear relation between the logarithm of the deprojected HI linewidth W_0 and the absolute I band magnitude M_I (with some Gaussian spread in M_I at given $logW_0$), how will data sets of [apparent magnitude, galaxy inclination angle, deprojected HI linewidth, right ascension, declination, redshift] appear to an observer with finite detection sensitivities and measurement errors in the near infrared and 21 centimeter bands? And how can those data sets be best compared against the model predictions to constrain β?

To address this question we have built Monte Carlo models that place our sample galaxies at the distances predicted by Struass *et al.*, assign to them a location in [$L_{60\mu}$, L_I, M_{HI}, $logW_0$, inclination angle i_{disk}] space constrained by realistic detection thresholds, and perturb their apparent I band magnitudes m_I and observed HI linewidths $W_{obs} = W_0\ sin(i_{disk})$ by realistic measurement errors. The resultant synthetic data sets are then analyzed in the same way we plan to treat the one actual dataset we have in hand. This produces likelihood functions for parameters derived from these datasets. (In practice, the derived quantity of interest will be the β_{var} value that minimizes the sample's inferred Tully-Fisher (TF) scatter.) Applying Bayes' Theorem then allows us to estimate

the relative likelihood that various values of β_{true} would have produced datasets whose inferred TF scatter was minimized by turning the β_{var} knob to a given value.

Section II: Properties of *IRAS* Model Predictions

Michael Strauss has kindly provided us predicted (relative) distances for each of our 4KVL objects at evenly spaced β values from .05 to 2 ($\Delta\beta = .05$). The distances provided us by Strauss were assessed by including the redshifts of galaxies in the 1.2 Jy $< F_{60\mu} <$ 2 Jy range; thus we must thank Karl Fisher for his permission to utilize these predictions, as these latter redshifts come from his thesis (Fisher 1992). These distances were assessed by methods described in ST and Yahil *et al.* (1991). Essentially, these authors:

(1) draw a sphere around *IRAS* galaxy j;

(2) assess the net gravitational acceleration imparted on galaxy j by all others in the sphere; the others are weighted to compensate for the portion of the 60μ luminosity function not visible at their distances;

(3) scale this acceleration by the assumed β value; an analog of Eqn. 1-17 then predicts the object's peculiar velocity $V^{\beta}_{pec_j}$;

(4) subtract the predicted $V^{\beta}_{pec_j}$ from galaxy j's redshift to revise its distance (in km sec^{-1});

(5) repeat (1) – (4) for each galaxy j;

(6) this has changed galaxy distances; repeat (1)-(5) until convergence.

In principle redshift may not be a single valued function of distance along a given line of sight. Strauss *et al.* estimate the distance of a galaxy as the average of D_1 and D_2, where

D_1 = closest distance predicting a redshift equalling $cz_j - 200$ km sec^{-1} , and

D_2 = furthest distance predicting a redshift equalling $cz_j + 200$ km sec^{-1} .

This method was tested against N-body models in Davis, Strauss and Yahil (1991) and found to recover galaxy distances for a wide range of realistic models. The method robustly handles triple valued zones, wherein three distances centered on a zone of strong infall all yield the same redshift.

The motion of the Local Group with respect to the sample is also predicted, as is an apparent microwave background radiation (MBR) dipole amplitude and direction.

Strauss *et al.* provided us with two sets of models: those for which the sphere radius in step (1) above was 10,000 km sec^{-1} , and those for which the radius in step (1) above was 20,000 km sec^{-1} ; these are referred to as SMALLR and STANDARD, respectively. The numerical index associated with each model, X, equals 20 times β; thus the files run from SMALLR.02 to SMALLR.40, and from STANDARD.02 to STANDARD.40, respectively. At the risk of confusion, we will label models by $X \equiv 20 \times \beta$ in what follows.

At a given X, SMALLR and STANDARD differ negligably in their predictions of the relative distances of the 4KVL sample objects; this presumably is due to our sample's 4000 km sec^{-1} edge resting well inside the region at which shot noise and other edge effects become important. They differ substantially in their predictions of the MBR dipole amplitude at a given X, however, suggesting that, if *IRAS* galaxies trace mass, a portion of the dipole is generated by rather distant objects.

Figure 1*a* plots the distances for the (entire 440 object) 4KVL sample predicted by SMALLR at $\beta = .25$ ($X = 5$) versus those predicted by STANDARD. Figure 1*b* offers the analogous plot for $\beta = 1.75$ ($X = 35$). As one might expect, at large X the two differ by larger amounts. A modest bias towards larger distances by STANDARD is also apparent.

Figure 1*c* plots SMALLR $X = 5$ distances for the 4KVL objects versus those for SMALLR $X = 35$, and 1*d* offers the same plot for STANDARD, simply to illustrate the larger range of distances at a given redshift produced by a larger value of β.

The MBR dipole amplitude that the *IRAS* models predict would be seen from the Local Group barycenter is listed for each X value in Tables I and II for SMALLR and STANDARD solutions, respectively. Note the relative stability of the direction despite enormous changes in amplitude. While SMALLR models predict an amplitude close to that observed with $X = 14 - 15$ ($\Omega \sim 0.6$ given $b_{IRAS} \equiv 1$), STANDARD models do so with $X \sim 8$ ($\Omega \sim .2$). The tables also give the additional motion the LG group must have for the observed MBR dipole of 614 km sec^{-1} towards $(l^{II}, b^{II}) = (269, +28$; Lubin *et al.* 1985) to be observed. This motion may either be a local effect (the Local Group deviating from its *IRAS*-predicted motion with respect to the *IRAS* sample) or a distant one (bulk motion of everything within $\sim$ 4000 km sec^{-1} with respect to the MBR). Implicit is the assumption that the MBR dipole is indeed due to the net motion of the Local Group with respect to the comoving frame, and not to intrinsic anisotropy.

The vast differences between SMALLR and STANDARD predictions for the MWB dipole suggest that, while the *IRAS* models may reproduceably predict the relative distances to the 4KVL galaxies, they poorly predict the LG motion with respect to that sample. Few body effects, perhaps highly nonlinear, may also effect the Local Group's net motion in ways not reflected in the sparse *IRAS* surveys. Deviation of actual LG motion with respect to the 4KVL sample from its predicted value will be discussed briefly as a 'nuisance parameter' in what follows.

Somewhat arbitrarily we restrict ourselves to SMALLR models in the rest of this work; this is perhaps justified by a better prediction of the MBR dipole amplitude at the β values near unity seemingly favored by data (*e.g.*, Dekel *et al.* 1993) and prejudice (*i.e.*, 'inflationary' cosmology; *cf.* Kolb and Turner 1990), and by presumably greater freedom from shot-noise effects at the sparsely populated edge of the 1.2 Jy sample.

Given a fixed 'true' X value, the distances of 4KVL object j at other X values may be expressed in magnitudes, where 'magnitude' comes from the ratio as

$$m(j; X_{var}|X_{true}) = 5\ log[d(j; X_{var})/d(j; X_{true})]. \qquad (6-1)$$

(Note that '*log*' denotes log_{10} here and in what follows.)

This quantity, averaged over all objects in the sample, reflects the average magnitude difference between various models that would be measured if a perfect 'standard candle' were available. Figures 2 offer the *rms* of this quantity for X_{true} values of 10, 20 and 30, respectively, with the models sampled by various subsamples of the *IRAS* 4KVL parent sample:

OKOBJ = 251 objects okay *a priori* for TF work,

JAN93 = 91 objects with reduced and standardized data as of 1/1/93,

OKNORTH = 105 OKOBJ objects with northern declinations,

OKSOUTH = 146 OKOBJ objects with southern declinations,

JAN93/N = 47 JAN93 objects at northern declinations, and

JAN93/S = 44 JAN93 objects at southern declinations.

One can imagine that, given perfect measurements of a perfect 'standard candle', the inferred dispersion in the candles' absolute magnitudes has been plotted as a function of X_{var}; thus X_{var} is a parameter 'knob' that may be turned until the apparent dispersion of candle magnitudes is minimized. We will in fact perform this experiment on Monte Carlo ensembles of synthetic datasets in the following sections, and characterize the distribution of knob settings that minimize the apparent TF scatter.

Observational errors, the intrinsic dispersion of the distance indicator used, and additional components of the flowfield not predicted by *IRAS* (if any), when expressed in magnitudes, all add in quadrature to fill up the rather sharp troughs seen in Figures 2. The motivation for a precise distance indicator ($\sigma_{mag} \lesssim 0.1$ mag, *e.g.*, Tonry 1991) is readily apparent.

Figures 2 also show that the detailed profile of *rms* magnitude difference between models depends to an extent upon just which galaxies are used to sample the flowfield. In particular, we note the emergence of a sharp downward kink at $X_{var} \sim 15$ in the response profile for $X_{true} = 20$ when the northern celestial hemisphere alone is considered. This appears to take place when the

gravitational action of the Virgo cluster becomes strong enough to pull a large number of objects into its triple valued zone, at which point a large number of objects is assigned similar distances near the cluster center.

Section III: Monte Carlo Generation of Synthetic Datasets

In order to create synthetic datasets analogous to the one we in fact possess, we posit that:

i - galaxies lie in some well-behaved locus in the space spanned by 60 micron luminosity, neutral hydrogen mass, disk rotation speed (reflected by HI spectral line width), and absolute I band magnitude;

ii - that galaxies lie at the distances predicted by one of the SMALLR models;

iii - that detection thresholds and observational errors are known,

and we use sequences of random numbers to select points from the probability density functions implicit in these postulates. Synthetic datasets (that is, values of α_j, δ_j, 60μ flux $F_{60\mu_j}$, apparent I band magnitude m_{I_j}, redshift cz_j, HI flux F_{HI_j}, HI linewidth $logW_{0_j}$, inclination angle i_{disk_j} for each galaxy j in a specified list) are created thereby and subject to the same analysis we will use on the unique dataset we actually possess.

Our models are constrained in that we insist that galaxies in a given list (*e.g.*, JAN93; OKOBJ) are retained in the sample.

The steps in our simulations are to:

1 - Posit that galaxies lie at distances predicted by one SMALLR model.

2 - Select the 4KVL subsample to be used (eg., JAN93; OKOBJ). Sky positions and redshifts in the Local Group 'rest frame' (cz_{LG}) are taken from our catalog. 'True' distances d_{T_j} come from SMALLR.X.

3 - Create data points [$F_{60\mu_j}$, m_{I_j}, W_{HI_j}, i_{disk_j}, F_{HI_j}] as detailed below, for each object j in the chosen subsample.

4 - Assess some statistic from the synthetic dataset created thereby, using the SMALLR models to convert apparent to absolute magnitudes as we do with the actual data.

5 - Repeat steps 3 and 4 N_{loop} times to get ensemble averages and standard deviations for the statistic of interest.

6 - Plot the statistic's average and *rms* versus actual value of the X parameter X_{true}.

7 - Assuming the statistic to be distributed in Gaussian form at given X_{true}, apply Bayes' Theorem and assess moments of posterior probability density to estimate the relative likelihood of various X_{true} given a measured value for the statistic.

The Monte Carlo method of step 3 entails in turn the following steps, whose elaboration is the purpose of this section.

1 - Assignment of Distances

Distances are assigned by files SMALLR.X for a given X_{true} value in the range $2 - 38$ (corresponding to an Ω range $.02 - 2.9$ if $b_{IRAS} \equiv 1$). Distances are expressed in units of km sec^{-1} ; the Hubble constant does not enter the analysis. 'Distance' in this context is thus shorthand for 'recession velocity of galaxy j from the Local Group expected if matter were evenly distributed'.

2 - Assignment of 60 Micron Luminosity

Yahil *et al.* (1991) determined the 60 micron luminosity function from the 1.9 Jy redshift survey. Its integral form is

$$\Psi(L) \propto (L/L_*)^{-\alpha} (1 + L/L_*)^{-\beta}, \qquad (6-2)$$

where $\alpha = 0.527$ (and is unrelated to right ascension), $\beta = 1.78$ (and is unrelated to the $\beta = \Omega^{0.6}/b_{IRAS}$ we discuss elsewhere), and $L_* = 6.2x10^9 h^{-2} L_\odot$ (H_0 being $100h$ km sec^{-1} Mpc^{-1}). $\Psi(L)$ gives the integral probability of $L_{60\mu}$ lying above value L; thus if some lower limit L_{min} is set, a normalization constant K must yield

$$\Psi(L_{min}) = K \times (L_{min}/L_*)^{-\alpha} \; (1 + L_{min}/L_*)^{-\beta} = 1. \qquad (6-3)$$

At distance d_T (in km sec^{-1}), an object with apparent 60 micron flux $F_{60\mu}$ in Janskys has 60 micron luminosity

$$L_{60\mu} = 2.5 \times 10^{-8} \; d_T^2 \; F_{60\mu} \; L_* \qquad (6-4)$$

(Strauss, personal communication).

For a given L_{min}, $L_{60\mu}$ is obtained from a 'random' variable uniformly distributed in the interval [0,1] (hereafter $R_k(0,1)$) by iterative solution of the equation

$$\Psi(L_{60\mu}) = R_1(0,1) \qquad (6-5)$$

for $L_{60\mu}$. R's subscript is intended to emphasize that successive invocations of R are independently generated, uncorrelated 'random' numbers.

We recall that the 4KVL sample is the union of two distinct sets:

a - objects satisfying $F_{60\mu} > 1.936$ Jy $\times(4000/cz_{LG})^2$,

and

b - objects satisfying $F_{60_\mu} > 1.936$ Jy $\times(4000/cz_{MB})^2$,

where cz_{LG}, cz_{MB} are object redshifts in the Local Group and MBR frames, respectively. Thus each galaxy was drawn from $\Psi(L)$ above an L_{min} given by

$$L_{min} = max[L_1, min(L_2, L_3)], \qquad (6-6)$$

where

$$L_1 = 1.936 \times 2.5 \times 10^{-8}\ d_T^2\ L_*, \qquad (6-7)$$

$$L_2 = 1.936 \times 2.5 \times 10^{-8}\ cz_{LG}^2\ L_*, \qquad (6-8)$$

and

$$L_3 = 1.936 \times 2.5 \times 10^{-8}\ cz_{MB}^2\ L_*, \qquad (6-9)$$

L_1 reflects the actual flux limit, while L_2, L_3 reflect the method we used to define our quasi volume limited sample. Note that in both this numerical experiment and in the one actually performed, this is the only role served by our knowledge of the actual microwave dipole (although it may prove to be a source of subtle bias, which we will investigate in future simulations).

3 - Assignment of HI Linewidth

We posit that a '60 micron Tully-Fisher relation' exists of form:

$$log(L_{60}/L_*) = a_1 + b_1\ logW_0 + \sigma_1 \times G_1(0,1), \qquad (6-10)$$

where W_0 is the deprojected HI linewidth in km sec^{-1} and $G_1(0,1)$ is a Gaussian 'random' deviate with zero mean and unit variance provided by Numerical Recipes' routine GASDEV (Press *et al.* 1986). G's subscript is used in this section to emphasize that successive invocations of GASDEV are uncorrelated. We may approximately state that, given L_{60}, $logW_0$ may be generated by

$$logW_0 = b_1^{-1}\ log(L_{60}/L_*) - b_1^{-1}\ a_1 - b_1^{-1}\ \sigma_1 \times G_1(0,1). \qquad (6-11)$$

We found in preliminary inspection of our data that $b_1 \sim 3.4$ and $b_1^{-1}\ \sigma_1 \sim .10$. The intercept a_1 was varied from -8.27 to -9.25 in our simulations; we find that values of $a_1 = -9.0$, in concert with the HI flux density limits imposed by various radiotelescopes, generate $< logW_0 > - cz$ trends in qualitative accord with that seen in our sample. The final inferred error bars on β are only weakly dependent upon the precise value of a_1.

4 - Assignment of HI Mass

The relationship between HI mass and HI linewidth was calibrated by Staveley-Smith and Davies (1989). (They also exploited it as a standard candle which, despite its large dispersion, enjoys complete freedom from internal and Galactic absorption.) We approximate their findings by:

$$log(M_{HI}/M_{\odot}) = a_2 + b_2\ logW_0 + \sigma_2 \times G_2(0,1), \qquad (6-12)$$

with $a_2 = 1.56$, $b_2 = 3.1$, and $\sigma_2 = 0.4$. For example, a galaxy with deprojected HI velocity width of 500 km sec^{-1} has, on average, an HI mass of 8.4×10^9 solar masses. In our models, we do not explicitly consider a range of values for a_2, as in principle we might, as infrared luminous objects may have more or less neutral hydrogen per unit mass than do optically selected objects. However, we vary constant a_1, which shifts the linewidth distribution and hence the HI mass distribution as well.

5 - Generation of Galaxy Inclination Angle

Consider a unit vector normal to a galaxy disk rooted at the disk center. It makes an angle i_{disk} ($0 \leq i_{disk} \leq 90$ degrees) with the line of sight (we do not distinguish between sides of the disk), and has azimuthal angle ψ and polar angle ϕ. The direction specified by (ψ, ϕ) is isotropically distributed but constrained so i_{disk} always lies above some i_{min}. Angles ϕ are generated by:

$$sin(\phi) = R_2(0,1). \qquad (6-13)$$

If $\phi > i_{min}$, then ψ can take on any angle between 0 and 90 degrees ($\psi_{min} = 0$ in Eqn. (6-15) below); if not, ψ must exceed a minimum value:

$$\psi_{min} = cos^{-1}[cos(i_{min})\ cos(\phi)], \qquad (6-14)$$

in order to yield a final $i_{disk} > i_{min}$. ψ is generated by:

$$\psi = \psi_{min} + (90° - \psi_{min}) \times R_3(0,1). \qquad (6-15)$$

Finally, i_{disk} is then generated by

$$cos(i_{disk}) \; = \; cos(\phi)\; cos(\psi). \qquad (6-16)$$

We apply our sample's nominal cutoff of $i_{min} > 45$ degrees in all our runs.

6 - Assessment of HI Flux Density

The transition probabilities for the spin flip of the electron magnetic dipole relative to that of the proton in isolated neutral hydrogen atoms allows a given HI mass to be associated with a given luminosity in the 21 centimeter line. Staveley-Smith and Davies (1989) provide the convenient formula:

$$M_{HI}/M_{\odot} = 2.36 \times 10^5 F_{HI}(cz/75)^2, \qquad (6-17)$$

where F_{HI} is in Jy km sec^{-1} , and cz is a galaxy's recession velocity (absent peculiar velocities) in km sec^{-1} . It is only here that an assumed value for the Hubble constant, 75 km sec^{-1} Mpc^{-1} in this case, has physical significance in our model. Note that in what follows, we use capital F_{HI} to denote integral fluxes (*e.g.*, Jy km sec^{-1}) and smallcase f_{HI} to denote flux density (*e.g.*, mJy).

Again by example, our hypothetical 500 km sec^{-1} rotator, placed at a distance of 3000 km sec^{-1} , yields an integrated HI flux of 22 Jy km sec^{-1} . The flux density in Jy depends on the apparent rotation velocity $W = W_0\; sin(i_{disk})$:

$$f_{HI} = F_{HI}/[W_0\; sin(i_{disk})]. \qquad (6-18)$$

f_{HI} has thus been determined by the previous two steps, and the above equations.

We now compare the galaxy's f_{HI} to the limits that characterize the telescopes operating in each declination range:

$$f_{tel} = 4 \text{ mJy}, -20° < \delta < 0 \text{ and } +38° < \delta < +90° \text{ (Jodrell Bank, Green Bank)};$$

$$f_{tel} = 1 \text{ mJy}, 0 < \delta < +38° \text{ (Arecibo)};$$

$$f_{tel} = 12 \text{ mJy}, -90° < \delta < -20° \text{ (Parkes)}.$$

If $f_{galaxy} < f_{tel}$, we return to step 2 and generate L_{60}, $logW_0$, M_{HI} and inclination anew.

7 - Placement upon I band Tully-Fisher Relation

The object's absolute I band magnitude is generated as

$$M_I = a_3 + b_3\, logW_0 + \sigma_3 \times G_3(0,1). \qquad (6-19)$$

Intercept a_3 is arbitrary since we apply no detection threshold to apparent I band magnitudes

$$m_I = M_I + 5log(d_T), \qquad (6-20)$$

and so we set $a_3 = 0$. We are free to do so because, once we decided to observe a galaxy with a CCD camera, we never failed to obtain an I band magnitude due to nondetection. b_3 has been set to -8 for all our models. $\sigma_3 = \sigma_{TF}^{intr}$, the intrinsic TF scatter, is varied as a quantity of interest between sets of models (but held constant when creating a given ensemble of synthetic datasets).

We note that several low latitude objects' magnitudes were unavailable due to excessive crowding from foreground stars, and that finite camera field of view at the Palomar 60 inch telescope also deprived us of a few northern objects of very large angular size. The effects of these *a posteriori* selection effects upon our results, if any, are not treated here.

8 - Add Observational Error to Linewidths and I band Magnitudes

Apparent I band magnitudes are independently perturbed in these simulations by

$$m_I \;\triangleleft\; m_I + \sigma_4 \times G_4(0,1). \qquad (6-21)$$

Based on our ability to reproduce isophotal magnitudes at $\Sigma_I = 23.5$ mag arcsec^{-2} to ~ 0.05 mag (Chapter 2), we have set $\sigma_4 = 0.05$ in all our simulations. As long as $\sigma_4 < \sigma_3$ by several factors, our results are not sensitive to σ_4's precise value.

Chapter 5 described our statistical correction of I band magnitudes to hypothetical face-on values. This exploited the apparent correlation between average isophotal surface brightness (within corrected isophotal apertures) and the logarithm of the axial ratio, $log(R) = log[sec(i_{disk})]$. That relation was found to have a slope of 1.44 ± 0.18. Thus we perturb the Monte Carlo m_I by an additional amount

$$m_I \;\triangleleft\; m_I + \sigma_5 \times G_5(0,1) \times log(R), \qquad (6-22)$$

where σ_5 is set to 0.18.

We found in Chapter 5 that our Parkes linewidths, when reduced twice independently by the same person (J.R.), were poorly reproduced as HI signal to noise ratio (S/N) declined. We assume this uncertainty to be due to ambiguity in baseline subtraction and visual signal discrimination. We crudely quantify its dependence upon S/N as

$$\sigma_{W_{obs}} = (20 - S/N), \quad S/N < 20, \qquad (6-23a)$$

$$\sigma_{W_{obs}} = 0, \quad S/N > 20, \qquad (6-23b)$$

where σ_{W_0} is in km sec^{-1} . As an example: for $< S/N >\sim 5$ as we typically get at Parkes, $< \sigma_{W_0} >\sim 15$ km sec^{-1} .

We found in Chapter 4 that inward-looking (*e.g.*, 'MAX') algorithms for measuring HI linewidths tend to suffer bias towards higher values at low HI S/N. Most linewidths we are compelled to take from the literature are generated by algorithms of this nature, and we thus will choose

to use our 'MAX' linewidths in actual data analysis. We crudely quantify the results of our Monte Carlo perturbed-linewidth experiments in Chapter 4 by defining an additive linewidth bias

$$b_{W_{obs}} = 20 \times (S/N)^{-0.74} \qquad (6-24)$$

in km sec^{-1} to the $W_{obs} = W_0\ sin(i_{disk})$ values generated in steps above.

Example: for $< S/N > \sim 5$ as we have at Parkes, $< b_{W_{obs}} > \sim 6$ km sec^{-1} .

Thus we add to a galaxy's *projected* (*i.e.*, observed) linewidth $W_{obs} = W_0\ sin(i_{disk}) = 10^{log[W_0\ sin(i_{disk})]}$ the noise and bias terms:

$$W_{obs} \quad \triangleleft \quad W_{obs} + \sigma_{W_{obs}} \times G_6(0,1) + b_{W_{obs}}. \qquad (6-25)$$

In our models, S/N is simply calculated as

$$S/N = f_{HI}/f_{tel} = F_{HI}/(W_0\ sin(i_{disk}))/f_{tel}. \qquad (6-26)$$

Thus in step VI above we effectively rejected all synthetic observations with $S/N < 1$.

We presume a galaxy's inclination angle is imperfectly determined by the ellipse fitting techniques described in Chapter 4; thus we perturb the actual Monte Carlo generated inclination angle by

$$i_{disk} \quad \triangleleft \quad i_{disk} + \sigma_6 \times G_7(0,1). \qquad (6-27)$$

We set $\sigma_6 = 3$ degrees in all our simulations.

Finally, we reassess $logW_0$, given the projected HI linewidth with its additive S/N-dependent error and bias terms, and deproject it by the latter perturbed inclination:

$$logW_0 \quad \triangleleft \quad log[W_{obs}/sin(i_{disk})]. \qquad (6-28)$$

Since we do not employ our actual HI fluxes as distance indicators nor to quantify the HI selection effects, we do not model the considerable error in HI flux determination, which in any case is dominated by systematic effects. The physical, not the catalogued, value of f_{HI} determines detection or nondetection in step 6 above.

Steps 1 – 8, performed for each galaxy in a subset of 4KVL, generate one synthetic dataset with the following data for each object:

$$\alpha, \delta, cz, m_I, F_{60\mu}, F_{HI}, W_{obs}, \text{ and } i_{disk}.$$

Section IV: Distributions of Inferred Tully-Fisher Relation Properties

$N_{loop} = 1000$ synthetic datasets were generated by the procedure detailed in the above section at each X_{true} value from 2 to 38 ($\Delta X = 2$). Parameter a_1 (zeroing the $log(L_{60\mu}) - logW_0$ relation, and implicitly determining the slope and intercept of the $< logW_0 > - cz$ relation) was set to -9.0 in the runs described here. A range of values for σ_3, the intrinsic scatter of the I band Tully-Fisher relation, from 0.25 to 0.45 mag was used.

The merit function whose distribution we have chosen to calculate is the value of X_{var} that minimizes the apparent Tully-Fisher scatter about a line fit to the plot of inferred absolute magnitude M_I versus log corrected HI linewidth $logW_0$. We do the fit two ways: 1 - by minimizing M_I residuals, and 2 - by minimizing $logW_0$ residuals. The corresponding X values are referred to as X^F_{fit}, X^B_{fit} in what follows.

For a given synthetic dataset, X_{var} for the model used to *interpret* (rather than generate) the data (*i.e.*, the knob setting) begins at 2. The model distances $d_T(j; X_{var})$ for galaxies 'j' at given X_{var} were used to turn apparent into absolute magnitudes:

$$M_I(j) \triangleleft m_I(j) - 5\, log[d_T(j; X_{var})]. \qquad (6-29)$$

A set of data points $[logW_{0_j}, M_{I_j}]$ results. A line is fit to it by unweighted least squares method (Numerical Recipes' FIT - Press *et al.* 1986). We found that weighting the individual data points by terms reflecting their error budget did not change the results we discuss below. Since the actual linewidth errors in the actual dataset are unknown to us, we prefer to treat the synthetic data sets as we do our actual one, and give points uniform weight. We speculate that the weighting terms do not affect the distribution of the random variable 'X_{var} knob setting at which apparent TF scatter is minimized' because the knob setting only takes on discrete values.

Note that if a traditional χ^2 statistic were being assessed, we would have to simultaneously fit three parameters: the TF slope, its intercept, and X. The present approach, in contrast, reduces the problem to one dimension and yields (admittedly biased) TF slope and intercept estimates as byproducts.

Separate fits minimizing the squared M_I and $logW_0$ residuals were performed for each synthetic dataset at each value of X_{var} from 2 to 38 ($\Delta X = 1$) and the X_{var} values X^F_{fit}, X^B_{fit} minimizing the M_I, $logW_0$ squared residuals, respectively, for each synthetic dataset were stored in their respective arrays. This specified the ensemble distributions for 'favored knob settings' X^F_{fit}, X^B_{fit}. We have found the distributions to be roughly Gaussian and we denote the mean and standard deviation for $X^{F,B}_{fit}$ given a value of X_{true} as $< X^{F,B}_{fit}|X_{true} >$, $\sigma_{X^{F,B}_{fit}|X_{true}}$, respectively.

Figures 3*a-f* show results for an intrinsic TF dispersion of $\sigma_3 = 0.45$ mag with the *IRAS* SMALLR models being sampled at the positions of the 91 4KVL/JAN93 objects. Squares and error bars represent ensemble averages and standard deviations for the N_{loop} trials at each X_{true}. Figure 3*a* depicts $< X^F_{fit}|X_{true} >$, $\sigma_{X^F_{fit}|X_{true}}$, while panel 3*b* shows the B-TF counterparts $< X^B_{fit}|X_{true} >$, $\sigma_{X^B_{fit}|X_{true}}$.

Figure 3*a* shows that, away from the extremes, the apparent 'forward TF' method (*i.e.*, that which minimizes *rms* M_I residuals; hereafter called 'F-TF') minimizes the apparent F-TF scatter σ^{F-TF}_{app} at an unbiased value of X_{var}. At $X \gtrsim 20$ ($\beta \gtrsim 1$), Figure 3*b* shows the apparent 'backward

TF' method (*i.e.*, that which minimizes *rms* $logW_0$ residuals; hereafter 'B-TF') yields an apparent B-TF scatter σ_{app}^{B-TF} at values of X_{var} slightly larger than the actual one X_{true} used to generate the synthetic datasets. We presume this modest bias to be at least partly due to the existence of the additive linewidth bias and to the linewidth-related HI detection thresholds, which we constrast with a lack of detection threshold or additive bias term for I band magnitudes.

Figures 3*c-d* show the ensemble mean and *rms* slopes from the F-TF, B-TF fits, respectively. Note that, as the inverse of the true slope of -8 is $-.125$, the B-TF slope is systematically biased steep by a significant amount. The effect is explained in Willick's thesis (WT; cf. Appendix C) as due to gradients in the $logW_0$ distribution coupled with linewidth measurement errors. A complementary bias skews the F-TF slope shallow, but the effect is much smaller in his models and negligable in ours.

Figures 3*e-f* show the F-TF and B-TF 'scatter' σ_{app}^{F-TF}, σ_{app}^{B-TF}, respectively, at their minimum values. The amplitude simply reflects the intrinsic TF scatter of 0.45 mag plus the various observational noise sources.

Figures 4*a-f* portray results for a simulation in which the *IRAS* SMALLR models are sampled at the positions of the entire 251 object 4KVL/OKOBJ sample for which we would have liked to get data. We note that the ensemble dispersions (error bars) drop by something like $\sqrt{N}$ as expected. The bias in X_{fit}^{B} appears to have actually somewhat increased at $X_{true} > \sim 25$. We note that the B-TF slopes, although showing less variance between synthetic datasets, remain biased at the same value of ~ -0.11, as the bias is a function of the observational and intrinsic TF scatter.

Figures 5 – 8 in turn represent runs for the following galaxy samples and values of σ_3:

Figure 5: $\sigma_3 = 0.35$ mag, sample = JAN93 ;

Figure 6: $\sigma_3 = 0.35$ mag, sample = OKOBJ ;

Figure 7: $\sigma_3 = 0.25$ mag, sample = JAN93 ;

Figure 8: $\sigma_3 = 0.25$ mag, sample = OKOBJ .

Note the decrease in the B-TF slope bias with decreasing intrinsic TF scatter as predicted by WT (Appendix C). Comparison of Figures 3 and 6 suggests that if the entire OKOBJ sample may be observed with superior HI or optical long slit Hα rotation curve spectra and the *IRAS* galaxies' TF scatter turns out to be $\sigma_3 \sim 0.35$ mag, this offers promise for a factor of $\sim$2 better constraint upon β than we believe possible with the present JAN93 dataset.

Section V: Bayes' Theorem and Confidence Limits on X_{true}

The Monte Carlo simulations described above provide us with ensemble distribution functions for measureable parameters X^F_{fit}, X^B_{fit} given what we hope are realistic models for the distribution of galaxies in their intrinsic properties, and for measurement errors and bias.

The temptation is to read error bars off panels *a*, *b* from Figures 3 – 8 for some value of X_{true} and state, 'the error in measuring X_{true} = some value is given by the error bars'. However, to associate a likeliest value of X_{true} and a range of X_{true} values compatible with a given, solitary measurement of X^F_{fit} or X^B_{fit}, we need to compute the relative likelihood each X_{true} value has of producing the one observational result we in fact obtained.

To assess the relative likelihood of various X_{true} producing an observed X^F_{fit} or X^B_{fit}, we apply Bayes' Theorem (BT). Given the probability densities $P(X)$, $P(Y)$ of events X, Y respectively and the conditional probabilities $P(X|Y), P(Y|X)$, we may write

$$P(Y|X)P(X) = P(X|Y)P(Y), \qquad (6-30)$$

implying

$$P(X|Y) = P(Y|X)P(X)/P(Y). \qquad (6-31)$$

Since $P(Y)$ may be expressed as the sum over X of terms $P(Y|X)P(X)$, we may rewrite the above equation as:

$$P(X|Y) = \frac{P(Y|X) \times P(X)}{\sum_X P(Y|X)P(X)} \qquad (6-32)$$

In English,

$$posterior = \frac{likelihood\ \ times\ \ prior}{evidence}$$

(Mackay 1992, hereafter MT; Loredo 1989).

Say X_{true} is the model parameter $20 \times \beta = 20 \times \Omega^{0.6}/b_{IRAS}$ that defines the actual velocity field and Y is the value of X_{var} in one's model that minimized the apparent TF scatter for one's dataset. Then the 'likelihood' $P(Y|X_{true})$ has been estimated by Monte Carlo integration over the various 'nuisance parameters' (*e.g.*, HI flux, galaxy inclination angle, uncertainty in internal extinction correction, it etc.) and its first and second moments are given by $< Y|X_{true} >$, $\sigma_{Y|X_{true}}$ respectively. We take $P(Y|X)$ to be a Gaussian with mean $= < X_{fit}|X_{true} >$ and standard deviation $\sigma_{X_{fit}|X_{true}}$ at given X_{true}:

$$P(X_{fit}|X_{true}) = \frac{1}{\sqrt{2\pi}\ \sigma_{X_{fit}|X_{true}}} exp\left\{\frac{(X_{fit} - < X_{fit}|X_{true} >)^2}{-2\ \sigma_{X_{fit}|X_{true}}}\right\}. \qquad (6-33)$$

(Here and in what follows, superscript 'F' or 'B' is implicit but not written.)

The 'prior' $P(X)$ is to be specified based on our theoretical prejudice or previous experimental results. In what follows we use two illustrative priors:

$$P(X_{true}) \ = \ constant, \ \ 2 \leq X_{true} \leq 39; \qquad (6-34a)$$

$$P(X_{true}) \ = \ 0, \ \ elsewhere \ \ (FLAT); \qquad (6-34b)$$

and

$$P(X_{true}) \ \propto cos^2\left\{\pi\frac{X_{true} - 20}{40}\right\}, \ 2 \leq X_{true} \leq 39; \qquad (6-35a)$$

$$P(X_{true}) \ = \ 0, \ elsewhere \ \ (BELL). \qquad (6-35b)$$

The latter prior favors $X_{true} = 20$ ($\Omega^{0.6}/b_{IRAS} = 1$) models and might be taken to reflect the latest observational results (*e.g.*, Dekel *et al.* 1993; Davis, pers. comm.) and theoretical prejudice (*e.g.*, 'inflation', anthropic arguments). The prior makes explicit that one's interpretation of an experimental result hinges upon one's prior ranking of hypotheses competing to explain that result.

Once the posterior probability $P(X_{true}|X_{fit})$ has been calculated by applying BT, its first and second moments tell us the average and spread for X_{true} values to be associated with a given observed X_{fit}:

$$< X_{true}|X_{fit} > = \frac{\{\sum_{X_{true}} X_{true} \times P(X_{true}|X_{fit})\}}{\sum_{X_{true}} P(X_{true}|X_{fit})} \qquad (6-36)$$

and

$$\sigma^2_{X_{true}|X_{fit}} = \frac{\sum_{X_{true}} \{(X_{true} - < X_{true}|X_{fit} >)^2 \times P(X_{true}|X_{fit})\}}{\sum_{X_{true}} P(X_{true}|X_{fit})}. \qquad (6-37)$$

Figures 9 – 14 reproduce in panels *a*,*b* the panels *a*,*b* of Figures 3 – 8. These we now associate with the respective likelihoods $P(X^F_{fit}|X_{true})$ and $P(X^B_{fit}|X_{true})$. Panels *c*,*e* represent $< X^F_{true}|X_{fit} >$ (squares) and $\sigma_{X_{true}|X^F_{fit}}$ (error bars) given the 'flat' and 'bell' priors, respectively. Panels *d*,*f* offer the analogous quantities for X^B_{fit}. It is these latter panels $c - f$ that quantify the accuracy (do the squares lie on the $y = x$ line?) and precision (how big are the error bars?) of our technique for 'measuring' β, as predicted by our simulations.

The role of the prior at extreme values of X_{fit} can be seen in panels *c*-*f* of Figures 9 – 14; the bell prior's prejudice against extreme values of X_{true} and towards the central value skews the model to be associated with a given measurement away from the $y = x$ line and towards X_{true}=20. The apparently subjective nature of prior choice, and its possibly dramatic effect on interpreting experimental results, may seem irrational, but proponents of Bayesian approaches (*e.g.*, MT; Loredo 1989; Weir, pers. comm.) insist that setting the prior simply makes explicit what we implicitly do in a standard χ^2 or maximum likelihood model fitting procedure anyway: we assign relative weights

to each of a set of competing hypotheses (discarding a much larger universe of hypotheses entirely), and adjust these weights in light of new data.

Section VI: Conclusions and Caveats

We have seen that setting the β 'knob' to a value at which a dataset's apparent Tully-Fisher relation shows minimum scatter can produce largely unbiased estimates of the density parameter in the presence of realistic Tully-Fisher scatter, observational errors, and selection effects. Error bars on estimates of β are seen to drop by roughly the square root the number of objects used to sample the flow, and roughly in proportion to the intrinsic scatter of the TF relation.

Figures 3 and 9 reflect a plausible model for our experiment: the JAN93 sample of 91 galaxies and an intrinsic TF scatter of 0.45 magnitudes. The numbers shown in panels *a-f* of Figure 9 are reproduced in Tables III and IV. As an example: suppose we find $X^F_{fit} = 20$ minimized the *rms* magnitude residuals of the inferred TF relation for the 91 galaxies we have observed to date. Table III suggests that $X_{true} = 20.2$ is the mean model to have given this result (if not the likeliest one: that is given by the mode of the posterior probability), and that $\sim 97\%$ of the X_{true} values that would give this result lie within the range $14.2 \leq X_{true} \leq 26.2$, or $0.71 \leq \beta \leq 1.3$. Given $b_{IRAS} \equiv 1$ these translate to a 'two-σ' Ω measurement of $1.02\ ^{+0.55}_{-0.45}$. We also note that, if Ω had the nucleosynthetic baryonic value of 0.2 ($X_{true} = 7.6$), then $P(X^F_{fit}|X_{true})$ tells us that we would virtually never observe $X^F_{fit} = 20$. Thus, while the [JAN93; $\sigma^{intr}_{TF} = 0.45$ mag] experiment cannot strongly constrain Ω (if we measure $\Omega = 1$, $\sim 97\%$ of the possible true values lie within ~ 0.6 to ~ 1.6), it can in principle reject the inflationary hypothesis, or, alternatively, demonstrate the dynamical effects of nonbaryonic matter on large scales. If longslit Hα rotation curves were to yield a Tully-Fisher relation of ~ 0.35 magnitudes' scatter for infrared-luminous galaxies, the models depicted in Figures 6 and 12 suggest that obtaining such data on the entire 251 object 'OKOBJ' sample would allow us to roughly double our current resolution upon the density parameter.

The 'POTENT' analysis of 493 galaxies gives '95% confidence limits' for β of $1.28\pm^{+0.75}_{-0.59}$; Dekel *et al.* 1993). Loosely speaking, then, our models suggest that 91 modest Tully-Fisher distance moduli to galaxies within the 4000 km sec^{-1} volume can constrain Ω better than can the larger peculiar velocity compilation fed to the 'POTENT' analysis. We suspect this is so because we go directly from the X_{true} parameter to an apparent TF diagram, whereas the 'POTENT' analysis first goes from magnitude and linewidth measurements to peculiar velocities, with all the attendent uncertainties in 'inferred distance' biases (*e.g.*, Roth 1991; Willick WT and 1993; Landy and Szalay 1992; Gould 1993) in full effect. The POTENT peculiar velocity field then must be heavily (and asymetrically) smoothed to beat down the random errors, as at $H_0 \times d = N \times 1000$ km sec^{-1} , a TF dispersion of even only 0.3 mag pulls measurements of $V_{pec} \lesssim N \times 150$ km sec^{-1} down to an effective signal to noise ratio below unity. The 'POTENT' velocity field is then integrated to generate the underlying potential and density. The *IRAS* distance field must be windowed and smoothed into a comparable density map. All these steps are bypassed if original (magnitude, linewidth) data are retained. We note that a similar approach was adopted by Faber and Burstein (FB) in fitting 'Virgo+Great Attractor+ Local Anomaly' models to the 7S elliptical and Aaronson *et al.* H band spiral galaxy data.

The trend in error bars for panels *c* of Figures 9 – 14 as σ_3 drops motivates the use of intrinsically very precise distance indicators. If the surface brightness fluctuation (SBF) technique (Tonry 1991) proves robust and the elliptical galaxies to which it applies can be found far enough from virialized cluster cores and triple-valued zones, an all sky sample of $\sim$ 100 SBF distances might constrain β to ~ 0.1 precision.

The modest deviations at $X^B_{fit} \gtrsim 25$ from the $y = x$ line seen in panels *b*, *d* of Figures 9 – 14 suggest that minimizing magnitude residuals yields slightly less biased estimates of Ω than does minimizing linewidth residuals. The numerous statements in the Tully-Fisher literature stating that linewidth residual minimization is to be preferred (*e.g.*, Tully 1988) are predicated on

the assumption that no selection effect favors some linewidths over others. For the Faber-Jackson experiment of Schechter (1980), often cited in this context, the assumption held: velocity dispersions were obtained for all galaxies that were observed spectroscopically. For the case of finite flux density thresholds at 21 centimeters and a nonunit slope for the $log(M_{HI}) - logW_0$ relation, the assumption clearly fails. On the contrary, in the present experiment it is the I band magnitude which suffers no instrumental bounds upon its value nor enters explicitly into the sample definition.

Although we have tried to make a realistic model for our *IRAS* 4KVL Tully-Fisher experiment, it is incomplete in several respects. For example, uncertainties in the Burstein-Heiles Galactic extinction estimates (BH) have not been introduced as a noise source, nor were they used to weigh model (or actual) data points, as they optimally might. Systematic trends in deviation from BH extinctions with sky position might profitably be modelled in light of recent revisions of A_B towards the Hydra-Centaurus complex. Our assumptions that outliers from mean relations between $logW_0$ and luminosities are Gaussian may require revision. Much larger simulations might allow us to relax the assumption of Gaussian distribution for $X_{fit}|X_{true}$ currently exploited to assess posterior probabilities. Insofar as our models may lack one or more significant 'nuisance parameters', our statements comparing our methods' leverage upon β to that of 'POTENT' must be taken as provisional.

Two physically motivated elaborations which belong in these models, but lie beyond the scope of the present thesis, are noted here:

A - Additional Flowfield Components

The possibility exists that the '*IRAS* galaxies trace mass' models are incomplete descriptions of the cosmic flowfield. As none perfectly predicts the microwave dipole vector, this must be true at some level. Our experiment is completely insensitive to any bulk motion of the entire 4000 km sec^{-1} radius 'ball of wax' with respect to the great beyond - except in that the MBR frame redshifts entered into the sample selection. (This manner of sample selection may induce subtle

biases, and this will be investigated by perturbing the actual MBR dipole and extracting other, hypothetical 4KVL samples from the 2 Jy survey). The mismatch between observed and *IRAS*-predicted microwave background may have a local origin, however, such that galaxy distances in fact are described by

$$d_T(j) = d_{IRAS}(j;X) + U_{dip} \times [l^{II}(j), b^{II}(j)] \odot [l^{II}_{dip}, b^{II}_{dip}], \qquad (6-38)$$

where $\odot$ denotes the dot product of the two unit vectors pointing towards the indicated directions l^{II}, b^{II} on the celestial sphere.

Figures 15 – 16 represent simulations like those of Figures 5, 11 ($\sigma_3 = 0.35$ mag; JAN93 models) but include a LG motion with respect to the 4KVL sample of

$$(U_{dip}, l^{II}_{dip}, b^{II}_{dip}) = (250 \text{ km sec}^{-1}\ , 210°, +10°)$$

reflected in the actual distances. This vector was inspired by the 'local anomaly' (FB; HM) believed to describe 'local' (on scales $\lesssim$ 500 km sec^{-1}) shear in the flowfield. We note that our simulation treats the vector $(250, 210, +10)$ as motion *above and beyond* that predicted by Strauss *et al.* - it is not as if the latter authors predicted no local shear whatsoever. If we entertain the possibility of such a dipolar deviation from their prediction, however, we see that in can notably skew estimates for X_{true} if not taken into account when modeling the (synthetic or real) datasets. In the example shown, we have artificially enhanced the local anomaly and the density parameter has predictably been overestimated thereby. We note that minimizing linewidth residuals appears to leave us a good deal more susceptible to the skewing of β estimates at $\beta \gtrsim 1$ than does the 'F-TF' approach.

If we choose not to (or lack sufficient data to) fit for the dipole in modelling the flowfield, the vector $(U_{dip}, l^{II}_{dip}, b^{II}_{dip})$ becomes another possible noise source or 'nuisance parameter' to be Monte Carlo sampled according to some probability density distribution inspired by, say, local anomaly models (Faber and Burstein 1988; Han and Mould 1990) or the cosmic virial theorem (Peebles 1980). If we do fit for the dipole, the flowfield model now has four parameters (X, U_{dip}, l^{II}_{dip}, b^{II}_{dip})

rather than one. A joint prior $P(X,\ U_{dip},\ l^{II}_{dip},\ b^{II}_{dip})$ must be specified to perform the Bayesian inversion to posterior probabilities. The prior may not factor to independent terms:

$$P_x(X)\ P_U(U_{dip})\ P_l(l^{II}_{dip})\ P_b(b^{II}_{dip}).$$

For example, the dipole may be constrained to reproduce that observed in the microwave background, or $< U^2_{dip} >$ may scale with Ω as predicted by the cosmic virial theorem. We will seek evidence for dipolar deviation from our best-fit X values in the next chapter, but the extension of the methods outlined above to these four parameter models lies beyond the scope of the present work. In practice, exclusion of nearby objects may largely decouple the β and $\mathbf{U}_{dip}$ problems.

Quadrupolar deviations from the $IRAS$ models could be induced if a structure lying beyond but near the edge of the 4KVL sample boundary enjoys a mass to light ratio significantly larger (or smaller) than the average for $IRAS$ galaxies. For example: the so-called 'Great Attractor' purported to lie beyond the Hydra and Centaurus clusters might be systematically undersampled by the $IRAS$ survey (Faber and Burstein 1988). An extension of our approach to '$IRAS$ + quadrupole' models likewise lies beyond the present work. It is unlikely that $\sim$ 100 objects across 4π steradians of sky can strongly constrain a weak quadrupolar deviation from the $IRAS$ models.

B - Covariant Residuals from Luminosity - Linewidth Relations

Our simulations assume that when a galaxy is over or under luminous in the I band at a given linewidth (relative to the mean at that linewidth), this bears no relation as to whether or not it is over or under luminous at 60 microns, or at 21 centimeters, at that same linewidth. That is, given the (already listed) relations:

$$log(L_{60}/L_*) = a_1 + b_1 logW_0 + \sigma_1 \times G_1(0,1), \qquad (6-10)$$

$$log(M_{HI}/M_\odot) = a_2 + b_2 logW_0 + \sigma_2 \times G_2(0,1), \qquad (6-12)$$

$$M_I = a_3 + b_3 logW_0 + \sigma_3 \times G_3(0,1), \qquad (6-19)$$

we called Numerical Recipes' GASDEV (Press et al. 1986) three separate times to generate the three uncorrelated sequential Gaussian random deviates $G_k(0,1)$.

Although the simplest model, this may not be conceptually or physically correct. Perhaps, at a given halo mass (reflected in linewidth), more gaseous galaxies made more stars, so that G_2 and G_3 are positively correlated. Perhaps at a given halo mass, all haloes get the same amount of neutral hydrogen gas and those who have processed more of it into stars have less HI left over; then G_2 and G_3 would be negatively correlated. Absorption of starlight and its reradiation in the far infrared by diffuse dust might couple G_1 and G_3.

Our sample has *a priori* limits on L_{60} (which are largely distance independent but may have subtle directional effects due to the way the MBR frame redshifts were used to select our sample) and *a posteriori* limits on M_{HI} which are strongly distance dependent as well as directional, due to the finite and site specific HI flux density detection thresholds encountered in our work. If the correlation coefficients

$$r_{13} = \frac{< G_1 \cdot G_3 > - < G_1 >< G_3 >}{\sqrt{< G_1^2 > - < G_1 >^2} \times \sqrt{< G_3^2 > - < G_3 >^2}} \qquad (6-39)$$

and

$$r_{23} = \frac{< G_2 \cdot G_3 > - < G_2 >< G_3 >}{\sqrt{< G_2^2 > - < G_2 >^2} \times \sqrt{< G_3^2 > - < G_3 >^2}} \qquad (6-40)$$

are nonzero, then these limits will skew M_I from its average value at given linewidth and could in principle skew $X_{fit}^{F,B}$.

The related problem of 'inferred distance bias' (known, for better or worse, as 'Malmquist' or 'Malmquist-like' bias in much of the literature) in the presence of covariant residuals has been discussed by Gould (1993). Gould showed that the 'Malmquist' correction routinely applied by direct mappers of peculiar velocities (*e.g.*, Dressler and Faber 1990; CT; Dekel *et al.* 1993) fail if objects are selected by apparent magnitude in one band, but distances are measured in another,

unless those bands' residual luminosities at fixed linewidth are perfectly (and positively) correlated ($r = +1$).

An empirical examination of related possible effects in the Pierce and Tully (1988) HI-based TF calibration of the Virgo and Ursa Major clusters was given by Mould *et al.* (1991). Although the results suffer tremendous shot noise, their experiments suggest that the angular diameter limits imposed in defining their southern cluster sample might induce spurious positive peculiar velocities as the I band TF residuals in Pierce and Tully's Virgo data show modest correlation with galaxy diameter. We note, however, that this discussion (as well as Gould's) pertain to peculiar velocity mapping with already-calibrated distance indicators, and not to model-fitting methods of the sort used in the present work.

We do note that samples may be divided up into halves above and below median values for critical parameters like f_{HI}; should the values for model parameters (*e.g.*, X_{fit}) obtained from such halves agree to within their estimated errors, they may be inferred to be largely free from such bias.

It is entirely possible that our X_{fit} statistics will remain robust to nonzero r_{13} or r_{23}, but we cannot assert so at present. Methods for generating correlated Gaussian variables are detailed in Meyer (1986) and will be applied to generating G_1, G_2, G_3 sequences in extensions of the present work.

Table I - predicted LG motion, *IRAS* SMALLR models

	predicted LG motion			add'l LG motion needed to match MBRD		
X	V_{LG}^{pred}	l_{LG}^{pred}	b_{LG}^{pred}	V_{LG}^{addl}	l_{LG}^{addl}	b_{LG}^{addl}
2	91	254	37	527	271	26
3	136	254	37	484	273	25
4	182	254	37	441	274	24
5	230	255	37	396	276	22
6	278	255	37	353	278	20
7	320	255	37	315	281	18
8	363	255	36	278	284	15
9	400	255	36	248	288	12
10	439	255	35	216	293	9
11	480	255	36	190	299	3
12	533	255	36	162	309	-9
13	566	254	35	156	321	-14
14	598	254	35	158	330	-21
15	641	254	35	159	344	-30
16	672	254	35	174	354	-35
17	706	254	34	190	7	-35
18	737	254	34	207	16	-36
19	778	254	34	235	25	-39
20	815	254	34	268	31	-38
21	849	255	34	290	38	-39
22	898	255	34	335	43	-40
23	927	255	34	363	45	-41
24	953	254	34	387	47	-40
25	995	255	35	425	51	-41
26	1033	254	35	463	51	-41
27	1045	255	34	468	55	-39
28	1089	256	34	510	57	-39
29	1127	255	34	547	58	-39
30	1169	256	34	587	60	-39
31	1211	256	34	629	61	-39
32	1229	255	35	650	60	-39
33	1261	254	35	684	59	-39
34	1297	255	34	716	61	-38
35	1332	255	35	750	62	-40
36	1369	256	35	784	64	-40
37	1398	256	36	814	65	-41
38	1403	256	35	818	65	-40
39	1424	256	35	838	65	-39
40	1465	256	35	879	66	-39

Table II - predicted LG motion, *IRAS* STANDARD models

	predicted LG motion			add'l LG motion needed to match MBRD		
X	V_{LG}^{pred}	l_{LG}^{pred}	b_{LG}^{pred}	V_{LG}^{addl}	l_{LG}^{addl}	b_{LG}^{addl}
2	151	248	41	476	274	23
3	232	247	41	408	279	20
4	317	248	41	341	284	13
5	394	248	42	288	290	5
6	485	248	42	243	301	-8
7	556	250	41	210	312	-21
8	636	249	40	225	332	-33
9	721	249	40	256	352	-44
10	788	250	40	293	8	-47
11	880	250	40	364	23	-49
12	965	250	40	437	33	-49
13	1042	250	39	504	39	-46
14	1120	251	38	572	45	-45
15	1198	252	37	638	51	-43
16	1299	251	36	735	54	-41
17	1405	250	36	842	55	-40
18	1524	250	36	956	57	-39
19	1649	251	35	1078	59	-38
20	1747	251	35	1172	61	-37
21	1878	251	35	1302	62	-38
22	1994	251	35	1417	63	-38
23	2113	252	35	1533	64	-37
24	2246	252	35	1666	65	-37
25	2306	253	36	1724	66	-38
26	2454	253	36	1870	67	-38
27	2519	254	36	1933	68	-38
28	2672	254	36	2086	69	-38
29	2723	254	36	2135	70	-38
30	2868	254	36	2280	70	-38
31	2907	252	37	2326	67	-39
32	3048	252	36	2465	68	-38
33	3120	253	36	2533	69	-38
34	3224	255	37	2636	71	-39
35	3327	255	38	2740	71	-40
36	3431	255	37	2842	72	-39
37	3450	256	39	2864	73	-41
38	3556	255	39	2969	72	-41
39	3699	255	37	3111	71	-39
40	3698	255	37	3109	72	-39

Table III - X_{F-TF} distributions, Monte Carlo models

	likelihood		'FLAT' posterior		'BELL' posterior	
X	$< X^F_{fit} >$	σ	$< X^{FLAT}_{var} >$	σ	$< X^{BELL}_{var} >$	σ
02	3.42	1.04	3.21	1.57	4.75	1.97
04	4.68	2.14	3.50	1.92	5.54	2.33
06	6.80	2.69	5.98	2.15	7.31	2.13
08	8.65	2.42	7.64	2.20	8.68	2.11
10	10.4	2.79	9.42	2.47	10.4	2.42
12	12.5	2.37	11.7	2.70	12.5	2.53
14	13.8	1.88	13.7	2.66	14.2	2.54
16	16.2	2.27	15.8	2.95	16.2	2.81
18	19.1	3.01	18.3	3.02	18.4	2.84
20	21.0	3.42	20.3	2.96	20.2	2.78
22	22.5	3.28	22.0	3.11	21.7	2.87
24	24.7	3.57	23.6	3.37	23.1	3.07
26	26.7	3.94	25.6	3.55	24.7	3.22
28	28.6	3.70	27.6	3.57	26.4	3.23
30	30.7	3.62	29.7	3.58	28.0	3.16
32	32.0	3.71	31.7	3.58	29.5	3.15
34	34.0	3.22	33.6	3.36	30.9	3.15
36	35.2	3.02	35.0	2.94	32.1	3.08
38	36.4	2.58	35.7	2.55	33.0	2.90

Mean and *rms* dispersion thereabout of the likelihood $P(X^F_{FIT}|X_{true})$, the posterior probability $P(X_{true}|X^F_{FIT})$, 'FLAT' prior, and the posterior probability $P(X_{true}|X^F_{FIT})$, 'BELL' prior. The likelihood has been estimated at each X_{true} by 1000 Monte Carlo synthetic datasets with the 91 galaxies of the 4KVL/JAN93 subsample drawn from a Tully-Fisher relation with intrinsic dispersion 0.45 mag.

First column is X_{true} for likelihood and X^F_{FIT} for posterior probabilities.

Table IV - X_{B-TF} distributions, Monte Carlo models

	likelihood		'FLAT' posterior		'BELL' posterior	
X	$< X^B_{fit} >$	σ	$< X^{FLAT}_{var} >$	σ	$< X^{BELL}_{var} >$	σ
02	3.11	0.56	4.17	1.96	5.86	2.18
04	3.71	1.39	4.42	2.17	6.34	2.37
06	5.46	2.58	7.02	2.11	8.09	2.09
08	7.64	2.80	8.60	2.12	9.43	2.21
10	9.70	3.31	10.3	2.58	11.2	2.64
12	12.2	2.87	12.4	2.80	13.2	2.73
14	13.9	2.10	14.2	2.82	14.7	2.74
16	15.8	2.42	16.0	3.13	16.3	3.00
18	19.1	3.55	18.2	3.29	18.4	3.08
20	21.0	3.82	20.3	3.06	20.2	2.87
22	22.8	4.02	21.7	3.04	21.5	2.84
24	25.0	4.06	23.1	3.24	22.7	3.00
26	27.6	4.60	24.7	3.42	24.0	3.16
28	29.8	4.26	26.5	3.45	25.6	3.23
30	31.7	3.84	28.3	3.39	27.1	3.20
32	33.5	3.67	30.3	3.42	28.6	3.17
34	35.1	2.91	32.5	3.52	20.0	3.25
36	36.3	2.28	34.5	3.26	31.3	3.34
38	37.1	1.86	35.3	2.94	32.1	3.29

Mean and *rms* dispersion thereabout of the likelihood $P(X^B_{FIT}|X_{true})$, the posterior probability $P(X_{true}|X^B_{FIT})$, 'FLAT' prior, and the posterior probability $P(X_{true}|X^B_{FIT})$, 'BELL' prior. The likelihood has been estimated at each X_{true} by 1000 Monte Carlo synthetic datasets with the 91 galaxies of the 4KVL/JAN93 subsample drawn from a Tully-Fisher relation with intrinsic dispersion 0.45 mag.

First column is X_{true} for likelihood and X^B_{FIT} for posterior probabilities.

FIGURE CAPTIONS - Chapter 6

Figure 1: distance - distance plots, *IRAS* models:(a) SMALLR versus STANDARD, $X = 5$; (b) ditto, $X = 35$; (c) $X = 5$ versus $X = 35$, SMALLR; (d) ditto, STANDARD.

Figure 2 (1): *RMS* magnitude differences between *IRAS* models: (a) reference model $X = 10$; (b) reference model $X = 20$; (c) reference model $X = 30$. Crosses refer to the *IRAS* models being sampled at the positions of the 91 4KVL objects with data as of 1 January 1993 (JAN93). Squares sample the *IRAS* models at the positions of all 251 *a priori* OK for TF 4KVL objects (OKOBJ).

Figure 2 (2): *RMS* magnitude differences between *IRAS* models: (d) reference model $X = 10$; (e) reference model $X = 20$; (f) reference model $X = 30$. Crosses sample the *IRAS* models at the positions of the OKOBJ objects at northern declinations. Squares sample the *IRAS* models at the positions of the OKOBJ objects at southern declinations.

Figure 2 (3): *RMS* magnitude differences between *IRAS* models: (g) reference model $X = 10$; (h) reference model $X = 20$; (i) reference model $X = 30$. Crosses sample the *IRAS* models at the positions of the JAN93 objects at northern declinations. Squares sample the *IRAS* models at the positions of the JAN93 objects at southern declinations.

Figure 3: Results of Monte Carlo experiment 1: Sample = JAN93; $\sigma_3 = 0.45$ mag. Panels shows ensemble mean (squares) and standard deviation (error bars) for: (a) model X_{var} value at which F-TF *rms* (M_I) residuals are minimized (hereafter X^F_{fit}); (b) model X_{var} value at which B-TF *rms* ($logW_0$) residuals are minimized (hereafter X^B_{fit}); (c) F-TF slope at $X_{var} = X^F_{fit}$; (d) B-TF slope at $X_{var} = X^B_{fit}$; (e) F-TF *rms* scatter, magnitudes, at $X_{var} = X^F_{fit}$; (f) B-TF *rms* scatter, $logW_0$ units, at $X_{var} = X^B_{fit}$.

Figure 4: Results of Monte Carlo experiment 2: Sample = OKOBJ; $\sigma_3 = 0.45$ mag. Panels (a) - (f) as defined in caption to Figure 3.

Figure 5: Results of Monte Carlo experiment 3: Sample = JAN93; $\sigma_3 = 0.35$ mag. Panels (a) - (f) as defined in caption to Figure 3.

Figure 6: Results of Monte Carlo experiment 4: Sample = OKOBJ; $\sigma_3 = 0.35$ mag. Panels (a) - (f) as defined in caption to Figure 3.

Figure 7: Results of Monte Carlo experiment 5: Sample = JAN93; $\sigma_3 = 0.25$ mag. Panels (a) - (f) as defined in caption to Figure 3.

Figure 8: Results of Monte Carlo experiment 6: Sample = OKOBJ; $\sigma_3 = 0.25$ mag. Panels (a) - (f) as defined in caption to Figure 3.

Figure 9: Results of Monte Carlo experiment 1: Sample = JAN93; $\sigma_3 = 0.45$ mag. Panels (a)-(b) reproduce those of Figure 3. Squares and error bars in panels (c), (e) show first and second moments of posterior probability density for X_{true} given by applying Bayes' Theorem (BT) to panel (a) under the assumption that the abscissa is distributed Gaussian with the plotted mean and standard deviation. Squares and error bars in panels (d), (f) do the same for application of BT to panel (b). Panels (c) - (d) utilize a flat prior over $2 \leq X \leq 39$. Panels (e)-(f) utilize a cos^2 prior peaking at $X = 20$ and dropping to zero at $X = 0$ and $X = 40$.

Figure 10: Results of Monte Carlo experiment 2: Sample = OKOBJ; $\sigma_3 = 0.45$ mag. Panels (a) - (f) as defined in caption to Figure 9.

Figure 11: Results of Monte Carlo experiment 3: Sample = JAN93; $\sigma_3 = 0.35$ mag. Panels (a) - (f) as defined in caption to Figure 9.

Figure 12: Results of Monte Carlo experiment 4: Sample = OKOBJ; $\sigma_3 = 0.35$ mag. Panels (a) - (f) as defined in caption to Figure 9.

Figure 13: Results of Monte Carlo experiment 5: Sample = JAN93; $\sigma_3 = 0.25$ mag. Panels (a) - (f) as defined in caption to Figure 9.

Figure 14: Results of Monte Carlo experiment 6: Sample = OKOBJ; $\sigma_3 = 0.25$ mag. Panels (a) - (f) as defined in caption to Figure 9.

Figure 15: Results of Monte Carlo experiment 7: Sample = JAN93; $\sigma_3 = 0.35$ mag; true distances = $IRAS(X_{true}) + 250$ km sec^{-1} to $(l^{II} = 210, b^{II} = +10)$. Panels shows ensemble mean (squares) and standard deviation (error bars) for: (a) $X^F_{fit}|X_{true}$; (b) $X^B_{fit}|X_{true}$; (c) F-TF slope at $X_{var} = X^F_{fit}$; (d) B-TF slope at $X_{var} = X^B_{fit}$; (e) $\sigma^{F-TF}_{X_{fit}}$, magnitudes; (f) $\sigma^{B-TF}_{X_{fit}}$, $logW_0$ units.

Figure 16: Results of Monte Carlo experiment 7: Sample = JAN93; $\sigma_3 = 0.35$ mag; true distances = $IRAS(X_{true}) + 250$ km sec^{-1} to $(l^{II} = 210, b^{II} = +10)$. Panels (a)-(b) reproduce those of Figure 15. Squares and error bars in panels (c), (e) show first and second moments of posterior probability density for $X_{true}|X^F_{fit}$ given by applying BT to panel (a) under the assumption that the abscissa in panel (a) is distributed Gaussian with the plotted mean and standard deviation. Squares and error bars in panels (d), (f) do the same for the application of BT to panel (b). Panels (c) - (d) utilize a flat prior over $2 \leq X \leq 39$. Panels (e)-(f) utilize a cos^2 prior peaking at $X = 20$ and dropping to zero at $X = 0$ and $X = 40$.

IRAS model distance predictions for 4KVL objects

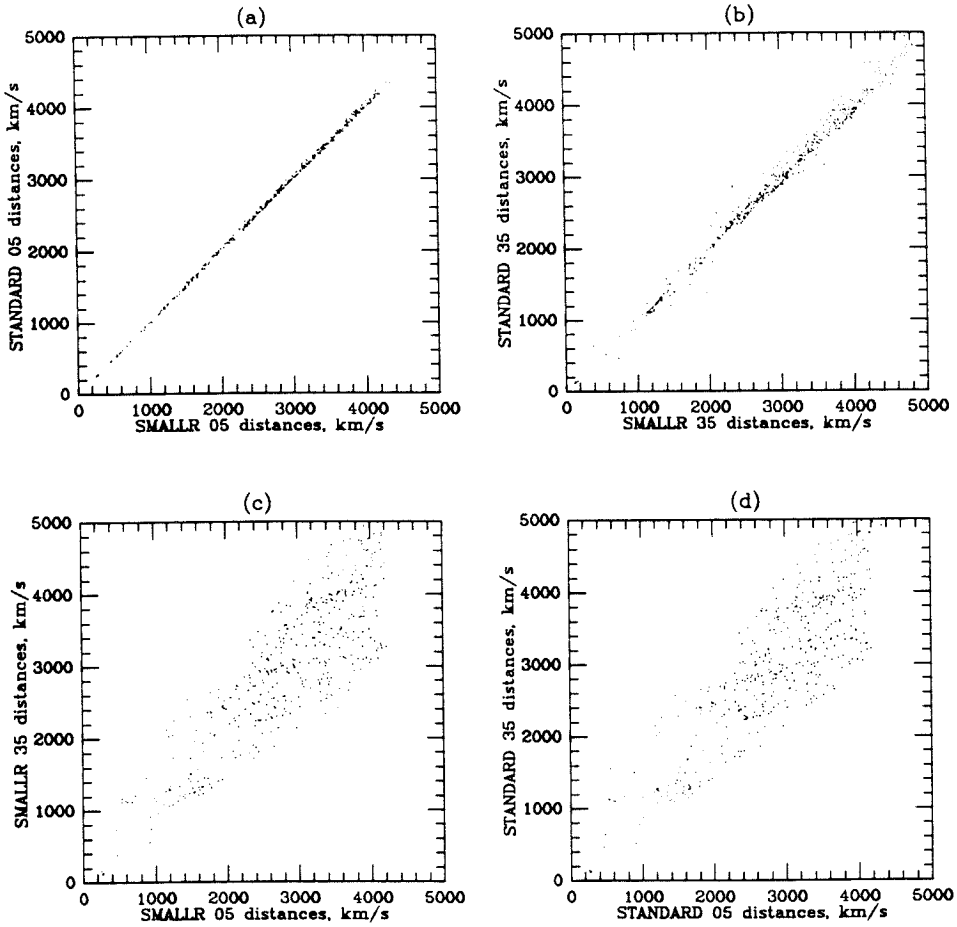

Figure 1

perfect standard candle IRAS response profiles

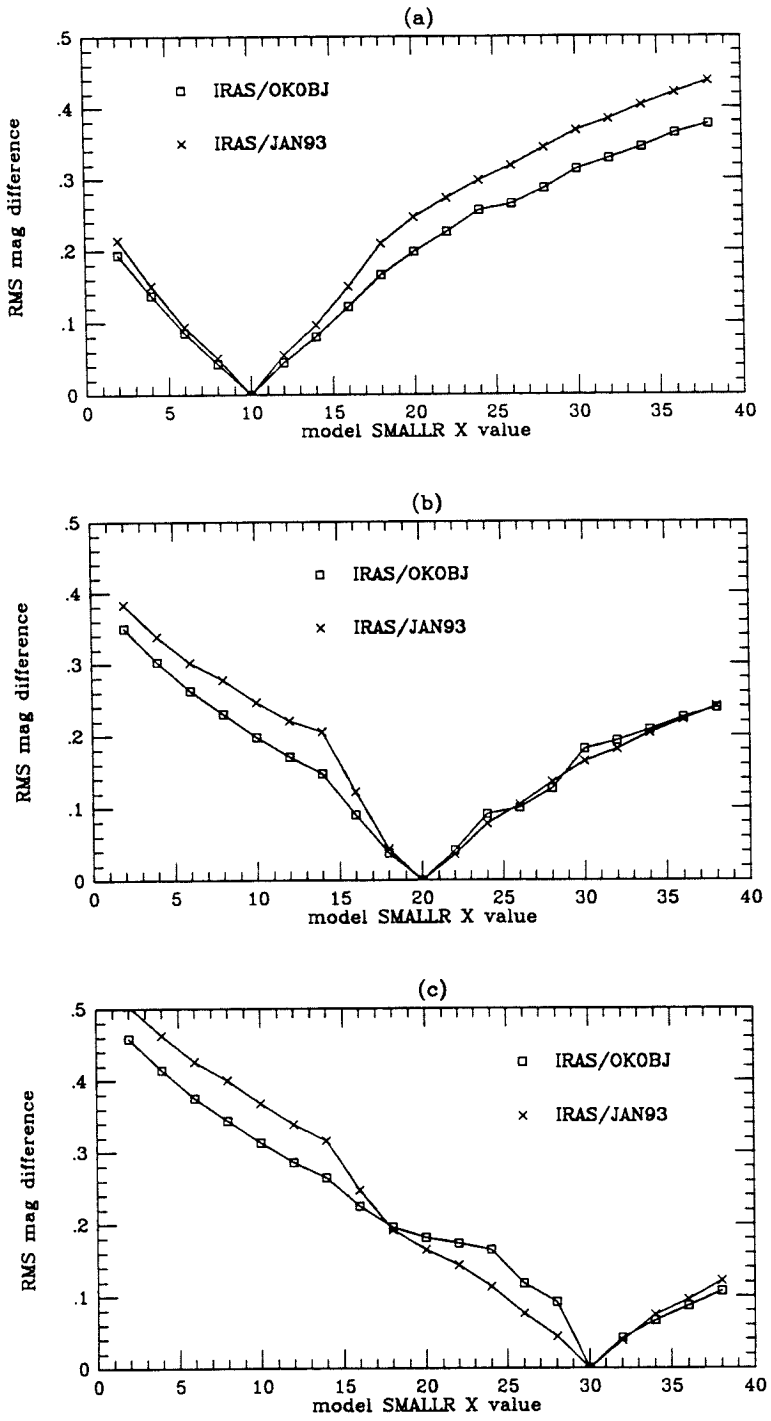

Figure 2(1)

perfect standard candle IRAS response profiles

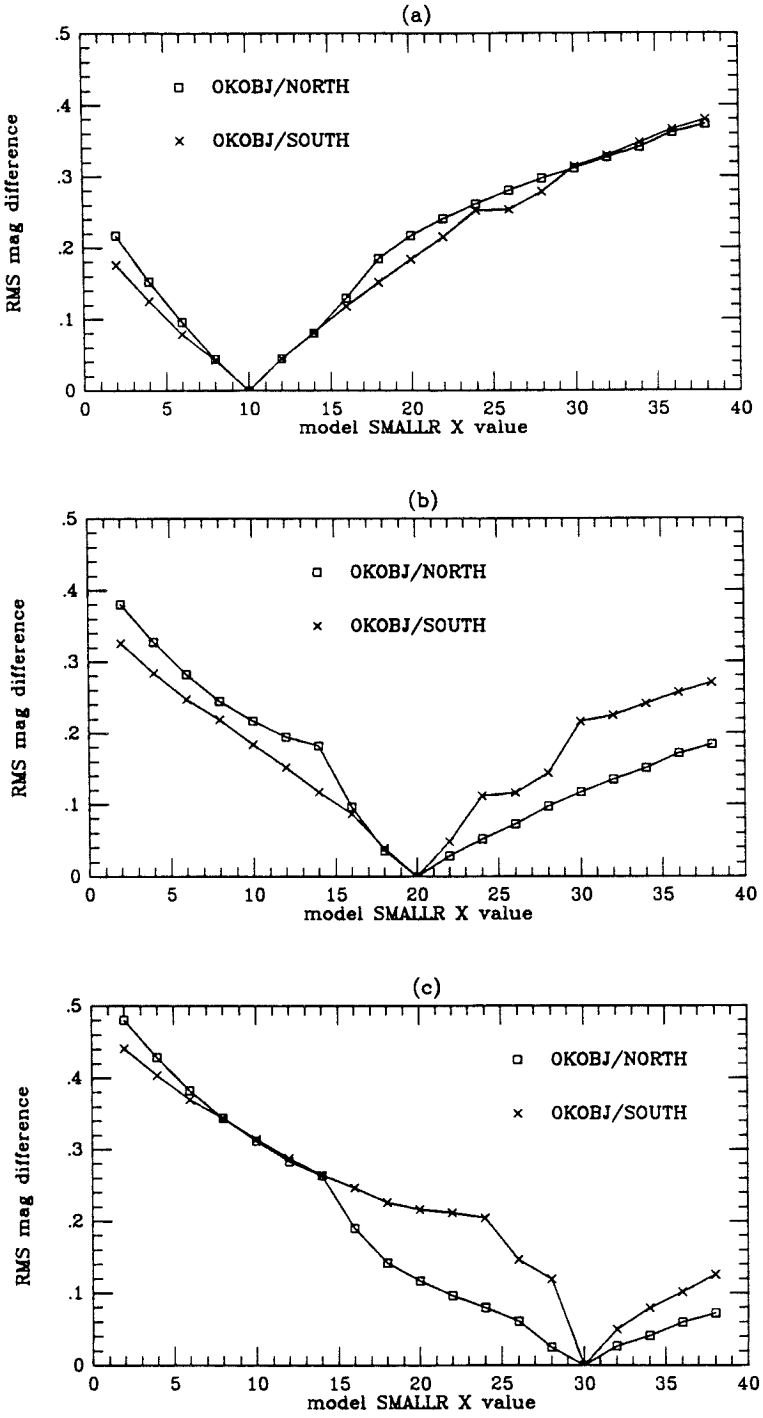

Figure 2(2)

perfect standard candle IRAS response profiles

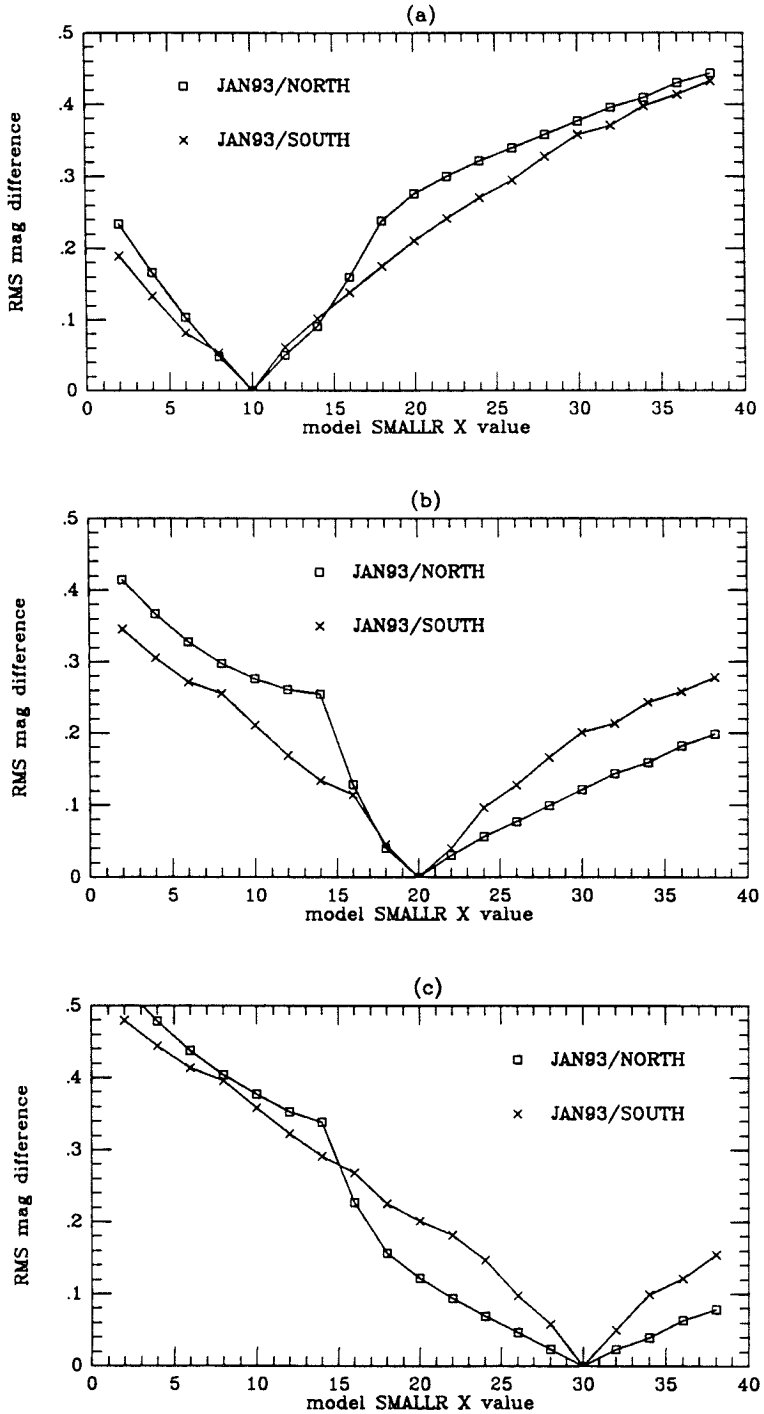

Figure 2(3)

sample = 4KVL/JAN93 (91 obj) / 1000 Monte-Carlo trials
I band Tully-Fisher scatter = 0.45 magnitudes

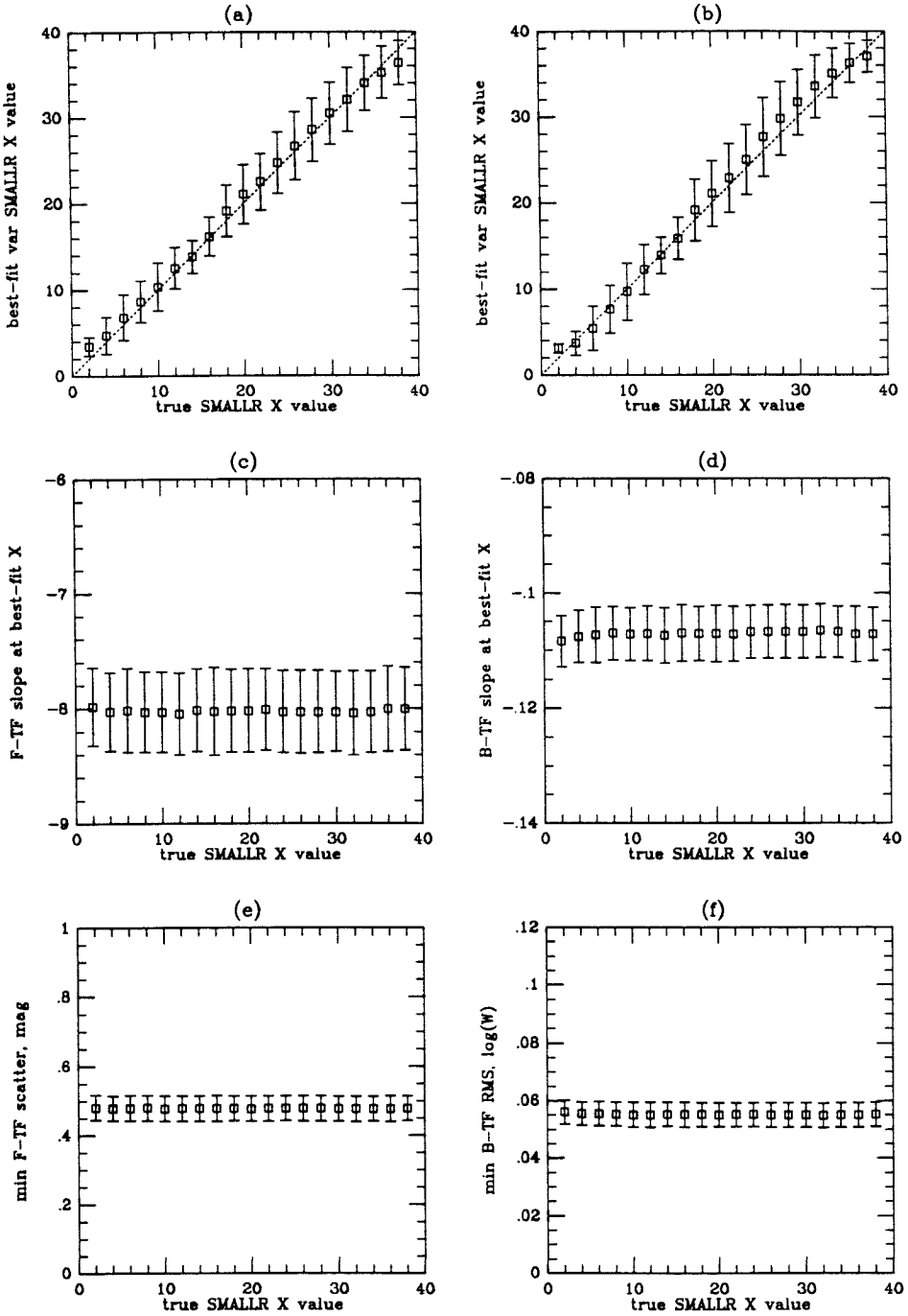

Figure 3

sample = 4KVL/OKOBJ (251 obj) / 1000 Monte-Carlo trials
I band Tully-Fisher scatter = 0.45 magnitudes

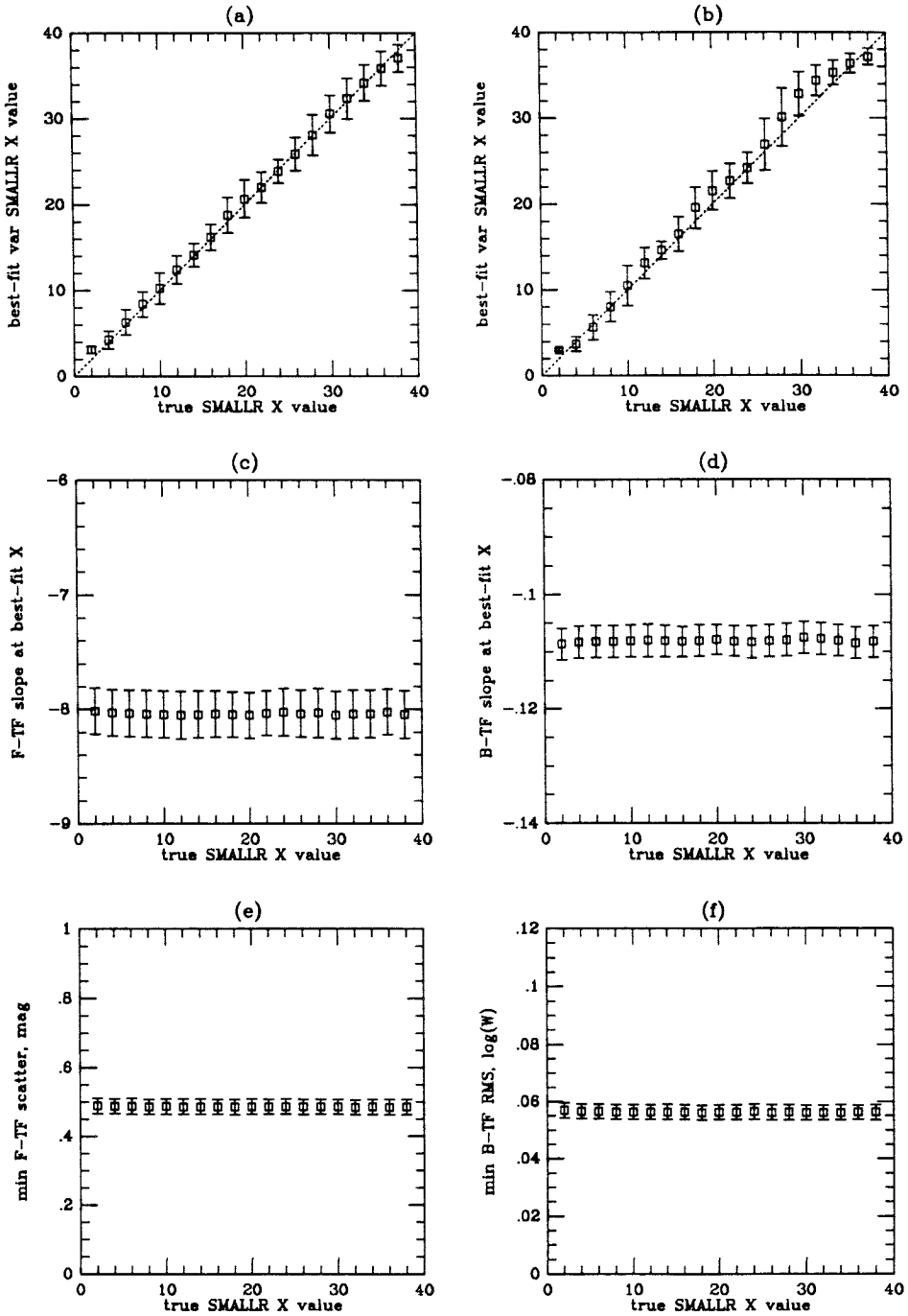

Figure 4

sample = 4KVL/JAN93 (91 obj) / 1000 Monte-Carlo trials
I band Tully-Fisher scatter = 0.35 magnitudes

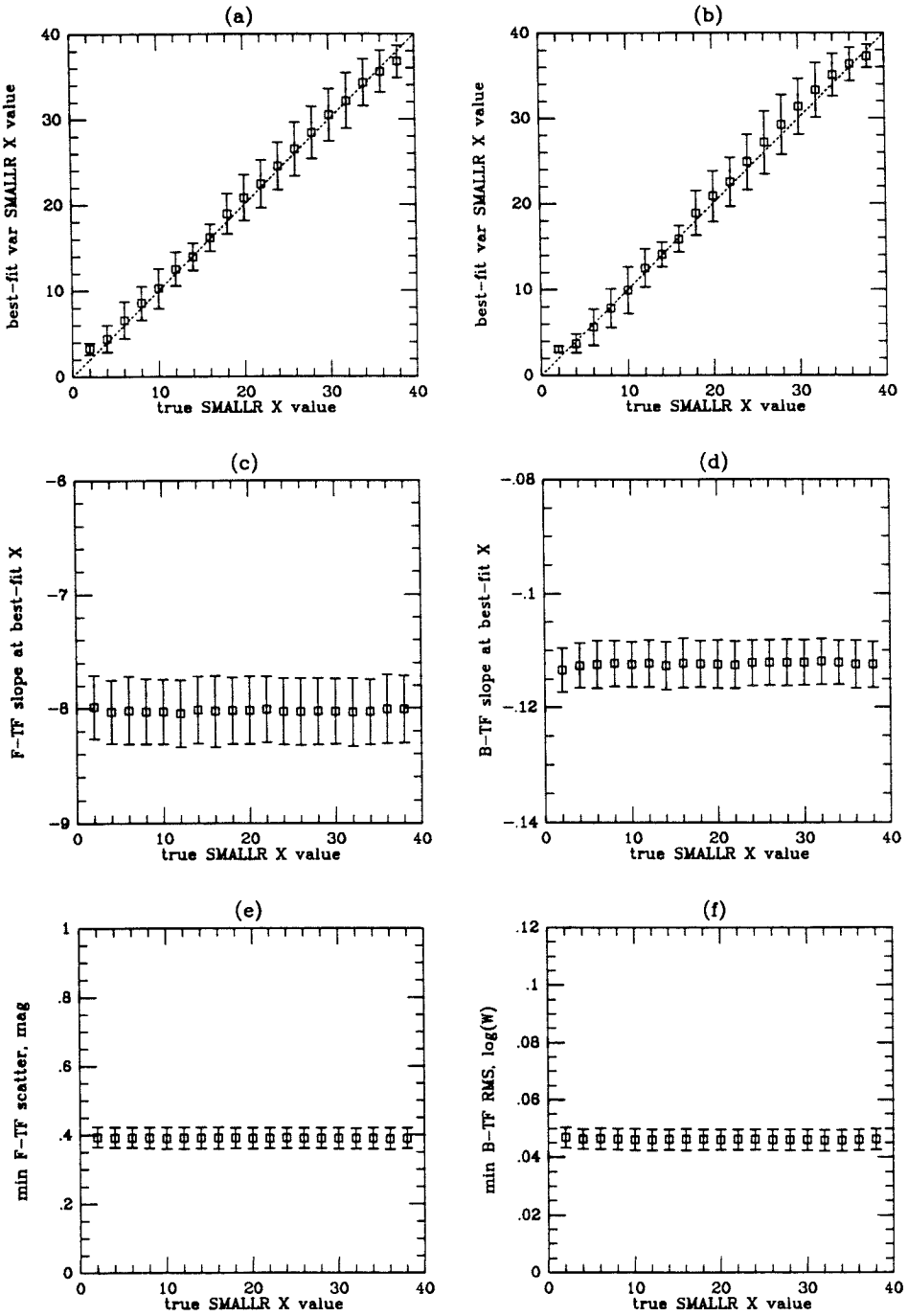

Figure 5

sample = 4KVL/0K0BJ (251 obj) / 1000 Monte-Carlo trials
I band Tully-Fisher scatter = 0.35 magnitudes

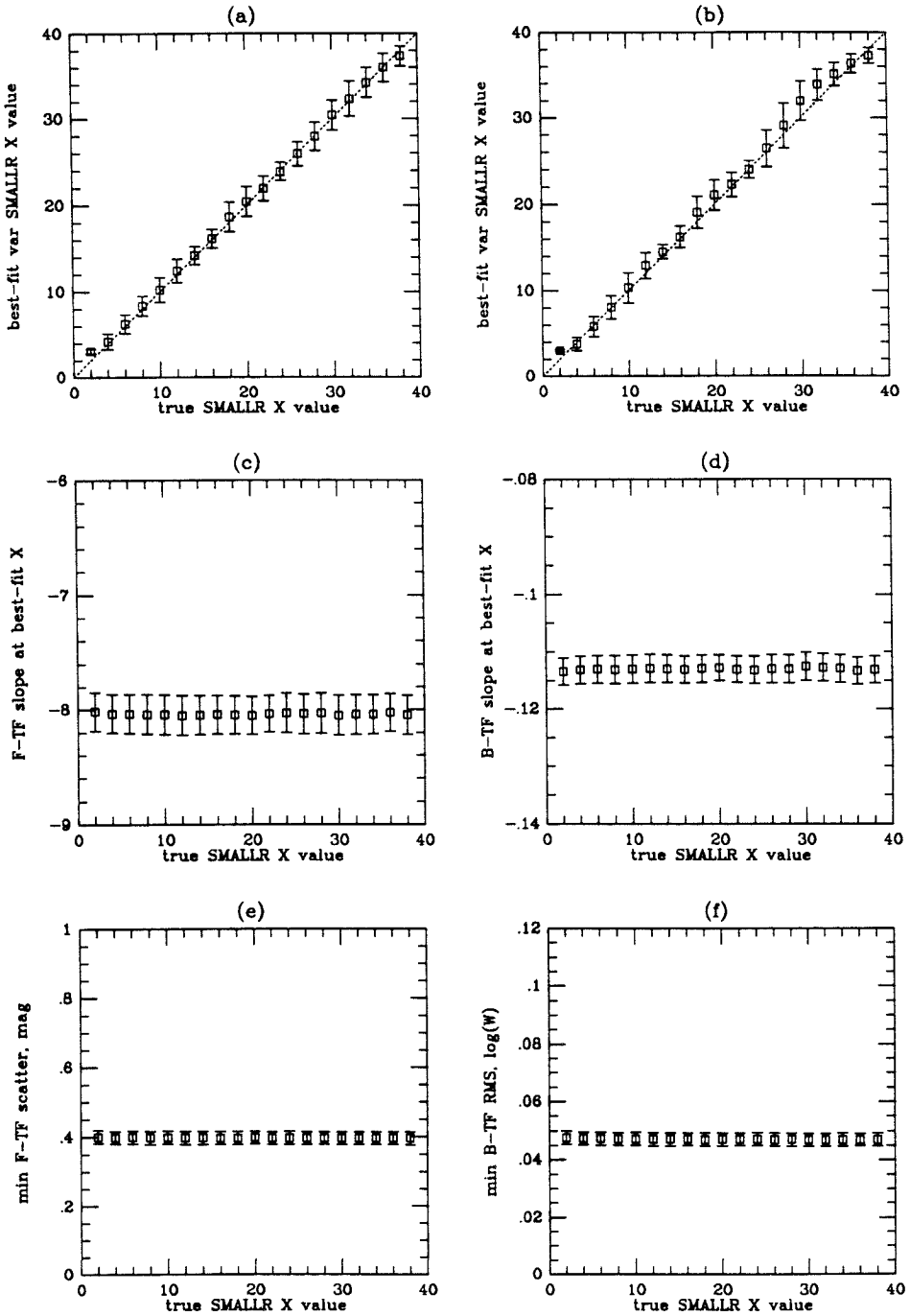

Figure 6

sample = 4KVL/JAN93 (91 obj) / 1000 Monte-Carlo trials
I band Tully-Fisher scatter = 0.25 magnitudes

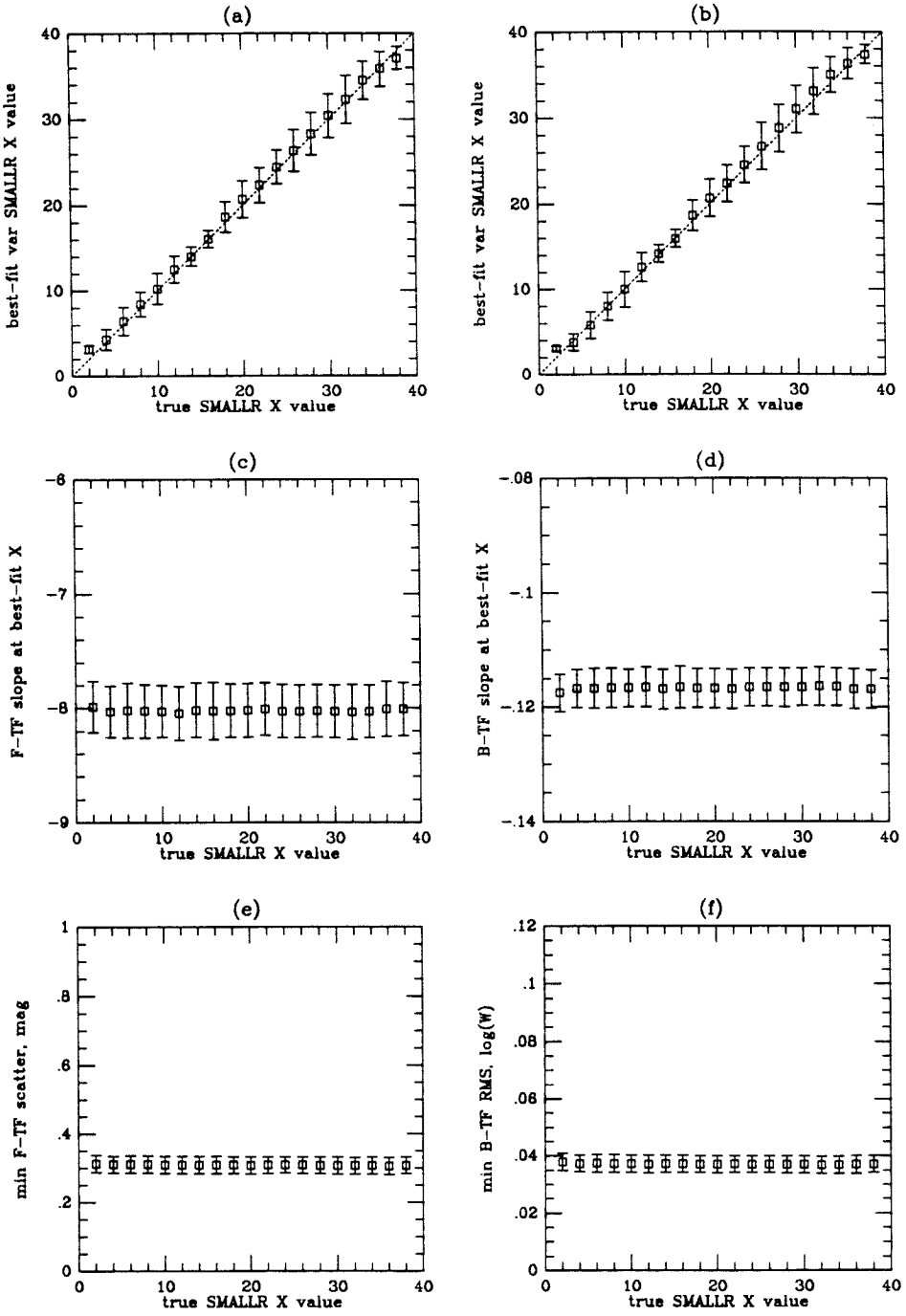

Figure 7

sample = 4KVL/OKOBJ (251 obj) / 1000 Monte-Carlo trials
I band Tully-Fisher scatter = 0.25 magnitudes

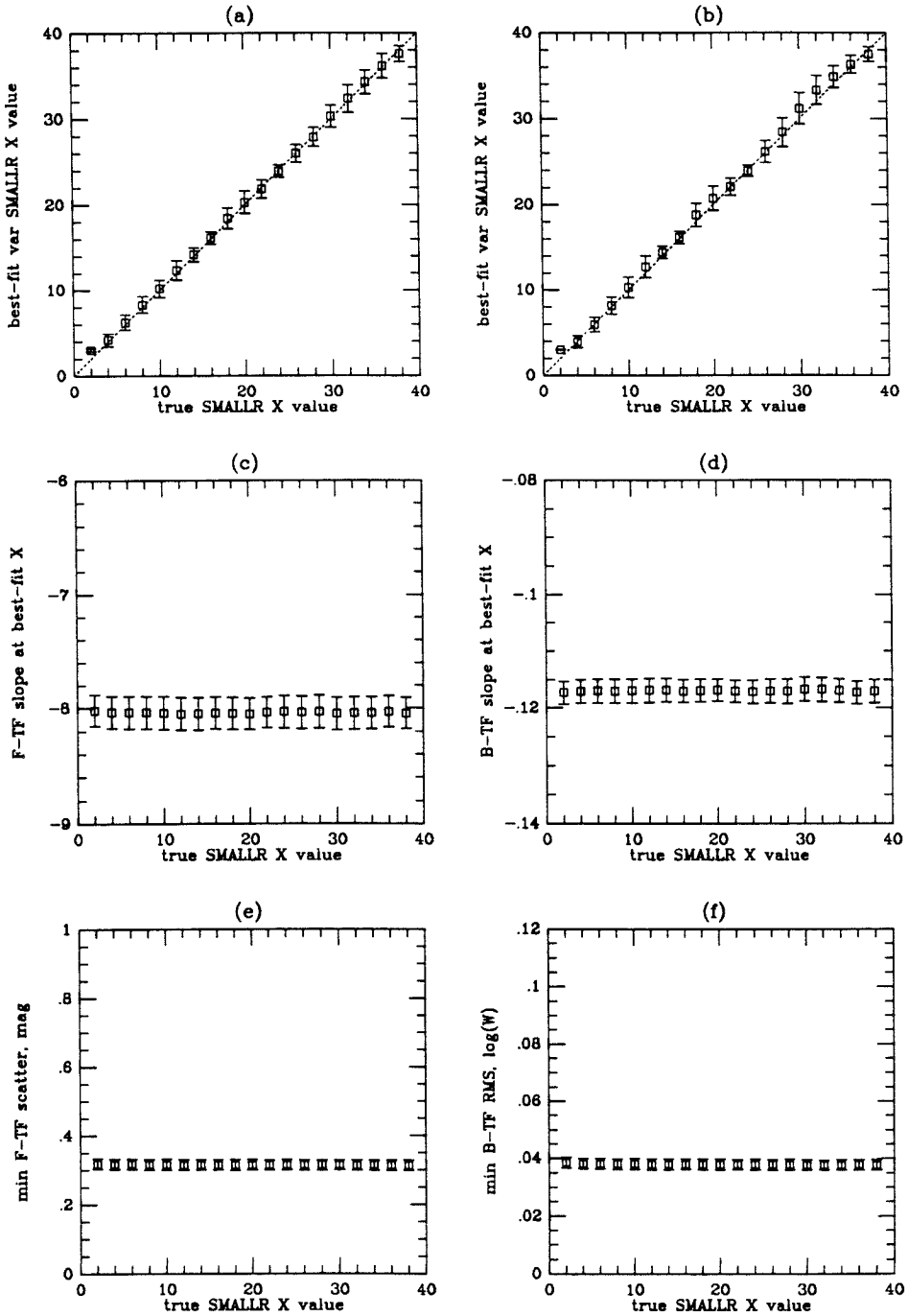

Figure 8

sample = 4KVL/JAN93 (91 obj) / 1000 Monte-Carlo trials
I band Tully-Fisher scatter = 0.45 magnitudes

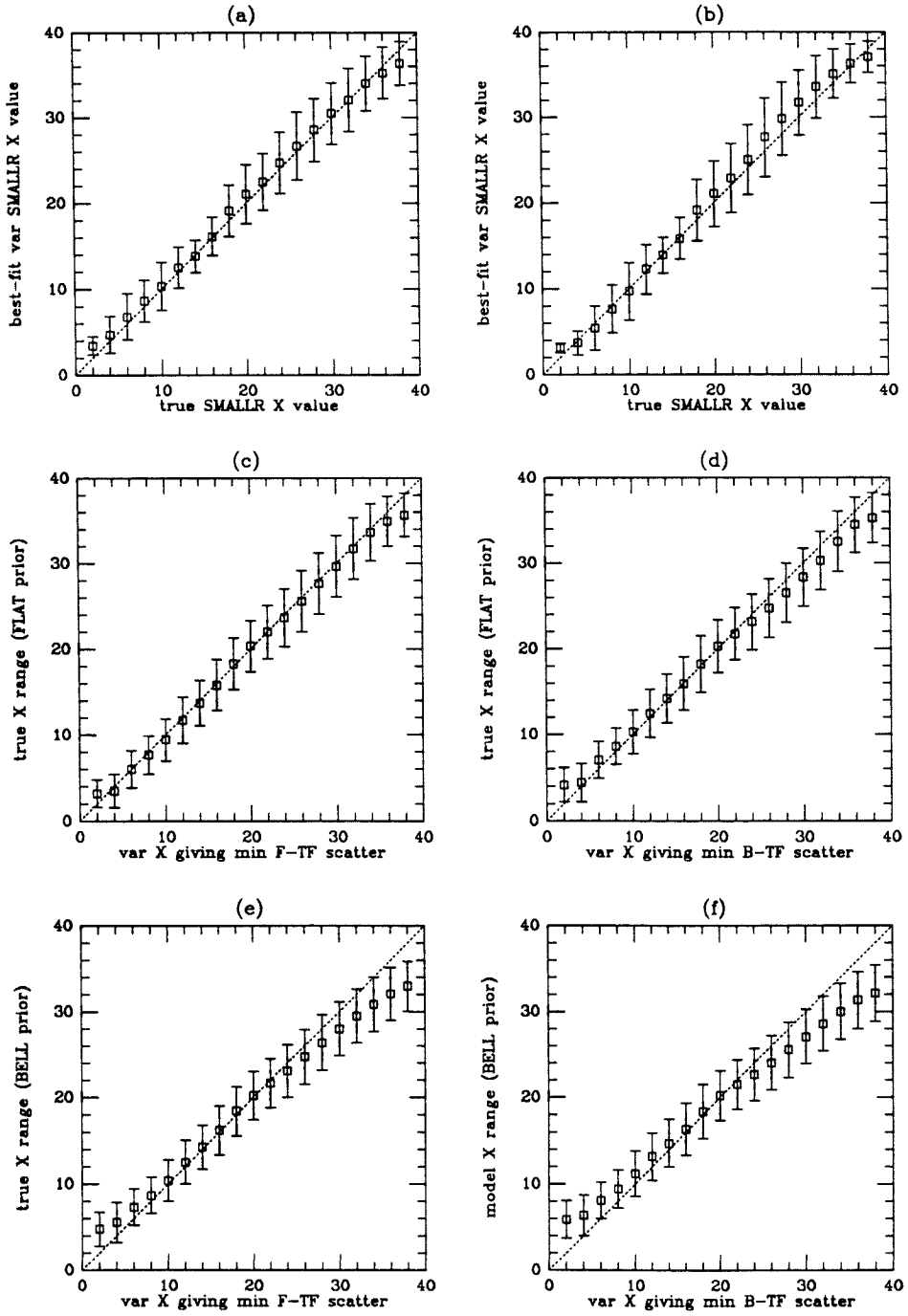

Figure 9

sample = 4KVL/OKOBJ (251 obj) / 1000 Monte-Carlo trials
I band Tully-Fisher scatter = 0.45 magnitudes

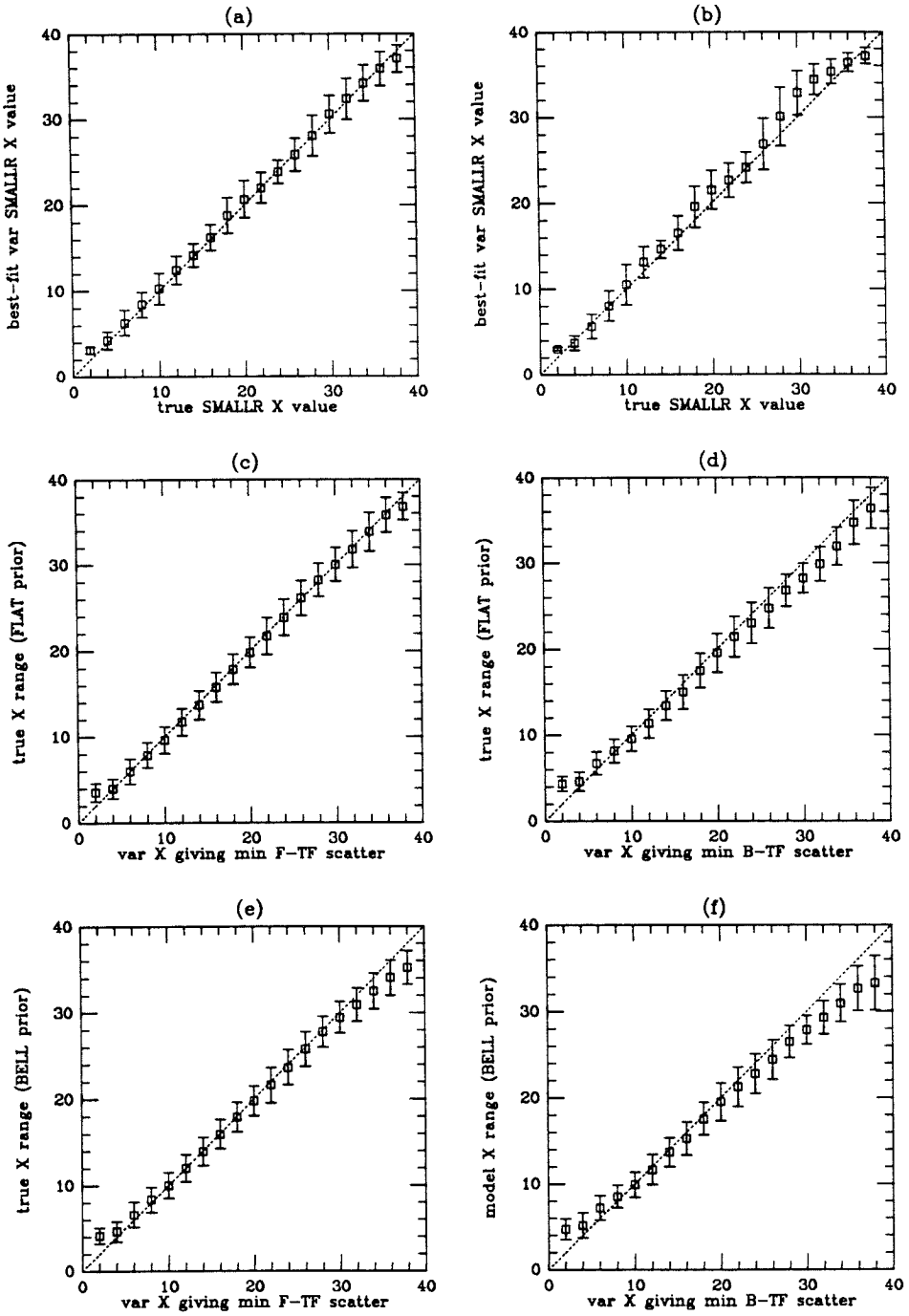

Figure 10

sample = 4KVL/JAN93 (91 obj) / 1000 Monte-Carlo trials
I band Tully-Fisher scatter = 0.35 magnitudes

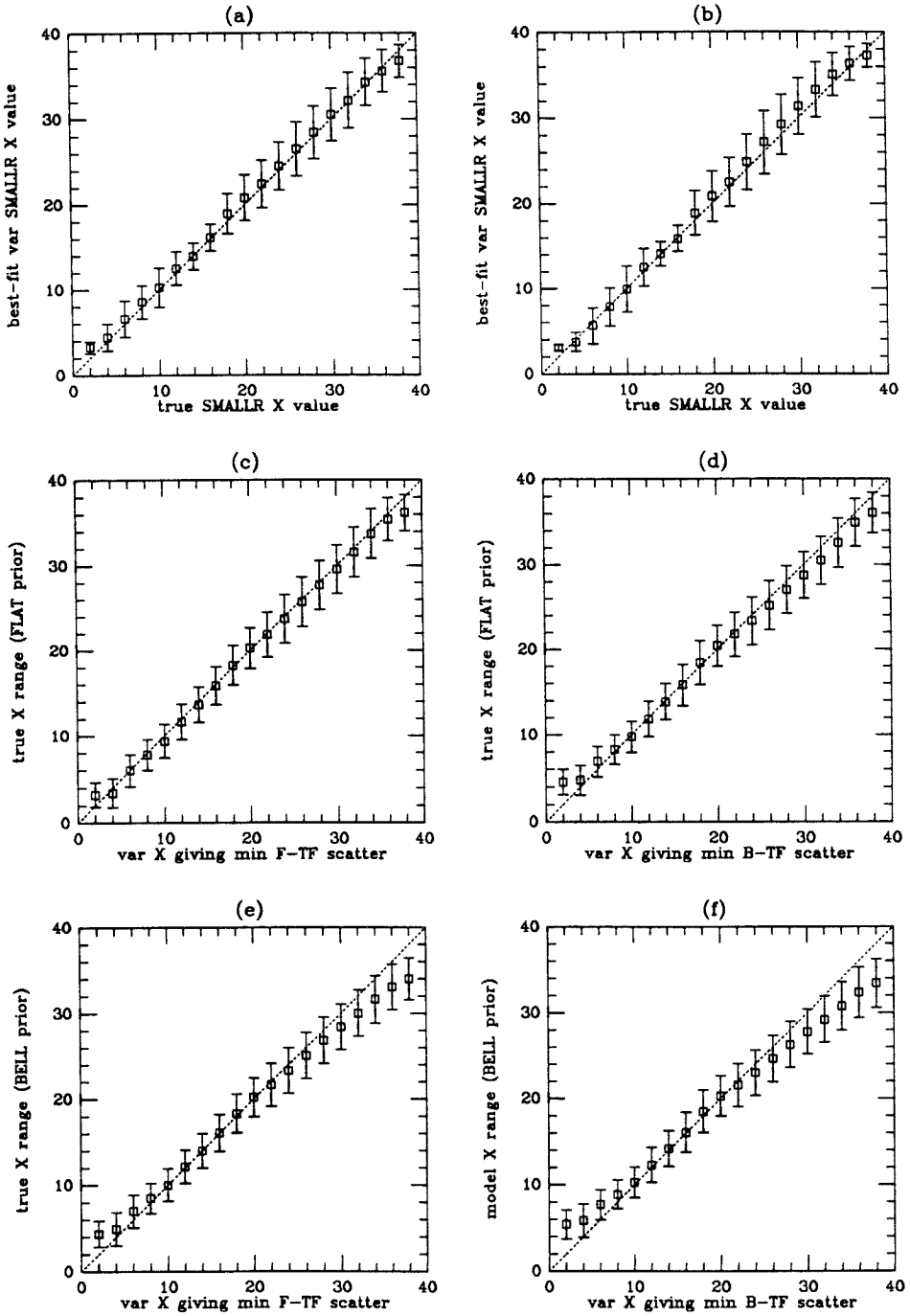

Figure 11

sample = 4KVL/0K0BJ (251 obj) / 1000 Monte-Carlo trials
I band Tully-Fisher scatter = 0.35 magnitudes

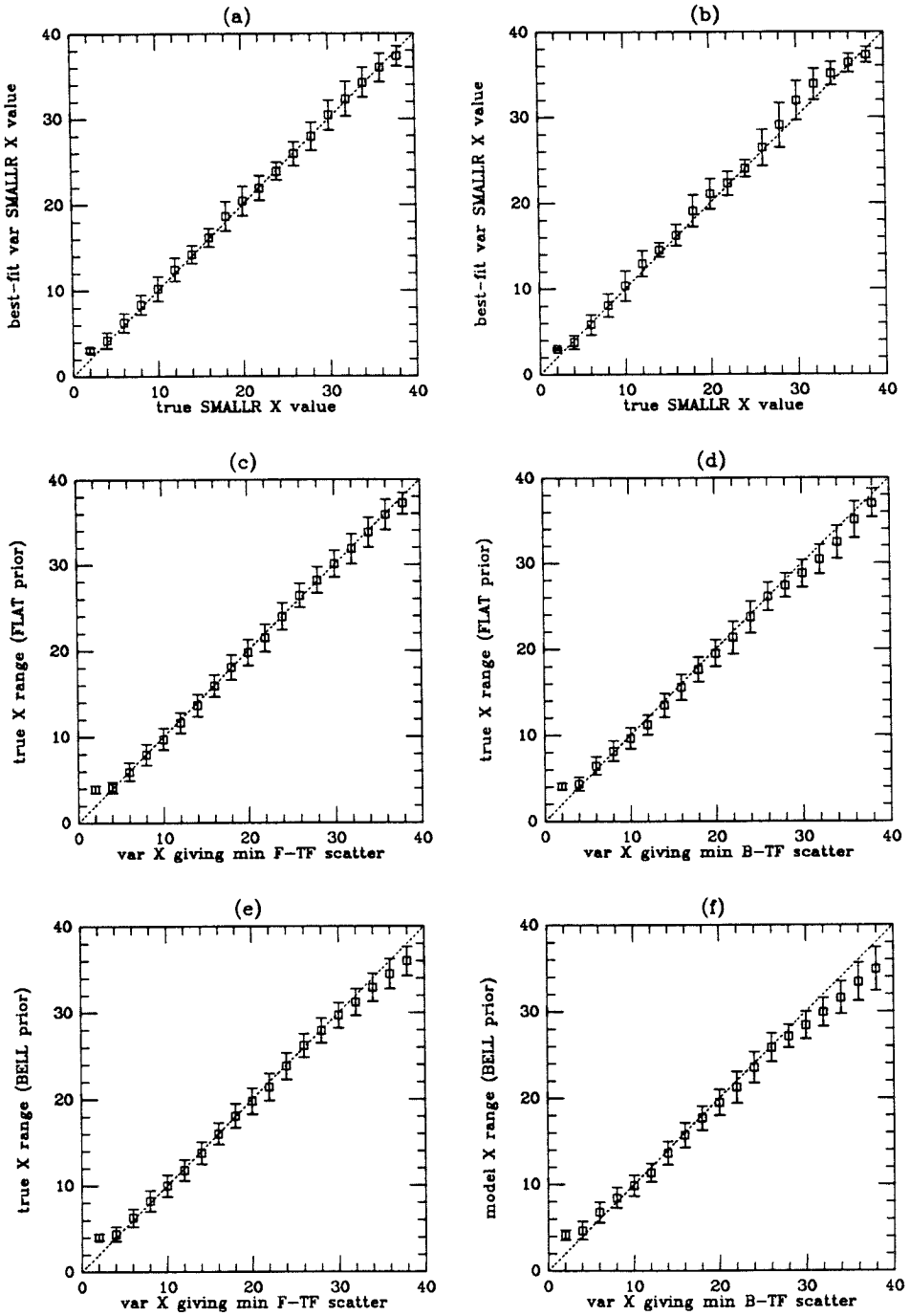

Figure 12

sample = 4KVL/JAN93 (91 obj) / 1000 Monte-Carlo trials
I band Tully-Fisher scatter = 0.25 magnitudes

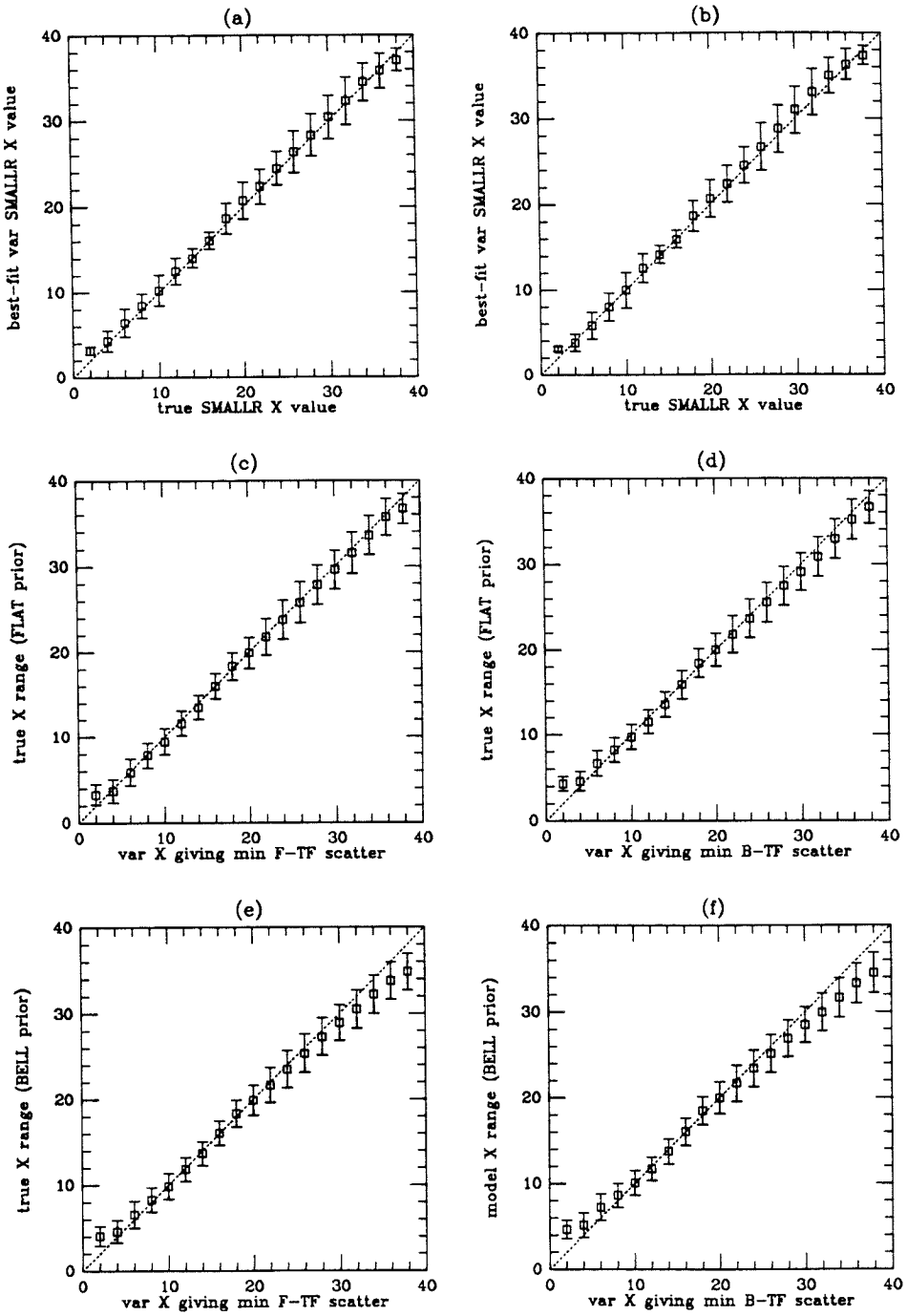

Figure 13

sample = 4KVL/0K0BJ (251 obj) / 1000 Monte-Carlo trials
I band Tully-Fisher scatter = 0.25 magnitudes

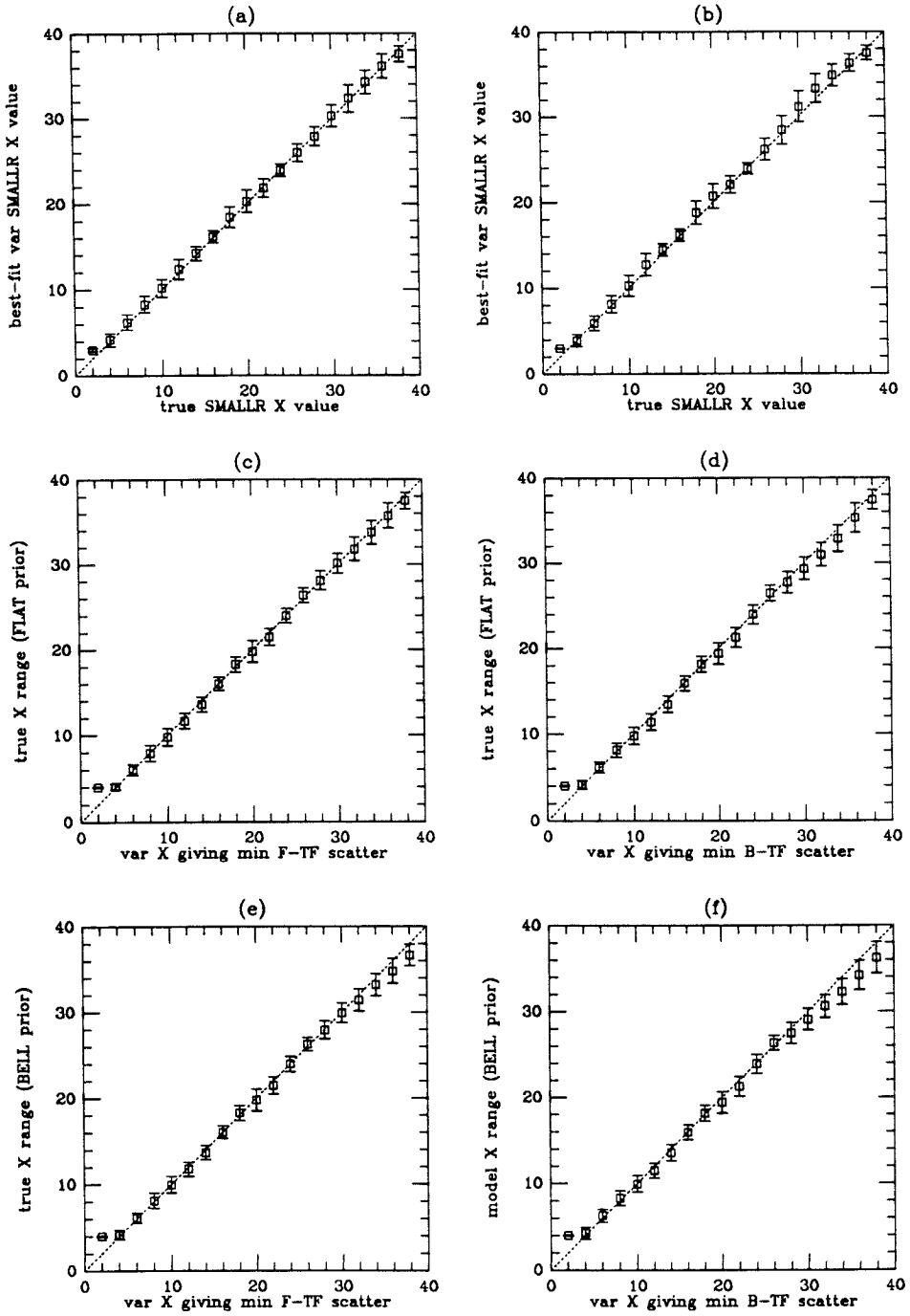

Figure 14

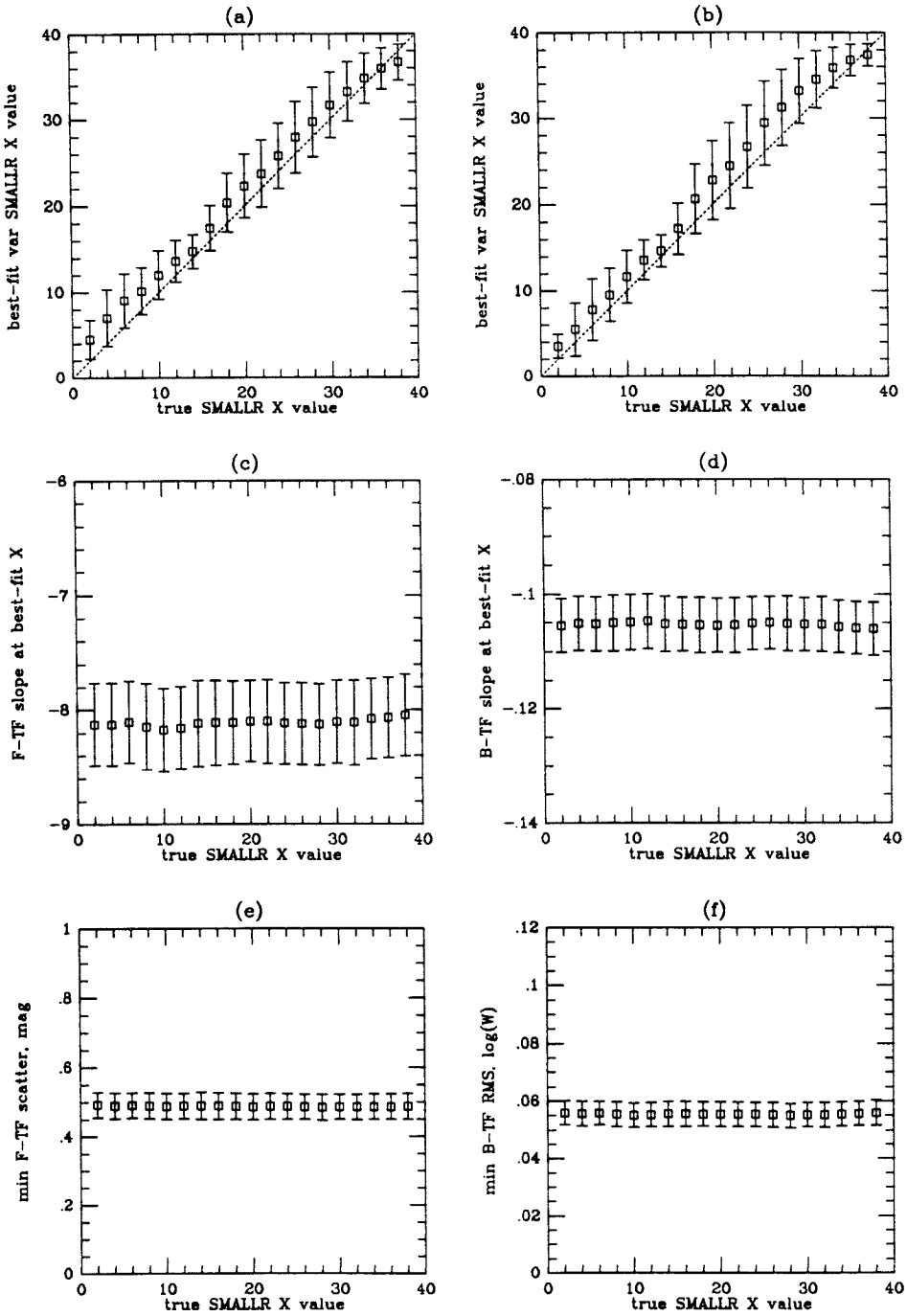
sample = 4KVL/JAN93 (91 obj) / 1000 Monte-Carlo trials
I band Tully-Fisher scatter = 0.45 magnitudes
true distances = IRAS + dipole (250 km/s, 210, +10)
(a)
best-fit var SMALLR X value
true SMALLR X value
(b)
best-fit var SMALLR X value
true SMALLR X value
(c)
F-TF slope at best-fit X
true SMALLR X value
(d)
B-TF slope at best-fit X
true SMALLR X value
(e)
min F-TF scatter, mag
true SMALLR X value
(f)
min B-TF RMS, log(W)
true SMALLR X value

Figure 15

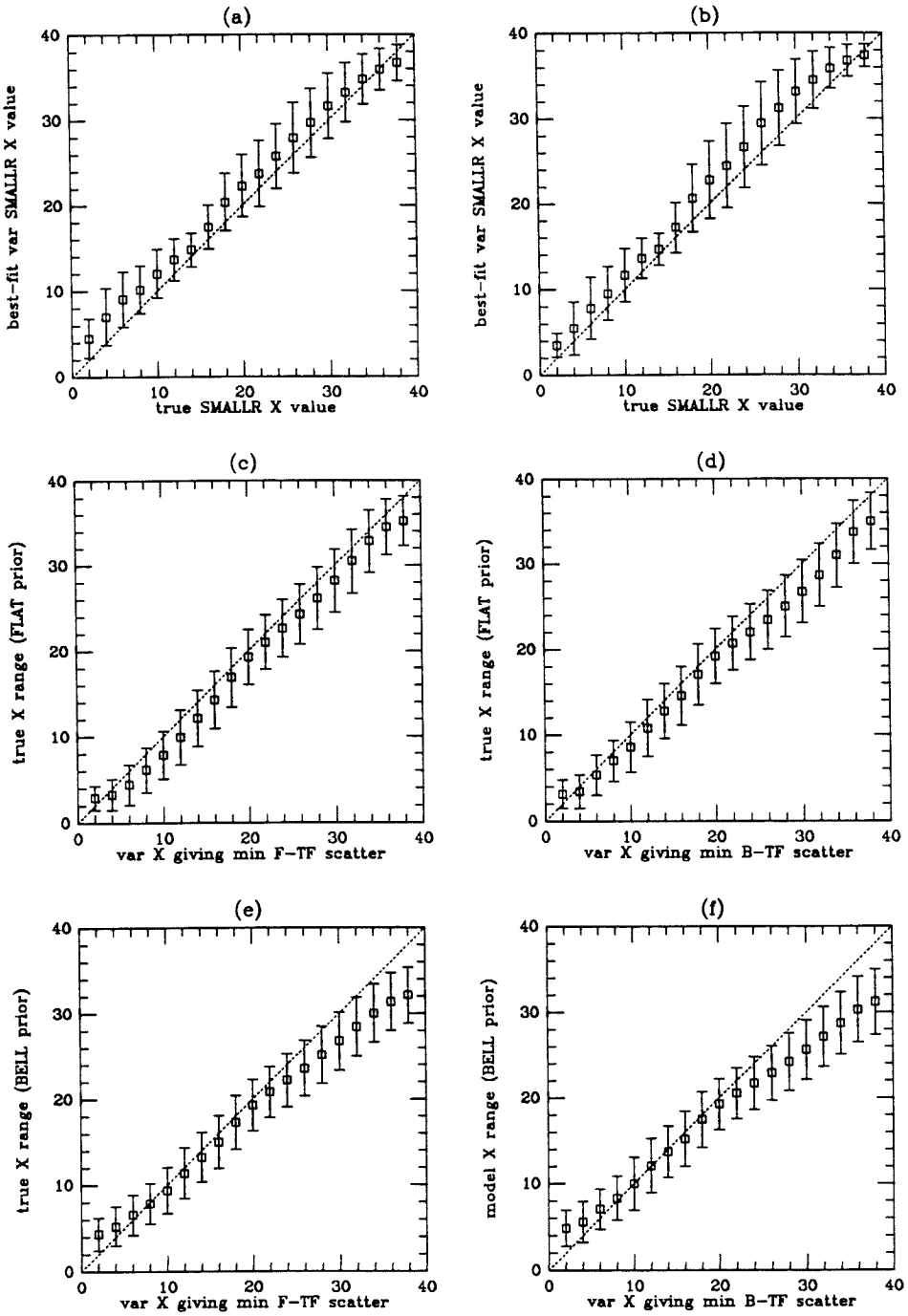
sample = 4KVL/JAN93 (91 obj) / 1000 Monte-Carlo trials
I band Tully-Fisher scatter = 0.45 magnitudes
true distances = IRAS + dipole (250 km/s, 210, +10)
(a)
best-fit var SMALLR X value
true SMALLR X value
(b)
best-fit var SMALLR X value
true SMALLR X value
(c)
true X range (FLAT prior)
var X giving min F-TF scatter
(d)
true X range (FLAT prior)
var X giving min B-TF scatter
(e)
true X range (BELL prior)
var X giving min F-TF scatter
(f)
model X range (BELL prior)
var X giving min B-TF scatter

Figure 16

Chapter 7 - Analysis of Current *IRAS* 4KVL Tully-Fisher Dataset

I. Introduction

We obtained HI data of 'acceptable' quality for $\sim$ 125 galaxies that also enjoy calibrated photometry from our CCD observations. Of these, $\sim$ 12 have only W_{50} values in HRCAT, a few lack BH extinction values, and a few lack updated photometric calibration as they lack V band frames and we did not generalize the photometric coefficients' update software to handle I-only cases. Our provisional galaxy sample of 91 objects (refered to as 'JAN93' in this thesis) falls far short of the 251 objects from our volume limited 4KVL sample suitable *a priori* for Tully-Fisher work, and this correspondingly drives the 'root N' noise up by $\sim$ 60% in estimates of β, as well as makes us more susceptible to shot noise in the sampling of the *IRAS*-predicted flowfield models. Despite these shortcomings, we have 136 points (because of multiple HI values for some objects) with which to measure one parameter (β, or $X = 20 \times \beta$), and our Monte Carlo models in the last chapter suggest that this allows us to place limits on β that are competitive with those offered by the 'POTENT' analysis of extant peculiar velocity data.

In this chapter, we describe the external HI data sources and the JAN93 subsample. We then interpret its apparent Tully-Fisher properties and utilize these, in conjunction with models like those of Chapter 6, to place limits on β. We then attempt to quantify which galaxies contribute most to this signal, and look for systematics in the TF residuals that may indicate biases or flowfield components not modeled by IRAS. We next inspect the ensemble properties of several well-defined subsets of the JAN93 subsample and discuss the doubts they cast upon straightforward interpretation of our dataset. Finally we conclude by describing avenues these results compel us to explore in future research.

II. External HI Sources and JAN93 Sample Definition

The Huchtmeier and Richter catalog of extragalactic neutral hydrogen observations (Huchtmeier and Richter 1989; hereafter HRCAT) attempts to comprehensively list all such observations through 1988. We searched a machine readable version of HRCAT provided by G. Bothun for all objects within 5 arcminutes of each 4KVL galaxy position and edited the list manually for misidentifications. We then screened for observations which we believe to be of acceptable quality by telescope, author and year of observation. The retained entries are listed separately for the Arecibo, Parkes, Jodrell Bank, Green Bank and Bonn telescopes in Tables I*a-e*, respectively. The entries are defined in detail in the introduction to HRCAT, which also gives the references. We note that the majority of HRCAT / Jodrell Bank observations we employ come from Lister Staveley-Smith and R. Davies; the Bonn data all originate with the compendium of Fisher and Tully (1981). We note that we list ALL suitable HRCAT entries, even if we currently lack photometry for an object. Only objects with a listed W_{20} were used in subsequent analysis. Objects with only W_{50} in HRCAT await graphical W_{50} to W_{20} conversion from the published profile plots.

Mathewson, Ford and Buchhorn (1992; hereafter MFB) performed an exhaustive survey of southern hemisphere galaxies, primarily to test for the 'backside infall' towards the putative 'Great Attractor'. HI data properties for MFB galaxies that also lie within the 4KVL sample are given in Table II. We thank Don Mathewson for providing us with a reprint of MFB and a computer tape of that papers' tables, from which Table II was drawn. (We also drew a handful of Galactic absorption coefficients for 4KVL objects not covered by BH/NED from MFB. MFB utilized the Galactic HI column density to estimate Galactic absorption.)

Table III lists 4KVL observations by J. R. Mould, G. Bothun, J. Huchra and team during a related program at Arecibo Observatory. '5' and '2' denote 50 and 20 % power levels, respectively, and 'M', 'P' indicate that this means 'percentage of mean power' or 'percentage of peak power' found in the profile. These data were reduced by Mould *et al.* using the Arecibo 'ANALYZ' package. We did not reprocess these data with SLAP. We thank the aforementioned observers for obtaining and

reducing these data on our behalf. We utilized '2P' in what follows for consistency with other sources.

Finally, the HI results described in Chapters 4 and 5 contribute to the sample.

When required, $1+z$ corrections were applied to the W_{20} values. HI entries were then matched with isophotal magnitudes at the $\Sigma_I = 23.5$ mag arcsec^{-2} level, corrected for internal and Galactic absorption and redshift related effects as in Chapter 3, Table I. Since repeated photometric observations enjoyed $\sim$ 0.05 magnitude consistency (Chapter 2), while multiple HI observations can differ wildly, we have averaged multiple photometric observations when available but retained one line in our TF files for each HI datum.

The resulting catalog as of January 1993 held 136 entries for 91 objects. We refer to this provisional sample as JAN93 throughout this thesis. Table IV lists the database numbers, names, positions and heliocentric redshifts of the 91 objects in the provisional JAN93 sample. Figure 1 shows its redshift histogram, with a median value around 2500 km sec^{-1} . HI nondetections clearly select against distant objects, robbing the sample of its *a priori* volume limited nature.

Systematic zeropoint offsets between datasets due to differences in dispersion, mean signal to noise ratio, and linewidth defining algorithms are certain to exist to some extent but are difficult to calibrate. Our simulations offer the hope that, within reason, our statistic 'X value at which apparent TF scatter is minimized' enjoys some robustness against this problem, but the situation is far from ideal, and the entire 4KVL OKOBJ 251 object sample should be reobserved at high dispersion in Hα, where the high occurence of line emission noted by the *IRAS* redshift survey should insure linewidths for a high fraction of the sample.

III. *IRAS* Model Distances and JAN93 Tully-Fisher Properties

A. Minimum TF scatter model

Corrected apparent isophotal I band CCD magnitudes at $\Sigma_I = 23.5$ mag arcsec^{-2} (hereafter referred to as apparent magnitudes m_I) were turned into absolute I band magnitudes M_I by using the distance $d(j; X_{var})$ (in km sec^{-1}) predicted for each galaxy j given $X = 20 \times \beta$:

$$M_I(j; X_{var}) = m_I(j) - 5log[10^{-5}\ d(j; X_{var})/75]. \qquad (7-1)$$

We note that setting H_0 to 75 affects the zero point of M_I but has no effect upon subsequent analysis.

Because the total TF error budget is dominated by a variable and poorly understood HI linewidth error, we perform unweighted fits to the data points in what follows. We note that our simulations showed no meaningful gain in constraining X resulted from weighing points according to their (in practice unknown) errors.

HI linewidths were corrected to face-on values by

$$W_0 = W_{obs}/sin(i_{disk}), \qquad (7-2)$$

where the inclination angle i_{disk} and its associated error are derived from the outer ellipses fit by 'GASP' to galaxy CCD images.

At a given SMALLR X_{var}, then, we have a list of points $[M_I(j; X_{var}), logW_0(j,k)]$, where k denotes independent HI observations for object j, *i.e.*, a Tully-Fisher dataset. Such tables were generated for the JAN93 subsample at integer X_{var} values from 2 to 39. Each had F-TF and B-TF lines fit by unweighted least-squares linefitting minimizing magnitude and $logW_0$ residuals, respectively. We assessed the *rms* scatter in magnitudes ($logW_0$ units) from the F-TF (B-TF) fits. The results are expressed in Figures 2*a-f*. We find that both the 'forward' and 'backward' TF fits favor X of 17 and that, at this best fit value, the F-TF relation has an apparent scatter of ~ 0.48 magnitudes. This scatter includes, of course, any systematic differences between the actual flowfield and that predicted by *IRAS*, and hence sets a upper limit on the scatter of the TF relation for

infrared luminous spiral galaxies (absent selection upon any significant TF second parameters; *cf.* Mould *et al.* 1991, appendix).

B. Monte Carlo Model for Error Budget and 'Response Profile'

We have performed Monte Carlo simulations generating synthetic datasets in exactly the manner of Chapter 6, but keeping X_{true} fixed at 17 and assessing ensemble averages and variances for the intercept, slope and scatter of the F-TF and B-TF at evenly spaced X_{var} values. a_1 (defined in Chapter 6) was set to -9.0 and σ_3, the intrinsic TF scatter, to 0.45 magnitudes. The results are shown in Figures 3*a-f*. The first four panels show the input ('true') values for the slope and intercept as dotted lines; as before, we find that the B-TF slope (and therefore its intercept) is biased. Both the models and the data show the close coupling of B-TF slope to F-TF scatter. However, the amplitude of the divergence between the F-TF and the (inverse of the) B-TF slopes (~ -4 versus ~ -12) is much greater in the data than in the models.

The detailed shape of the 'response profile' (TF scatter versus X_{var}) is rather different than seen in the data. The 'response profile' can be seen as the ideal *rms* mag difference between SMALLR models (such as plotted in Figures 2 of the last chapter) filled up in quadrature with intrinsic TF scatter and data error. The response profile may be skewed by LG motion with respect to the JAN93 sample above and beyond that predicted by Strauss *et al.* ; alternatively, nonlinear dynamics towards the Virgo cluster may be hashing up the central portion of a response profile whose asymptotic behavior more closely resembles that of an $X_{true} < 17$ model.

Although our simulation generates a minimum F-TF scatter much like seen in the data, the B-TF scatter is notably lower ($\sim 0.056 = 0.45/8$ in model versus ~ 0.067 in data). The difference corresponds to 0.037 in $logW_0$ (or $\sim$ 50 km sec^{-1} of additional linewidth noise and/or bias at $logW_0 = 2.75$), suggesting that in our actual experiment, the intrinsic TF scatter is something like $\sim$ 0.35 mag, but the linewidth noise and bias are each two or three times higher than suggested

by Eqns. 6-23, 6-24. Thus the external HI sources, particularly those from HRCAT, may suffer substantially higher noise and/or bias than our own HI data. That such is plausible is illustrated in Figure 4, where HRCAT W_{20} entries for galaxies we observed at Jodrell Bank are plotted versus the Jodrell values we obtained in 1989-90; we note that in all cases HRCAT entries trend towards higher W_{20}, and that the points on the diagonal come principally from Staveley-Smith and Davies (SSDI, SSDII), who used the same spectrometer and reduction methods as we. The absence of points to the left of the diagonal provides circumstantial evidence for the bias effects discussed towards the end of Chapter 4.

With this motivation we set $\sigma_3 = 0.35$ mag and multiplied the original model linewidth errors (Eqn. 6-23) by 2 and the original model linewidth bias (Eqn. 6-24) by 3 for a second set of models. The resulting figures do not significantly differ from Figures 3 and the apparent error ratio $\sigma^{app}_{F-TF}/\sigma^{app}_{B-TF}$ remains at exactly the same value of 8.7. Comparing with error ratios from our models (wherein the TF slope is known), we take the error ratio from the data $\sigma^{app}_{F-TF}/\sigma^{app}_{B-TF} = 7.2$ to indicate that the actual TF slope for our sample is perhaps somewhat shallower than -7; if $b^{true}_{F-TF} = -6.5$, then the F-TF slope suffers $\sim$ 2 units bias, while the (inverse of the) B-TF slope $b^{-1,\,true}_{B-TF}$ suffers $\sim$ 6 units bias; such asymmetric slope bias would accord with the predictions of Willick's (WT) simulations. (In fact, his simulations show the ratio of slope biases $[b^{-1,\,app}_{B-TF} - b^{-1,\,true}_{B-TF}]/\,[b^{app}_{F-TF} - b^{true}_{F-TF}]$ to be $\sim$ 3 at a 'cluster depth', or *rms* magnitude difference, of ~ 0.45 magnitudes.)

Our failure to generate F-TF / B-TF slope divergence in our models as great as that seen in our data is certainly a shortcoming of our analysis but one whose resolution lies beyond the scope of the present work. It may indicate that some conspiracy of the selection effects is rendering the effective $logW_0$ distribution or the 60μ luminosity function steeper than those used in our simulations.

C. 'Best Fit' TF Relation and Residuals Therefrom

The I band TF relation inferred by model SMALLR.17 is plotted for the 91 JAN93 objects (136 points) in Figure 5. The F-TF and B-TF fits are shown as dotted and dashed lines, respectively. We note the small dynamic range in $logW_0$ and speculate that it derives from the sharp effective $L_{60\mu}$ cutoff in the sample definition. The I band TF relations implied by models SMALLX (7,12,17,22,27,32) are shown in Figure 6 to illustrate the modest gains in apparent TF scatter provided by turning the β knob.

Figures $7a - r$ show F-TF (M_I) and B-TF ($logW_0$) residuals $\delta M_{I|logW_0}$, $\delta logW_{0|M_I}$ from the dotted and dashed lines, respectively, of Figure 5. These residuals are plotted versus cz, α, δ, l^{II}, b^{II}, $|b^{II}|$, i_{disk}, $F_{60\mu}$ and f_{HI}. The lack of correlation with i_{disk} show that in the mean, observables have been corrected in an unbiased fashion for galaxy inclination. The null results for HI and 60μ flux densities suggest that neither M_{HI} nor $L_{60\mu}$ is a significant second parameter to the I band TF relation. (Some HRCAT references lacked HI fluxes, hence the points with unphysical zero HI flux density.) The null F-TF result for $|b^{II}|$ suggests that BH absorptions in the mean are consistent at $|b^{II}| \gtrsim 10$ degrees.

The hints of sinusoidal B-TF residuals variation with position angles $(\alpha, \delta, l^{II}, b^{II})$ are not generally reflected in their F-TF counterparts, casting doubt on a dynamical origin for these sinusoidal patterns. However, Figures $8a - r$ juxtapose the B-TF residuals plots with plots of $logW_0$ itself versus the quantities cz, α, δ, l^{II}, b^{II}, i_{disk}, $F_{60\mu}$ and f_{HI}. These demonstrate that, although flowfield modeling pulls in some of the $logW_0$ scatter, the sinusoidal trends are intrinsic to $logW_0$ itself. (Note that the $logW_0$ plots are not model dependent.) Simulations as described in the last chapter, but with $\sim$ 250 km sec^{-1} excess LG motion (above and beyond that predicted by the *IRAS* models) with respect to the JAN93 sample can generate sinusoidal variations in $< logW_0 >$ versus position angle of a few tenths' amplitude, since $logW_0$ is slaved to L_{60} and deviant LG motion creates a dipolar difference between distance and redshift. We have not yet quantitatively accounted for the apparent sinusoidal variation in $logW_0$ seen in our data.

The greater than unit slope for the $log(M_{HI}) - logW_0$ relationship discussed in the last chapter generates a modest increase in $< logW_0 >$ with redshift when finite HI flux density limits are in effect. Our models predict a significantly sharper slope for $< logW_0 >$ versus cz (9×10^{-5}) than that seen in our data ($2 \times 10^{-5} \pm 8 \times 10^{-6}$; see Figure 8*a*). Nevertheless, the ensemble average for synthetic JAN93 datasets given $a_1 = -9.0$ is $< logW_0 >= 2.60$; our actual data give $< logW_0 >= 2.64$. This provides some *a posteriori* justification for our choice of $a_1 = -9.0$ in the models of this and the previous chapter.

D. Zonal Analysis of JAN93 Geographical Subsets

In section *B* we found that $X_{var} = 17$ yielded F-TF and B-TF relation of minimum scatter, but the asymptotic behavior of the 'response profile' (plot of σ_{TF}^{app} versus X_{var}) suggested a lower value. We would like to know if aspects of the 'response profile' may be attributed to different portions of the sample. In this section we study the 'response profiles' for various subsets of the JAN93 dataset.

F-TF and B-TF slopes, intercepts and scatters at X_{fit}^F, X_{fit}^B, respectively are listed for various subsets of JAN93 in Tables V$a - b$. Asterisks denote the JAN93 subsets whose X_{fit}^F and X_{fit}^B wildly disagree. The response profiles from which the numbers derive are plotted in Figures 9 - 14. The left columns in Figures 9- 14 show F-TF scatter versus X_{var}; the right columns show B-TF scatter versus X_{var}.

Figures $9a - f$ contrast the response profiles of the entire JAN93 dataset with those of the northern and southern celestial hemispheres. The hemispheres yield radically different profiles. Figures $10a - f$ provide the analogue for Galactic hemispheres. Monte Carlo experiments such as described in Chapter 6, sampling the *IRAS* predictions at the positions of the JAN93 objects at $\delta > 0$ do show a milder version of the sharp downward kink at $X \sim 15$, as do the 'perfect standard candle' curves in Figures $2d - i$ of Chapter 6, but do not predict a significant divergence between

the N and S values for X_{fit} unless an enormous ($>$ 500 km sec^{-1}) dipole term is added to the SMALLR distance predictions.

Figures $11a-l$ show response profiles for a range of subsets chosen by cz_{LG}. At redshifts beyond that of the Virgo cluster the profiles show somewhat consistent behavior, albeit with a poorly constrained minimum at $X_{var} < 20$. At redshifts below the JAN93 median of $\sim$ 2500 km sec^{-1} , however, the rapid rise of σ^{app}_{F-TF} at $X_{var} \gtrsim 20$ and the bump at $X \sim 15$ return with a vengeance. The trend for B-TF slope to hover at extreme values ~ -0.05 (= -1/20!) suggests that this subset is poorly fit by the IRAS predictions at any value of X_{var}.

Finally, we select objects by the cosine of their angular distance on the celestial sphere from the following points: the Perseus-Pisces (PP) system ($\alpha = 1^h, \delta = +20°$; Figures $12a-f$), the 'Great Attractor' ($l^{II} = 300°, b^{II} = +20°$; Figures $13a-f$), and M87 (Figures $14a-f$). In each case we consider the hemisphere centered on the point of interest (panels a, b), the complimentary hemisphere (panels c, d) and all points 30 or more degrees from the point of interest (panels e, f). Figures $12e-f$ show that exclusion of the Perseus-Pisces region yields a response profile most nearly like that of the whole dataset. Figures $13e-f$ likewise show that excluding the objects in the foreground of the 'Great Attractor' does not markedly alter the response profile. The extremely low X_{fit} for the P-P hemisphere (Figures $12a-b$) suggests that infall of objects between us and P-P into the latter is gentler than predicted by the *IRAS* models; this may be related to Willick's (WT; 1990) and Courteau's (CT) findings that galaxies in the P-P and its foreground show peculiar velocities more negative than might be expected given P-P's dominance in redshift maps.

Excising the Virgo cluster (*i.e.*, retaining objects whose angular distance from M87, θ_{M87}, exceeds 30 degrees; panels $14e-f$), however, yields a response profile whose form closely matches that obtained by adding $\sigma^{intr}_{TF} \sim 0.48$ mag in quadrature to the intrinsic response profiles for $X_{true} = 10$ depicted in Chapter 6, Figure $2a$. The Virgo results suggest that the unusual kink in the JAN93

response profile derives from this region, and that it pushes the X value yielding minimum TF scatter up towards $X_{fit} \sim 18$ from lower values.

The cluster exclusion results may simply indicate variations in the (infrared) 'M/L' ratio (where L in fact denotes the number density of $IRAS$ galaxies, not the luminosity density). Whether such variations can also account for the marked N/S hemisphere discrepancies seen in our data remains to be determined. That the exclusion of the sky region centered on the 'Great Attractor' did not significantly change the appearance of the response profile, nor shift its minimum from $X^F_{fit} = 17$, suggests that the structure does not possess a wildly discrepant 'M/L' value. The dramatic effect of excluding Virgo may result from the nonlinear dynamics encountered crossing the cluster center, or from a shortcoming of the $IRAS$ methodology in triple valued zones.

E. Iterative Ranking of Data Points by Sensitivity to X

We saw in Section 2 that the response profile shown in Figure 2e does not resemble that of ensemble averages of simulations with X_{true} set to 17. We seek to find which data points [$m_I(j)$, $logW_0(j;k)$], where k denotes independent HI sources for object j, provide the asympotic behavior of Fig. 2e, which suggests a lower value for β, and which generate the actual minimum of $X_{true} = 17$, and to rank the data points by some quantitative measure of the sensitivity they have to X_{var} ($i.e.$, to β).

From the F-TF line fits described by Figures 1(a, c, e), each data point (j,k) has a magnitude residual $\delta M^{X_{var}}_{(j,k)}$ at fixed linewidth. A plot of $|\delta M^{X_{var}}_{(j,k)}|$ versus X_{var} can then be called the 'response profile' of data point (j,k). The response profiles of individual data points show complicated behavior, but can be broken into three classes: (i) - those rising monotonically as X_{var} runs from 2 to 38; (ii) - those dropping monotonically along the same run of X_{var}, and (iii) - those showing a minimum at intermediate X_{var}. These three classes are illustrated schematically in Figure 15a. We find 31 (of 136) points fall in class (i), 34 in class (iii), and the remaining 71 in class (iii). Of those

71, 46 hit bottom at $X_{var} < 20$ and the remaining 26 at $X_{var} > 20$. Only 8 data points actually have their response profile hit bottom at $X_{var} = 17 \pm 1$. Thus the data lean towards X_{var} values below 20 (i.e., towards β less than unity), but the final sample response profile seems to result from an unstable balance between those of individual datapoints favoring extreme values.

We define two statistics to describe the response profiles $|\delta M^{X_{var}}_{(j,k)}|$ of points (j,k). One simply measures the total drop in 'distance' from the best fit TF line:

$$P_{(j,k)} = |\delta M^{max}_{(j,k)}| \; - \; |\delta M^{min}_{(j,k)}|, \qquad (7-3)$$

while the other attempts to normalize $P_{(j,k)}$ for how good the best fit is:

$$Q_{(j,k)} = P_{(j,k)} - |\delta M^{min}_{(j,k)}| = |\delta M^{max}_{(j,k)}| - 2|\delta M^{min}_{(j,k)}|. \qquad (7-4)$$

P more closely determines which points actually affected the solutions, while Q perhaps better determines which points end up fitting the models best. We admit the *ad hoc* nature of P and Q; they are not motivated by theory. Figure 15*b* depicts two hypothetical profiles which have equal P but different Q. The lower Q profile may ride higher than the other because it suffers from an abberent magnitude or linewidth measurement, because it is intrinsically over or under luminous at fixed linewidth compared to the global TF relation, or because it samples space at a point where the *IRAS* models poorly predict the flowfield.

To study the relationship between P, Q and the response profile for the JAN93 dataset as a whole, we performed the following iterative procedure:

1 - fit F-TF lines (*i.e.*, minimize M_I residuals) to entire JAN93 dataset at each X_{var} in [2,39];

2 - assess response profiles $|\delta M^{X_{var}}_{(j,k)}|$ and derivative statistics $P_{(j,k)}$ (or $Q_{(j,k)}$) for each point (j,k);

3 - rank data points (j,k) by P (or Q);

4 - select points within the upper 75% of ranked P (or Q) values;

5 - fit F-TF lines to the subset made in step (4) at each X_{var} in the range [2-39]; assess F-TF scatter of subset points about each line fit; record X_{var} yielding minimum scatter ($X_{fit}^{P,Q}$);

6 - assess magnitude residuals $|\delta M_{(j,k)}^{X_{var}}|$ of ALL points (j,k) from the F-TF line fit to the subset determined in step (5);

7 - return to step 2 and repeat N_{loop} times.

Step 6 gives each data point (j,k) a chance to rejoin the 'in' crowd on each pass. We feel this is important in light of the arbitrariness in just what data lie in hand at present, and in just how points are ranked by P or Q on the first pass.

After N_{loop} passes, the fraction of passes $f_{(j,k)}^{P,Q}$ during which a point (j,k) was in the accepted subset can be plotted versus (j,k), or versus any other property of point (j,k), such as object position or redshift. Global response profiles $[\sigma_{TF}^{app}(X_{var})]$ for subsets ranked by $f_{(j,k)}^{P,Q}$ then indicate what the statistically favored objects have to say about β.

We performed the above sequence of steps, using P and Q separately as quality parameters, with 250 iterations for each run.

Figure 16*a* shows a sky map of P on the first pass through the loop (all 136 points are present). Figure 16*b* shows the analogous map for Q. P ranges from 0 to about 1.3; Q, from $-.5$ to $\sim$1.3. These maps show that both P and Q increase about the major sources of gravitation in our volume: Virgo, Centaurus and Perseus-Pisces. A fourth region near $\alpha \sim 4^h$, $\delta \sim -50°$ seems to stand out as well.

In what follows, Figures 17 - 19 pertain to the P-rank sequence; Figures 20 - 22, to that for Q.

Figure 17*a* shows the inclusion frequency from P-looping, $f^P_{(j,k)}$, clustered about 0.75 as expected, for each of the 136 points. The vertical lines delimit the aformentioned separate HI data sources:

1 - HRCAT / ARECIBO,

2 - HRCAT / PARKES,

3 - HRCAT / JODRELL BANK,

4 - HRCAT / GREEN BANK ,

5 - HRCAT / EFFELSBERG,

6 - ROTH *et al.* / JODRELL BANK,

7 - ROTH *et al.* / PARKES,

8 - MATHEWSON / PARKES,

9 - MOULD *et al.* / ARECIBO.

Figure 18*a* shows the analogous plot for the Q loop. Although the plots differ, in each case we note that abrupt changes in the $f^{P,Q}_{(j,k)}$ profile tend to take place at boundaries between datasets. Thus $f^{P,Q}_{(j,k)}$ profiles may offer an *a posteriori* method for searching for systematic offsets between data sets that contribute to peculiar velocity maps with heterogeneous input. We note that both P and Q disfavor our Parkes and Jodrell data as well as the Arecibo data from HRCAT. Whether this is due to the location at which those datasets sample the flowfield or to systematic zeropoint offsets arising from resolution or width algorithm effects is not clear thus far.

Figures 17*b* and 18*b* show the runs of favored knob values $X^{P,Q}_{fit}$ for the P and Q loops, respectively.

Figures 19$a-c$ show the P loop inclusion frequency $f^P_{(j,k)}$ versus α_j, δ_j and cz_{LG_j}. The Q loop analogues is given by Figures 20$a-c$. While the Q loop inclusion frequency $f^Q_{(j,k)}$ shows essentially flat response to each of these variables, P loop inclusion frequency $f^P_{(j,k)}$ seems to disfavor points in the southern celestial hemisphere, points at high redshift, and, perhaps, points in the foreground of

the 'Great Attractor'. This may be a data quality filter, or simply selection against points where the flowfield is quieter and hence less informative about β.

Figure 21*a* shows the response profiles of the P loop subsets [$f^P_{(j,k)}$ > median (squares)] and [$f^P_{(j,k)}$ < median (crosses)]. These subsets' response profiles roughly parallel those of the northern and southern subsets seen in the previous section. They show that the points that tend to have the rate highest in P yield a response curve like that seen for the entire sample, with a minimum near $X_{var} = 17$. Figure 21*b* offers the response profiles for the P loop subsets ['upper 75% in ordered list of $f^P_{(j,k)}$' (squares)] and ['lower 75% in ordered list of $f^P_{(j,k)}$' (crosses)].

Figures 22$a - b$ are the analogous response profiles for the data points restricted by Q loop inclusion frequency. Q, in contrast with P, favors data that yield the smoother, lower $\sigma^{app}_{F-TF}(X_{var})$ response profile. This may be because the monotonic data point response profiles $|\delta M^{X_{var}}_{(j,k)}|$ in class (i) discussed above tend to have higher amplitude than those in class (ii). If Q indeed reflects how well points fit the model in an absolute as well as in a differential sense, the preferred profiles (squares) in Figures 22 suggest that the data points (j,k) favoring low X fit the IRAS models better than do their complement. This is consistent with the fact that the squares in Figures 22 well match the response profile expected for observations of model $X \sim 10$, whereas no pure *IRAS* model predicts a bump like that seen in the profiles that bottom out near $X_{var} \sim 17$.

Although not plotted, we note that neither $f^P_{(j,k)}$ nor $f^Q_{(j,k)}$ appears to correlate with V_{diff}, the separation between the distances D_1, D_2 (in km sec^{-1} ; defined in Chapter 6, Section II) averaged by Yahil *et al.* (1991) in their Method 2 to remain robust to triple valued zones. V_{diff} is a measure of how much the Hubble flow is retarded by an attractive mass, and tends to be greater near cluster centers. This lack of correlation surprises us.

Figures 23$a - c$ shows histograms of X^F_{fit} for the P and Q loops, as well as for 250 bootstrap samples obtained by sampling with replacement at random from the parent dataset. We see

that directed sampling of the dataset yields the modal value for X^F_{fit} more often than does blind subsampling.

P loop inclusion frequency $f^P_{(j,k)}$ is mapped on the sky in Figure 24*a*, and its Q loop analogue in panel *b*. We see the former map disfavors data in the south, while the latter map shows no directional trend. Recalling further that $f^Q_{(j,k)}$ appears blind to redshift cz as well, we suspect that the Q statistic indeed discriminates against points that poorly fit the *IRAS* models, not because of systematic departures from the *IRAS* predictions by the actual flowfield, but because of poor data quality.

F. Dipolar Trends in Tully Fisher Residuals

In this section we seek to measure whether a significant dipole exists in the F-TF, B-TF residuals ($\delta M_{I|logW_0}$, $\delta logW_{0|M_I}$) from the TF relations fit to the datapoints $[M_I(j;X_{var}), logW_0(j;k)]$ at X_{var} from 2 to 39. To do so we simply assess the residual magnitude

$$\delta M_I(j,k;X_{var}) = M_I(j;X_{var}) \; - \; (a_F + b_F \; logW_0(j;k)) \qquad (7-5)$$

or linewidth

$$\delta logW_0(j,k;X) = logW_0(j,k) \; - \; (a_B + b_B \; M_I(j;X)) \qquad (7-6)$$

where (a_F, b_F), (a_B, b_B) are the F-TF, B-TF (intercept, slope) pairs, respectively. The residuals' net dipoles are assessed as:

$$\mathbf{P}_F^{X_{var}} =$$

$$= \sum_{j,k} \delta M_{j,k}^{X_{var}} cos(\alpha_j) cos(\delta_j) \; \mathbf{r_x} +$$

$$+ \sum_{j,k} \delta M_{j,k}^{X_{var}} sin(\alpha_j) cos(\delta_j) \; \mathbf{r_y} +$$

$$+ \sum_{j,k} \delta M_{j,k}^{X_{var}} sin(\delta_j)\ \mathbf{r_z} \qquad (7-7)$$

or

$$\mathbf{P}_B^{X_{var}} =$$

$$= \sum_{j,k} \delta log(W_0)_{j,k}^{X_{var}} cos(\alpha_j) cos(\delta_j)\ \mathbf{r_x} +$$

$$+ \sum_{j,k} \delta log(W_0)_{j,k}^{X_{var}} sin(\alpha_j) cos(\delta_j)\ \mathbf{r_y} +$$

$$+ \sum_{j,k} \delta log(W_0)_{j,k}^{X_{var}} sin(\delta_j)\ \mathbf{r_z} \qquad (7-8)$$

where $\mathbf{P}$ denotes a vector and $\mathbf{r_x}$, $\mathbf{r_y}$, $\mathbf{r_z}$ are unit vectors in the $(\alpha = 0^h, \delta = 0°)$, $(\alpha = 6^h, \delta = 0°)$, $(\delta = +90°)$ directions, respectively.

The amplitude, right ascension and declination $\alpha_{dip}^{F,B}$, $\delta_{dip}^{F,B}$ of either $\mathbf{P}_{dip}$ can then be calculated from the amplitudes of the $\mathbf{r_x}$, $\mathbf{r_y}$,and $\mathbf{r_z}$ terms.

The F-TF results are shown in Figures $25a-d$. Stars in panel a show $|\mathbf{P}_{dip}^F|$, while those panel b shows the same quantity normalized by the *rms* TF scatter $\sigma_{F-TF}^{app}(X_{var})$ at each X_{var}. Squares and error bars show the ensemble mean and standard deviation obtained by scrambling the list of $\delta M(j,k;X_{var})$ while keeping the list of α_j, δ_j fixed. These panels suggest that the residuals show a significant dipole at all X_{var} and that the dipole amplitude is minimized at $X_{var} = 12$. Panels c and d show the actual (stars) and scrambled (squares) dipole directions α_{dip}^{F-TF}, δ_{dip}^{F-TF}. They show that while the amplitude appears robust, the direction is rather ill determined. Figures $26a-d$ offer the analogous plots for B-TF. We note that the F-TF dipole reflects where galaxies are systematically overluminous at a given linewidth, while the B-TF dipole reflects the opposite. At $X_{var} = 12$, the F-TF dipole lies at Galactic coordinates $(l^{II}, b^{II}) \sim (145, +25)$, whereas the B-TF dipole lies opposite $(l^{II}, b^{II}) \sim (260, +15)$; that these two average to $\sim (200, +20)$, within ~ 10 degrees of the 'local anomaly' given by Han and Mould (1990) may reflect a detection of LG motion along this axis

in excess of that predicted by $IRAS$ of $\sim$ 2500 x $[10^{(0.2\times0.06)} - 1]$ $\sim$ 70 km sec^{-1} (2500 being the sample median redshift, and 0.06, the dipole amplitude).

To our surprise, we found the plots of residuals' dipole amplitude differed little when points within 30 degrees of M87 were excluded from the fits and from the dipole assessment. This is shown in Figures 27 - 28. Furthermore, the (F-TF, B-TF) average dipole direction lies at (l^{II}, b^{II}) $\sim$ $(190, -10)$, again close to the direction of the 'local anomaly'. (These directional agreements may well be fortuitious.)

Before associating the dipolar trend in our data with systematic departures from the $IRAS$ predictions, however, we must wonder whether any anisotropy in TF residuals would be expected even from samples obeying pure $IRAS$ flowfields. This was investigated with Monte Carlo simulations identical to those described in the previous Chapter. Six runs were performed with true SMALLR X_{true} values of 7, 12, 17, 22, 27, and 32. The dipole amplitude response profiles $|\mathbf{P}_{dip}^{F-TF}|$ versus X_{var} are shown in Figures $29a - f$.

We see that even when the LG is given no excess motion with respect to the JAN93 sample (*i.e.*, when $U_{dip} = 0$; cf. Eqn. 6-38), the F-TF and B-TF residuals exhibit a dipole of amplitude comparable to those we see in our data. The amplitude curves show strong sensitivity to X_{var} only at low values of X_{true}, presumably because some measure of the LG's local motion is a small fraction of the average peculiar velocity at large β. Qualitatively the $X_{true} = 12$ model dipole response profile ($|\mathbf{P}_{dip}^{F-TF}|$ versus X_{var}) resembles that seen in the data, and the amplitudes are comparable. Thus the physical interpretation of the data profile as excess 'local anomaly' offered above is suspect.

The models do NOT produce a significant divergence between the F-TF and B-TF dipole directions such as seen in the data. Perhaps in this, as in the F-TF / B-TF slope divergence, severe nongaussian outliers are corrupting the results.

We note in closing that the current sample size seems inadequate for measuring quadrupolar deviations from the *IRAS* predictions; the experimental particulars required to constrain such trends will be calibrated with future simulations.

IV: Comments - Conclusions - Caveats

A. Constraints Upon the Density Parameter

We have assessed the apparent TF relations $[M_I(j;X_{var}), logW_0(j,k)]$ of the JAN93 dataset of 136 datapoints for 91 objects at SMALLR X_{var} values of 2 to 39 and sought the TF relation yielding minimum scatter. We found that scatter was minimized at $X_{var} = 17$, but that the response profiles (TF scatter versus X_{var}) showed asymptotic behavior more like those produced by Monte Carlo models wherein X in fact has substantially lower values. The apparent F-TF scatter bottomed out at $\sigma^{app}_{F-TF} \sim 0.48$ magnitudes.

Throwing caution to the winds and assuming that the models of Chapter 6 reflect all important noise sources, we may associate the $\sigma_3 = 0.45$ mag runs with this result and refer to that chapter's Table III for the relevant posterior probabilities. Interpolating between the listed results for $X^F_{fit} = 16$ and $X^F_{fit} = 18$, we find that the mean X_{true} to have yielded $X^F_{fit} = 17$ is 17.25 ± 2.93 (67%) given the 'bell' prior; this translates to '2σ' β limits of 0.86 ± 0.28. If the 'bias' factor b_{IRAS} is set to unity, the inferred $\sim 95\%$ confidence limits on Ω are $0.78^{+0.46}_{-0.40}$. We compare this result with that of the 'POTENT' / *IRAS* program of Dekel *et al.* (1993), who state their mean result and 95% confidence limits on β as $1.26^{+0.75}_{-0.59}$, and with Davis and Tonry, whose surface brightness fluctuations distance moduli to 37 elliptical galaxies give them β within the 0.9 - 1.1 range (Davis, informal seminar; precise definition of confidence limit unstated). We note further that the 'POTENT' result (but not ours nor Davis and Tonry's) is susceptible to what the amplification of apparent infall towards overdense regions by what is currently called 'inhomogeneous Malmquist bias' (*e.g.*, Roth

1991; Landy and Szalay 1992) and that Dekel *et al.* estimate this may boost Ω (at $b_{IRAS} = 1$) by ~ 0.16, at least at the low end of their β range. Thus these three estimates of β appear to enjoy consistency within their stated confidence intervals.

If we dictate that $\Omega \equiv 1$, we may then infer from our $X_{fit} = 17$ result constraints on the '*IRAS* galaxy / mass contrast ratio' (usually if unfortunately called the 'bias' factor; Kaiser 1984): $b_{IRAS} = 1.16^{+0.56}_{-0.28}$. Such limits are consistent with the parsimonious hypothesis that *IRAS* galaxies trace the underlying mass contrast field. We note that the optical to *IRAS* bias factor (b_{opt}/b_{IRAS}) is found to be $\sim 1.5 - 2.0$ (Strauss *et al.* 1992), and the optical bias factor is believed to not exceed ~ 1.5 (Valls-Gabaud, Alimi and Blanchard 1989).

Using the 'flat' prior in place of 'bell' does not significantly change our inferences; nor does using the B-TF result in place of F-TF. We favor F-TF, however, because of our lack of a detection threshold to apparent I magnitudes, and because our simulations suggest X^F_{min} is less biased than X^B_{min} in the presence of our particular experimental constraints.

The response profiles of the '$\theta_{M87} > 30$ degrees' and the 'frequency of inclusion by Q ranking > median' subsets better match those expected from pure *IRAS* models with $X_{true} \sim 10$, lacking the troublesome kink at $X_{var} \sim 15$. This, as well as the disappearance of the kink with removal of only a handful of objects at low redshift suggests that associating the minima in the JAN93 response profiles at $X_{var} = 17$ with a 'detection' of $\Omega \sim 0.8$ is premature.

The marked change in response profiles obtained by excluding low redshift objects may be related to the redshift analogue of 'inhomogeneous Malmquist' bias, wherein thermal dispersion in redshift carries points preferentially away from caustics in redshift space. This effect plagues 'method 2' programs at small distances (Faber and Burstein 1988). Virgo is the most prominent virialized region encompassed in our 4000 km sec^{-1} limit.

The '$\theta_{M87} > 30$ degrees' subset, yielding minimum σ^{app}_{F-TF} at $X_{var} = 12$, indicates a lower value of $\Omega \sim 0.4$; the 'Q loop' subset, yielding $X^{F-TF}_{fit} = 9$, an even lower value ($\Omega \sim 0.25$). Table III of Chapter 6 suggests the following '2σ' confidence intervals for β:

subset	2σ β range, 'bell'	2σ β range, 'flat'
$\theta_{M87} > 30°$	0.63 ± 0.24	0.60 ± 0.26
Q loop, $f >$ median	0.49 ± 0.23	0.44 ± 0.24

If $b_{IRAS} \equiv 1$, these translate to Ω ranges:

subset	2σ Ω range, 'bell'	2σ Ω range, 'flat'
$\theta_{M87} > 30°$	$0.46^{+0.33}_{-0.25}$	$0.43^{+0.35}_{-0.26}$
Q loop, $f >$ median	$0.30^{+0.28}_{-0.19}$	$0.25^{+0.28}_{-0.18}$

Alternatively, if $\Omega \equiv 1$, these numbers suggest 'bias' factors of $b_{IRAS} \sim 1.5$ ('$\theta_{M87} > 30°$') to $b_{IRAS} \sim 2$ ('Q loop'), with large confidence regions.

These latter, lower limits on Ω are only marginally consistent with those of Davis and Tonry and of the 'POTENT' group (although the possibility exists that the latter group has substantially underestimated the 'enhanced infall' bias upon Ω).

Our finding that Q loop inclusion frequency appears uncorrelated with position or redshift suggests it indeed serves as a data quality index. Thus we are inclined to favor these latter results, based on favored data points, over those based on the entire JAN93 dataset including the problematic Virgo region. Given our heterogeneous and incomplete dataset and the numerous qualifications we must state regarding our analysis, however, we hesitate to claim a precise determination of the density parameter. As in the case of the passionately contested Hubble parameter, it appears that

systematic effects outweigh shot noise and random errors in limiting the power of our experiment. We hope to have provided a modicum of realism in our simulations of this experiment, and must content ourselves with the fact that the universe, as well as the observations we make of it, has turned out to be rather messier.

B. Cautionary Remarks

We note again that our Monte Carlo calibrated '2σ' error bars with $\sim$ 100 galaxy distances imply greater precision than the 95% confidence region based on $\sim$ 500 objects stated by Dekel *et al.* As noted before, we expect that this results from the latter groups' heavy smoothing of the *IRAS* density and 'POTENT' velocity fields, and from the general deviation of actual 'Malmquist' biases from the corrections applied. Our method remains closer to the data (no peculiar velocities are explicitly calculated, nor smoothing applied) and sidesteps the 'enhanced infall' bias. We stress that our models may well be lacking one or more significant 'nuisance parameters' that would generate further imprecision or inaccuracy upon the X_{true} values associated with the measured X_{fit}. In particular, residual LG motion with respect to the sample should be treated as a further 'nuisance parameter' in the next round of posterior probability assessments.

The joint likelihood of $(X_{fit}, \sigma_{TF}^{app})$ should be assessed at each X_{true} so that the observed value of the apparent TF scatter at X_{fit} can be explicitly included into the posterior probabilities for X_{true}. This will, however, require substantially more computation than did the models described in Chapter 6.

As mentioned before, our models assume that neither 60 micron luminosity nor HI mass act as 'second parameters' for the $(M_I - logW_0)$ relation. The lack of correlation between TF residuals and HI or 60μ flux density supports these assumptions in at least an *a posteriori* sense. Relaxing them in a next generation of models will allow the possibility of 'HI detection threshold bias' or '60μ selection bias' upon Ω to be investigated.

Excluding the datapoints generating the wrinkle at $X_{var} \sim 15$ in the JAN93 response profiles amounts to using the profiles' asymptotes, rather than the precise minimum, to measure Ω. These asymptotes can be skewed by LG motion with respect to the 4KVL sample in excess of that predicted by *IRAS*. That the asymptotic behavior of response profiles shows considerable covariance between X_{true} and residual LG motion is shown in Figures $30a - f$, which depict simulations with (X_{true}; U_{dip}, l^{II}_{dip}, b^{II}_{dip}) settings of

(14; 0, 0, 0) - panels a, b;

(17; 300 km sec^{-1} , 30, -10) - panels c, d;

and

(11; 250 km sec^{-1} , 210,+10) - panels e, f,

respectively. (The axis of deviant motion was inspired once again by the 'local anomaly' of Han and Mould 1990.) Although the *IRAS* models are not expected to mispredict the local anomaly by several hundred km sec^{-1} , any possible covariance between the deviation vector $\mathbf{U}_{dip}$ and Ω needs to be assessed in the next generation of Monte Carlo simulations. We note, however, that any such covariance may be 'marginalized' by treating the deviant motion vector $\mathbf{U}_{dip}$ as a nuisance parameter in the Monte Carlo simulations predicting likelihood functions for $X_{fit}|X_{true}$. The prior distribution of such deviant motions might be inspired by the cosmic virial theorem or constrained by dense local peculiar velocity samples like that in preparation by Pierce (pers. comm.). We expect that in a sparse volume limited sample lacking many local ($cz \lesssim 500$ km sec^{-1}) objects, a LG deviation from *IRAS* models less than several hundred km sec^{-1} will be difficult to directly measure. This statement awaits qualification by further modeling, however.

C. Future Work

i - Computational

Although incomplete, our simulations do offer the tantilizing prospect that uniform, all sky samples of galaxies obeying well established $\sigma \sim 0.4$ mag distance indicator relations hold promise for constraining the density parameter. The effects several complications have upon our ability to constrain Ω, as well as observational tests that might reveal those complications, can be explored profitably by modelling. Such complications fall into three classes: (a) systematic flowfield departures from the *IRAS* predictions, which might most profitably be explored by successive terms in multipole expansion; (b) systematic differences between different subsets of the global dataset, whether due to procedural, instrumental or sample selection differences, and (c) complications, such as nonlinearity or second parameter effects, in the intrinsic distance indicator relations themselves.

We hope that an extension of our simple minded 'minimize distance indicator scatter' approach can be applied to the heterogeneous dataset currently used in the *IRAS* / 'POTENT' comparison, and that some version of our iterative data quality assessment can highlight systematic differences between the individual datasets used in that study. The all sky sample of $\sim$ 440 elliptical galaxies whose photometry and velocity dispersions were obtained by the 'Seven Samurai' seems an obvious candidate for our analysis, as long as these objects, which tend to populate denser regions than do spirals, enjoy reliable *IRAS* predictions. The 'Samurai' sample may also provide sufficient sky coverage to seek quadrupolar deviations from the *IRAS* models.

The use of Bayes' Theorem to assign relative probabilities to competing hypotheses seems a more natural way to interpret our results than do the traditional χ^2 based statistics, and we look forward to its (far from trivial) extension to additional parameters describing the flowfield and / or the distance indicator relations. In principle, the 'evidence' term normalizing the posterior probabilities in Bayes' Theorem can be compared between classes of models in order to quantify Occam's razor (Loredo 1989; Mackay 1992). A compelling (if heretical) alternative to the *IRAS* models is to suggest a Tully-Fisher zeropoint that varies monotonically with galaxy number density. Suppose that some values for a linear form of that relation's slope and intercept are found to best

fit the data. Comparing the 'evidence' can in principle determine which class of models (peculiar velocities versus zeropoint variations) more economically describes the data in hand.

ii - Observational

Because (a) Hα rotation curve amplitudes have been shown to closely correlate with HI profile linewidths, (b) *IRAS* galaxies exhibit strong emission lines, and (c) longslit spectroscopy is more nearly surface brightness than flux limited, lessening nondetection of distant objects, Hα longslit spectroscopy along galaxy major axis should be sought for the present sample and extensions thereof.

The completion of the 1.2 Jy *IRAS* redshift survey (Fisher, FT) allows galaxies of the same intrinsic 60 micron luminosity to be found out to a new volume limit of $4000 \times \sqrt{2/1.2} = 5200$ km sec^{-1} . This will double the volume of space sampled and envelop much larger portions of the regions dominated by the Perseus-Pisces and Hydra-Centaurus complexes. Photometric and spectroscopic measurements for this extended sample could be obtained in two or three years' (occasionally cloudy!) observation (twice yearly photometric and spectroscopic observations in each hemisphere).

The utility of distance indicators with greater precision is strongly evident in our simulations. A sample of even $\sim$ 100 distance moduli good to $\sim$ 0.10 mag provided by surface brightness fluctuation measurements on elliptical galaxies (Tonry 1991) could provide sensitive constraints upon Ω and upon flowfield departures from the *IRAS* models. Simulations like those presented in this thesis can quantify the gains expected from such a program, and perhaps guide the choice of 'test particles' in the presence of finite observing and reduction capacity.

Table I*a* - SELECTED ARECIBO OBSERVATIONS FROM *HRCAT*

obj	HI flux		$V_{\odot;HI}$	W_{50}	W_t	t	ref
1	Int	13.6	2308		426	5	488
29	Int	76.4	2461		460	5	488
43	Int	12.56	1532	291	313	3	452
47	Int	1.4	3901		283	5	488
49	Int	0.92	4026		184	3	565
70	Int	6.84	4076	116	325	3	452
73	Int	8.4	3823		473	5	488
75	Int	6.52	3923	311	344	3	454
100	Int	5.39	3952	133	89	3	467
109	Int	20.21	2251	348	324	3	467
114	Int	4.48	3960	341	290	3	467
139	Int	7.753	3104	261	315	4	489
141	Int	5.26	2722	316	294	3	467
150	Int	239.0	555		393	5	488
154	Int	13.40	3083	305	273	3	467
154	Int	12.86	3084	285	316	4	489
170	Int	25.59	4102	538	570	4	489
193	Int	282.0	804		459	5	488
226	Int	9.482	1978	300	327	4	489
276	Int	5.92	3709		279	3	529
361	Int	2.631	3824	400	406	4	489
424	Int	42.3	2381		385	5	488
426	Int	35.3	2678	430	477	4	543
433	Int	9.14	3554	270	285	3	454
434	Int	9.91	3487	292	306	3	454
437	Int	8.9	4261		326	3	488

Table I*b* - SELECTED PARKES OBSERVATIONS FROM *HRCAT*

obj	HI flux		$V_{\odot;HI}$	W_{50}	W_t	t	ref
65	Int	135.1	1634	369	396	4	550
79	Int	130.2	1502	203	230	4	550
164	Int	49.8	2632	390	417	4	552
169	Int	28.8	2889	402	427	4	550
169	Int	22.0	2629	411	451	4	552
195	Int	32.2	2153	289	307	4	552
231	Int	20.5	2688	265	282	4	550
285	Int	21.7	3005	486	508	4	550
368	Int	30.9	3836	330	348	4	550
411	Int	42.4	3012	394	421	4	552

Table Ic - SELECTED JODRELL BANK OBSERVATIONS FROM *HRCAT*

obj	HI flux		$V_{\odot;HI}$	W_{50}	W_t	t	ref
1	Int	16.6	2318	405	433	4	473
6	Int	62.6	1654	213	324	4	473
11	Int	756.3	238	420	444	4	523
29	Int	103.6	2474	444	488	4	473
51	Int	159.2	1273	378	404	4	473
68	Int	95.6	1204	417	466	4	523
78	Int	45.4	2457	316	346	4	473
150	Int	269.2	553	370	381	4	473
157	Int	41.1	2724	341	360	4	523
158	Int	126.2	1118	437	482	4	523
167	Int	16.6	3095	311	329	4	473
170	Int	30.7	4118	497	560	4	523
193	Int	246.0	801	437	468	4	473
203	Int	59.2	1864	393	428	4	523
206	Int	50.6	1730	409	442	4	473
207	Int	31.6	2696	495	517	4	523
303	Int	94.0	1153	257	281	4	473
310	Int	23.1	3378	420	445	4	473
313	Int	27.8	2267	290	327	4	473
332	Int	15.4	1912	383	397	4	473
345	Int	83.5	1924	423	471	4	473
353	Int	44.3	3144	334	355	4	473
354	Int	16.9	3292	642	681	4	473
370	Int	23.3	2373	370	403	4	523
421	Int	179.4	818	492	521	4	473
424	Int	32.3	2382	350	371	4	523
434	Int	13.2	3487	306	321	4	523

Table I*d* - SELECTED GREEN BANK OBSERVATIONS FROM *HRCAT*

obj	HI flux		$V_{\odot;HI}$	W_{50}	W_t	t	ref
1	FH	3.81	2316		403	4	373
1	Int	14.30	2301		444	4	515
50	Int	59.7	1402		331	4	203
56	Int	17.69	3884	319	287	3	498
67	Int	40.2	2079		386	4	203
67	FH		2099		383	4	373
67	Int	40.70	2087		402	4	515
68	FH	24.50	1210		440	4	373
68	Int	94.30	1202		451	4	515
73	Int	11.70	3816		513	4	515
78	Int	43.80	2459		349	4	515
78	FH	9.06	2460		326	4	373
98	Int	14.04	3087	411	390	3	498
101	Int	15.99	3791	395	317	3	498
106	Int	13.33	3567	348	315	3	498
109	Int	32.2	2261		358	4	203
110	Int	3.40	3064	175	141	3	498
117	Int	3.28	3510	264	250	3	498
134	Int	18.63	2170	278	240	3	498
150	Int	243.50	557		399	4	515
158	Int	109.2	1131		488	4	203
167	FH	5.18	3076		350	4	373
193	Int	306.60	800		475	4	515
203	Int	54.89	1868		411	4	466
207	FH	7.56	2696		509	4	373
223	Int	48.08	1460		348	4	466
228	FH	3.01	862		298	4	373
241	Int	2.78	2179		126	4	466
243	Int	16.60	2989		384	4	466
246	FH	8.79	2285		542	4	373
247	Int	105.10	1736		385	4	515
248	Int	92.50	1808		353	4	515
251	FH	2.87	2559		422	4	373
251	Int	27.68	2539		449	4	466
255	Int	14.29	2394		272	4	466
256	Int	61.12	1523		410	4	466
258	Int	4.74	1119		132	4	466
271		56.8	3106		472	4	203
271	FH	14.83	3117		446	4	373
271	Int	50.27	3111		471	4	466
284	Int	24.3	1743		330	4	203
284	FH	7.00	1743		347	4	373
284	Int	23.38	1736		349	4	466

Table I*d* - GREEN BANK OBSERVATIONS FROM *HRCAT*, page 2/2

obj	HI flux		$V_{\odot;HI}$	W_{50}	W_t	t	ref
303	Int	95.2	1155		291	4	203
311	Int	39.7	2557		417	4	203
333	Int	37.9	2117		465	4	203
337	Int	50.30	1734		444	4	515
338	Int	9.91	2780		412	4	466
345	FH	16.61	1930		467	4	373
345	Int	77.30	1921		460	4	515
348	FH	8.49	1867		358	4	373
348	Int	44.50	1961		582	4	515
348	Int	44.50	1859		377	4	515
353	Int	49.90	3392		368	4	515
354	Int	20.10	3313		697	4	515
360	Int	17.5	1963		362	4	203
370	Int	23.4	2376		386	4	203
385	Int	11.4	2426		307	4	203
385	FH	4.18	2409		292	4	373
385	Int	14.60	2417		304	4	515
418	Int	19.69	4219		485	3	498
421	Int	237.3	817		528	4	203
421	Int	257.60	817		537	4	515
424	Int	37.6	2382		362	4	203
426	Int	56.7	2665		472	4	203
434	Int	13.5	3491		323	4	203

Table I*e* - SELECTED EFFELSBERG OBSERVATIONS FROM *HRCAT*

obj	HI flux		$V_{\odot;HI}$	W_{50}	W_t	t	ref
3	FH	36.34	1587		504	4	373
22	FH	9.98	1487		383	4	373
29	FH	22.05	2473		490	4	373
44	FH	2.43	1983		119	4	373
51	FH	35.35	1275		402	4	373
65	FH	37.59	1639		403	4	373
66	FH	7.33	1503		224	4	373
90	FH	9.89	1216		316	4	373
150	FH	44.07	554		395	4	373
158	FH	26.41	1125		478	4	373
169	FH	7.05	2900		425	4	373
193	FH	66.53	804		466	4	373
199	FH	157.7	734		290	4	373
206	FH	12.48	1731		433	4	373
231	FH	5.06	2689		317	4	373
232	FH	20.67	1993		385	4	373
269	FH	11.36	2185		380	4	373
303	FH	20.96	1156		291	4	373
401	FH	11.63	2799		517	4	373
421	FH	51.41	819		531	4	373
427	FH	9.73	1609		280	4	373

Table II - 4KVL OBJECTS OBSERVED AT PARKES BY MATHEWSON *et al.*

obj	w_{50}	*err*		w_{20}	*err*		F_{HI}	*rms*	*S/N*
3	230	2	2	243	1	2	183.	18.	26.
12	214	4	3	226	3	0	18.	9.	9.
15	211	6	6	219	2	2	17.	8.	7.
51	192	2	2	204	2	5	176.	25.	23.
65	187	1	2	205	3	5	176.	22.	25.
66	91	2	3	105	3	6	35.	13.	15.
67	176	2	7	197	2	4	44.	12.	13.
77	127	3	4	142	3	3	59.	13.	19.
79	102	1	1	113	1	1	148.	19.	42.
90	152	3	4	163	2	2	42.	13.	12.
156	143	4	5	154	4	7	45.	24.	8.
157	175	2	2	180	2	0	23.	10.	10.
164	190	1	1	198	2	3	55.	14.	17.
169	205	2	2	215	3	4	18.	9.	10.
179	178	13	22	218	17	0	24.	10.	7.
195	134	3	10	162	11	4	28.	13.	9.
210	132	14	2	144	9	10	13.	7.	8.
232	180	2	2	187	2	2	66.	21.	14.
260	183	3	4	195	2	7	23.	9.	10.
269	181	5	5	199	3	3	60.	17.	12.
285	248	15	2	253	2	0	27.	9.	10.
287	149	5	6	173	3	9	24.	8.	11.
323	175	12	3	183	2	9	24.	9.	10.
334	174	2	10	188	4	0	19.	9.	8.
348	160	4	5	169	2	4	35.	13.	11.
350	169	3	2	176	2	8	47.	17.	11.
367	227	3	3	246	15	0	24.	9.	8.
379	120	2	1	146	6	2	24.	8.	16.
401	252	2	2	263	4	2	60.	13.	15.
409	197	2	2	202	3	0	21.	10.	8.
411	192	2	2	203	8	0	39.	19.	8.
412	61	2	2	80	7	2	36.	18.	16.
417	187	5	31	231	15	3	16.	8.	6.

Table III - MOULD *et al.* ARECIBO OBSERVATIONS OF 4KVL OBJECTS

obj	F_{HI}	*err*	V_{HI}	W_{5M}	W_{2M}	W_{5P}	W_{2P}
2	9.84	1.29	4207	339	366	314	348
8	3.31	1.42	4245	527	616	297	517
19	23.76	2.54	2519	386	423	360	394
28	55.30	3.38	3116	446	480	421	463
39	18.71	1.35	3739	297	330	262	313
43	22.87	1.79	1530	329	364	308	342
43	24.95	4.23	1534	331	375	308	358
82	7.23	2.00	2122	316	333	293	326
105	9.85	1.04	2905	568	586	546	572
109	23.35	0.82	2254	350	382	326	352
114	5.76	0.88	3961	348	383	322	372
130	3.93	0.70	4126	353	409	330	373
139	7.94	1.06	3107	272	295	252	286
141	4.86	1.27	2721	327	348	311	336
159	9.91	1.25	2404	263	286	243	268
170	27.42	1.11	4107	565	595	525	576
361	2.68	1.03	3819	412	479	380	414
378	7.09	1.19	2290	375	392	368	385
384	15.17	0.87	3915	442	470	406	440
408	1.56	0.70	3414	354	385	228	363
408	1.46	0.96	3441	254	383	219	304
433	13.39	1.76	3554	290	320	270	296
434	12.88	1.38	3489	316	338	295	329
435	6.41	1.40	4208	341	381	314	348
437	12.13	1.24	4264	330	354	314	339

Table IV - JAN93 sample object list

obj	NGC	UGC	ESO	α_{1950}	δ_{1950}	$cz_{\odot}$
1	7817	19		0 01	20 28	2342
2		148		0 13	15 48	4156
8	192	401		0 36	0 35	4210
19		903		1 19	17 19	2320
28	697	1317		1 48	22 06	3109
33	827	1640		2 06	7 44	3438
43	972	2045		2 31	29 05	1548
66	1385		482 16	3 35	-24 39	1503
69		2866		3 45	69 56	1232
71	1482		549 33	3 52	-20 38	1655
77	1559		84 10	4 17	-62 53	1292
79	1566		157 20	4 18	-55 03	1487
80	1591		484 25	4 27	-26 49	4127
82				4 29	29 23	2047
90	1792		305 06	5 03	-38 02	1216
91	1803		203 18	5 04	-49 38	4145
93			553 20	5 09	-20 29	3997
98		3354		5 43	56 05	3085
99	2076			5 44	-16 48	2422
106		3511		6 38	65 15	3567
109	2339	3693		7 05	18 51	2252
114		3780		7 14	34 10	3980
115	2369		122 18	7 16	-62 15	3237
117		3828		7 20	58 03	3217
132	2601		60 05	8 25	-67 57	3234
134	2633	4574		8 42	74 16	2156
136			563 28	8 48	-21 46	2611
139	2738			9 01	22 10	3102
141	2764			9 05	21 38	2707
150	2903			9 29	21 43	539
154	2990	5229		9 43	5 56	3198
159	3094	5390		9 58	16 00	2477
163			263 23	10 12	-43 22	3032
167	3183	5582		10 17	74 25	3076
169	3223		375 12	10 19	-34 00	2900
170	3221	5601		10 19	21 49	4085
179	3318		317 52	10 35	-41 22	2910
193	3521	6150		11 03	0 14	804
203	3672			11 22	- 9 31	1861
204	3683	6458		11 24	57 09	1686
206	3717		439 15	11 29	-30 01	1731
207	3735	6567		11 33	70 48	2696
210			266 15	11 38	-44 12	3113
223	4030			11 57	- 0 49	1463

Table IV - JAN93 sample object list - continued

obj	NGC	UGC	ESO	α_{1950}	δ_{1950}	$cz_{\odot}$
226	4045			12 00	2 15	1942
228	4102	7096		12 03	52 59	862
231			380 01	12 12	-35 13	2689
232	4219		267 37	12 13	-43 02	1993
246	4501	7675		12 29	14 41	2321
247	4527	7721		12 31	2 55	1730
248	4536	7732		12 31	2 27	1814
251	4602			12 38	- 4 51	2559
255	4658			12 42	- 9 48	2407
256	4666			12 42	- 0 11	1516
260			323 25	12 49	-38 45	4060
265	4793	8033		12 52	29 12	2487
269	4835		269 19	12 55	-45 59	2185
271	4939			13 01	-10 04	3117
280			219 41	13 10	-49 12	3518
284	5054			13 14	-16 22	1743
285	5064		220 02	13 16	-47 38	2982
287			269 85	13 16	-47 01	2893
303	5248	8616		13 35	9 08	1156
310	5351	8809		13 51	38 09	3631
313	5383	8875		13 55	42 05	2258
316	5430	8937		13 59	59 34	2819
332	5678	9358		14 30	58 08	1929
333	5676	9366		14 31	49 40	2104
334			272 23	14 36	-44 06	2911
337	5719			14 38	- 0 06	1688
338	5728			14 39	-17 02	2834
348	5861			15 06	-11 07	1855
349	5833		42 03	15 06	-72 40	3071
350			581 25	15 10	-20 29	2277
352	5900	9790		15 13	42 23	2551
353	5905	9797		15 14	55 41	3391
354	5908	9805		15 15	55 35	3309
357	5937			15 28	- 2 39	2754
360	5962	9926		15 34	16 46	1963
361	5990	10024		15 43	2 34	3809
367			69 02	16 15	-70 01	3452
370	6181	10439		16 30	19 55	2372
378	6574	11144		18 09	14 58	2261
396		11540		20 19	66 34	2490
401	6925		463 04	20 31	-32 09	2799
409			48 02	21 30	-76 34	3901
411	7083			21 31	-64 07	3049
414			404 36	22 07	-36 20	3028
422			534 09	22 35	-26 06	3395
426	7541	12447		23 12	4 15	2607
434	7678	12614		23 25	22 08	3489

Table V*a* - F-TF properties at X_{fit} for JAN93 subsets

subset	N_{pts}	N_{obj}	a_F	b_F	σ	X_{fit}
all JAN93	136	91	-10.95	-4.37	0.49	17
$\delta > 0$	70	47	-6.38	-6.07	0.42	18
$\delta < 0$	66	44	-12.36	-3.82	0.46	5
$b^{II} > 0$	95	63	-8.9	-5.14	0.43	17
$b^{II} < 0$	41	28	-12.4	-3.83	0.51	7
$cz_{LG} < 2500$	64	42	-17.2	-1.89	0.49	4
$cz_{LG} > 1000$	128	88	-10.5	-4.52	0.48	6
$cz_{LG} > 1500$	117	82	- 9.0	-5.11	0.44	22
$cz_{LG} > 2000$	94	66	-7.23	-5.76	0.43	12
$cz_{LG} > 2500$	72	49	-7.93	-5.52	0.43	12
$cz_{LG} > 3000$	45	33	-6.42	-6.08	0.41	17
$0 \geq \theta_{PP} \geq 90°$	44	31	-12.2	-3.88	0.52	5
$90 \geq \theta_{PP} \geq 180°$	92	60	-9.79	-4.82	0.42	17
$\theta_{PP} > 30°$	121	82	-11.22	-4.27	0.49	17
$0 \geq \theta_{GA} \geq 90°$	89	57	-13.0	-3.64	0.47	17
$90 \geq \theta_{GA} \geq 180°$	47	34	-8.52	-5.24	0.46	15
$\theta_{GA} > 30°$	115	79	-10.6	-4.50	0.51	17
$0 \geq \theta_{M87} \geq 90°$	95	63	-9.26	-5.01	0.42	17
$90 \geq \theta_{M87} \geq 180°$	41	28	-11.9	-4.03	0.54	6
$\theta_{M87} > 30°$	118	78	-10.3	-4.61	0.48	12

Table V*b* - B-TF properties at X_{fit} for JAN93 subsets

subset	N_{pts}	N_{obj}	a_F	b_F	σ	X_{fit}
all JAN93	136	91	0.77	-0.083	0.067	17
$\delta > 0$	70	47	0.54	-0.093	0.051	23
$\delta < 0$	66	44	0.66	-0.088	0.070	2
$b^{II} > 0$	95	63	0.55	-0.093	0.058	22
$b^{II} < 0$	41	28	0.99	-0.072	0.069	2
$cz_{LG} < 2500$	64	42	1.43	-0.053	0.074	19
$cz_{LG} > 1000$	128	88	0.73	-0.085	0.066	6
$cz_{LG} > 1500$	117	82	0.68	-0.087	0.058	39
$cz_{LG} > 2000$	94	66	0.56	-0.093	0.055	14
$cz_{LG} > 2500$	72	49	0.47	-0.097	0.057	12
$cz_{LG} > 3000$	45	33	0.67	-0.088	0.052	39
$0 \geq \theta_{PP} \geq 90°$	44	31	1.10	-0.067	0.068	2
$90 \geq \theta_{PP} \geq 180°$	92	60	0.46	-0.097	0.060	18
$\theta_{PP} > 30°$	121	82	0.80	-0.083	0.068	2
$0 \geq \theta_{GA} \geq 90°$	89	57	0.99	-0.074	0.068	2
$90 \geq \theta_{GA} \geq 180°$	47	34	0.75	-0.084	0.058	39
$\theta_{GA} > 30°$	115	79	0.83	-0.080	0.069	18
$0 \geq \theta_{M87} \geq 90°$	95	63	0.48	-0.096	0.057	22
$90 \geq \theta_{M87} \geq 180°$	41	28	1.08	-0.070	0.069	2
$\theta_{M87} > 30°$	118	78	0.73	-0.085	0.065	10

Figure Captions - Chapter 7

Figure 1: Histogram of 91 'JAN93' object redshifts cz_{LG} in Local Group frame.

Figure 2: F-TF and B-TF 'response profiles' for JAN93 dataset. 'F-TF' denotes linefits minimizing y *rms* residuals, $x = logW_0$, $y = M_I = m_I - 5\ log(d_{model})$; 'B-TF' denotes linefits minimizing y *rms* residuals, $y = logW_0$, $x = M_I = m_I - 5\ log(d_{model})$. X_{var} is index of $IRAS$ (SMALLR) model predicting distances d_{model}. (a) F-TF intercept versus X_{var}; (b) B-TF intercept versus X_{var}; (c) F-TF slope; (d) B-TF slope; (e) F-TF *rms* residuals amplitude (hereafter 'scatter of TF relation'); (f) B-TF scatter versus X_{var}. Both F-TF and B-TF show minimum scatter at $X_{var} = 17$.

Figure 3: 'Response profile' of Monte Carlo 'observation' of an $X_{true} = 17$ universe sampled at the positions and redshifts of the JAN93 objects. Panels (a-f) as defined in caption to Figure 2. Dotted lines in panels (a-d) reflect 'true' values of intercept and slope imposed in model. As before, B-TF slope bias towards steeper values (in mag / logW units) is minimized at $X_{var} = X_{true}$.

Figure 4: Linewidth values W_{20} from our Jodrell Bank 1989/90 runs versus W_{20} for same objects, where available, from Huchtmeier and Richter 1989 (HRCAT). The diagram provides indirect evidence for bias effects discussed in Chapter 4.

Figure 5: Apparent Tully Fisher [M_I, $logW_0$] diagram for JAN93 sample (91 objects; 136 points). Distances predicting M_I given observed m_I derive from the SMALLR $X = 17$ model. Dotted line is F-TF fit; dashed line is B-TF fit.

Figure 6: Apparent Tully Fisher [M_I, $logW_0$] diagrams for JAN93 sample. Distances predicting M_I given observed m_I derive from the SMALLR models: (a) $X_{var} = 7$, (a) $X_{var} = 7$, (b) $X_{var} = 12$, (c) $X_{var} = 17$, (d) $X_{var} = 22$, (e) $X_{var} = 27$, (f) $X_{var} = 32$.

Figure 7(1): F-TF residuals ($\delta M_{I|logW_0}$), left column, and B-TF residuals ($\delta logW_{0|M_I}$), right column, from the F-TF, B-TF fits to the JAN93 dataset at $X_{fit} = 17$, versus: (a-b) cz_{LG}, (c-d) α, (e-f) δ.

Figure 7(2): F-TF residuals ($\delta M_{I|logW_0}$), left column, and B-TF residuals ($\delta logW_{0|M_I}$), right column, from the F-TF, B-TF fits to the JAN93 dataset at $X_{fit} = 17$, versus: (g-h) l^{II}, (i-j) b^{II}, (k-l) $|b^{II}|$.

Figure 7(3): F-TF residuals ($\delta M_{I|logW_0}$), left column, and B-TF residuals ($\delta logW_{0|M_I}$), right column, from the F-TF, B-TF fits to the JAN93 dataset at $X_{fit} = 17$, versus: (m-n) i_{disk}, (o-p) $logF_{60\mu}$, (q-r) f_{HI}.

Figure 8(1): Corrected linewidths $logW_0$, left column, and B-TF residuals ($\delta logW_{0|M_I}$), right column, from the F-TF, B-TF fits to the JAN93 dataset at $X_{fit} = 17$, versus: (a-b) cz_{LG}, (c-d) α, (e-f) δ.

Figure 8(2): Corrected linewidths $logW_0$, left column, and B-TF residuals ($\delta logW_{0|M_I}$), right column, from the F-TF, B-TF fits to the JAN93 dataset at $X_{fit} = 17$, versus: (g-h) l^{II}, (i-j) b^{II}, (k-l) $|b^{II}|$.

Figure 8(3): Corrected linewidths $logW_0$, left column, and B-TF residuals ($\delta logW_{0|M_I}$), right column, from the F-TF, B-TF fits to the JAN93 dataset at $X_{fit} = 17$, versus: (m-n) i_{disk}, (o-p) $logF_{60\mu}$, (q-r) f_{HI}.

Figure 9: F-TF scatter, magnitudes, left column, and B-TF scatter, $logW_0$ units, right column, about F-TF, B-TF line fits, respectively, to subsets of JAN93 dataset as functions of X_{var} (hereafter called 'subset response profiles'): (a-b) entire JAN93 sample; (c-d) objects at $\delta > 0$; (e-f) objects at $\delta < 0$.

Figure 10: JAN93 subset response profiles: (a-b) entire JAN93 sample; (c-d) objects at $b^{II} > 0$; (e-f) objects at $b^{II} < 0$.

Figure 11(1): JAN93 subset response profiles: (a-b) objects with $cz_{LG} < 2500$ km sec^{-1} ; (c-d) objects with $cz_{LG} > 1000$ km sec^{-1} ; (e-f) $cz_{LG} > 1500$ km sec^{-1} .

Figure 11(2): JAN93 subset response profiles: (g-h) objects with $cz_{LG} > 2000$ km sec^{-1} ; (i-j) objects with $cz_{LG} > 2500$ km sec^{-1} ; (k-l) $cz_{LG} > 3000$ km sec^{-1} .

Figure 12: JAN93 subset response profiles delimited by sky angle θ_{PP} of objects from center of Perseus-Pisces system: (a-b) $\theta_{PP} < 180°$; (c-d) $\theta_{PP} > 180°$; (e-f) $\theta_{PP} > 30°$.

Figure 13: JAN93 subset response profiles delimited by sky angle θ_{GA} of objects from the nominal position of the 'Great Attractor': (a-b) $\theta_{GA} < 180°$; (c-d) $\theta_{GA} > 180°$; (e-f) $\theta_{GA} > 30°$.

Figure 14: JAN93 subset response profiles delimited by sky angle θ_{M87} of objects from M87, equated with the center of the Virgo cluster: (a-b) $\theta_{M87} < 180°$; (c-d) $\theta_{M87} > 180°$; (e-f) $\theta_{M87} > 30°$.

Figure 15: Schematic 'F-TF individual datapoint (j,k) response profiles' $|\delta M|^{X_{var}}_{I|logW_0}(j,k)$. (a) monotonically ascending, monotonically descending and nonextreme minimum profiles (types *i* - *iii*, respectively); (b) 'Sensitivity' $[P(j,k) = |\delta M|^{max}_{I|logW_0}(j,k) - |\delta M|^{min}_{I|logW_0}(j,k)]$ and 'quality' $[Q(j,k) = P(j,k) - |\delta M|^{min}_{I|logW_0}(j,k)]$ parameters illustrated.

Figure 16: (a) Sky map of 'sensitivity' parameter P for 136 JAN93 data points (j,k) on first pass through iterative P loop. Symbol size is proportional to P. (b) Sky map of 'quality' parameter Q on first pass through Q loop. Symbol size is proportional to $Q - 0.5$.

Figure 17: Results from successive F-TF solutions to JAN93 subsets iteratively chosen by relative $P(j,k)$ value (hereafter 'P loop'): (a) frequency of inclusion versus datapoint index for 136 JAN93

datapoints; vertical lines delimit HI data sources listed in Chapter 7 text; (b) run of X_{fit}^{sub} values yielding minimum F-TF scatter versus iteration number.

Figure 18: Results from successive F-TF solutions to JAN93 subsets iteratively chosen by relative $Q(j,k)$ value (hereafter 'Q loop'): (a) frequency of inclusion versus datapoint index; (b) run of X_{fit}^{sub} values yielding minimum F-TF scatter versus iteration number.

Figure 19: P loop inclusion frequency (as plotted in Figure 17*a*) $f_{(j,k)}^{P}$, versus: (a) α, (b) δ, (c) cz_{LG}.

Figure 20: Q loop inclusion frequency (as plotted in Figure 18*a*) $f_{(j,k)}^{Q}$, versus: (a) α, (b) δ, (c) cz_{LG}.

Figure 21: F-TF response profiles (F-TF scatter versus X_{var}) for subsets of JAN93 chosen by P loop inclusion frequency $f_{(j,k)}^{P}$. (a) $f_{(j,k)}^{P} >$ median value, squares, and $f_{(j,k)}^{P} <$ median value, crosses. (b) Points (j,k) in upper 75% of dataset as ranked by $f_{(j,k)}^{P}$, squares, and points in lower 75% so defined, crosses.

Figure 22: F-TF response profiles (F-TF scatter versus X_{var}) for subsets of JAN93 chosen by Q loop inclusion frequency $f_{(j,k)}^{Q}$. (a) $f_{(j,k)}^{Q} >$ median value, squares, and $f_{(j,k)}^{Q} <$ median value, crosses. (b) Points (j,k) in upper 75% of dataset as ranked by $f_{(j,k)}^{Q}$, squares, and points in lower 75% so defined, crosses.

Figure 23: Histograms of X_{fit}^{sub} values yielding minimum F-TF scatter to subsets of JAN93 dataset chosen by (a) P loop iteration, (b) Q loop interation, and (c) blind subsampling with replacement ('bootstrap').

Figure 24: (a) Sky map of P loop inclusion frequency for 136 JAN93 data points (j, k). Symbol size is proportional to $f^P_{(j,k)} - 0.5$ (b) Sky map of Q loop inclusion frequency. Symbol size is proportional to $f^Q_{(j,k)} - 0.55$.

Figure 25: 'F-TF dipole response profiles', or properties of the net dipole $\mathbf{P}^{F-TF}_{dip}$ of the magnitude residuals from the F-TF line fits versus X_{var}, for the entire JAN93 dataset. Stars represent actual dipole; squares and error bars, the first and second moments from 100 dipoles assessed by randomizing the list of magnitude residuals while keeping (α, δ) fixed. (a) dipole amplitude, magnitudes; (b) dipole amplitude divided by F-TF scatter at same X_{var}; (c) dipole right ascension α, degrees; (d) dipole declination δ, degrees.

Figure 26: 'B-TF dipole response profiles', or properties of the net dipole $\mathbf{P}^{B-TF}_{dip}$ of the $logW_0$ residuals from the B-TF line fits versus X_{var}, for the entire JAN93 dataset. Stars represent actual dipole; squares and error bars, the first and second moments from 100 dipoles assessed by randomizing the list of $logW_0$ residuals while keeping (α, δ) fixed. (a) dipole amplitude, $logW_0$ units; (b) dipole amplitude divided by B-TF scatter at same X_{var}; (c) dipole right ascension α, degrees; (d) dipole declination δ, degrees.

Figure 27: Analogue of Figure 25 ('F-TF dipole response profile') for subset of JAN93 database with $\theta_{M87} > 30°$. (a) dipole amplitude, magnitudes; (b) dipole amplitude divided by F-TF scatter at same X_{var}; (c) dipole right ascension α, degrees; (d) dipole declination δ, degrees.

Figure 28: Analogue of Figure 26 ('B-TF dipole response profile') for subset of JAN93 database with $\theta_{M87} > 30°$. (a) dipole amplitude, magnitudes; (b) dipole amplitude divided by B-TF scatter at same X_{var}; (c) dipole right ascension α, degrees; (d) dipole declination δ, degrees.

Figure 29: 'F-TF dipole amplitude response profiles' ($|\mathbf{P}^{F-TF}_{dip}|$ versus X_{var}) for Monte Carlo simulations of observations of universes obeying pure *IRAS* (SMALLR) models with X_{var} values:

(a) $X_{var} = 7$, (b) $X_{var} = 12$, (c) $X_{var} = 17$, (d) $X_{var} = 22$, (e) $X_{var} = 27$, (f) $X_{var} = 32$. Squares and error bars represent ensemble mean and standard deviation therefrom.

Figure 30: Partial 'response profiles' (F-TF scatter, left column, and B-TF slope, right column) for Monte Carlo 'observations' of universes obeying '$IRAS$ + dipole' models at the positions and redshifts of the 91 JAN93 objects. (X; U_{dip}, l^{II}_{dip}, b^{II}_{dip}) values for three models are listed: (a-b) (14; 0, 0, 0); (c-d) (17; +250, 210, +10); (e-f) (11; -300, 210, +10).

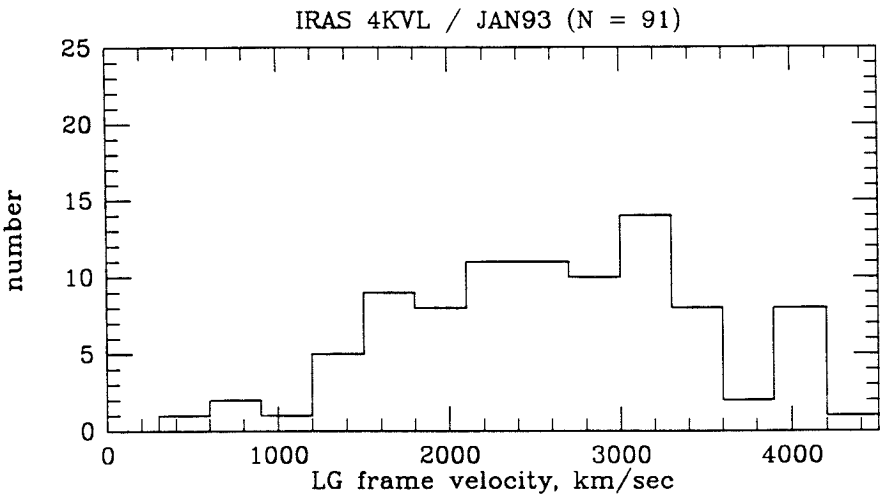
IRAS 4KVL / JAN93 (N = 91)
number
25
20
15
10
5
0
0
1000
2000
3000
4000
LG frame velocity, km/sec

Figure 1

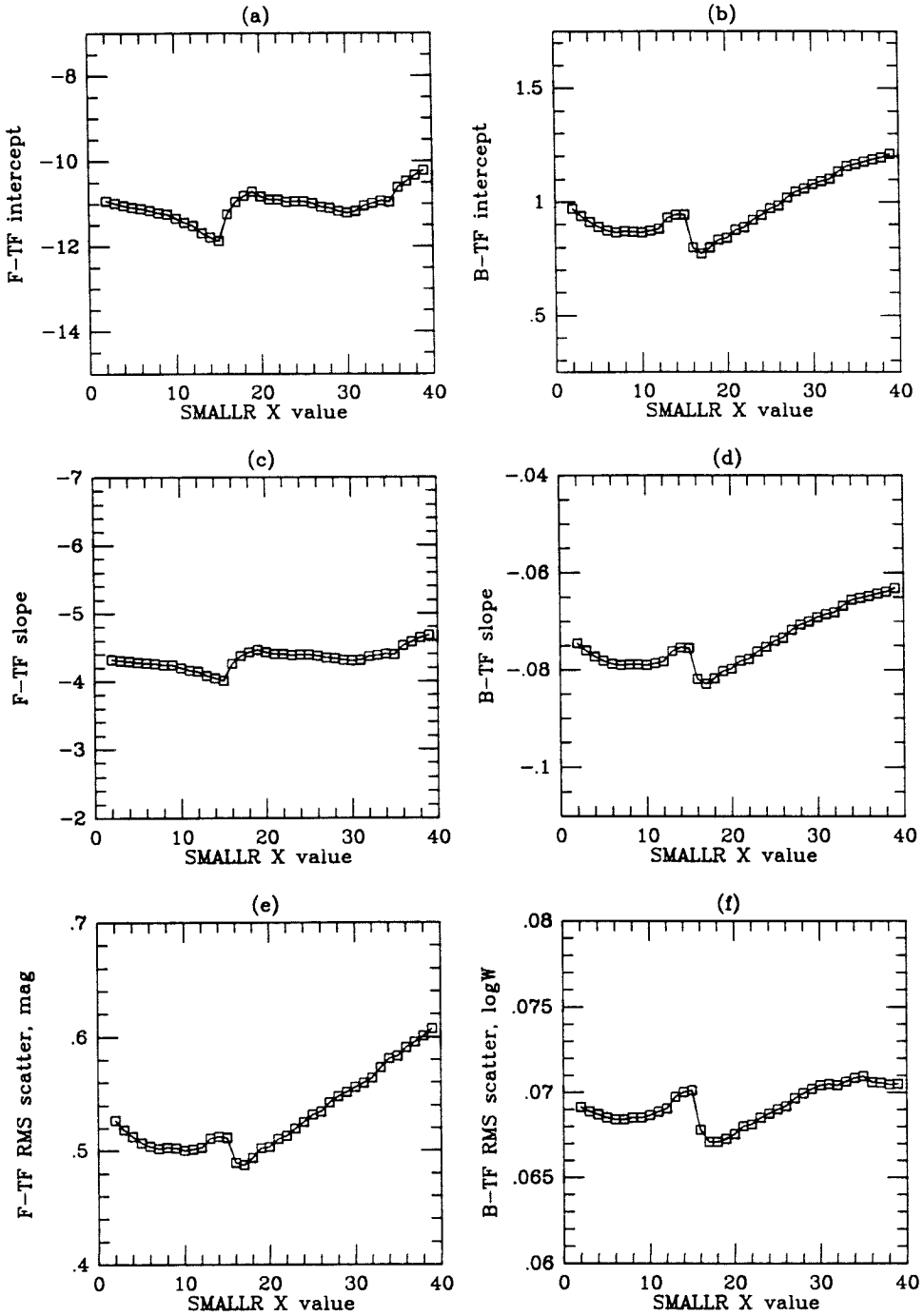
SAMPLE = 4KVL/JAN93 (91 obj)
I band Tully-Fisher response profiles
left = F-TF (mag resids) / right = B-TF (logW resids)
(a)
F-TF intercept
SMALLR X value
(b)
B-TF intercept
SMALLR X value
(c)
F-TF slope
SMALLR X value
(d)
B-TF slope
SMALLR X value
(e)
F-TF RMS scatter, mag
SMALLR X value
(f)
B-TF RMS scatter, logW
SMALLR X value

Figure 2

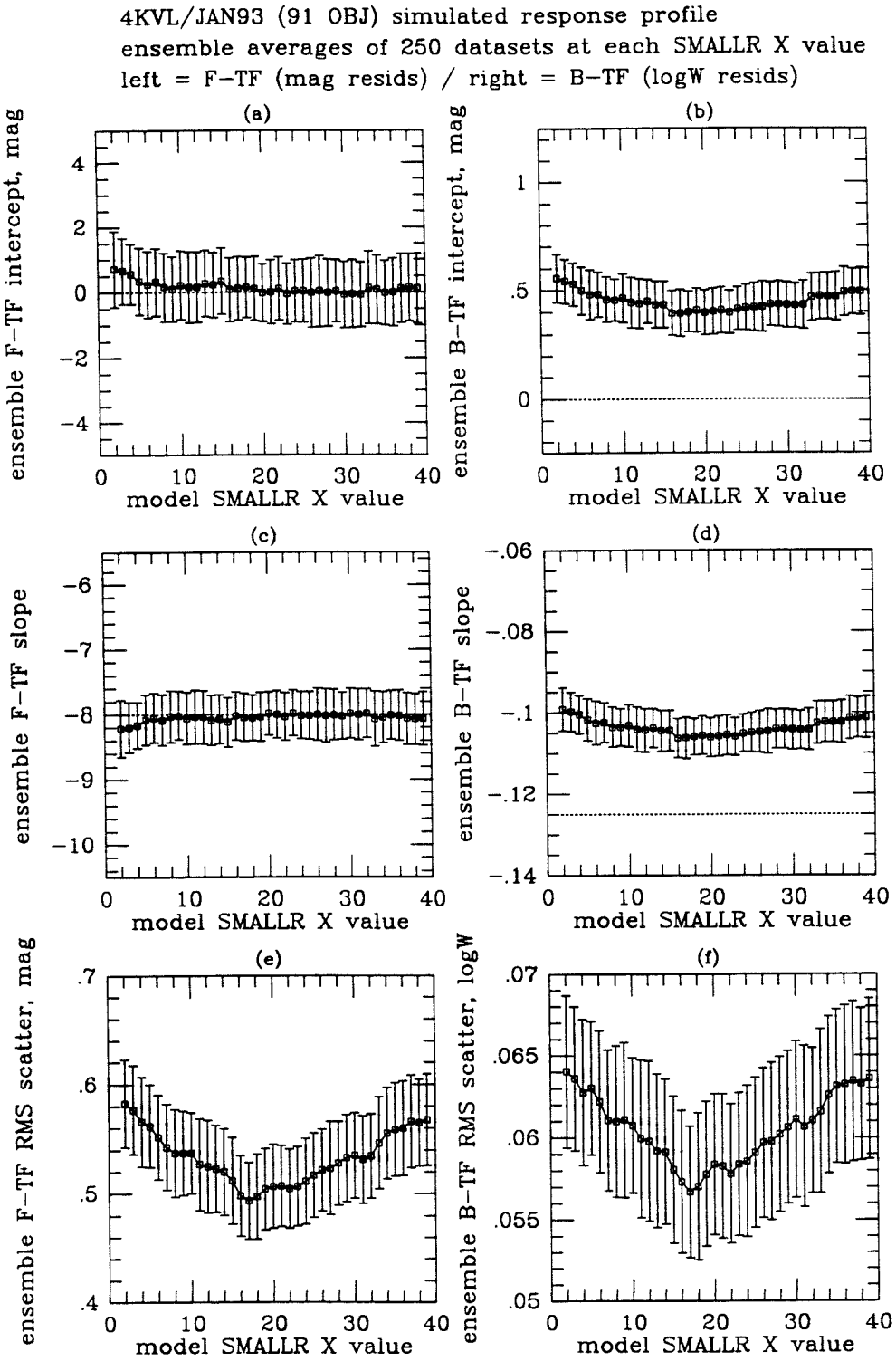
4KVL/JAN93 (91 OBJ) simulated response profile
ensemble averages of 250 datasets at each SMALLR X value
left = F−TF (mag resids) / right = B−TF (logW resids)
(a)
(b)
(c)
(d)
(e)
(f)
ensemble F−TF intercept, mag
ensemble B−TF intercept, mag
ensemble F−TF slope
ensemble B−TF slope
ensemble F−TF RMS scatter, mag
ensemble B−TF RMS scatter, logW
model SMALLR X value

Figure 3

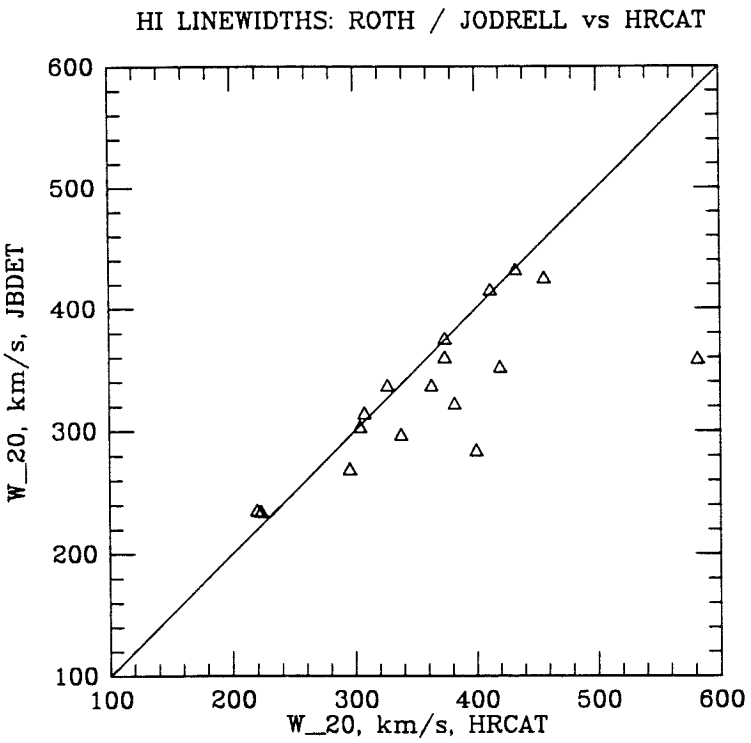
HI LINEWIDTHS: ROTH / JODRELL vs HRCAT
W_20, km/s, JBDET
W_20, km/s, HRCAT
100
200
300
400
500
600

Figure 4

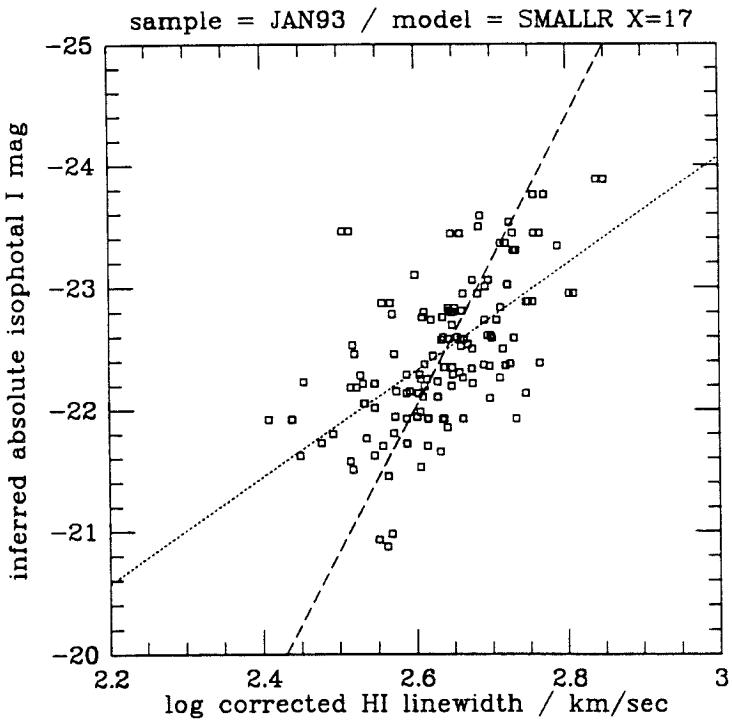
sample = JAN93 / model = SMALLR X=17
inferred absolute isophotal I mag
-25
-24
-23
-22
-21
-20
2.2
2.4
2.6
2.8
3
log corrected HI linewidth / km/sec

Figure 5

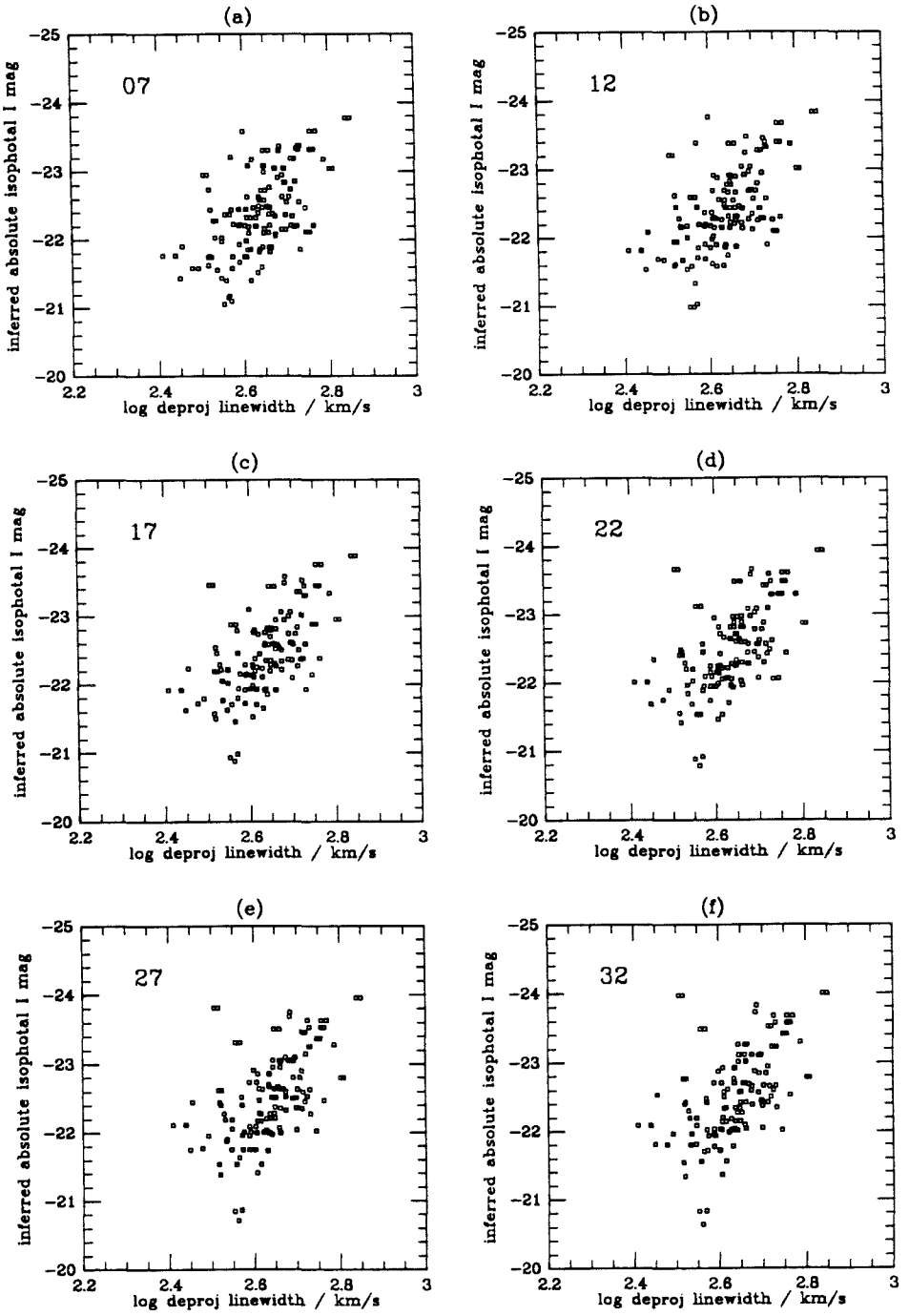
SAMPLE = 4KVL/JAN93 (91 obj)
I band apparent Tully-Fisher relations
models = SMALLR X, X = [7, 12, 17, 22, 27, 32]
(a)
07
(b)
12
(c)
17
(d)
22
(e)
27
(f)
32
inferred absolute isophotal I mag
log deproj linewidth / km/s
-25
-24
-23
-22
-21
-20
2.2
2.4
2.6
2.8
3

Figure 6

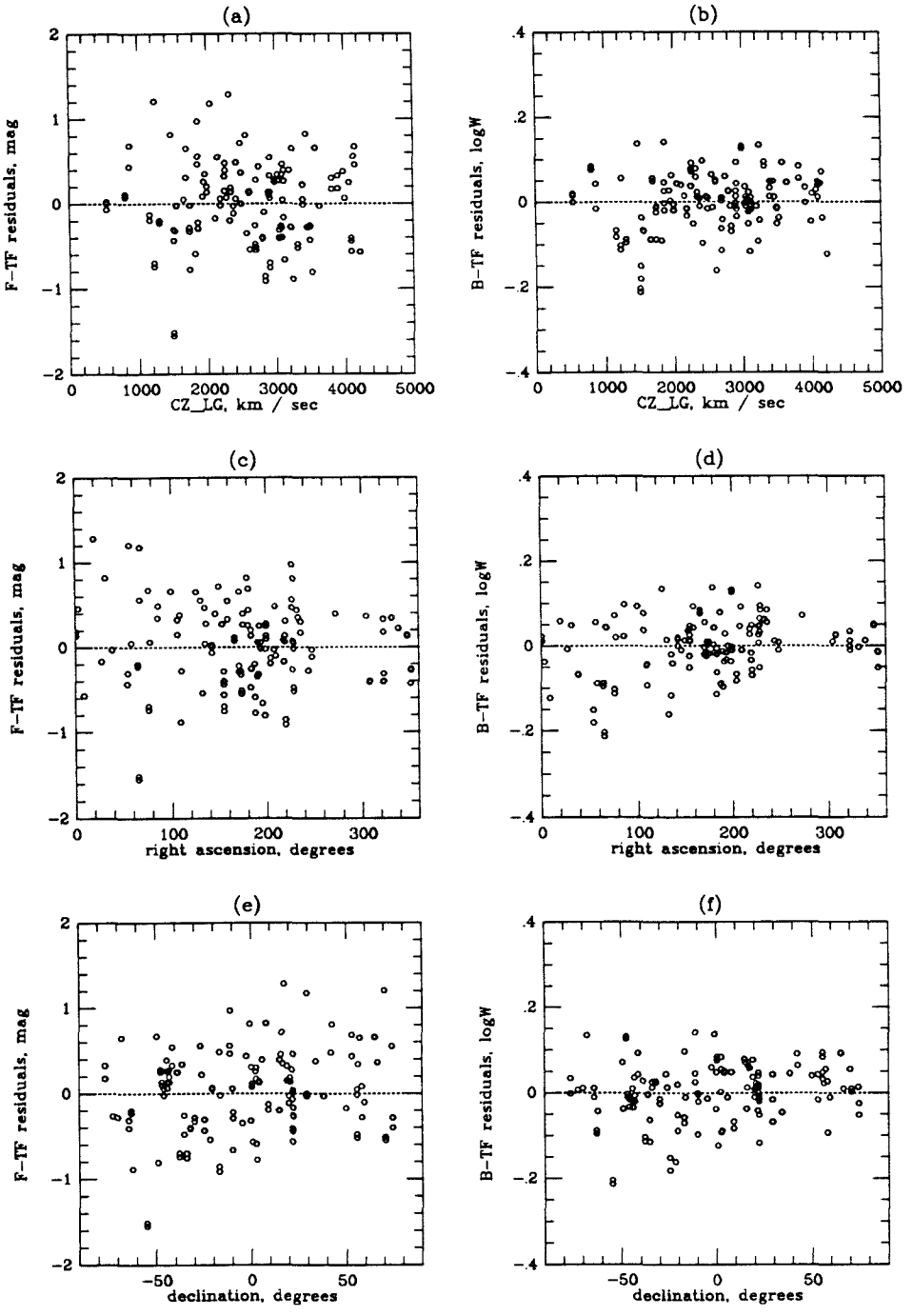
SAMPLE = 4KVL/JAN93 (91 obj)
I band apparent Tully-Fisher residuals trends
left = F-TF (mag) / right = B-TF (logW)
(a)
(b)
(c)
(d)
(e)
(f)
F-TF residuals, mag
B-TF residuals, logW
CZ_LG, km / sec
right ascension, degrees
declination, degrees

Figure 7(1)

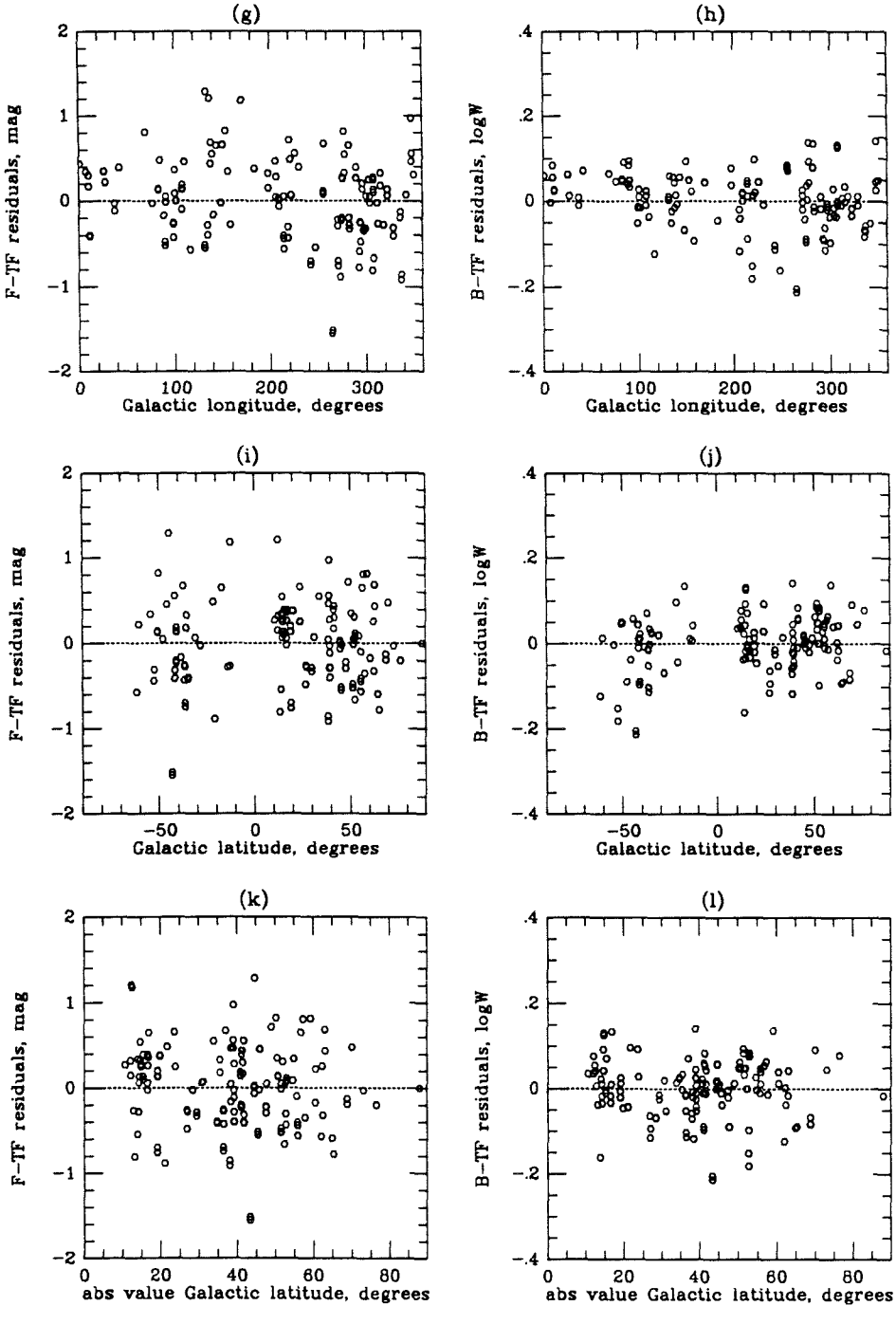
SAMPLE = 4KVL/JAN93 (91 obj)
I band apparent Tully-Fisher residuals trends
left = F-TF (mag) / right = B-TF (logW)
(g)
(h)
(i)
(j)
(k)
(l)
F-TF residuals, mag
B-TF residuals, logW
Galactic longitude, degrees
Galactic latitude, degrees
abs value Galactic latitude, degrees

Figure 7(2)

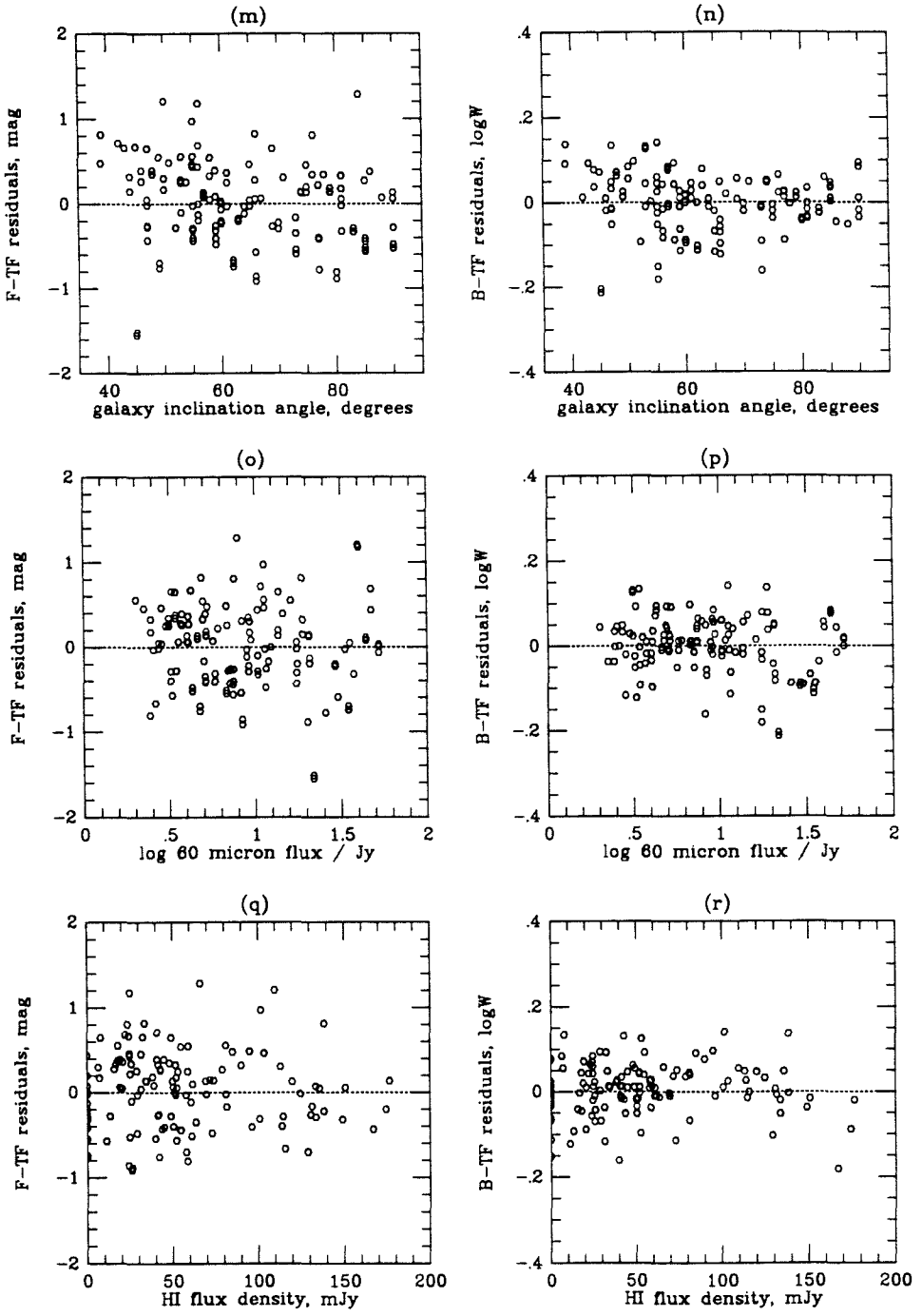
SAMPLE = 4KVL/JAN93 (91 obj)
I band apparent Tully-Fisher residuals trends
left = F-TF (mag) / right = B-TF (logW)
(m)
(n)
F-TF residuals, mag
B-TF residuals, logW
galaxy inclination angle, degrees
galaxy inclination angle, degrees
(o)
(p)
log 60 micron flux / Jy
log 60 micron flux / Jy
(q)
(r)
HI flux density, mJy
HI flux density, mJy

Figure 7(3)

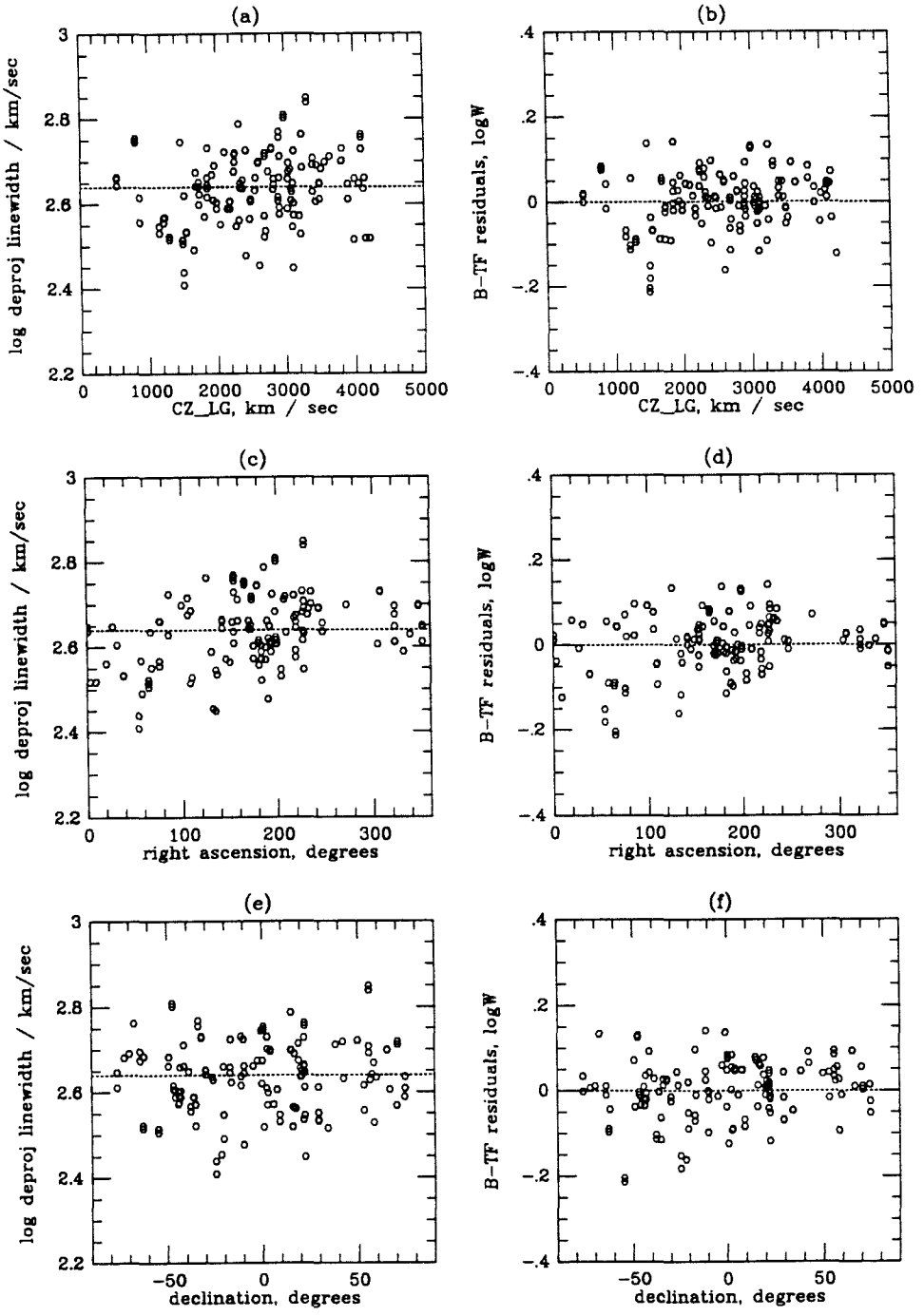
SAMPLE = 4KVL/JAN93 (91 obj)
I band TF residuals, logW trends
left = logW / right = B-TF (logW resids)
(a)
(b)
(c)
(d)
(e)
(f)
log deproj linewidth / km/sec
B-TF residuals, logW
CZ_LG, km / sec
right ascension, degrees
declination, degrees

Figure 8(1)

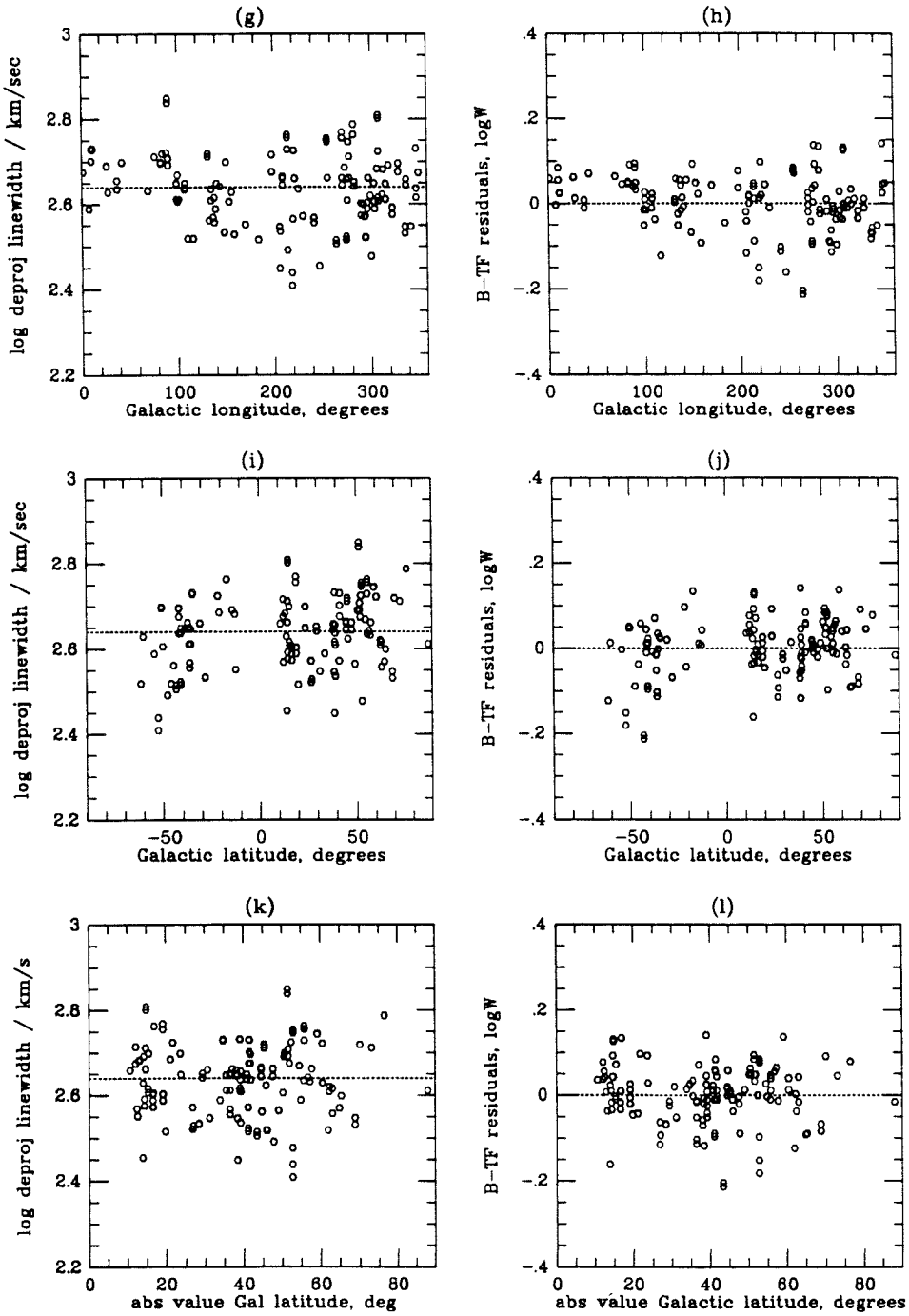
SAMPLE = 4KVL/JAN93 (91 obj)
I band TF residuals, logW trends
left = logW / right = B-TF (logW resids)
(g)
(h)
(i)
(j)
(k)
(l)
log deproj linewidth / km/sec
log deproj linewidth / km/s
B-TF residuals, logW
Galactic longitude, degrees
Galactic latitude, degrees
abs value Gal latitude, deg
abs value Galactic latitude, degrees

Figure 8(2)

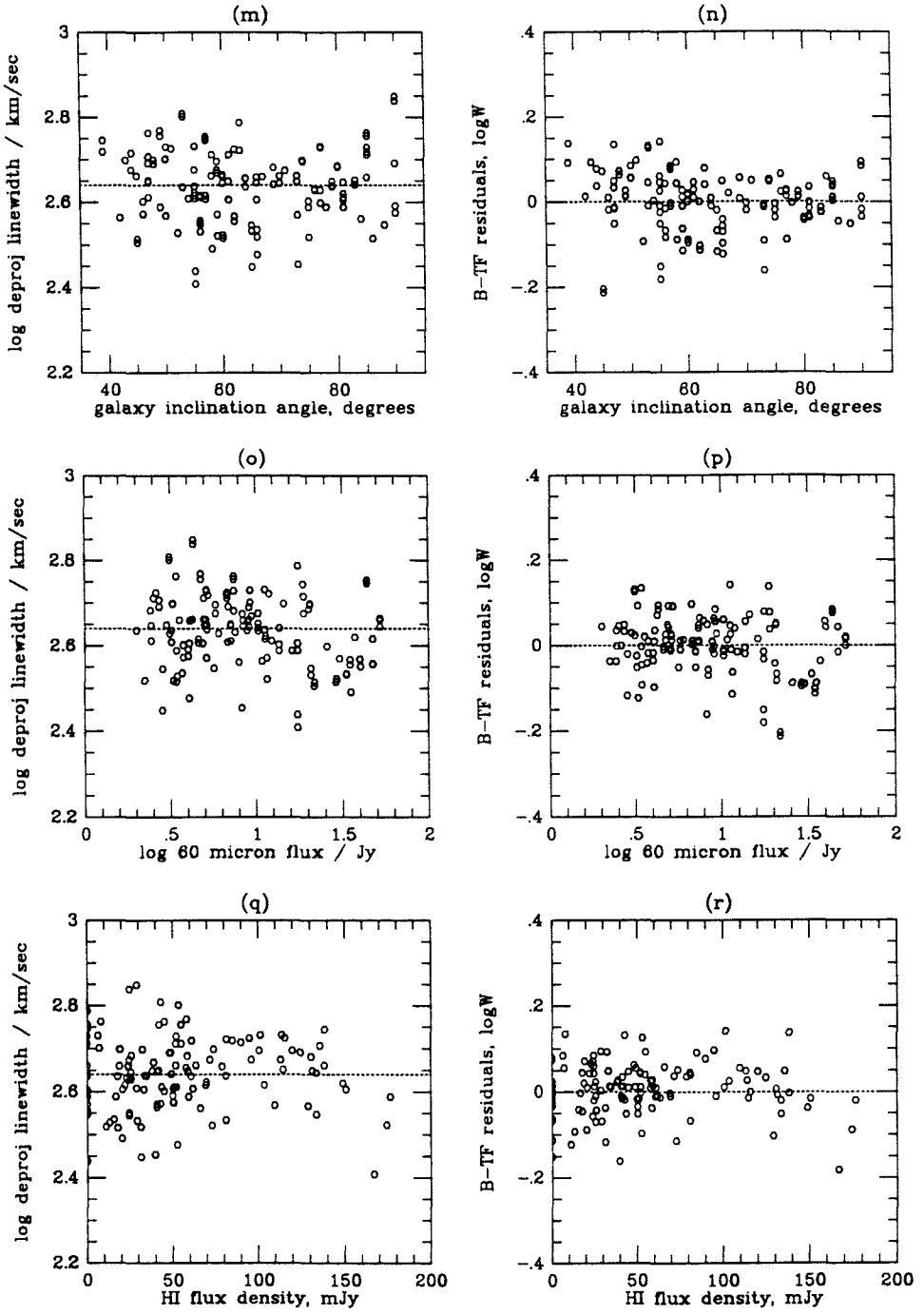
SAMPLE = 4KVL/JAN93 (91 obj)
I band TF residuals, logW trends
left = logW / right = B-TF (logW resids)
(m)
(n)
(o)
(p)
(q)
(r)
log deproj linewidth / km/sec
B-TF residuals, logW
galaxy inclination angle, degrees
log 60 micron flux / Jy
HI flux density, mJy

Figure 8(3)

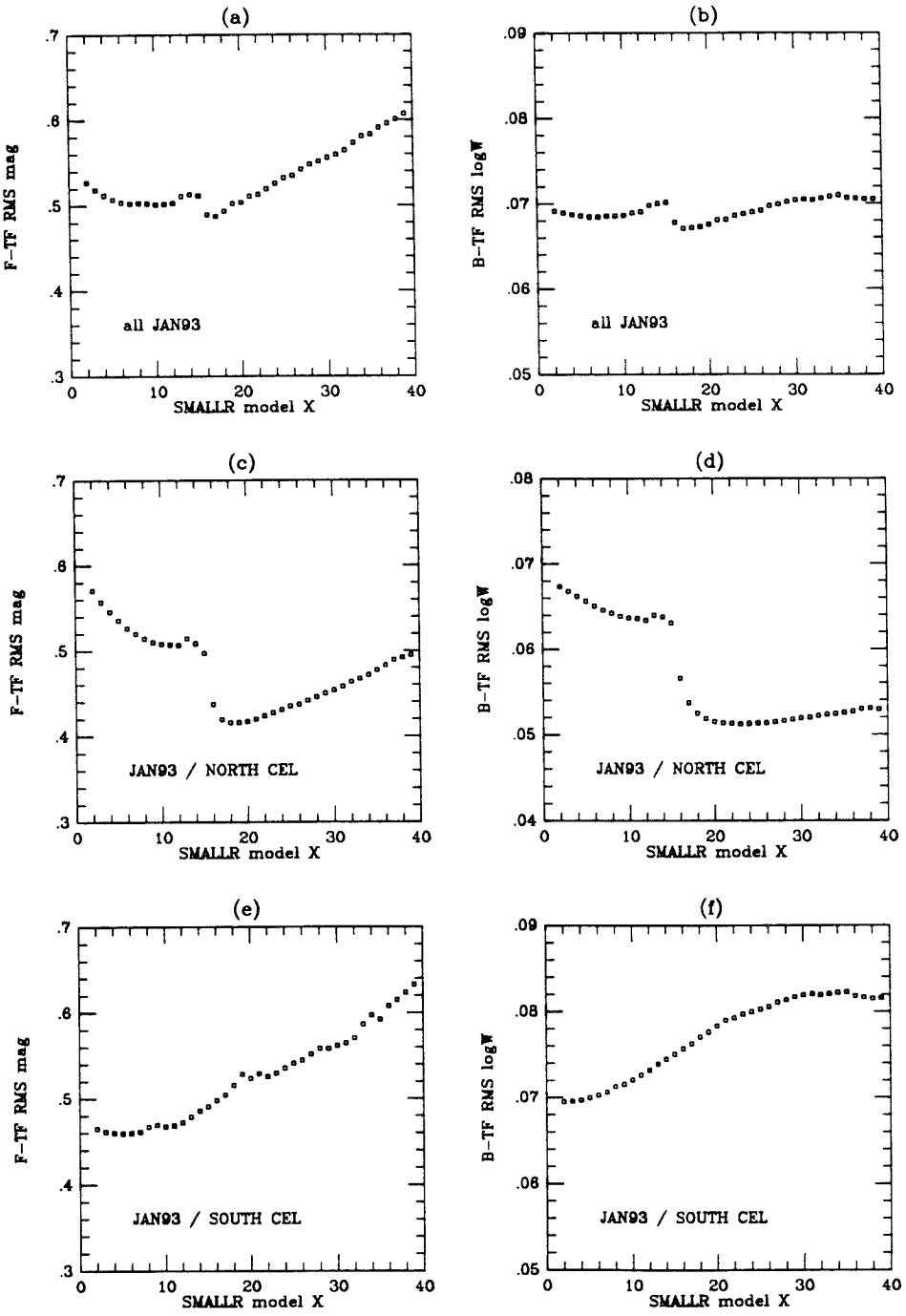
SAMPLE = 4KVL/JAN93 (91 obj) / SUBSETS
I band Tully-Fisher response profiles
left = F-TF (mag resids) / right = B-TF (logW resids)
(a)
(b)
(c)
(d)
(e)
(f)
F-TF RMS mag
B-TF RMS logW
SMALLR model X
all JAN93
JAN93 / NORTH CEL
JAN93 / SOUTH CEL

Figure 9

SAMPLE = 4KVL/JAN93 (91 obj) / SUBSETS
I band Tully–Fisher response profiles
left = F–TF (mag resids) / right = B–TF (logW resids)

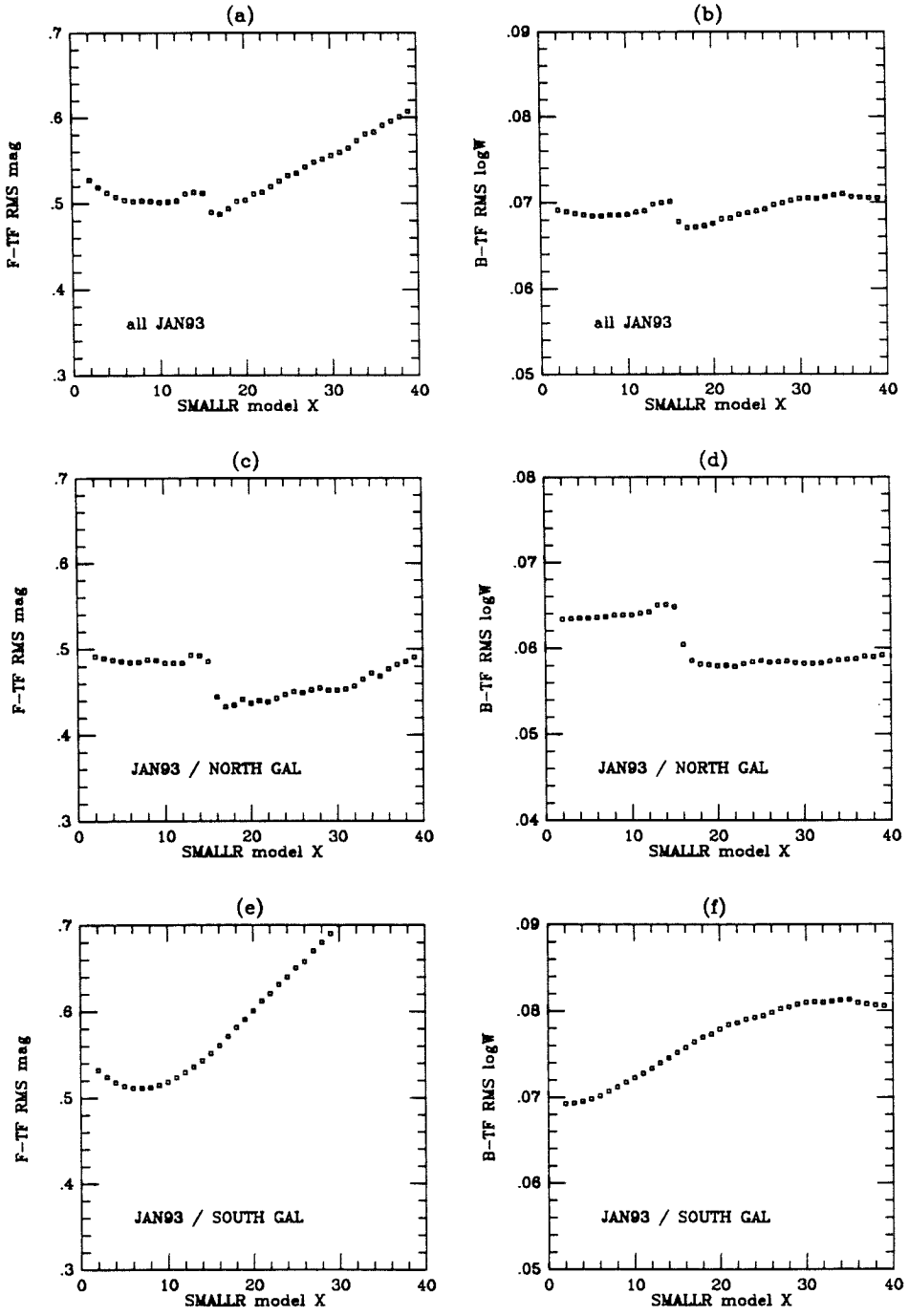

Figure 10

SAMPLE = 4KVL/JAN93 (91 obj) / SUBSETS
I band Tully-Fisher response profiles
left = F-TF (mag resids) / right = B-TF (logW resids)

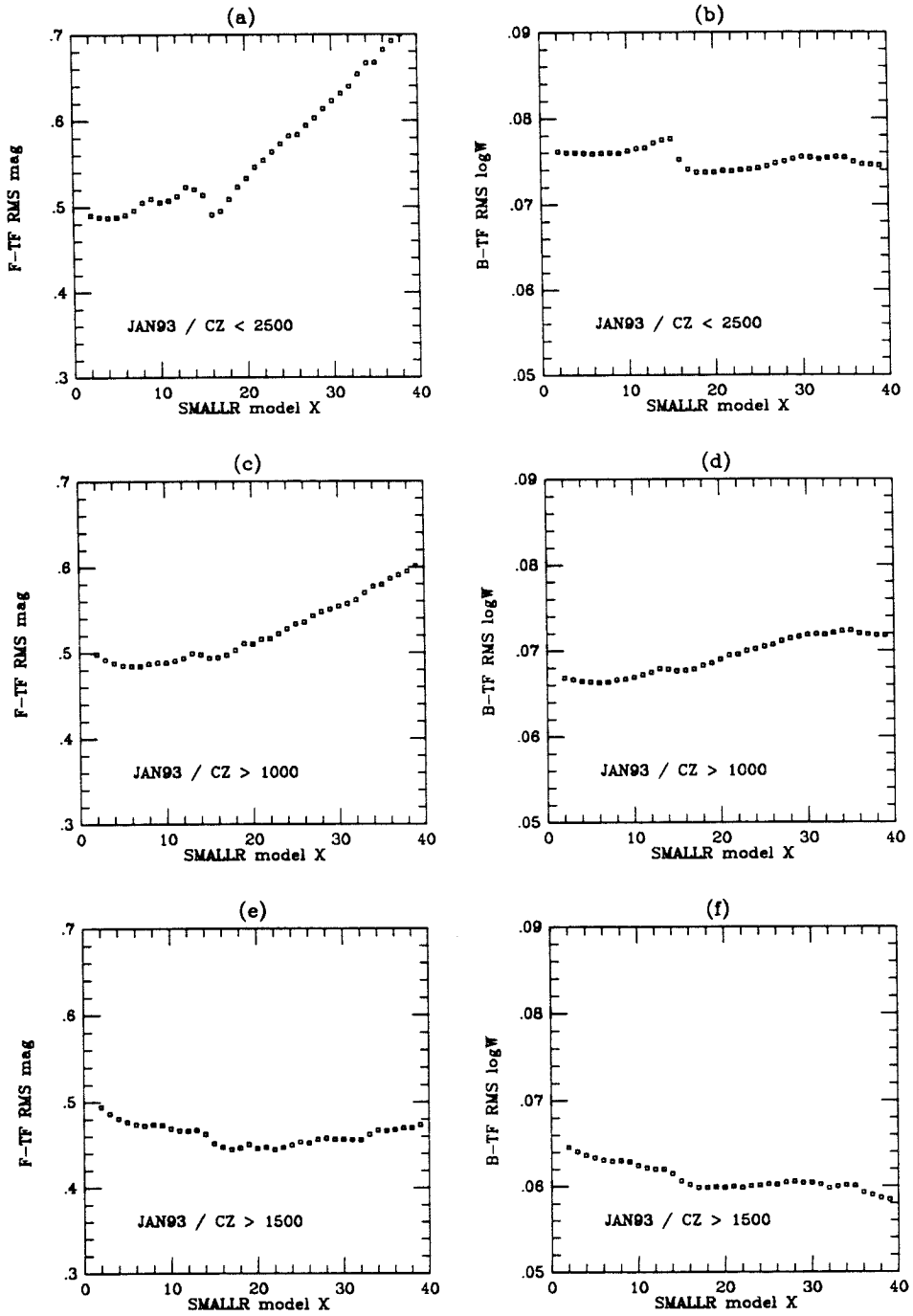

Figure 11(1)

SAMPLE = 4KVL/JAN93 (91 obj) / SUBSETS
I band Tully–Fisher response profiles
left = F–TF (mag resids) / right = B–TF (logW resids)

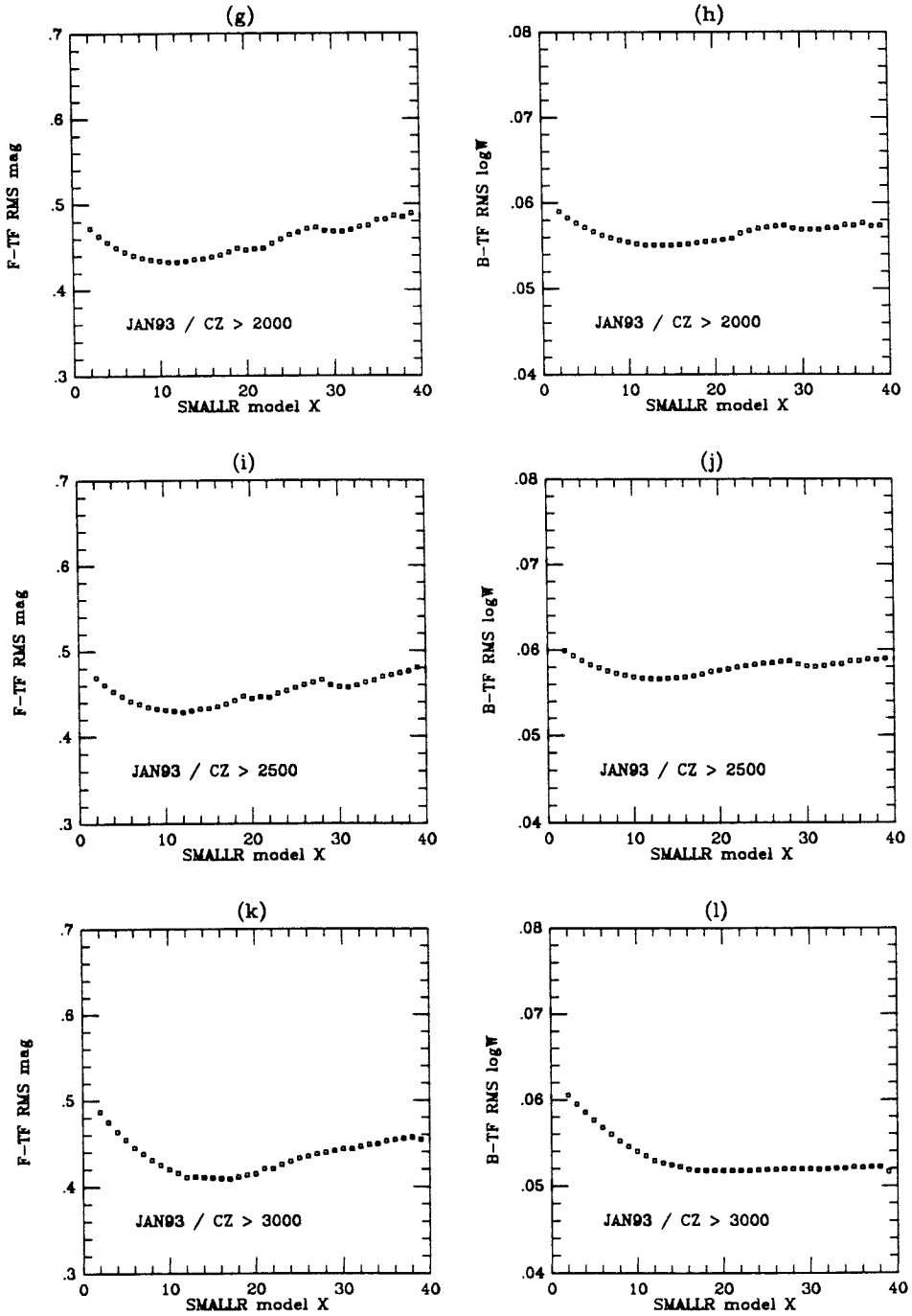

Figure 11(2)

SAMPLE = 4KVL/JAN93 (91 obj) / SUBSETS
I band Tully-Fisher response profiles
left = F-TF (mag resids) / right = B-TF (logW resids)

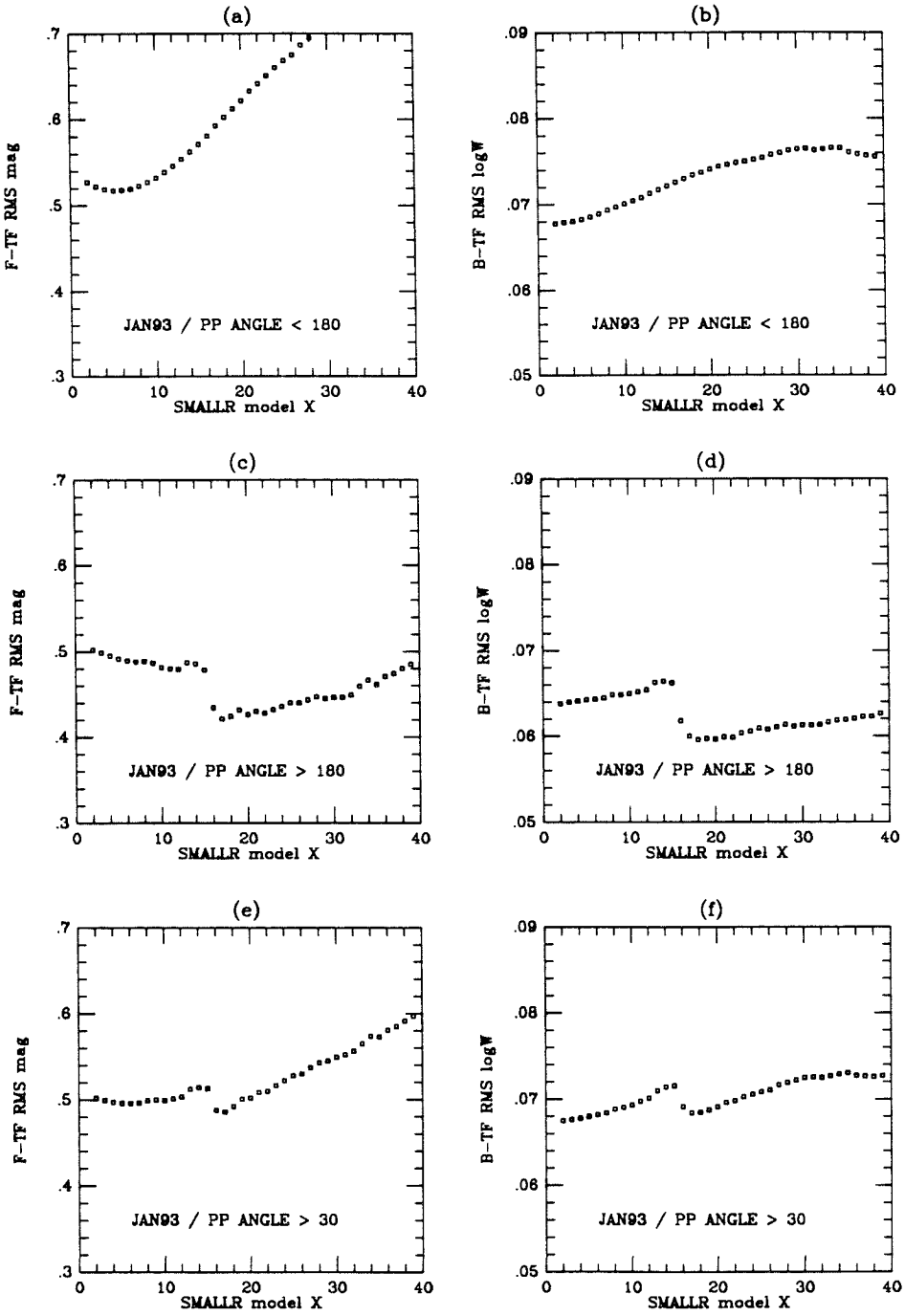

Figure 12

SAMPLE = 4KVL/JAN93 (91 obj) / SUBSETS
I band Tully-Fisher response profiles
left = F-TF (mag resids) / right = B-TF (logW resids)

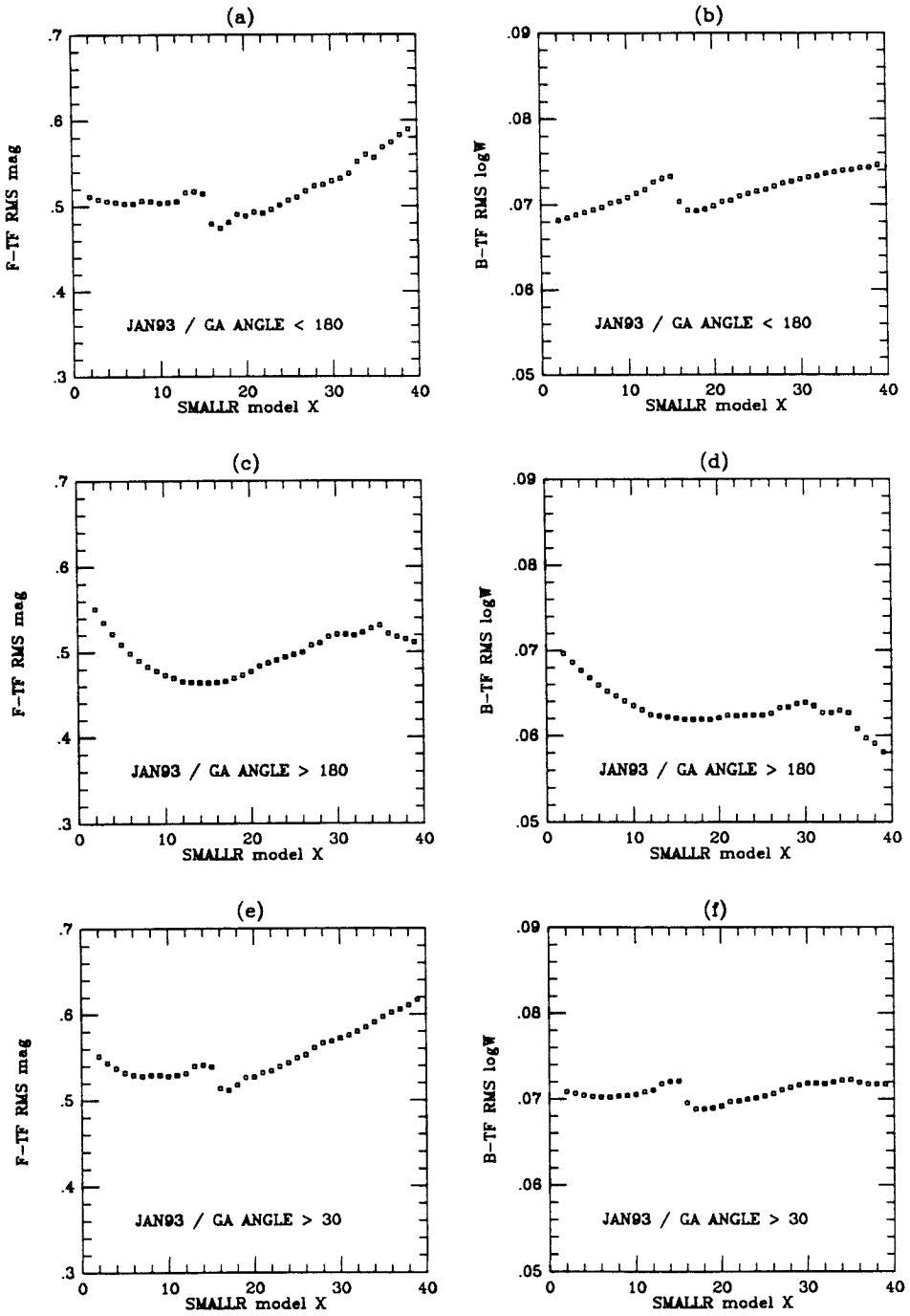

Figure 13

SAMPLE = 4KVL/JAN93 (91 obj) / SUBSETS
I band Tully-Fisher response profiles
left = F-TF (mag resids) / right = B-TF (logW resids)

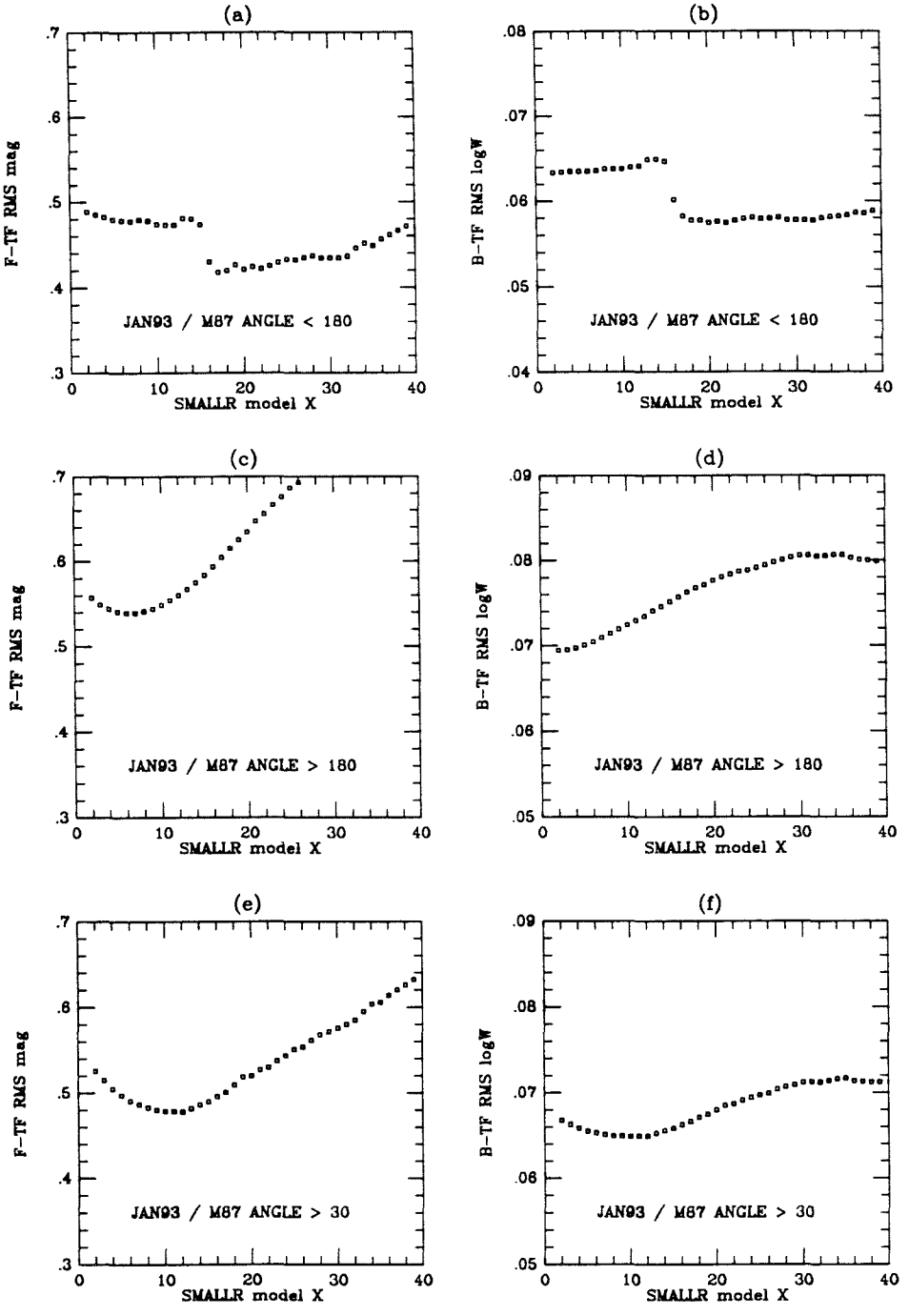

Figure 14

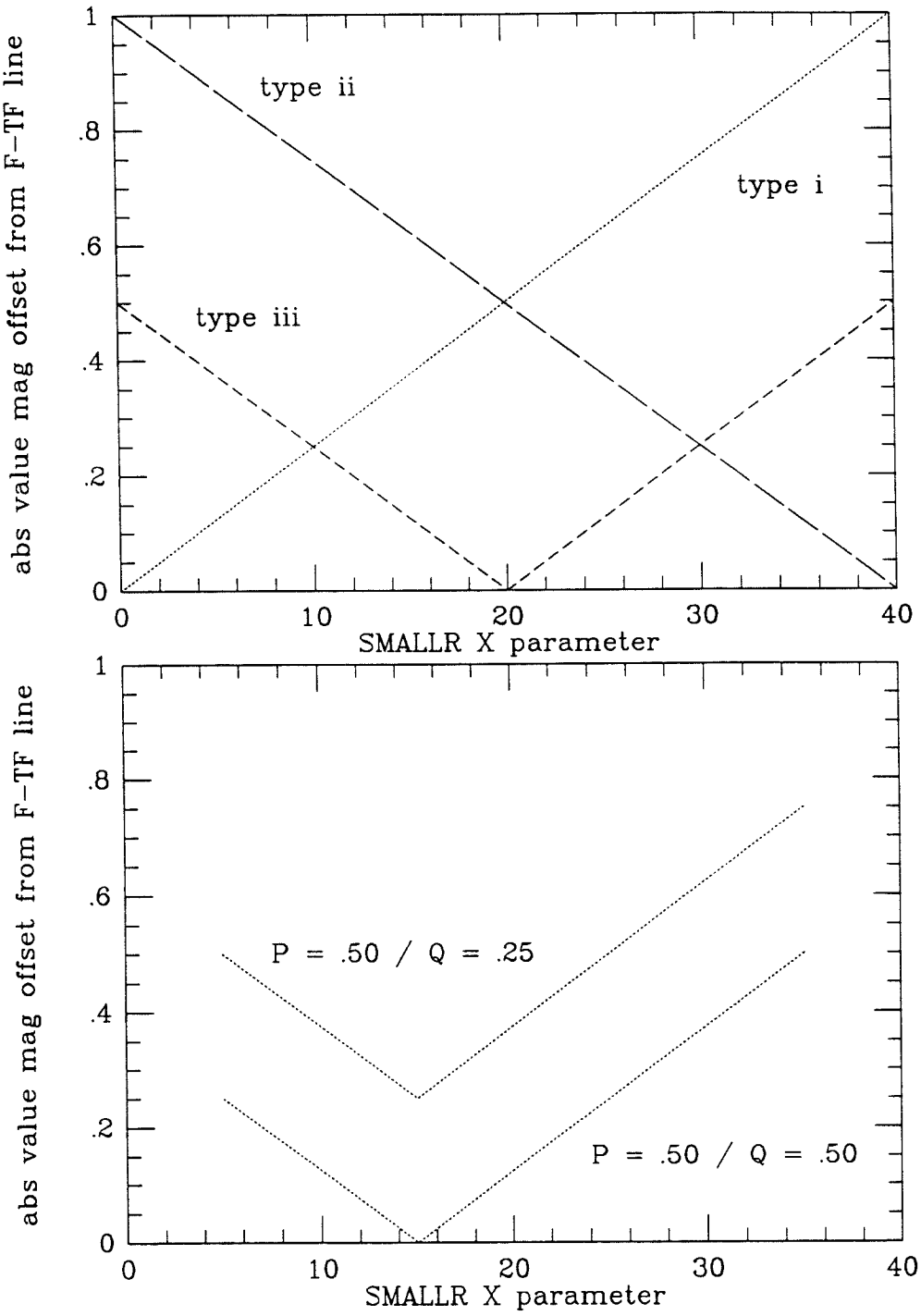
abs value mag offset from F-TF line
1
.8
.6
.4
.2
0
type ii
type i
type iii
0
10
20
30
40
SMALLR X parameter
abs value mag offset from F-TF line
1
.8
.6
.4
.2
0
P = .50 / Q = .25
P = .50 / Q = .50
0
10
20
30
40
SMALLR X parameter

Figure 15

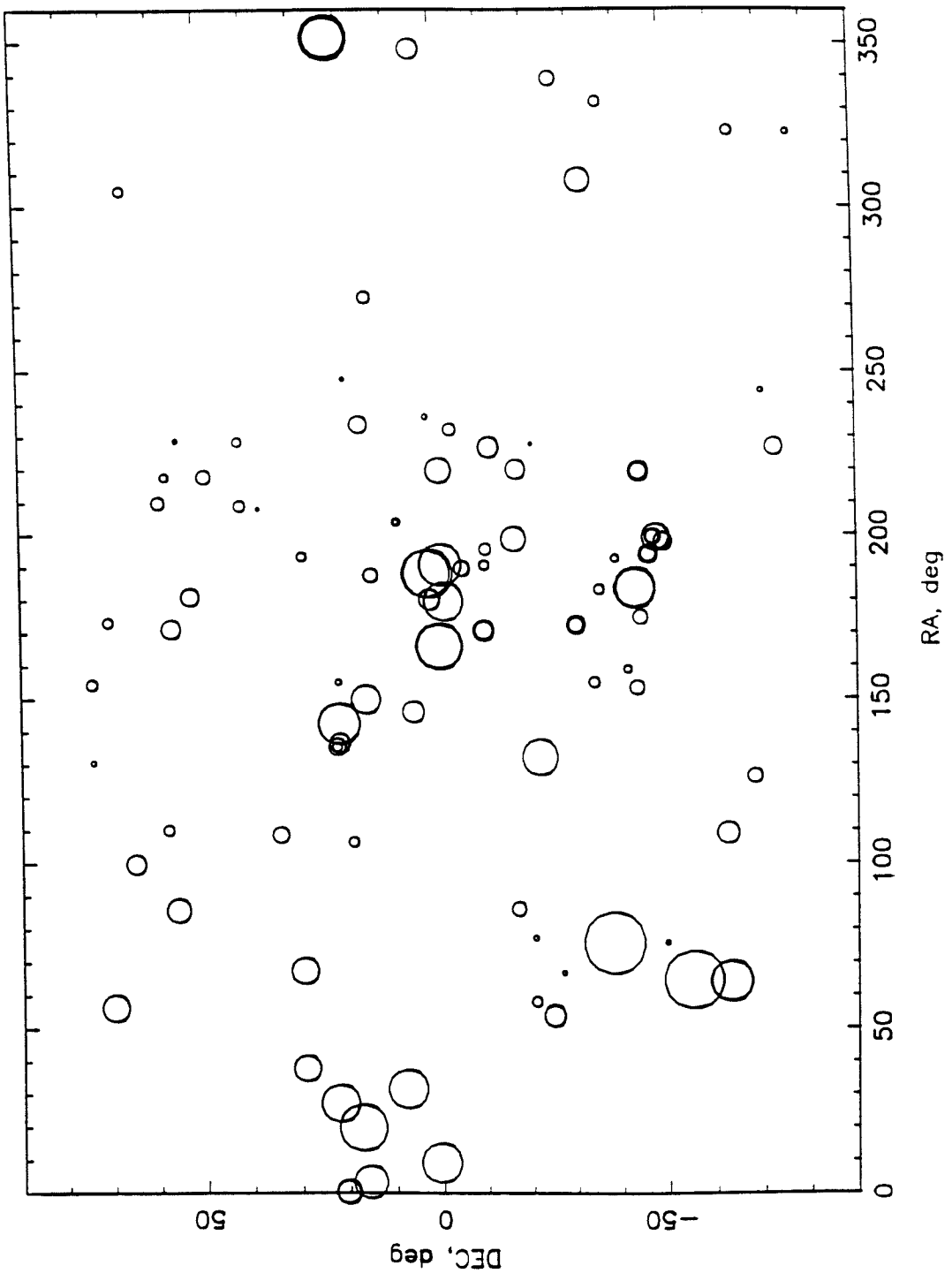

Figure 16a

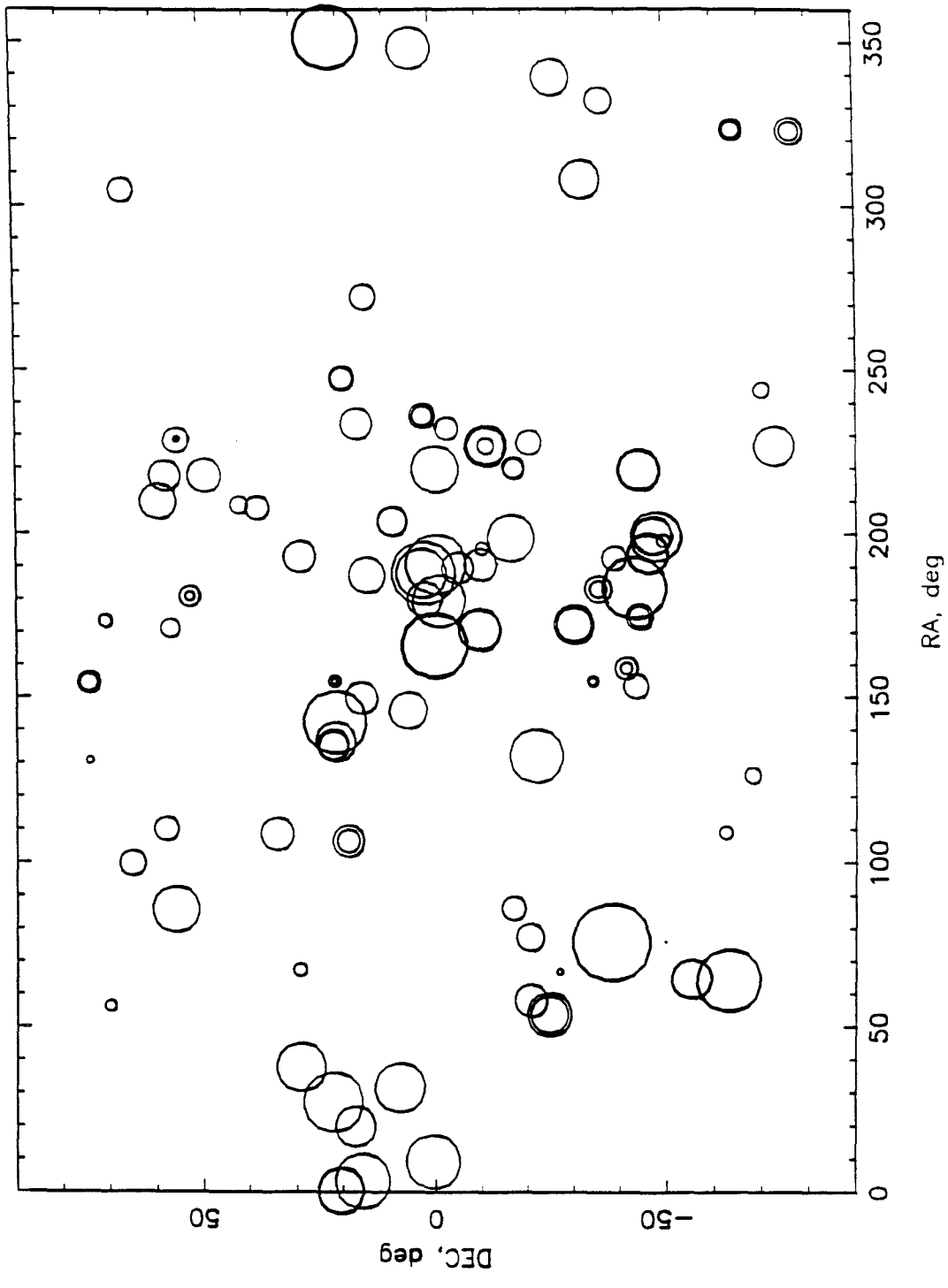

Figure 16b

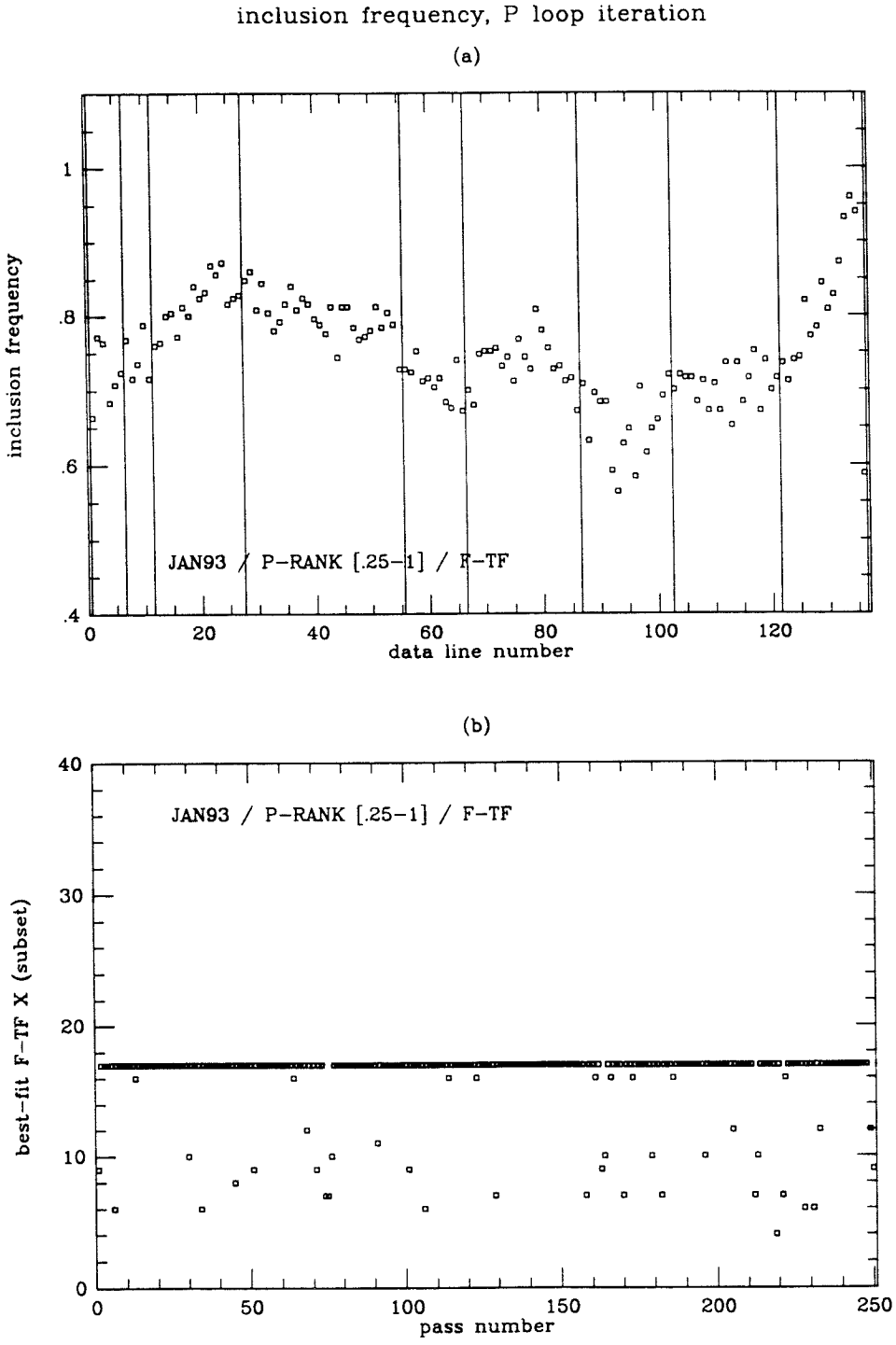
inclusion frequency, P loop iteration
(a)
inclusion frequency
1
.8
.6
.4
JAN93 / P-RANK [.25-1] / F-TF
0
20
40
60
80
100
120
data line number
(b)
best-fit F-TF X (subset)
40
30
20
10
0
JAN93 / P-RANK [.25-1] / F-TF
0
50
100
150
200
250
pass number

Figure 17

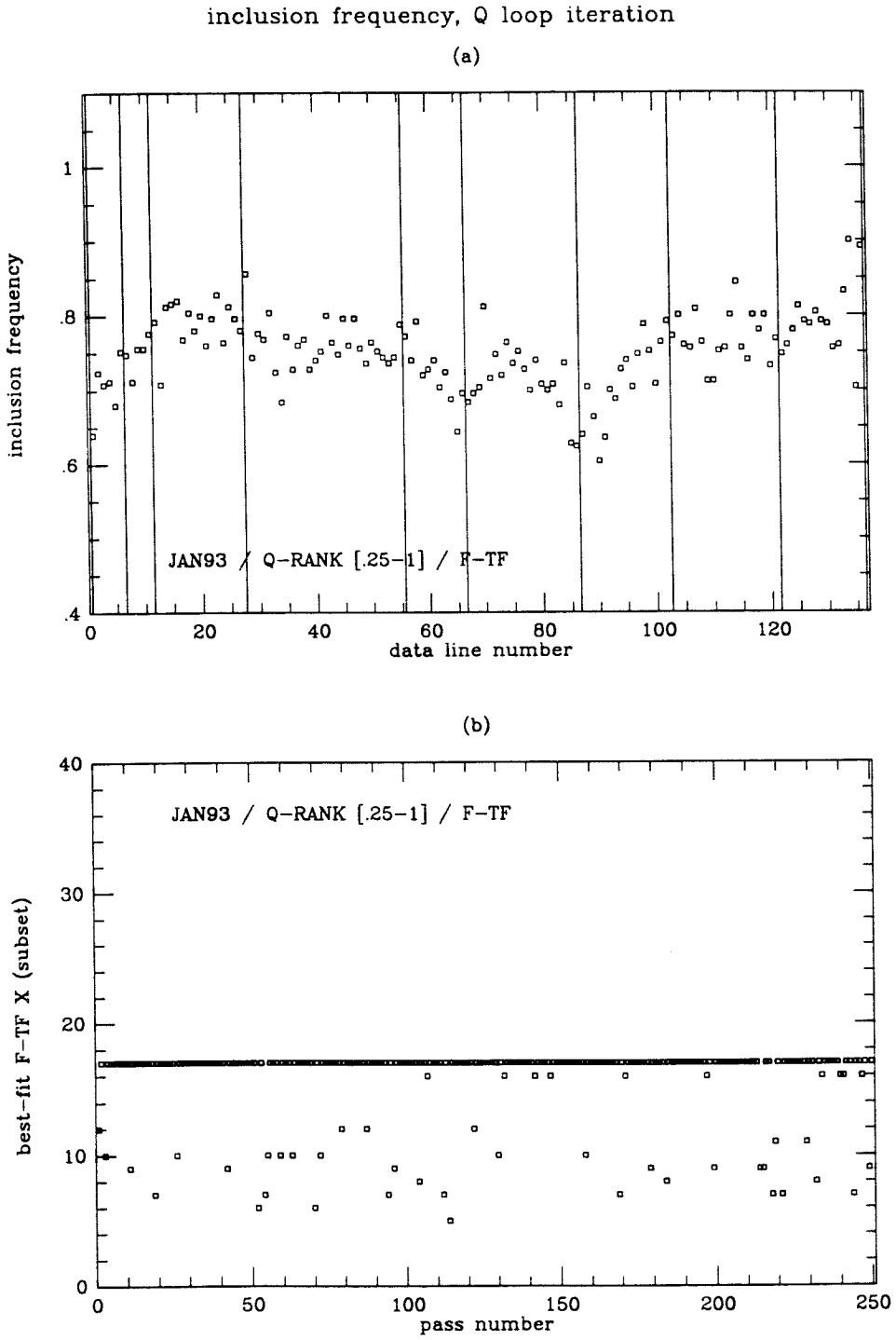
inclusion frequency, Q loop iteration
(a)
inclusion frequency
1
.8
.6
.4
0
20
40
60
80
100
120
data line number
JAN93 / Q-RANK [.25-1] / F-TF
(b)
best-fit F-TF X (subset)
40
30
20
10
0
0
50
100
150
200
250
pass number
JAN93 / Q-RANK [.25-1] / F-TF

Figure 18

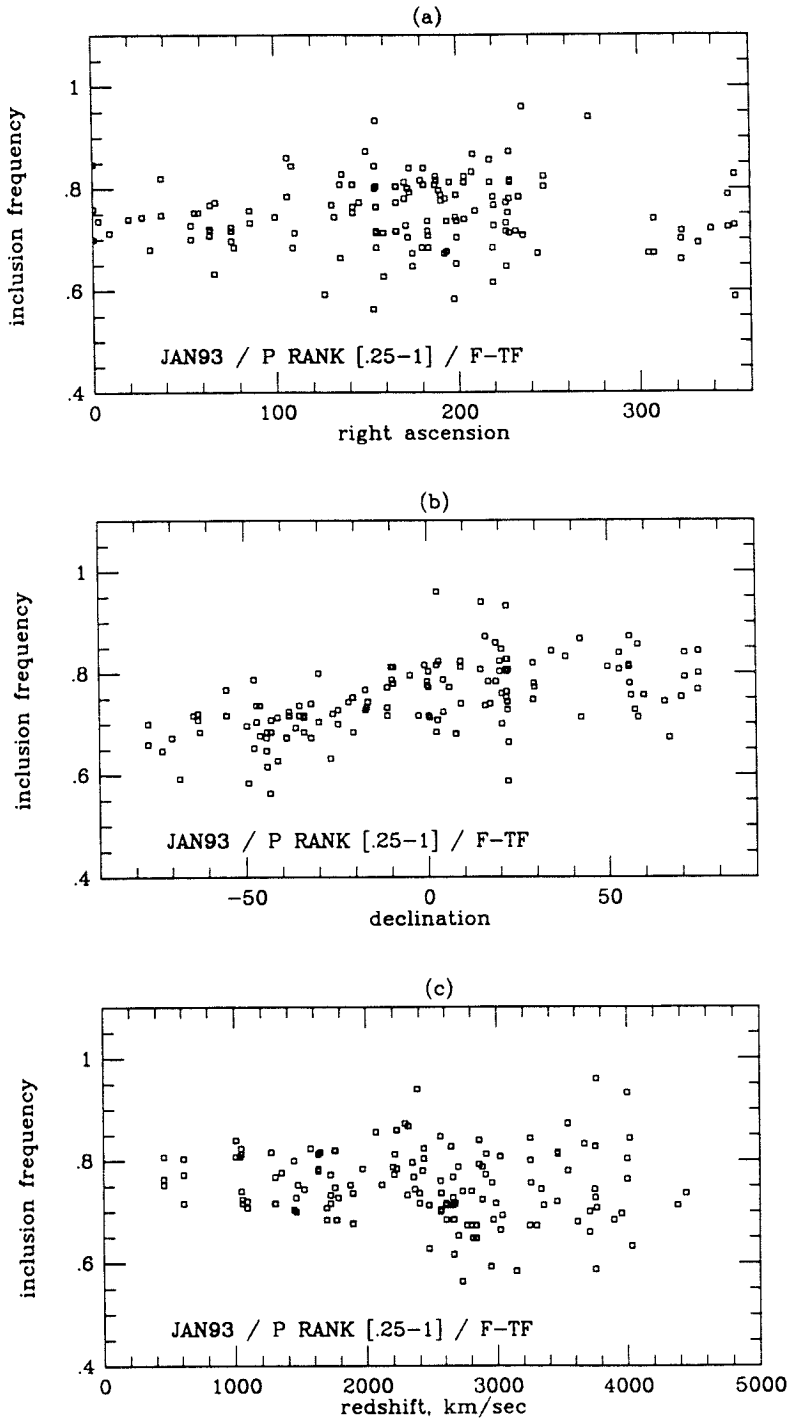
inclusion frequency, P loop iteration
(a)
inclusion frequency
1
.8
.6
.4
JAN93 / P RANK [.25-1] / F-TF
0
100
200
300
right ascension
(b)
inclusion frequency
1
.8
.6
.4
JAN93 / P RANK [.25-1] / F-TF
-50
0
50
declination
(c)
inclusion frequency
1
.8
.6
.4
JAN93 / P RANK [.25-1] / F-TF
0
1000
2000
3000
4000
5000
redshift, km/sec

Figure 19

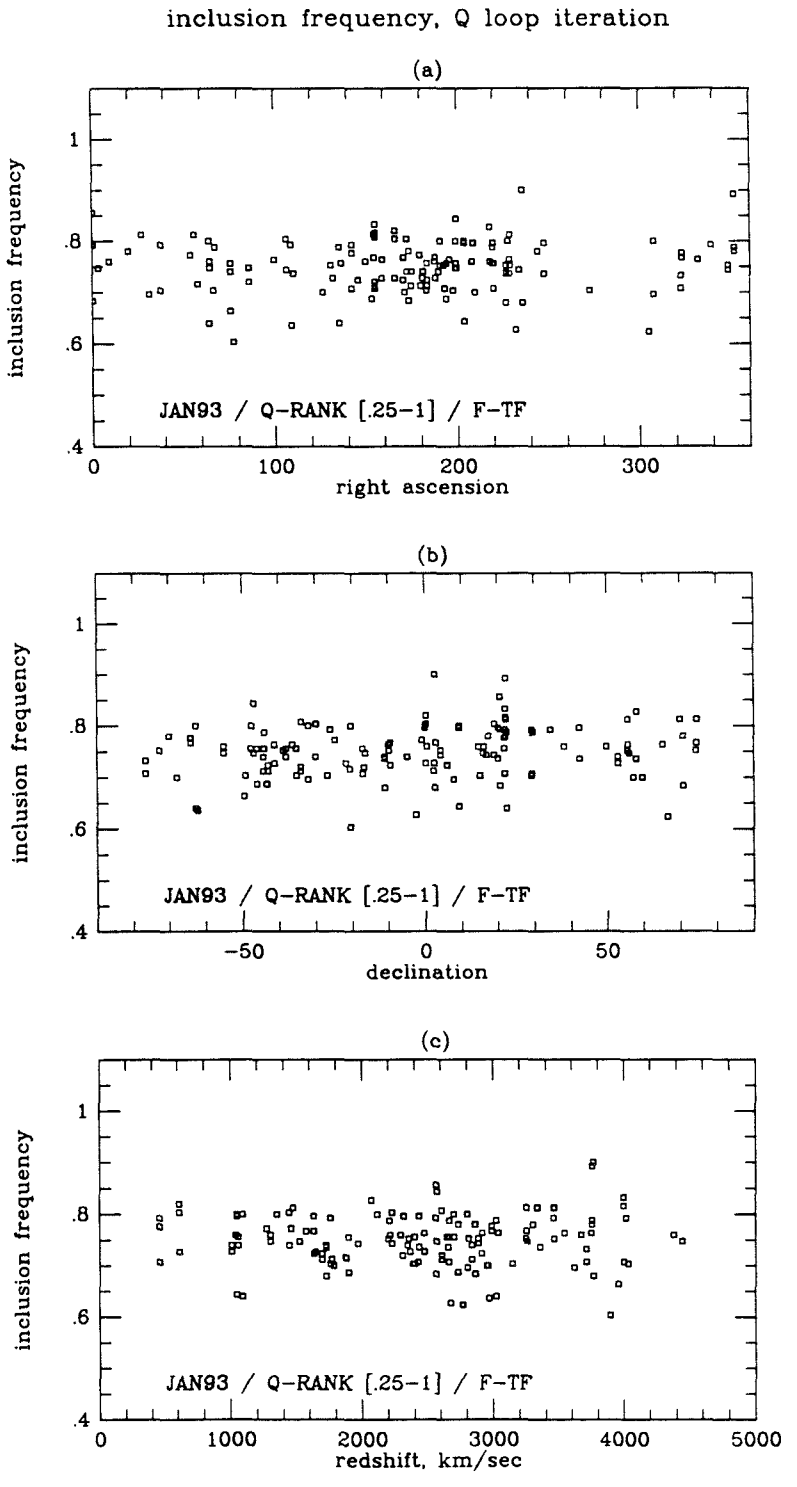
inclusion frequency, Q loop iteration
(a)
inclusion frequency
1
.8
.6
.4
JAN93 / Q-RANK [.25-1] / F-TF
0
100
200
300
right ascension
(b)
inclusion frequency
1
.8
.6
.4
JAN93 / Q-RANK [.25-1] / F-TF
-50
0
50
declination
(c)
inclusion frequency
1
.8
.6
.4
JAN93 / Q-RANK [.25-1] / F-TF
0
1000
2000
3000
4000
5000
redshift, km/sec

Figure 20

response profiles for subsets ranked by incl freq, P loop

(a)

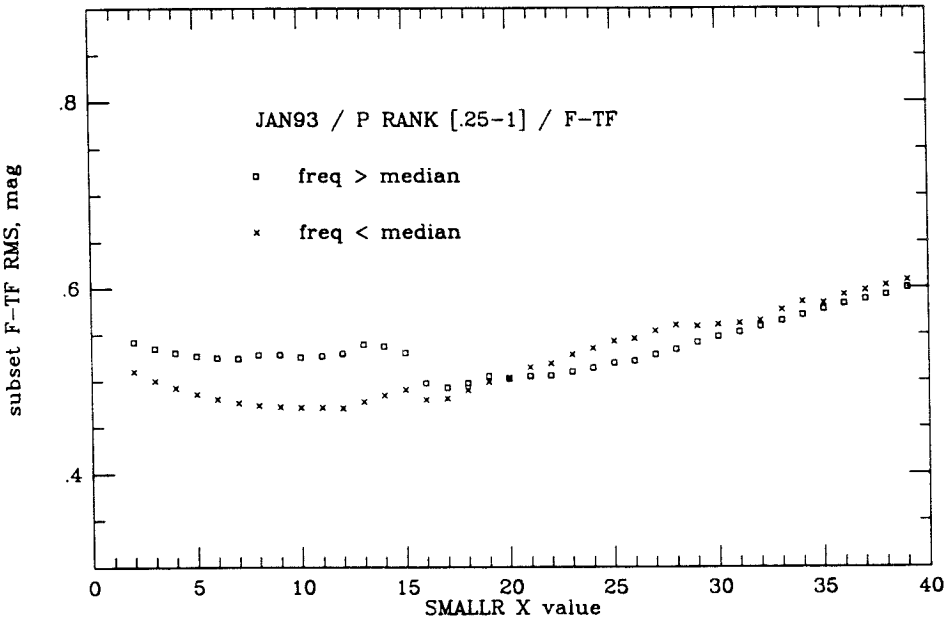

(b)

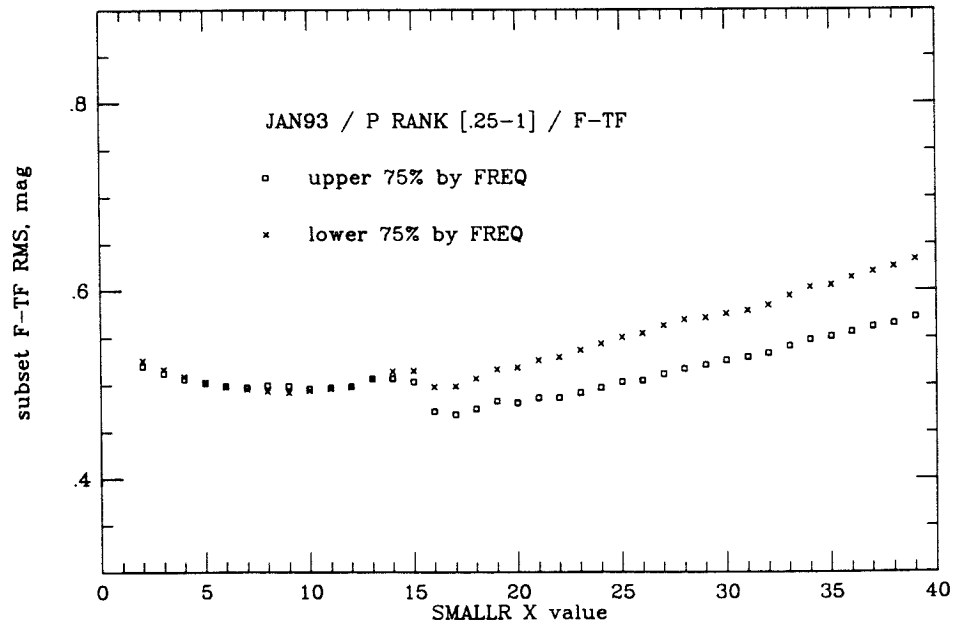

Figure 21

response profiles for subsets ranked by incl freq, Q loop

(a)

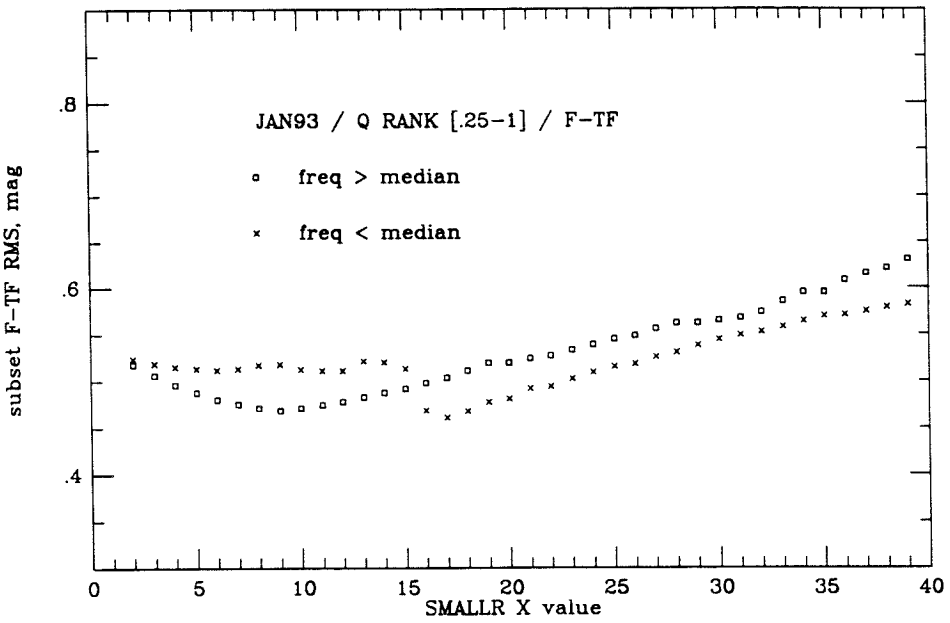

(b)

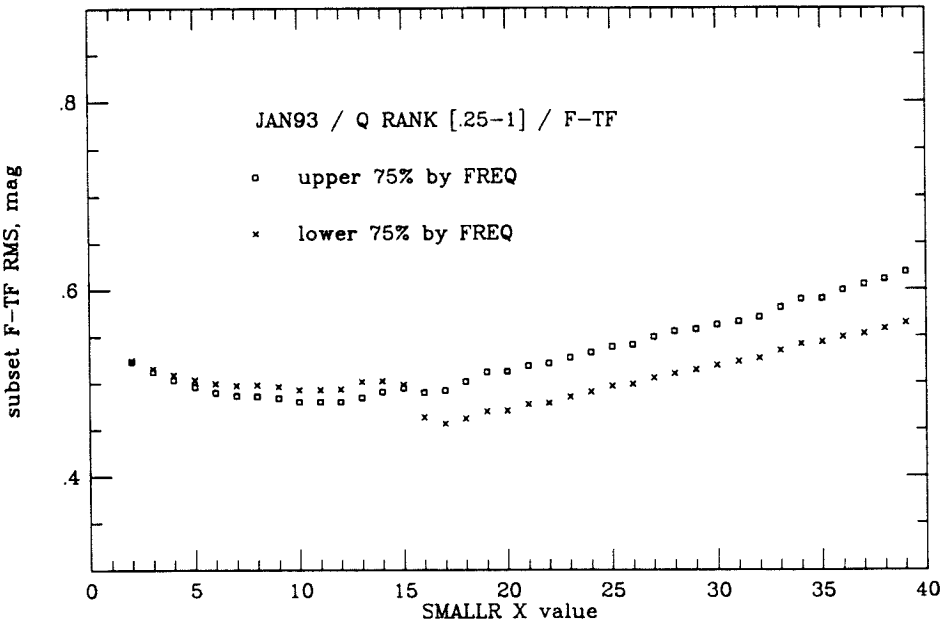

Figure 22

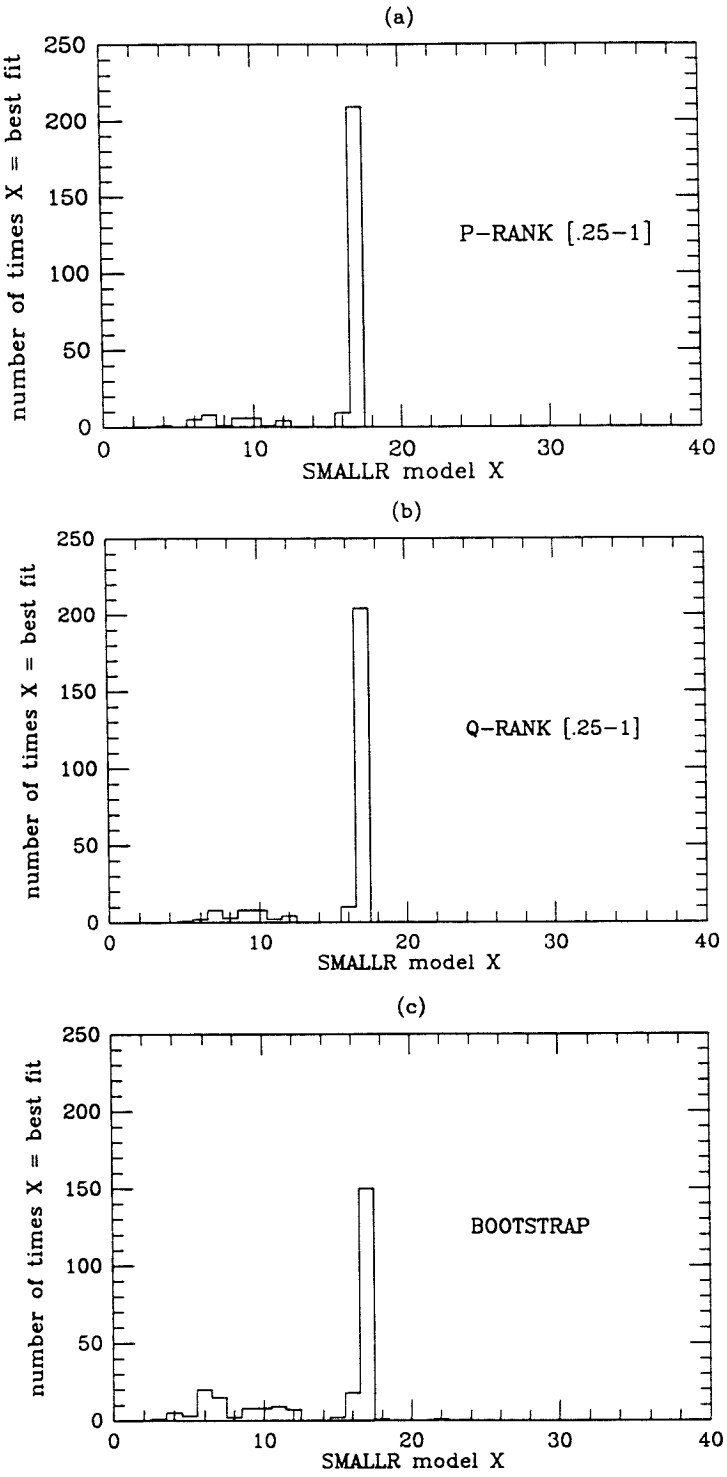
(a)
number of times X = best fit
250
200
150
100
50
0
0
10
20
30
40
SMALLR model X
P-RANK [.25-1]
(b)
number of times X = best fit
250
200
150
100
50
0
0
10
20
30
40
SMALLR model X
Q-RANK [.25-1]
(c)
number of times X = best fit
250
200
150
100
50
0
0
10
20
30
40
SMALLR model X
BOOTSTRAP

Figure 23

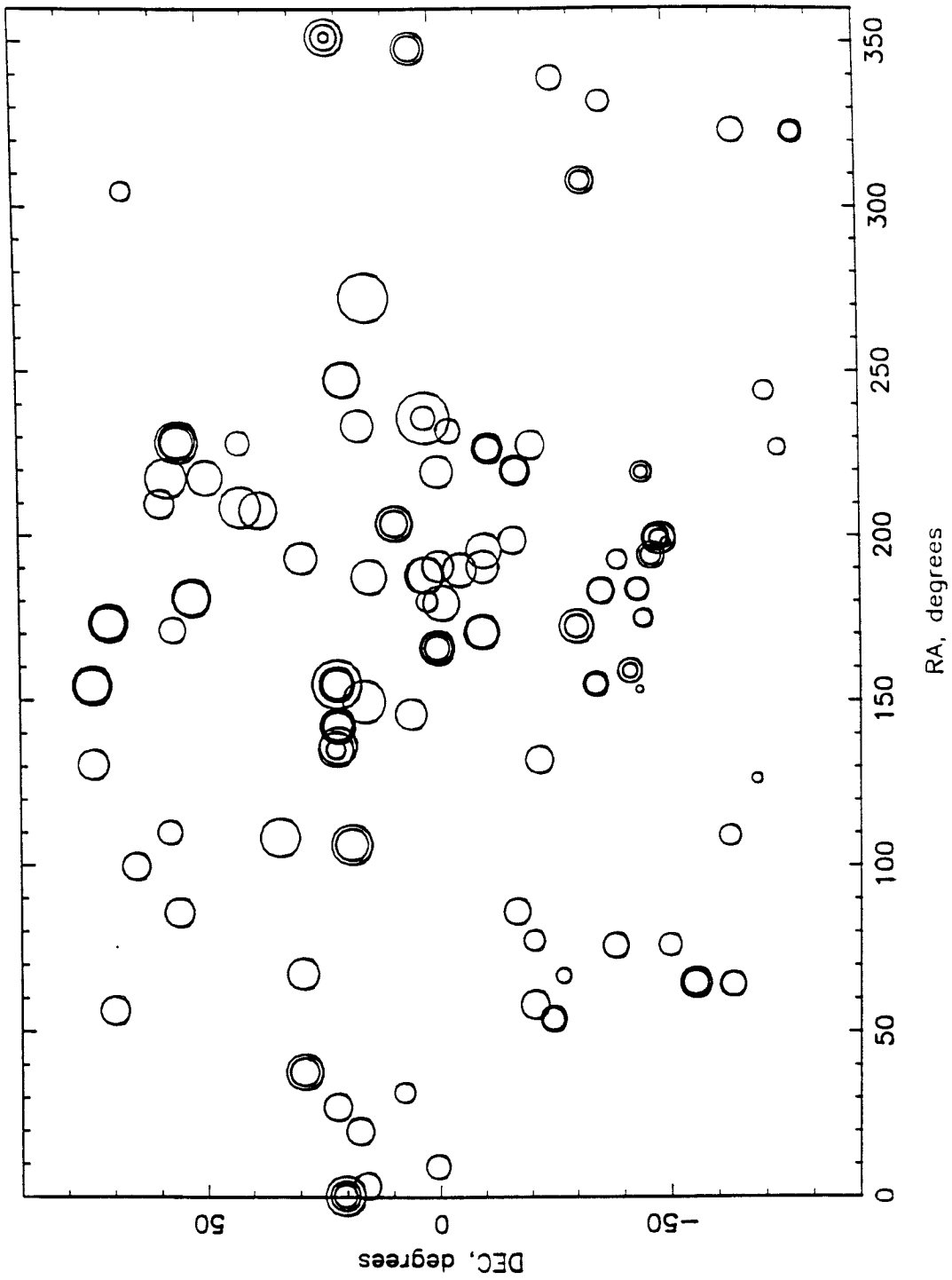

Figure 24a

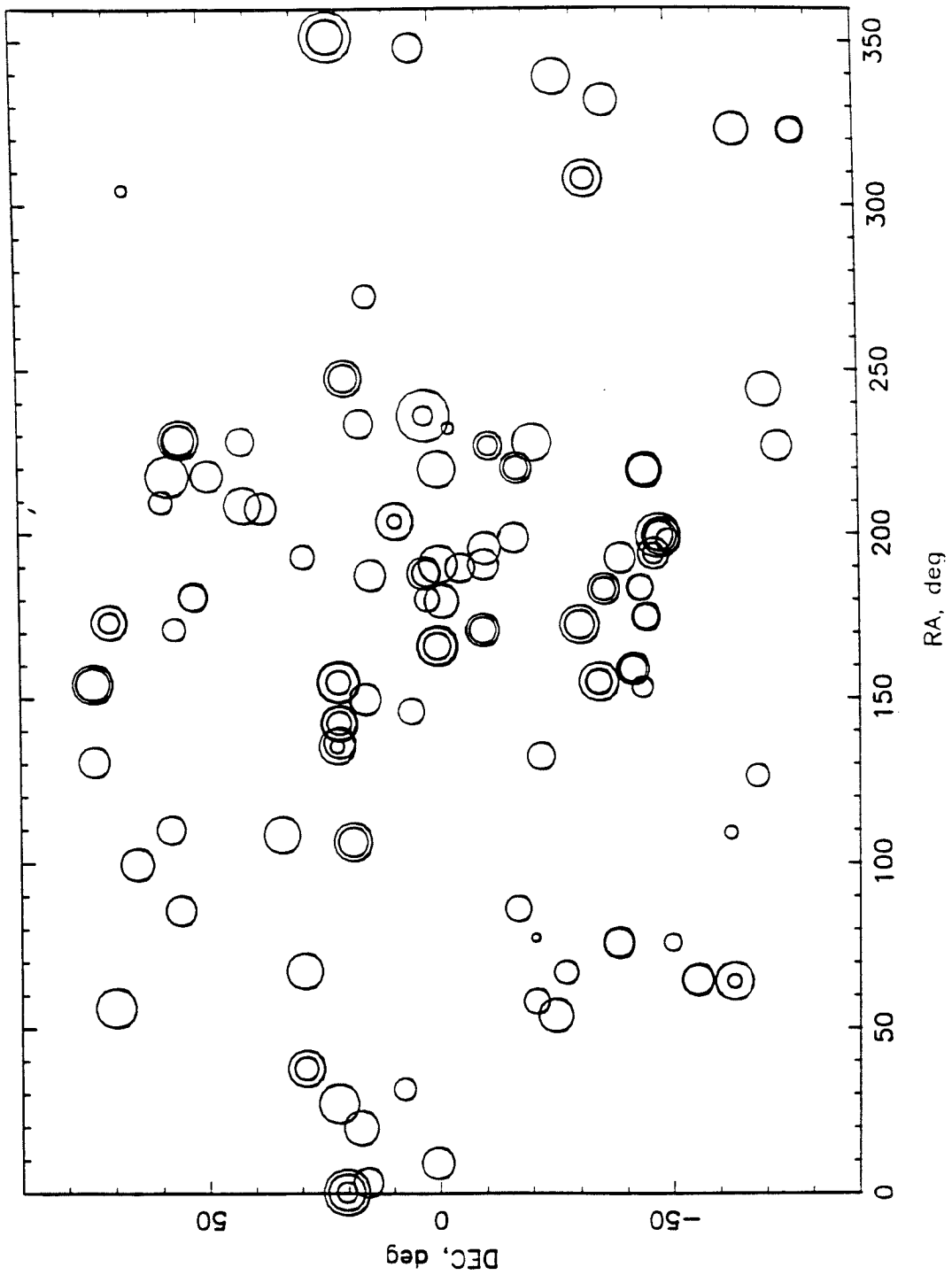

Figure 24b

magnitude residuals dipole response profiles / JAN93

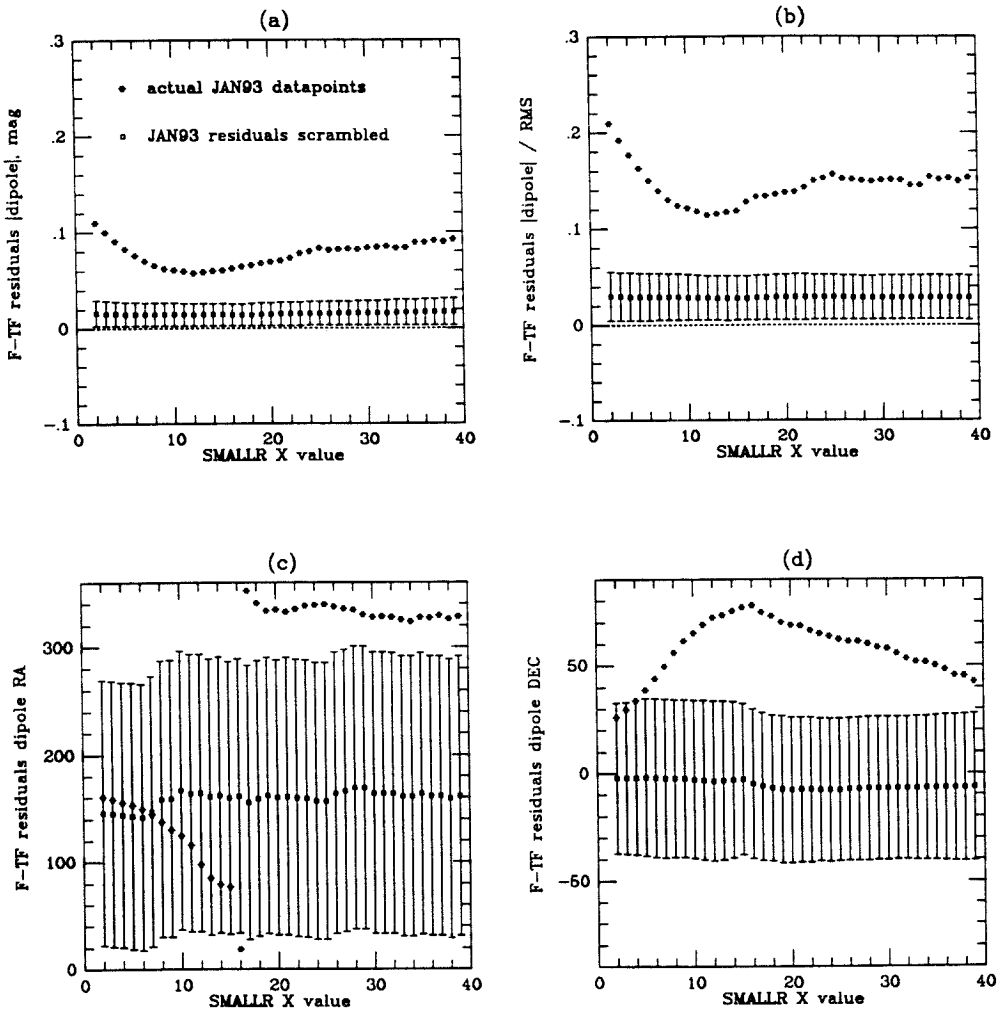

Figure 25

logW residuals dipole response profiles / JAN93

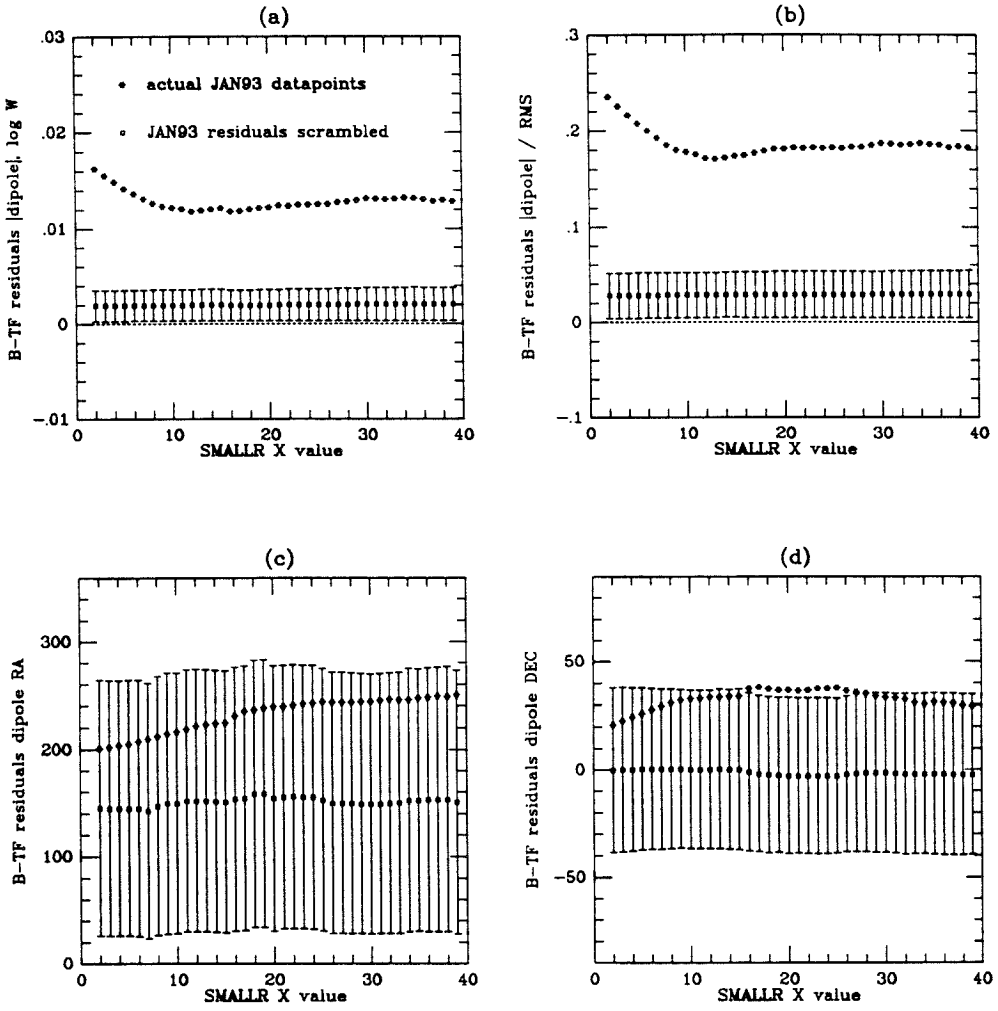

Figure 26

magnitude residuals dipole response profiles
sample = JAN93 / M87 angle > 30 degrees

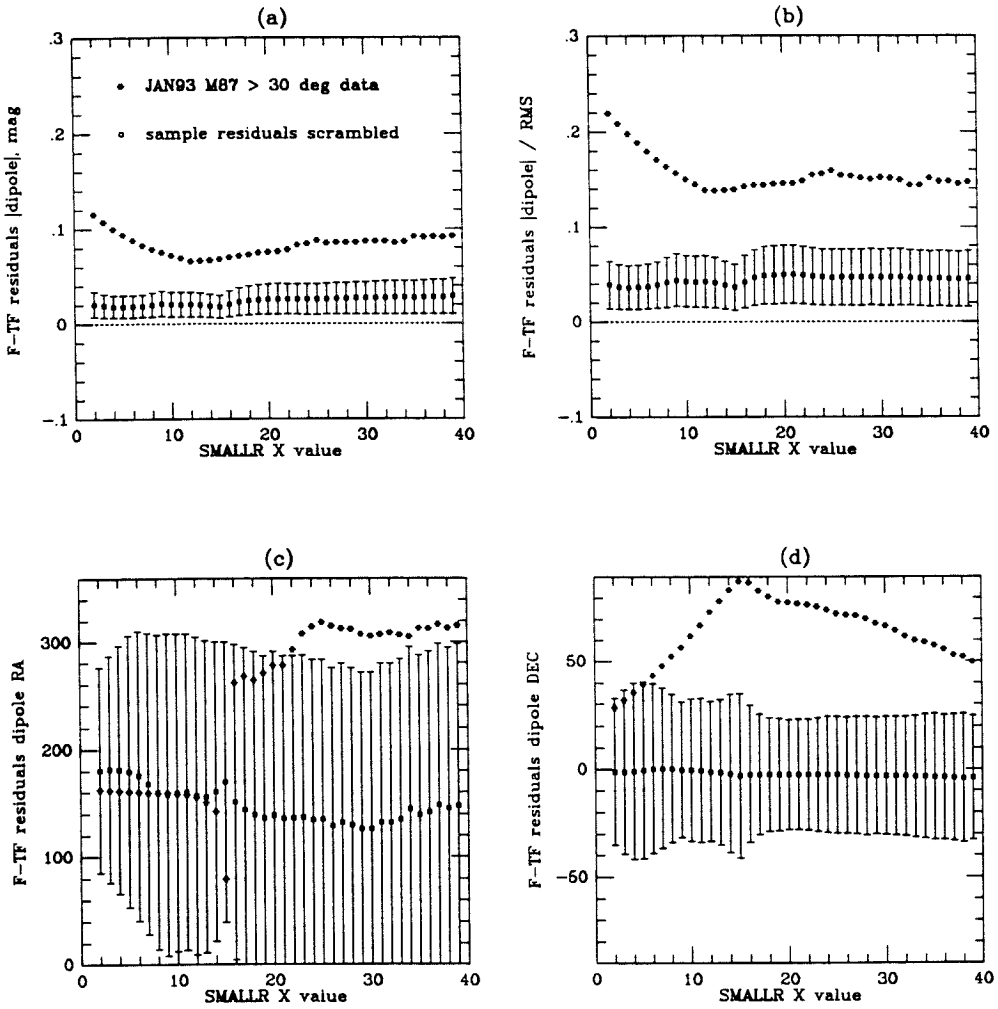

Figure 27

logW residuals dipole response profiles
sample = JAN93 / M87 angle > 30 degrees

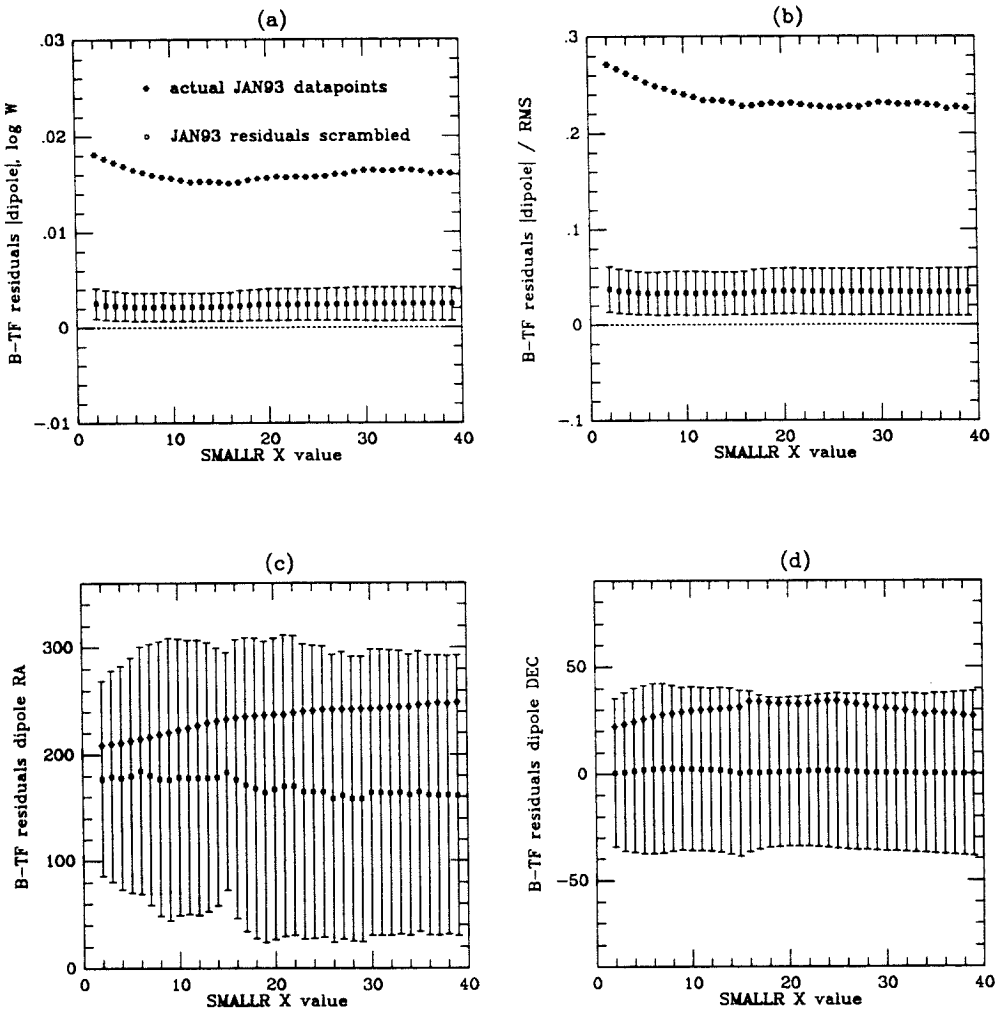

Figure 28

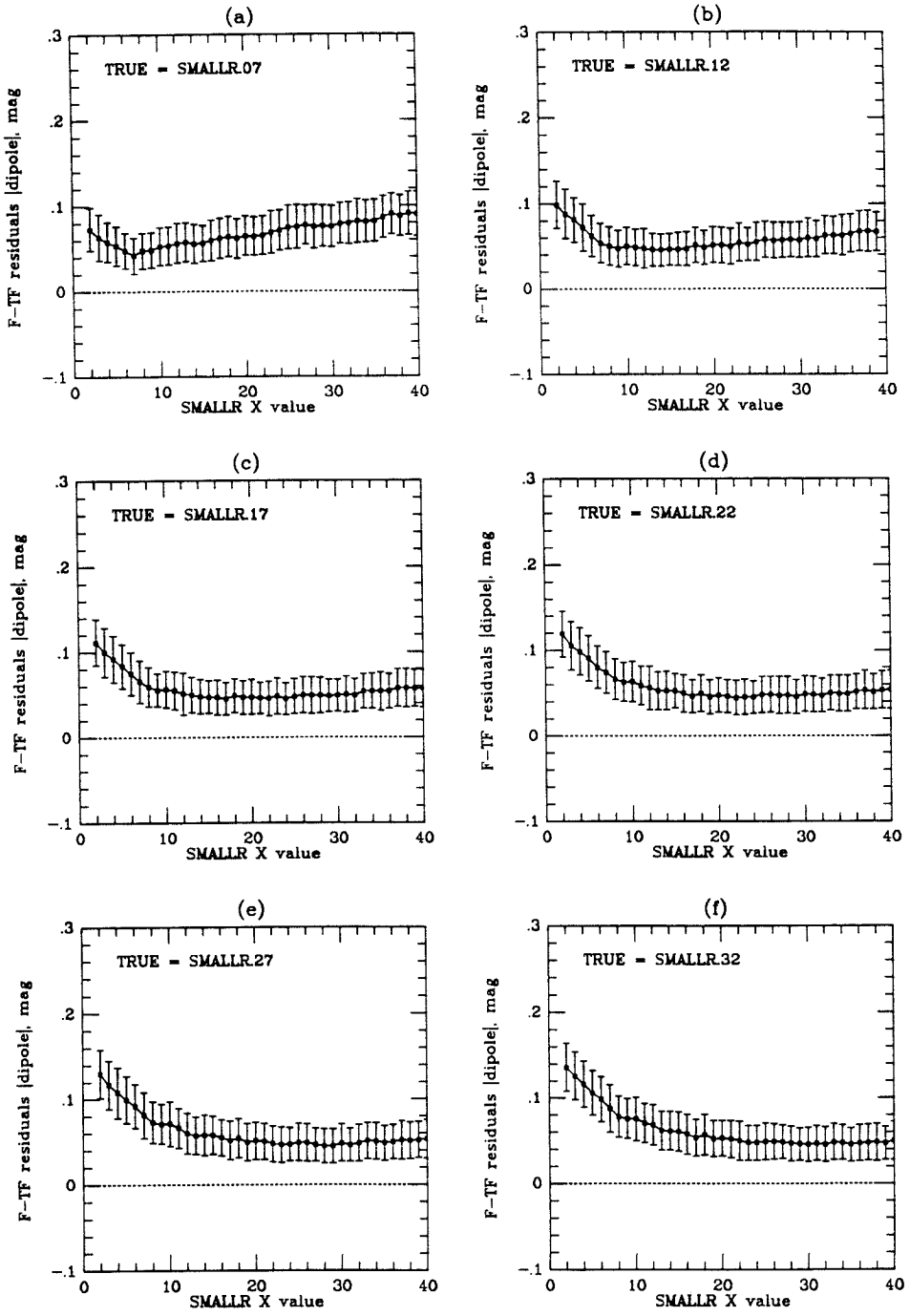
magnitude residuals dipole response profiles
Monte Carlo simulations / sample = JAN93
SMALLR X = [7, 12, 17, 22, 27, 32]
(a)
TRUE = SMALLR.07
(b)
TRUE = SMALLR.12
(c)
TRUE = SMALLR.17
(d)
TRUE = SMALLR.22
(e)
TRUE = SMALLR.27
(f)
TRUE = SMALLR.32
F-TF residuals |dipole|, mag
SMALLR X value

Figure 29

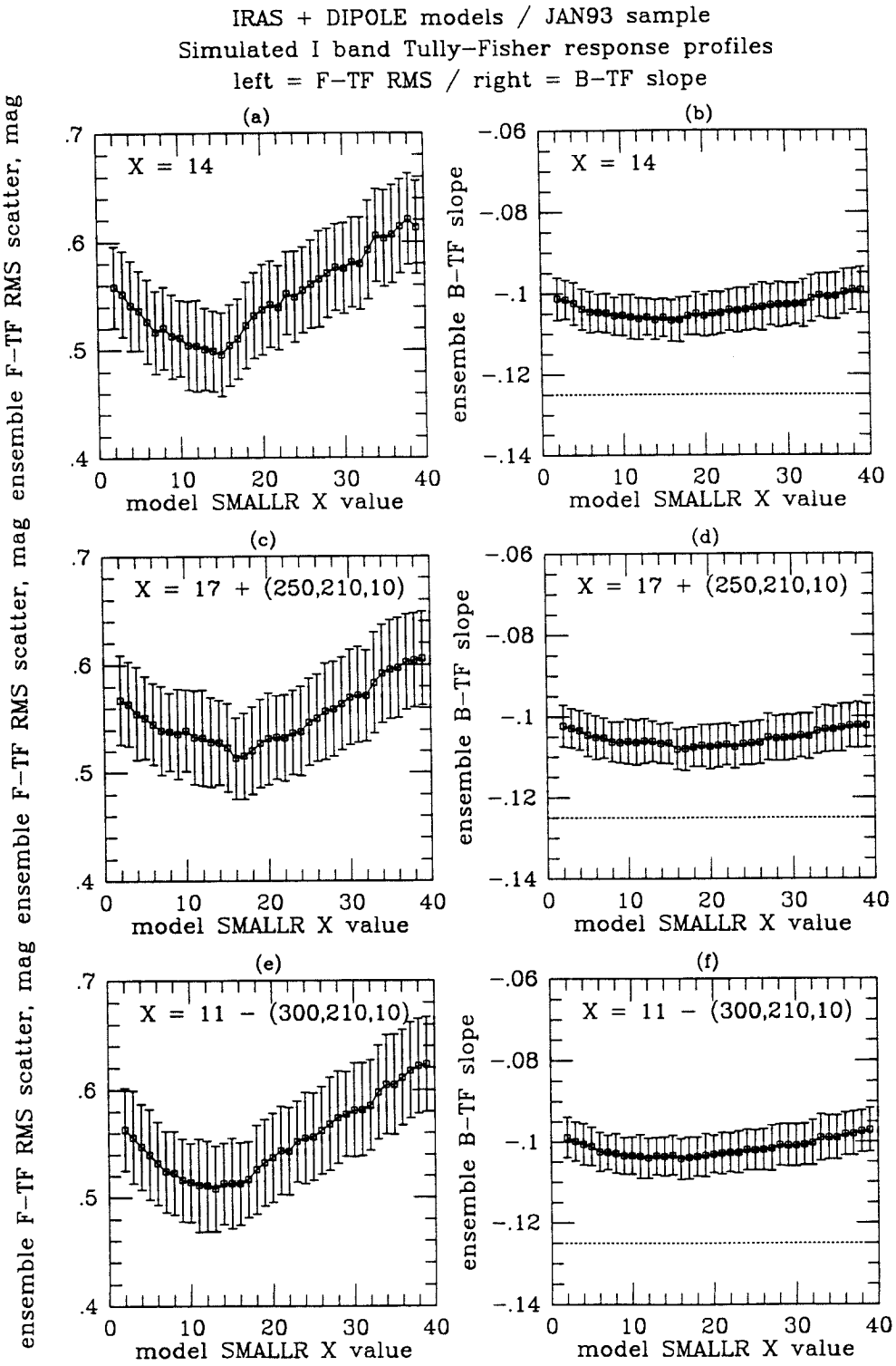
IRAS + DIPOLE models / JAN93 sample
Simulated I band Tully-Fisher response profiles
left = F-TF RMS / right = B-TF slope
(a)
X = 14
(b)
X = 14
(c)
X = 17 + (250,210,10)
(d)
X = 17 + (250,210,10)
(e)
X = 11 - (300,210,10)
(f)
X = 11 - (300,210,10)
ensemble F-TF RMS scatter, mag
ensemble B-TF slope
model SMALLR X value

Figure 30

References

Aaronson, M. *et al.* 1982. *Astrophys. J.* **258:**64.

Aaronson, M. *et al.* 1986. *Astrophys. J.* **302:**536.

Bertschinger, E. and Dekel, A. 1989. *Astrophys. J.* **336:**L5.

Bicay, M. D. and Giovanelli, R. 1986. *Astron. J.* **91:**705.

Branch, D. 1992. *Astrophys. J.* **392:**35.

Burstein, D. and Heiles, C. 1982. *Astron. J.* **87:**1165 (BH).

Carroll, S. M., Press, W. H., and Turner, E. L. 1992. *Ann. Rev. Astron. Astrophys.* **30:**499.

Christian, C. A. *et al.* 1985. *Publ. Astr. Soc. Pac.* **97:**363.

Courteau, S. 1992. Ph. D. thesis, University of California, Santa Cruz (CT).

Cousins, A. W. J. 1976. *Mem. Roy. Astr. Soc.* **81:**25.

DaCosta, G. S. 1992. In *Astronomical CCD observing and reduction techniques.* Howell, S. B., ed. San Francisco: Astronomical Society of the Pacific.

Davies, R. D. , Staveley-Smith, L. and Murray. J. D. 1989. *Mon. Not. Roy. Astr. Soc.* **236:**171 (DSSM).

Davis, M. *et al.* 1982. *Astrophys. J.* **253:**423.

Davis, M., Strauss, M. A., and Yahil, A. 1991. *Astrophys. J.* **372:**394.

Dekel, A. *et al.* 1993. Preprint; submitted to *Astrophys. J.*

de Vaucauleurs, G., de Vaucauleurs, A. and Corwin, H. 1976. *Second reference catalog of bright galaxies.* University of Texas Press (RC2).

Djorgovski, S., de Carvalho, R., and Han, M. S. 1989. In *The extragalactic distance scale.* van den Bergh, S. and Pritchet, C. J., eds. San Francisco: Astronomical Society of the Pacific.

Djorgovski, S. and Davis, M. 1987. *Astrophys. J.* **313:**59.

Dressler, A. *et al.* 1987. *Astrophys. J.* **313:**42.

Dressler, A. and Faber, S. M. 1990. *Astrophys. J.* **354:**13.

Faber, S. M. and Burstein, D. 1988. In *Large-scale motion in the universe.* Rubin, V. C. and Coyne, G. V., eds. Princeton University Press.

Faber, S. M. and Jackson, R. E. 1976. *Astrophys. J.* **204:**668.

Felten, J. E., and Isaacman, R. 1986. *Rev. Mod. Phys.* **58(3):**689.

Fisher, J. R. and Tully, R. B. 1981. *Astrophys. J. Supp.* **47:**139.

Fisher, K. 1992. Ph. D. thesis, University of California, Berkeley (FT).

Gilliland, R. L. 1992. In *Astronomical CCD observing and reduction techniques.* Howell, S. B., ed. San Francisco: Astronomical Society of the Pacific.

Gould, A. 1993. Preprint.

Graham, J. A. 1982. *Publ. Astr. Soc. Pac.* **94:**244.

Gramann, M. 1992. Preprint; to appear in the *Astrophys. J.* (Letters).

Gunn, J. E. 1978. In Gunn, J. E., Longair, M. S., and Rees, M. J. *Observational cosmology.* Sauverny: Geneva Observatory.

Han, M. S. and Mould, J. R. 1990. *Astrophys. J.* **360:**448.

Han, M. S. 1991. Ph. D. thesis, California Institute of Technology (HT).

Han, M. S. 1992. *Astrophys. J.* **391:**617.

Harrison, E. 1981. *Cosmology: the science of the universe.* Cambridge University Press.

Howell, S. B., ed. 1992. *Astronomical CCD observing and reduction techniques.* San Francisco: Astronomical Society of the Pacific.

Hubble, E. 1929. *Proc. Nat. Acad. Sci.* **15:**168.

Huchtmeier, W. and Richter, O.-G. 1989. *HI observations of galaxies.* New York: Springer (HRCAT).

James, P. A., Joseph, R. D., and Collins, C. A. 1991. *Mon. Not. Roy. Astr. Soc.* **248:**444.

Janesick, J. and Elliott, T. 1992. In *Astronomical CCD observing and reduction techniques.* Howell, S. B., ed. San Francisco: Astronomical Society of the Pacific.

Kaiser, N. 1984. *Astrophys. J.* **284:**L49.

Kolb, E. W. and Turner, M. S. 1990. *The early universe.* Menlo Park: Addison-Wesley.

Kraus, J. D. 1986. *Radio astronomy, 2nd ed.* Powell (OH): Cygnus-Quasar Books.

Landolt, A. 1973. *Astron. J.* **78:**989.

Landolt, A. 1983. *Astron. J.* **88:**439.

Landolt, A. 1992. *Astron. J.* **104:**340.

Landy, S. D. and Szalay, A. S. 1992. *Astrophys. J.* **391:**494.

Lawden, D. F. 1982. *An introduction to tensor calculus, relativity and cosmology (3rd ed.).* New York: Wiley.

Lewis, B. M. 1983. *Astron. J.* **88:**962.

Loh, E. D. and Spillar, E. J. 1986. *Astrophys. J.* **307:**L1.

Loredo, T. 1989. In *Maximum entropy and Bayesian methods.* Fougere, P., ed. Dordrecht: Kluwer Academic.

Lubin, P. M., Villela, M. P., Epstein, G. L., and Smoot, G. F. 1985. *Astrophys. J.* **298:**L1.

Lutz, T. E. and Kelker, D. H. 1973. *Publ. Astr. Soc. Pac.* **85:**573.

Lynden-Bell, D. *et al.* 1988. *Astrophys. J.* **326:**19.

Mackay, D. J. C. 1992. Ph. D. thesis, California Institute of Technology (MT).

Madore, B. F. and Tully, R. B., eds. 1986. *Galaxy distances and deviations from universal expansion.* Dordrecht: Reidel.

Mathewson, D. S., Ford, V. L., and Buchhorn, M. 1992. *Astrophys. J.* **389:**L5.

Meyer, S. L. 1986. *Data analysis for scientists and engineers.* Evanston (IL): Peer Management Consultants Ltd.

Mould, J. R. *et al.* 1991. *Astrophys. J.* **383:**467.

Peebles, P. J. E. 1980. *The large-scale structure of the universe.* Princeton University Press.

Picard, A. 1991. *Astron. J.* **102:**445.

Pierce, M. J. and Tully, R. B. 1988. *Astrophys. J.* **330:**579.

Press, W. H. *et al.* 1986. *Numerical recipes.* Cambridge University Press.

Roth, J. 1991. Preprint; rejected by *Nature.*

Rubin, V. C. *et al.* 1976. *Astron. J.* **81:**687;719.

Rubin, V. C. and Coyne, G. V., eds. 1988. *Large-scale motion in the universe.* Princeton University Press.

Sandage, A. 1963. *Astrophys. J.* **138:**863.

Schechter, P. L. 1980. *Astron. J.* **85:**801.

Schild, R. E. 1983. *Publ. Astr. Soc. Pac.* **95:**1021.

Silk, J. 1989. *Astrophys. J.* **345:**L1.

Smith, S. 1936. *Astrophys. J.* **83:**23.

Smoot, G. F. *et al.* 1992. *Astrophys. J.* **396:**L1.

Staveley-Smith, L. 1985. Ph. D. thesis, Manchester University (SST).

Staveley-Smith, L. and Davies, R. D. 1987. *Mon. Not. Roy. Astr. Soc.* **224:**953 (SSDI).

Staveley-Smith, L. and Davies, R. D. 1988. *Mon. Not. Roy. Astr. Soc.* **231:**833 (SSDII).

Staveley-Smith, L. and Davies, R. D. 1989. *Mon. Not. Roy. Astr. Soc.* **241:**787.

Strauss, M. A. 1989. Ph. D. thesis, University of California, Berkeley (ST).

Strauss, M. A. *et al.* 1992. *Astrophys. J. Supp.* **83:**29.

Tonry, J. 1991. *Astrophys. J.* **373:**L1.

Tonry, J. and Schneider, D. P. 1988. *Astron. J.* **96:**807.

Tully, R. B. and Fisher, J. R. 1977. *Astron. Astrophys.* **54:**661.

Tully, R. B. and Fouque, P. 1985. *Astrophys. J. Supp.* **58:**67.

Tully, R. B. 1988. *Nature.* **334:**209.

Valls-Gabaud, D., Alimi, J.-M., and Blanchard, A. 1989. *Nature.* **341:**215.

Villumsen, J. V. and Davis, M. 1986. *Astrophys. J.* **308:**499.

Weinberg, S. 1972. *Gravitation and cosmology.* New York: Wiley.

Whitford, A. E. 1958. *Astron. J.* **63:**201.

Willick, J. A. 1990. *Astrophys. J.* **351:**L5.

Willick, J. A. 1992. Ph. D. thesis, University of California, Berkeley (WT).

Willick, J. A. 1993. Preprint.

Yahil, A. *et al.* 1991. *Astrophys. J.* **372:**380.

Zwicky, F. 1933. *Helv. Phys. Acta* **6:**110.